LOCKHEED MARTIN ENERGY RESEARCH LIBRARIES

3 4456 0515189 4

ORNL-5108

Cy 1

GAS-COOLED REACTOR PROGRAMS

HIGH-TEMPERATURE GAS-COOLED REACTOR BASE-TECHNOLOGY PROGRAM PROGRESS REPORT

January 1, 1974 - June 30, 1975

J. H. Coobs - P. R. Kasten

OAK RIDGE NATIONAL LABORATORY
CENTRAL RESEARCH LIBRARY
DOCUMENT COLLECTION
LIBRARY LOAN COPY
DO NOT TRANSFER TO ANOTHER PERSON
If you wish someone else to see this document, send in name with document and the library will arrange a loan.

OAK RIDGE NATIONAL LABORATORY
OPERATED BY UNION CARBIDE CORPORATION FOR THE ENERGY RESEARCH AND DEVELOPMENT ADMINISTRATION

Printed in the United States of America. Available from
National Technical Information Service
U.S. Department of Commerce
5285 Port Royal Road, Springfield, Virginia 22161
Price: Printed Copy $12.75; Microfiche $2.25

This report was prepared as an account of work sponsored by the United States Government. Neither the United States nor the Energy Research and Development Administration/United States Nuclear Regulatory Commission, nor any of their employees, nor any of their contractors, subcontractors, or their employees, makes any warranty, express or implied, or assumes any legal liability or responsibility for the accuracy, completeness or usefulness of any information, apparatus, product or process disclosed, or represents that its use would not infringe privately owned rights.

ORNL-5108
Distribution
Category UC-77

Contract No. W-7405-eng

GAS-COOLED REACTOR PROGRAMS

HIGH-TEMPERATURE GAS-COOLED REACTOR BASE-TECHNOLOGY PROGRAM PROGRESS REPORT FOR JANUARY 1, 1974, THROUGH JUNE 30, 1975

J. H. Coobs, Program Manager
P. R. Kasten, Program Director

Date Published: November 1976

LOCKHEED MARTIN ENERGY RESEARCH LIBRARIES
3 4456 0515189 4

OAK RIDGE NATIONAL LABORATORY
Oak Ridge, Tennessee 37830
operated by
UNION CARBIDE CORPORATION
for the
ENERGY RESEARCH AND DEVELOPMENT ADMINISTRATION

ACKNOWLEDGMENT

This report was edited by Sigfred Peterson of the Metals and Ceramics Division. Typing and composition were by the Metals and Ceramics Reports Office under the supervision of Meredith R. Hill.

CONTENTS

FOREWORD xi

SUMMARY xiii

1. PRESTRESSED CONCRETE PRESSURE VESSEL DEVELOPMENT 1

1.1 INTRODUCTION 1

1.2 PCRV THERMAL CYLINDER EXPERIMENT 2

1.2.1 Correlation of Analytical Results with Model Test Data 5

1.2.2 Investigations of Tendon Corrosion Problems 11

1.3 DEVELOPMENT OF ANALYTICAL METHODS FOR PCRVs 13

1.3.1 Computer Capability Development 13

1.3.1.1 Two-Dimensional Plane-Axisymmetric Codes . 13

1.3.1.2 Three-Dimensional Codes 17

1.3.1.3 Support Programs 19

1.3.2 Review of Methods for Analysis of PCRVs 19

1.4 HEAD FAILURE STUDIES 20

1.4.1 Prestressing System 21

1.4.2 Sealing and Instrumentation 21

1.4.3 Test Results 24

1.4.4 Analytical Studies 24

1.5 CONCRETE STRUCTURAL MODEL TESTS 28

1.5.1 Background 28

1.5.2 Initial Structural Models Test Series: Grouted vs Nongrouted Prestressing Tendon Behavior 29

1.5.3 Experimental Investigation 29

1.5.3.1 Concrete Laboratory 29

1.5.3.2 Grouted or Nongrouted Tendon Investigation 30

1.6 LINER AND PENETRATION STUDIES 38

1.7 CONCRETE PROPERTIES IN A NUCLEAR ENVIRONMENT 43

1.8 INSTRUMENTATION EVALUATION AND DEVELOPMENT 48

1.8.1 Background 48

1.8.2 Concrete Embedment Instrumentation: Present Status . 50

1.8.3 Instrumentation Evaluation Program 53
1.8.3.1 General Gage Performance Characteristics . 53
1.8.3.2 Gage Performance in Representative PCRV Environment 54
1.8.3.3 Gage Performance in Extreme Environments . 55
1.8.4 Overview of Acoustic Emission for In-Service Structural Integrity Monitoring of PCRVs 56
1.8.4.1 Background 56
1.8.4.2 Applications to PCRVs 58
1.9 LONG-TERM CREEP AND MOISTURE MIGRATION STUDIES 59
1.10 REFERENCES 63
2. STRUCTURAL MATERIALS 67
2.1 INTRODUCTION 67
2.2 MECHANICAL PROPERTIES 67
2.2.1 Tensile Testing 67
2.2.2 Creep Testing in HTGR Primary Coolant Environment . 73
2.2.2.1 Background 73
2.2.2.2 Environmental Test Facilities 74
2.2.2.3 Environmental Creep Tests 77
2.2.3 Subcritical Crack Growth Studies 81
2.2.3.1 Material 81
2.2.3.2 Equipment and Procedures 83
2.2.3.3 Results and Discussion 88
2.2.4 Low-Cycle Fatigue Life Testing 95
2.2.4.1 Fatigue Behavior of 2 1/4 Cr-1 Mo Steel . . 95
2.2.4.2 Fatigue Behavior of Hastelloy X 126
2.3 CORROSION OF STEAM GENERATOR MATERIALS 128
2.3.1 Injection Loops 128
2.3.1.1 Tests in the 9 Cr-1 Mo Steel Loop 129
2.3.1.2 The Inconel 625 Loop 133
2.3.2 The Influence of Heat Flux on the Corrosion of 2 1/4 Cr-1 Mo Steel 135
2.3.3 The Inconel 617 Test Loop 138
2.4 REFERENCES 139

3. FISSION PRODUCT TECHNOLOGY STUDIES 143
3.1 INTRODUCTION 143
3.2 FISSION PRODUCT RELEASE FROM COATED PARTICLE FUELS 143
3.2.1 Mathematical Description of Fission Product Transport in Coated Fuel Particles During Postirradiation Anneal Experiments 144
3.2.2 Release of Fission Products During Postirradiation Anneals 144
3.2.3 Fission Product Release During Irradiation 152
3.2.4 Review of Coated Fuel Particle Stability 153
3.3 TRANSPORT OF STRONGLY ADSORBED SPECIES IN POROUS MEDIA . . 154
3.3.1 Applicable Transport Theories 155
3.3.1.1 Vapor or Gas-Phase Transport 155
3.3.1.2 Adsorbed Phase Transport 156
3.3.1.3 Coupled Vapor-Adsorbed Phase Transport . . 157
3.3.2 Laboratory Experiments 159
3.3.3 Review of Peach Bottom HTGR Fuel Element Postirradiation Examination Data 166
3.4 RADIONUCLIDE DISTRIBUTIONS IN AN HTGR 181
3.4.1 Analysis of Tritium Distribution and Release 181
3.4.2 Iodine Behavior in an HTGR 182
3.5 FISSION PRODUCT SURVEILLANCE IN THE PEACH BOTTOM HTGR . . . 184
3.5.1 Fuel Element Examinations 185
3.5.1.1 Postirradiation Examination Procedures . . 187
3.5.1.2 Results for Driver Fuel Element E06-01 . . 188
3.5.2 Primary Circuit Gamma Activity Scans 197
3.5.3 Coolant Sampler Results 200
3.6 REFERENCES 203
4. HTGR KERNEL MIGRATION AND IRRADIATED FUEL CHEMISTRY 205
4.1 INTRODUCTION 205
4.2 KERNEL MIGRATION STUDIES 205
4.2.1 Theory and Initial Analyses of Oxide Kernel Migration in HTGR Particles 205
4.2.2 Current KMC Data for Oxides and Carbides 208
4.2.3 WAR UC_2 Kernel Vaporization 210

4.3 GAS PRESSURE MEASUREMENTS 214
4.4 THE CHEMICAL BEHAVIOR OF HTGR FUELS 219
4.5 REFERENCES 222
5. COOLANT CHEMISTRY: THE STEAM-GRAPHITE REACTION 225
5.1 INTRODUCTION 225
5.2 ANALYSIS OF COOLANT IMPURITY COMPOSITION DATA OBTAINED DURING FORT ST. VRAIN HTGR STARTUP 225
5.3 COMPUTER SIMULATION OF LABORATORY-SCALE STEAM-GRAPHITE REACTION EXPERIMENTS 227
5.4 REFERENCES 228
6. HTGR FUEL QUALIFICATION 229
6.1 INTRODUCTION 229
6.2 FUEL PARTICLE PROCESS DEVELOPMENT AND QUALIFICATION 230
6.2.1 Resin Kernel Studies 230
6.2.2 Particle Coating Process Development 236
6.2.2.1 Pyrolytic Carbon Deposition 236
6.2.2.2 SiC Deposition Process Development 242
6.2.2.3 Evaluation of Compounds Other than MTS . . 247
6.3 FUEL ROD FABRICATION DEVELOPMENT AND QUALIFICATION 247
6.4 CHARACTERIZATION OF PYROCARBON COATINGS 249
6.4.1 OPTAF Technique 250
6.4.2 X-Ray Diffraction Techniques 255
6.4.3 Etching Techniques 257
6.4.4 Transmission Electron Microscopy (TEM) 263
6.4.5 Chemical Characterization of PyC 266
6.5 IRRADIATION TESTS IN HFIR TARGET FACILITY 267
6.5.1 Capsules HT-12 Through -15 267
6.5.1.1 Thermal Analysis 268
6.5.2 Irradiation Test Capsules HT-17, -18, and -19 . . . 269
6.5.3 Irradiation Tests HT-20 Through 23 276
6.5.4 Irradiation Experiments HT-24 and -25 283
6.5.5 Test Capsules HT-26 and -27 285
6.5.6 Irradiation Test Capsules HT-28, -29, and -30 . . . 286
6.5.6.1 Capsule Design 287

6.5.6.2 Experimental Objectives 288
6.5.6.3 Capsule Loading, Operation, Fluence, and Burnup 292
6.6 IRRADIATION TESTS IN HFIR REMOVABLE BERYLLIUM FACILITIES . 296
6.6.1 Capsules HRB-4 and -5 296
6.6.2 Capsule HRB-6 296
6.6.3 Capsules HRB-7 and -8 303
6.6.3.1 Capsule Design 305
6.6.3.2 Preparation of Test Specimens 305
6.6.3.3 Capsule Operation 311
6.6.3.4 Thermal Analysis 319
6.6.3.5 Postirradiation Examination 319
6.6.4 Capsules HRB-9 and -10 336
6.6.4.1 Capsule Design 336
6.6.4.2 Preparation of Test Specimens 337
6.6.4.3 Capsule Operation 346
6.6.4.4 Postirradiation Examination 352
6.7 IRRADIATION TESTS IN THE ORR 360
6.7.1 OF-1 Capsule 360
6.7.1.1 Capsule Operation 361
6.7.1.2 Postirradiation Examination 365
6.7.1.3 Thermal Analysis 374
6.7.2 Capsule OF-2 377
6.7.2.1 Description of the OF-2 Capsule and Fuel Specimen Holders 378
6.7.2.2 Design Thermal Analysis 381
6.7.2.3 Description of OF-2 Fuel Specimens 385
6.7.2.4 Fuel Rods 387
6.7.2.5 Capsule Irradiation 392
6.8 IRRADIATION TESTS IN PROTOTYPE REACTORS 395
6.9 NUCLEAR ANALYSIS IN SUPPORT OF IRRADIATIONS 396
6.9.1 Characteristics of the HFIR Facilities 397
6.9.2 Characteristics of the ORR Facilities 402
6.9.3 Development of the CACA Code 406

6.9.4 Summary of Graphite Damage Terminology 406
6.9.5 Development of a Gamma and Fission Calorimeter (GAFI) 407
6.9.6 Development of Dosimetry Materials 408
6.10 CAPSULE THERMOMETRY 411
6.10.1 Johnson Noise Thermometer Development 414
6.10.2 Low-Cross-Section Thermocouple Development 416
6.10.3 Thermometry in HRB Capsules 418
6.10.4 Thermometry in ORR Capsules 426
6.10.5 Correction of Tungsten-Rhenium Thermocouple Data . 428
6.10.5.1 Analytic Method 428
6.10.5.2 Empirical Method 430
6.11 PERFORMANCE ASSESSMENT OF COATED PARTICLE FUELS 436
6.11.1 Thermal Analysis 436
6.11.1.1 HT Capsules 436
6.11.1.2 HRB Capsules 437
6.11.1.3 ORR Capsules 439
6.11.1.4 Recycle Test Elements 439
6.11.1.5 Dragon Reactor Experiment 440
6.11.2 Mechanical Analysis of HT-12, -13, -14, and -15 Experiments 440
6.11.3 Coated Particle Failure Analysis 441
6.11.3.1 Failure Mechanisms 441
6.11.3.2 Irradiated Microsphere Gamma Analyzer System 446
6.11.3.3 Statistical Basis for Failure-Fraction Determinations 450
6.11.4 Performance Comparison of Candidate Fissile Fuels . 457
6.11.5 Effect of Fissile Kernel Diameter on Operating Temperatures of Large HTGRs 460
6.11.6 Dynamic Testing of HRB Capsules 462
6.11.7 Reaction of Fission Products with SiC 465
6.12 REFERENCES 467
7. CHARACTERIZATION AND STANDARDIZATION OF GRAPHITE 475
7.1 INTRODUCTION 475

7.2 PROGRAM OBJECTIVES AND DESIGN CRITERIA 475
7.3 DESIGN OF ORR FACILITY AND 900°C CREEP CAPSULE 478
7.4 REFERENCE 484

FOREWORD

The Gas-Cooled Reactor Programs being carried out at the Oak Ridge National Laboratory contribute to the development and evaluation of high-temperature gas-cooled reactors (HTGRs) and of gas-cooled fast reactors (GCFRs). These programs are sponsored by the U.S. Energy Research and Development Administration (ERDA) and include the Thorium Utilization Program (HTGR Fuel Recycle Development Program), the HTGR Base Program, the HTGR Safety Program, and the GCFR Program. This report covers work performed on the HTGR Base Program.

Major incentivies for developing HTGRs are the prospects for economically attractive power production, improved fuel utilization, the potential for obtaining low environmental impact at a diversity of plant sites, the potential for high-temperature direct cycle and process heat applications, and the pertinence of the component technology to GCFRs. The good neutron economy and fuel performance permit high burnup and associated low fuel-cycle costs. The high-temperature capability of the graphite core structure enables reactor plant operation at high thermodynamic efficiency, and thus requirements for heat dissipation to the environment are relatively low. Excellent fission product retention by the coated fuel particles leads to coolant circuits with low radioactivity levels. Further, the high exposures attainable with HTGR fuels permit the development of economic fuel recycling.

The organization of this report is based on an orderly presentation of the development work being performed under the Base Technology Program. The program includes testing and evaluation of prestressed concrete reactor vessels (PCRVs) and primary circuit structural materials under possible reactor conditions, fission product behavior studies, fuel and coolant chemistry studies, and an emphasis on fabrication, characterization, irradiation testing, and performance evaluations of fuel and fuel elements.

In work on PCRVs, correlation of the operating data with analytical models for concrete behavior and an investigation of tendon corrosion completed the work on the Thermal Cylinder Experiment. Additional testing of materials, instrumentation, and concrete models and analytical work on concrete behavior were carried out, and the programs involving creep and moisture migration in concrete were completed by documentation of final results.

The new program on structural materials studies involving mechanical properties and corrosion of primary circuit materials became very active during this period. A series of creep test rigs operating in HTGR primary coolant environment were commissioned and testing was begun, and studies on subcritical crack growth and low-cycle fatigue failure in materials were carried out. The corrosion testing of steam generator materials involves isothermal, cyclic, and heat flux testing of candidate materials in a loop at a fossil-fired steam plant.

The experimental programs on fission product technology and fuel and coolant chemistry are all presently included in Base Program work. The behavior and release of fission products in fuel particles have been studied for several years, and these studies are closely related to present investigations of fission product behavior in graphite and in the coolant circuit of the Peach Bottom HTGR. Fuel chemistry studies have emphasized the migration of fuel in a temperature gradient and the oxygen potential in fuel during various stages of fuel element life. Finally, coolant chemistry studies have emphasized steam-graphite reaction kinetics and involve a careful analysis of Fort St. Vrain start-up data to obtain new information on reaction rates.

HTGR fuel development work at ORNL is largely concerned with evaluating, understanding, and improving fuel performance and with studying the behavior of certain fission products, including their effects on fuel performance. Coated-particle fuel studies involve irradiation testing, with emphasis on demonstration of satisfactory fuel and materials performance at the required fuel burnup and fast-neutron fluences. An important part of the program involves irradiation testing and evaluation of fuels produced in prototype recycle facilities. In these tests, the High Flux Isotope Reactor (HFIR) has proved highly useful as an irradiation facility; we also utilize an in-core facility at the ORR, which provides relatively large volumes for testing fuel bodies. Preparations are nearly complete for the use of a second in-core facility at ORR for the measurement of irradiation creep of moderator and reflector graphites.

All our development work is coordinated closely with similar development work at General Atomic Company to supplement and verify their test results without unnecessary duplication of effort. Work on gas-cooled reactors is also being performed in Europe, with significant efforts being carried out on the HTGR concept by the Dragon Project in England and at KFA in West Germany. Associated information pertaining to HTGR research and development work is obtained through the ERDA/Dragon HTGR Agreement and the ERDA/KFA Exchange Arrangement. These exchange programs include information on fuel characterization, testing, and performance, fuel reprocessing, fission product behavior, materials behavior, and reactor safety. The exchange of information is facilitated by occasional visits and exchanges of materials for testing as well as the formal exchange of published documents. Interactions between the ORNL and overseas programs are reported where appropriate.

SUMMARY

1. PRESTRESSED CONCRETE PRESSURE VESSEL DEVELOPMENT

Postmortem studies of the ORNL Thermal Cylinder Model have been completed. The thermal cyclinder experiment was designed to provide a means for evaluating present capability to predict time-dependent stress-strain behavior of Prestressed Concrete Reactor Vessels under typical design and off-design operating conditions. The results of studies conducted to determine reasons for observed disagreement between the model test data and calculated results show that the primary factors are the fairly large scatter in comparable concrete embedment gage data and an apparent deficiency in the analytical creep algorithm for the thermal transient condition. Laboratory studies were conducted to identify the mechanism of corrosion of the thermal cylinder model axial tendons. The preferred hypothesis that ammonium carbonate was responsible for the failures was not confirmed; however, high concentrations of nitrates caused cracking of stressed tendon wires in a very short time. The tendon failures have been attributed to stress-corrosion cracking of the wires in the rather unique environment provided by the thermal cylinder model.

The major effort under the analysis methods development task has been to develop basic computer capability and to review the state of the art of PCRV analysis methods. Both two-dimensional (SAFE/CRACK and CREEP/PLAST) and three-dimensional (NØNSAP) finite element codes have been made operational on the ORNL computer, and a diagnostic code has been developed for checking element specification errors.

Under the PCRV head failure studies being conducted at the University of Illinois, two vessel models have been tested, and computer programs for analyzing the heads have been made operational. Design and construction of a prestressing apparatus and development of a liner system were necessary before the models could be post-tensioned and pressurized to failure.

Plans have been finalized for evaluating PCRV concrete embedment instrumentation and structural model studies at ORNL. Representative commercial instrumentation has been procured, and testing under simulated PCRV environment has begun. We will also study the adequacy and structural advantages of grouted over ungrouted tendons in a PCRV.

The ORNL laboratory for casting and testing structural models and related concrete specimens has been completed. A series of instrumented prestressed concrete beams having either grouted or ungrouted tendons will be used to evaluate structural behavior, corrosion resistance, new grouting and concrete materials, and tendon monitoring techniques.

A program has been initiated to determine fracture toughness characteristics of the ferritic components of the steel used for PCRV penetrations and closures. The forging and plate materials are being obtained

by General Atomic Company (GA) from the materials being used in fabricating PCRV metallic components. Initial testing completed thus far indicates that the forging materials exceed the impact and strength requirements for SA-508 class 1 steel.

Literature was reviewed to determine current knowledge of concrete properties in a nuclear environment. There is a serious lack of basic understanding of behavior of mass concrete at elevated temperatures, of irradiation effects, and of the migration of moisture in massive structures such as a PCRV. The traditional types of small plain concrete laboratory specimen tests were judged as being incapable of providing the data required to understand the behavior of a large prestressed concrete structure. A recommendation was made that realistic PCRV structural models be developed and tested to obtain the required data.

A survey of available commercial concrete embedment instrumentation has been completed, representative instruments have been procured, and an evaluation program has been planned. Work has also begun to determine capability of present commercial acoustic emission systems for in-service monitoring of PCRV structural integrity. Based on information obtained thus far, plans have been made to procure an acoustic emission monitoring system for use in the initial structural model study of grouted prestressing tendons.

Reports have been published on the U.S. Army Waterways Experiment Station moisture migration experiment and the University of Texas long-term concrete creep tests. The major portion of this research was completed in 1972; however, funding limitations have deferred preparation and publication of the final reports to the present time.

2. STRUCTURAL MATERIALS

A program was initiated in late 1973 to provide an appropriate data base for the selection of materials for primary circuit and steam generator components of a large commercial HTGR. Studies include high-temperature mechanical properties testing and steam corrosion testing.

Mechanical Properties

Tensile test results of isothermally annealed 2 1/4 Cr-1 Mo steel and 9 Cr-1 Mo steel up to 593°C (1100°F) were similar to and consistent with data from the *Nuclear Systems Materials Handbook*. Hastelloy S was stronger than Hastelloy X in tensile tests up to 816°C (1500°F). At 871°C (1600°F) tensile strengths were identical.

Facilities were developed to creep test materials in simulated HTGR helium. Ten systems were built, and developments relating to specimen design, extensometry, and the environmental system are described. Initial creep test results on 2 1/4 Cr-1 Mo steel, 9 Cr-1 Mo steel, and Hastelloy X in HTGR helium are reported.

Subcritical crack growth data on 2 1/4 Cr-1 Mo steel have been obtained with six closed-loop electrohydraulic machines that operate in either air, helium, or steam. These data show that (1) increasing temperature increases crack growth rate except in the strain aging range 315–430°C (600–800°F), (2) decreasing cycle frequency increases cyclic crack growth rate at high temperatures, (3) increasing the mean stress level increases crack growth rate, and (4) steam and helium may retard crack growth rate compared with air.

The low-cycle fatigue behavior of 2 1/4 Cr-1 Mo steel in air is reported. Major test parameters included strain- or load-range, temperature, cycle form and frequency, and hold times. Strain aging caused a peak in fatigue life at 800°C. Decreasing the strain rate decreased fatigue life. A compressive or tensile hold period decreased fatigue life.

Corrosion of Steam Generator Materials

A variety of materials including 2 1/4 Cr-1 Mo steel, 9 Cr-1 Mo steel, type 304 stainless steel, type 410 stainless steel, Incoloy 800, Inconel 600, Inconel 625, Hastelloy N, and Ebrite 26-1 were exposed to oxygenated, chloride-containing wet-dry steam environments. When exposed to stresses within the elastic range no failures due to pitting or stress-corrosion cracking occurred after times up to 6475 hr at 385°C (725°F). At high strains (~7%) as-welded Incoloy 800, Hastelloy N, and Ebrite 26-1 were extremely susceptible to cracking.

After 6000 hr at specimen temperatures of 510 to 540°C (950–1005°F) heat flux (126 kW/m^2) increased the corrosion rate of 2 1/4 Cr-1 Mo steel about 1.5 times that observed in isothermal steam corrosion tests at 538°C (1000°F).

3. FISSION PRODUCT TECHNOLOGY STUDIES

The extent to which relationships between fuel particle stability and temperature and irradiation histories had been established was reviewed. Experimental data are sparse. Moreover, companion studies of techniques for identifying coating failures suggest that some of the stability data are suspect because the optical methods used are unreliable.

The mathematical framework for use in studies of fission product release from intact fuel particles had been developed, and the experimental studies were reoriented somewhat to test theoretical predictions and assumptions, and to provide more detailed information on initial and boundary conditions. Partly for these reasons, a micro grinding technique was developed to obtain concentration profiles within the pyrolytic carbon coatings.

Studies of cesium transport through graphite septa indicate that, in general, more than one diffusion mechanism operates. Good correlation of laboratory and fuel element postirradiation examination data has been obtained under the assumption that simple Fickian diffusion of the cesium through the graphite is perturbed by a mechanism that can be described mathematically as a first-order irreversible reaction.

Analyses of tritium and iodine distributions in an HTGR have been completed. Most of the tritium that is available for release is due to the $^{3}He(n,p)T$ reaction. Plateout on coolant circuit surfaces can significantly affect iodine release.

Gamma-activity scans at selected stations along the Loop 1 coolant circuit of the Peach Bottom HTGR were made during this period to augment similar data taken earlier; samples of coolant helium were likewise taken at locations upstream and downstream of the steam generator. Both sets of data affirm previous observations that cesium behavior during the early part of Core 2 operation was due to releases experienced during Core 1 operation, but that cesium breakthrough from Core 2 fuel had unmistakenly occurred.

Postirradiation examination of Peach Bottom HTGR driver fuel element E06-01 has been completed. As anticipated, ^{134}Cs and ^{137}Cs displayed greatest mobility; moreover, analysis of the cesium concentration profiles in the sleeve of this fuel element indicates that transport through the sleeve was indeed due to cesium directly, rather than to the corresponding xenon precursors.

4. HTGR KERNEL MIGRATION AND IRRADIATED FUEL CHEMISTRY

The main objective of this 1.5-man-year program is the understanding of the kinetic processes and thermodynamics of the fuel, fission product, coating system to a degree that permits identification and quantitative description of failure mechanisms and improved fuel performance by means of kernel chemistry modification.

Kernel Migration Studies

During this reporting period the kinetic studies have concentrated primarily on determining the experimental kernel migration coefficients (KMC) for a wide variety of current or potential HTGR kernel compositions. In-reactor KMC data have been obtained on about 450 particles in the postirradiation-examination program for $Th_{0.84}U_{0.16}C_2$, UO_2, ThO_2, and $Th_{1-z}U_zO_2$ (including both ^{233}U and ^{235}U). Qualitative migration observations have been made in-reactor on $UC_{0.4}N_{0.6}$ and $UO_{1.50}N_{0.38}$. The significant new in-reactor information obtained in these studies concerned the latter two compositions; both the oxynitride and the carbonitride exhibited unacceptable fuel-coating interactions and are not considered to be viable HTGR fuel compositions. The new KMC information

obtained on the other oxide and carbide fuel kernel compositions was generally consistent with KMC information reported previously. However, some discrepancy was noted between in-reactor and laboratory KMC values for $Th_{0.84}U_{0.16}C_2$. Also, extensive UO_2 migration data from several installations were used to demonstrate that the KMC plot correlated the data as well as a plot based on rate control by $CO-CO_2$ diffusion.

Laboratory determinations of KMC values have been made for unirradiated UC_2, ThC_2, $Th_{0.84}U_{0.16}C_2$, ThO_2, and $UO_{1.65}N_{0.25}$. This part of the ORNL program was accomplished in its entirety during this reporting period; kernel migration was measured in a total of approximately 1100 particles. The ORNL KMC data for the unirradiated carbides agreed quantitatively with that published by GA; UC_2 was thus used as an internal standard in all experiments involving other kernel compositions. Migration was observed in ThO_2 particles. This was the first known observation of migration in unirradiated stoichiometric oxide kernels; the KMC values agree with those for the extrapolated in-reactor behavior of ThO_2. Laboratory KMC values for $UO_{1.65}N_{0.25}$ were approximately comparable with the extrapolated in-reactor behavior of UO_2. Attempts to make as-coated UO_2 migrate have not been successful.

UC_2 Kernel Evaporation

Heating of weak-acid-resin-derived (WAR) Biso UC_2 particles at 1800 to 1900°C resulted in the quantitative loss of 50% or more of the uranium from all the particles in about 550 hr; no loss was observed from Biso particles containing fully dense UC_2 kernels. No quantitative theoretical explanation for this evaporation phenomenon has yet been developed. It may be associated with the surface area of the WAR kernel, which is 1000 times higher than that for dense UC_2. The apparent activation energy is about kJ/mole (100,000 cal/mole); this and the containment properties of the SiC layer on the fissile particles apparently preclude any problem with uranium loss at nominal HTGR temperatures.

HTGR Kernel Chemistry

This part of this program involves investigations of kernel chemistry during fission. In the experimental portion of the work, approximately 100 particles have been broken and the released gases collected. This has revealed the behavior of the oxygen release as CO pressure within the oxide particles as a function of burnup and temperature. These studies have concentrated primarily on Biso ThO_2 particles irradiated in the HT-12, -13, -14, and -15 experiments in HFIR to as high as about 18% FIMA. These burnup levels are unique to HFIR irradiations and provide information that extends approximately 2.5 times beyond the nominal burnup for HTGR ThO_2 particles. Also, the validity of the ORNL experimental technique was verified by an ORNL-AERE-OSGAE intercomparison that used particles from a single U.K. irradiation. The theoretical portion of the kernel chemistry studies is directed to applying the thermodynamic literature

to the interpretation of the observed interactions between fuel, fission products, and coating. The phases present in the WAR UO_2-UC_2 kernel have been calculated as a function of initial UC_2 content and burnup; the same phases are apparently present at all HTGR temperatures.

5. COOLANT CHEMISTRY: THE STEAM-GRAPHITE REACTION

Examination of the Fort St. Vrain HTGR primary coolant impurity levels that were obtained while the reactor was operated at the 2% power level indicated much higher CO_2/CO concentration ratios than expected. This anomaly is postulated to be due to the radiolytic reaction between steam and graphite.

A computational program has been developed to assist in the analysis of laboratory steam-graphite reaction kinetics investigations.

6. HTGR FUEL QUALIFICATION

Fuel Particle Process Development and Qualification

Resin kernel studies included carbonization of the weak-acid resin (WAR) kernels, which have been loaded with uranium nitrate, to produce UO_2 dispersed in a porous carbon matrix, and conversion, whereby a controlled amount of the UO_2 is converted to UC_2. Both Amberlite and Duolite resins were considered in these studies.

Differential thermal analysis (DTA) and thermogravimetric analysis (TGA) were used to define critical reaction regions during the carbonization process (200–500°C). The heating rate through the critical carbonization range had a strong effect on the properties of the final product.

The carbon-to-uranium ratio is a significant parameter in the conversion step. Values above 5.8 were necessary to prevent agglomeration. The Duolite resin exhibits less tendency to agglomerate during conversion than Amberlite resin. The partially converted resin kernels were shown to be a mixture of the phases UO_2, UC_2, and UC_xO_{1-x}. The amount and proportion of these phases can be controlled by temperature variation and the addition of hydrogen or carbon monoxide to the fluidizing gas stream. The presence of these phases suggests the possibility of uranium volatilization during conversion, although losses of only 0.02% have been detected under a "worst case" condition (very rapid carbonization cycle).

Microradiographic examination of coated WAR fuels has shown that under certain conditions a substantial amount of uranium can be transferred from the kernel to the buffer. This transfer occurs during

annealing of the inner LTI coating at 1800°C and during deposition of the SiC layer. This "fuel dispersion" is worst for fuels with high conversion ratios (high proportion UC_2).

Pyrocarbon (PyC) coating studies included both optimization of the coating process and variation of coating process parameters to determine the effects on measurable properties. Under PyC coating process development, the major work was associated with the use of MAPP gas to replace propylene for deposition of LTI coatings. Calculations have shown that MAPP gas should result in approximately 50% as much heat absorption as does propylene during the coating process, yielding a considerable improvement in temperature control of the coating process. Experiments verified this calculation.

The process parameters for LTI coating deposition were systematically varied to provide a range of coating microstructures for irradiation testing and development of characterization techniques. The parameters varied included deposition temperature, MAPP gas concentration, total fluidizing gas flow rate, and bed volume. Specimens prepared by varying the process parameters were tested in the HT-28 through -30 irradiation capsules.

Permeability of LTI coatings is of particular concern. An additional experiment was conducted to investigate the effect of process variables on LTI coating permeability. Leaching of coated particles with Cl_2 was used as a measure of the LTI permeability. The data suggest that application of a seal coat to the outer LTI surface reduces LTI permeability, but further testing is needed to prove this conclusively. As stated earlier, kernels with high conversion ratios appear to be most susceptible to Cl_2 attack through permeable LTI coatings.

Silicon carbide coating studies included an evaluation of the effects of coating conditions on coating characteristics when methyltrichlorosilane (MTS) is used as the source of SiC. The principal variables in this study were MTS flux, H_2/MTS ratio, and coating temperature. We reached a good understanding of the influence of these variables on the microstructure of the SiC coating deposited. In addition, alternate coating compounds were considered as potential replacements for MTS (because of the corrosive nature of the HCl, which is a by-product of MTS). No alternatives produced coatings of equal quality to those produced by MTS, but much more work is needed in this area.

Fuel Rod Fabrication Development and Qualification

In-block carbonization is the reference fabrication process for large HTGR fuel elements. Because of the size of the equipment and process complexity of this method, alternatives are being considered. Carbonization in packed alumina beds has been considered, but this is not easily adapted to remote operation required for fuel refabrication. A quick-setting thermosetting resin that would permit carbonization of

fuel rods in graphite trays without additional mechanical support is being sought. Several candidates have been investigated, but no suitable ones have yet been found. These investigations are continuing at a low level of effort.

Characterization of Pyrocarbon Coatings

Techniques under development for PyC characterization include optical anisotropy (OPTAF), x-ray determination of the Bacon anisotropy factor (BAF), oxygen plasma etching, small-angle x-ray scattering (SAXS), transmission electron microscopy (TEM), and chemical characterization. Characterization efforts have been concentrated on specimens prepared for irradiation testing. These specimens were fabricated with coating deposition conditions systematically varied to provide ranges of microstructures for correlation with irradiation performance.

Work on OPTAF during the reporting period was only moderately successful. Mechanical problems were encountered with the apparatus, which could be overcome with tedious manual manipulation, but which will probably preclude automating the equipment. Several batches of coatings were successfully characterized, and a comparison of measurements made on the same particles at ORNL and KFA Jülich showed good agreement.

Two preliminary experiments using x-ray diffraction techniques demonstrated the technical feasibility of this method for characterizing the coating of a single particle. The major problem with microspheres is to sufficiently collimate the incident and diffracted beams so that meaningful crystallographic information could be obtained from a relatively small volume of LTI coating. Powder patterns from crushed coating samples revealed considerable information on turbostratic stacking, crystallite size, and degree of graphitization in the PyC coatings. Work began on a method for direct determination of preferred orientation in PyC coatings on particles. This technique is of interest because it is fairly rapid and can be quantitative. Development of this method is continuing.

Several etching techniques have been investigated for PyC characterization, including oxygen plasma oxidation, electrolytic etching, and cathodic etching. The etching patterns in PyC structures have been correlated with irradiation performance of Biso PyC coatings. Frequently the microstructural features revealed were below the resolution limit for optical microscopes, so a scanning electron microscope (SEM) was used. Well defined microstructures were produced by plasma oxidation, whereas the structures revealed by cathodic etching were less well defined. Cathodic etching has therefore been abandoned. A brief investigation of electrolytic etching yielded encouraging results. On coatings that had failed under irradiation, continuous circumferential bands of structure were observed after electrolytic etching. No such band structure was observed in a batch of particles that had survived irradiation. While electrolytic etching did reveal microstructural differences between

batches of particles that had failed and had survived irradiation, the differences were less well defined than those produced by plasma oxidation. Therefore, electrolytic etching has not been developed further.

Development of techniques for examination of PyC coatings by transmission electron microscopy (TEM) has been fruitful. Coatings with both "tangled" and "ordered" structures have been observed, and the structure appears to be related to deposition conditions. Work during the reporting period has been aimed at further delineating the microstructures of PyC coatings and at correlating the features in these structures with deposition conditions and resistance to fast-neutron damage. Coatings from batches that had been irradiated in the HT-12 through -15 and HT-17 through -19 series were examined. Coatings that demonstrated poor irradiation survival possessed coherently diffracting regions from one-fifth to one-quarter of the volume of the growth features in which they appeared. Coatings that demonstrated good survival consisted of much smaller coherently diffracting regions within growth features. Further examination of good performing coatings revealed structural features of essentially two sizes.

Irradiation Tests in HFIR Target Facility

HFIR Target Capsules reported in this section include HT-12 through -30. These experiments are in various stages of completion. Capsules through HT-23 have been reported in previous Annual Reports, while Capsules HT-24 through -30 are reported for the first time here. A major effort was expended to improve capabilities for calculating operating temperatures in HT capsules, which are not instrumented. This work is discussed briefly in the HT-12 through -15 section. Capsules HT-17 through -19 were designed to test the importance of various coating parameters on irradiation performance. This series has been investigated extensively for correlations between microstructure and performance. Coatings from archives have been subjected to numerous characterization techniques in an attempt to find some property or microstructural parameter that correlates well with irradiation performance. The HT-20 through -23 series was irradiated to provide specimens for physical property measurement. It was intended to measure the influence of irradiation on thermal expansion and thermal conductivity of HTGR fuel rods. Coated inert particles were included in both slug injected and extruded fuel rods with varying particle loadings. The HT-24 through -25 series was designed as a test of candidate shim materials. Capsules HT-26 and -27 were a test of particle-matrix interaction. Experimental problems not related to the performance of the fuel limited the amount of information gained from these capsules. Irradiation performance of LTI coatings and ZrC coatings (produced by LASL) on both loose particles and in bonded beds was tested in HT-28 through -30.

Irradiation Tests in HFIR Removable Beryllium Facilities

Capsules reported in this section include HRB-4 through -10. These experiments are in various stages of completion. Capsules through HRB-8 have been discussed in previous annual reports. Capsules HRB-9 and -10 are reported for the first time here. Topical reports have been prepared on all HRB experiments through HRB-8. The HRB-4 and -5 series was the first major test of the weak-acid-resin-derived (WAR) fissile fuel. The favorable performance of WAR fuel in these capsules and subsequent tests at GA on WAR fuel led to a selection of this as the reference recycle fuel. The WAR fuel was tested further in HRB-7 through -10. In HRB-9 and -10 several stoichiometries were tested, ranging from WAR UO_2 to WAR UC_2. Intermediate stoichiometries of 85% oxide 15% carbide and 50% oxide 50% carbide performed very well. The 25% oxide 75% carbide fuel showed fair performance but displayed considerably more fission product attack of the SiC layer than the fuels containing higher proportions of oxide.

Irradiation Tests in ORR

Two experiments are discussed in this section, the OF-1 capsule, which completed irradiation during the reporting period, and the OF-2 capsule, which began irradiation at the end of the reporting period. Considerable work was done developing procedures for thermal analysis of OF-type capsules. This work is described in the OF-1 section. The fuel irradiated in OF-1 was $Th_{0.8}U_{0.2}O_2$, which was the reference recycle fuel at the time the experiment was planned. The switch (described earlier) of reference to the WAR fissile fuel made the performance data from the OF-1 capsule somewhat obsolete even before the irradiation was completed. However, some of the problems noted with particle-matrix interaction in the HRB-4 and -5 capsules were not present in OF-1. This result was somewhat surprising, as some interaction had been anticipated. The OF-2 capsule contains all WAR fissile fuel. The test is doubly significant because the same fuel has been tested in HRB-9 and -10 under more accelerated conditions, and OF-2 serves as a lead capsule for the Fort St. Vrain Test Element Program, where the same fissile fuel fabricated in engineering-scale equipment will be irradiated to full exposure under real-time HTGR conditions.

Irradiation Tests in Prototype Reactors

The Peach Bottom Recycle Test Elements (RTE) were fabricated and irradiated under the sponsorship of the Thorium Utilization Program. These elements were inserted into the reactor in July 1970. Three of the seven elements were removed and examined before the October 1974 shutdown of the Peach Bottom Reactor. The remaining four elements began examiation during the reporting period, and this examination is expected to be completed by the end of FY 1976. A brief summary of this work is included in this report, and a complete report is included in the Thorium Utilization Program Progress Report (ORNL-5128).

An experiment was begun in January 1975 in the Dragon Reactor. Operation of Dragon was terminated in Fall 1975, and no examination of the test specimens is planned. A brief summary of that experiment is contained in this report.

Nuclear Analysis in Support of Irradiations

Flux mapping experiments have been conducted in the HFIR and ORR. These experiments and the computational analyses that accompany them have been conducted to determine the spatial variations of neutronic parameters required for the design and operation of test capsules in these reactors. Computational models have been developed and tested. These models accurately calculate spatial variations of neutron fluxes and energy spectra in the ORR, and efforts are under way to provide the same quality of information for the HFIR. Replacement of the beryllium reflector in HFIR in 1975 required experiments before and after replacement to determine whether the experimental environment experienced by HFIR capsules had changed.

A computer program (CACA) was written to provide calculations of the neutronic-related engineering parameters required during the design and operation of irradiation capsules. A development program was started to produce a calorimetric device for direct measurement of gamma and/or fission heat rates in selected materials.

Capsule Thermometry

The HRB capsules have been used as vehicles for testing of improved thermocouple designs aimed at increasing the accuracy and reliability of temperature measurements. Centerline thermometers in HRB capsules must withstand temperatures as high as 1500°C for up to 6000 hr and neutron fluences of 3×10^{22} n/cm^2 (thermal) and 8×10^{21} n/cm^2 (fast). Temperature accuracy of 10°C is desirable for experimental determination of fuel thermal conductivities and diffusion kinetics in the coated particle fuels.

Chromel vs Alumel thermocouples have performed well in the graphite sleeve regions of the HRB capsules (experiencing temperatures of up to 900°C) but are not suitable for centerline temperature measurement. Tungsten-rhenium thermocouples have suitable temperature range and out-of-reactor stability but experience large decalibration drifts in-reactor due to transmutation of rhenium to osmium. Thermocouples using refractory materials with low neutron cross section could be useful to 1500°C, but are still in the early stages of development. Ultrasonic thermometers also have suitable temperature ranges, but also show unfavorable decalibration characteristics in-reactor. A Johnson noise thermometer (JNT) has been successfully tested in one HRB capsule for 4500 hr at 1250 to 1500°C and experienced no apparent decalibration. The JNT is an absolute thermometer, and its development represents the main thrust of the thermometer development program.

Performance Assessment of Coated Particle Fuels

Information gained through irradiation testing is interpreted and applied to process and equipment development and specification writing. Most of the attention during this reporting period has been directed at thermal analysis and the determination of failed particle fractions. A little work was done to adapt computer models for coated particle mechanical analysis for use in direct evaluation of the data from loose particle irradiations in HT capsules. Dynamic testing methods were studied briefly to determine whether our thermal analysis procedures could be improved through such testing, but we concluded that the additional information would not justify the cost. The studies of fission product reaction with SiC represent a new field, where additional work is planned for the future.

7. CHARACTERIZATION AND STANDARDIZATION OF GRAPHITE

The values for both the primary and secondary creep coefficients for graphites in HTGRs are required for the safety and design calculations for these reactors. Such primary and secondary creep coefficients for high-temperature fast-neutron-induced creep are to be determined for compressive stresses in the Oak Ridge Research Reactor (ORR) in position E-5. The work is primarily for and critical to HTGRs, but it should also be useful for other systems that involve graphite in their designs, such as fusion reactors.

The materials selected for these tests are grades H-327, an anisotropic graphite used in the Fort St. Vrain Reactor; H-451 and TS-1240, both coarse-grained, near-isotropic grades of graphite that are two of the principal candidates for 1000-MW(e) HTGR application; and AXF-8QBG, a fine-grained near-isotropic grade of graphite. These are to be irradiated under test conditions of compressive stresses of 13.8 and 20.7 MPa (2000 and 3000 psi); temperatures of 900, 600, and 1150°C listed in the order of priority, accumulating increments of fluence of approximately 1×10^{21} n/cm^2 (>0.18 MeV) per set of specimens per test temperature until each set of specimens has accumulated fluences in excess of 8×10^{21} n/cm^2, full design fluence of the HTGR. Accompanying each set of compressively stressed graphite specimens in each test for each test temperature is a matching set of unstressed (control) specimens. Both the control (unstressed) and stress specimens shall be measured in the unirradiated condition and at the end of each increment of fluence accumulation for dimensions, longitudinal and shear sonic moduli, and other property data required for constitutive equations for primary and secondary creep coefficients.

A minor rearrangement of the ORR loading pattern meets the neutron flux requirements for the irradiation facility; however, the accuracy, precision, and the complexity of the tests to acquire suitable data for the determination of the creep coefficients require a well-designed

complex irradiation capsule and facility with sophisticated equipment for the test control, data acquisition, and data processing. The design of the first capsule OC-1 for the 900°C test, the first of the OC-series of capsules, was completed. The necessary instruments and controls to operate the capsules as well as a Digital Equipment Corporation PDP 11/40 computer with ancillary equipment to control capsule temperatures and to handle other facets of the experiment during irradiation have been procured. Algorithms have been developed to relate the various capsule thermocouple temperatures to the specimen tempeatures and thus permit the computer to adjust the heaters to the required operating levels. The first capsule, OC-1, is scheduled for insertion into the ORR during January 1976.

1. PRESTRESSED CONCRETE PRESSURE VESSEL DEVELOPMENT

J. P. Callahan

1.1 INTRODUCTION

The present reporting period marks a transition from the original program of Prestressed Concrete Reactor Vessel (PCRV) Development to a redirected and amplified new program. The Thermal Cylinder Experiment was designed to provide a final culmination to the original program. Its primary purpose was to provide the experimental data required to evaluate present capability for predicting time-dependent behavior of a PCRV during simulated HTGR operating conditions. During the present reporting period, we completed postmortem studies of the model. These studies were conducted to identify causes of observed disagreement between model test data and results calculated with the SAFE/CRACK finite element analysis, and to identify the mechanism of corrosion of the model axial prestressing tendons. Section 1.2 describes the last of the planned studies pertaining to this very important experiment.

The new PCRV Research and Development Program is divided into the following eight tasks:

Task 1. PCRV Analytical Studies

Task 2. PCRV Head Failure Studies

Task 3. Concrete Properties in Nuclear Environment

Task 4. Long-Term Creep and Moisture Migration

Task 5. Investigation of Tendon Corrosion

Task 6. Liners and Penetration Studies

Task 7. Instrumentation Evaluation and Development

Task 8. Concrete Structural Model Tests

Sections 1.3 through 1.8 describe progress made under the various tasks, consisting of state-of-the-art reviews, planning, and in some cases initiation of new research. New studies under Tasks 4 and 5 have been delayed by the need for completing studies conducted under the previous PCRV Research and Development Program.

In addition to the Thermal Cylinder Model postmortem studies described in Sect. 1.2, work is under way to document an extensive study of moisture migration and time-dependent behavior of concrete. Laboratory testing was completed in 1972 with the exception of eight long-term creep specimens, which remained under sustained loading at the University of Texas. The reports published thus far and results of the long-term creep tests are discussed in Sect. 1.9.

1.2 PCRV THERMAL CYLINDER EXPERIMENT — J. P. Callahan

The thermal cylinder experiment was designed to provide information for evaluating the capability of analytical methods to predict stress-strain behavior of the barrel portion of a single-cavity PCRV, as shown in Fig. 1.1, under typical design and off-design operating conditions. The 1/6-scale model shown schematically in Fig. 1.2 was a thick-walled cylinder having a height of 1.22 m (4 ft), a thickness of 0.46 m (1.5 ft), and an outer diameter of 2.06 m (6.75 ft). It was prestressed both axially and circumferentially and subjected to 4.83 MPa (700 psi) internal pressure together with a thermal crossfall imposed by heating the inner surface of the cylinder to 66°C and cooling the outer surface to 24°C. Since the test was designed to study behavior of the barrel section of a massive concrete structure such as the Fort St. Vrain Nuclear Generating Station PCRV, all exposed surfaces were sealed to prevent moisture loss, and the top and bottom of the model were insulated thermally to prevent heat flow in the axial direction.

The experiment was designed to utilize information developed from previously reported studies of concrete materials properties, triaxial creep, instrumentation, analysis methods, and structural models. The initial 460 days of testing were divided into time periods that simulated prestressing, heat-up, reactor operation, and refueling. At the conclusion of the simulated refueling period, the model was repressurized, and a narrow circumferential band at the inner surface was heated to 232°C for 84 days to produce an off-design hot-spot condition.

Comparisons of experimental strain gage data with time-dependent analysis predictions obtained by use of the SAFE/CRACK finite element

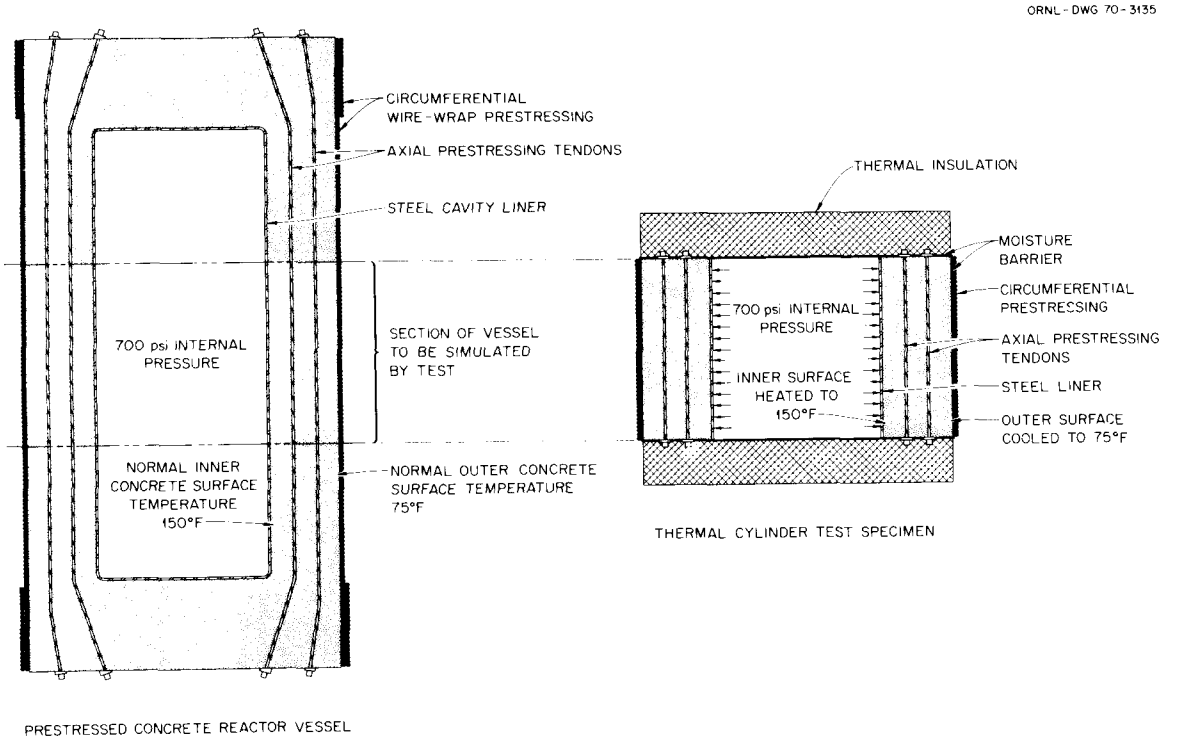

Fig. 1.1. Relationship of Thermal Cylinder Test Specimen to Prestressed Concrete Reactor Vessel. Internal pressure is 4.8 MPa, inner surface temperature is 66°C, and outer surface temperature is 24°C.

computer program indicated generally good agreement for the normal vessel operating period; however, the analysis tended to underestimate heating strains and overestimate mechanical loading strains.

Postmortem examinations of the model have revealed corrosion of the axial prestressing tendons, with a number having failed during both normal operating periods and hot-spot testing periods. The only other detrimental effect of the hot spot was a substantial reduction in strength of the concrete within an 80-mm distance from the heating element.

The model test was completed in December 1972, and preliminary results were reported.[1] Detailed comparisons of experimental data with calculated results obtained with the SAFE/CRACK code were also presented.[2]

During the present reporting period we have investigated the causes of the observed disagreement between the experimental data and calculated

results, and we have conducted laboratory studies in attempting to identify the causes of the axial tendon corrosion. These studies are described in the following sections.

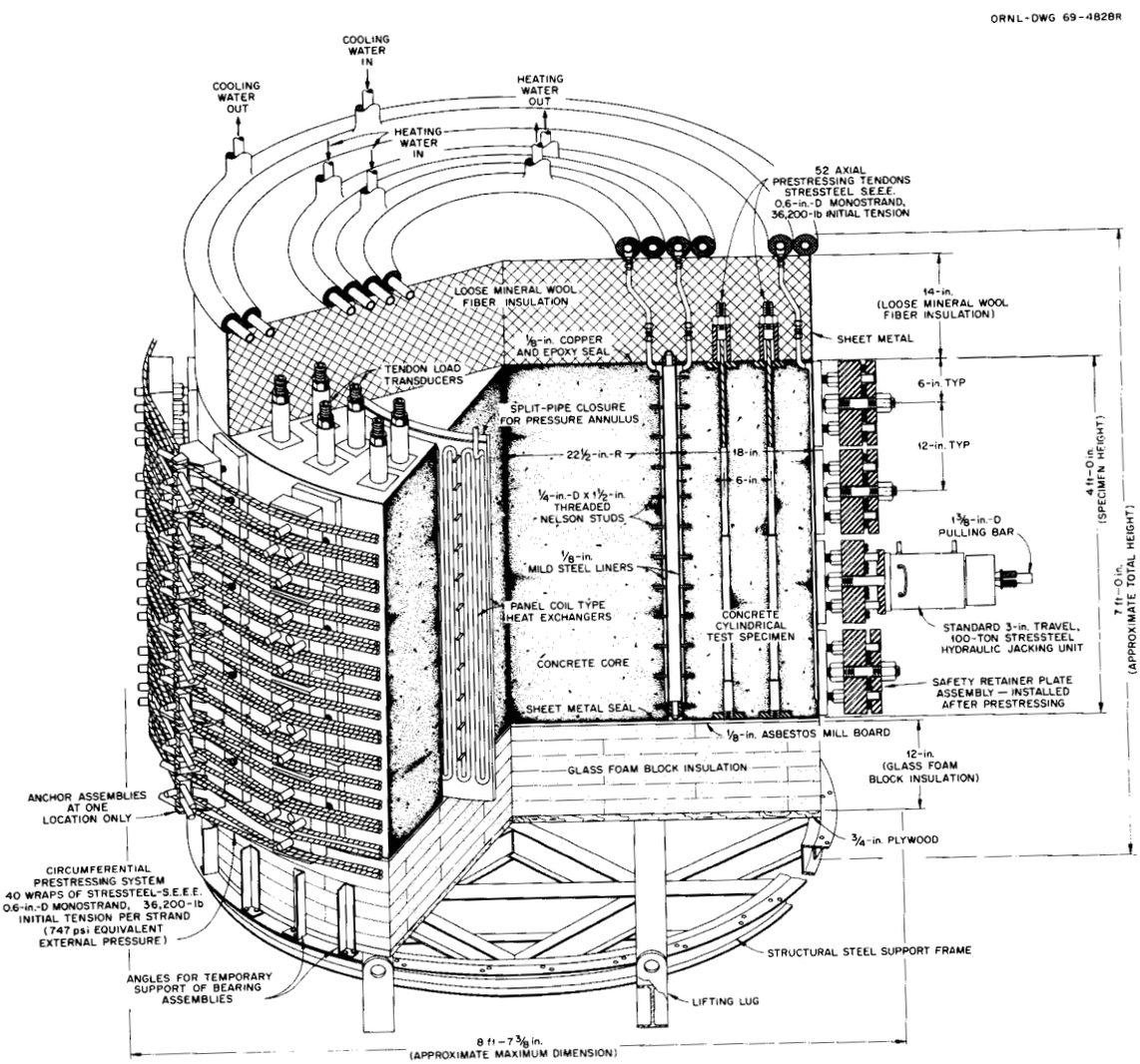

Fig. 1.2. Isometric of Thermal Cylinder Test Structure. To convert dimensions, 1 in. = 25.4 mm, 1 ft = 0.305 m. Initial tension per strand is 0.161 MN, equivalent to 5.15 MPa external pressure.

1.2.1 Correlation of Analytical Results with Model Test Data — W. G. Dodge and D. N. Fanning

The differences between the analytical results obtained by use of the SAFE/CRACK finite element code[3] and the results obtained from the ORNL Thermal Cylinder model embedded strain transducers seemed to be excessive when compared with similar results found in the published literature.[4–6] To obtain a better feel for the accuracy of the experimental results and to identify any trends, it is desirable to compare the results from groups of gages whose readings should be essentially the same. Due to the model design (Fig. 1.2) the effect of end restraints on the strain distribution near the midplane should be negligible. Hence it is reasonable to ignore differences in the axial position. With the additional assumption that the loading is axisymmetric the only relevant positional parameter for grouping is the radial position of the gages.

A significant number of gages were located in the neighborhood of three radial positions: 76 mm (3 in.) from the inside wall, at mid-thickness, and 76 mm (3 in.) from outside wall. These positions will be referred to as the inside, middle, and outside positions, respectively. The strain-time histories shown in Figs. 1.3 through 1.5 indicate that a number of gages at each location exhibit similar trends throughout the life of the test but have significant differences in strain magnitudes. Some of these differences we thought to be due to the fact that the circumferential prestressing was not uniformly distributed, as assumed in the axisymmetric analysis, but was locally applied through steel bearing pads. These pads were approximately 0.20 m (8 in.) wide and had a center-to-center circumferential spacing of 0.46 m (18 in.). The effect of this nonuniformity in the loading should be particularly significant for the outer gages but could also be expected to have some effect throughout the thickness, as the model wall thickness was the same as the pad spacing.

To investigate the effect of nonuniform loading of the model due to the circumferential prestressing, a thin slice from mid-height in a sector of the vessel was analyzed by use of a radial loading obtained

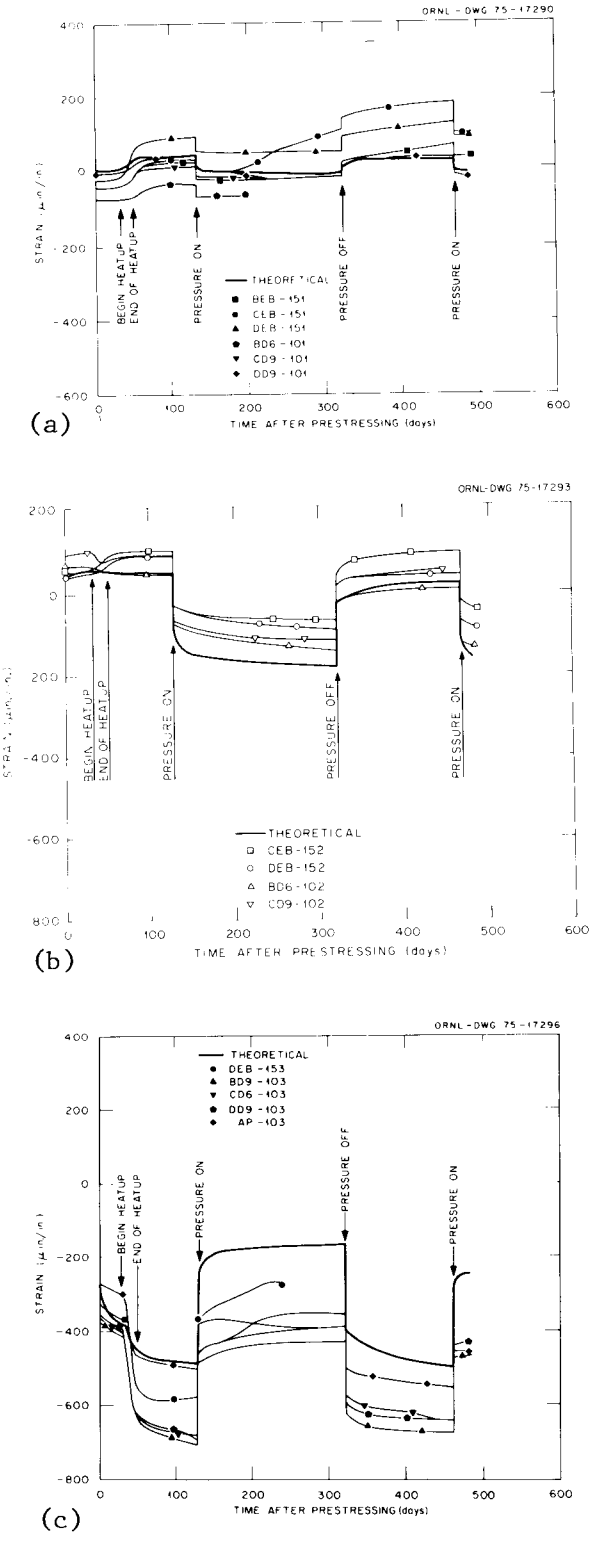

Fig. 1.3. Strain 76 mm (3 in.) from Inside Wall of Thermal Cylinder Model Test Section. (a) Axial. (b) Radial. (c) Circumferential.

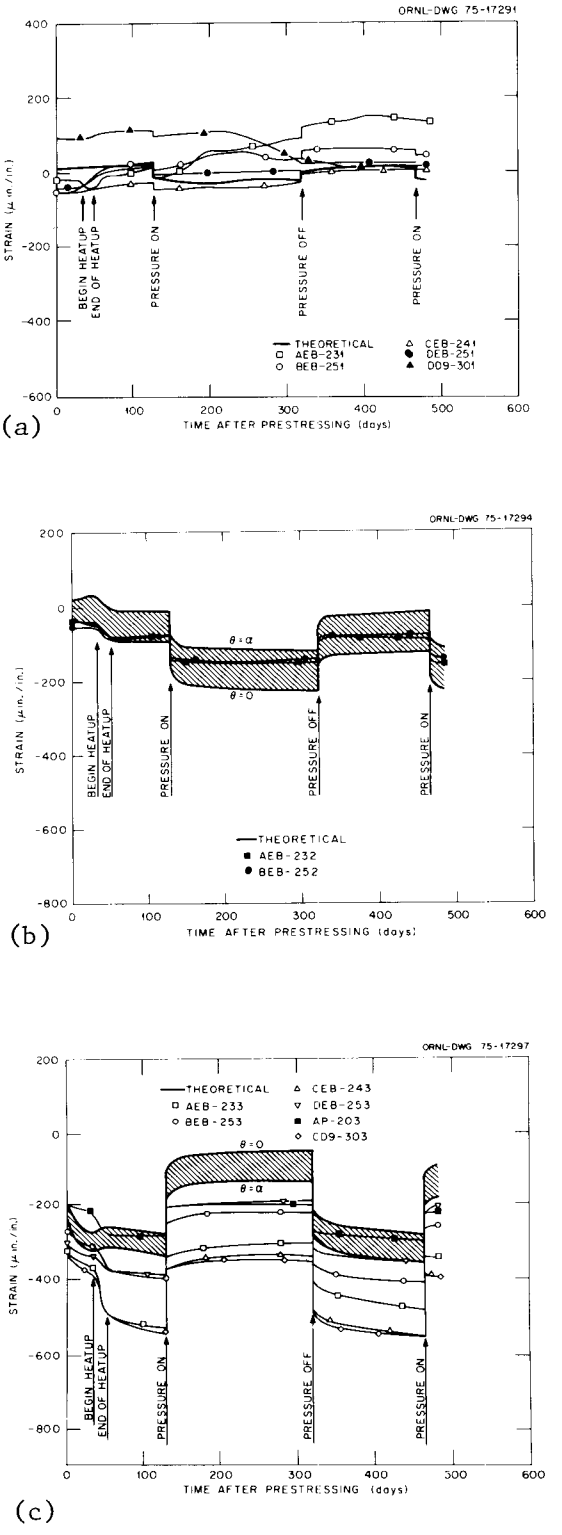

Fig. 1.4. Strain at Midthickness of Thermal Cylinder Model Test Section. (a) Axial. (b) Radial. (c) Circumferential.

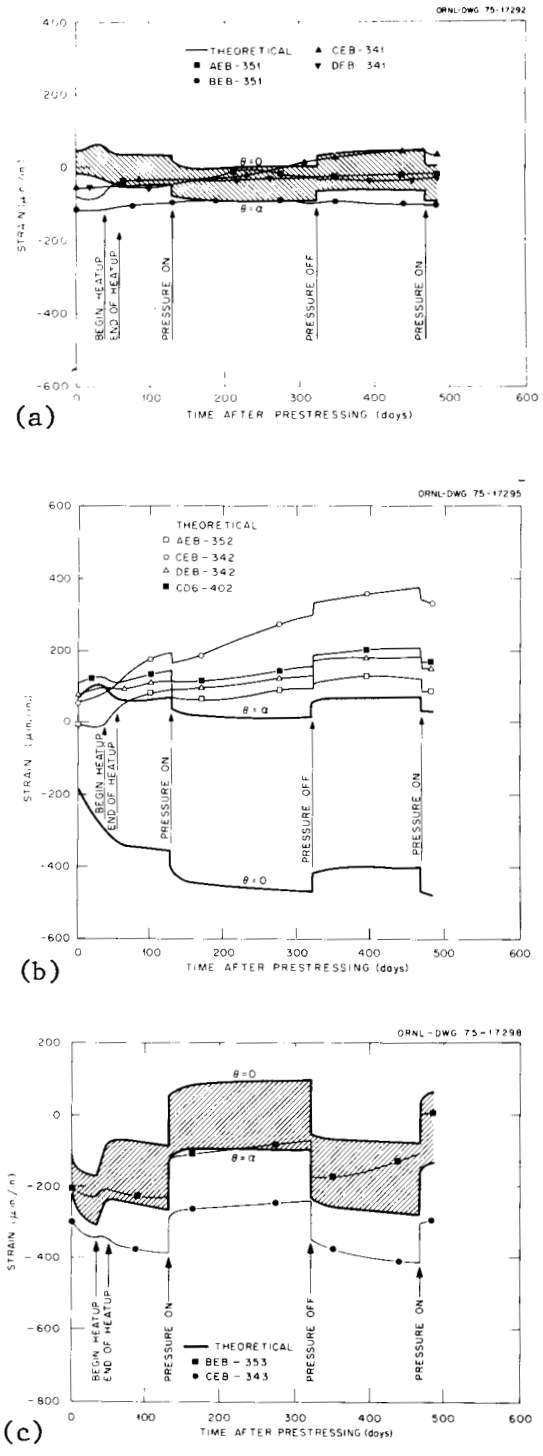

Fig. 1.5. Strain 76 mm (3 in.) from Outside Wall of Thermal Cylinder Model Test Section. (a) Axial. (b) Radial. (c) Circumferential.

from an analysis of the force transmitted by the prestressing through the bearing pads. Figure 1.6 shows the finite element mesh, loading conditions, and boundary conditions imposed in the analysis. In addition, a constant axial stress was applied to simulate the effect of the axial prestressing. The results from this analysis for radial positions along a ray passing through the center of a pad ($\theta = 0$) and radial positions midway between adjacent pads ($\theta = \alpha$) are shown on the Figs. 1.3 through 1.5. The effect of the nonuniformity in the loading is significant at the outside positions (Fig. 1.5) but insignificant at the inside position (Fig. 1.3). Aside from properly accounting for the positive radial strains measured at the outside positions [Fig. 1.5(b)] and better agreement for the axial results [Figs. 1.3(a), 1.4(a) and 1.5(a)], the results from the plane and axisymmetric analyses are essentially the same. Thus the differences in strain readings within each grouping cannot be explained by the nonuniformity of loading on the outside wall.

The close agreement between the results of the axisymmetric and the plane analysis and the fact that for most cases the analytical results lie within the distribution of strain results give a degree of credibility to the accuracy of the analysis, one significant exception being the circumferential strains occurring during vessel heat-up. The results given in Figs. 1.3(c) and 1.4(c) indicate that the algorithm used for calculating creep strains[7] significantly underestimates the strains occurring during vessel heat-up. The creep rate of concrete is known to be approximately proportional to the stress and strongly dependent on the temperature; consequently, the effect of errors in the creep calculations will be most pronounced for the higher stress components at locations having the greatest temperature change; namely, for the circumferential strains at the inside and middle locations [Figs. 1.3(c) and 1.4(c)]. It should be noted that if the observed disagreement between calculated and experimental strains during heat-up had been due to an incorrect value of the coefficient of the thermal expansion, an equal error would have been produced in the axial and radial strains at these locations, but such an error is not evident

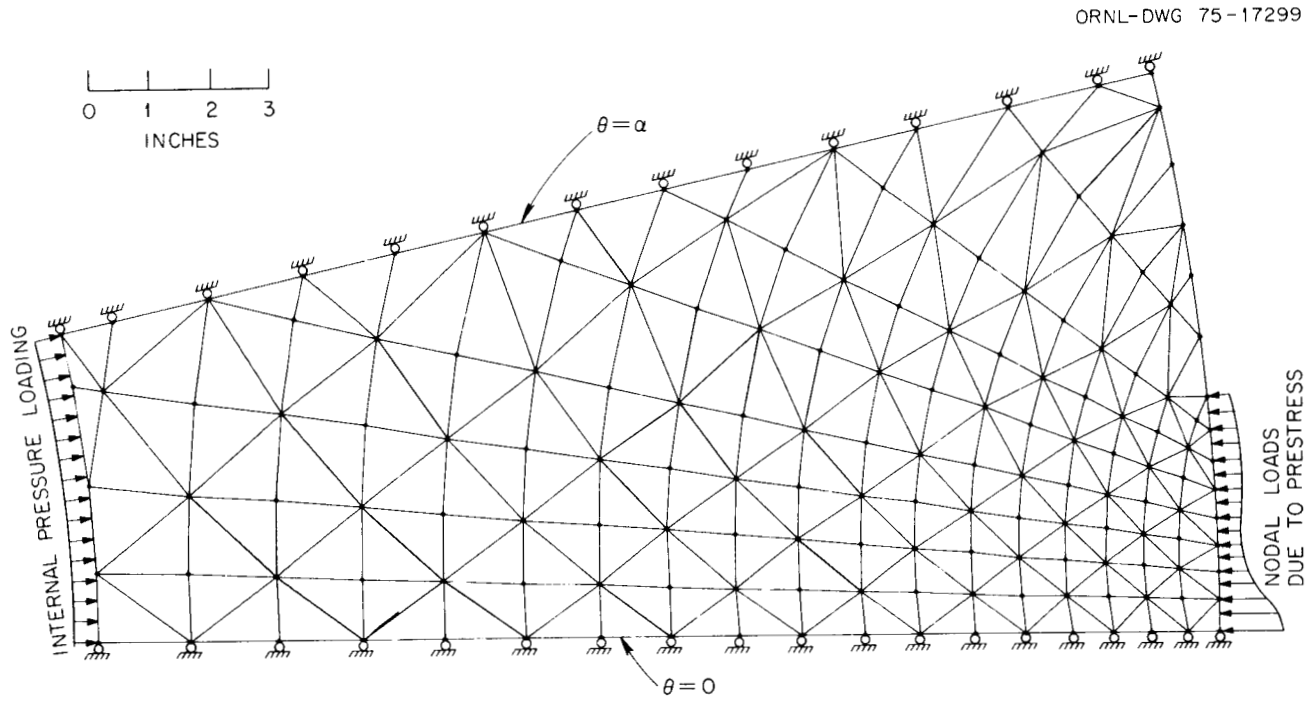

Fig. 1.6. Plane Slice at Mid-Height of Thermal Cylinder Model.

[Figs. 1.3(a) and (b), 1.4(a) and (b)]. The axial and radial stresses at these locations are very low; thus the corresponding creep strains are small and even a relatively large percentage error in their calculated values will not be significant. It also should be noted that if the analytical results were corrected for the discrepancy during heat-up, close agreement between the analytical and experimental results would be obtained for the remaining portions of the test.

To ensure that the discrepancy during heat-up was not the result of an incorrect coding of the creep algorithm, the algorithm was independently recoded. There was very little difference in the results from the two independent codings, indicating that the error is fundamental to the algorithm and not the result of improper coding. As the code reproduced the specified isothermal creep curves and the calculated creep during isothermal conditions seemed to agree with the corresponding experimental results for the thermal cylinder, the probable source of error is in the mathematical generalization of the isothermal creep data to the thermal transit case. Although the algorithm implemented in the SAFE/CRACK code is widely used, the results of this study and other published results[8—10] indicate that it underestimates the accumulated creep strain during thermal transit conditions. The effect of this error would probably be less for an actual PCRV than in this test because the heat-up is slower, occurs at a later concrete age, and occurs in some cases after vessel pressurization and hence at lower stress levels.

In conclusion, the results of this investigation indicate the need for better embedded gages and/or better techniques for embedding these gages, as the scatter present in the results reduces their effectiveness in the validation of vessel design and analysis. The consistency of the two analytical results tends to verify the accuracy of the viscoelastic finite element algorithm in the SAFE/CRACK code; however, there appears to be a deficiency in the creep algorithm for the thermal transient case. Additional fundamental research is required to correct a possible deficiency in the theory.

1.2.2 Investigations of Tendon Corrosion Problems — D. A. Canonico and J. C. Griess

In May 1973 the PCRV thermal cylinder test was terminated. During detensioning of the axial prestressing tendons, we discovered that a number of the inner-row 7-wire tendons had failed during the lifetime of the experiment. Figure 1.7 shows a typical failed tendon. An investigation showed that individual wires in the tendons had failed both before and after the hot-spot test. Figure 1.8 is a composite showing a typical fracture surface of one wire from a failed tendon. The failures initiated from a flat area, which is readily seen in the photomacrograph of the wire (Fig. 1.8). A scanning electron microscopy (SEM) investigation of the fractured surfaces was conducted. Figure 1.8 contains a scanning electron micrograph of the flat area. There are no indications of striations on the fracture surface. This, plus other visual evidence, led to the conclusion that the tendon failures were due to stress-corrosion cracking (SCC) of the wires until the net section was incapable of maintaining the prestress load (∿70% of the ultimate tensile strength).

An investigation sought the SCC mechanism by which the wires could have failed. Newly disassembled ducts that contained failed tendons were found to be "wet". An analysis of the "wet" wax showed it to contain about 2.5% H_2O and 50 ppm nitrate. A strong ammonia odor was associated with a newly disassembled tendon duct. This odor suggested a high nitrogen content, which was later attributed to the use of an incorrectly formulated epoxy resin in the region of the bottom anchor plates. A mechanism involving NH_4^+ and carbonate (CO_3^{2-}) from the concrete was postulated. A laboratory study was conducted to assess this hypothesis. U-bend wire samples (from seven-wire-strand circumferential tendons) were exposed at 70°C to ammonium carbonate and ammonium nitrate solutions. Cracking occurred in 0.2 *M* solution of ammonium nitrate in three days. Specimens exposed to 0.1, 0.2, 0.5, and 1.0 *M* and saturated ammonium carbonate solutions for 94 days at 70°C did not fail. Subsequent tests (with fresh ammonium carbonate solutions) to which 50 ppm nitrate (as $NaNO_3$) was added were conducted. No evidence of cracking was observed after 100 days at 66°C. This study showed that the steel from which the tendons

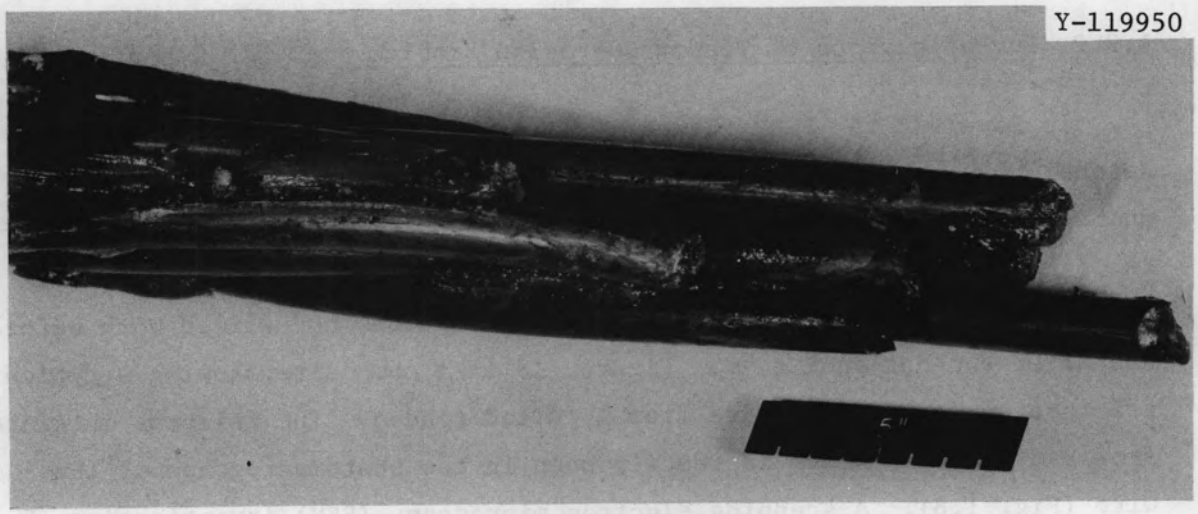

Fig. 1.7. Typical Tendon Failure.

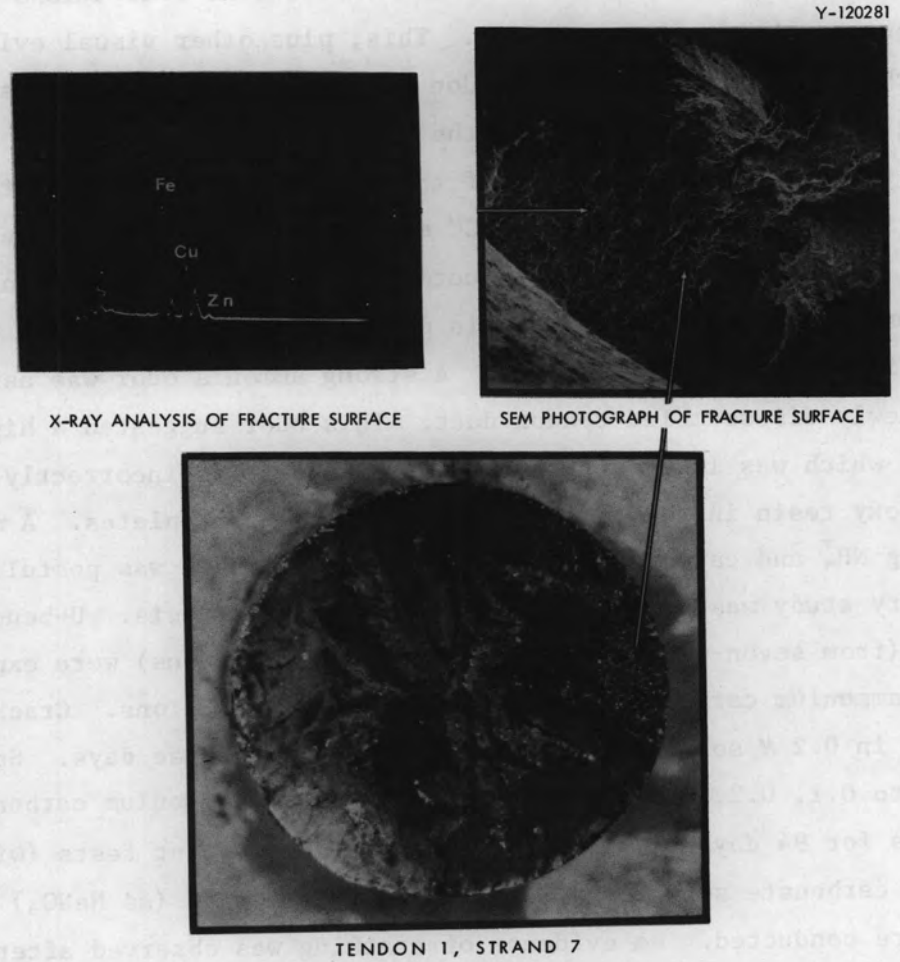

Fig. 1.8. Fractographic Examination of Failure Surface in a Wire from a failed Tendon. The flat area in the photomacrograph was viewed and analyzed in the scanning electron microscope. There is a definite indication of sulfur in the flat area of the fracture surface.

were made is susceptible to SCC in ammonium nitrate solutions, but no cracking was noted in solutions that contained only 50 ppm nitrate. (The 50 ppm nitrate is in the range of concentrations found in the liquid in contact with the failed tendons.)

The hypothesis that ammonium carbonate was responsible for the failure was not proven. It was shown, however, that high concentrations (6000 ppm) of nitrates caused cracking in highly stressed tendon wires in a very short time. It is conceivable that in the thermal cylinder test the nitrate concentration could have been high enough to be responsible for the tendon failures.

An interim report[11] describing the early facets of this investigation has been published.

1.3 DEVELOPMENT OF ANALYTICAL METHODS FOR PCRVs — W. G. Dodge and D. N. Fanning

During the first year of activity under this task area, the major thrust has been directed toward establishing required basic analytical capabilities. This effort consisted of obtaining operational basic computer software and developing appropriate material constitutive relations for concrete.

1.3.1 Computer Capability Development

A survey was made of available computer programs applicable to the analysis of PCRVs. Four finite element codes were obtained and made operational on the ORNL computers. The basic capabilities, status, and projected use of these programs are as follows.

1.3.1.1 Two-Dimensional Plane-Axisymmetric Codes

The SAFE/CRACK and CREEP/PLAST codes were selected from this category. Both were developed under the direction of Y. R. Rashid and have many similarities in content and logic structures. This parallelism reduces the effort required to become familiar with their internal operations.

SAFE/CRACK. This program was developed at GA for the analysis of PCRV structures and remains one of GA's primary analysis tools. The concrete is discretized by use of constant-strain triangular elements having linear viscoelastic time-dependent material properties. A hereditary integral formulation is used for the time-dependent analysis, with temperature effects incorporated by a time-shift in the basic creep functions.[7] Concrete failure under combined stresses is implemented by changing the material behavior so as to model the force transmission of the crack.[12] The material properties for those elements exceeding the failure criteria are changed from isotropic to orthotropic so that the element stiffness perpendicular to the crack becomes zero while full stiffness is maintained parallel to the crack. Elastic-perfectly plastic membrane and uniaxial elements are available for modeling the steel-bonded reinforcement and vessel liner.

Because SAFE/CRACK is used by GA for PCRV analysis we have devoted a rather extensive effort to become familiar with this code. The theoretical basis of the major algorithms and their implementation have been reviewed. In particular, the algorithms associated with the element formulations, creep computations, and the solution procedure have been extensively examined, and certain modifications have been incorporated to improve the logic structure and/or computational efficiency. The portion of the code related to the calculation of relaxation functions for time-dependent material response was completely reprogrammed, and many comment cards were introduced throughout the code to improve the internal documentation.

In the ORNL version of this code, the algebraic equations that resulted from finite element discretation are solved using the Gauss-Seidel iterative method.[13] This method offers two distinct advantages over the more commonly used direct methods of solution. Because it is necessary to allocate storage only for the nonzero coefficients of the stiffness matrix, core storage requirements are significantly reduced, and the final solution accuracy is not affected by accumulation of round-off errors beyond that occurring within a single row operation. The main difficulty with the method is that slow convergence often leads to an excessive number of iterations before a satisfactory solution is obtained.

The two most widely used methods for accelerating the convergence are the over-relaxation method and the Aitken's extrapolation formula,[13] both of which were employed in the original version of SAFE/CRACK. Much of our early difficulty with the code was related to these acceleration techniques. Although our proficiency improved with experience, we were unable to develop a consistent and reliable solution procedure based on these techniques. This difficulty was resolved by the development of a completely new acceleration method based on variational principles. (We also incorporated a direct solution algorithm as a possible backup.)

The system of algebraic equations to be solved is of the from

$$[K]\{\delta\} = \{F\} \tag{1}$$

where [K] is an $n \times n$ matrix called the stiffness matrix, $\{\delta\}$ is the $n \times 1$ vector of generalized displacements, and $\{F\}$ is the $n \times 1$ vector of generalized forces. These equations arise as a necessary condition that the total potential energy of the elastic system be a local minimum. For any set of generalized displacements $\{\delta'\}$ satisfying the constraint conditions the total potential energy is given by

$$V = U + \Omega \ , \tag{2}$$

where

$$U = 1/2 \ \{\delta'\}^T[K]\{\delta'\} \tag{3}$$

is called the total strain energy, and

$$\Omega = - \ \{\delta'\}^T\{F\} \tag{4}$$

is the potential energy of the generalized forces. The vector $\{\delta'\}$ satisfying Eq. (1) and the constraint conditions on displacements yields a minimum for the total potential energy, V.

The new acceleration scheme is based upon the use of the iterative approximations as trial functions for minimizing the total potential energy.

Let $\{D\}$ be the approximation of the solution of Eq. (1) after the ith iteration of the Gauss-Seidel method and $\{\Delta\}$ be the change in the solution during the $(i + 1)$th iteration. A new approximation of the solution, $\{\delta'\}$, is constructed as a linear combination of $\{D\}$ and $\{\Delta\}$:

$$\{\delta'\} = a\{D\} + b\{\Delta\} \ , \tag{5}$$

where a and b are constants to be determined by requiring that V be a minimum. The minimum requirement yields

$$\frac{\partial V}{\partial a} = \frac{\partial V}{\partial b} = 0 \ . \tag{6}$$

The values of a and b satisfying the above equations are

$$a = \frac{h_1\{\Delta\}^T\{F\} - h_3\{D\}^T\{F\}}{h_1^2 - h_2h_3} \tag{7a}$$

$$b = \frac{h_1\{D\}^T\{F\} - h_2\{\Delta\}^T\{F\}}{h_1^2 - h_2h_3} \tag{7b}$$

where

$$h_1 = \{D\}^T[k]\{\Delta\} \ , \tag{7c}$$

$$h_2 = \{D\}^T[K]\{D\} \ , \tag{7d}$$

$$h_3 = \{\Delta\}^T[K]\{\Delta\} \ . \tag{7e}$$

After the values of a and b are determined, the iterative procedure is restarted using the value of $\{\delta'\}$ given by Eq. (5).

This acceleration procedure has been used successfully for a broad range of problems having quite different convergence properties and has produced rapid and stable convergence in all cases. The procedure may be applied repeatedly during the solution process, and the overall convergence does not seem to be very sensitive to the number of iterations

between application since the longer the interval, the larger the value of b, and the greater the resulting acceleration for each application of the procedure. Typically, solution convergence is obtained in 1/5 to 1/20 the number of iterations required for the nonaccelerated procedure.

The advantages of the iterative procedure over direct solution methods become more pronounced in incremental inelastic problems because a realistic estimate of the starting vector is generally available. For three-dimensional problems, the reduced core requirements become increasingly important. Also, because the iterative method is independent of the bandwidth of the [K] matrix, it is theoretically possible to develop a procedure for automatic mesh redefinition to account for crack propagation. Thus, the method offers an exceptional potential for reducing the cost of inelastic analysis of multicavity PCRVs and for improving the accuracy by which crack propagation problems can be modeled.

Various test cases were run on the SAFE/CRACK code to validate its accuracy, including an analysis of the ORNL Thermal Cylinder test, which was discussed in Section 1.2.1 of the report. Our opinion is that the code is functionally correct in its present form. Because SAFE/CRACK is two-dimensional, with limited applicability to multicavity PCRV analysis, further development does not seem to be justified.

CREEP/PLAST.[14] This computer program is currently the primary analysis tool for the LMFBR High-Temperature Structural Design Methods task at ORNL and has consequently received extensive check-out. Thus, it provides a convenient tool for validation of equivalent features in the SAFE/CRACK code, and we have used it for this purpose. In its present form the code is capable of performing elastic-plastic and nonlinear creep computations using constitutive models appropriate to metals. In the future the code may be useful for evaluating the use of plasticity models in describing nonlinear behavior of concrete and the use of rate-type models for time-dependent response of concrete.

1.3.1.2 Three-Dimensional Codes

At this time no nonproprietary three-dimensional finite element codes are capable of analyzing nonlinear and/or time-dependent effects

in PCRVs. In the selection of suitable three-dimensional codes it was anticipated that further development would be required, and particular attention was given to those factors that affect the amount of effort required for implementing modifications. The two most important factors considered are the degree of internal and external documentation and a modular logic structure. Both the codes selected in this category were developed at the University of California and share many similarities in content and logic structure. They are moderately well structured, very well documented, and widely used.

NØNSAP.[15,16] This program is designed for linear and nonlinear, static and dynamic analysis of two- and three-dimensional structures by the finite element method. Variable node isoparametric elements are available for continuum discretization, and various material models are available to represent elastic, hyperelastic (nonlinear elastic), and hypoelastic (elastic-plastic) material behavior. One particularly interesting feature is a tension cut-off capability for modeling geological materials. Unfortunately, the majority of these material models are implemented only for the two-dimensional case, and the time-dependent material response (creep) model is not available. Also, only an in-core solution algorithm exists, thus limiting the maximum problem size. The latter limitation is not now viewed as a serious restriction, but if in future studies it should become so, the introduction of out-of-core solution algorithm should not be a major problem.

Basically, NØNSAP is an efficient, modular, and easily modified general analysis code. Consequently it is an effective tool for conducting research pertaining to nonlinear analysis procedures, and simultaneously it offers the capability of efficient solution of a variety of practical problems related to PCRV structures. At present, the code is operational, and many of its features have been tested. We are becoming familiar with the internal logic so as to be in a position to incorporate appropriate constitutive models for concrete and make other modifications to improve the modeling capabilities.

STATIC/SAP.[17] This program is a predecessor to NØNSAP, and much of the coding is similar. The fundamental difference is that STATIC/SAP is

only a linearly elastic code, hence its capabilities are restricted. However, there are distinct advantages associated with this code: there is greater operational experience with it, it is simpler, and it contains an out-of-core solution algorithm. We do not anticipate any further development for this code but will use it to provide parallel validation of NØNSAP. If necessary, we may extract the solution algorithm from this code for inclusion into NØNSAP.

1.3.1.3 Support Programs

In addition to the four finite element codes discussed previously, two support computer programs were developed to provide error diagnostic capabilities for the finite element mesh definition. Both programs also provide plots of all nodes and elements making up the complete mesh.

The program CHECK/2D provides a diagnostic capability for the plane/axisymmetric two-dimensional programs by preparing a plot of all element boundaries that are specified only once by the element cards. If no errors exist in the element specifications, only the outline of the structure will appear on this plot. Any element specification error will produce internal lines within the structure.

The program CHECK/3D provides diagnostic capability for the three-dimensional programs by plotting all element boundary surfaces that are specified only once. Any element specification error will produce internal surfaces within the structure. Both programs provide an absolute validation of the correctness of the finite element mesh definition.

1.3.2 Review of Methods for Analysis of PCRVs

To ensure that our efforts in the development of analytical capabilities are properly directed and profit from previous experience, an extensive effort was devoted to the review of published information. Two consultants, Prof. Z. P. Bazant of Northwestern University and Prof. R. H. Gallagher of Cornell University, are participating in this effort. The findings will be published in a report on the state-of-the-art of analysis methods for PCRVs. The document discusses the relationship between the design philosophy and the types of analyses required

(linear elastic, time-dependent, and inelastic), the various constitutive relations that are used to describe material behavior, and the implementation of these behavior models in finite element computer codes.

1.4 HEAD FAILURE STUDIES — M. A. Sozen and W. C. Schnobrich (University of Illinois)

The immediate objective of the project activities for the first year was to develop experimental techniques and to reassemble computer programs to study the shear strength of flat end slabs of cylindrical vessels, with various arrangements of penetrations in the end slab.

The overall dimensions of the two vessels tested are shown in Fig. 1.9. One of the test vessels had a solid end slab while the other had six 0.13-m (5-in.) penetrations distributed symmetrically around a 0.20-m (8-in.) radius.

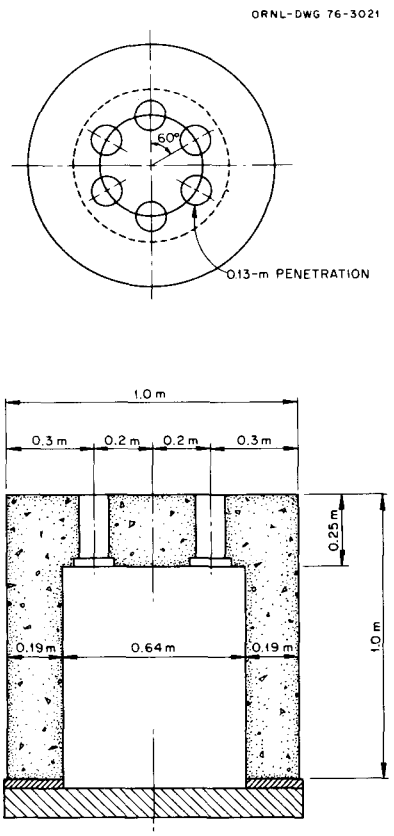

Fig. 1.9. Overall Dimensions of Test Vessel.

1.4.1 Prestressing System

The end slab is made of plain concrete (without conventional steel reinforcement). Tensile stresses created during loading are counteracted by the compressive stresses generated by the circumferential and vertical prestressing.

Because no commercial source was available for applying the circumferential prestressing force with the variability that would be required in the course of the project, we elected to develop a system for circumferential prestressing in the laboratory. Figure 1.10 shows the prestressing rig currently being used.

The system uses a dead weight of 680 kg (1500 lb) to develop the prestressing force such that the total force of the 2.0-mm (0.08-in.) prestressing wire is approximately 3.3 kN (750 lb) as continuously recorded by a transducer connected to the last pulley. The test vessel is seated on a platform, which is rotated by an electric motor providing the prestressing force. The travel of the prestressing steel is regulated by a friction wheel. The 680-kg (1500-lb) weight is maintained at constant elevation by continually adjusting the normal force on the friction wheel with the brake lever.

The prestressing force is provided by a series of bands, each of which occupies a height of 0.10 m (4 in.) on the vessel wall and comprises approximately 300 turns. The bands are spaced on 0.20-m (8-in.) centers. The total prestressing operation takes approximately two days.

The vertical or longitudinal prestress is provided by sixty 19-mm (3/4-in.) stress steel rods, as shown in Fig. 1.11. Fifteen of these rods are instrumented and calibrated to measure changes in stress during the test.

1.4.2 Sealing and Instrumentation

One of the critical tasks in the testing of each vessel is the internal seal or liner, which has to hold the pressure after cracking of the inside surface of the vessel and rotation of the head. Developmental work led to the sandwich liner shown in Fig. 1.12.

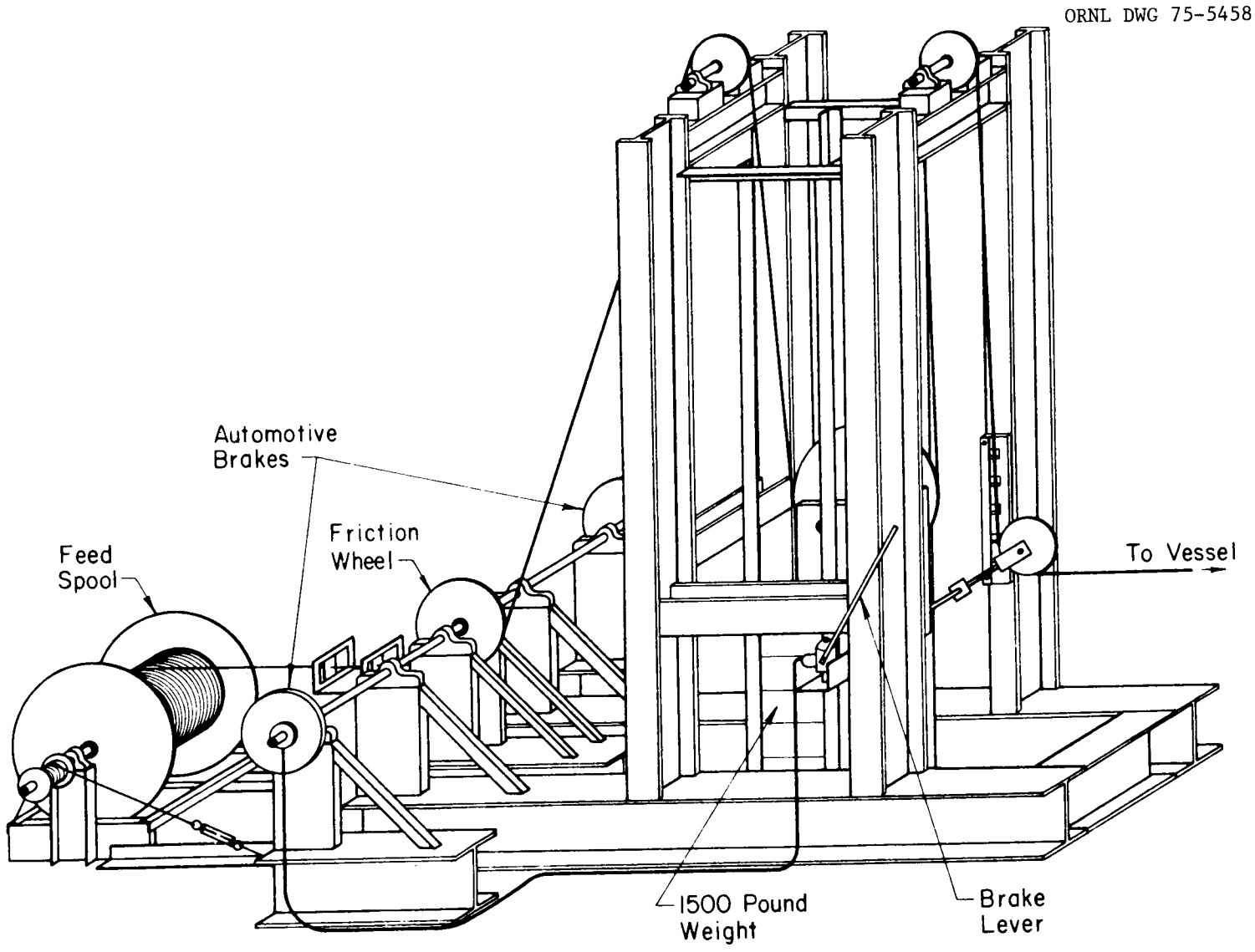

Fig. 1.10. Prestressing Apparatus for PCRV Head Failure Study Model.

ORNL-DWG 76-3022

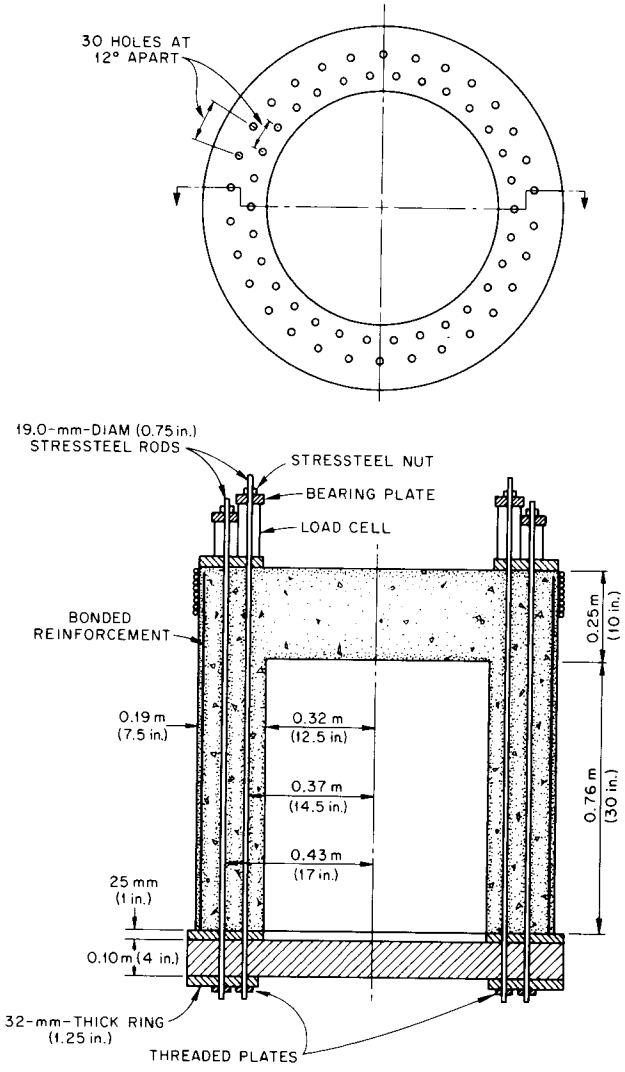

Fig. 1.11. Arrangement of Vertical Prestressing Rods.

ORNL-DWG 76-3023

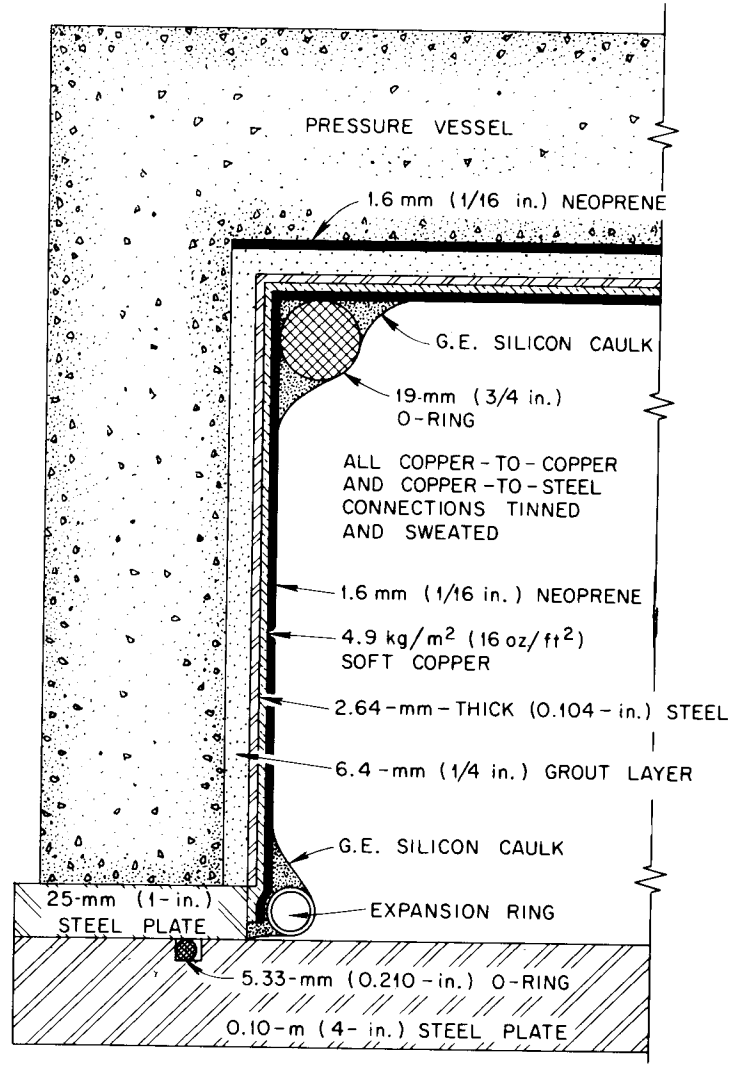

Fig. 1.12. Vessel Lining (Horizontal Scale Exaggerated).

A hollow steel cylinder with one end open is built from 2.6-mm (0.104-in.) steel plate to fit in the concrete vessel, resting on a 6.4-mm (0.25-in.) grout layer. The inside surface of the hollow steel cylinder is lined with a 1.9-kg/m^2 (16-oz/ft^2) soft-copper plate, which is soldered to the steel ring at the open end of the concrete vessel. The copper plate is, in turn, lined by a 1.6-mm (1/16-in.) membrane of neoprene. A 19-mm (3/4-in.) O-ring is placed at the reentrant corner and covered by a generous layer of silicone caulk. An expansion ring, which pushes the liner membrane against the steel ring at the open end of the concrete vessel, is also covered by caulk. The seal between the steel closure plate and the test vessel is provided by a 5.3-mm (0.21-in.) O-ring.

In addition to instrumentation for measuring the prestressing forces, the internal pressure, and crack patterns, electrical resistance gages measure the strains on concrete at two surfaces of the end slab as well as in the penetrations.

1.4.3 Test Results

Both specimens failed as a result of shear in the end slab in a manner similar to the failures described by Karlsson and Sozen.[18] Figure 1.13 shows the measured relationship between the internal stress and deflection at the center of slab. The observed close relationship between the strength and deformation properties of these two vessels, one of which has virtually half its cross-sectional area at a radius of 0.20 m (8 in.) removed, is noteworthy and confirms the observation made by Karlsson and Sozen.

1.4.4 Analytical Studies

The analysis of the vessel heads using the element approach requires an efficient program to adequately treat the nonlinear phase of the study in an incremental manner. After experiments with several existing programs

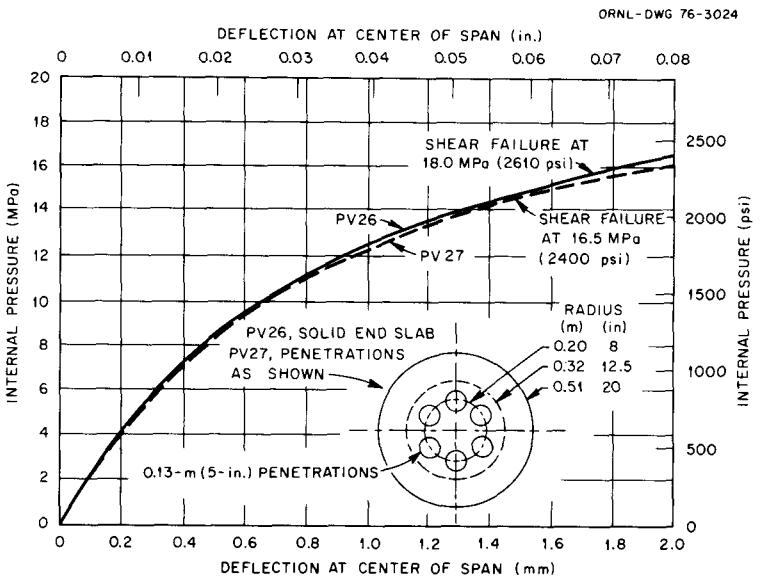

Fig. 1.13. Measured Pressure-Deflection Relationship.

of both the general purpose and the special purpose types we concluded that several programs tailored to the particular problem represented an effective approach.

The cracking program adapts a combined incremental-iterative procedure. The structure is loaded monotonically (with increments determined by the user). Within each increment the program performs a number of iteration cycles to achieve an equilibrium solution under the applied loads plus all the residual forces being redistributed as a result of the nonlinear action. The frequency at which the tangential stiffness matrix is updated is user selected.

A major problem in the application of the procedure is the specification of the nonlinear properties of concrete under the wide variety of possible stress combinations. A number of programs have used an elastic-plastic material characterization with the failure surface determined by the choice of yield criterion. Such programs have worked successfully mostly on problems insensitive to the compressive stress conditions. For the head problem this type of material specification is inadequate. Thus the constitutive relations incorporated in the program are based on an

empirical model of a general curved shape for the concrete. Based on the selected stress-strain characteristics the stresses which the material can stand, the residual stresses, and the instantaneous moduli are determined. The flow diagrams for the basic algorithms used with principal tensile or compressive stresses are shown in Figs. 1.14 and 1.15.

The program allows two-dimensional axisymmetric or three-dimensional isoparametric elements to be selected along with a general nonlinear concrete stress-strain relationship. In its current formulation, it does not accept decaying stress-strain conditions.

The program is currently being employed to investigate the stress fields in the cryptodome configurations developed in the recent test specimens.

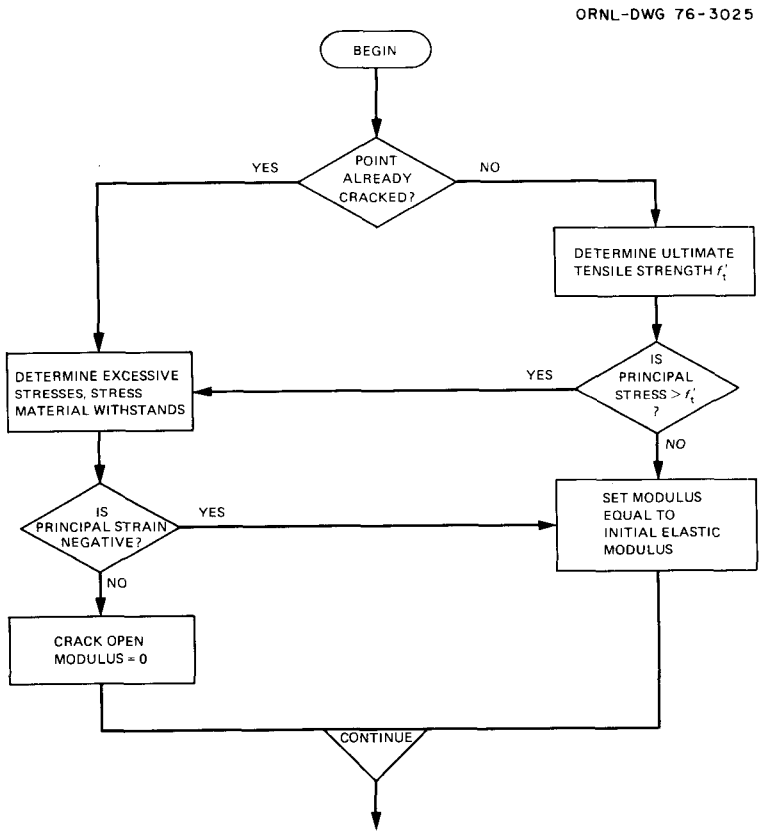

Fig. 1.14. Basic Algorithm for Handling Principal Tensile Stresses.

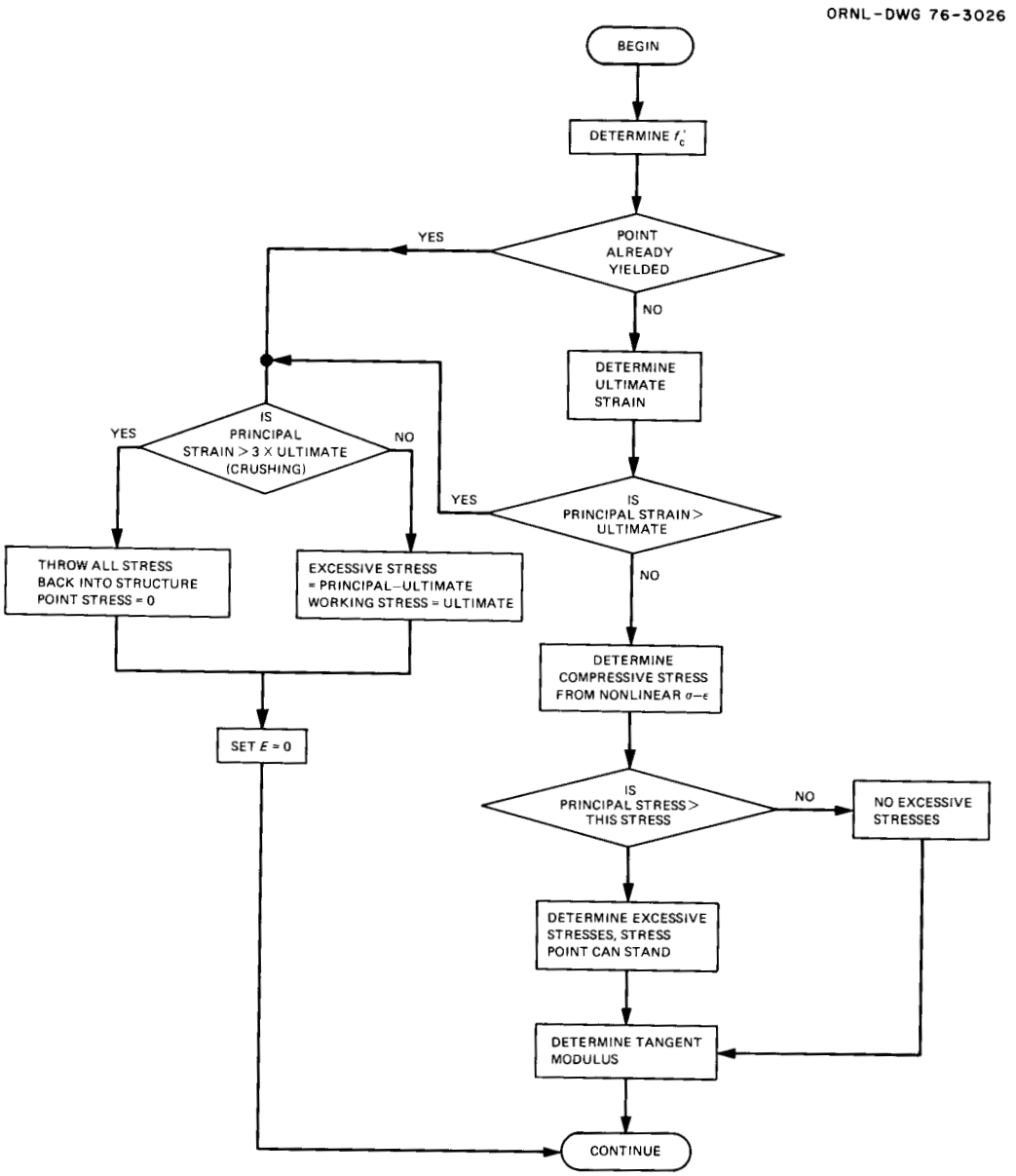

Fig. 1.15. Basic Algorithm for Handling Principal Compressive Stresses.

1.5 CONCRETE STRUCTURAL MODEL TESTS — D. J. Naus

1.5.1 Background

Prestressed concrete reactor vessels (PCRVs) are generally massive thick-walled, right-circular cylinders having flat heads. They are either of the single-cavity or multicavity type. Analysis of these structures is extremely difficult because of their complexity, varying loading conditions, time-dependent material behavior, and changing environments. Their design is based on the premise that catastrophic failure is virtually impossible since sufficient conventional reinforcing steel and prestressing steel are contained in the concrete matrix to ensure that the structural behavior is nonbrittle. Thus, if failure ever happened, it would be a progressive process occurring in small increments.

During development of PCRVs as containment structures for nuclear reactors many models were fabricated, tested, and analyzed to verify designs and to develop and refine existing failure analyses. In fact, models have been tested for all PCRVs that have been built to date. Despite the considerable research data obtained through model studies, there is still a definite continuing need for model studies associated with PCRV development. In many of the previous investigations the data are of limited use because only limited ranges of variables were investigated, research efforts were conducted independently and the data are applicable only to the particular model study, and the models were fabricated from "model" concretes and tested in environments not adequately representative of the material state in the PCRV. (Results cannot be related to the 20 to 30-year design life.)

The series of model tests to be conducted under this task will be designed to provide input for development of new and/or refinement of existing analytical techniques for describing PCRV long-term time, temperature, and load-dependent behavior. Initially, the models will involve relatively simple structural members. The structural models will then increase stepwise in complexity until they represent a PCRV or major portions of a PCRV. Loading and environments will be designed to simulate long-term PCRV operating conditions. The models will generally be of sufficient size so that representative PCRV materials may be utilized.

1.5.2 Initial Structural Models Test Series: Grouted vs Nongrouted Prestressing Tendon Behavior

As a result of a request[19] from GA for information on use of grouted tendons in PCRVs, the initial structural models test series has been designed to investigate the relative performance of grouted vs nongrouted tendons. If grouted tendons perform adequately in PCRVs, reduced overall costs and improved performance may be affected.* Before accepting *a priori* the use of grouted tendons, further experimentation is required to evaluate grouted tendon systems, especially in potentially aggressive environments.

1.5.3 Experimental Investigation

The present experimental effort is divided into two phases: (1) development of a concrete laboratory capable of batching, mixing, and casting the required structural models, and (2) an evaluation of the relative performance of grouted and nongrouted prestressing tendons. The work that has been completed during this reporting period includes the development of the concrete structural model laboratory and development of a test program for the grouted tendon study.

1.5.3.1 Concrete Laboratory

The in-house laboratory for batching, mixing, casting, and testing of concrete structural models has been completed. Basic equipment contained in the laboratory includes: coarse and fine aggregate storage facilities, sieves for aggregate gradations, hoppers for batching the dry concrete ingredients and transporting the concrete while in a plastic condition, batching scales, a 0.17-m^3-capacity (6-ft^3) concrete mixer especially designed for optimum efficiency, a 0.07-m^3 (2.5-ft^3) and a 0.02-m^3 (0.7 ft^3) mixer suitable for casting relatively small models,

---

*Initial costs of grouted and nongrouted tendons are approximately equal, but the surveillance costs for nongrouted tendons over the 20 to 30-year design life of the structure may cost as much as the prestressing system itself. In addition, grouted tendons provide increased ultimate moment capacity, better crack control, improved anchorage efficiency, and elimination of dynamic effects resulting from tendon fracture.

and external and internal vibrators for compaction of the concrete in the molds. Equipment is available for determination of the following concrete properties: compressive strength, splitting-tensile strength, unit weight, air content, slump, time of set, and modulus of rupture.

Two testing machines have been obtained for the laboratory: a 1.78-MN (400-kip) hydraulic machine and a 0.24-MN (55-kip) structural test system. The 1.78-MN hydraulic machine is primarily for concrete materials property evaluations, and the 0.24-MN closed-loop electro-hydraulic system will be used for structural testing of the models. In addition to its 0.24-MN capacity, the system has a 0.15-m (6-in.) stroke, the capability of being programmed for constant loading, constant deformation rate, or a wide variety of ramp loading functions, as well as dynamic and cyclic loading capability.

1.5.3.2 Grouted or Nongrouted Tendon Investigation

A test program to assess the relative behavior of grouted and non-grouted tendons has been developed. The experimental investigation is to be divided into studies of: (1) structural behavior, (2) corrosion behavior, (3) new materials, and (4) tendon monitoring techniques. Post-tensioned beams fabricated from representative PCRV materials will be used as the primary structural elements.

1.5.3.2.1 Specimen Geometry, Materials, and Specimen Fabrication. To simplify the testing and analysis requirements, beam structural elements have been selected as the primary members to be used in the investigation. A beam geometry of 0.15 m wide by 0.305 m deep by 3.1 m long (6 in. by 12 in. by 10 ft) was selected accoring to criteria that the beam be of sufficient size that flexural members are accurately modeled, that representative prestressing steel types and quantities may be used, and that the beam and material properties specimens be cast from one concrete mix. An analysis has been conducted to ensure that specimens of the geometry selected will fail in flexure after steel yielding and that ultimate loads are within the capacity of the structural test system.

A 19-mm (3/4 in.) maximum aggregate size concrete with design properties representative of the mix specified for the Summit Power Station [compressive strength = 45 MPa (6500 psi), modulus of elasticity = 31—45 GPa ($4.5—6.5 \times 10^6$ psi), and Poisson's ratio = 0.15—0.25] will be used for specimen fabrication. Type II cement will be used in the investigation. Seven-wire 13-mm-diam (0.5-in.) lo-lax grade 270 strand has been selected as the post-tensioning reinforcement since this strand is representative of presently used prestressing. The quantity (area) of steel provided by one strand will classify the beams as underreinforced and thus the steel will yield before failure of the beam.

Specimens cast from each mix will be one beam test specimen, three 0.15-m-diam by 0.305-m (6- by 12-in.) compression test cylinders, three 0.10-m-diam by 0.20-m (4-by 8-in.) splitting-tensile test cylinders, and three 0.08 by 0.10 by 0.46 m (3 by 4 by 18 in.) modulus of rupture test prisms. Slump, air content, and unit weights will be determined for each mix. The beam structural elements will be cast in steel molds, and the procedure followed will include: placement and attachment of the flexible conduit in the mold, concrete placement, compaction by vibration, leveling of exposed surface, and covering with wet burlap and plastic to minimize moisture loss. Companion control specimens will be cast according to appropriate ASTM standards. From 20 to 24 hr after casting the specimens will be removed from their molds, conduit temporarily sealed, and the specimens coated with a brittle shellac-type material to prevent moisture loss and thus simulate mass concrete conditions. The specimens will be cured for 21 days in the laboratory environment. After specimen curing, the strand reinforcement will be inserted into the conduit and post-tensioned to the desired prestressing level taking into account losses due to deformations and anchorage seating. Tendons slated for grouting will be grouted by the following procedure: place beam with one end elevated so the grout will have to be pumped uphill; flush conduit with an alkaline water solution; blow out residual water with compressed air that is dry and oil free; pump grout into conduit until it flows freely and uniformly from the elevated end; close uphill opening; maintain grout pressure 1 min; and seal lower end. The beams will be tested approximately seven days after grouting.

1.5.3.2.2 Grouted vs Nongrouted Tendon Behavior. Relative behavior of grouted and nongrouted post-tensioned beam structural elements will be assessed. The beam geometry presented in Fig. 1.16 will be used for this phase of the investigation. Tests to be conducted will include static flexure, dynamic flexure, and fatigue.

Approximately seven static flexure tests will be conducted. Three of the tests will be grouted post-tensioned tendons having effective prestressing levels of 0.5, 0.6, and 0.7 times f_s' where f_s' is the ultimate tensile strength of the prestressing strand.* Three companion ungrouted post-tensioned beams with the same effective prestressing levels will be tested. The beams will be loaded at the "third points" so that the central length of the beam will not be subjected to external shear forces. The beams will be loaded at a rate of 73 N/sec (1000 lb/min). After the first crack occurs loading will be temporarily stopped and held until cracks can be marked and measured. The beams will then be loaded in increments of 4.45 to 8.9 kN (1—2 kips) until failure occurs by crushing of the concrete, excessive deflection, or strand failure. Cracks will be marked and measured at each load increment. Deflections at the third points and at the center of the beam will be continuously monitored as well as strains in the beam. One additional grouted post-tensioned flexure member will be tested with one end anchorage loosened to determine the effects of a simulated defective anchorage on performance.

Six tests are planned to provide an indication of the rate of loading on relative performance of grouted and nongrouted post-tensioned beams. Three grouted tendon beams will be tested at loading rates of 0.73, 7.3, and 73 kN/sec (10, 100, and 1000 kips/min). A companion non-grouted beam will also be tested at each load rate. Loads and deflections will be monitored during the tests.

An indication of the relative performance of grouted and nongrouted post-tensioned beams subjected to cyclic loadings such as might occur during the pressurization-depressurization phases in a PCRV will be

---

*Unless otherwise specified $0.6f_s'$ will be used as the effective prestressing level for all post-tensioned beam elements.

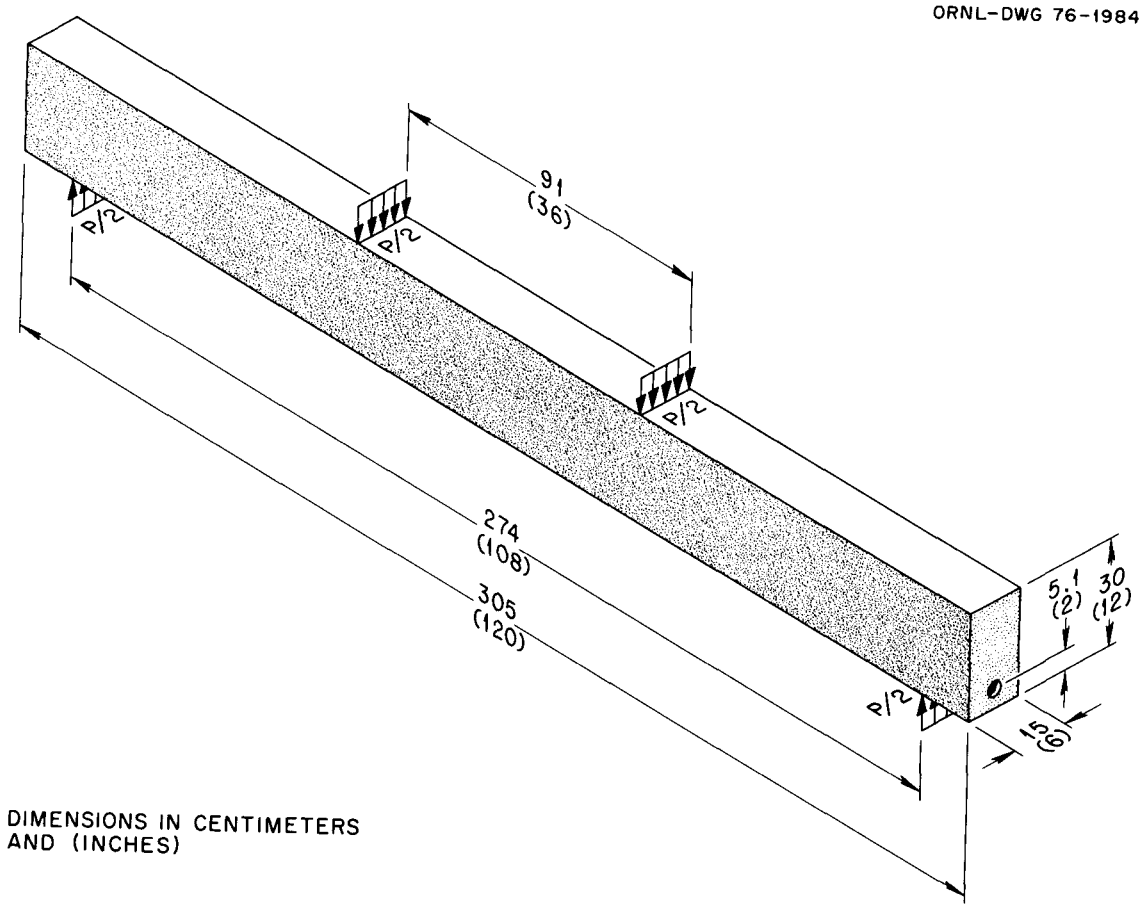

Fig. 1.16. Flexure Test Specimen.

provided by six fatigue tests. Three beams each for the grouted and nongrouted condition will be cycled in flexure at load levels that produce corresponding stress levels in the prestressing ranging from 60 to 80, 60 to 70, and 50 to 70% of f_s'. The specimens will be cycled at a rate of 1 Hz (60 cycles/min)* until either failure occurs or 10^6 load cycles have been applied. Data will be obtained during the tests on load-deflection, cracking (number, depth, width), and number of cycles to failure.

---

*This slow rate of loading is to ensure that the loading frequency is sufficient below the fundamental natural frequency of the beam (≈30 Hz).

1.5.3.2.3 Corrosion Resistance. The corrosion protection provided by grouting of tendons will be evaluated and compared with control (nongrouted-nonprotected) and a conventionally used protection system (No-ox-id or Visconorust 2090P-4). The test fixture presented in Fig. 1.17 will be used to apply loads to the tendons housed in conduits. The specimens will be subjected to a 0.2 *M* NH_4NO_3 solution, which has been shown[11] to produce relatively rapid corrosion failures in prestressing tendons. A total of nine specimens will be tested, in which a nongrouted-nonprotected (control) specimen, a nongrouted-protected (No-ox-id or Visconorust 2090P-4) specimen, and grouted-protected specimen will each be tested for load levels representing 0.6, 0.7, and 0.8 times f'_s. Relative times to failure will be determined.

1.5.3.2.4 New Materials. Potential new materials for tendon grouting and structural applications will be briefly investigated. The material systems include polymer silica and fast-setting refractory cements developed at Southwest Research Institute, and steel-fiber-reinforced concrete, which has been used extensively for pavement applications where flexure stresses are high.

Polymer silica materials are materials that react at a predetermined activation temperature to produce a material system that can withstand service temperatures of 538 to 1093°C (1000—2000°F), obtain compressive strengths of 69 to 138 MPa (10,000—20,000 psi), and develop excellent adhesion to metals. The fast-setting refractory cements cure at room temperature, develop 41 MPa (6000 psi) compressive strength in 24 hr, resist heat cycling and continuous exposure to 1093°C (2000°F), and develop excellent adhesion to metals. The materials will be evaluated as grouting materials. Tests to be conducted include: volume change and bleeding, which will be measured by placing the materials in a cylindrical mold 0.10 m diam by 0.25 m high (4 by 10 in.) and measuring bleed water and shrinkage (or expansion) on curing; compressive strength and rate of strength gain evaluated by testing 51-mm (2-in.) cube specimens; tensile strength measured by conducting splitting-tensile strength tests on 51-mm cubes and modulus of rupture tests on 25-mm (1-in.) by 25-mm by 0.305-m (12-in.) prisms; bond strength evaluated with the "pull-out"

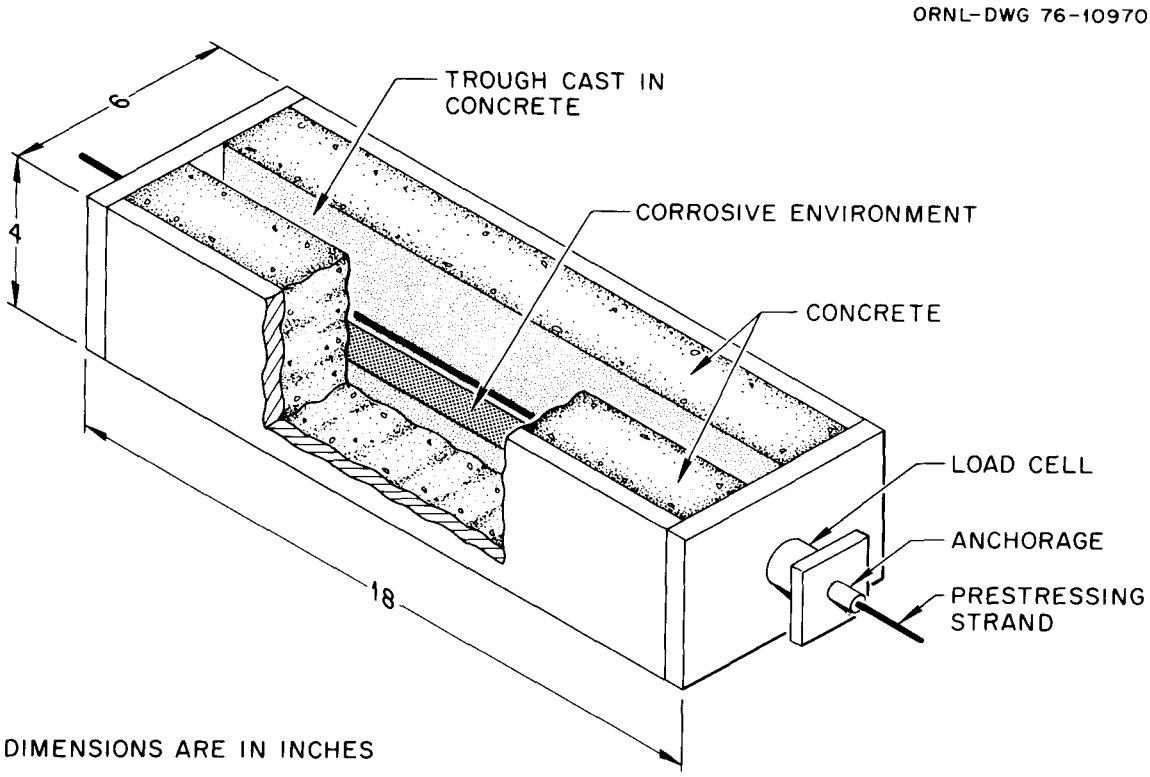

Fig. 1.17. Corrosion Test Setup. Overall Dimensions are 0.10 by 0.15 by 0.45 m.

test setup presented in Fig. 1.18; pumpability and performance evaluated by grouting and testing of a flexure specimen with the geometry presented in Fig. 1.16; and the bond development length* determined on a specimen of the geometry of Fig. 1.16 by grouting the tendon, curing, releasing the anchorage at one end, and measuring with a mechanical gage concrete surface strains at the level of the prestressing.

Fiber-reinforced concrete is concrete consisting of hydraulic cements containing fine or fine and coarse aggregates and discontinuous, discrete fibers, which are blended into concrete during the mixing cycle. The addition of fibers to concrete increases its strength, ductility, and resistance to dynamic loading. An indication of the performance of fibrous concrete as a prestressed member will be assessed by casting

*Bond development length will be defined as the length required for a tendon to develop maximum stress when the anchorage is released.

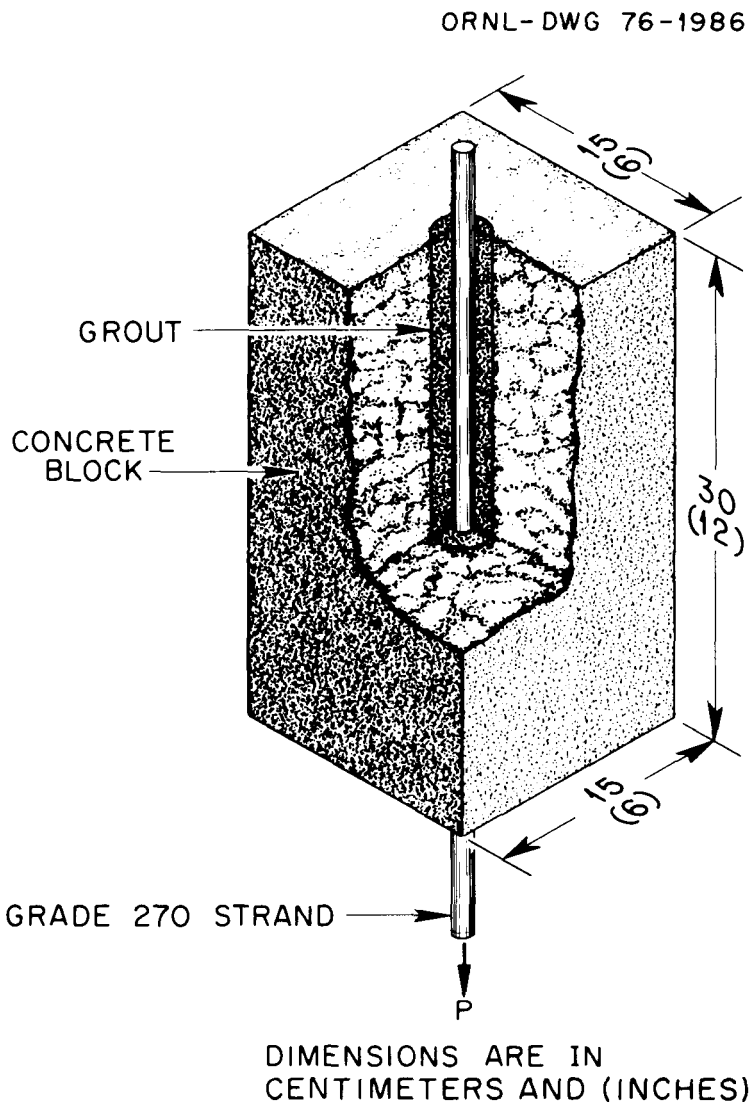

Fig. 1.18. Bond Strength Test Specimen.

six fibrous concrete beams with the geometry presented in Fig. 1.16. Three grouted and three nongrouted beams will be tested with active prestressing levels of 0.5, 0.6, and 0.7 times f'_s for each type beam. Grouting and testing procedures will be identical to those used for the grouted vs nongrouted tendon behavior tests. The relative performance of the fibrous concrete flexure members will be determined by comparing the results with those obtained in the grouted vs nongrouted tendon behavior tests.

1.5.3.2.5 Tendon Monitoring Techniques. Associated with the instrumentation evaluation and development work discussed in Sect. 1.8, a phase of this investigation will be conducted to provide input to an assessment of acoustic emission as a technique for monitoring the structural integrity of PCRVs. The ability of the technique to detect and locate flaws in concrete composite members will be studied. Basic tests will be conducted to identify concrete microcracking and fracture, prestressing tendon fracture, and tendon slippage.

Concrete compression cylinders 0.152 m diam by 0.305 m long (6 by 12 in.) and modulus of rupture specimens 0.076 by 0.102 by 0.458 m (3 by 4 by 18 in.) will be used. The specimens will be strain gaged before testing, and the strain output during testing used to indicate first concrete microcracking (first deviation from linear load-strain curve). A transducer will be attached to each specimen to record emissions during testing. The level of intensity and frequency of emissions will be related to the various stages of concrete fracture.

Prestressing strand will be tested in direct tension by procedures identical to those used to obtain material properties for the prestressing strand. The strand will be instrumented so that stress-strain curves may be obtained during testing. Transducers will be attached both at the ends of the strand (strand used as a wave guide) and perpendicular to the strand. Level of intensity and frequency of acoustic emission during testing will be recorded. The data obtained will be related to the inelastic phenomena occurring in the strand during loading to failure.

The third stage of the acoustic emission study will combine the concrete and prestressing steel into a composite system. The primary mechanism investigated will be prestressing slip. To simplify testing and remove many of the extraneous noises that could mask the data, the specimen geometry of Fig. 1.18 will be used. To simulate tendon slippage a section of the tendon embedded in the concrete will be either wrapped with black electrician's tape or coated with grease. Transducers will be attached to both the concrete and prestressing strand to obtain noise

level and frequency data during testing. Three additional specimens having the geometry of Fig. 1.16 will be tested in flexure. Each specimen will contain a different simulated region of unbonding. Acoustic emissions will be used to determine flaw location and thus provide an indication of the ability of acoustic emission to locate flaws. When practical, acoustic emission data will be obtained during the other test phases.

1.6 LINER AND PENETRATION STUDIES — R. K. Nanstad and D. A. Canonico

Although the PCRV is constructed primarily of prestressed concrete, the penetrations and closures have several thick-section steel members within the vessel. For these components, Section III, Division 2 (ref 20) of the *ASME Boiler and Pressure Vessel Code* refers to the rules of Division 1, Section III and, thus, to the fracture toughness requirements of that document.[21] The toughness requirements in Division 1 were developed for materials used in light-water reactor (LWR) systems. The steels used for PCRV penetrations and closures are different from LWR materials, and the consequences of failure are probably not as severe as for the LWR vessel. Thus, the program was motivated by a need to develop realistic requirements for the PCRV ferritic materials and applications. The objectives of the program are as follows:

1. to define a reference fracture toughness curve for ferritic components of the HTGR primary pressure boundary similar to the K_{IR} curve in Appendix G of Ref. 21,
2. to define a temperature indexing procedure for this curve based on standard materials qualification tests (Charpy V-notch and dropweight) similar to the RT_{NDT} procedure of Ref. 21,
3. to obtain a sufficiently large quantity of fracture toughness data so that a statistically meaningful evaluation of the data can be conducted as a tool to help assess the probability for component failure.

The testing program will include five heats of SA-508 Class 1 steel forgings, five heats total of SA-537 Classes 1 and 2 steel plate, one heat of SA-387 Grade D steel plate, one heat each of SA-182 F11 and F22

forging materials as well as various combinations of plate-to-plate, forging-to-forging, and plate-to-forging weldments. Both weldment and heat-affected zone (HAZ) samples will be tested for weld material properties. Another group of the high-temperature alloy materials will be thermally aged for periods up to 10,000 hr to study the effects of temper embrittlement under simulated HTGR environmental conditions. The testing program will include such tests as Charpy V-notch (C_V) and drop weight impact, subsize and standard [12.8 mm (0.505 in.)] tensile, and, various sized compact tension specimens as well as instrumented pre-cracked Charpy specimens for static and dynamic fracture toughness. Some of the forging materials have been received and testing has been initiated. More recently, some plate material has been received and plans are under way for fabricating test specimens.

Initial testing was performed on the forging material, SA-508 Class 1 (designated F1, F2, etc.). We discovered that the supplier made the material according to a case of the *ASME Boiler and Pressure Vessel Code, Case 1332-6* (1972), which allows some variation in composition requirements. In addition, test sections removed from the cylindrical forgings included the quenched ends of the forgings. There is some question as to the requirements of Section III, ASME Code relative to these forgings. Briefly, one method requires that test specimens be removed at a location (1/4) t (t is nominal thickness) from any surface and at least 1 t from any second surface [i.e., (1/4) t by t]. The other method applies to "very thick and complex forgings" and allows test specimens to be removed 19 mm (3/4 in.) from one surface and 38 mm (1 1/2 in.) from a second surface (i.e., 19 by 38 mm). Only one of the forging sections received (F1) is of a sufficient size to allow limited specimen testing by the (1/4) t by t method. The concern, then, is that testing of specimens obtained from a section close to a quenched edge may produce properties superior to those more representative of the bulk material in the forgings. Because of the importance of reporting fracture toughness and other mechanical property data that are representative to their application, our investigations have thus far concentrated on

characterizing full section properties of forgings F1 and F2. F1 contains greater than 1 t of material, while F2 contains about 1 t.

The chemical composition of F1 is provided in Table 1.1. The test sections, F1-1 and F2-2, were removed from cylindrical forgings of about 4.3 m diam by 0.13 to 0.15 m thick by 2.1 m long (14 ft by 5–6 in. by 7 ft). The forgings were austenitized at 849 to 893°C for 5 hr and water quenched, then tempered at 621 to 639°C for 9 hr. After removal, test sections were subjected to a simulated postweld heat treatment (PWHT) at 593 to 621°C for 13 to 16 hr and furnace cooled. Charpy V-notch impact specimens were machined from the forgings in the CA (circumferential specimen with an axial notch) orientation, while subsize tensile specimens [4.6-mm-diam by 31.8-mm (0.18 × 1.25-in.) gage section] were machined in the circumferential orientation.

Hardness traverses were performed on the sections before and after the PWHT. Contours of constant hardness are shown in Fig. 1.19 for section F1-1. The figure shows, as expected, that hardness decreases from surface to center of the forging. It is apparent that the PWHT softens the material throughout the thickness. Although the differences are not great on an absolute scale, especially in view of usually accepted accuracy of hardness testing, both diagrams show that the cooling rate was greater from the outer surface of the forging during the quenching treatment. The precise quenching procedure is not known. Figure 1.19 indicates the approximate positions of specimens that would be removed by either the (1/4) t by t or 19 by 38 mm methods. From the absolute hardness numbers, we would not expect substantial differences in properties obtained by either method.

The results of tensile testing at room temperature for F1 are given in Table 1.2. The results obtained by the Japanese Steel Works (JSW) are very close to ours. The only significant differences are in the elongation values, which are difficult to compare precisely because of the different size tensile specimens used. At any rate, all specimens satisfied the requirements of SA-508 Class 1 and Case 1332-6.

Table 1.1. Chemical Composition of Forging F1

	Content, wt %												
	C	Si	Mn	P	S	Ni	Cr	Mo	V	Cu	Sn	B	As
Specification[a]	0.35	0.15–0.35	0.40–0.90[b]	0.025	0.025	0.40	0.25	0.10	0.05				
JSW	0.16	0.27	1.27	0.008	0.009	0.37			<0.01				
ORNL	0.17	0.30	1.27	0.010	0.007	0.40	0.20	0.12	0.003	0.05	0.02	0.0003	0.004

[a]Maximum allowed or range for SA-508 Class 1.

[b]Code case 1332-6 allows up to 1.35 Mn provided C < 0.30.

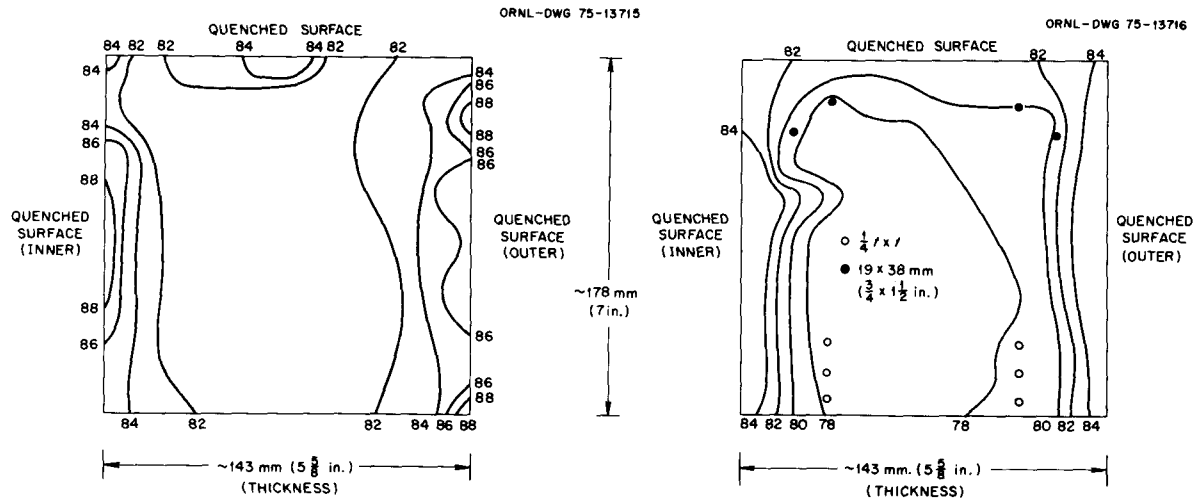

Fig. 1.19. Contours of Constant Rockwell B Hardness in Forging F1 Before (left) and After (right) Postweld Heat Treatment. Points on right-hand diagram show locations from which specimens would be taken by two sampling methods.

Table 1.2. Tensile Data for Forging F1 at 22°C.

Analysis	Sample Location	Strength, MPa (ksi)		Elongation[a] (%)	Reduction of Area (%)
SA-508 Cl-1		241(35) min	483–655 (70–95)	20 min	38 min
JSW	Unknown	345(50)	510(74)	38	77
ORNL	(1/4)t × t	345(50)	496(72)	30	78
ORNL	19 × 32 mm	372(54)	517(75)	24	78

[a]The SA-508 Cl 1 specification is for 50.8 (2 in.) gage length. The ORNL data were obtained on subsize specimens, 4.6 mm (0.18 in.) diam by 31.8 mm (1.25 in.) gage length.

The results of C_V impact tests are shown in Fig. 1.20. The minimum requirement stipulated by SA-508 Class 1 is that at 4.4°C the average value of a set of three specimens must be at least 20.3 J (15 ft-lb) with no specimen lower than 13.5 J (10 ft-lb). The figure shows C_V energy versus temperature for ORNL (1/4) *t* by *t* specimens, JSW specimens (location unknown), and the SA-508 minimum requirement. There is much scatter in the transition range, but that is not unusual. Obviously, the material exceeded the impact toughness requirement by stopping the impact hammer [input energy = 325.4 J (240 ft-lb)] at −7°C. The sensitivity in the transition range was dramatically shown by two adjacent specimens removed from a location near the center of the section. Both specimens were tested at −73°C, and one specimen absorbed 317.3 J (234 ft-lb) while the other absorbed only 29.8 J (22 ft-lb). Another specimen at −73°C stopped the hammer. It is apparent that the C_V results reported by JSW at −7°C and −23°C are substantially lower than the ORNL results. The JSW data, however, more than adequately satisfy the SA-508 criteria. It is not known at this time why such significant differences in impact energy were obtained.

Because of some of the wide differences in behavior of various specimens, metallography, chemical analyses, and electron microprobe studies are being conducted to determine if local variations in microstructure or chemical content might be the cause of such variations. Figure 1.21 shows micrographs of a broken specimen near the center of the forging. The large irregular patches seen in both views are under examination at this time. Testing of forging F2 has shown results that are similar to those presented for F1.

Thus, it is apparent that the material examined to date exceeds the impact and strength requirements for SA-508 Class 1 steel. In fact, a primary concern at this point is that the material is atypical of this class of material, so it could not be used to establish standard toughness criteria. In that regard, then, the further results of fracture toughness testing will have to be analyzed with that perspective.

In addition, there is no evidence at this point, at least with the particular forgings examined, that qualification testing with specimens

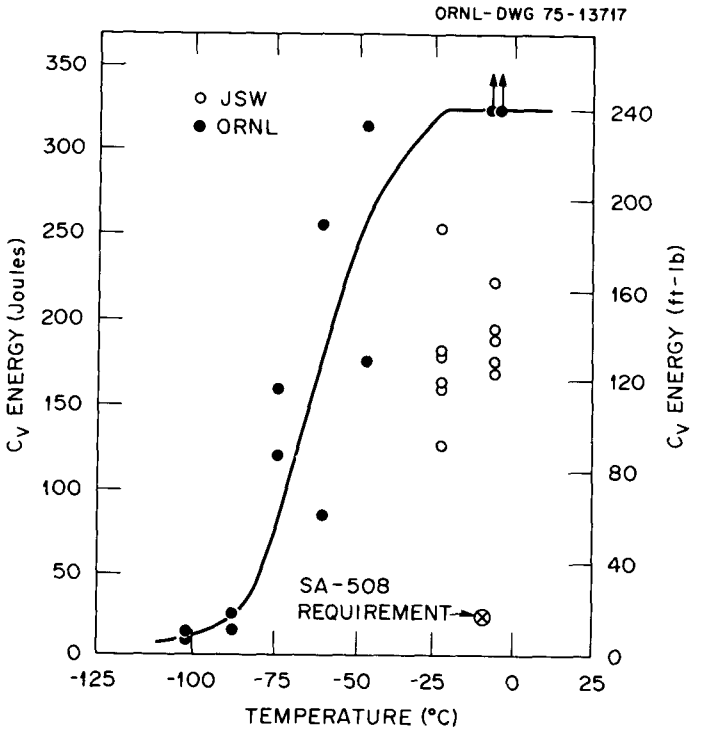

Fig. 1.20. Variation of C_V Energy with Temperature for Forging F1 after Postweld Heat Treatment — (1/4) t by t Specimens.

from the 19 by 38 mm location would result in significantly better results than those from the (1/4) t by t location.

Further tests of the forging materials will include drop weight tests, standard 12.8 mm (0.505-in.) tensile tests, pre-cracked Charpy tests, and various sized compact tension specimens for fracture toughness tests. Plate materials will be tested similarly.

1.7 CONCRETE PROPERTIES IN A NUCLEAR ENVIRONMENT — R. K. Nanstad

The initial objective of this task was to conduct a critical literature review of the properties of plain concrete in a nuclear environment. Development of a program plan for experimentation was planned for FY 1976, but imposed budget limitations deferred implementation of the task. A detailed topical report has been prepared as a result of this review.[22] The following is a summary of the report.

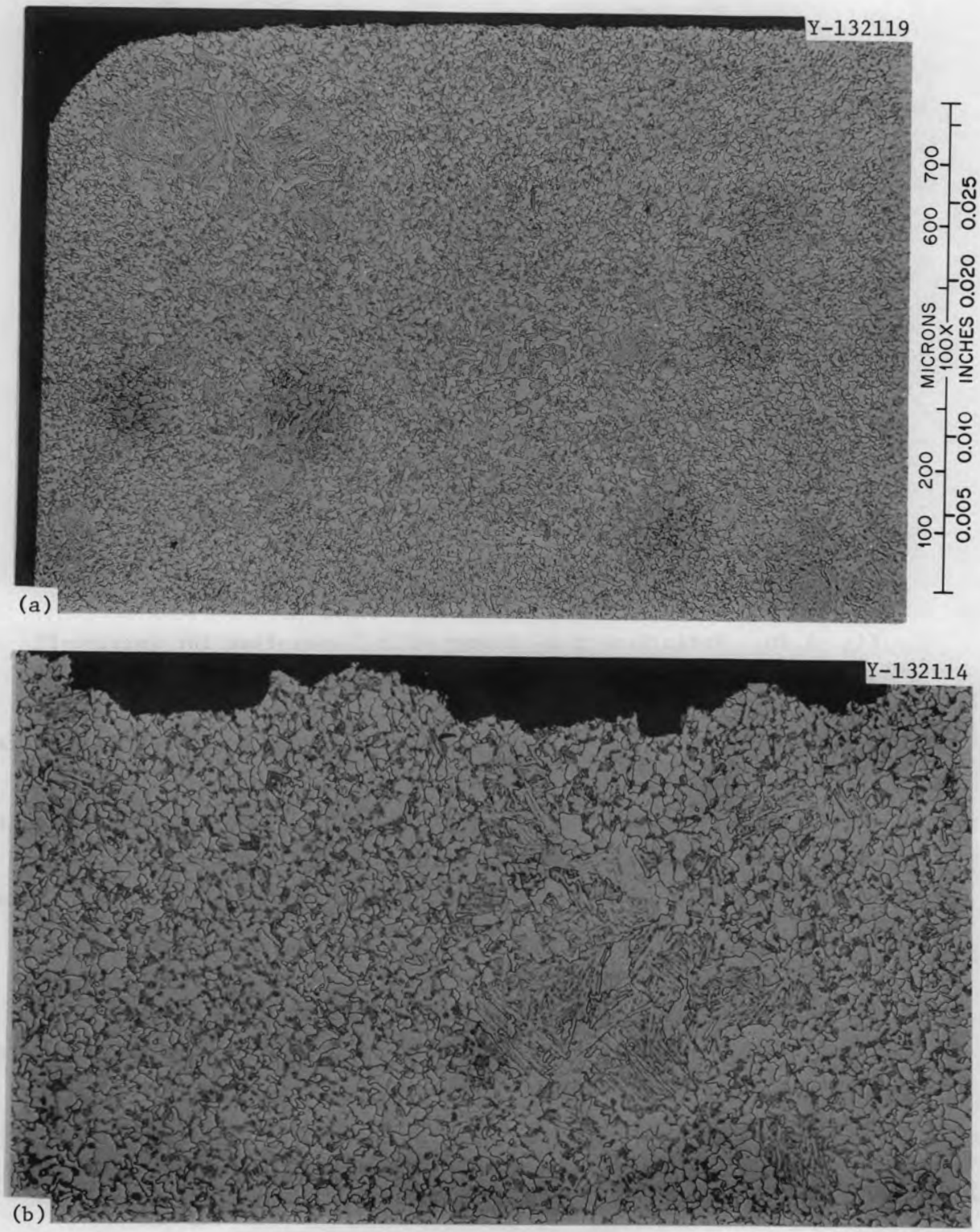

Fig. 1.21. Microstructure from Two Regions of a Fractured Charpy Specimen Taken from Near the Center of Forging F1. (a) 100×. (b) 200×.

The use of a prestressed concrete reactor vessel (PCRV) for nuclear power reactors was first proposed in 1954. Since that time, PCRVs have been constructed for many gas-cooled reactors in France, England, and the United States. Because of their redundant design with regard to safety, prestressed concrete vessels are being considered for other types of energy systems. This review was conducted to determine the state-of-the-art technology of plain concrete used in a PCRV for the high-temperature gas-cooled reactor (HTGR). The report considers the effects of current and projected PCRV operating conditions on concrete properties and the possible effects on the structural behavior of the vessel.

A brief description of typical PCRVs and the design philosophy are provided as well as a general discussion of concrete materials used in PCRV-type structures. The report emphasizes throughout that concrete is a general term for a class of materials that can vary widely in their properties and applications. It is a recognized fact that direct comparison of available research results on concrete structures is extremely difficult because of the differences in mixture design, constituents, curing procedures, curing time, age at testing, test procedures, and moisture conditions. For example, the moisture condition of concrete alone is a major topic. Mass concrete is known to lose its free moisture very slowly. However, temperature gradients will influence the rate of moisture migration, and the free moisture content has a direct effect on the mechanical and physical properties of plain concrete.

The review centered on representative published research reports, which have considered the effects of temperature on such properties as compressive strength, tensile strength, modulus of elasticity, Poisson's ratio, shrinkage and creep, coefficient of thermal expansion, and thermal conductivity. Additionally, the effects of multiaxial loading and the mechanisms involved in temperature effects are discussed. Other topics include the effects of local hot spots on the vessel concrete and model testing.

A normalized comparison of all data reviewed on compressive strength and elastic modulus showed that those properties decreased with increases

in temperature, time of exposure, free moisture content, and number of thermal cycles (generally, tensile properties parallel compressive properties). Graphs are provided to present data from both sealed and unsealed specimens tested at room temperature (after exposure to an elevated temperature) and at the exposure temperature. Specimens are sealed with various kinds of impervious materials so that free moisture will be retained within the concrete to simulate the conditions in a mass concrete structure. Sealed concrete generally showed more deterioration at elevated temperatures than unsealed specimens, with the degree of deterioration increasing substantially above 100°C. As could be expected for the wide range of variables represented, the scatter in results is substantial. The most conservative interpretation of the data would suggest losses of 70% and 60% in compressive strength and elastic modulus, respectively, at 150°C. In contrast, the most liberal interpretation could show improvements in both properties over those at room temperature. Limestone aggregate concrete appears most susceptible to degradation at temperatures over 100°C, while silica aggregate concrete appears to have high resistance to elevated temperatures.

Elevated temperatures enhance the creep of concrete; however, a maximum in the curve of specific creep rate versus time has been reported at temperatures in the range 50 to 150°C. The specific creep of sealed specimens, at least below 100°C, is less than for unsealed specimens.

As temperature increases and drying proceeds, the thermal conductivity of concrete decreases. The coefficient of thermal expansion also decreases with loss of moisture but increases very slightly with temperature up to 250°C.

The biaxial state of stress is of most interest for massive structures such as the PCRV, and the most reliable data indicate at ambient temperatures a maximum biaxial compressive strength of 1.25 times uniaxial strength. The development of compression test equipment that minimizes end restraints is imperative to the understanding of concrete behavior under multiaxial loadings as well as for the collection of reliable design data. The observance of a critical stress level, which could be as low as 50% of ultimate strength, in biaxial testing deserves serious consideration for its ramifications to structural integrity.

Conclusive evidence is lacking for radiation effects on normal structural concretes. The *ASME Boiler and Pressure Vessel Code* allows for an exposure to concrete of 1.0×10^{21} neutrons/cm^2. However, severe damage may occur at a total neutron fluence of 10^{19} to 10^{20} neutrons/cm^2. Thus, the ASME Code should be reevaluated in light of this data.

Although there is not much data on moisture migration in mass concrete at sustained temperatures over 100°C, moisture migration increases and should require serious evaluation.

The limited data available indicate that hot spot temperatures of 200 to 250°C for up to three months exposure will not cause serious damage to the concrete at locations away from steel reinforcing. However, cracking may occur at concrete reinforcement junctions. Although there is no evidence to suggest that sustained exposure of normal concretes to current PCRV normal operating conditions will result in any significant loss of properties, the lack of knowledge concerning moisture migration in mass concrete and the strong effects of temperatures above 100°C on plain concrete with retained free moisture do not give support for PCRV operation above current limits or for postulated off-design accident conditions.

The report provides many recommendations for further study. A major recommendation is to perfect the design, testing, and evaluation of PCRV structural models. It is not felt that testing of small plain concrete specimens using accepted methods can provide data for predicting the behavior of a large prestressed concrete structure. The ultimate goal of the model testing program, which would include simultaneous small specimen testing, should be the development of an analytical procedure that will describe the model behavior and also identify the contribution of various plain concrete properties. Thus, reasonable predictions of PCRV behavior could hopefully be derived from small specimen laboratory test results.

Other recommendations include: development of multiaxial equipment and testing techniques to measure strength and creep properties, investigation of critical stress levels, refinement of techniques for testing sealed specimens both above and below 100°C, improving the resistance of limestone concrete to elevated temperatures (primarily over 100°C), and

more detailed chemical and microscopic studies of sealed concrete exposed to high temperatures. Additional studies necessary for extensions of present PCRV design include: moisture migration studies at temperatures over 100°C, testing to verify the occurrence and/or validity of a maximum in the creep or creep rate versus temperature curve for sealed concrete, concrete material development to maximize resistance to temperature, and determination of radiation effects on plain concrete and the doses at which significant deterioration initiates.

It is felt that a detailed feasibility study of other vessel concepts such as the hot liner and segmented concrete designs should be performed. A study is also recommended to establish more precise standardization for concrete mixtures used for nuclear applications.

The report provides an unusual amount of detailed information obtained from the published literature. The intent was to show the great variations in materials and testing procedures used to obtain the available published "concrete" properties. The conclusion was reached that any discussion of concrete properties for a particular structural application requires a more specific description than the term "concrete."

1.8 INSTRUMENTATION EVALUATION AND DEVELOPMENT — D. J. Naus

1.8.1 Background

Instrumentation of PCRVs is required to determine strain distributions, deflections, stresses, temperature distributions, crack magnitudes and locations, forces in prestressing, and free moisture content. The quantities measured are used to assess the safety and reliability of PCRVs for short- and long-term operation, to assess correctness of calculations and assumptions of analytical techniques, and to assess the complex behavior of the vessels, especially monitoring of structural integrity for extended periods of operation. The methods of measurement are dictated by cost, life expectancy, accuracy, recording or data acquisition requirements, and long-term stability at normal and elevated temperatures and under irradiation.

The measurement of stress (or strain) in concrete structures is much more complex than it might appear at first. Concrete is a heterogeneous material composed of a hydrated portland cement paste matrix, which may contain unhydrated cement particles, voids, water, and fine and coarse aggregate particles. Behavior of the concrete material system is a function of the relative quantities of its constituents and their response to loading and environmental influences. Characteristics of concrete include a nonlinear stress-strain response, changing values of elastic modulus and strength properties, time-dependent deformation, and differences in tensile and compressive behavior. To further complicate stress and strain measurements in concrete, the loadings are often biaxial or triaxial, measurement of one quantity can influence the results of another quantity, and the instrumentation to measure quantities of interest (stress, strain, moisture, temperature) generally must be embedded in the concrete and thus disturb the continuity of the material if the properties of the instrument are not properly matched to the concrete properties.

Numerous commercial concrete embedment instrumentation systems are presently available and are designed for measurement of strain, stress, and moisture. Since a major safety consideration of a PCRV is that its structural integrity be monitored over its lifetime, the instrumentation systems must provide reliable data for extended periods of time (20—30-year vessel design life). However, effective installation methods, long-term stability, and reliability of the sensing elements in a PCRV environment have not been established.

The investigations being conducted under this task are designed to provide information on the performance of instrumentation for PCRVs. Instrumentation systems for measurement of temperature, prestressing forces, concrete cracking, stress, strain, and moisture are being examined. Acoustic emission as a possible technique for structural integrity monitoring of PCRVs is also being investigated. The work covered in this reporting period is divided into three areas: (1) establishment of current instrumentation state of the art, (2) development of an experimental program for instrumentation evaluation and development, and (3) conduction of an overview of acoustic emission.

1.8.2 Concrete Embedment Instrumentation: Present Status

Well developed and reliable methods exist for measurement of temperature and prestressing forces and detection of concrete cracks. Temperatures are often measured with the same instrumentation used for reading stress or strain; also, readings are readily obtained with thermocouples or thermistors. Forces in nongrouted prestressing tendons are routinely monitored by use of load cells or strain gage techniques. PCRVs have been designed so that cracks that may develop in the concrete as a result of unusual loading conditions are readily detectable by visual techniques, crack gages, acoustic emission, or possibly holography. Strain, stress, and moisture determination, however, are not as well established as the above.

Strain measurements can assess the distribution of short-term stress, evaluate concrete creep and shrinkage and its effects on prestressing, and provide data for future designs. Problems in strain measurement in PCRVs arise from the concrete environment within which the gages must operate and from reactor operation (i.e., gage installation factors, highly alkaline humid environment, elevated temperature, and radiation). Strain in concrete has been measured by electrical resistance, acoustic, electrical inductance, electrical capacitance, fluidic, and mechanical techniques. Table 1.3 summarizes the characteristics of several commercially available strain measurement devices. Since PCRVs are a relatively new development and the environment within which the gages must operate is unique, data are inadequate to evaluate the effects of temperature, irradiation, and stability on gage performance over the 20 to 30-year design life of the vessels. Consequently, laboratory investigations conducted in representative environments are required.

Evaluation of the relaxation of stress and the identification of highly stressed regions in PCRVs are important from both structural integrity (safety) and design considerations. Strain measurements cannot directly identify time-dependent stresses because the measured strain in PCRVs also contains creep, shrinkage, and thermal components; stress may be induced without a corresponding strain; the modulus of elasticity of the concrete depends on environmental time factors; and the state of

Table 1.3. Strain Gage Instrumentation for PCRVs

Type	Gage Length (cm)	Gage Length (in.)	Strain[a] Range (με)	Temperature Range (°C)	Temperature Range (°F)	Sensitivity[a] (με)	Gage Factor	Stability	Approximate Cost/Gage ($)	Comments
Electrical Resistance										
Unbonded wire Type A	10–50	4–20	1050–2100	65	150	2–6	2	Fair	35–75	Proven reliability
Unbonded wire Type B	10–25	4–10	+500 to −1000	−30 to +70	−20 to +158	4–7	2	Fair	35–40	Proven reliability
Unbonded wire Type C	10+	4+	3000	120	250	5	2.2	Good	100	Contains built-in standard
Polyester encapsulated	1–13	1/2–5	20,000	200	400	10	2	Poor	5–20	Stability in moist environment questionable, volume change of plastic
Metal encapsulated	15	6	limited by carrier	−45 to +65	−50 to +150	10	2.1	Fair	25	Bond deterioration under cyclic load, embedment difficult
Single wire	5–15	2–6	±20,000	−200 to >300	−320 to >600		2	Good	55–150	High-temperature use, small cross section requires careful placement
Semiconductor	0.1–1	1/16–1/2	+3000 to −10,000	−70 to +500	−100 to +1000		50–250	Good	18–25	Very limited concrete application, stable, high-temperature use
Acoustic										
Vibrating wire Type A	7–14	3–5.5	>1000	80	180	0.5		Good	85–95	Used extensively
Vibrating wire Type B	14	5.5	>1000	80	180	0.5		Good	75	Used extensively
Vibrating wire Type C	10	4.0	±1500			<0.5		Good	195	Dual wire, temperature compensation
Vibrating wire Type D	13	5.0	+1000 to −2000			0.5		Good	160	Temperature measurement capability
Vibrating wire Type E	10	4.0	±1500	−40 to +80	−40 to +175	0.1		Good	150	Temperature measurement capability
Radiofrequency cavity	21	8.3	3600	to 850	to +1570[b]	1.2		Good		Expensive, requires special signal generation equipment
Inductance gage	10	4	30,000			±10		Good	200–300	Stable, low gage modulus, limited number of gages fabricated

[a] "Microstrain" units: fractional strain × 10^6.

[b] Range stated is for short-term exposure; for extended exposure, 93°C (200°F).

stress is primarily multiaxial. In regions of a PCRV where stress determinations are required, direct measurement is most desirable. Stress can be measured in plugs or on flat plates embedded in the concrete. The stress plug method requires observation of optical patterns related to a stress state, so the plugs must be used on the surface or provided with an observation hole. The flat plate or stress meter, which relates the deflection of a plate to stresses, is limited to compressive stresses, requires temperature corrections, is limited to temperatures below 88°C (190°F), and is large and expensive. Table 1.4 presents available stress meters for embedment in concrete. More detailed evaluation of these meters needs to be conducted in representative PCRV environments, and there is a definite need for development of a stress meter that will measure tensile stresses in concrete.

The loss of moisture or its movement from one section of a concrete structure to another influences the concrete properties, particularly neutron shielding and thermal conductivity but also shrinkage, creep, loss of prestressing force, and cracking. Moisture can be determined in concrete by neutron or gamma-ray absorption, electrical resistivity, dielectric constant, or filament length change. Neutron source techniques for internal concrete moisture measurement require an access tube for insertion of a probe, are highly temperature sensitive, have questionable accuracy, and are not economically amenable to automatic data acquisition. Disadvantages of the electrical resistivity techniques include questionable long-term stability, results influenced by concrete materials properties (calibration curve), and limited accuracy. Changes in dielectric constant may be related to moisture content, but the long-term stability is questionable and temperature effects must be considered. Length change of a filament is limited to relatively low temperatures and must be temperature compensated. In general, the accuracy of the above techniques for moisture determinations in concrete is only within ±20%, so the information obtained is more qualitative than quantitative. Determination of the long-term stability and the development of more reliable and accurate free moisture measurement devices are required for use in PCRVs.

Table 1.4. Stress Meters for PCRVs

Type	Extent, m(in.)	Thickness		Stress Range		Temperature Range		Sensitivity		Approximate Cost/Gage ($)	Comments
		(mm)	(in.)	MPa	(psi)	(°C)	(°F)	(kPa)	(psi)		
I	0.18(7) diam	15	0.6	2.8–10.3	400–1500	<65	<150	20–70	3–10	250	Inability to measure tensile stresses; measures temperature
II	0.16(6 1/4) diam	13	1/2	2.8–11.7	400–1700	−25 to 70	−15 to 160	28–41	4–14	200	Inability to measure tensile stresses; measures temperature
III	0.070 × 0.14 (2 3/4 × 5 1/2)	2.4	3/32	0–34	0–5000	−20 to 90	0 to 190	±7	±1	270	Requires hydraulic lines; reliability and accuracy questionable

1.8.3 Instrumentation Evaluation Program

We are evaluating and developing embedment instrumentation for strain, stress, and moisture determinations in PCRVs. During the present reporting period strain instrumentation was primarily considered. Commercially available concrete embedment strain sensors and their associated readout instrumentation were procured, characteristics of the instrumentation to be evaluated were identified, and an evaluation program was planned. A limited number of commercial stress cells have also been obtained for evaluation.

Polyester-encapsulated electrical resistance, wound-wire resistance, single-filament resistance, and vibrating wire concrete embedment strain gages are to be evaluated relative to general performance, performance in a representative PCRV environment (stability, accuracy), and performance in extreme environments.

1.8.3.1 General Gage Performance Characteristics

The general performance characteristics of commercially available strain gage instrumentation are to be assessed. Characteristics to be considered include: range, sensitivity, accuracy, response, data acquisition requirements, cost factors, accuracy of calibration information supplied by manufacturers, and resistance to damage during construction. The range, sensitivity, accuracy, response, data acquisition requirements, and cost factors will be primarily obtained from data supplied by the manufacturers; however, during the experimental portions of the gage

evaluations program the manufacturer's performance data will be checked. Calibration data and gage durability during PCRV construction will be evaluated through laboratory investigations.

The accuracy of calibration data supplied with each gage by the manufacturers will be checked. Strain gages will be cast in 0.15-m-diam by 0.53-m-long (6 by 21-in.) cylindrical test specimens with the gage aligned with the cylinder axis. Only one type of gage will be cast in each test specimen. One day after casting, the test specimens will be sealed with an epoxy coating to reduce moisture migration and thus minimize shrinkage effects. Mechanical gage points [0.20 m (8 in.) gage length] will be installed two days after casting at 120° intervals around each specimen's circumference, and during the curing period (>28 days) readings will be taken using a mechanical gage and compared with those obtained from the embedded gages. Just before the cylinders are tested, strain gages will be installed 180° apart aligned with the cylinder axis. The cylinders will be loaded in compression in small increments, and strain readings will be obtained at each increment. The results obtained from the embedded gages will be compared with those obtained from the electrical resistance strain gages and mechanical gages and used to evaluate the accuracy of supplied calibration information.

Whether or not the gages require embedment in a briquette for protection during construction will be determined by monitoring gage performance after the gages are subjected to simulated PCRV construction sequences. The gages will be positioned in a form and the concrete placed and vibrated with an internal vibrator. Variables considered will be the length of vibration (5—30 sec) and location of the internal vibrator relative to the gages [adjacent to gage to 0.46 m (18 in.) from gage].

1.8.3.2 Gage Performance in Representative PCRV Environment

Each type of gage will be evaluated for accuracy and stability in a representative PCRV environment. A sealed test specimen 0.41 m diam by 1.02 m long (16 by 40 in.) cast from representative PCRV concrete will be used. It will contain a stress cell, thermocouples, and at least one of each type of strain measurement devices. After curing, the concrete

specimen will be placed into a uniaxial loading frame containing a hydraulic ram by which compressive forces may be applied. Before loading, the cylinder will be heated with a thermal blanket. The specimen will be subjected to load and thermal cycles to simulate the pressurization-depressurization and heat-up cool-down cycles, respectively, to which a PCRV would typically be subjected. Stress, strain, and temperature will be read throughout the test. Gage stability and accuracy will be assessed by comparing stress readings from the stress cell(s) to readings from a calibrated hydraulic loading ram (loads converted to stress since cylinder has a known area), strain readings from embedded gages to readings obtained from mechanical gages, and temperature readings obtained from the stress and strain measurement devices and the thermocouple outputs.

Pending location of a suitable source and costs not being prohibitive, the performance of the embedment strain gages under irradiation will be evaluated. Samples of each of the gages will be subjected to radiation exposures of approximately 10×10^{20} neutrons/cm^2, the exposure limit for concrete set by the ASME Code.[20]

1.8.3.3 Gage Performance in Extreme Environments

The embedment strain measurement devices will also be tested under nontypical operating conditions, such as overpressurization or overheating. Test series planned include environments corresponding to: (1) 100% relative humidity, (2) elevated temperature and pressure, and (3) radiation exposures in excess of limits prescribed in the ASME Code.

Evaluation in 100% relative humidity will be conducted in two phases, in an environment more severe than normally encountered in service. Initially each type of strain measurement device will be placed into a basic water solution (water plus cement) simulating the concrete moisture environment that the gage would see. Strain and resistance to ground will be read as a function of time. In the second phase another gage of each type will be placed into a water bath. Temperatures and pressures will be varied up to 65.5°C (150°F) and 3.5 MPa (500 psi), respectively. Strain and resistance to ground will be read.

The second test series will use the 0.41-m-diam by 1.02-m-long (16- by 40-in.) concrete specimens for gage evaluations in a representative PCRV environment. The specimens will be subjected to temperatures above 65.5°C and uniaxial stresses above 3.5 MPa. Gage performance will be evaluated in the same manner as it was for the evaluations in the representative PCRV environment.

Exposure of the strain gages to excessive irradiation will be considered in the third test series. Gage performance will be monitored to exposures exceeding 10×10^{10} neutrons/cm^2.

1.8.4 Overview of Acoustic Emission for In-Service Structural Integrity Monitoring of PCRVs

1.8.4.1 Background

Techniques used for nondestructive testing of nuclear power facilities to evaluate their safety and to assure their maximum availability have included dye penetration, computerized remote ultrasonic evaluation, holographic techniques, and remote television coverage. Application of many of these techniques is time consuming and costly. Relatively recent advancements in nondestructive testing utilizing acoustic emission have made this system potentially viable for in-service monitoring of the structural integrity of pressure vessels.

Acoustic emissions are small-amplitude elastic stress waves generated during material deformation resulting from a mechanical or thermal stimulus. The stress waves are detected by transducers as small displacements on the specimen surface. The emissions are classified as being either continuous or burst. Continuous acoustic emissions are low-level, high-signal-density emissions such as might be observed during tension testing of unflawed specimens. Burst acoustic emissions are generated when a plastic zone or microcracks form at a crack tip, or crack extension occurs. Characterization of these stress wave emissions provides an insight into the type of inelastic deformation occurring: amplitude of the stress wave emission indicates the magnitude of flaw extension, rate of stress wave emission indicates the rate of flaw propagation, and the total acoustic emission energy generated is proportional to the loss of structural integrity.

Instrumentation systems for acoustic emission monitoring generally include transducers, preamplifiers, filters, processors, and recorders. Transducers (sensors), when stimulated by stress waves, transform the mechanical excitations into electrical signals. Piezoelectric crystals, specially designed for the 20 kHz frequency range of interest, are generally used as transducers because of their high sensitivity and stability. The signal from the transducer is fed to a preamplifier, which is located as close as possible to the transducer to provide a good signal-to-noise ratio and to match impedances (long cables may be used without adversely affecting signal-to-noise ratio). Emerging from the preamplifier the electrical signals are processed by signal conditioners such as: filters (enable selective rejection of certain unwanted signals), main amplifiers (provide a variable and calibrated gain), and discriminators (selectively reject signals having certain spatial or temporal characteristics). After conditioning, the electrical signals generally exceed 1 V and are ready for processing. Several processing techniques are available, including those that: count the number of times the signal crosses a threshold value of 1 V (number of crossings is proportional to magnitude of the acoustic emission signal and thus an approximate measure of the energy or severity of the event), extract electrical energy by an energy module (compares count and energy), count number of events and not threshold crossings, perform spectral analysis, and perform amplitude distribution. Presentation of the data may be by punched tape, printed tape, magnetic tape or disk, cathode ray oscilloscope display, or graphic plotters.

Flaws may be located by use of data from an array of three or more coupled transducers. Location of an acoustic source is usually established through analysis of differences in time of propagation of the stress wave emissions to the multiple sensor array. A typical sequence of events for flaw location on a two-dimensional surface may be described as follows. An acoustic event produces an expanding spherical wave, which impacts one of the transducers, starting a clock. The time of arrival of the stress wave to the other transducers of the array is established. When the rate of propagation of the stress wave in the material and the arrival times

are known, a locus of points (circle for two-dimensional case) may be established for each transducer to indicate possible locations of the source. The intersection of the circles identifies the flaw location.* Commercially available flaw location systems use analog or digital computers to perform all analyses. Statistical methods may be incorporated into the system for data processing to develop probability maps for the structure being investigated so that areas with a high probability of containing flaws may be identified. Tentative advantages of acoustic emission include: access to entire vessel is not required; 100% of the vessel volume may be inspected; the vessel may be monitored in service; the system possesses the capability to detect, locate, and categorize the approximate severity of a growing defect; and the technique requires minimal time. Potential disadvantages or problem areas of the system, which must be overcome, include: background noise, which may mask defect emissions, will have to be filtered out; hydrotest stresses (proof tests) are not truly representative of in-service stresses; time-temperature annealing effects may influence results; the vessel should be continuously monitored so all events may be identified; and, unless the instrumentation is permanently mounted, down time is required for instrumentation and calibration before each test.

1.8.4.2 Applications to PCRVs

The state of the art of acoustic emission has advanced very rapidly in the last few years through numerous applications. In fact, at least one company has developed an acoustic emission system that is being used to inspect nuclear power plant coolant systems and metallic containment vessels. However, only limited applications of acoustic emission have been made to concrete material systems.

Results obtained from acoustic emission applications to concrete material systems tend to indicate that onset and failure progression can be detected, stress wave emission characteristics may be correlated to

---

*Flaw location in a pressure vessel may be established to an accuracy of approximately one-half the vessel wall thickness.

material modulus of elasticity, loading levels can be evaluated nondestructively, flaws may be located, and the sensitivity of acoustic emissions for detection of failure processes and deformation in materials is superior to conventional techniques. The results are sufficiently encouraging to indicate that acoustic emission may be feasible for in-service monitoring of the structural integrity of PCRVs.

1.9 LONG-TERM CREEP AND MOISTURE MIGRATION STUDIES — J. P. Callahan

An extensive study was undertaken under the earlier PCRV Research and Development Program to evaluate creep behavior of concrete under various uniaxial, biaxial, and triaxial states of stress while it was exposed to temperatures of 24 and 65.6°C. The study was divided into two phases. One phase, conducted at the U.S. Army Engineers Waterways Experiment Station [Interagency Agreement AT-(40-1)-3636], consisted of an experimental study of creep behavior of concretes made with three different aggregate types (chert, limestone, and graywacke). The final report is being prepared at the Waterways Experiment Station.

The second phase conducted at the University of Texas (Subcontract 2864) consisted of an in-depth study of creep behavior of a limestone aggregate concrete selected as most typical for use in constructing PCRVs in the United States. The last phase of this investigation consisted of subjecting 0.15-m-diam by 0.41-m (6 by 16 in.) cylindrical concrete specimens to sustained uniaxial compressive stresses of 4.1 and 16.5 MPa (600 and 2400 psi) for periods up to 5 years. The 12 cylinders encompassed curing periods of 90, 183, and 365 days and both as-cast (sealed after initial moist curing) and air-dried (unsealed after curing) conditions. The strains were monitored with vibrating wire strain gages that were embedded in the specimens, as shown in Fig. 1.22.

The total strain-time relationships of the specimens are shown in Figs. 1.23 and 1.24. Unstressed shrinkage specimens were included in the overall study; however, the results were inconsistent, and additional specimens would be required to accurately estimate the shrinkage. Since the strains resulting from the 16.5 MPa loading were relatively large, the

error resulting from omission of shrinkage appears to be small. However, the error will probably have a more significant effect on the estimated creep behavior of the 4.1 MPa test specimen.

A comparison of the creep strain-time relationships for specimens under 16.5 MPa stress shown in Fig. 1.23 generally indicates that concrete having longer curing periods exhibited smaller axial and radial creep strains; however, this effect diminished with time and in one case,

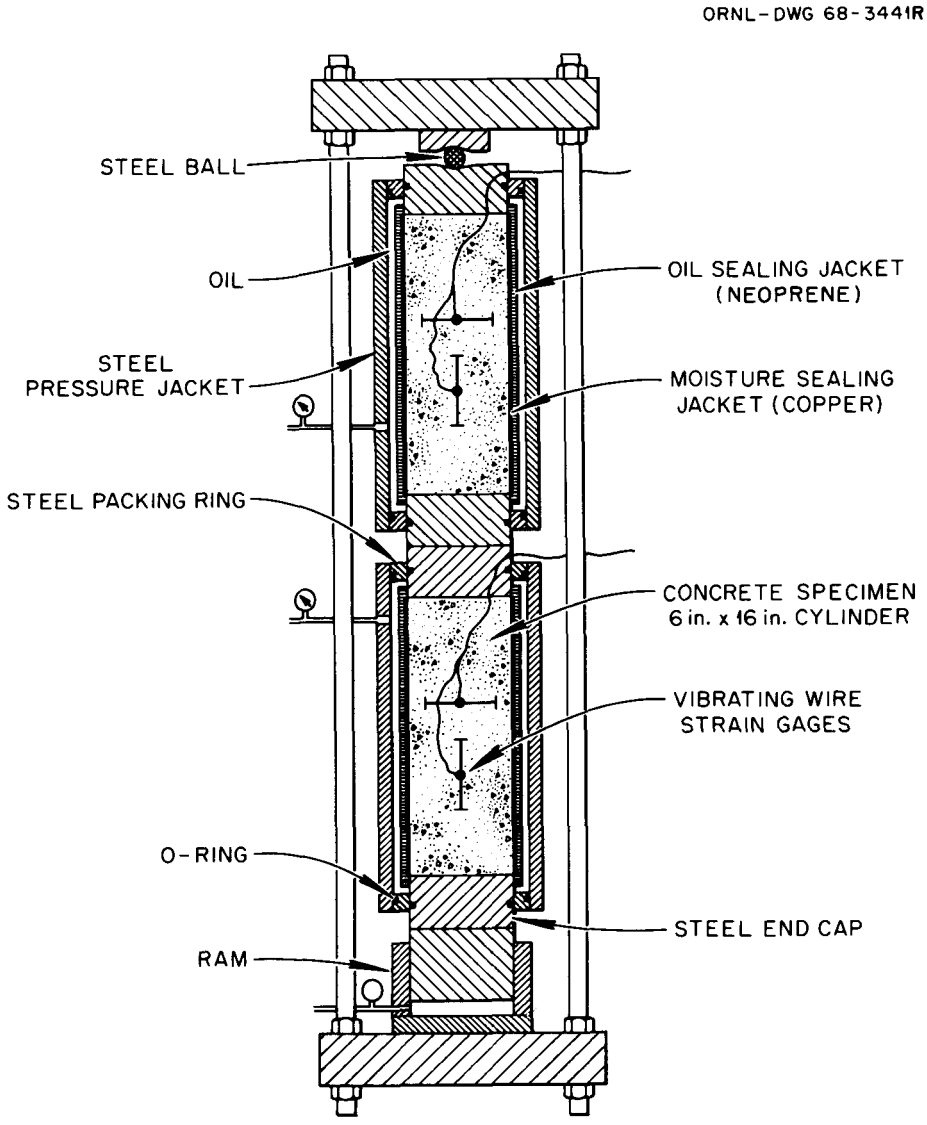

Fig. 1.22. Triaxial Test Unit Used at The University of Texas.

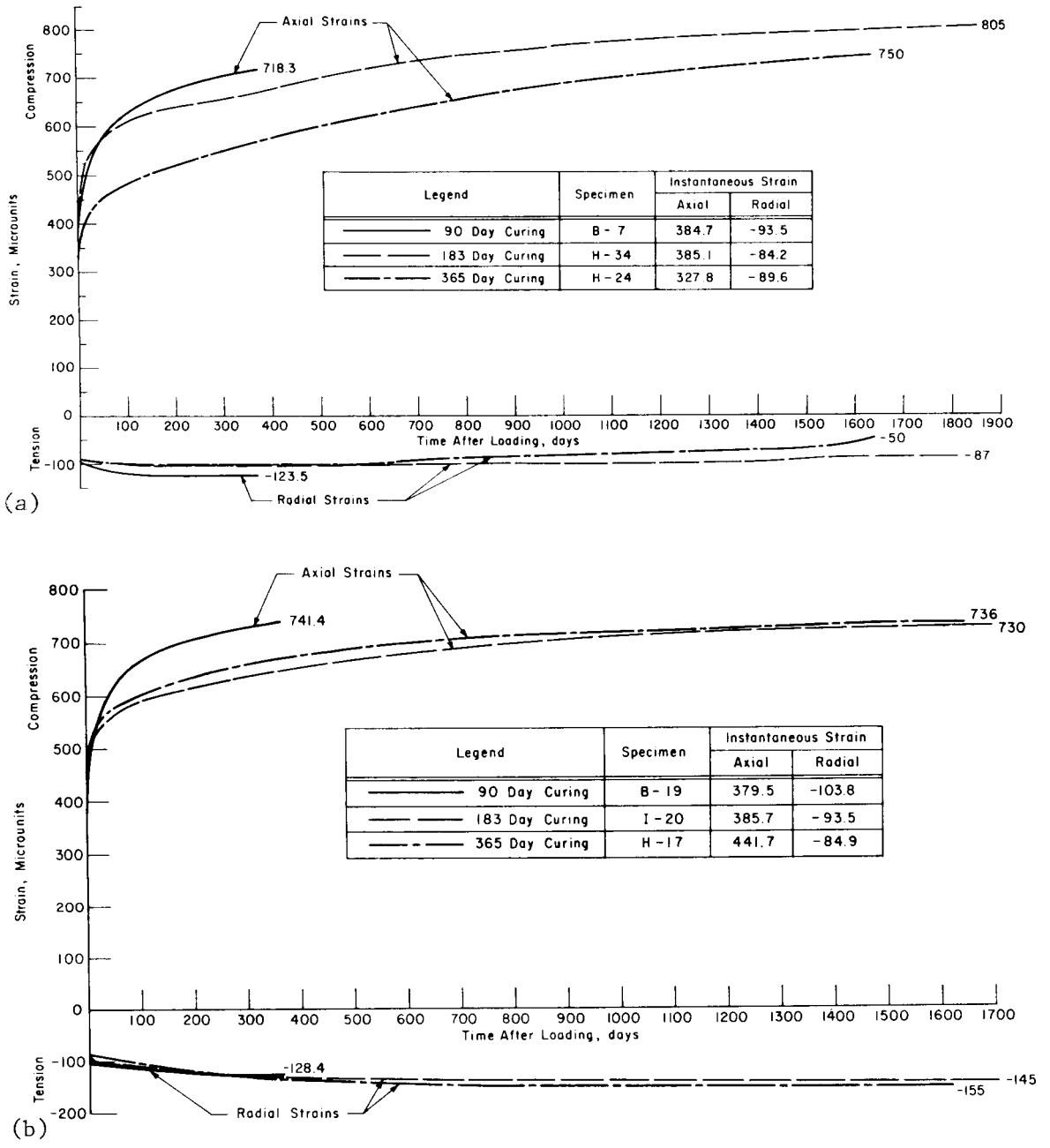

Legend	Specimen	Instantaneous Strain	
		Axial	Radial
90 Day Curing	B - 7	384.7	-93.5
183 Day Curing	H - 34	385.1	-84.2
365 Day Curing	H - 24	327.8	-89.6

Legend	Specimen	Instantaneous Strain	
		Axial	Radial
90 Day Curing	B - 19	379.5	-103.8
183 Day Curing	I - 20	385.7	-93.5
365 Day Curing	H - 17	441.7	-84.9

Fig. 1.23. Total Axial and Radial Strain Relationships with Uniaxial Stress of 16.5 MPa (2400 psi). (a) As-cast specimens. (b) Air dried. University of Texas drawings.

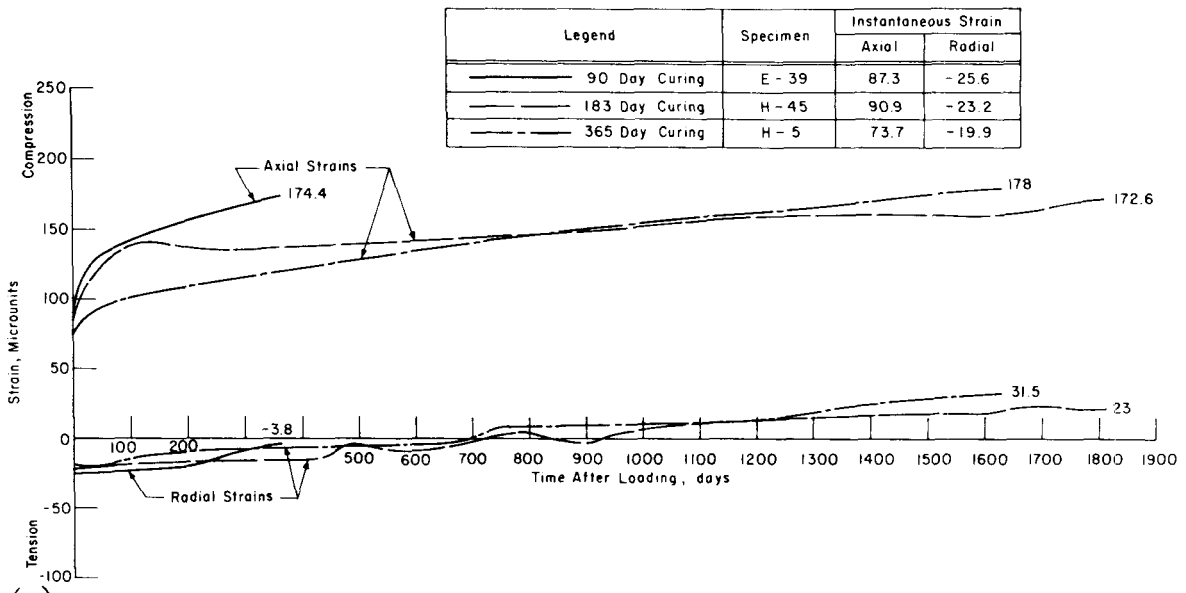

(a)

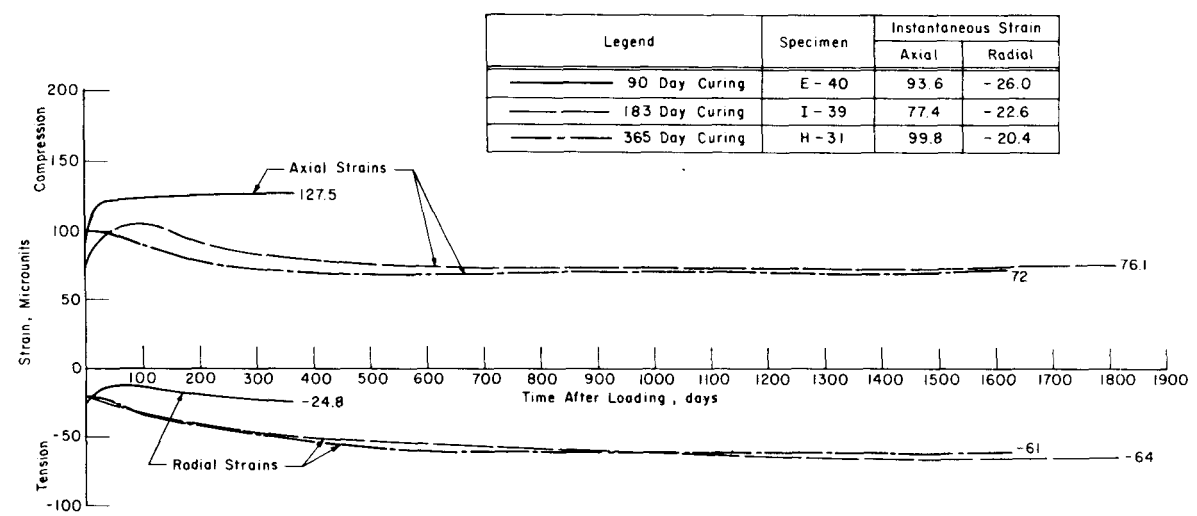

(b)

Fig. 1.24. Total Axial and Radial Strain Relationships with Uniaxial Stress of 4.1 MPa (600 psi). (a) As-cast specimens. (b) Air dried. University of Texas drawings.

Fig. 1.23(b), the curves actually crossed. A similar trend is also evident for specimens stressed at 4.1 MPa, although it is not as pronounced because of the low stress level and the omission of shrinkage effects.

The air-dried specimens exhibited larger axial creep strains than the as-cast specimens regardless of age at loading. During the first 2.5 years, the creep strains of as-cast specimens at any given time were approximately 82% of those of the air-dried specimens for the same loading. During the next 2.5 years, the two specimen types appeared to approach the same absolute creep strain, even though after five years of loading the concrete specimens continued to creep. The findings of the long-term creep tests were reported.[23]

A report on the U.S. Army Engineers Waterways Experiment Station moisture migration experiment has also been published.[24] It contains results of an experimental study of moisture migration in a pie-shaped specimen representing the flow path through the cylindrical wall of a PCRV.

1.10 REFERENCES

1. J. P. Callahan, R. S. Valachovic and G. C. Robinson, "PCRV Thermal Cylinder Test," *GCR Programs Annu. Progr. Rep. Dec. 31, 1972*, ORNL-4911, pp. 181–209.
2. J. P. Callahan and G. C. Robinson, "The Thermal Cylinder Test," *GCR Programs Annu. Progr. Rep. Dec. 31, 1973*, ORNL-4975, pp. 173–216.
3. S. C. Lu and C. M. Charman, *SAFE/CRACK Users' Manual*, GA-A-13035 (December 1974).
4. D. Carlton, J. R. Smith, and G. N. Bellwood, "Prestressing and Proof Pressure Testing of the Wylfa Prestressed Concrete Pressure Vessels and Comparison of Measured Data With Predicted Performance," pp. 319–52 in *Proc. First Int. Conf. on Structural Mechanics in Reactor Technology*, (Berlin, 1971), Vol. H, Commission of the European Communities, Brussels.
5. F. Bremer, "Practice With Model Techniques," pp. 7–13 in *Conference on Model Techniques for Prestressed Concrete Pressure Vessels*, The British Nuclear Society, London, 1969.

6. J. R. Smith, "Problems in Assessing the Correlation Between the Observed and Predicted Behavior of Models," pp. 81–89 in *Conference on Model Techniques for Prestressed Concrete Pressure Vessels*, The British Nuclear Society, London, 1969.

7. Y. R. Rashid, "Nonlinear Analysis of Two-Dimensional Problems in Concrete Creep," *J. Appl. Mech.* 94: 475–82 (1972).

8. E. M. Wallo, R. L. Yuan, J. L. Lott, and C. E. Kesler, *Sixth Progress Report Prediction of Creep in Structural Concrete from Short-Time Tests*, University of Illinois, Theoretical and Applied Mechanics Department Report 658 (1965).

9. S. Arthanari and C. W. Yu, "Creep of Concrete Under Uniaxial and Biaxial Stresses at Elevated Temperatures," *Magazine of Concrete Research* 19(60): 149–56 (September 1967).

10. R. S. Taylor and A. J. Williams, "The Design of Prestressed Concrete Pressure Vessels with Particular Reference to Wylfa," pp. 446–55 in *Proc. Third Int. Conf. on Peaceful Uses of Atomic Energy, Geneva, 1964*, Vol. 8, United Nations, New York, 1965.

11. D. A. Canonico, *Second Interim Report on PCRV Thermal Cylinder Axial Tendon Failures*, ORNL-TM-4764 (November 1974).

12. Y. R. Rashid, "Ultimate Strength Analysis of Prestressed Concrete Pressure Vessels," *Nucl. Engr. Des.* 7(4): 333–44 (April 1968).

13. A. M. Cohen, *Numerical Analysis*, John Wiley and Sons, New York, 1973.

14. Y. R. Rashid, *Theory Report for Creep-Plast Computer Program*, GEAP-10546 (January 1972).

15. K. J. Bathe, H. Ozdemir, and E. D. Wilson, *Static and Dynamic Geometric and Material Nonlinerar Analysis*, UC SESM 74-4, Structural Engineering Laboratory, University of California, Berkeley (1974).

16. K. J. Bathe, E. L. Wilson, and R. H. Iding, *NONSAP: A Structural Analysis Program for Static and Dynamic Response of Nonlinear Systems*, UC SESM 74-3, Structural Engineering Laboratory, University of California, Berkeley (1974).

17. *Finite Element Analysis of Mine Structures, Final Report to Denver Mining Research Center, U.S. Department of the Interior, Bureau of Mines*, Department of Civil Engineering, University of California, Berkeley, Contract 0110231 (1972).

18. B. I. Karlsson and M. A. Sozen, "Prestressed Concrete Deep Slabs with Openings," *Nucl. Eng. Des.* 25(2): 290—300 (July 1973).

19. F. S. Ople, GA, private communication to J. P. Callahan, ORNL, Jan. 22, 1975.

20. *ASME Boiler and Pressure Vessel Code, Sect. III, Div. 2, Code for Concrete Reactor Vessels and Containments,* American Society of Mechanical Engineers, New York, 1975; this document is also American Concrete Institute Standard 359-74.

21. *ASME Boiler and Pressure Vessel Code, Sect. III, Div. 1, Rules for Construction of Nuclear Power Plant Components,* American Society of Mechanical Engineers, New York, 1975.

22. R. K. Nanstad, *A Review of Concrete Properties in a Nuclear Environment,* ORNL/TM-5497 (October 1976).

23. T. W. Kennedy, *Long Term Creep Behavior of Concrete,* ORNL-Sub-3899-1 (Research Report 3899, The University of Texas) (January 1975).

24. J. E. McDonald, *Moisture Migration in Concrete,* ORNL-TM-5051 (Technical Report C-75-1; U. S. Army Engineer Waterways Experiment Station) (May 1975).

2. STRUCTURAL MATERIALS

P. L. Rittenhouse and J. R. DiStefano

2.1 INTRODUCTION

Many of the metallic materials in the primary and steam generator circuits of the HTGR operate in temperature ranges where their mechanical properties are time dependent (i.e., within their creep range). Because of this, it is necessary to consider both elastic-plastic and creep behavior in design, performance, and safety analyses. This requires that detailed and accurate information on creep, fatigue, crack growth, etc. be available as input to the formulation of high-temperature structural design methods and the development of failure criteria. Additionally, the analysis of the long-term behavior of HTGR metallic materials must include consideration of the effects of environment (steam/water and/or primary coolant helium) and thermal aging on properties.

The objective of the tasks described in the sections that follow is to obtain specific data and information needed to improve the basis for design analysis and performance evaluations of steam generator and primary circuit components and materials of the large commercial HTGR. The current target date for these tasks is 1979 and corresponds to the scheduled completion of the FSAR for the first unit large HTGR.

2.2 MECHANICAL PROPERTIES — C. R. Brinkman and P. L. Rittenhouse

2.2.1 Tensile Testing — P. L. Rittenhouse

All HTGR materials that are being used in mechanical property studies have been procured under applicable ASTM-ASME specifications, and "certificates of test" documenting room-temperature properties and composition have been obtained and filed. In addition, to further characterize these materials, tensile tests have been conducted on each material (from room temperature through appropriate elevated temperatures) in known heat treatment conditions. The results of these tests are described below.

Tests at room temperature and at 210 to 593°C (500–1100°F) in 55.5°C (100°F) increments were conducted on three heats (Babcock and Wilcox heats 36202, 72768, and X-6216) of 2 1/4 Cr-1 Mo steel tubing. These heats, currently being tested in our environmental creep program (see Sect. 2.2.2), were isothermally annealed [i.e., austenitized at 927°C (1700°F) and then held for 2 hr at 704°C (1300°F), cooling rates controlled both from 927 to 704°C (1700 to 1300°F) and from 704°C (1300°F) to room temperature] before tensile testing. The 0.2% offset yield strengths and ultimate tensile strengths determined for these heats are shown in Table 2.1. Yield strength values tend to follow the trend of the "expected minimum yield strength vs temperature" curve given[1] in Code Case 1592, but a number of our experimentally determined values fall somewhat below the subject curve. These values are, however, consistent with minimum yield strengths recently incorporated into the *Nuclear Systems Materials Handbook*. Ultimate tensile strengths, with an intermediate-temperature maximum at about 371°C (700°F), are also consistent with Handbook data.

Specimens of 9 Cr-1 Mo steel, an alloy that has been considered a backup to 2 1/4 Cr-1 Mo in steam generator applications, have also been tested at temperatures to 593°C (1100°F). Results from tests on isothermally annealed (see heat treatment for 2 1/4 Cr-1 Mo given in previous paragraph) 13-mm (1/2-in.) plate material (G. O. Carlson Heat 316381-1A) are given in Table 2.2. Both the 0.2% offset yield and ultimate strengths are, as expected, quite similar to those for the 2 1/4 Cr-1 Mo material.

Tensile tests have also been performed on two nickel-base alloys, Hastelloy X and Hastelloy S. Hastelloy X is the current material of design for the hot ducting (core outlet to the steam generator) of the HTGR, while Hastelloy S is an alternate candidate for this application. Results of the tests on 13-mm (1/2-in.) plate Hastelloy X (Cabot Corp. Heat 2600-3-4936) and 16-mm-diam (5/8-in.) Hastelloy S rod (Cabot Corp. Heat 8635T) are shown in Tables 2.3 and 2.4, respectively. All the tests on Hastelloy S and some on Hastelloy X (see notation in Table 2.3) were run at a rate of 0.4%/min through failure. However, most of the tests on Hastelloy X were run at 0.4%/min through yielding and then at 1.6%/min

Table 2.1. Tensile Strength Data for Three Heats of Isothermally Annealed 2 1/4 Cr-1 Mo Steel

Test	Heat	Temperature		Tensile Strength			
				0.2% Yield		Ultimate	
		(°C)	(°F)	(ksi)	(MPa)	(ksi)	(MPa)
14496	72768[a]	24	75	32.4	223	69.0	476
14497	72768	24	75	32.1	221	69.0	476
14159	72768	24	75	33.3	230	65.5	452
14162	72768	24	75	34.2	236	68.3	471
14498	36202[b]	24	75	36.2	250	73.5	507
14105	36202	24	75	37.3	257	73.1	504
14106	36202	24	75	36.7	253	72.8	502
14199	36202	24	75	32.7	225	72.7	501
14492	X-6216[b]	24	75	35.4	244	72.3	498
14493	X-6216	24	75	34.9	241	71.6	494
14494	X-6216	24	75	35.0	241	71.6	494
14495	X-6216	24	75	34.8	240	71.7	494
14152	72768	260	500	25.9	179	56.3	388
14153	72768	260	500	25.8	178	55.5	383
14154	36202	260	500	27.5	190	60.3	416
14155	36202	260	500	28.3	195	60.0	414
14151	X-6216	260	500	28.6	197	61.6	425
14111	X-6216	260	500	28.1	194	58.5	403
14066	72768	315	600	25.0	172	57.1	394
14068	72768	315	600	22.4	154	56.9	392
14071	36202	315	600	27.8	192	61.3	423
14073	36202	315	600	27.6	190	61.7	425
14158	X-6216	315	600	27.0	186	59.8	412
14501	X-6216	315	600	27.5	190	64.0	441
14502	72768	371	700	23.7	163	62.1	428
14070	72768	371	700	26.4	182	66.3	457
14086	36202	371	700	25.9	179	64.6	445
14503	36202	371	700	26.0	179	65.5	452
14067	X-6216	371	700	26.3	181	63.3	436
14069	X-6216	371	700	27.2	188	62.8	433
10489	72768	427	800	23.9	165	57.9	399
14091	72768	427	800	20.7	143	57.6	397
14505	72768	427	800	25.8	178	59.2	408
14504	36202	427	800	24.7	170	63.4	437
14094	36202	427	800	29.4	203	62.0	427
14075	X-6216	427	800	26.1	180	60.2	415
14088	X-6216	427	800	27.7	191	56.7	391
14092	72768	482	900	23.5	162	52.5	362
14093	72768	482	900	26.7	184	52.5	362
14506	72768	482	900	22.7	157	52.3	361
14095	36202	482	900	19.1	132	56.6	390
14096	36202	482	900	18.7	129	56.5	390
14087	X-6216	482	900	23.3	161	54.5	376
14097	X-6216	482	900	25.5	176	55.3	381
14101	72768	538	1000	21.1	145	44.1	304
14104	72768	538	1000	19.2	132	44.2	305
14109	36202	538	1000	23.1	159	47.3	326
14511	36202	538	1000	24.4	168	47.9	330
14098	X-6216	538	1000	23.6	163	48.2	332
14100	X-6216	538	1000	22.0	152	46.1	318
14102	72768	593	1100	16.8	116	34.7	239
17513	72768	593	1100	19.3	133	33.9	234
14512	36202	593	1100	19.7	136	36.8	254
14108	36202	593	1100	21.1	145	37.3	257
14097	X-6216	593	1100	19.7	136	36.2	250
14099	X-6216	593	1100	21.9	151	36.2	250

[a]Carbon content 0.10%.

[b]Carbon content 0.12%.

Table 2.2. Tensile Strength Data for Isothermally Annealed 9 Cr-1 Mo Steel

Test	Temperature		Tensile Strength			
			0.2% Yield		Ultimate	
	(°C)	(°F)	(ksi)	(MPa)	(ksi)	(MPa)
14130	25	77	38.6	266	76.0	524
14131	25	77	39.9	275	75.4	520
14132	25	77	38.7	267	75.5	521
14133	25	77	40.3	278	76.1	525
14134	260	500	29.6	204	66.4	458
14135	260	500	29.0	200	66.0	455
14136	316	600	28.0	193	63.9	441
14137	316	600	28.2	194	64.5	445
14138	371	700	27.1	187	63.8	440
14139	372	700	27.1	187	63.3	436
14140	427	800	27.8	192	59.8	412
14141	427	800	25.6	177	59.0	407
14142	482	900	24.7	170	52.3	361
14143	482	900	24.1	166	52.3	361
14144	538	1000	22.3	154	40.3	278
14145	538	1000	23.3	161	41.2	284
14146	593	1100	19.7	136	30.0	207
14147	593	1100	19.5	134	29.7	205

Table 2.3. Tensile Properties of Hastelloy X (Heat 2600-3-4936)

Test	Temperature		Tensile Strength, ksi(MPa)		Elongation (%)	Reduction of Area (%)
	(°C)	(°F)	0.2% Yield	Ultimate		
14892	22	72	52.0(358)	110.5(762)	50.5	59.8
14893	22	72	50.6(349)	110.8(764)	51.5	59.2
14894	22	72	50.8(350)	110.8(764)	51.9	61.4
14895	149	300	42.1(290)	98.9(682)	51.1	60.6
14899[a]	149	300	41.8(288)	97.3(671)	51.5	59.8
14896	288	550	36.0(248)	96.0(662)	52.8	57.9
14897	288	550	35.4(244)	94.4(651)	53.7	55.9
14814	288	550	35.5(245)	95.2(656)	54.4	55.4
14813	427	800	32.4(223)	91.0(627)	56.5	56.9
14813	427	800	34.0(234)	91.2(629)	49.8	
14809	482	900	28.0(193)	90.4(623)	59.0	43.6
14810	482	900	34.0(234)	90.2(622)	55.9	38.4
14811	482	900	31.8(219)	90.1(621)	58.4	48.2
14807	538	1000	34.6(239)	85.8(592)	49.9	40.9
14808	538	1000	32.1(221)	86.5(596)	48.8	31.4
14804	593	1100	31.9(220)	84.9(585)	53.3	40.9
14805	593	1100	32.4(223)	85.1(587)	53.1	41.9
14806	593	1100	33.7(232)	84.3(581)	51.5	43.0
14802	649	1200	31.1(214)	73.6(507)	39.7	35.9
14803	649	1200	30.9(213)	73.6(507)	39.7	39.4
14799[a]	704	1300	32.4(223)	61.6(425)	48.5	41.7
14800	704	1300	31.2(215)	65.5(452)	37.3	33.6
14801	704	1300	30.8(212)	66.7(460)	37.6	35.9
14790[a]	760	1400	31.2(215)	46.4(320)	73.3	99.7
14791[a]	760	1400	31.5(217)	62.2(429)	75.6	99.7
14796	760	1400	31.5(217)	55.8(385)	66.6	55.8
14798	760	1400	29.9(206)	55.2(381)	68.1	57.0
14792[a]	816	1500	32.1(221)	34.9(241)	87.2	99.4
14793[a]	816	1500	33.7(232)	34.8(240)	72.2	99.7
14794[a]	816	1500	33.5(231)	34.5(238)	74.6	99.8
14795	816	1500	30.9(213)	34.9(241)	81.2	81.4
14797	816	1500	32.7(225)	41.7(288)	86.0	69.6
14815[a]	871	1600	23.4(161)	24.0(165)	79.8	88.9
14898[a]	871	1600	23.6(163)	24.3(168)	84.4	88.2

[a]Constant strain rate of 0.4%/min through failure; all other tests at this rate through yielding and then 1.6%/min.

Table 2.4. Tensile Properties of Hastelloy S (Heat 8365T)

Test	Temperature		Strength, MPa (ksi)		Elongation (%)	Reduction of Area (%)
	(°C)	(°F)	0.2% Yield	Ultimate Tensile		
15324	22	72	457 (66.3)	934 (135.5)	50.8	69.2
15325	22	72	466 (67.6)	931 (135.0)	52.8	68.1
15326	22	72	455 (66.0)	924 (134.0)	51.6	60.1
15355	22	72	465 (67.4)	929 (134.8)		61.6
15327	149	300	425 (61.6)	879 (127.5)	52.4	61.7
15328	149	300	417 (60.5)	880 (127.6)	51.2	53.3
15329	288	550	376 (54.6)	852 (123.6)	53.7	60.4
15330	288	550	363 (52.7)	850 (123.2)	52.2	43.4
15331	288	550	368 (53.4)	858 (124.4)	48.4	54.8
15332	427	800	350 (50.7)	836 (121.2)	50.4	54.5
15333	438	820	366 (53.1)	852 (123.5)	52.6	41.7
15334	482	900	348 (50.5)	829 (120.2)	51.6	38.9
15335	482	900	361 (52.3)	835 (121.1)	47.1	50.9
15336	482	900	359 (52.0)	837 (121.4)	50.9	41.2
15337	538	1000	359 (52.0)	818 (118.6)	49.2	45.4
15338	538	1000	333 (48.3)	805 (116.8)	52.8	35.2
15339	593	1100	330 (47.8)	789 (114.4)	45.6	39.0
15340	593	1100	363 (52.6)	793 (115.0)	45.3	36.3
15341	593	1100	367 (53.3)	786 (114.0)	62.6	43.7
15342	649	1200	358 (51.9)	654 (94.9)	94.4	74.1
15343	649	1200	363 (52.7)	655 (95.0)	96.0	76.5
15344	649	1200	365 (52.9)	652 (94.5)	96.2	75.6
15345	704	1300	345 (50.0)	496 (71.9)	83.7	82.1
15346	704	1300	349 (50.6)	494 (71.7)	93.1	83.0
15354	704	1300	355 (51.5)	501 (72.7)	81.9	80.2
15347	760	1400	314 (45.6)	365 (52.9)	79.6	85.0
15348	760	1400	345 (50.0)	362 (52.5)	81.7	86.0
15349	816	1500	276 (40.0)	278 (40.3)	93.9	86.6
15350	816	1500	259 (37.5)	262 (38.0)	71.0	86.0
15351	816	1500	276 (40.0)	282 (40.9)		93.7
15352	871	1600	173 (25.1)	175 (25.4)	78.2	90.6
15353	871	1600	175 (25.4)	178 (25.8)	78.7	85.6

to failure. The only property that seemed to be significantly affected by this difference in test method was reduction of area [e.g., at 760°C (1400°F) reduction of area was <60% for the two-stage rate and >79% for the other]. Comparison of the data for the two materials leads to the conclusion that — at least in terms of tensile properties — Hastelloy S is a stronger material than Hastelloy X at temperatures up to and including 816°C (1500°F). At 871°C (1600°F) the strengths of the two are almost identical.

2.2.2 Creep Testing in HTGR Primary Coolant Environment — P. L. Rittenhouse

2.2.2.1 Background

Alloys employed in the construction of primary and steam generator circuit components will be exposed to high-temperature helium containing low levels of impurities (H_2, CO, CH_4, and H_2O) for the design lifetime (30—40 years) of the plant. Although the helium primary coolant is — by conventional standards — extremely pure and characterized by low oxidation and carburization potentials, reactions between HTGR alloys and these impurities will occur. A number of studies conducted in Europe have demonstrated — depending upon alloy, temperature, and impurity species, levels, and ratios — various degrees and types of gas-metal reactions (e.g., selective oxidation of alloying elements and carburization) and consequent effects on creep behavior.[2—5]

The creep rupture and creep strain data being obtained (both in air and in simulated HTGR primary coolant helium) in the task described in this section should identify any effects of the helium environment on the creep behavior of selected HTGR structural alloys. Such effects, if found, can then be incorporated into design to ensure the functionability, integrity, and safety of the system. Currently, major emphasis in the subject task is on 2 1/4 Cr-1 Mo ferritic steel and Hastelloy X, but some testing of 9 Cr-1 Mo steel has been undertaken and plans have been developed for studying Inconel 617. Similar tests on Alloy 800H are in progress at the General Atomic Company (GA) under ERDA/RRD sponsorship.

2.2.2.2 Environmental Test Facilities

Conventional high-precision creep testing (i.e., in air) involves — in brief — load train systems for applying uniaxial loads with a minimum of bending stresses, extensometry to monitor the strain that accrues with time, and furnaces and controls for maintaining the desired test temperature within narrow limits for long periods of time. Testing in a controlled environment adds substantially to the above in complexity, effort, and cost. The ten systems we are now using for environmental tests required extensive development related to the design of the specimen, the load train, extensometry, the environmental chamber, and — particularly — to the methods for supplying and monitoring the helium environments. Some of the details of the environmental creep systems are described in the paragraphs that follow.

The creep specimens are loaded conventionally through calibrated lever arms. The load train itself is designed to minimize bending loads by the use of U-joints and the elimination of threaded connections. This practice is carried over to the specimens (see Fig. 2.1) by attaching them to the load train with tapered fittings clamped over each end. The environmental chamber is constructed of austenitic stainless steel pipe (enclosed in the furnace bore) with water-cooled flanges and metal bellows at each end. The bellows are provided to further facilitate alignment of the load train. U-cup seals, lightly lubricated to minimize friction, are used where the polished pull-rods enter and exit the environmental chamber. This allows a positive environmental seal and, yet, permits application of load and unrestricted specimen extension. The bores of the environmental chambers were seasoned (preoxidized) before use.

Three Chromel vs Alumel thermocouples are attached equidistantly along the specimen gage length to monitor temperature. The three-zone furnace surrounding the environmental chamber bore is shunted to achieve a maximum of 2°C (3.6°F) difference over the 25.4-mm (1-in.) gage length. The control thermocouple is placed in the annulus between the chamber and the furnace to avoid any possibility of reaction between the thermocouple materials and the helium environment and possible consequent changes in

ORNL-DWG 75-14128

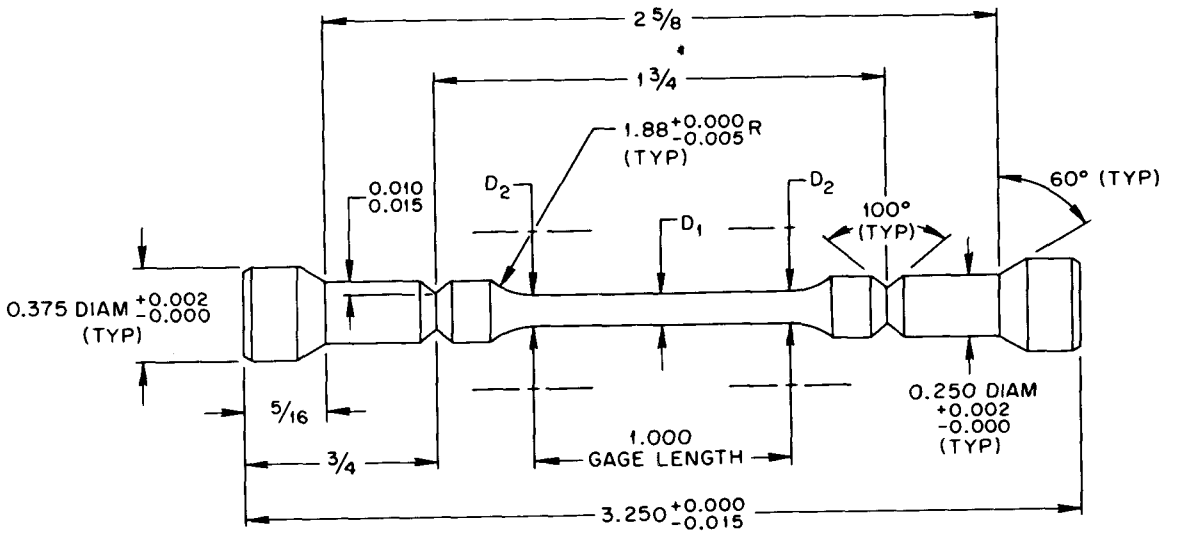

NOTE: ALL DIMENSIONS IN INCHES

$D_1 = 0.125 \pm 0.001$ DIAM

D_2 = FROM 0.0010 TO 0.0015 GREATER THAN D_1

Fig. 2.1. Details of Creep Specimens for Environmental Tests. To convert dimensions to millimeters, multiply by 25.4.

thermocouple output. Before any test specimen is brought to temperature and loaded, the environmental chamber is evacuated and then backfilled with helium.

Provision of a system for supplying, monitoring, and controlling the simulated HTGR primary coolant helium environment has been the most difficult step in facility preparation. The three types of systems that were considered are (1) premixed (tank) gas supply, (2) once-through dynamic-mix supply, and (3) recirculating loop dynamic-mix supply. The first — premixed — can be provided with the lowest cost, is the most versatile (e.g., each test chamber can, if desired, operate with a different environment), but does not offer continuous on-line control of impurity levels. Early concerns relative to gas stability (i.e., possible changes in impurity levels in the tanks during storage and use) and cleanliness were, and continue to be, dispelled by our experience in use of this method. Before we adopted this method of supply, tanks containing controlled additions of H_2, CO, and CH_4 to helium were prepared

and bled from 7 MPa (1000 psia) to 0.34 MPa (50 psia) over a 600-hr period. (A normal period for tank use in test is <300 hr.) No changes in impurity levels were detected during this period. A schematic of the premixed system is shown in Fig. 2.2.

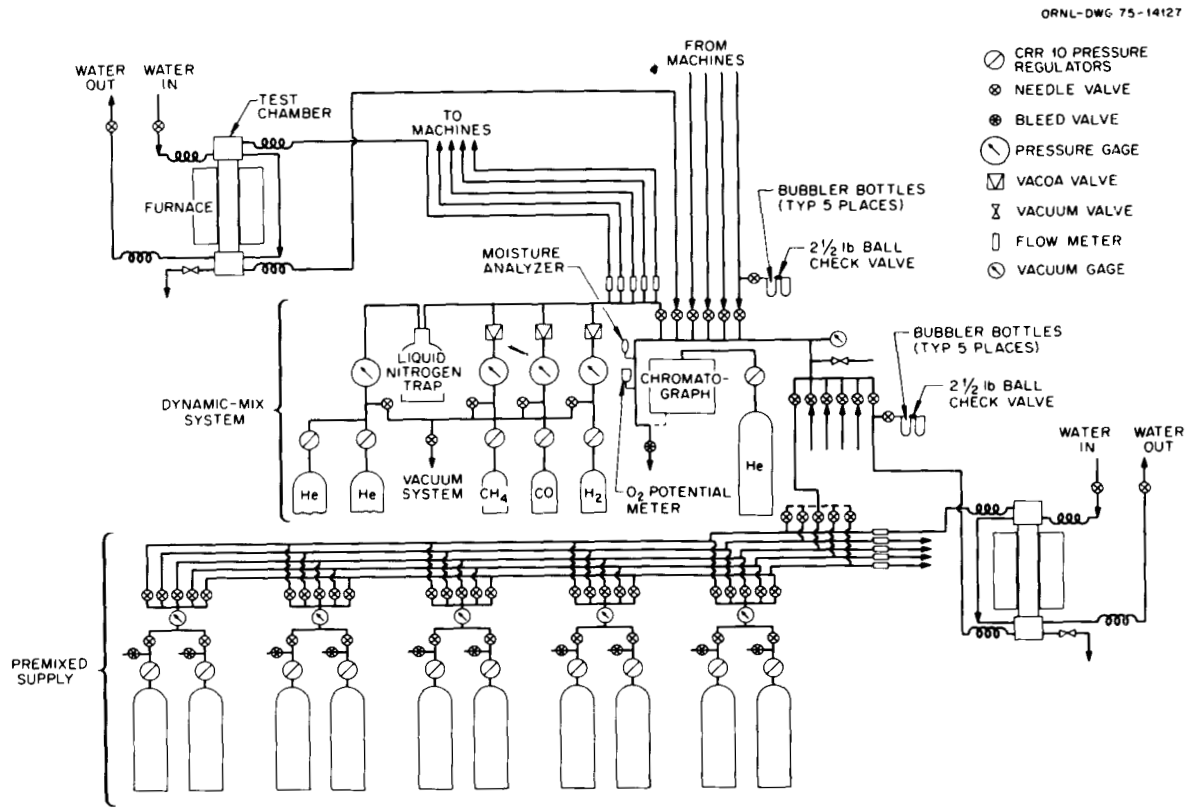

Fig. 2.2. Schematic Diagram of Premixed and Dynamic-Mix Systems for Environmental Supply.

Once-through dynamic-mix systems can provide simulated HTGR primary coolant helium by continuous additions of hydrogen etc. (through micrometering valves) to high-purity helium. Such systems are intermediate in cost and versatility. We have constructed such a system (see Fig. 2.2) but have had serious problems in establishing control and calibration. Modifications — in details rather than general concept — to correct these deficiencies are in progress. We have also considered dynamic-mix recirculating loops, which are attractive from the standpoint of helium cost

and long-term stability of the helium environment. These systems are, however, of minimum versatility, and their construction costs far exceed those that could be considered in our program.

The impurity levels in the helium supply are monitored entering and leaving the environmental creep chambers on a scheduled basis. No significant entrance-to-exit differences are observed when flows through each chamber exceed 25 cm^3/min. (Flows have generally ranged from 30 to 50 cm^3/min.) Levels of H_2, CO, and CH_4 are measured with a gas chromatograph. It offers an additional leak-check feature by indicating N_2 and O_2 levels. Water vapor content of the gas is followed with a separate moisture analyzer, and a solid-state oxygen potential meter (continuously on-line) is used as the oxygen partial pressure reference. System pressure is normally 0.15 to 0.18 MPa (1.5—1.8 atm).

2.2.2.3 Environmental Creep Tests

The first two of our ten creep frames for environmental testing were completed, and preliminary testing began in December 1974. Since April 1975, all frames have operated essentially continuously. The environment for all tests has been supplied from premixed tanks containing controlled additions of H_2, CO, and CH_4. Typical impurity levels in the simulated HTGR primary coolant helium are given in Table 2.5. Estimates of impurity levels to be expected in steam-cycle gas cooled reactors are also shown in Table 2.5. Comparison shows that our test environments are within the range of those expected.

The matrix of environmental creep tests in progress or completed at the end of the reporting period is given in Table 2.6. Available strain-time data through 3000 hr of test are shown in Table 2.7. The three tests on isothermally annealed (see Sect. 2.2.1 for heat treatment) 2 1/4 Cr-1 Mo [Heat X-6216, 593°C (1100°F), 69 MPa (10 ksi) Tests 15023, 15045, and 15047] were designed to check the reproducibility of test results from machine to machine. At the end of 3000 hr the total strains for these three tests were 0.94, 0.87, and 0.94%, respectively. Comparison of total strains for these tests at various time increments, up to and including 3000 hr (see Table 2.7), indicates quite good reproducibility of results. Test

15045 was discontinued at 3160 hr (total strain of 0.90%, see Fig. 2.3). The other two 593°C (1100°F), 69 MPa (10 ksi) tests on 2 1/4 Cr-1 Mo are continuing.

Table 2.5. Impurity Levels in Simulated and Estimated HTGR Primary Coolant Helium

Impurity	Impurity Levels, μatm[a]			
	Simulated Coolant	Estimates for Reactor Coolant		
		Minimum[b]	Expected[c]	European[d]
H_2O	3–22[e]	<1	50	f
CH_4	30–40	20	50	20–50
CO	12–26	10	450	2–50
CO_2		<1	<2	
H_2	275–400	200	1500	100–500
O_2	$<10^{-16}$	10^{-19}	10^{-16}	$\ll 10^{-3}$
N_2		<1	<1	<10

[a]μatm = ppm by volume × system pressure in atm; 1 μatm corresponds to a partial pressure of 0.1 Pa.

[b]General Atomic Company estimate for totally leak-free steam generator, at equilibrium after start-up.

[c]Estimate based on General Atomic Company Technical Specification limits.

[d]Based on discussions with Dragon Project and UKAEA.

[e]Water vapor levels vary day-by-day and have been as high as 22 μatm and as low as 3.0 μatm. Average level is about 8 μatm.

[f]Strongly dependent on time in life, reactor design, etc.

Tests 15058 and 15377 have also been completed. The first — Hastelloy X, Heat 2600-3-4936, 704°C (1300°F), 138 MPa (20 ksi) — ruptured after 4044 hr with a total strain of 21.4%. The period of second-stage creep (constant minimum strain rate of 0.0017%/hr) started about 500 hr into the test and continued approximately 1100 hr. The creep curve is shown in Fig. 2.4.

Table 2.6. Current Environmental Creep Tests

Test	Test Frame	Material	Heat	Temperature (°C)	Temperature (°F)	Stress (MPa)	Stress (ksi)	Comments
15023	I-168	2 1/4 Cr-1 Mo	X-6216	593	1100	69	10	
15045	I-160	2 1/4 Cr-1 Mo	X-6216	593	1100	69	10	Discontinued at 3160 hr (0.90% strain)
15046	I-161	2 1/4 Cr-1 Mo	X-6216	593	1100	103	15	
15047	I-169	2 1/4 Cr-1 Mo	X-6216	593	1100	69	10	
15058	I-162	Hastelloy X	2600-3-4936	704	1300	138	20	Ruptured at 4044 hr (21.4% strain)
15363	I-163	9 Cr-1 Mo	316381-1A	538	1000	103	15	
15369	I-164	2 1/4 Cr-1 Mo	36202	538	1000	103	15	
15373	I-166	2 1/4 Cr-1 Mo	36202	482	900	207	30	In 3rd-stage creep at about 500 hr
15374	I-165	2 1/4 Cr-1 Mo	36202	482	900	172	25	In 3rd-stage creep at about 800 hr
15377	I-167	9 Cr-1 Mo	316381-1A	482	900	172	25	Discontinued after 1317 hr because of erratic strain readings
15771	I-160	Hastelloy X	2600-3-4936	704	1300	172	25	
15772	I-167	Hastelloy X	2600-3-4936	649	1200	172	25	
15792	I-162	Hastelloy X	2600-3-4936	704	1300	138	20	

Table 2.7. Strain-Time Data From Environmental Creep Tests

Time (hr)	Total Strain, %, for Each Test[a]									
	15023	15045	15046	15047	15058	15363	15369	15373	15374	15377
200	0.22	0.17	0.20	0.14	1.56	0.14	0.35	1.70	0.64	0.35
400	0.29	0.23	0.38	0.17	2.23	0.18	0.59	2.07	0.72	0.39
600	0.34	0.27	0.55	0.22	2.67	0.23	0.83	2.43	0.80	0.42
800	0.39	0.32	0.73	0.28	3.03	0.28	1.04	2.92	0.90	0.46
1000	0.44	0.36	0.87	0.34	3.31	0.33	1.22	3.45	1.01	0.49
1200	0.49	0.41	0.99	0.40	3.65	0.37	1.39	4.17	1.16	
1400	0.54	0.45	1.11	0.45	3.97	0.42	1.56	4.96	1.36	
1600	0.59	0.50	1.22	0.52	4.34					
1800	0.64	0.54	1.34	0.58	4.78					
2000	0.69	0.59	1.46	0.64	5.23					
2200	0.74	0.64	1.57	0.70	5.81					
2400	0.79	0.69	1.69	0.76	6.37					
2600	0.84	0.75	1.80	0.82	7.04					
2800	0.89	0.81	1.92	0.88	7.86					
3000	0.94	0.87	2.03	0.94	8.82					

[a]See Table 2.6 for test details.

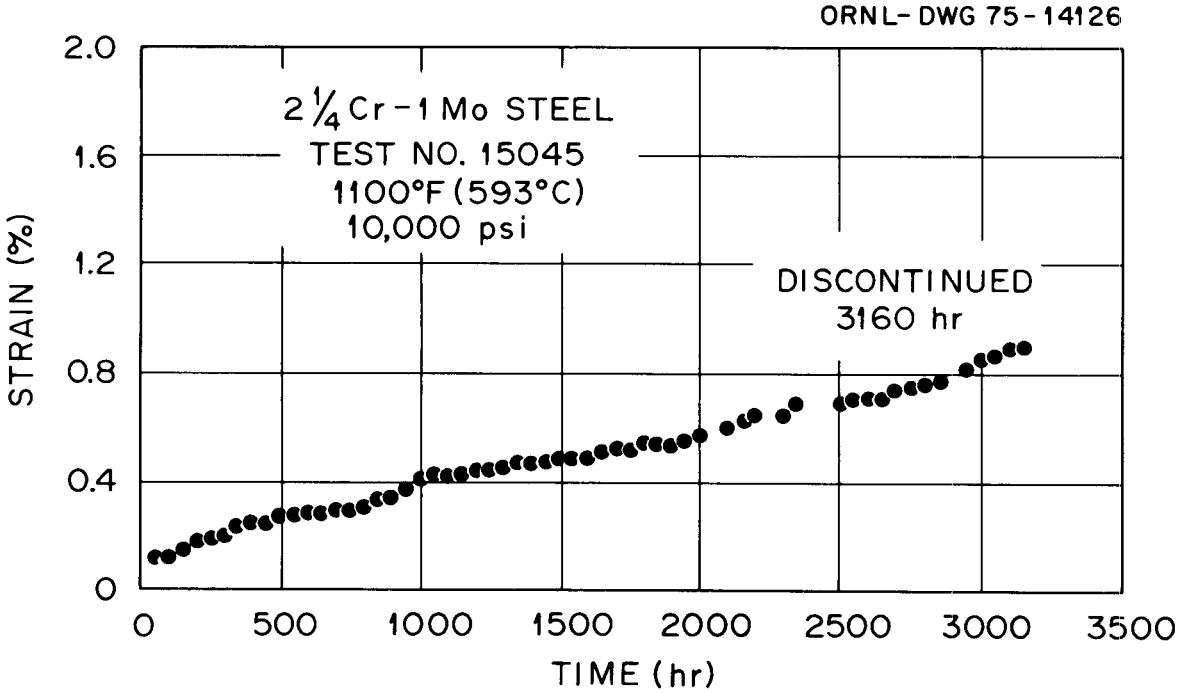

Fig. 2.3. Creep Curve for 2 1/4 Cr-1 Mo Test 15045 at 69 MPa (10 ksi) and 593°C (1100°F).

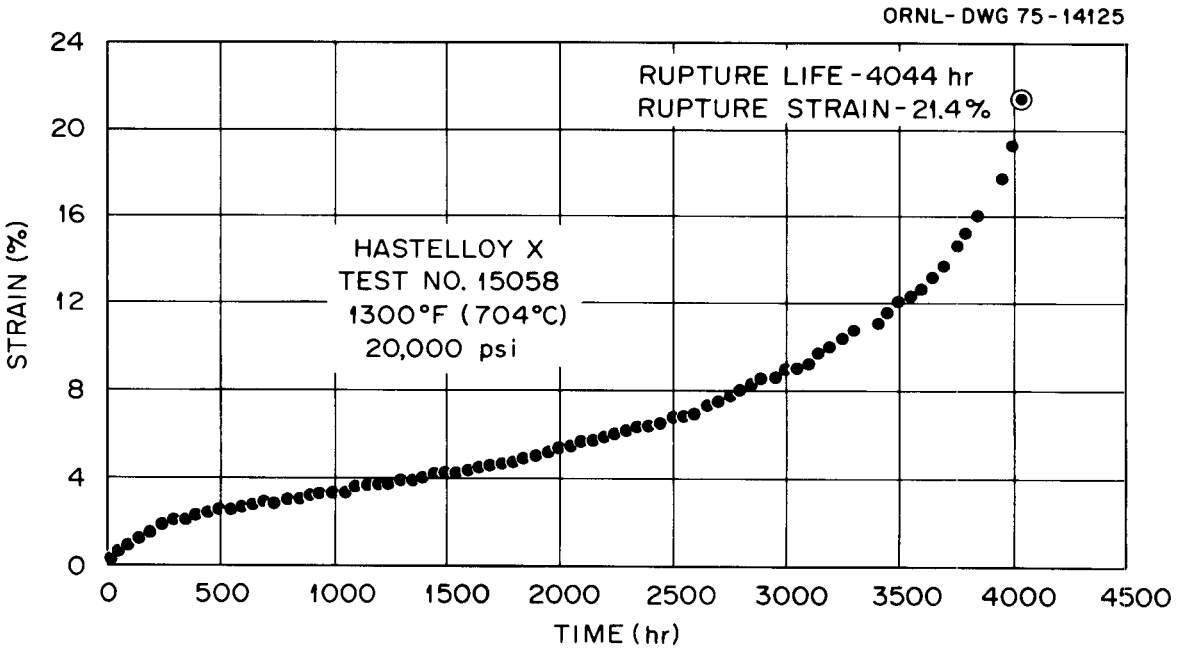

Fig. 2.4. Creep Curve for Hastelloy X Test 15058 at 138 MPa (20 ksi) and 704°C (1300°F).

Test 15377 [9 Cr-1 Mo steel, Heat 316381-1A, 482°C (900°F), 172 MPa (25 ksi)] was discontinued at 1319 hr because of continuously erratic strain readings. Strain at this point was about 0.6% but fluctuations up to a total strain of 0.9% had been observed. (No such difficulties have been encountered in any of our other tests.) Details and comments on all other tests are given in Table 2.6. Comparison tests in air will begin in the Fall of 1975.

Preliminary metallographic results from the three completed tests (15045, 15058, and 15377) have been obtained. Cross sections of the specimens were mounted, mechanically polished, and examined metallographically. The surface of the 9 Cr-1 Mo specimen [exposed just over 1300 hr at 482°C (900°F) appeared to be covered by an oxide film some 1 to 2 μm in thickness [see Fig. 2.5(a)]. The 2 1/4 Cr-1 Mo specimen (15045) exposed 3160 hr at 593°C (1100°F) showed evidence of what seems to be a selective oxidation to a depth of about 5 μm [see Fig. 2.5(b)]. Finally, the Hastelloy X specimen (15058), which was exposed just over 4000 hr at 704°C (1300°F) shows little if any surface film but exhibits grain boundary penetrations ranging up to 50 μm [see Fig. 2.5(c)]. The form of the attack (i.e., penetrations) and its physical appearance are consistent with other observations,[6] but the depth of attack is somewhat greater than for these comparable tests at 760°C (1400°F). The observations described here should be considered preliminary awaiting the completion of metallographic examination and the results of other ongoing tests.

2.2.3 Subcritical Crack Growth Studies — W. R. Corwin

2.2.3.1 Material

The material used in this study to date has been 2 1/4 Cr-1 Mo ferritic steel from 1-in. plates of Babcock and Wilcox Heat 20017. The material received an isothermal anneal [e.g., 927 ± 15°C (1700 ± 27°F) for 1 hr; cool at maximum of 83°C/hr (150°F/hr) to 704°C (1300°F) and hold for 2 hr; cool to room temperature at maximum of 5°C/min (9°F/min). Its

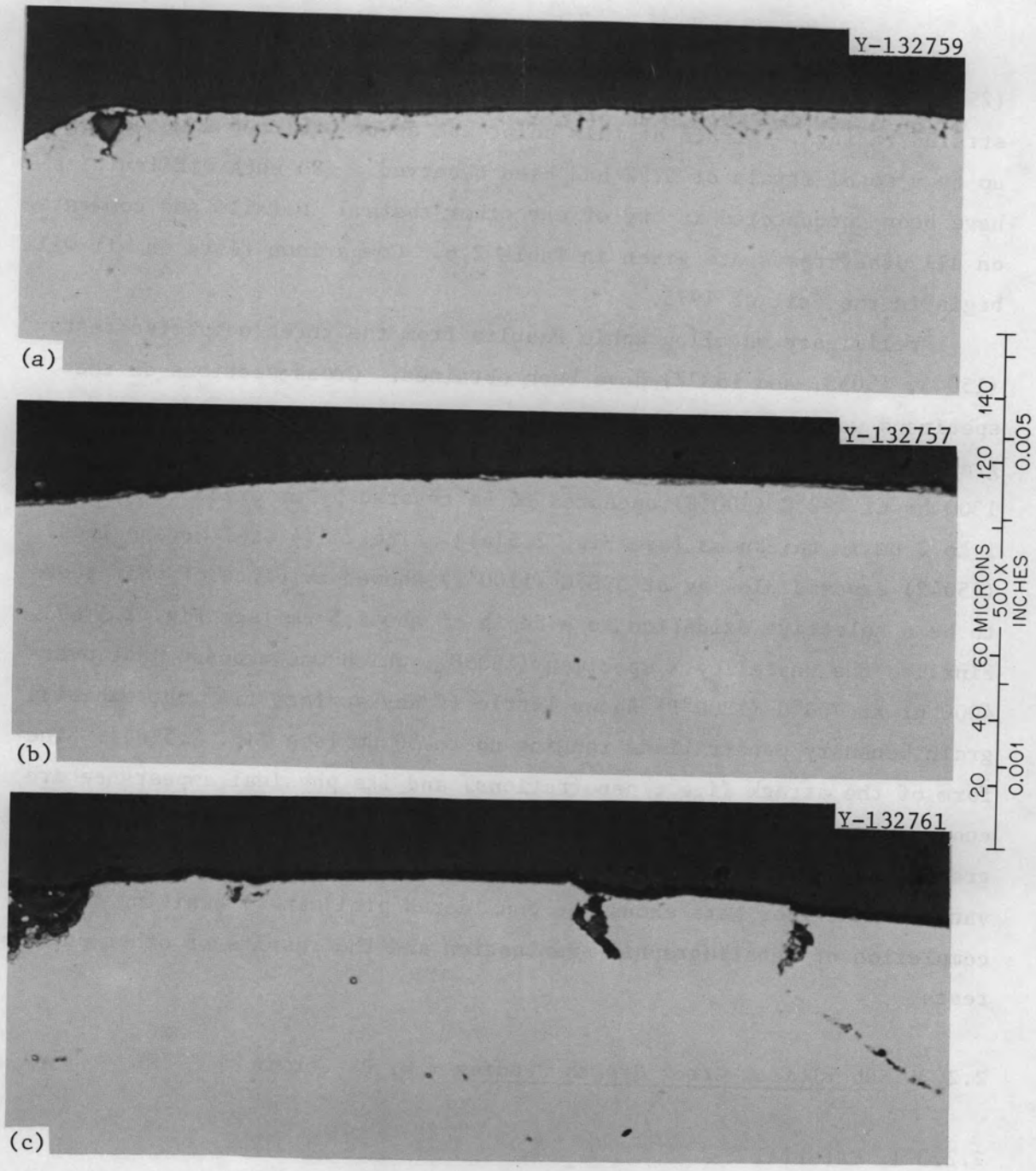

Fig. 2.5. Surface Cross Sections of Creep Specimens Exposed in Simulated HTGR Helium. (a) 9 Cr-1 Mo 1317 hr at 482°C (900°F). (b) 2 1/4 Cr-1 Mo 3160 hr at 593°C (1100°F). (c) Hastelloy X 4044 hr at 704°C (1300°F).

chemical composition, according to an ORNL analysis, in wt % is

C	Mn	Si	Cr	Mo	Ni	S	P
0.135	0.57	0.37	2.2	0.92	0.16	0.016	0.012

The grain size is ASTM 4 to 5, and its mechanical properties are reported elsewhere.[7]

2.2.3.2 Equipment and Procedures

Three closed-loop electro-hydraulic testing machines have been prepared for high-temperature subcritical fatigue crack growth (SFCG) testing in air and are currently operating full time on this study. Two of these systems are equipped with clamshell furnaces and the third with induction heating. A fourth test machine, available for part-time use, is equipped with a circulating-air furnace. It is currently in use about half time in this study. Another closed-loop machine with a circulating-air furnace has been modified to permit testing in steam. The steam is produced from distilled water in a generator outside the system and is supplied slightly above atmospheric pressure. This steam is piped into a stainless steel jacket that surrounds the specimen and is entirely within the furnace.

Testing in simulated HTGR primary coolant is done on another closed-loop machine, which is fitted with a cold-wall vacuum furnace that has been specially modified for these environmental tests. The vacuum capability of the system is used only to evacuate the test chamber before backfilling with the test gas. This gas is supplied from cylinders premixed to the specifications described in Sect. 2.2.2.2.

When completed, the gas monitoring system will consist of three on-line detection devices. A gas chromatograph will detect all major impurity gas species except for O_2 at very low levels and H_2O. These will be handled, respectively, by a solid-state oxygen potential meter and a moisture analyzer sensitive to approximately 1 ppm. Currently only the moisture analyzer is installed and operating. All other impurities are being detected by mass-spectrometer analysis of gas samples

taken during testing. (Installation of the remaining detection devices is scheduled for fall of 1975.)

Specimens in use in this study include those of compact tension (CT), wedge opening load (WOL), and center notched (CN) geometries. Comparison tests have shown no appreciable differences in results from specimens of these geometries. Most tests in air have used the WOL type for reasons of experimental convenience. All tests in steam use the WOL type and all in helium use the CT type. These choices are dictated by equipment capabilities.

Crack growth rate is a function of stress intensity applied to a crack: $da/dN = C(\Delta K)^n$, where a = crack length, N = number of cycles, ΔK = change in stress intensity factor, C, n = constants. Several methods for crack length determination have been investigated: visual observation, crack opening displacements (COD) electric potential crack followers, and fatigue surface markings. Regardless of the method or methods used in any given test, the values of da/dN and ΔK are determined by use of a standard two-point divided difference technique.[8]

To assure the validity of SFCG tests, a question that must be addressed is, what is the upper limit of crack length beyond which the calculated ΔK expressions are no longer valid because of the limitations of linear elastic fracture mechanics (LEFM). Determining exact departure from LEFM conditions during testing is not yet possible, but approximations can be made. The basic problem for load-controlled tests is to determine at what crack length the macroscopic stress state is such that near the crack tip gross yielding or inelastic deformation occurs. One method is to use a simple strength of materials approach and calculate the net section stress in the vicinity of the crack tip without including the stress concentrating effects of the crack.

For a WOL-type specimen this includes both a tension component and a bending component, whereas for a center-notch specimen only a tension component is required. This approach gives a net section tensile stress S_n for the center-notch specimen of

$$S_n = P/(w - 2a)T \ , \qquad (1)$$

where P is the applied load, w is the specimen width, $2a$ is the total tip to tip crack length, and T is the specimen thickness.

A similar expression for the WOL-type specimen, which assumes a bending moment arm equal to the crack length plus one-half the remaining ligament width, is

$$S_n = \frac{P}{(w - a)T} \left[1 + \frac{3(a + w)}{w - a}\right]. \tag{2}$$

This expression has been applied to the data using a yield criterion of $0.9\sigma_{ys}$, where σ_{ys} is either the monotonic or cyclic yield strength. The results are shown in Table 2.8 and appear to provide an overly conservative lower limit for ΔK. Other approaches were also investigated and are based primarily on observation of the specimen itself. As gross plastic flow begins the specimen naturally thins locally at the crack tip and a shear lip is formed. The crack length at which a shear lip forms has been measured on several specimens for the three testing temperatures investigated. The results contain enough scatter that drawing conclusions based on such measurements is difficult. The major source of inaccuracy is determining exactly where the shear lip begins. Minute perturbations on the edge of the crack face begin almost at the onset of testing and very gradually increase and coalesce with increasing crack length. At specimen failure the shear lip has become prominent, but choosing the point where plane stress conditions begin to dominate is highly subjective and, as a result, is a poor indicator of the onset of overall ligament yielding.

Post-test measurements of local specimen thickness versus crack length, however, appear to reproducibly indicate the upper limit beyond which the ΔK expressions referred to above should be considered invalid or at best questionable for correlating plane strain crack growth data. The method for determining these points is illustrated in Fig. 2.6 for three specimens at 593°C (1100°F). Local thickness measurements along the crack length taken on each specimen after the completion of its test were normalized by dividing each by the original specimen thickness (see Table 2.9). The normalized thickness measurements were then plotted versus the normalized crack length, a/w, as shown in Fig. 2.6.

Table 2.8. Apparent Limits of LEFM for Several Specimens as Computed by Eq. (2).

Test Temperature (°F)	Test Temperature (°C)	R[a]	Monotonic Yield Limits[b] a/w	Monotonic Yield Limits[b] K_{max} ksi (in.)$^{1/2}$	Monotonic Yield Limits[b] ΔK ksi (in.)$^{1/2}$	Cyclic Yield Limits[b] a/w	Cyclic Yield Limits[b] K_{max} ksi (in.)$^{1/2}$	Cyclic Yield Limits[b] ΔK ksi (in.)$^{1/2}$
Room		0.05	0.5550	21.53	20.46	0.5825	23.51	22.35
950	510	0.033	0.5120	19.98	19.32	0.5593	23.40	22.63
950	510	0.05	0.5120	19.98	18.98	0.5593	23.40	22.23
950	510	0.2	0.5120	19.98	15.98	0.5593	23.40	18.72
950	510	0.5	0.5120	19.98	9.99	0.5593	23.40	11.70
1100	593	0.05	0.4735	18.63	17.70	0.5380	22.07	20.91

[a] R is the ratio of the minimum tensile load to the peak tensile load.

[b] To convert K_{max} and ΔK to MPa m$^{1/2}$, multiply by 1.099.

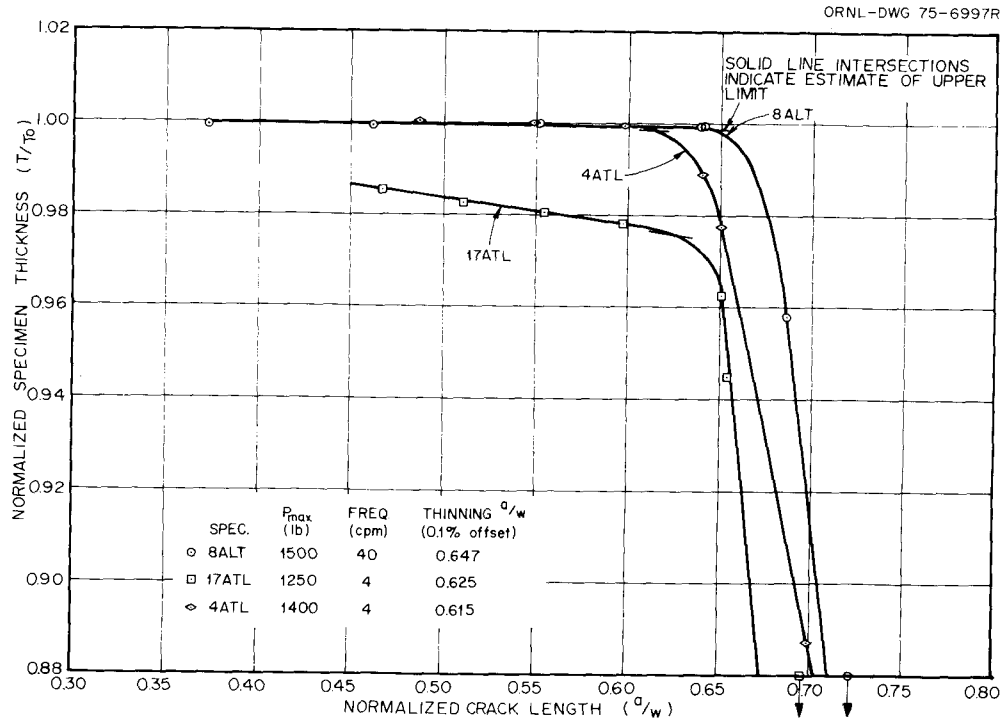

Fig. 2.6. Limits of Plane Strain Crack Propagation of 2 1/4 Cr-1 Mo Steel at 593°C (1100°F) in Air with R = 0.05.

Table 2.9. Thickness Along Crack Length of 2 1/4 Cr-1 Mo Steel Fatigue Crack Propagation Specimens Tested at 593°C (1100°F)

Specimen	Maximum Load (lb)	Maximum Load (kN)	R	Frequency (cpm)	Thickness, in. (mm) T_0, original	Thickness, in. (mm) T, local	Normalized Thickness, T/T_0	Normalized Crack Length a/w
8 ALT	1500	6.67	0.05	40	0.5042 (12.807)	0.5030 (12.776)	0.9976	0.3745
						0.5030 (12.776)	0.9976	0.4638
						0.5025 (12.764)	0.9966	0.5531
						0.5000 (12.700)	0.9917	0.6405
						0.5000 (12.700)	0.9917	0.6424
						0.4830 (12.268)	0.9580	0.6870
						0.3852 (9.784)	0.7104	0.7209
17 ATL	1250	5.56	0.05	4	0.5013 (12.733)	0.4941 (12.550)	0.9856	0.4682
						0.4925 (12.510)	0.9824	0.5113
						0.4913 (12.479)	0.9801	0.5555
						0.4902 (12.451)	0.9779	0.5988
						0.4823 (12.250)	0.9621	0.6521
						0.4733 (12.022)	0.9441	0.6540
						0.4240 (10.770)	0.8458	0.6956
						0.3234 (8.214)	0.6451	0.7239
4 ATL	1400	6.23	0.05	4	0.5040 (12.802)	0.5040 (12.802)	1.0000	0.4881
						0.5033 (12.784)	0.9986	0.5497
						0.5023 (12.758)	0.9966	0.5991
						0.4982 (12.654)	0.9885	0.6420
						0.4927 (12.515)	0.9776	0.6508
						0.4470 (11.354)	0.8869	0.6964
						0.3030 (7.696)	0.6012	0.7847

In this manner it is easily seen where significant thinning begins, even in specimen 17 ATL, where a small amount of thinning is apparent before necking (possibly due to creep or ratchetting effects). To consistently obtain an estimate of the upper limit value of a/w, the intersection of the curve and a line offset 0.1% below its upper linear portion was taken. This value of a/w was then used to determine the limiting K_{max} and ΔK values for each test shown in Table 2.10. Three conclusions may be drawn: (1) As would be expected, the maximum stress intensity factor that can be obtained without specimen yielding decreases with increasing temperature, presumably because of temperature-related material softening. (2) At 593°C (1100°F), where there is a strong frequency effect, as shown in Fig. 2.6, the limiting K_{max} decreases with decreasing frequency for similar reasons. (3) The limiting K_{max} for a given set of temperature and frequency conditions seems to decrease with decreasing maximum load. This is indicated by comparing the three tests at 510°C (950°F) or the two at 593°C (1100°F) at 4 cpm. This conclusion is also supported by comparing the functional forms of S_n and K_{max} for the WOL specimen. Within the region of interest S_n increases faster with increasing crack length than does K_{max}. Therefore, to cover a larger region of stress intensity, tests with low P_{max} may be required physically to obtain low da/dN values, and tests with high P_{max} and short crack length may be required to obtain high da/dN values yet still be within the LEFM regime.

2.2.3.3 Results and Discussion

The aim of the experimental portion of this program is twofold. First, sufficient data are desired over appropriately varied testing conditions to allow parameterization of the fatigue crack growth behavior of 2 1/4 Cr-1 Mo in air as a function of temperature, frequency, and mean stress level in the region of interest. This will provide a sound base for demonstrating any effect of environment on crack growth behavior. The remainder of the effort involves testing in steam and simulated HTGR primary coolant helium.

To date, the preponderence of data obtained has been in air. This is to expected considering the added difficulty of running elevated-temperature SFCG tests in controlled environment and the extra time and

Table 2.10. Apparent Upper Limits of Plane Strain Crack Propagation for 2 1/4 Cr-1 Mo Steel as Indicated by Specimen Thinning at the Crack Tip

Specimen	Temperature (°C)	Temperature (°F)	R	Maximum Load (lb)	Maximum Load (kN)	Frequency (cpm)	Thinning, a/w (0.1% offset)	Limiting Stress Intensity Factors, ksi $\sqrt{in.}$ K_{max}	(MPa $\sqrt{m}$)	ΔK	(MPa $\sqrt{m}$)
1 ATL	Room		0.05	1250	5.56	420	0.770	55.00	(60.44)	52.25	(57.42)
4 ALT	510	950	0.033	1512	6.72	40	0.654	35.12	(38.59)	33.96	(37.32)
1 CLT	510	950	0.05	1750	7.78	200	0.623	35.72	(39.25)	33.93	(37.28)
6 CTL	510	950	0.5	1450	6.45	50	0.650	33.35	(36.65)	16.67	(18.32)
Average	510	950						34.73	(38.16)		
17 ATL	593	1100	0.05	1250	5.56	4	0.625	25.69	(28.23)	24.40	(26.81)
4 ATL	593	1100	0.05	1400	6.23	4	0.615	27.48	(30.20)	26.11	(28.69)
Average	593	1100				4		26.58	(29.23)	25.26	(27.76)
8 ALT	593	1100	0.05	1500	6.67	40	0.647	33.67	(37.00)	31.99	(35.15)

effort that has been necessary in equipment development. For the most part, all equipment is now operational, and the rate of data collection will henceforth be determined roughly by equipment availability, as described earlier.

Some of the first variables investigated in this study were specimen geometry and orientation within the rolled plate. A comparison of results from WOL, CT, and CN geometries revealed no noticeable effect at room temperature (see Fig. 2.7). Additionally, no differences in behavior were found between specimens in which the crack advanced parallel to or transverse to the plate rolling direction (WOL specimens 1 ATL and 1 ALT, respectively, in Fig. 2.7). Similar comparisons at 510°C (950°F) are shown in Fig. 2.8. As at room temperature, no differences are apparent.

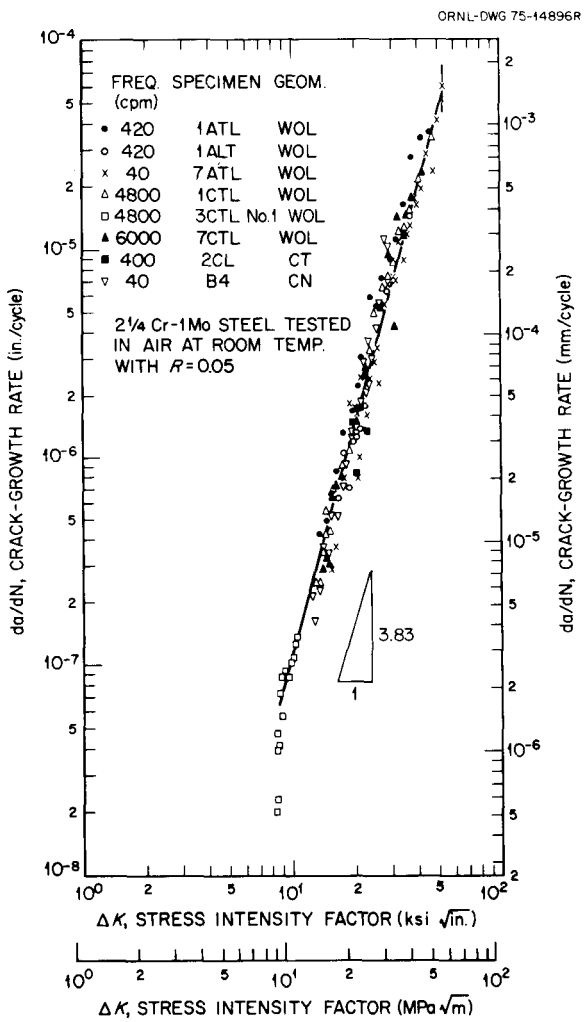

Fig. 2.7. Effects of Frequency, Specimen Geometry, and Orientation on SFCG at Room Temperature.

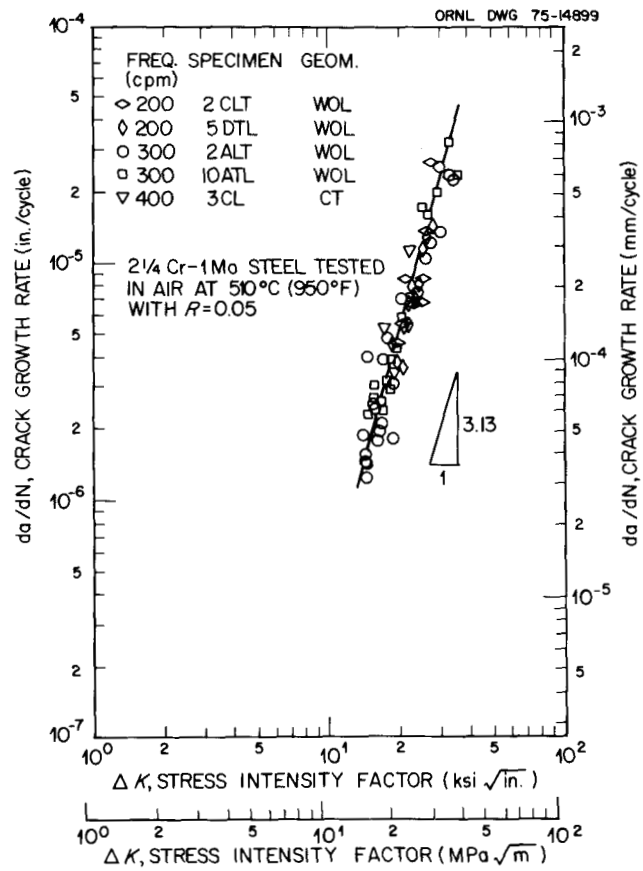

Fig. 2.8. Effects of Frequency, Specimen Geometry, and Orientation on SFCG at 510°C (950°F).

Investigations of frequency effects have begun at room temperature, 510°C (950°F), and 565°C (1100°F). At room temperature there is no effect of frequency in the range 0.67 to 100 Hz (40–6000 cpm) (see Fig. 2.7). At 510°C (950°F) no effects are seen in the range 3.3 to 6.7 Hz (200–400 cpm) (Fig. 2.8) nor would any be expected at higher frequencies. Tests at frequencies below 3.3 Hz (200 cpm) are, however, planned. At 593°C (1100°F), a temperature well into the creep range, strong frequency effects occur, as is evident in Fig. 2.9. Crack growth rate increases by roughly a factor of 2.5 when the frequency drops from 0.67 to 0.067 Hz (40 to 4 cpm). A wider range of frequencies will be examined at this temperature.

The work to date on the temperature dependence of crack-growth rate is also summarized in Fig. 2.9, with the composite lines representing room temperature and 510°C (950°F) behavior and the data points behavior

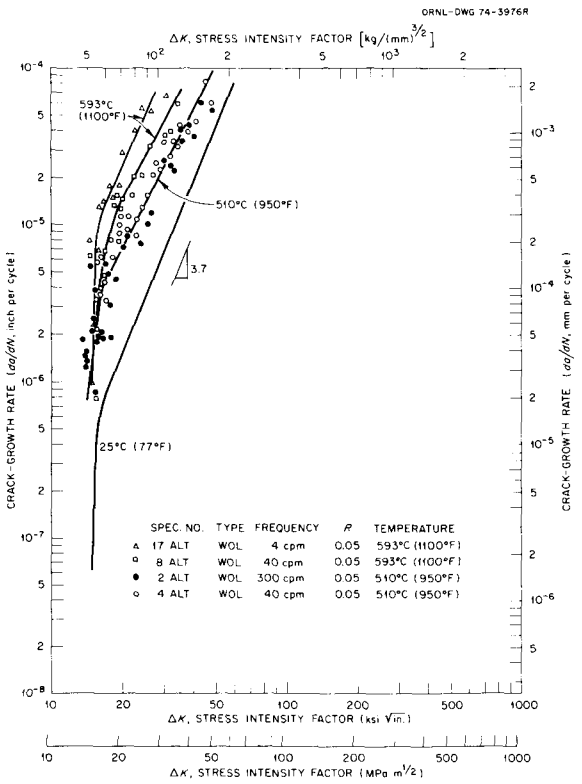

Fig. 2.9. Effects of Frequency and Temperature on SFCG from Room Temperature to 593°C (1100°F).

at 593°C (1100°F). The crack-growth rate clearly increases with increasing temperature; however, the 593°C (1100°F) data are not strictly comparable with those for the lower temperatures because the test frequencies are different and significant effects of frequency are associated with this higher temperature. Tests are planned at 204, 371, 454, and 593°C (400, 700, 850, and 1100°F) — all at 6.7 Hz (400 cpm) — to further examine temperature effects.

Since most of the 2 1/4 Cr-1 Mo structural components in the HTGR will operate with some mean load, tests have been performed over a range of mean stress levels. The results of tests at 510°C (950°F) at several values of R ratio (minimum load/maximum load) show (see Fig. 2.10) that increasing the mean stress increases the crack-growth rate. This type of behavior has been examined by Walker.[9] He has concluded that essentially the crack grows only while it is open at the tip. Since the crack tip is not open

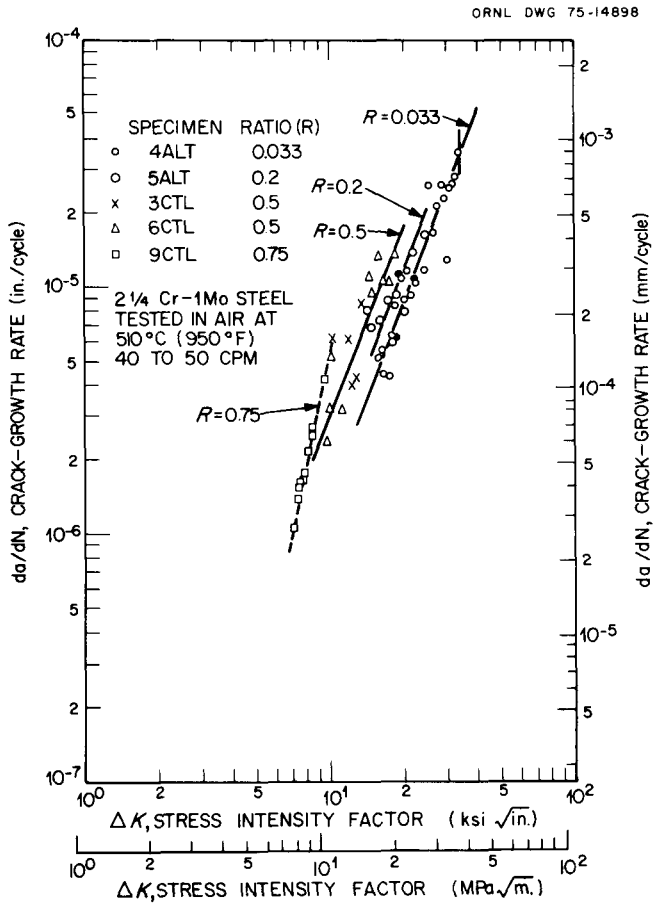

Fig. 2.10. Effects of Mean Stress on SFCG at 510°C (950°F).

during the entire load cycle (reversed plastic stresses keep the crack tip closed below a given load level). Walker has devised an effective stress intensity factor, which is used in place of ΔK to normalize crack growth rate data taken with different R ratios. The effective stress intensity factor, K_{eff}, is given by:

$$K_{eff} = K_{max}(1 - R)^m \quad , \tag{3}$$

where m is a material constant. The data in Fig. 2.10, with $0.003 \leq R \leq 0.5$, are normalized well by this equation using a value of m between 0.5 and 0.6. Optimization of m is currently under way. However, the data for test 9CTL (R = 0.75) are not normalized by the equation.

This is presumably because at R = 0.75 the crack is never closed, and hence the basis for K_{eff} is invalid. Further, nonlinear effects due to creep may also be important.

Tests in steam to date have been concentrated at 510°C (950°F). Results of the two tests shown in Fig. 2.11 indicate little or no effect of steam environment on the SFCG behavior of 2 1/4 Cr-1 Mo steel at 510°C (950°F) with R = 0.05 at a frequency of 3.3 Hz (200 cpm). The composite line for similar tests in air (taken from Fig. 2.8) virtually splits the data from the steam tests, and the agreement is certainly within experimental error. Comparison tests are currently under way in air and steam at 510°C (950°F) and 67 MHz (4 cpm).

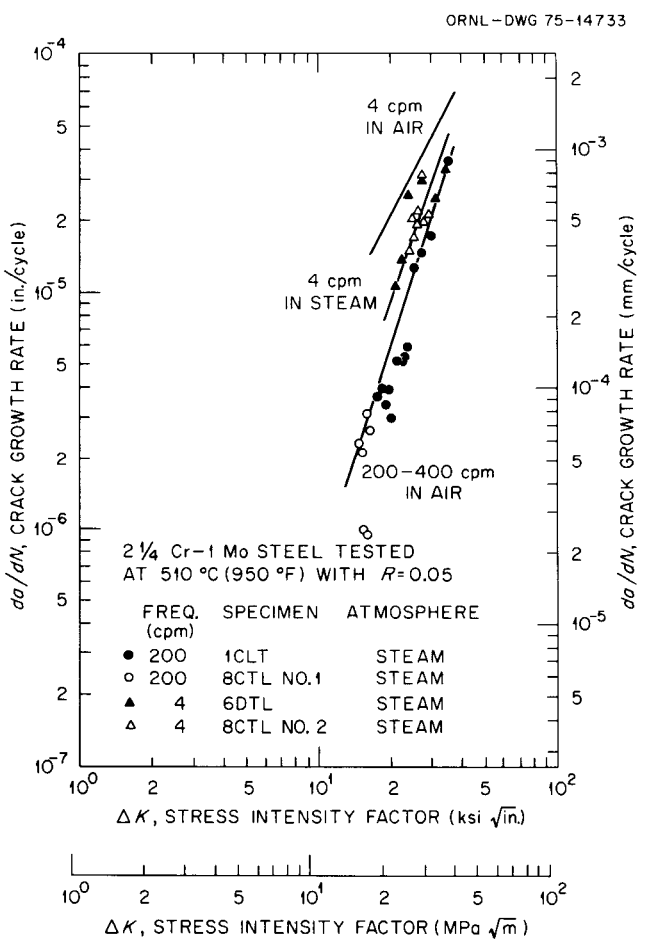

Fig. 2.11. Effects of Steam Environment at 510°C (950°F).

System check-out and initial testing in helium at 510°C (950°F), frequencies of 0.67 to 0.83 Hz (40–50 cpm), and R = 0.005 have been completed. After a lengthy shakedown period, it now appears that reproducible results can be generated. Direct comparison of this HTGR helium data with air data is not possible at this time because of the lack of 0.67-Hz (40-cpm) air data at 510°C (950°F). However, some tentative conclusions can be made. As seen in Fig. 2.12, the linear (stage 2) growth rate (above the knee of curve) is lower in HTGR helium than in air. On the basis of the air data at 593°C (1100°F), if there is a frequency effect in air at 510°C (950°F), changing test frequencies from 3.3–6.7 Hz (200–400 cpm) down to 40 cpm would probably increase the growth rate. This would increase even further the difference in crack-growth rate between air and HTGR helium at 510°C (950°F). The present indication that a simulated HTGR primary coolant environment is beneficial relative to air in terms of crack growth rate is still tentative. Significantly more work will be needed to confirm this conclusion.

2.2.4 Low-Cycle Fatigue Life Testing — J. P. Strizak

2.2.4.1 Fatigue Behavior of 2 1/4 Cr-1 Mo Steel

Fatigue testing of 2 1/4 Cr-1 Mo steel is currently under way at several temperatures to define material behavior under cyclic loading conditions and to establish the design base for design-oriented correlations. The following types of tests are either under way or planned:

Low-cycle fatigue
High-cycle fatigue
Fatigue, strain rate sensitivity
Creep fatigue tests
  Short term
  Long term
Tensile tests
  Constant strain rate to failure
  Cyclic stress-strain curve
  Interrupted fatigue
  Block or multiple-step fatigue

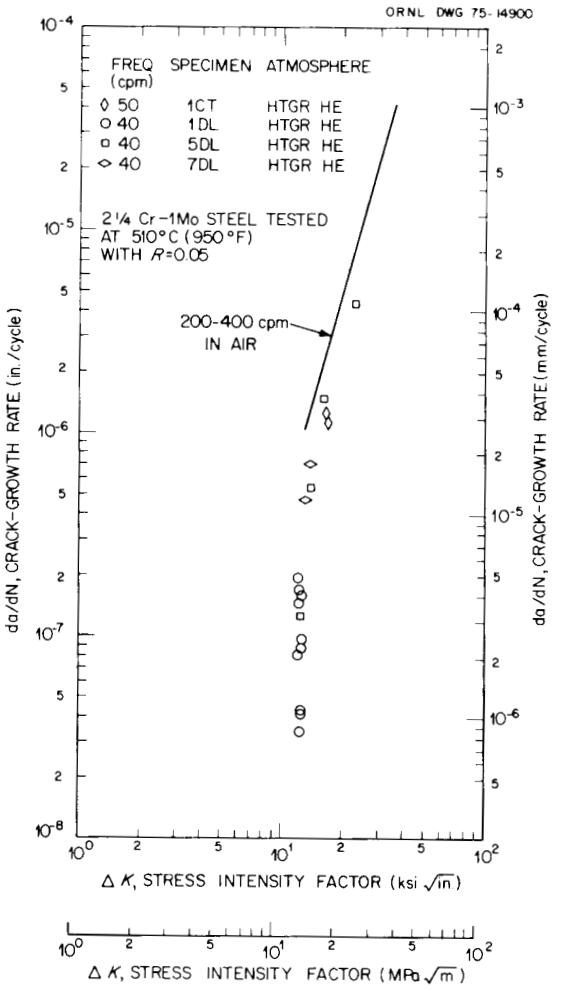

Fig. 2.12. Effects of Simulated HTGR Primary Coolant at 510°C (950°F).

Combined mode

Mixed mode

Mean strain fatigue

Fatigue of weld metal and weldments

Notched fatigue

Stable crack growth

Combined push-pull axial and torsion

Aging and test environment

Strain and load-controlled fatigue tests in air are under way at temperatures from room to 538°C (1000°F). Two commercial heats of 25-mm-thick (1-in.) Croloy plate are being tested. Specimens were prepared

from material in either the annealed (furnace cooled) or isothermally annealed condition. The isothermal annealing treatment is described in Sect. 2.2.3.1.

Hourglass-shaped specimens were prepared for both the load- and strain-controlled tests from the plate material, with the major axis of the specimen parallel to the rolling direction of the plate. Tests were performed on closed-loop, electro-hydraulic testing machines; strain-controlled tests employed a diametral extensometer and a simple analog computer to convert directly measured diametral strain to axial strain.

Results reported herein were obtained from three test laboratories: Mar-Test, Battelle Memorial Institute — Columbus, and Oak Ridge National Laboratory. Additional strain- and load-controlled data were obtained through the courtesy of General Atomic Company (GA). The chemical composition of the material tested in the GA program is compared with the ORNL heats in Table 2.11.

Table 2.11. Chemical Analysis of the 2 1/4 Cr-1 Mo Steel

Product Form	Heat	Chemical Composition, wt %								ASTM Grain Size
		C	Mn	Si	Cr	Mo	Ni	S	P	
Plate (ORNL)	20017	0.135	0.57	0.37	2.2	0.92	0.16	0.016	0.012	4–5
Plate (ORNL)	3P5601	0.145	0.53	0.40	2.18	0.94	0.30	0.019	0.014	7–8
Pipe (GA)	1	0.11	0.47	0.35	2.89	0.96	0.26	0.009	0.013	4–5
Pipe (GA)	2	0.11	0.35	0.23	2.42	0.92	0.04	0.025	0.008	7–8
Pipe (GA)	3 (27479)	0.119	0.35	0.27	2.30	0.96	0.20	0.022	0.009	5

Tensile data for the GA heats 1, 2, and 3 are compared with data obtained on the ORNL heat 20017 in Fig. 2.13(a). Results from tensile tests conducted on ORNL heat 3P5601 are plotted in Fig. 2.13(b). Generally, good agreement was found in comparing the tensile properties for the several heats and heat treatments. Indications of strain aging in the intermediate temperature range are apparent from the ductilities and strengths shown in Fig. 2.13. Results of the strain- and load-controlled

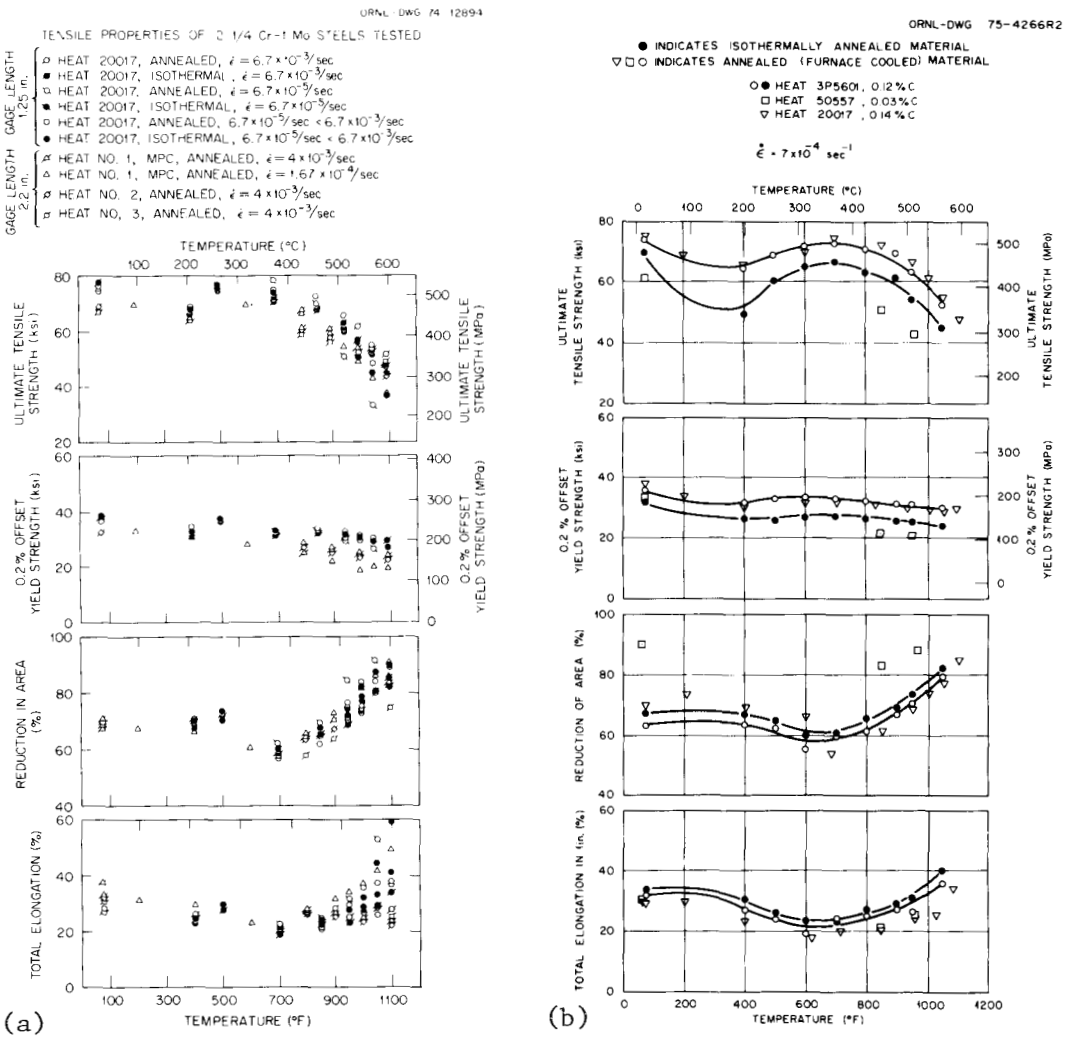

Fig. 2.13. Tensile Properties of 2 1/4 Cr-1 Mo Steel. (a) Several heats tested at various strain rates. Gage lengths given are 31.8 and 55.9 mm. (b) Heat 3P5601 tested at a strain rate of 6.7×10^{-4}/sec.

fatigue tests are plotted as elastic, plastic, and total strain range versus cycles to failure in the illustrations described below.

In Fig. 2.14 the results are plotted for strain-controlled tests conducted at both room temperature and 316°C (600°F). Data for both the elastic and plastic components of strain show linearity when plotted on log-log coordinates; hence, the room-temperature data were best fitted with simple power-law equations by least squares analysis. Extrapolation of the elastic and plastic best fit lines, followed by summation, permitted a reasonable extrapolation of the total strain range for the room-temperature

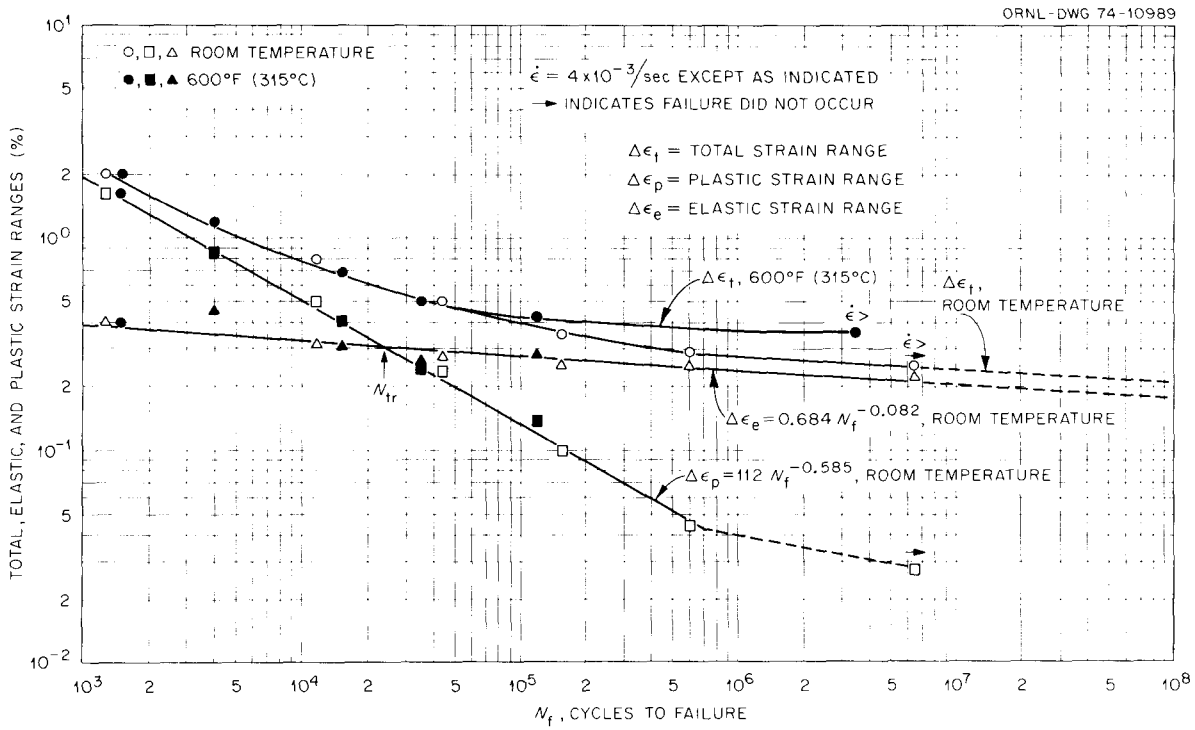

Fig. 2.14. Total, Elastic, and Plastic Strain Range Versus Cycles to Failure for Isothermally Annealed 2 1/4 Cr-1 Mo Steel at Room Temperature and 316°C (600°F), Showing Transition Fatigue Life, N_{tr}. Total strain range data points marked $\dot{\varepsilon}$> were obtained from tests started in strain control at the indicated strain rate but changed to load control and a higher strain rate after several hundred thousand cycles and an indication of load stability.

data out to 10^8 cycles to failure. Comparing the 316°C (600°F) fatigue data, obtained from limited tests, with the room-temperature data shows that little difference in fatigue life occurs in this temperature range within the low-cycle region. However, at cyclic lives exceeding approximately 60,000 cycles, there is a strong indication that the fatigue life of this material at 316°C (600°F) exceeds that at room temperature.

In Fig. 2.15 the results are plotted for strain-controlled tests conducted at 371°C (700°F). A distinct break occurred in the otherwise linear (log-log) plot of plastic strain range versus cycles to failure, resulting in a bilinear (log-log) data plot. The data were fitted similarily to the room-temperature data.

Results are plotted in Fig. 2.16 from both strain- and load-controlled tests conducted at 427°C (800°F). Distinct breaks occurred in the

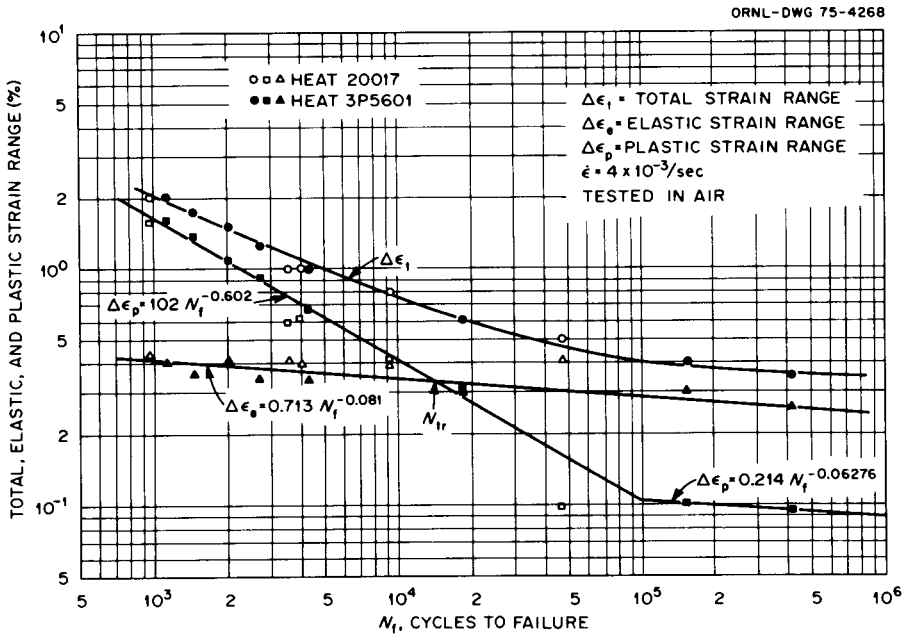

Fig. 2.15. Total Elastic and Plastic Strain Range Versus Cycles to Failure for Isothermally Annealed 2 1/5 Cr-1 Mo Steel at 371°C (700°F), Showing Transition Fatigue Life, N_{tr}.

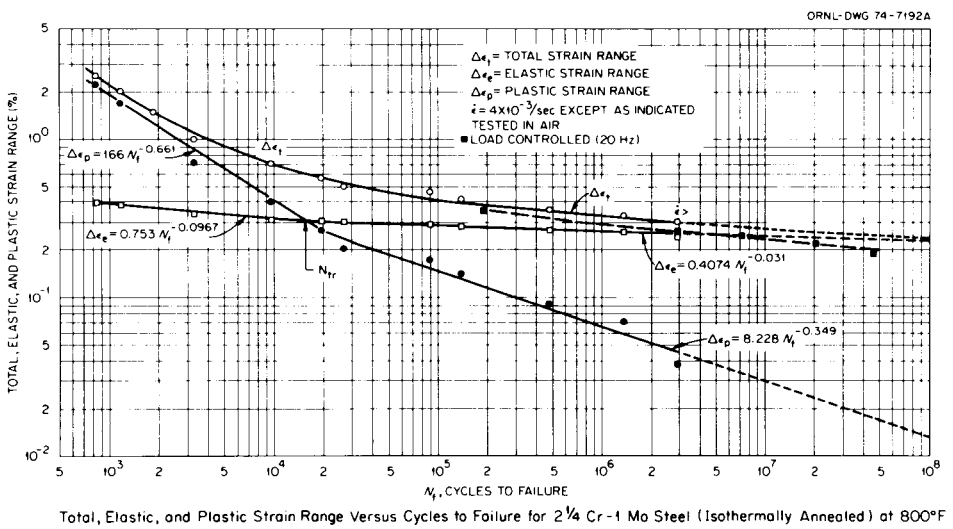

Total, Elastic, and Plastic Strain Range Versus Cycles to Failure for 2¼ Cr-1 Mo Steel (Isothermally Annealed) at 800°F (427°C) Showing Transition Fatigue Life, N_{tr}.

Fig. 2.16. Total, Elastic, and Plastic Strain Range Versus Cycles to Failure for Isothermally Annealed 2 1/4 Cr-1 Mo Steel at 427°C (800°F), Showing Transition Fatigue Life, N_{tr}. Extrapolations of data obtained from tests conducted in strain control are compared with data obtained from tests conducted in load control. In tests marked $\dot{\varepsilon}$>, strain rate increased after load stability was obtained.

otherwise linear (log-log) plots of both elastic and plastic strain range versus cycles to failure, resulting in bilinear (log-log) data plots. The data were fitted and the total strain range was extrapolated similarly to the room-temperature data. The results of the load-controlled tests shown over the range of 1.87×10^5 to 1.45×10^7 cycles to failure were not considered in the extrapolation of the strain-controlled data. An estimate of the stabilized strains achieved for the load-controlled tests, which was used to compare the load-controlled cyclic lives with the strain-controlled lives, was obtained from the cyclic stress-strain curves presented later. Alternatively, excellent agreement was found when the strains obtained from the cyclic stress-strain curve were compared with the appropriate values of stress divided by the appropriate dynamic Young's modulus. The single exception was the test conducted at a stress level that resulted in failure at about 187,500 cycles. In this case the strain was taken from the cylic stress-strain curve for this material. As shown in Fig. 2.16, the results of the load-controlled tests are not necessarily consistent with results or extrapolated results of the strain-controlled tests, even out in the ultrahigh-cycle range (i.e., $>10^7$ cycles) where the strain is nearly all elastic. There are several possible explanations for this behavior. These are: (1) cyclic hardening followed by softening of the material, although it occurs primarily during the first part of a given test, may complicate the strain history of a test conducted in load control; (2) some ratchetting of the load-controlled specimen may result in a nonzero mean load spectrum; (3) normal scatter in the data within the high-cycle region may result from subtle differences in surface finish, residual stress levels, etc.; and (4) experimental techniques may differ subtly, since the load-controlled tests, with the single exception of the test that failed at approximately 187,500 cycles, were conducted in a different laboratory than the strain-controlled tests.

Results of both the load- and strain-controlled tests obtained at 538°C (1000°F) are compared in Fig. 2.17. The load-controlled data were obtained by Brookhaven National Laboratory[10] on a different heat of Croloy (0.145% C in the annealed condition). An extrapolation of the data on total strain range versus cycles to failure, giving an indication of

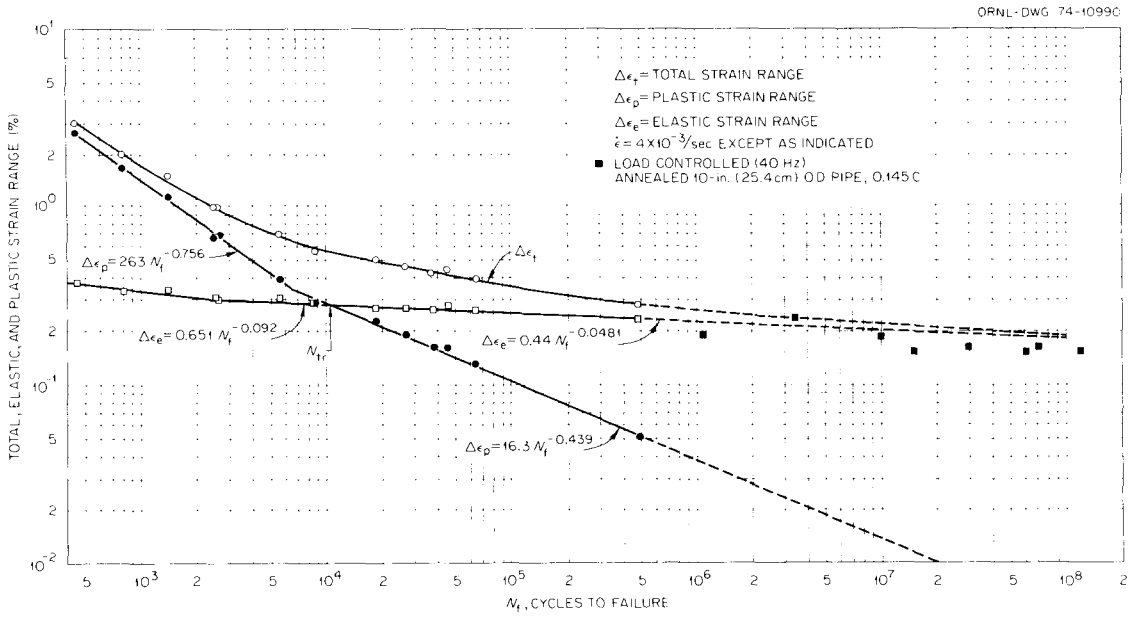

Fig. 2.17. Total, Elastic, and Plastic Strain Range Versus Cycles to Failure for Isothermally Annealed 2 1/4 Cr-1 Mo Steel at 538°C (1000°F), Showing Transition Fatigue Life, N_{tr}. Extrapolations, $\Delta\varepsilon_t$, of data obtained from strain-controlled tests are compared with data obtained from high-cycle load-controlled tests.

expected failure to 10^8 cycles, was similarly constructed from the elastic and plastic strain range values. Again, the results of the load-controlled tests fall below the extrapolated curve for the strain-controlled test data.

Figure 2.18 contains 593°C (1100°F) data received from GA and shows best fit lines for plastic and elastic strain ranges and the sum of these lines yielding total strain range vs cycles to failure.

A composite plot of total strain range versus cycles to failure is given in Fig. 2.19. This figure compares lines drawn through the strain-controlled test data points and associated extrapolations given in Figs. 2.14 through 2.18 in the 427 to 538°C (800–1000°F) range and at room temperature. Figures 2.15 through 2.18 demonstrate that the plastic ($\Delta\varepsilon_p$) and the elastic ($\Delta\varepsilon_e$) components of the total strain range ($\Delta\varepsilon_t$) can be expressed as simple power law relationships, thus:

$$\Delta\varepsilon_t = \Delta\varepsilon_p + \Delta\varepsilon_e \ , \qquad (4)$$

$$\Delta\varepsilon_t = AN_f^{-a} + BN_f^{-b} \ . \tag{5}$$

However, because of the bilinearity of the plastic strain range line when plotted on log-log coordinates, values of the constants A and a depend on strain range, as indicated in Table 2.12.

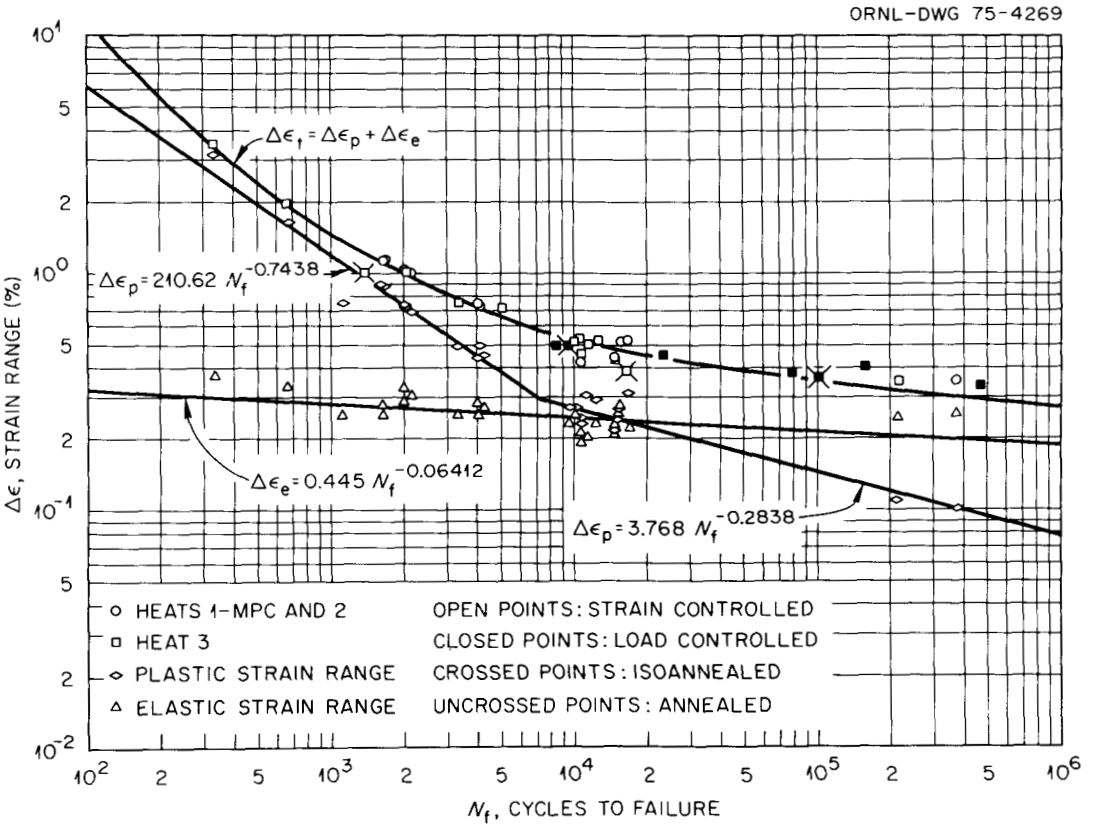

Fig. 2.18. Total, Elastic, and Plastic Strain Range Versus Cycles to Failure for Annealed and Isothermally Annealed 2 1/4 Cr-1 Mo Steel at 593°C (1100°F). Best fit lines for plastic and elastic strain ranges and the sum of these lines for the total strain range are shown.

Cycling specimens in strain control resulted in initial rapid (primary) hardening followed by either gradual (secondary) hardening, softening, or near stability as cycling continued, as evidenced by changes in load required to maintain the prescribed total axial strain range, $\Delta\varepsilon_t$. The amount of secondary hardening or softening depended upon $\Delta\varepsilon_t$ and temperature, with a tendency toward continuous hardening at the higher strain

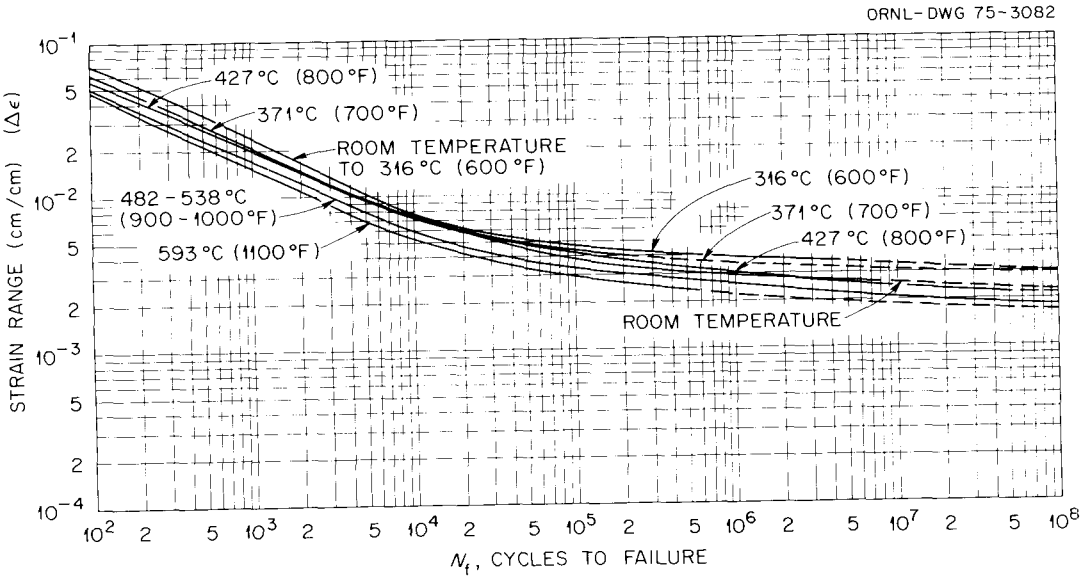

Fig. 2.19. Best Fit Fatigue Curves for Annealed and Isothermally Annealed 2 1/4 Cr-1 Mo Steel. $\dot{\varepsilon} \approx 4 \times 10^{-3}$/sec.

Table 2.12. Values for the Elastic and Plastic Strain Range Constants for Strain-Controlled Tests Conducted at a Strain Rate of 4×10^{-3}/sec

Temperature (°C)	Temperature (°F)	N_f Range (cycles)	Values of Constants in $\Delta\varepsilon_t = AN_f^{-a} + BN_f^{-b}$			
			A	a	B	b
Room		$\leq 6 \times 10^5$	112	0.585	0.684	0.082
315	600	$< 6 \times 10^4$	112	0.585	0.684	0.082
		$> 6 \times 10^4$	1.03	0.164	0.684	0.082
371	700	$< 10^5$	102	0.683	0.713	0.081
		$> 10^5$	0.214	0.063	0.713	0.081
427	800	$< 1.8 \times 10^4$	166	0.661	0.407	0.031
		$> 1.8 \times 10^4$	8.23	0.349	0.407	0.031
539	1000	$< 1 \times 10^4$	263	0.756	0.440	0.048
		$> 1 \times 10^4$	16.3	0.439	0.440	0.048
593	1100	$< 7.5 \times 10^3$	210.6	0.744	0.445	0.064
		$> 7.5 \times 10^3$	3.768	0.284	0.445	0.064

ranges, say 2%, and softening at lower strain ranges. Increasing the temperature reduced the amount of secondary hardening at the higher strain ranges and increased the softening at the lower strain ranges. Examples of this hardening-softening behavior, as evidenced by changes in the stress range, $\Delta\sigma$, with fraction of cycle life over the temperature range of room temperature to 538°C (1000°F) are shown in Figs. 2.20 through 2.24 for both a high- and low-strain-range test at each temperature.

A summary plot of both the half-life ($N_f/2$) stress and plastic strain range as functions of temperature for several total strain ranges ($\Delta\varepsilon_t$) is given in Fig. 2.25. The plots of these independent variables indicate only slight temperature sensitivity [excluding dynamic strain aging effects at 371°C (700°F)] until temperatures above about 427°C (800°F) are obtained. Strain aging in the range 316 to 427°C (600—800°F) complicates the high-cycle fatigue life in that material tested at 316°C (600°F) shows superior resistance to fatigue life compared with material tested at room temperature, as shown in Fig. 2.19. Cyclic stress-strain curves were obtained with $N_f/2$ values of the stress-range and are compared with monotonic curves in Figs. 2.26 through 2.29.

Based on existing data on GA heat 3 over the temperature range from 427 to 538°C (800—1000°F) (data not shown), comparison of the strain-controlled cyclic lives of annealed and isothermally annealed material shows that little difference in lifetime is presently apparent from these heat treatment variations. However, differences in cyclic stress-strain behavior do occur, and variations in lifetimes are apparent when the materials are tested in load control. Figure 2.28 compares the cyclic stress-strain curves for heat 20017 in the isothermally annealed condition and heat 3 in both the annealed and isothermally annealed conditions. Heat 3 material in the isothermally annealed condition cyclically hardens to higher values of stress than does the annealed material when loaded under strain control. Thus, in strain control higher loads were required to achieve the programmed strain range for the isothermally annealed material than for the same material in the annealed condition. Comparing the cyclic stress-strain response of the two heats in the isothermally annealed condition in Fig. 2.28 reveals that some heat-to-heat variations exist.

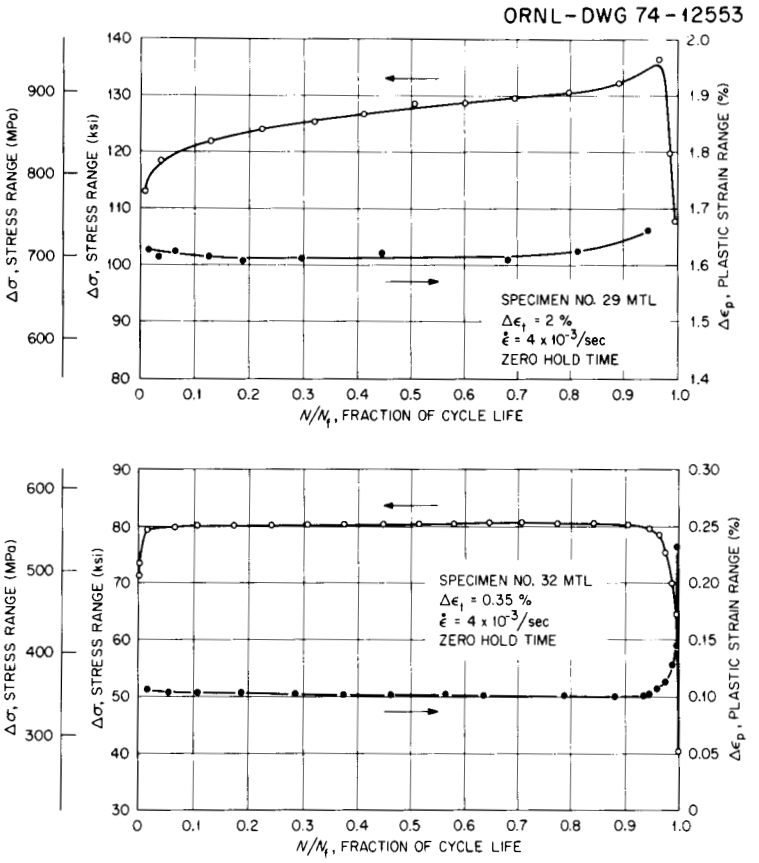

Fig. 2.20. Stress and Plastic Strain Ranges as Functions of Fraction of Cyclic Life for Isothermally Annealed 2 1/4 Cr-1 Mo Steel, Heat 20017, at Room Temperature.

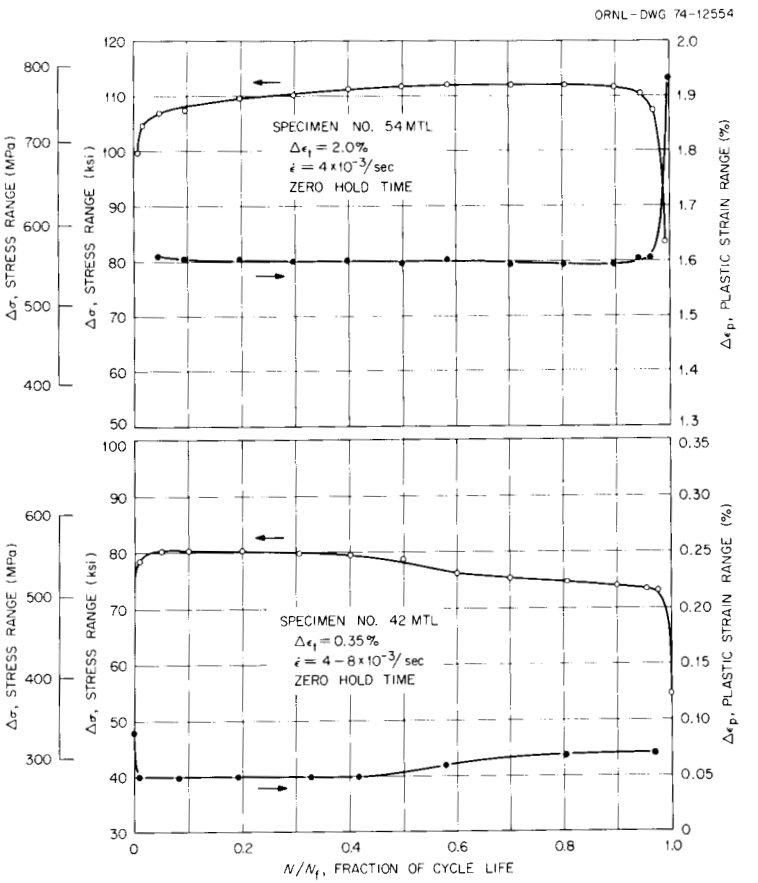

Fig. 2.21. Stress and Plastic Strain Ranges as Functions of Fraction of Cyclic Life for Isothermally Annealed 2 1/4 Cr-1 Mo Steel, Heat 20017, at 315°C (600°F).

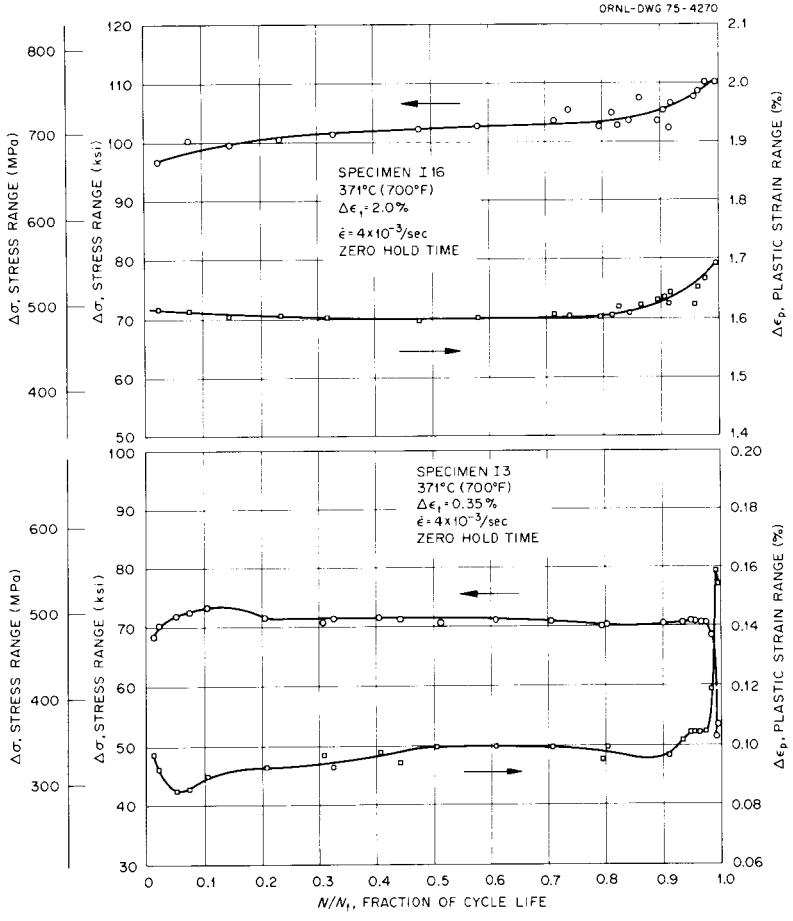

Fig. 2.22. Stress and Plastic Strain Ranges as Functions of Fraction of Cyclic Life for Isothermally Annealed 2 1/4 Cr-1 Mo Steel, Heat 3P5601, at 371°C (700°F).

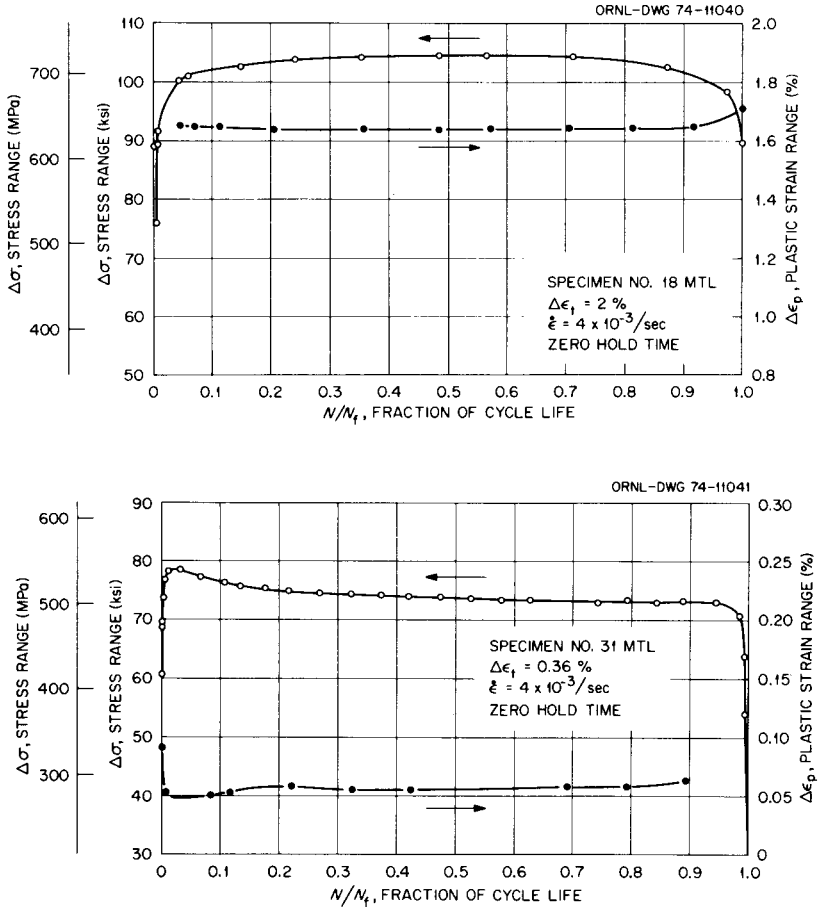

Fig. 2.23. Stress and Plastic Strain Ranges as Functions of Fraction of Cyclic Life for Isothermally Annealed 2 1/4 Cr-1 Mo Steel, Heat 20017, at 427°C (800°F).

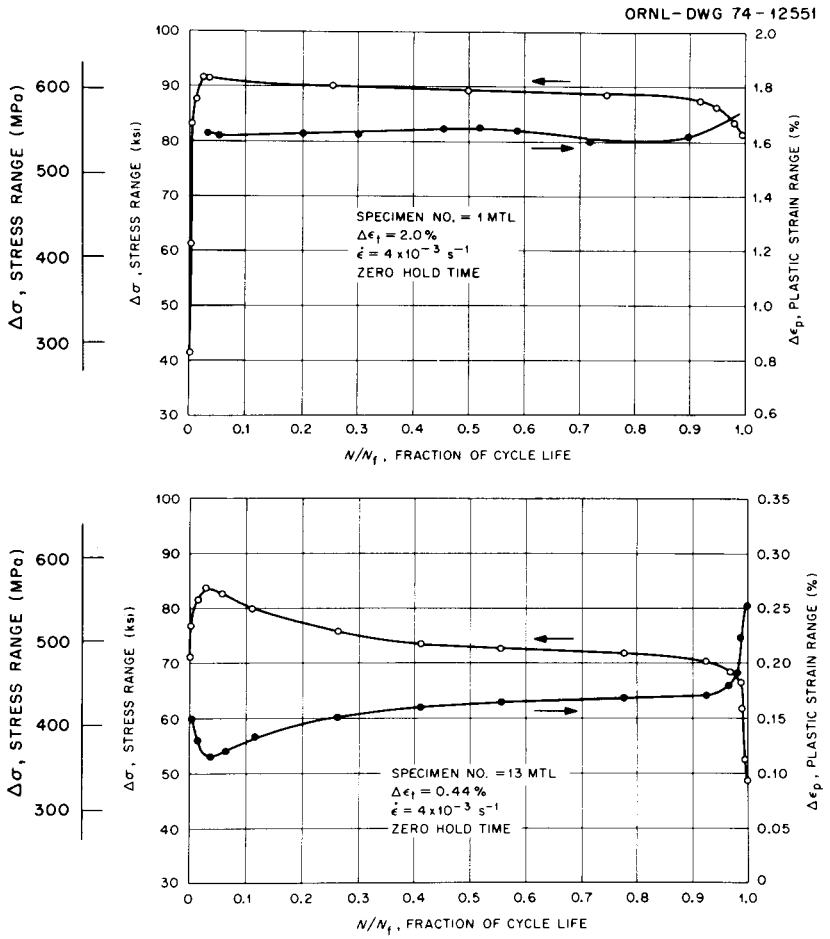

Fig. 2.24. Stress and Plastic Strain Ranges as Functions of Fraction of Cyclic Life for Isothermally Annealed 2 1/4 Cr-1 Mo Steel, Heat 20017 at 538°C (1000°F).

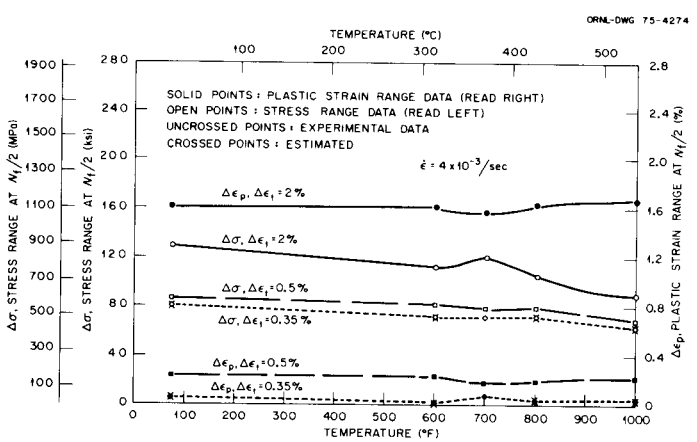

Fig. 2.25. Stress and Plastic Strain Ranges at $N_f/2$ as Functions of Temperature at Several Total Strain Ranges ($\Delta\varepsilon_t$).

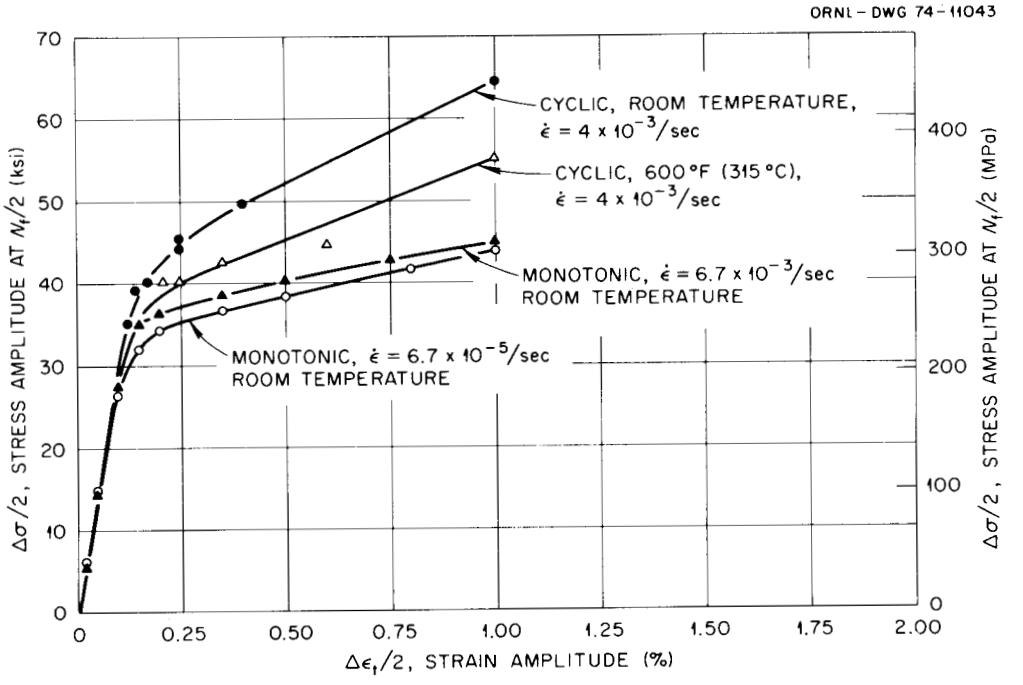

Fig. 2.26. Comparison of the Cyclic and Monotonic Stress-Strain Curves for Isothermally Annealed 2 1/4 Cr-1 Mo Steel at Room Temperature and 316°C (600°F).

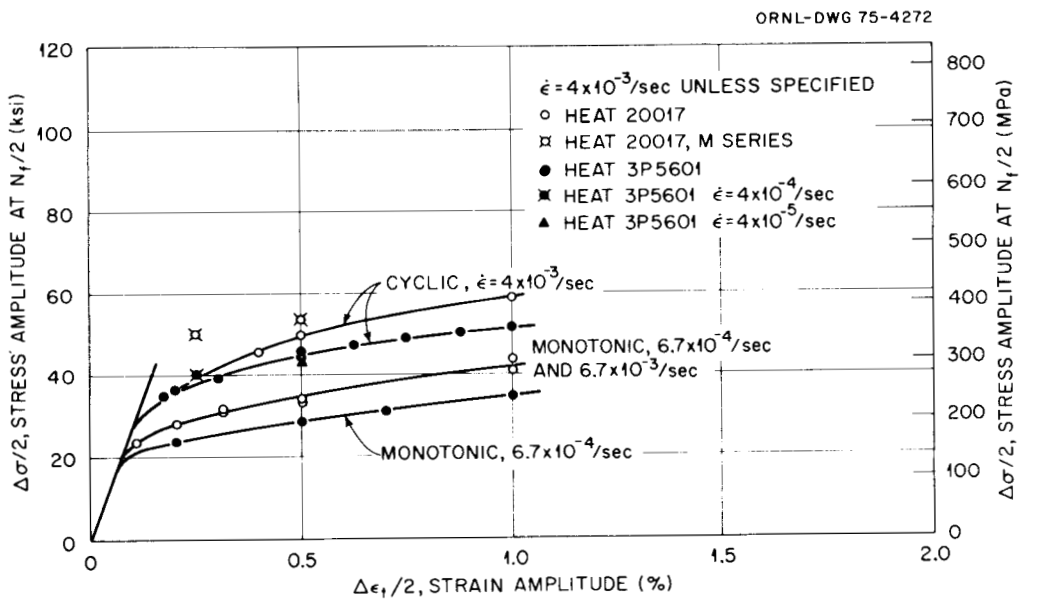

Fig. 2.27. Comparison of the Cyclic and Monotonic Stress-Strain Curves for Isothermally Annealed 2 1/4 Cr-1 Mo Steel at 371°C (700°F).

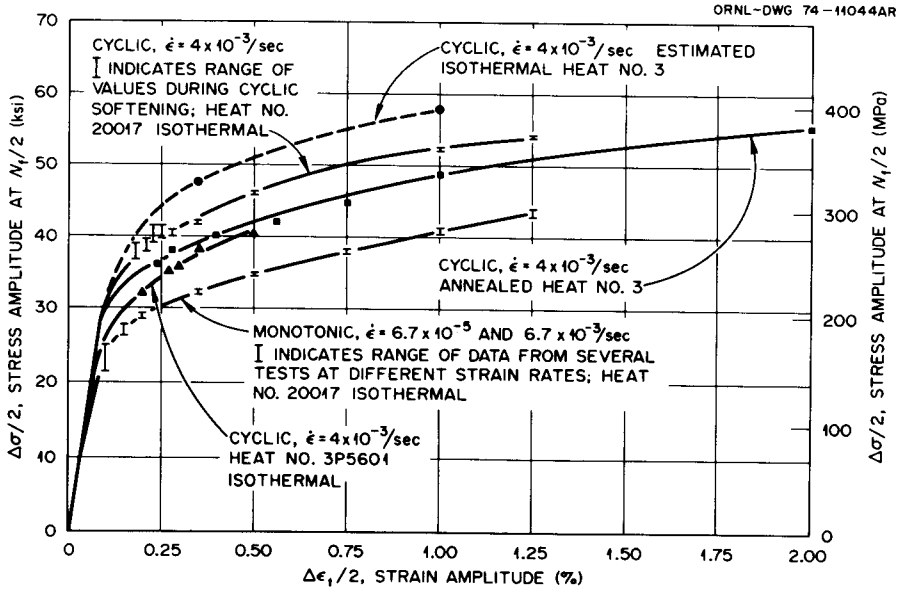

Fig. 2.28. Comparison of the Cyclic and Monotonic Stress-Strain Curves for Isothermally Annealed and Annealed 2 1/4 Cr-1 Mo Steel at 427°C (800°F).

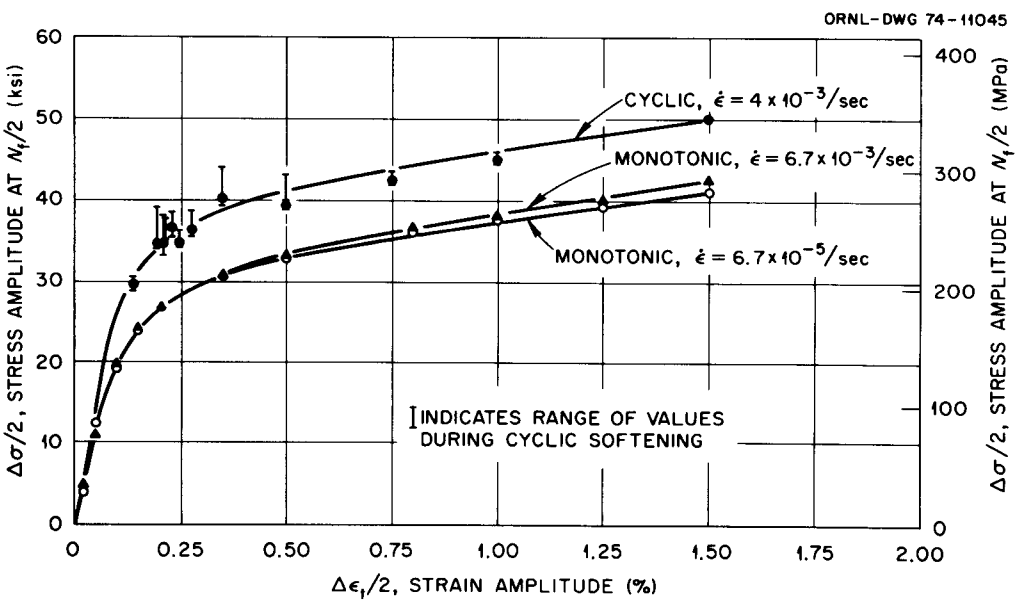

Fig. 2.29. Comparison of the Cyclic and Monotonic Stress-Strain Curves for Isothermally Annealed 2 1/4 Cr-1 Mo Steel at 539°C (1000°F).

Similarly, the overall fatigue lives of the two ORNL heats, 20017 and 3P5601, differ little at 371°C (700°F) in the isothermally annealed condition (see Fig. 2.15). However, some differences in both cyclic and monotonic flow response are apparent from the plots given in Fig. 2.27.

Portions of the cyclic stress-strain curves for these materials obeyed a simple expression of the form

$$\Delta\sigma/2 = A(\Delta\varepsilon_p/2)^n \ , \tag{6}$$

where $\Delta\sigma/2$ and $\Delta\varepsilon_p/2$ are the stress amplitudes and plastic strain amplitudes, respectively, taken at half the cyclic life ($N_f/2$). The constants A and n depend on material, temperature, and strain rate. Isothermal plots of the data on log-log coordinates are shown in Fig. 2.30. Differences in cyclic stress-strain response between the annealed and isothermally annealed material are again apparent for heat 3, particularly at 593°C (1100°F).

As indicated earlier, strain aging is apparent in 2 1/4 Cr-1 Mo over the temperature range from 316 to 427°C (600–800°F), as seen in the tensile properties of this material. To determine the influence of dynamic strain aging on fatigue life several compressive hold time and lower strain-rate continuous cycling fatigue tests were conducted at 371°C (700°F). The data shown in Fig. 2.31 indicate a degradation in fatigue life with decreasing strain rate achieved by either hold periods or a lower cyclic frequency.

Continuous cycling strain-controlled fatigue tests conducted with either tensile or compressive hold periods are also under way. These tests are necessary to define the design creep-fatigue curves. Figure 2.32 contains the results of hold time tests conducted to date over the range from 371 to 539°C (700–1000°F). In these plots cycle life reduction factors and changes in the plastic strain range are compared for various strain ranges and temperatures as functions of hold time. The cycle life reduction factor is defined as the ratio of the cycles to failure, N_h, for a given strain range, temperature, and hold time divided by the corresponding cycles to failure, N_f, from a test conducted under identical

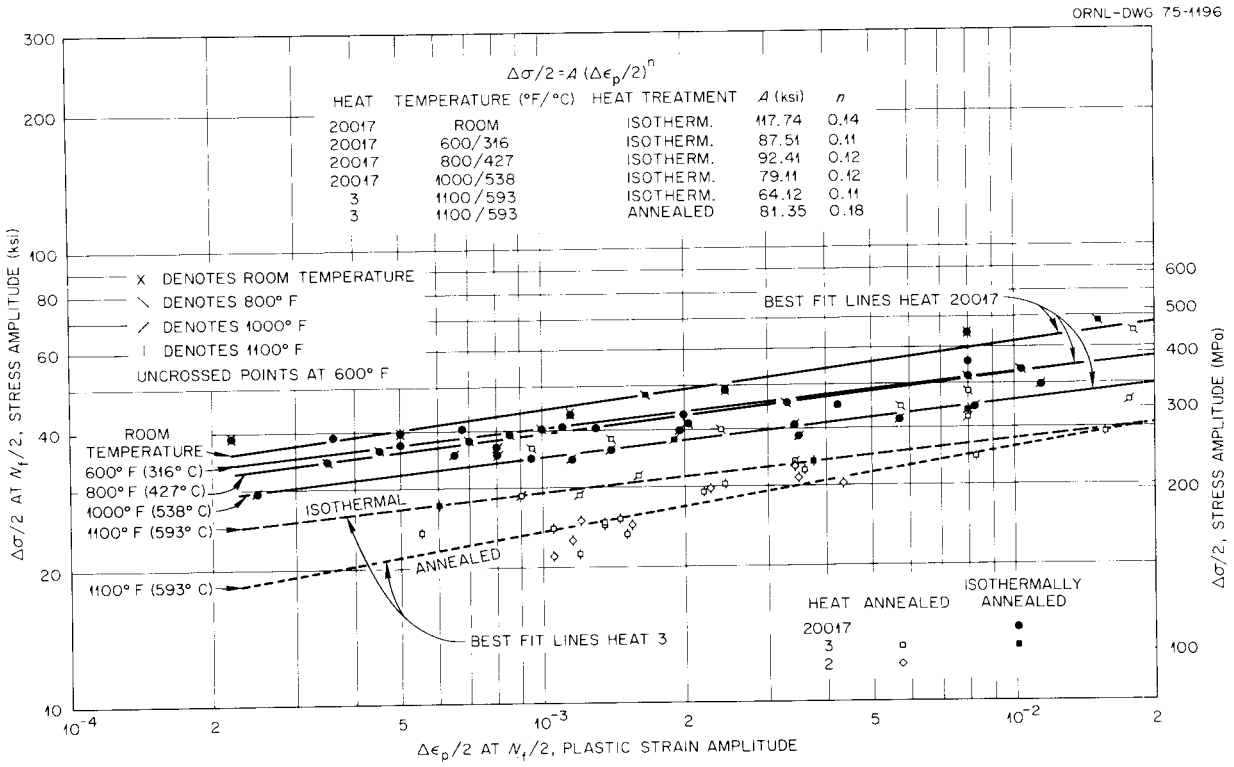

Fig. 2.30. Stress Amplitude as a Function of Plastic Strain Amplitude for several Heats of 2 1/4 Cr-1 Mo Steel.

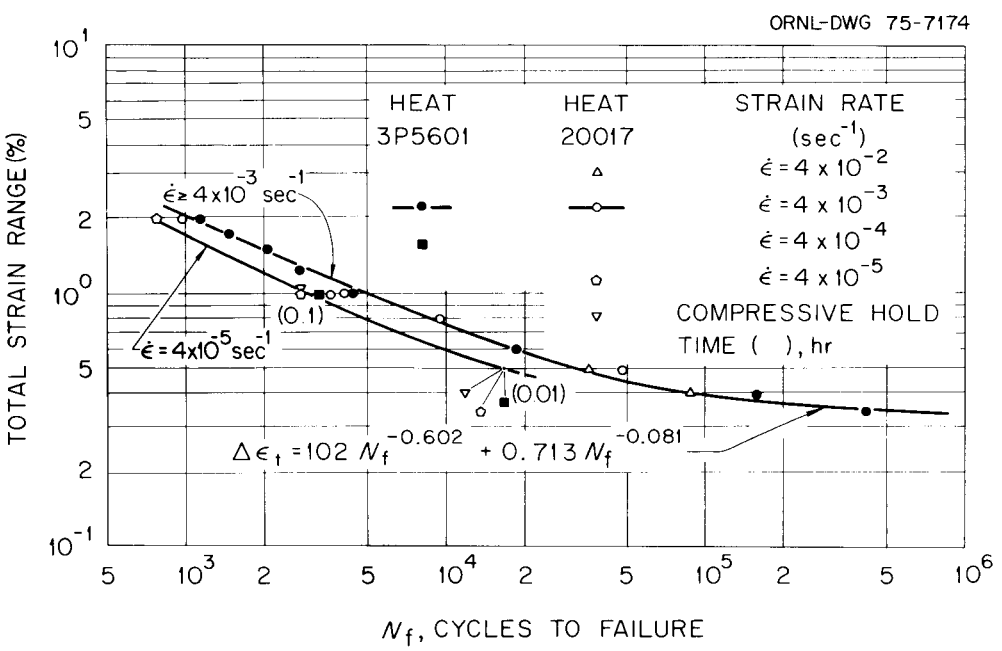

Fig. 2.31. Total Strain Range, $\Delta\varepsilon_t$, vs Cycles to Failure at 371°C (700°F), Showing the Influence of Strain Rate on the Strain-Controlled Fatigue Properties of 2 1/4 Cr-1 Mo Steel.

ORNL-DWG 75-4277A

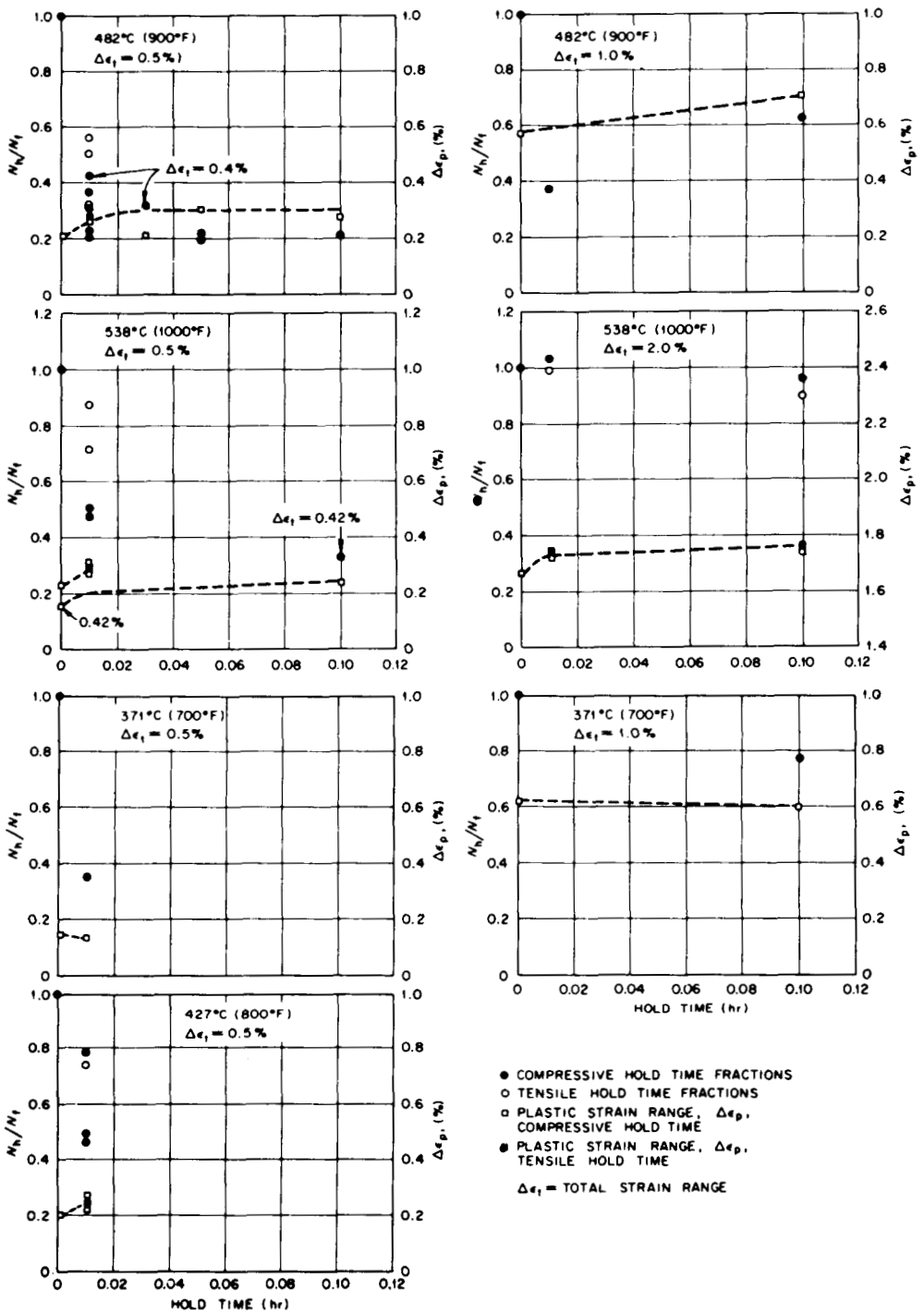

Fig. 2.32. Cyclic Life Reduction Factors for Several Strain Ranges as Functions of Strain-Controlled Hold Times (Compressive or Tensile) at Four Temperatures. N_h = cyclic life with indicated hold time. N_f = cyclic life without hold time.

conditions without a hold time. The interim data were plotted this way so that the reader might compare the influence of various hold times, both tensile and compressive, on the fatigue life in tests conducted at various strain ranges and temperatures. From these plots the following preliminary conclusions concerning the behavior of 2 1/4 Cr-1 Mo steel were made:

1. There is a deleterious hold-time effect at all temperatures considered. However, the hold-time effect at 371°C (700°F) appears to be due to strain aging rather than creep, since the value of the $N_f/2$ plastic strain range actually decreases in comparison with the similar no-hold-time test.

2. The hold-time effect is greater at lower strain ranges (i.e., $\Delta\varepsilon_t$ = 0.4 or 0.5%) than at higher strain ranges. At low strain ranges compressive hold times seem to be more deleterious than the corresponding tensile hold times. Since compressive effects do occur in elevated-temperature design this finding has engineering significance and, therefore, compressive hold-time tests have been emphasized.

3. Over the temperature range and hold times employed to date, very short hold times (e.g., 0.01 hr) had a marked influence on the low-strain-range fatigue life of this material. Low strain ranges and fairly low temperatures have been particularly emphasized to date in order to obtain data approaching actual design conditions and to provide the data base for comparison with predictions based on data taken at higher temperatures and higher strain ranges.

Figure 2.33 compares peak stresses and plastic strain ranges achieved as functions of fraction of cycle life for specimens tested with and without hold times for similar test conditions. At low strain ranges there is a considerable apparent drop in the peak stress range introduced as a consequence of the hold times at this temperature. Also, the plastic strain range shows a marked increase.

The particularly damaging effect of compressive hold periods is somewhat contrary to earlier findings[11] on other materials, and requires investigation. One suggestion[12] has been that compressive holds tend to create a mean tensile stress and thus enhance crack propagation, leading

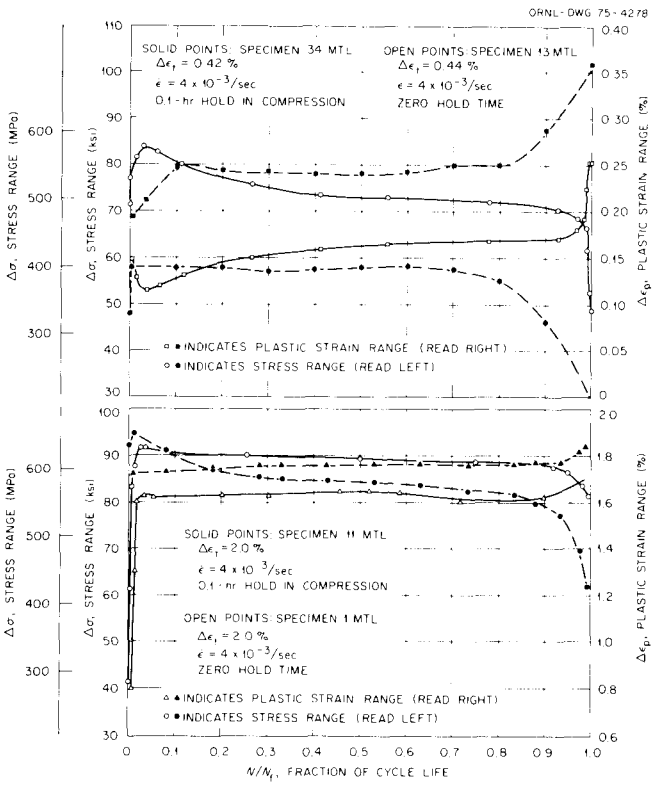

Fig. 2.33. Stress and Plastic Strain Ranges as Functions of Fraction of Cyclic Life for 2 1/4 Cr-1 Mo Steel (Isothermally Annealed) at 538°C (1000°F). Tests conducted with and without hold times are compared.

to decreased cyclic life. An investigation of this effect, however, has shown no noticeable trend in this direction for the current data, as shown in Fig. 2.34 for two different temperatures.

Several methods for the analysis of creep-fatigue data have been proposed, including the strain range partitioning approach,[13] the linear summation of damage approach,[14] the frequency modification approach,[15] the ductility exhaustion approach,[16] and others. Most methods require a complete spectrum of data, including a range of hold times, strain ranges, etc. However, data obtained in the current program are as yet incomplete, making analysis by these latter methods difficult. Interim results have been obtained, however, by the methods of strain range partitioning and linear summation of damage.

The linear summation of damage approach is that currently used for actual design.[14] Briefly, the method consists of separately identifying

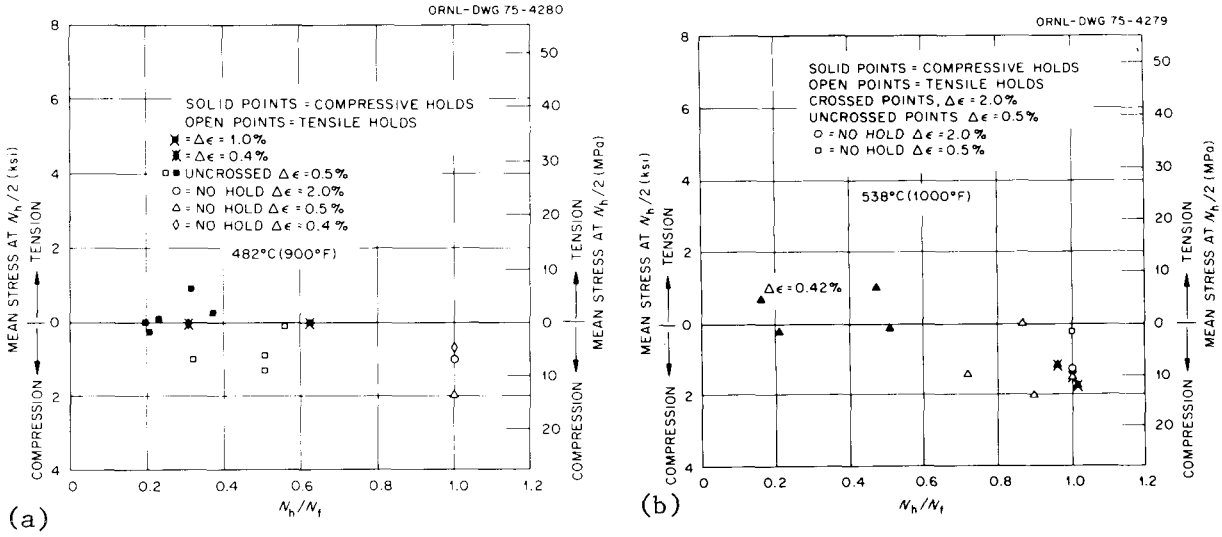

Fig. 2.34. Half-Life Mean Stresses for Isothermally Annealed 2 1/4 Cr-1 Mo Steel Heat 20017. (a) At 482°C (900°F). (b) At 538°C (1000°F).

creep and fatigue "damage fractions." If these two types of damage fractions combine linearly, then the sum of the two damage fractions should be equal to unity:

$$D_c + D_F = 1 \ , \tag{7}$$

where

$$D_c = \Sigma\Delta t/t_r = \text{creep damage fraction}, \tag{8}$$

$$D_F = N_h/N_f = \text{fatigue damage fraction} \ . \tag{9}$$

Here, N_h is the number of cycles to failure with hold times and N_f is the number of cycles to failure that would have been expected with no hold time. At 427°C (800°F) N_f was determined from actual data at a given strain range, while 538°C (1000°F) data were used to establish N_f at both 538 and 482°C (1000 and 900°F). For the calculation of creep damage, D_c, Δt is the time increment at a given stress and t_r is the expected rupture life (taken from the *NSM Handbook*) at that stress and test temperature. In the present case, the calculation of creep damage is complicated,

however, by the fact that the hold times are strain controlled, and thus the stress relaxes during each hold period. Therefore the term $\Delta t/t_r$ for each cycle must be evaluated by integration over the relaxation curve so that the creep damage in one cycle becomes

$$D_c^1 = \int_0^{t_r} dt/t_r \ , \tag{10}$$

where t_r is now the rupture life expressed as a function of the continuously changing stress.

The integrals in Eq. (10) have been evaluated by first fitting a Gittus-type equation[17] to the relaxation curves, such that

$$\ln(\sigma_0/\sigma) = At^{\alpha} \ , \tag{11}$$

where σ_0 = maximum stress, σ = a stress somewhere on the relaxation curve corresponding to time t, A,α = constants. Solving this equation for stress as a function of time yields the relationship

$$\sigma = \exp(\ln \sigma_0 - At^{\alpha}) \ . \tag{12}$$

Equation (12) then allows the integral in Eq. (10) to be evaluated numerically by Simpson's rule by use of a model for t_r previously developed[18] at ORNL. The entire analysis is performed by means of the DAMAGE computer program.[19]

This integration technique involves knowledge of actual relaxation curves, and cannot readily be performed separately for each cycle. An approximation was therefore used. The procedure was to perform the integration on a representative relaxation curve obtained at the half-life ($N_f/2$) and to multiply the creep damage during this cycle by the total number of cycles to failure, such that

$$D_c = N_h \int dt/t_r \ . \tag{13}$$

It should be noted that Campbell,[14] in a similar analysis of type 304 stainless steel, defined failure as the point at which the stress range had decreased 5% from its stabilized value rather than actual specimen separation. For fatigue damage, this definition makes no significant difference, since N_h and N_f would both be defined in this way. For creep damage calculations performed to date, the damage per cycle is so small (10^{-6}–10^{-4}) that there is again no meaningful difference. Actual specimen separation was used here to be consistent with previous work[20] in the current program.

Figure 2.35 shows a "damage summation diagram" calculated for results obtained to date at 427, 482, and 538°C (800, 900, and 1000°F) by the above technique, while Fig. 2.36 shows the result of life predictions obtained by rewriting Eq. (7) as

$$N_{\mathrm{PRED}} = N_f(1 - D_c) \ . \tag{14}$$

Tests involving tensile holds are correlated well by this technique, while the correlation for tests involving compressive holds is considerably less effective. Such a result is not surprising since the data used to establish

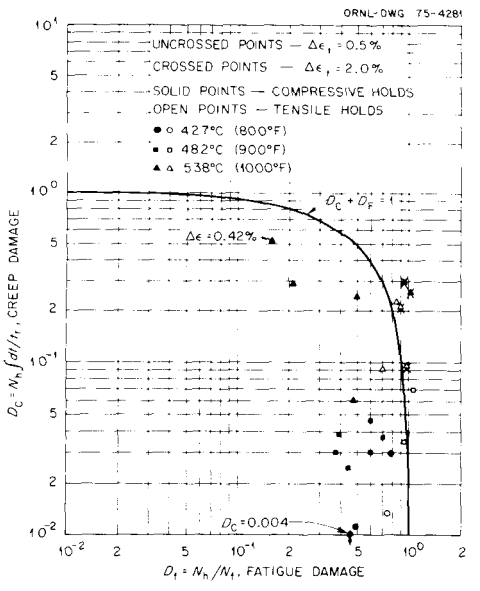

Fig. 2.35. Results of Linear Summation of Damage Analysis of Hold-Time Fatigue Data for Isothermally Annealed 2 1/4 Cr-1 Mo Steel.

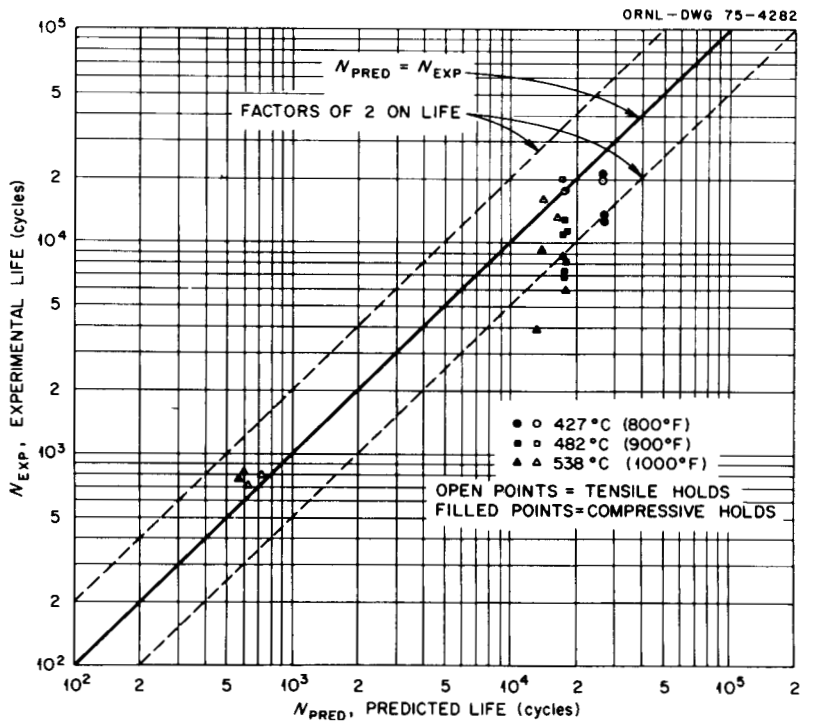

Fig. 2.36. Comparison of Experimental Hold-Time Fatigue Lives with Predicted Lives Calculated by the Linear Summation of Damage Approach.

the t_r values were all from tensile creep-rupture tests. Meaningful correlation of tests involving compressive or combined tensile-compressive holds would probably require data from cyclic creep-rupture tests such as those reported by Halford.[21]

For design applications, the values of t_r and N_f in Eqs. (8) and (9) are replaced by t_D and N_D, where t_D and N_D are design limits on rupture life and fatigue life, respectively. Thus, the design damage criterion becomes

$$\Sigma \frac{\Delta t}{t_D} + \frac{N_n}{N_D} < 1 \ . \tag{15}$$

The strain range partitioning approach involves partitioning the plastic strain range traversed by a cycling specimen into four types:

$\Delta\varepsilon_{pp}$ = tensile plastic strain reversed by compressive plastic strain,

$\Delta\varepsilon_{cc}$ = tensile creep strain reversed by compressive creep strain,

$\Delta\varepsilon_{cp}$ = tensile creep strain reversed by compressive plastic strain,

$\Delta\varepsilon_{pc}$ = tensile plastic strain reversed by compressive creep strain.

Here, "plastic" strain is defined as time-independent inelastic strain, while "creep" strain is defined as time-dependent inelastic strain.

Test results obtained to date at 427, 482, and 538°C (800, 900, and 1000°F) include either tensile or compressive hold periods at constant strain. Thus, in this case, the types of strain involved are $\Delta\varepsilon_{pp}$, $\Delta\varepsilon_{cp}$, and $\Delta\varepsilon_{pc}$ only, where $\Delta\varepsilon_{cp}$ and $\Delta\varepsilon_{pc}$ are defined by

$$\Delta\varepsilon = \Delta\sigma_r/E \ , \tag{16}$$

where $\Delta\sigma_r$ is the total change in stress due to relaxation and E is Young's modulus at test temperature.

Application of the strain range partitioning approach involves two steps. First, "life relationships" must be formulated whereby $\Delta\varepsilon_{pp}$, $\Delta\varepsilon_{cp}$, and $\Delta\varepsilon_{pc}$ are related respectively to N_{pp}, N_{cp}, and N_{pc}, where N_i is the expected cycle life of a specimen cycled in pure $\Delta\varepsilon_i$ strain. Formulation of a life relationship for $\Delta\varepsilon_{pp}$-N_{pp} was reported previously.[20] However, the present data do not involve enough different strain ranges or enough creep strain to enable formulation of $\Delta\varepsilon_{cp}$-N_{cp} and $\Delta\varepsilon_{pc}$-N_{pc} relationships. Such relationships for annealed 2 1/4 Cr-1 Mo steel, which were generated at high strain ranges, have been reported previously.[13] Thus, the present approach was to use our $\Delta\varepsilon_{pp}$-N_{pp} relationship[20] and $\Delta\varepsilon_{pc}$-N_{pc} and $\Delta\varepsilon_{cp}$-N_{cp} relationships reported by Manson et al.[13]

Once the life relationships are established, the next step is to formulate a damage rule to predict cyclic lives for tests involving mixtures of the various types of strain. One approach might be to again formulate a linear rule such that

$$D_{pp} + D_{cp} + D_{pc} + D_{cc} = 1 \ , \tag{17}$$

where, for example, D_{cp} is a "damage fraction" calculated for $\Delta\varepsilon_{cp}$ strain by

$$D_{cp} = N/N_{cp} \ . \tag{18}$$

However, recent experience has suggested that an "iteraction damage rule"[22] is more appropriate.[23] Employing this rule, for example, D_{cp} would be given by

$$D_{cp} = \frac{\Delta\varepsilon_{cp}}{\Delta\varepsilon_{\text{inel}}} \left(\frac{N}{N_{cp}}\right) \ , \tag{19}$$

where $\Delta\varepsilon_{\text{inel}}$ is the total inelastic strain range and N_{cp} is the life corresponding to a pure $\Delta\varepsilon_{cp}$ strain equal to $\Delta\varepsilon_{\text{inel}}$.

In the present analysis, the interaction damage rule has been used, although the relationships taken from Manson et al.[13] had been established by the linear damage rule. Such an approach requires caution, but it turns out that the values of $\Delta\varepsilon_{cp}$ and $\Delta\varepsilon_{pc}$ from the linear rule technique[13] are of the same order of magnitude as the $\Delta\varepsilon_{\text{inel}}$ values for the present data, while the $\Delta\varepsilon_{\text{inel}}$, $\Delta\varepsilon_{cp}$, and $\Delta\varepsilon_{pc}$ values from ref. 13 are generally somewhat higher than those for the present data. Therefore, the current technique of summing damage by the interaction rule using the linearly determined[13] life relationships has an advantage in that it makes extrapolation of the life relationship line unnecessary.

With the life relationships and the damage summation rule established, the remaining step is "simply" to determine $\Delta\varepsilon_{pp}$, $\Delta\varepsilon_{cp}$, and $\Delta\varepsilon_{pc}$ for a given test. Here again, in the present analysis, values have been obtained from a representative cycle at $N_f/2$. For example, in a test with a tensile hold period, $\Delta\varepsilon_{cp}$ is defined by Eq. (16) and $\Delta\varepsilon_{pp}$ is given by

$$\Delta\varepsilon_{pp} = \Delta\varepsilon_{\text{inel}} - \Delta\varepsilon_{cp} \ . \tag{20}$$

However, there is somewhat of a complication in the determination of $\Delta\sigma$. At the beginning of a hold period, the stress undergoes a sudden rapid decrease ($\Delta\sigma_i$) followed by a period of more gradual decrease. Diercks[24] has attributed such a decrease for type 304 stainless steel to a strain-rate effect caused by a sudden change from the ramp strain rate to the zero strain rate of the hold period, and has thus suggested that the strain

$$\varepsilon_{in} = \Delta\sigma_{in}/E \ , \tag{21}$$

might be considered plastic rather than creep strain. Furthermore, there is some indication that plastic strains accumulated during relaxation and creep strains are not equivalent.[25] The current results have been obtained by treating the entire plastic strain due to relaxation as creep, but the effect is being examined closely. Life predictions obtained by the strain range partitioning approach are shown in Fig. 2.37. All predictions are within a factor of 2 on life, and are considerably better than those obtained through the linear summation of damage method (Fig. 2.36). If the strain ε_{in} were plastic rathen than creep, the predictions should be overconservative. Indeed, there is some tendency to underpredict, although several lives were overpredicted.

Analysis by these two methods will continue, including attempts to identify creep failure behavior under cyclic conditions and a further investigation of the plastic strain increase during relaxation. Also, analysis by other techniques will begin as more data become available. Thus, both descriptions of material behavior and comparisons of analytical methods will be obtained.

In order to understand the softening and hardening behavior that occurs as a function of temperature and strain range as well as to characterize microstructural changes that occur during dynamic strain aging, transmission electron microscopy studies (TEM) have been initiated. These studies are being conducted on material adjacent to the fracture (fatigue) surface (minimum diameter of the hourglass specimen), as well as at various positions remote from the fatigued section for comparison.

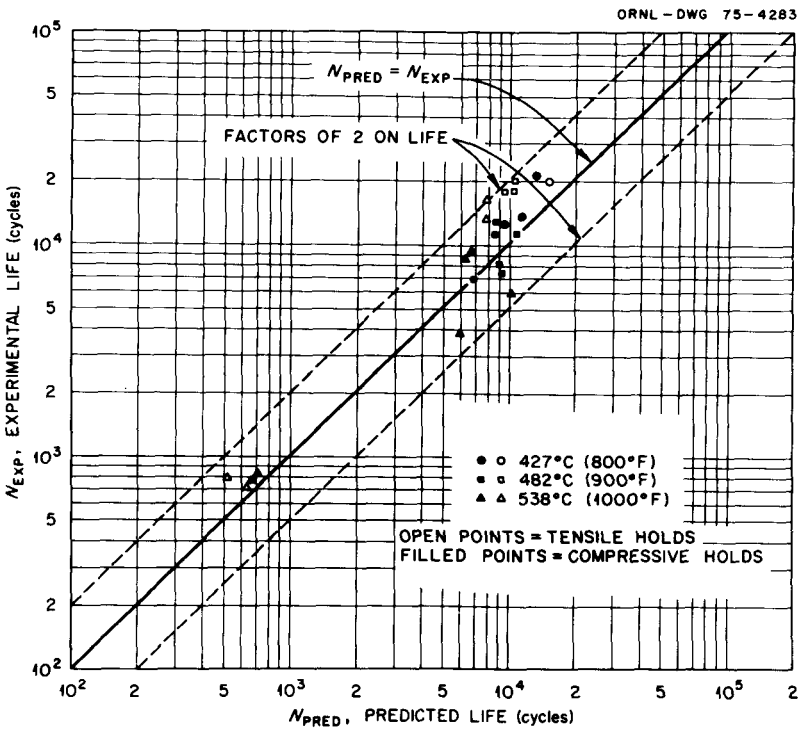

Fig. 2.37. Comparison of Experimental Hold-Time Fatigue Lives with Predicted Lives Calculated by the Strain Range Partitioning Approach.

To date we have examined two specimens that were tested at 427°C (800°F). Specimens 18MTL and 31MTL were tested at total strain ranges of 2 and 0.36%, respectively. Specimen 18MTL cyclically hardened initially quite rapidly (primary hardening) and then continued to harden at a decreasing rate throughout most of test, while specimen 31MTL hardened rapidly during the first few cycles and then softened at a decreasing rate throughout the remainder of the test.[25] Cyclic softening at all temperatures results in deviations from the Coffin-Manson law for linearity of plastic strain range versus cyclic life when plotted on log-log coordinates.

Transmission electron micrographs taken of various samples from specimen 31MTL (0.36%) at increasing distances from the fatigue fracture surface are shown in Figs. 2.38 and 2.39. Micrographs of specimen 18MTL (2%) are shown in Fig. 2.40. Figure 2.41 shows a region in the head of the specimen that saw no plastic straining during the fatigue tests.

Fig. 2.38. Representative Areas from a High-Cycle Fatigue Specimen (31MTL) 0.69 mm (0.027 in.) from Fracture Surface. 25,000×.

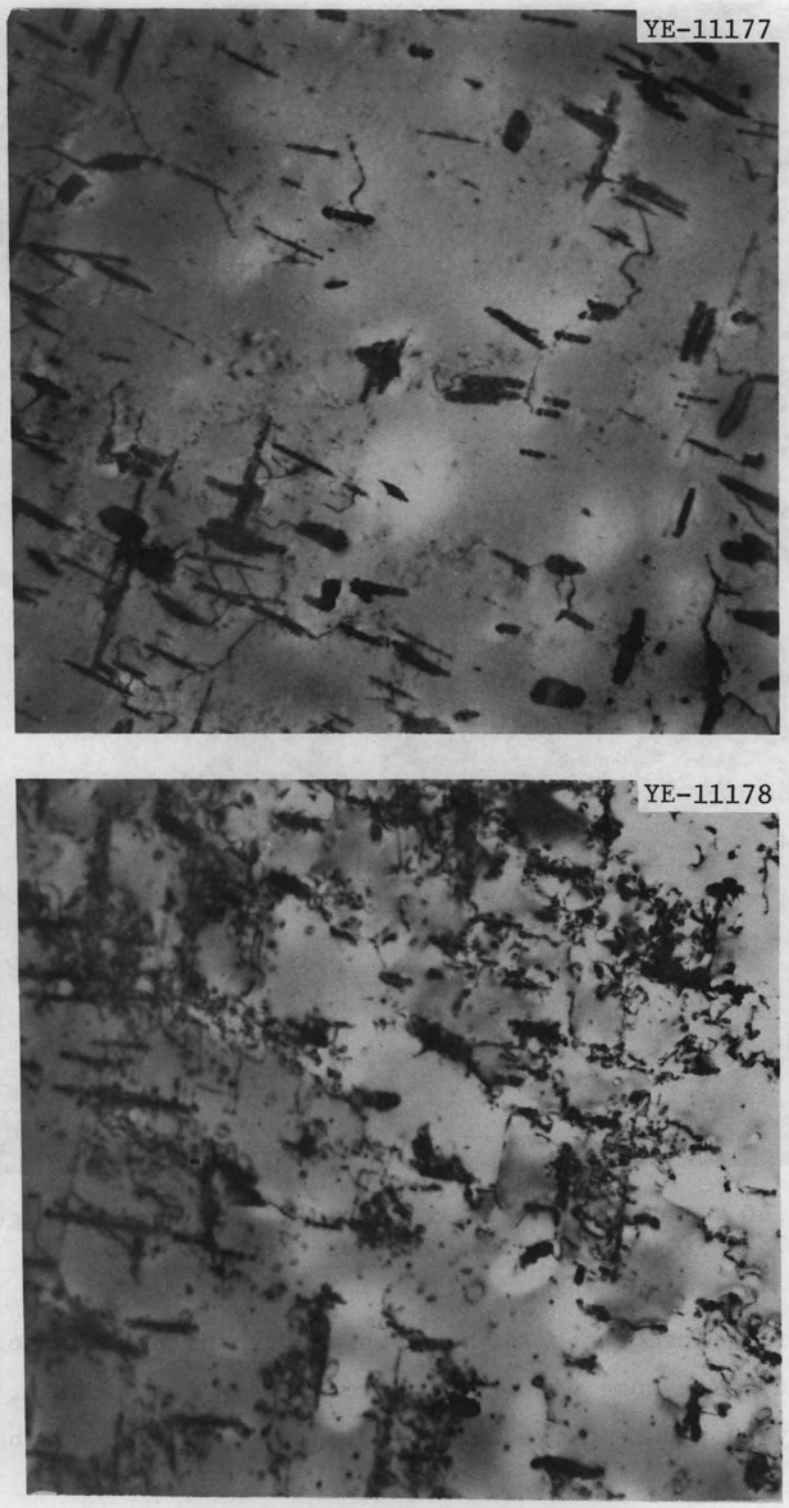

Fig. 2.39. Representative Areas from a High-Cycle Fatigue Specimen (31MTL) 2.06 mm (0.081 in.) from Fracture Surface. 25,000×.

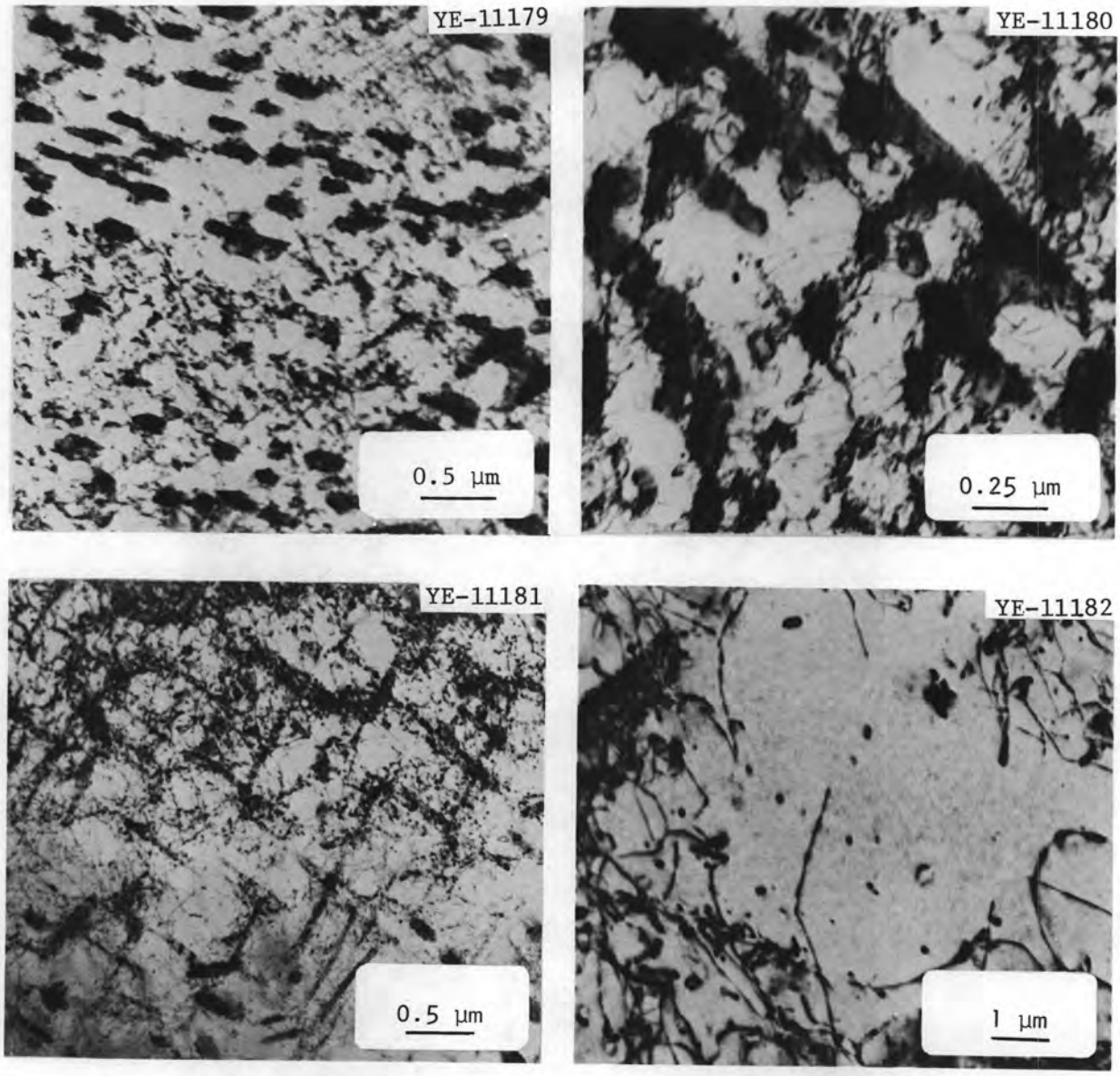

Fig. 2.40. Representative Areas from a Low-Cycle Fatigue Specimen (18MTL) 1.37 mm (0.054 in.) from Fracture Surface.

These electron micrographs show a complex precipitate morphology and distribution, with some dislocation-precipitate interaction, which is particularly apparent in the high-strain-range test specimen in Fig. 2.41.

2.2.4.2 Fatigue Behavior of Hastelloy X

Presently, a test matrix for characterizing the fatigue behavior of Hastelloy X (Heat 2600-3-4936) is being prepared. Low-cycle strain-controlled

Fig. 2.41. Region from Unstressed Specimen Showing Dislocation Structure in Region with Comparable Precipitate Density to Fig. 2.40. 25,000×.

fatigue testing in air will be performed over the temperature range 482 to 1204°C (900–2200°F). The types of tests under consideration at this time involve continuous cycling low-cycle fatigue, strain-rate sensitivity, creep-fatigue (hold time effects), aging, and test environment. The purpose of this work is to scope the possible effects of HTGR primary coolant environment on fatigue behavior.

Plans are being formulated for aging Hastelloy X (Heat XX01A305) over the temperature range 538 to 982°C (1000–1800°F) as well as Inconel 617 over the range 538 to 871°C (1000–1600°F) for periods of 2500, 10,000, and 20,000 hr.

Some 45 hourglass-shaped specimens are now on hand, and limited low-cycle fatigue data on as-received (solution annealed) as well as 2500-hr-aged material should be available by December 1975.

Design of an environmental chamber for fatigue testing in a helium environment is currently under way. This chamber will be used in conjunction with an existing low-cycle, strain-controlled fatigue testing machine to scope the possible effects of HTGR primary coolant environment on fatigue behavior of both Hastelloy X and 2 1/4 Cr-1 Mo.

2.3. CORROSION OF STEAM GENERATOR MATERIALS — J. C. Griess, J. H. DeVan, W. A. Maxwell,* and P. L. Rittenhouse

The purpose of this program is to determine the corrosion behavior of selected materials that are planned or being considered for use in nuclear steam supply systems in both pure steam and in steam under faulted conditions. The actual testing of materials is performed by the Southern Nuclear Department of the NUS Corporation under contract to Oak Ridge National Laboratory. The test facilities are located at the Bartow Plant of the Florida Power Corporation in St. Petersburg, Florida, and use steam taken directly from the fossil-fueled electrical generating plant. Since the results from this program are useful to high-temperature reactors in general, funding is provided by both the HTGR and LMFBR projects. During the present report period work has been primarily concerned with the effect of chlorides on the stress-corrosion cracking of several alloys in steam and on a determination of the influence of heat flux on the corrosion of 2 1/4 Cr-1 Mo steel by pure superheated steam.

2.3.1 Injection Loops

During this report period two injection loops were operated to investigate the effect of chloride on the corrosion of potential steam generator materials in steam. The geometry of these loops is shown in Fig. 2.42. Steam from the Bartow plant superheater entered at the top of the loop, passed through a section with heaters, and then entered

---

*NUS Corp., Clearwater, Florida 33515.

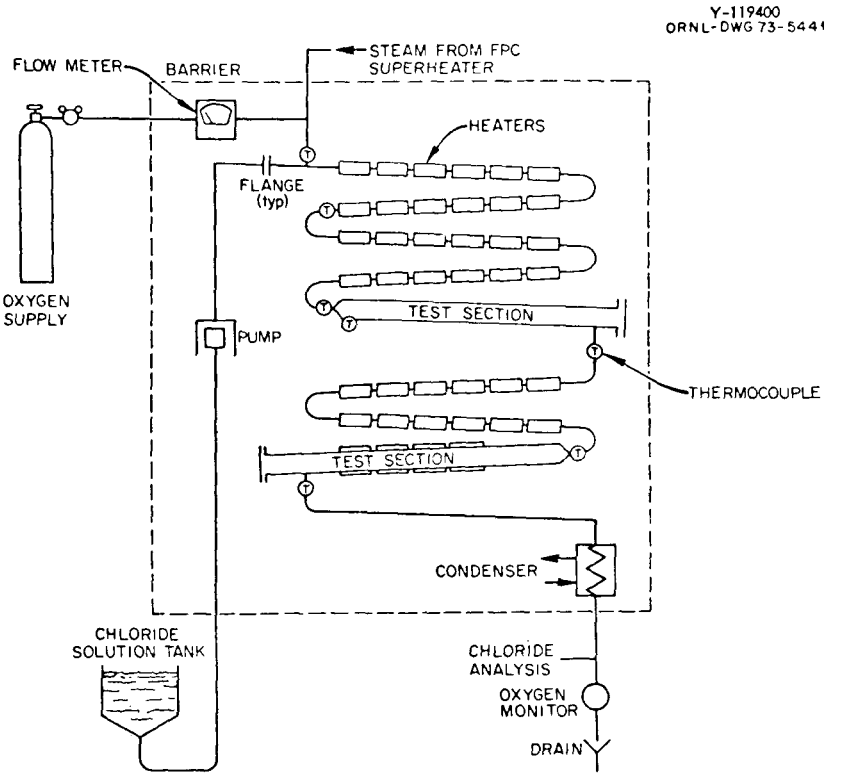

Fig. 2.42. Schematic of Loop Facility Used for Studying Corrosion Effects of Impurities in Steam.

an autoclave where test specimens were exposed. Another heated section preceded the second autoclave, and this was followed by a condenser and/or letdown valve. As indicated, liquids with both dissolved salts and gases could be added to the steam as it entered the loop, and concentrations of additives were chemically determined in the condensate. One loop was constructed from 9 Cr-1 Mo steel and the second from Inconel 625.

2.3.1.1 Tests in the 9 Cr-1 Mo Steel Loop

During the past report period two tests were completed in this loop. In the first test, Test 11, the environment consisted of superheated steam at 482°C (900°F) and 11.2 MPa (1625 psi) containing 2 ppm chloride as sodium chloride. Steam flowed through the loop at the rate of 22.7 kg/hr (50 lb/hr). Throughout this test the oxygen level was below 0.007 ppm. Small rectangular strips of Incoloy 800 and 2 1/4 Cr-1 Mo steel were placed

in test about 1500 hr after the run started; constant-stress tubular specimens were exposed for the entire test period. The former specimens were weighed periodically and the latter were inspected for cracks (leaks).

The configuration of the constant-stress specimens is shown in Fig.2.43. The inner tube, which served as the test specimen, was machined to the desired wall thickness and was welded into the outside tube centered by the spacer rings. In the early specimens a small-diameter tube was welded to the 3.2-mm (1/8 in.) hole in the outer tube, the annulus between the inner and outer tubes was evacuated, and the small tube was welded shut. In some specimens where the outside diameter of the inner tube could be matched closely to the inside diameter of the outer tube, the rings were eliminated. Also, in the more recently fabricated specimens the evacuation tube was replaced by a plug, which was electron-beam welded in place in a vacuum chamber. The steam pressure in the loop produced the constant stress on the specimen, the stress being a function of the wall thickness of the inner tube. In this test stresses ranged between S_m and $2S_m$.* Alloys tested included 2 1/4 Cr-1 Mo and 9 Cr-1 Mo steels, type 304 stainless steel, Incoloy 800, Inconel 600, and Inconel 625. Specimens of all were made from seamless tubing both with and without autogenous welds parallel to their axes. A total of 62 such specimens started the test.

Early in this run two brief temperature excursions occurred while the pressure remained constant. As a result, eight of the most highly stressed specimens (five 2 1/4 Cr-1 Mo steel, two 9 Cr-1 Mo steel, and one Inconel 625) failed and were removed from test. Accurate temperature measurements during the excursion were not available, but temperatures as high as 593 to 649°C (1100–1200°F) were estimated. Under these circumstances, a ductile collapse of some of the most highly stressed specimens

---

*S_m is a time-independent primary stress limit specified in ASME Code Case 1592 as the lowest of: (1) 1/3 minimum ultimate tensile strength at room temperature, (2) 0.367 times minimum ultimate tensile strength at temperature of application, (3) 2/3 of the minimum yield strength at room temperature, (4) 2/3 of the minimum yield strength at temperature of application (ferritic), (5) 0.90 of the minimum yield strength at temperature of application (austenitic).

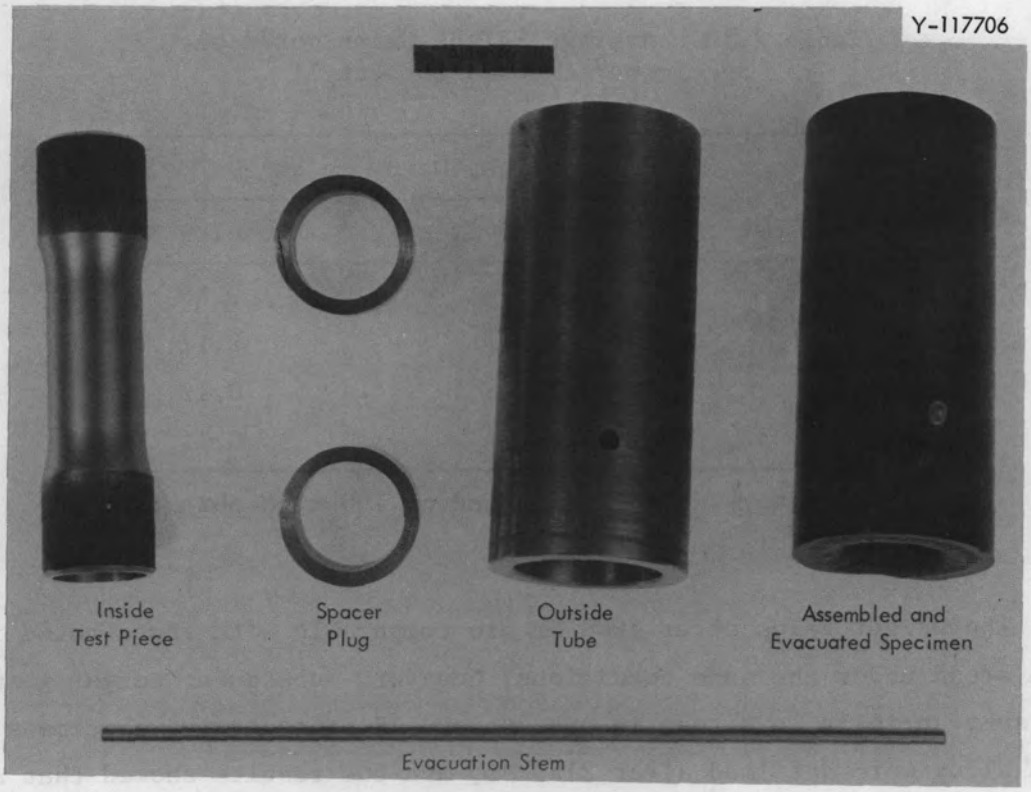

Fig. 2.43. Components of Constant-Stress Tubular Specimen.

was not unexpected. All the failed specimens except one were stressed at $2S_m$ at 482°C (900°F) and 11.2 MPa (1625 psi) steam pressure; the other specimen was 2 1/4 Cr-1 Mo steel stressed to 1.5 S_m. Examination of the remaining specimens immediately after the temperature excursions showed no apparent damage, and they were returned to test.

Test 11 lasted 4626 hr. At the end of the test no failures were noted. The number of constant-stress specimens of each alloy that survived the test were: 16 — 2 1/4 Cr-1 Mo steel; 24 — Incoloy 800 (grade 2); 4 — 9 Cr-1 Mo steel; 4 — type 304 stainless steel; 3 — Inconel 625; and 3 — Inconel 600. About half of each type contained an axial weld in the gage section.

Average weight gain data noted on the coupons are shown in Table 2.13.

Table 2.13. Average Weight Gains Noted on Specimens[a] Exposed in Test 11

Time (hr)	Weight Gain, mg/cm^2	
	2 1/4 Cr-1 Mo Steel	Incoloy 800
1008	1.63	0.10
2000	1.69	0.11
2375	1.73	0.12
3120	1.82	0.11

[a]Specimens initially ground on 100-mesh abrasive belt grinder.

The weight gains after 1000 hr are comparable with those noted in pure steam under the same conditions; however, subsequent weight gains are substantially less than in pure steam. Representative specimens of each alloy were defilmed after 3120 hr, and the results showed that at least 95% of the amount of metal lost was present in the film or scale. There were numerous wide shallow pits, 13 to 25 μm deep, (0.5—1.0 mil), on the steel specimens, but in spite of this the attack was less than expected from data obtained in pure steam.

All the constant-stress specimens and most of the coupons from Test 11 were also exposed in Test 12. This test operated under exactly the same conditions as the previous test except 8 ppm O was added to the steam. Test 12 was terminated on June 30, 1975, after 5958 hr.

Only one Inconel 600 tubular specimen developed a leak during this test, and examination showed that the leak resulted from a crack in the electron-beam closure weld. All other tubular specimens showed neither leaks nor significant change in appearance as a result of oxygen added to the environment.

Weight changes on the coupons were erratic because some scale was apparently lost. Some but not all oxide was converted to Fe_2O_3, and part of this appeared to be only loosely attached to the surface. A determination of actual corrosion rates in this latter environment awaits

descaling of the specimens. Although the results are not complete at this time, the data indicate that the presence of chloride ion dissolved in steam, either in the presence or absence of oxygen, did not have a significant detrimental effect on any of the materials tested. In fact, in the absence of oxygen the presence of chloride in the steam actually appeared to inhibit the oxidation of 2 1/4 Cr-1 Mo steel and Incoloy 800.

Test 12 was the last test to be performed in the 9 Cr-1 Mo steel loop, and the loop is being removed from the power plant to make room for a new facility (see Section 2.3.3). This loop will be thoroughly inspected when it is dismantled, and mechanical property data will be acquired to see if prolonged service at 482°C (900°F) has produced any changes from the before-test condition.

2.3.1.2 The Inconel 625 Loop

During this report period two extended tests were made in this loop, and in each case the temperature of the loop was alternated every 24 hr between a superheated and a saturated steam condition at constant pressure. Thus, the specimens were alternately exposed to wet and dry steam. This type of operation simulated a condition that could exist in the entrance region of a superheater in a drum-type steam generator, where a few droplets of water may escape separation in the entrainment separators.

In the first test, designated 2A, only U-bend specimens of a variety of alloys were exposed to steam containing chloride and oxygen. The pressure and oxygen concentration were held constant at 11.2 MPa (1625 psi) and 8 ppm, respectively. The temperature was cycled between 385 and 318°C (725 and 605°F). During the superheat part of the cycle the chloride concentration (as NaCl) was maintained at 4.2 ppm for the first 3146 hr and 2.7 ppm (as $CaCl_2$) for the rest of the test. The chloride concentration during the saturated part of the cycle was increased to 10 ppm regardless of the salt that was used.

The results of this test have been reported.[26] Generally, they showed welded U-bend specimens of Incoloy 800 (not subsequently heat treated) to be highly susceptible to cracking. However, unwelded and

welded-and-annealed specimens of Incoloy 800 resisted cracking. Hastelloy N and Ebrite 26-1 were extremely susceptible to cracking and the ferritic steels — 2 1/4 Cr-1 Mo and type 410 stainless steel — did not crack. Single small cracks were found in Inconel 600, Inconel 625, and Hastelloy X specimens but none were found in Inconel 601.

In addition to the severity of the test environment, the materials in the above test were highly strained (∿7% max). Consequently, a second test was conducted in which only constant-stress specimens as shown in Fig. 2.43, were exposed at stresses within the elastic range. The environmental conditions and temperatures were identical to those just described. The specimens exposed were: 35 — 2 1/4 Cr-1 Mo steel; 20 — Incoloy 800 (grade 2); 12 — type 304L stainless steel; and 12 — Inconel 625. Approximately half of each type contained an axial autogenous weld in the test section, and about equal numbers of each type were stressed to 0.5 S_m, S_m, and 1.5 S_m at 385°C (725°F). The test lasted 6475 hr, with the specimens being removed and examined at several intermediate times.

No specimens failed because of either pitting or stress-corrosion cracking throughout the test. However, 27 of the 2 1/4 Cr-1 Mo steel specimens, about equal numbers welded and unwelded, failed because of general wall thinning. All specimens stressed to 1.5 S_m or S_m [wall thicknesses of 0.5 or 0.8 mm (0.02 or 0.030 in.)] failed, whereas none of those stressed at 0.5S_m [wall thickness 1.5 mm (0.06 in.)] failed, although significant general attack on all surfaces was apparent. One additional failure occurred in an Inconel 82 weld that joined an inner test section of type 304 stainless steel to the outer tube. The failure did not extend into the stainless steel.

The high rate of general attack on the low-alloy steel specimens was not unexpected in the oxygenated, chloride-containing, wet-dry environment. However, the absence of cracking in the Incoloy 800, and particularly in the type 304L stainless steel specimens, was unexpected. In all cases at least a part of the test specimen was exposed to an aqueous chloride solution during the saturated part of the test, as indicated by the water line on the specimens. Although the specimens were stressed at levels below the yield point, stresses and oxygen and chloride concentrations

should have been high enough to produce cracking. The absence of cracking in the Inconel 625 specimens was expected in view of only very limited cracking in the severly strained U-bend specimen. General attack was minimal on the Incoloy 800, type 304 stainless steel, and Inconel 625.

As of July 1, 1975, the Inconel 625 loop was placed on standby. The condition of this loop is excellent (no loop failures during its life) and it could be placed in service again on short notice.

2.3.2 The Influence of Heat Flux on the Corrosion of 2 1/4 Cr-1 Mo Steel

The effect of heat flux on the corrosion of 2 1/4 Cr-1 Mo steel was investigated in equipment shown schematically in Fig. 2.44. Steam at a mass flow rate of 272 kg/hr (600 lb/hr) was adjusted to 468°C (875°F) and then divided into two equal parallel streams. Each stream was passed over a single heated specimen and then over a group of isothermal specimens before being condensed and removed from the system as condensate.

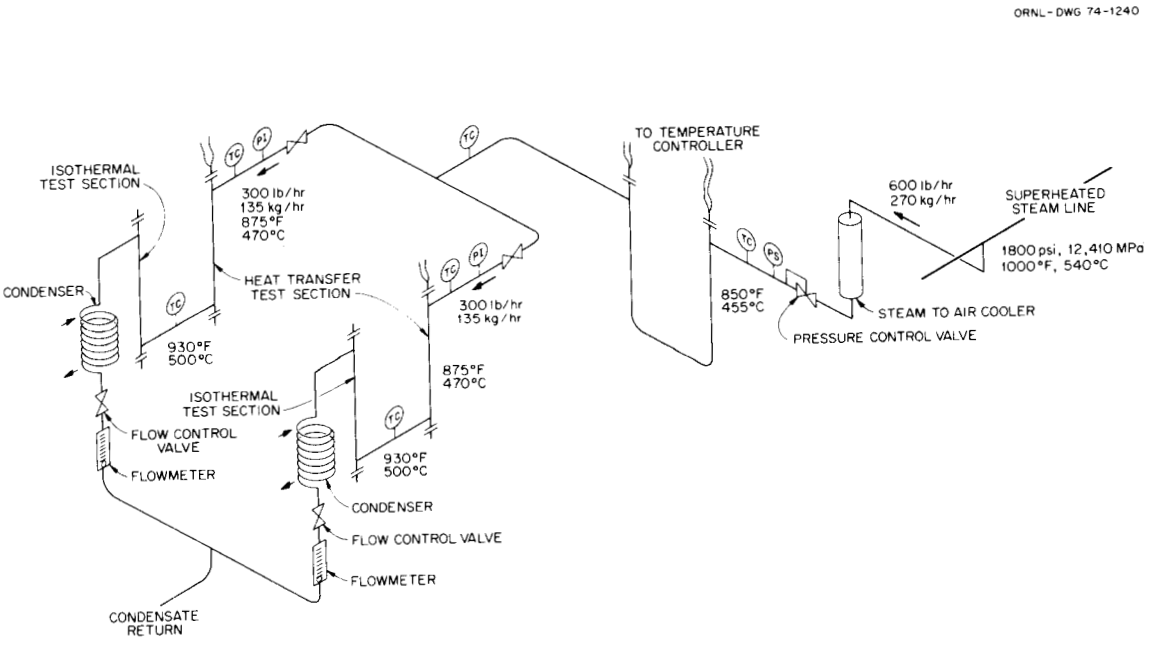

Fig. 2.44. Schematic of Heat Transfer Corrosion Test Facility.

The heat-flux specimens were tubes 0.80 m (31.5 in.) long with an inside diameter of 12.40 mm (0.488 in.) and an outside diameter of 14.40 mm (0.567 in.). The specimens were carefully weighed before test. A Calrod heater fitted snuggly inside the tube, which was heated only over the center 0.61 m (24 in.) of its length. Water-cooled seals were used on each end to define the heated length, and a liner with a 1.65-mm (0.065-in.) annulus directed the steam flow past the specimen. Table 2.14 shows the conditions of the first series of tests.

Table 2.14. Operating Conditions for Heat-Transfer Corrosion Tests

Bulk steam temperature, °C (°F)	
Inlet	468(875)
Outlet	499(930)
Specimen surface temperature, °C (°F)	
Inlet	510(950)
Outlet	540(1005)
Electrical heat input, kW (Btu/hr)	3.5(11,900)
Average heat flux, kW/m^2 (Btu hr^{-1} ft^{-2})	126(40,000)
Steam pressure, MPa (psig)	10.5(1525)
Steam mass flow rate, kg/hr (lb/hr)	272(600)
Steam velocity, m/sec (ft/sec)	13(43)

The isothermal specimens were made from short lengths of the same tubing used for the heated tests. They were exposed to steam at 499°C (930°F) flowing at 9.5 m/sec (31 ft/sec). All specimens were weighed at intermediate times, and some were removed for descaling.

At the conclusion of a heat transfer test, the heater was removed and the specimen was reweighed. In some cases metallographic sections were taken, and in all cases the oxidation products were chemically removed with Clark's solution (1000 ml 37% HCl + 20 g Sb_2O_3 + 50 g $SnCl_2$), followed by reweighing. From the three weighings both the amount of metal oxidized and the weight of oxide were determined. The pertinent results obtained from the first six heat-flux specimens are shown in Table 2.15.

Table 2.15. Summary of Results from the First Six Heat-Transfer Specimens

Exposure Time (hr)	Metal Oxidized (mg/cm^2)	Average Penetration (μm)	Weight of Oxide (mg/cm^2)	Average Oxide Thickness[a] (μm)	Oxide Retained on Specimen[b] (%)
585[c]	10.1	12.7	14.2	27.3	102
585[c]	12.5	15.7	15.9	30.6	92
951	11.3	14.2	d		
2007	13.4	17.0	17.6	33.8	95
3026	20.4	25.9	23.2	44.6	83
5989	31.2	39.6	29.7	57.1	67

[a]Based on an oxide (Fe_3O_4) density of 5.2 g/cm^3.

[b]Assumes all metal oxidized was converted to Fe_3O_4.

[c] Two test runs at 585 hr.

[d]Specimen was damaged in removing the heater and a significant amount of oxide was lost.

The visual appearance of the oxide formed on the heat transfer specimens during the short-time tests was the same as that observed on isothermal specimens exposed to steam between 482 and 538°C (900 and 1000°F). For about the first 2000 hr the oxide was uniform and adhered well to the metal. The specimen that was exposed for 2000 hr showed only one small area on the hot end where oxide had spalled. At 3000 hr some oxide had spalled over most of the surface, and at 5989 hr the entire surface had undergone random spallation and regrowth of oxide. This fact is clearly shown by the decreasing amount of oxide retained on the specimen as the test duration increased (Table 2.15). As a result the surfaces of both the 3000- and 6000-hr specimens were rough to the touch. A typical example of the nature of the oxide is shown in Fig. 2.45, which is a cross-section view taken near the inlet end (lower temperature end) of the 6000-hr specimen. The lack of adherence of the oxide to the metal, the differences in oxide thickness, and the porosity of the oxide are in sharp contrast to the oxide usually found on isothermal specimens exposed in the same temperature range.

Although the data are incomplete and additional tests are being run, the preliminary results indicate that the high heat flux used in the tests

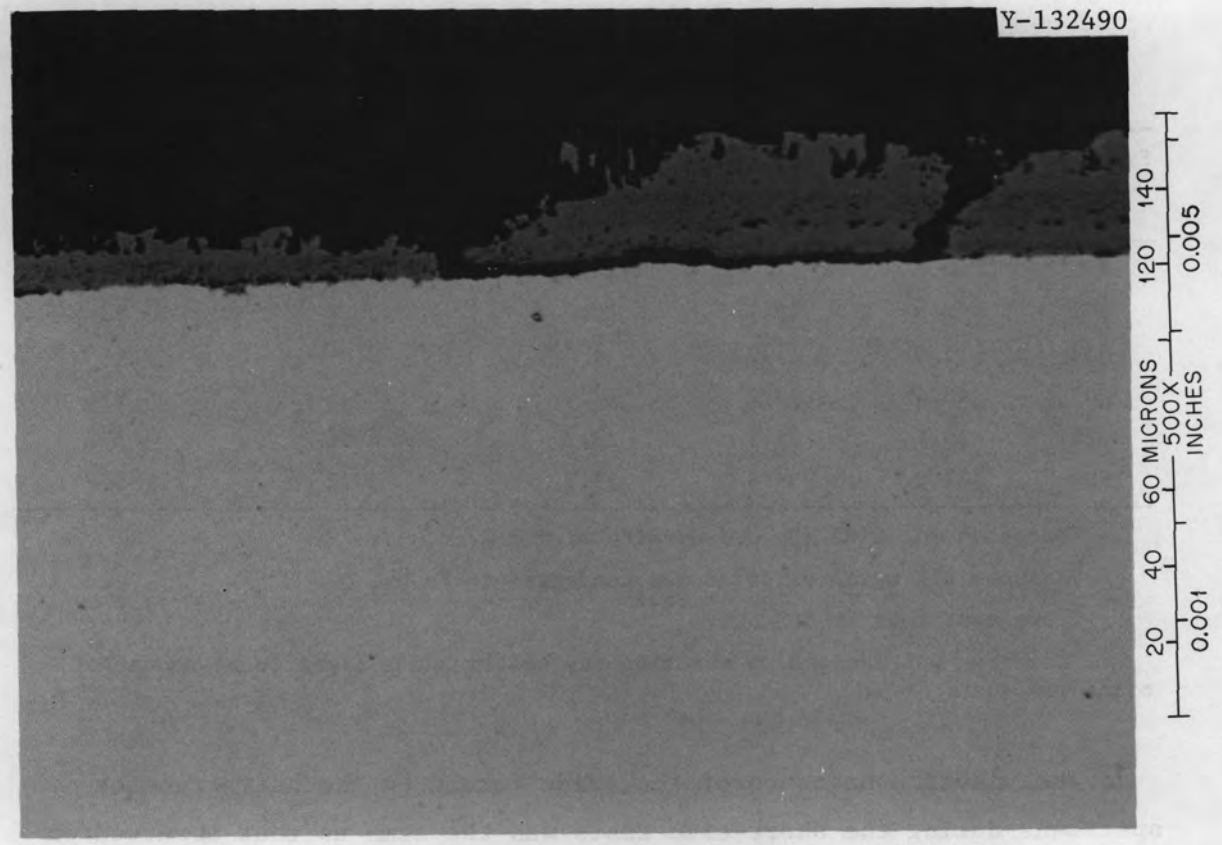

Fig. 2.45. Cross-Section View of the 6000-hr Heat-Transfer Specimen from Near the Entrance Region.

to this time had a detrimental effect on the corrosion of 2 1/4 Cr-1 Mo steel. After 6000 hr the extent of corrosion was about 1.5 times greater than observed[27] in isothermal tests conducted at 538°C (1000°F).

The isothermal specimens appeared to behave normally. Their weight changes were in reasonable agreement with the data obtained in other isothermal tests[27] conducted at 482°C (900°F).

2.3.3 The Inconel 617 Test Loop

A new test loop constructed entirely of Inconel 617 is being prepared to replace the 9 Cr-1 Mo steel loop at the Bartow plant. All the material needed to complete the loop is on hand, and some of the welding has been successfully completed. This loop should be ready to begin shakedown tests in October 1975, and exposure of test specimens should begin the following month. The geometry of the loop is the same as that shown in

Fig. 2.42, although in the initial test impurities will not be injected into the incoming steam.

For the initial tests, specimens will be exposed to pure superheated steam at 482°C (900°F) in one autoclave and 538°C (1000°F) in the other. Materials will include 2 1/4 Cr-1 Mo and 9 Cr-1 Mo steel, HT-9 (Sandvik), type 304 stainless steel, Incoloy 800, and Inconel 617. In addition to annealed coupons, specimens of 2 1/4 Cr-1 Mo welded to Incoloy 800, Incoloy 800 welded to Incoloy 800, and Inconel 617 welded to Inconel 617 will be exposed both as flat coupons and as highly strained U-bends. All flat specimens will be weighed at intermediate times, and at these times some of the specimens will be replaced with new ones. Thus, during this test, which is tentatively scheduled to last for 15,000 hr, the oxidation rates of all materials can be determined.

2.4 REFERENCES

1. "Case 1592," pp. 327–442 in *1974 Code Cases (ASME Boiler and Pressure Vessel Code)*, American Society for Mechanical Engineers, New York, 1974.
2. C. Tyzak et al., "The Behavior of Constructional Materials in Mark III Helium Cooled Reactors," paper presented at U.K. Conference on Gas-Cooled Reactors, London, May 1972.
3. D. S. Wood, M. Farrow, and W. T. Burke, "A Preliminary Study of the Effect of Helium Environment on the Creep and Rupture Behavior of Type 316 Stainless Steel and Incoloy 800," pp. 213–28 in *Effects of Environment on Material Properties in Nuclear Systems* (Proceedings of the International Conference on Corrosion, London, July 1–2, 1971), Institution of Civil Engineers, London, 1971.
4. H.G.A. Bates and K. Bøye, "A Review of the Results of the Corrosion Creep Tests at C.I.I.R Oslo and a Preliminary Appraisal of Their Application to H.T.R. Design," Paper 2 in *Dragon Project Metals Information Meeting, London, December 6–7, 1973*, DPTN/486.
5. H. Willermoz et al., "Effect of Various Parameters on the Behavior of Iron-Chromium-Nickel Alloys in the Presence of Impurities Contained in Helium," paper presented at Dragon Project Metals Information Meeting, London, December 6–7, 1973.

6. F. N. Mazandarany and P. L. Rittenhouse, *Effects of Service Environments on the Behavior of HTGR Steam Generator Structural Materials*, GA-A-13553 (July 15, 1975).

7. R. L. Klueh, *Heat Treatment Effects on the Tensile Properties of 2 1/4 Cr-1 Mo Steel*, ORNL-5144 (May 1976).

8. C. R. Brinkman, M. K. Booker, J. P. Strizak, W. R. Corwin, J. L. Frazier, and J. M. Leitnaker, *Interim Report on the Continuous Cycling Elevated Temperature Fatigue and Subcritical Crack Growth of 2 1/4 Cr-1 Mo Steel*, ORNL-TM-4993 (December 1975).

9. E. K. Walker, "An Effective Strain Concept for Crack Propagation and Fatigue Life with Specific Applications to Biaxial Stress Fatigue," p. 225 in *Proc. Air Force Conf. Fatigue and Fracture of Aircraft Structures and Materials*, H. A. Wood et al., eds., AFFDL-TR-70-144 (1970).

10. Brookhaven National Laboratory, private communication.

11. C. E. Jaske, J. S. Perrin, and H. Mindlin, "Low Cycle Fatigue of Reactor Structural Materials," *React. Technol.* 15(3): 185–207 (Fall 1972).

12. L. F. Coffin, Jr., "Fatigue at High Temperature — Prediction and Interpretation," *Proc. Inst. Mech. Eng. London* 188: 109–27 (September 1974).

13. S. S. Manson, G. R. Halford, and M. H. Hirschberg, *Creep-Fatigue Analysis by Strain-Range Partitioning*, NASA-TM-X-67838 (1971).

14. R. D. Campbell, "Creep Fatigue Interaction Correlation for 304 Stainless Steel Subjected to Strain-Controlled Cycling with Hold Times at Peak Strain," *J. Eng. Ind.* 93: 887–92 (1971).

15. L. F. Coffin, Jr., "Predictive Parameters and Their Application to High Temperature, Low Cycle Fatigue," pp. 643–54 in *Proc. Int. Conf. Fract. 2nd, 1969*, Chapman and Hall, London.

16. J. F. Polhemus, C. E. Spaeth, and W. H. Vogel, "Ductility Exhaustion Model for Prediction of Thermal Fatigue and Creep Interaction," pp. 625–35 in *Fatigue at Elevated Temperatures, ASTM Spec. Tech. Publ.* 520, American Society for Testing and Materials, Philadelphia, 1972.

17. J. H. Gittus, "Implications of Some Data on Relaxation Creep in Nimonic 80 A," *Phil. Mag.* 9: 749 (1964).

18. M. K. Booker, T. L. Hebble, D. O. Hobson, and C. R. Brinkman, "Mechanical Property Correlations for 2 1/4 Cr-1 Mo Steel in Support of Nuclear Reactor Systems Design," paper F 8/9 in *Transactions of the 3rd International Conference on Structural Mechanics in Reactor Technology* (London, UK, 1–5 Sept. 1975), Vol. 2, Part F, Commission of the European Communities, Luxembourg, 1975.

19. M. K. Booker and B.L.P. Booker, "DAMAGE," unpublished computer program.

20. C. R. Brinkman, M. K. Booker, and J. P. Strizak, "Fatigue Behavior of 2 1/4 Cr-1 Mo Steel," *Mechanical Properties Test Data for Structural Materials Quart. Progr. Rep. Jan. 31, 1975,* ORNL-5104. pp. 220–31.

21. G. R. Halford, *Cyclic Creep-Rupture Behavior of Three High-Temperature Alloys,* NASA-TN-D-6309 (1971).

22. S. S. Manson, "The Challenge to Unify Treatment of High Temperature Fatigue — A Partisan Proposal Based on Strainrange Partitioning," pp. 744–75 in *Fatigue at Elevated Temperatures, ASTM Spec. Tech. Publ.* 520, American Society for Testing and Materials, Philadelphia, 1972.

23. G. R. Halford, NASA Lewis Research Center, private communications.

24. D. R. Diercks, "Strain-Range-Partioning Analysis of Tension-Hold-Time Data for Type 304 Stainless Steel," *Mechanical Properties Test Data for Structural Materials Quart. Progr. Rep. Jan. 31, 1975,* ORNL-5104, pp. 3–13.

25. C. R. Brinkman, J. P. Strizak, and C. O. Stevens, "Fatigue Behavior of 2 1/4 Cr-1 Mo Steel," *Mechanical Properties Test Data for Structural Materials Quart. Progr. Rep. Oct. 31, 1974,* ORNL-5103, pp. 220–31.

26. J. C. Griess, J. P. Hammond, and W. A. Maxwell, *Effects of Chloride and Caustic on the Cracking Behavior of Several Materials Under Alternate Wet and Dry Steam Conditions,* ORNL-TM-4995 (September 1975).

27. H. S. Isaacs and W. A. Maxwell, *Fuels and Materials Development Program Quart. Progr. Rep. Mar. 31, 1974,* ORNL-TM-4620, pp. 16–23.

3. FISSION PRODUCT TECHNOLOGY STUDIES

A. P. Malinauskas

3.1 INTRODUCTION

The subject matter of this chapter primarily concerns the release of radiologically significant fission products from coated particle fuel, and the subsequent distribution of these fission products among core and primary circuit components. The data derived from these investigations are sought for several reasons; these range from providing source term information for use in systems response analyses to the establishment of criteria for fission product retention in candidate fuel types.

Major emphasis during this reporting period has concerned the time-temperature-radiation interrelationships as they determine fuel particle stability, cesium release from intact fuel particles, and tritium and iodine distributions in an HTGR, and extensive postirradiation examinations of selected Peach Bottom HTGR driver fuel elements. In addition, a study of cesium transport through graphite has been undertaken. A report of this investigation, which is sponsored by the Division of Physical Research, USERDA, is included here for sake of completeness.

3.2 FISSION PRODUCT RELEASE FROM COATED PARTICLE FUELS — M. T. Morgan, R. B. Evans III, R. L. Towns, and L. L. Fairchild

The purpose of these studies is to describe fission product transport in pyrocarbon-coated fuel particles. Related objectives include a comparison of the effectiveness of various coatings in retaining fission products, a determination of fission product release (primarily cesium) during postirradiation anneals, the measurement of cesium concentration profiles in particle coatings by a grinding technique, and analyses of irradiated coated particles to determine loss of fission products during irradiation.

Mathematical models were developed to describe fission product release during postirradiation anneals and comparisons were made with experimental data. These exercises gave a reasonable interpretation of most of the experimental observations. The experimental results

provided a range of diffusion coefficients for various fission products in pyrocarbon coatings and indicated that some fraction of fission products is essentially trapped in the kernels. Also a constant driving potential for cesium diffusion in the outer coatings during anneals of highly irradiated coated particles was demonstrated. In addition, irradiation experiments were reviewed to establish the degree of conservatism of coated particle stability diagrams, which are being used in computer codes for calculations of fission product release.

3.2.1 Mathematical Description of Fission Product Transport in Coated Fuel Particles During Postirradiation Anneal Experiments

A report that reviewed various solutions of the diffusion equation as are applicable to studies of fission product release from coated fuel particles was issued. An abstract of this report[1] follows:

> This report is concerned with several integrated forms of the diffusion equation that might be used to interpret and correlate cesium (and perhaps strontium) release data obtained from postirradiation anneals of pyrocarbon-coated fuel particles. Emphasis is placed on the role of the initial and boundary conditions as influenced by source concentration levels, permanent trapping in the source, and partition coefficients between the source and coating. It is assumed that release rates are controlled by the source potential and the diffusivity of the coating (with and without an external film or evaporation coefficient). A review of the equations, coupled with considerations of correlation procedures, indicates the need for complementary experiments that will give independent measurements of the trapped fraction and boundary concentrations.

3.2.2 Release of Fission Products During Postirradiation Anneals

A comprehensive review of previous studies of fission product release from coated fuel particles during postirradiation anneal has been completed, and a report issued. An abstract of the report[2] follows:

This report contains the data, results, and evaluations of postirradiation annealing studies of coated HTGR fuel particles. The purpose of the studies was to compare the capability of various pyrocarbon coatings for retaining fission products, including strontium, barium, and cerium, but primarily cesium. Experimental methods for annealing and examining coated particles are discussed. Constant-potential diffusion equations were used to calculate diffusion coefficients and the concentrations in the outer coating at the buffer-to-outer-coating interface. The results revealed kernel trapping effects and have indicated the possibility of a cesium concentration limit of about 2×10^{19} atoms/cm^3 in low-temperature-deposited isotropic pyrocarbon coatings of high density. Diffusion coefficients for cesium in the low-temperature-deposited isotropic pyrocarbon coatings were found to be an order of magnitude higher than in high-temperature-deposited isotropic pyrocarbon coatings. The diffusion coefficients obtained will be useful in determining the maximum cesium release from similar coated particle fuel during irradiation. Data concerning a trapped fraction and a concentration limit can direct further research which might provide more accurate estimations of cesium release from coated particles during irradiation.

These annealing studies were continued to verify the existence of a constant-potential driving force for cesium in highly irradiated coated particles, to provide additional experimental correlation with mathematical models, and to define the effects of temperature and burnup on kernel trapping effects. A major effort was placed on annealing pyrocarbon-coated UO_2 particles that had been irradiated to 11% and 22% FIMA at temperatures below 800°C. These coated particles were from batch OR-1010-SB, which was also the source of particles studied extensively in the previous experiments. The OR-1010-SB coated particles had thin sacrificial layers over the outer coatings. These layers

were ground off before annealing. Nine coated particles from each of the two irradiations were annealed at 1400°C. Three coated particles from each group were removed at 119 hr for grinding, and the remainder were annealed for a total of 1914 hr. Average cesium releases are plotted in Fig. 3.1. These curves are linear between 25 and 50 hr annealing time. An expanded plot would show a departure from linearity beginning at about 45 hr. The linear part of the curve corresponds to constant-potential diffusion. The part of the curve beyond 45 hr, which corresponds to diffusion from a depleting source, would be expected to continue to curve downward, finally approaching a horizontal asymptote, which is determined by the fraction of available cesium. The increase in slope, which is seen in both curves, is unexpected and may be similar to abrupt changes in release rates that had been observed in previous experiments.[2]

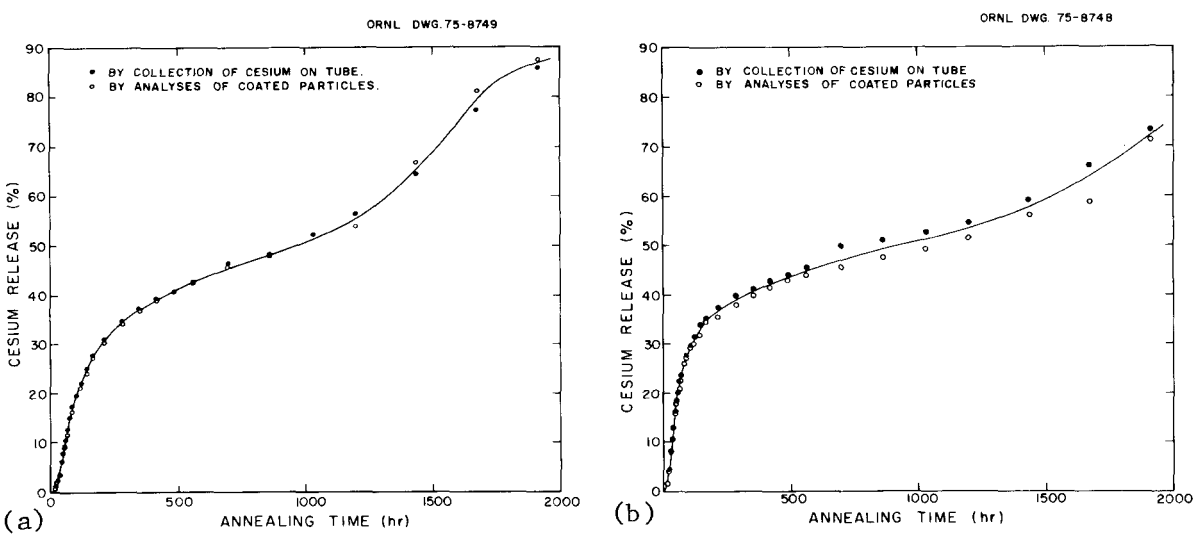

Fig. 3.1 Cesium Release During Anneals at 1400°C of Pyrocarbon Coated UO_2 Particles Irradiated to (a) 11% FIMA and (b) 22% FIMA.

To demonstrate that the linear part of the release curve represents diffusion from a source at a constant potential, other particles from the same irradiations were annealed at 1400°C for 24, 30, 36, and 42 hr. These coated particles were then ground to determine concentration profiles in the coatings. A sketch of the grinding apparatus is shown in

Fig. 3.2. Three separate motions are provided, as indicated in the figure, to maintain particle spheroidicity. Other details are self explanatory.

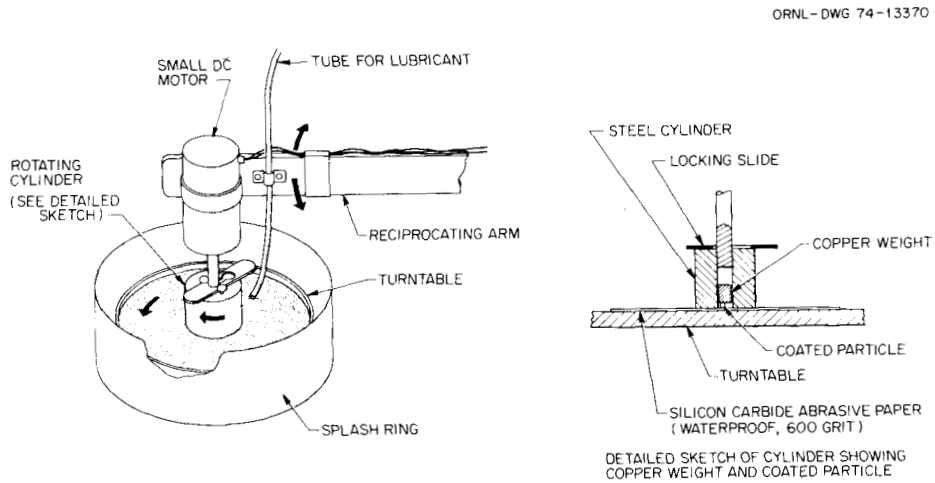

Fig. 3.2. Coated Particle Grinder.

A typical concentration profile is shown in Fig. 3.3. The stepped profile indicates the thickness of the layers removed. The curved line was calculated from the equation for constant-potential diffusion in a spherical shell:[1]

$$C(r) = C(a)\left[1 + \left(\frac{ab}{rl} - \frac{b}{l}\right)\right] - C(b)\left(\frac{ab}{rl} - \frac{b}{l}\right), \qquad (1)$$

where

$C(r)$ = cesium concentration at radial distance r,
$C(a)$ = cesium concentration at radial distance a,
$C(b)$ = cesium concentration at radial distance b,
a = radius at buffer-to-outer-coating interface,
b = radium at outer surface, and
l = coating thickness.

The intercept of the curve with the vertical line at b gives a concentration at the surface of 1.4×10^{18} atoms/cm^3; however, the

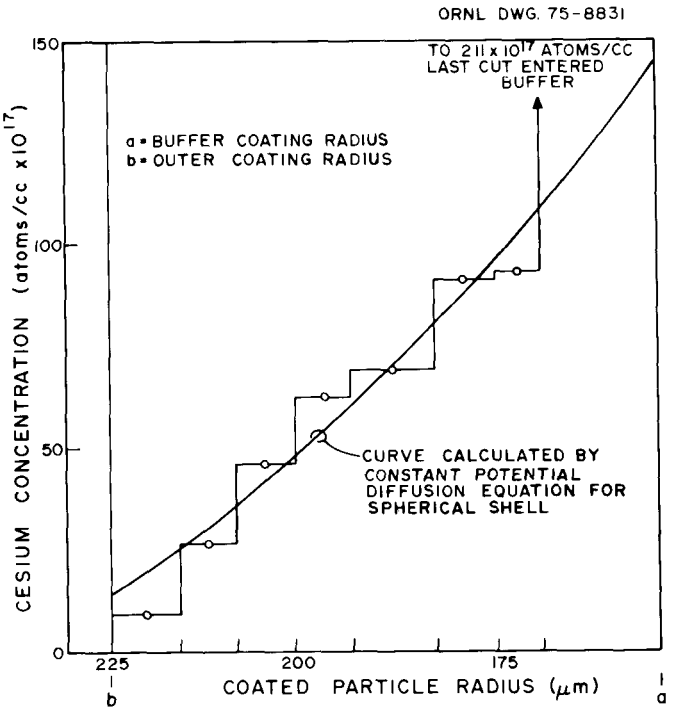

Fig. 3.3. Cesium Concentration Profile in Pyrocarbon Coating of UO_2 Particle Irradiated to 11% FIMA and Annealed 30 hr at 1400°C.

average concentration in the initial cut is below the calculated line, thus indicating a steep concentration gradient just below the coated particle surface. The intercept at $r = a$ indicates an approximate concentration $C(a)$ of 1.4×10^{19} atoms/cm^3. In Table 3.1, the average values of $C(a)$ obtained from concentration profiles of coated particles annealed between 24 and 36 hr at 1400°C are compared with $C(a)$ values obtained from the slope and intercept of release curves. The difference

Table 3.1. Average Cesium Concentration at $r = a$ in OR-1010-SB Coated Particles Irradiated to 11% and 22% FIMA

Source of Data	Sacrificial Layers	av conc, atoms/cm^3, at Each Burnup		Particles Measured	
		11% FIMA	22% FIMA	11%	22%
Concentration profiles	Removed	1.2×10^{19}	1.4×10^{19}	6	6
Release curves	Intact	1.2	1.0	11	4
Release curves	Removed	2.8	3.4	9	9

in the values of $C(a)$ that were obtained from the release curves with and without removal of the sacrificial layers is unexplained.

Cesium concentration profiles which were obtained from coated particles removed from the annealing series at 24, 30, 36, 42, and 119 hr are displayed in Fig. 3.4. Concentration ratios $C(r)/C_a^0$ are plotted, where C_a^0 represents the initial cesium concentration at $r = a$ averaged from profiles at 24, 30, and 36 hr annealing time. The straight-line portions represent least squares fits of the data but exclude points at positions below 0.1 and above 0.86. These data confirm that a constant driving potential for cesium transport in the outer coating exists between 24 and 36 hr annealing time. The points close to the outer boundary, position 0, show the steep concentration gradient mentioned earlier.

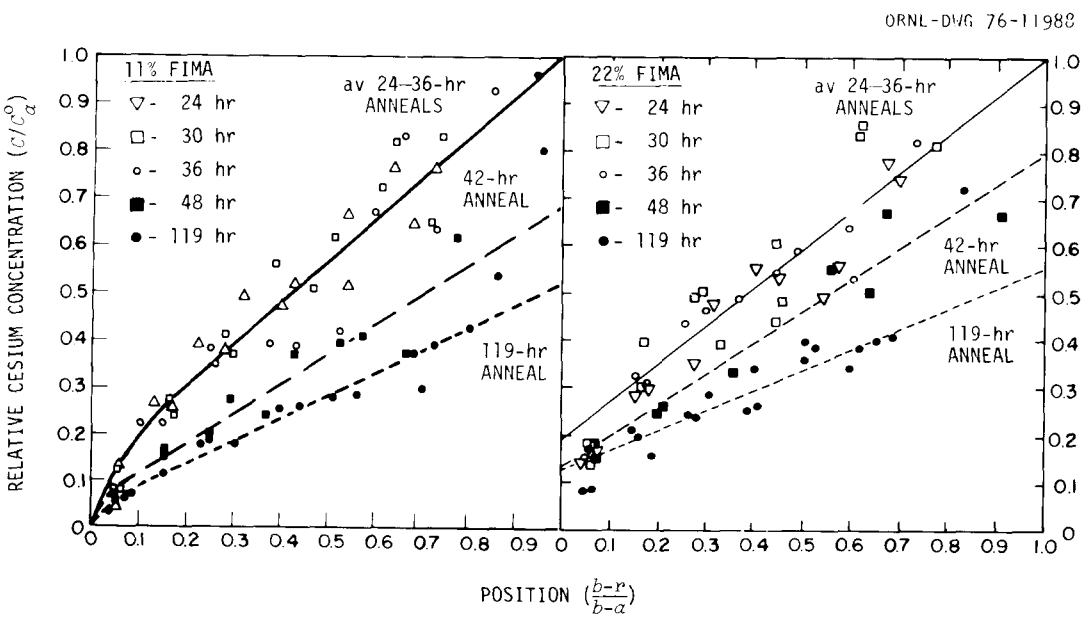

C = ^{137}Cs CONCENTRATION

C_a^0 = INITIAL ^{137}Cs CONCENTRATION AT a

r = RADIAL POSITION

a = RADIUS OF POSITION-OUTER COATING INTERFACE

b = RADIUS OF OUTER BOUNDARY

Fig. 3.4. Cesium Concentrations in Pyrocarbon Coatings of Batch OR-1010-SB Particles after Irradiation to Two Burnups and Annealing at 1400°C.

Release from bare UO_2 kernels has likewise been studied to gain an understanding of the extent to which this mechanism controls release from the coated particle as a whole. Although release studies had been made with 22%-FIMA-irradiated UO_2 kernels that had been annealed 300 hr at 1250°C, with no kernel fragmentation observed,[2] extension of the studies to 1400°C anneals has been complicated by persistent kernel disintegration.

Kernels were obtained from batch OR-1010-SB particles that had been irradiated to 11 and 22% FIMA. In the first attempt to anneal the kernels, by bringing them directly to the 1400°C anneal temperature, all the kernels broke. In the next attempt kernels were annealed 24 hr at 1250°C before proceeding to 1400°C. Of six kernels used in this test, three still disintegrated at 1400°C, one completely to dust and the other two to several large fragments. The kernel that disintegrated to dust was discarded; the other two fragmented kernels and three intact kernels were used in the anneals at 1400°C. The kernels were not removed from the tungsten annealing tubes for analysis in these experiments to avoid excessive handling, which might have caused further fragmentation, contamination of the upper end of the tube where released cesium is deposited, or possible loss of sample. Since the cesium released is deposited more than 13 mm away from the kernel, the kernel could be shielded while the deposited cesium on the upper end of the tube was assayed with a gamma-ray spectrometer.

Observed cesium release in these experiments is presented graphically in Fig. 3.5. (The initial datum point on each curve represents cesium released from the kernels during annealing of the intact coated particles before grinding.) At about 240 hr annealing time, two of the tungsten tubes were broken and replaced. This apparently caused the cesium release rate to increase abruptly. To determine whether the removal of the small concentration of cesium in the tubes adjacent to the kernels (less than 1% of cesium remaining in the kernels) had affected the release rate, kernels 1 and 5 were removed from their respective annealing tubes and the tubes were annealed at 1600°C to lower the cesium concentrations in the area near the kernel. The maximum cesium activity in the

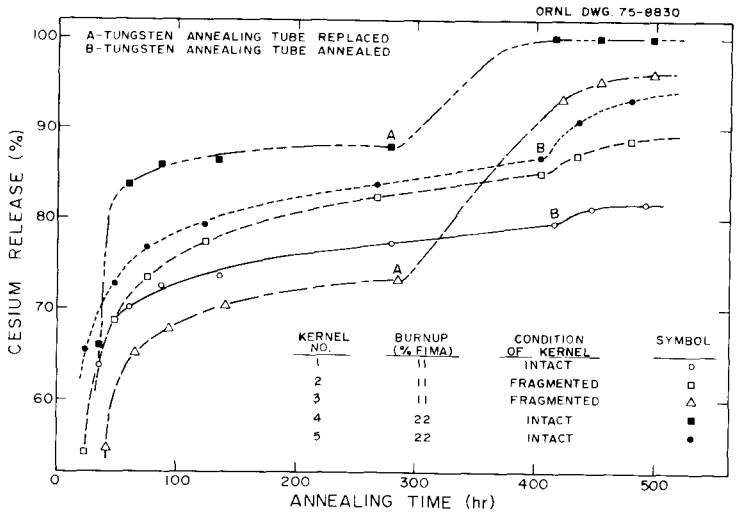

Fig. 3.5. Cesium Release from Bare Kernels during Anneals at 1400°C.

space surrounding the kernels was calculated to be less than 1×10^{16} atoms/cm^3 before the heat treatment at 1600°C. The cesium activity dropped from 1118 to 274 dis/sec in the bottom of tube 1, and from 431 dis/sec to near zero in the bottom of tube 5. The kernels were replaced and annealed as before. The release rate from kernel 5 increased significantly, but that from kernel 1 increased only slightly. Also, an increase in release rate was noted from kernel 2, even though the concentration of cesium in the tube had not been changed. A previous experiment was also reviewed; this involved anneals of four intact coated particles at 1400°C in which the tubes and thimbles used in the tubes were changed. No change in release rates occurred, although the activity changes in the tubes exceeded those in the current experiments.

It was concluded that the cesium concentrations in the tubes adjacent to the kernels are insufficient to significantly affect the cesium release rate. The results of these experiments indicate a rapid release of cesium in 50 hr to approximately 70 and 80% from the kernels irradiated to 11 and 22%, respectively, and a very slow diffusion rate after 50 hr. The higher release fraction would be expected at the higher burnup because of increased porosity.

3.2.3 Fission Product Release During Irradiation

This study is currently centered on Biso-coated ThO_2 particles, batches OR-1840 and OR-1849, which had been irradiated in capsules HT-12 through -15. A disagreement between the number of coating failures as determined by visual inspection and those determined by coated particle gas pressure measurement prompted a more thorough investigation. Samples of the coated particles were analyzed by gamma-ray spectroscopy, leached with hot chlorine at 1000°C, and inspected visually under the stereo microscope before and after leaching. They are now being reanalyzed by gamma spectroscopy. The failure determinations obtained thus far are presented in Table 3.2.

Table 3.2. Failures in Biso-Coated Particles from Capsules HT-12 Through HT-15 as Determined by Different Methods

Capsule	Average Temperature (°C)	Burnup (% FIMA)	Fast (>0.18 MeV) Fluence (n/cm^2)	Visual Failures (%)	Gas Pressure Test, Numbers of Particles[a]		Hot Chlorine Leach		
							Failures, %		Number Leached
					Failed	Tested	By ThO_2 Collected	By Particle Activity	
			Holder 8, Batch OR-1840, Design[b] 402-25-50						
HT-12	1090	1	3×10^{21}	0		0	0	0	16
HT-13	1190	3	6	0	0	6	5	6	16
HT-14	1250	7	9	0	3	3	80	94	16
HT-15	1260	10	11	0		0	76	100	6
			Holder 21, Batch OR-1840, Design[b] 402-25-50						
HT-12	1370	1	4	0		0	0	0	16
HT-13	1460	6	8	0	0	10	0	0	16
HT-14	1500	13	14	0	3	8	14	19	16
HT-15	1500	16	16	93		0			0
			Holder 13, Batch OR-1849, Design[b] 508-79-75						
HT-12	1180	1	3	0		0	0.3	0	16
HT-13	1270	5	7	0		0	0	0	12
HT-14	1320	9	11	0	2–3	6	58	75	8
HT-15	1330	11	13	0	2	3	70	88	8
			Holder 26, Batch OR-1849, Design[b] 508-79-75						
HT-12	1450	1	4	0	0	3	5	6	16
HT-13	1520	6	9	0	0	6	0	0	16
HT-14	1550	14	14	0	0	5			0
HT-15	1550	16	16	3	0	5	0	0	8

[a]Failures determined by absence of fission gas during pressure measurements.

[b]Design gives kernel diameter, buffer thickness, and outer coating thickness, all dimensions in micrometers.

The results indicate that some defective coatings may not be detected by visual inspection. As seen under the scanning electron microscope (SEM), the surfaces of some, but *not* all, of the defective coatings

appear to be porous. Further comparisons with sound coatings are desirable and have been planned. Although faint lines were observed in several coated particles at high magnification under the optical microscope, the SEM examination of two of these showed the lines to be merely surface features. No cracks were found in the eight coated particles examined under the SEM. One definitely cracked coating and three with holes were detected by visual inspection after leaching. These holes apparently developed during leaching of defective particles.

A comparison between the failures detected by crude beta-gamma activity measurements on individual particles after leaching with those determined by the amount of ThO_2 collected during leaching indicates good agreement. The total amount of ThO_2 was based on the average kernel diameter; consideration was made for loss of ThO_2 by burnup and transmutation during irradiation.

The results also show a significantly higher failure fraction in two samples of coated particles irradiated at lower temperatures, but from the same batch (compare HT-14-8 with HT-14-21, and HT-15-13 with HT-15-26). Note that the burnup in the high-temperature holders exceeds that of the low-temperature holders in the same irradiation capsule. Since the failures do not appear to be gross pressure vessel failures, the cause of failure remains to be determined.

The analytical data for the calculation of fission product loss during irradiation are now being assembled and evaluated.

3.2.4 Review of Coated Fuel Particle Stability

The stability of HTGR fuel particles as a function of burnup, fast neutron fluence, irradiation time, and temperature, but without regard for effects of coating parameters was reviewed. A report of this review has been issued;[3] an abstract of the report follows:

> This report reviews the stability of coated fuel particles in high-temperature, gas-cooled reactors as a function of burnup, fast-neutron fluence, irradiation time, and temperature; the effect of coating design parameters was not considered. The purpose of the review is to establish limits of coated particle

performance and, in particular, to validate diagrams in which coating failure during abnormal temperature excursions is plotted vs previous irradiation time.

3.3 TRANSPORT OF STRONGLY ADSORBED SPECIES IN POROUS MEDIA* — R. B. Evans III and A. L. Sutton, Jr.

The purpose of this investigation is to identify and describe mathematically those mechanisms that control the transport of strongly adsorbed species in porous media. Diffusion of cesium through graphite components of HTGR fuel elements is a good example of such systems, since most of the activity in HTGR cooling circuits results from cesium isotopes that leak out of coated fuel particles,[1] either as noble gas precursors or in the metallic state,[2,3] then adsorb and migrate through the graphite that surrounds the fuel regions. The subject investigation comprises a dual effort. It concerns correlation of data from laboratory experiments involving small graphite specimens subjected to short-term diffusion anneals (with cesium), and analyses of cesium diffusion profiles that correspond to long-term cesium exposures in the Peach Bottom HTGR. It is felt that the only way to develop a viable phenomenological model for cesium diffusion is to test its applicability to both long- and short-term experimental results.

Accordingly, this report consists of two major parts, a brief review of our bench-scale techniques and results, followed by a detailed summary of attempts to correlate diffusion profiles in reactor components that were studied under the auspices of various HTGR surveillance programs. In the laboratory, transport of cesium through graphite is being studied at temperatures ranging from 600 to 1000°C, wherein cesium could exist as a metallic vapor, but more likely (in view of its strong adsorption tendencies)[4] as a mobile adsorbed species on graphite surfaces. Here, we seek information about migration diffusion rates, reported in the form of diffusion coefficients, and the possible effects of other surface phenomena that might perturb the overall migration patterns. In addition, we are interested in the relative roles of vapor-phase and adsorbed-phase mechanisms.

---

*This work is sponsored by the Division of Physical Research, USERDA.

3.3.1 Applicable Transport Theories

3.3.1.1 Vapor or Gas-Phase Transport

Consider the transport of gas *1* in a porous medium that is saturated with helium. Gas *1* could be a stable isotope (^{134}Xe), a radioactive precursor (^{137}Xe) or even metallic ^{137}Cs; gas *2* is helium, and the medium is graphite. The equation for gas *1* diffusion in this system is given by

$$\vec{J}_1 = -D_1 \nabla C_1 + \delta_1 y_1 \vec{J} - (1 - \delta_1) y_1 \vec{J}_V \ . \tag{2}$$

The $\vec{J}$s represent molar fluxes, D_1 is an overall effective diffusion coefficient, C_1 is the partial density of gas *1* (concentration), δ_1 is a ratio of coefficients and is unity if free-molecule flow is negligible, y_1 is the mole fraction of gas *1*, and $\vec{J}$ and $\vec{J}_V$ are the net flux and that part of the net flux that results from forced flow, respectively. Note that $\vec{J}$ is $\vec{J}_1 + \vec{J}_2$, and each of these is the sum of a diffusive and viscous contribution; e.g., $\vec{J}_1 = \vec{J}_{1_D} + \vec{J}_{1_V}$, $\vec{J} = \vec{J}_V + \vec{J}_D$. Thus, the last two terms of Eq. (2) can be rearranged to yield

$$[(2\delta_1 - 1) y_1 \vec{J}_V + \delta_1 y_1 \vec{J}_D] \approx y_1 \vec{J}_V \ .$$

The approximate form at right arises when $\vec{J}_V > \vec{J}_D$ and $\delta_1 \to 1$. This means that the net forced flow will overwhelm the diffusive term, and that the data will concern high-permeability graphites at moderate pressures or moderate-permeability media at high pressures.

Another expression for a gas undergoing radioactive decay during flow is developed from the continuity equation for gas *1*,

$$-\nabla \cdot \vec{J}_1 = \varepsilon \frac{\partial C_1}{\partial t} + \varepsilon \lambda_1 C_1 \ , \tag{3}$$

where ε is the porosity of the medium and λ is the decay constant. The companion relationship for both gases, assuming that gas *1* is very dilute, is

$$-\nabla\cdot\vec{J}_V = \varepsilon\lambda_1 C_1 \quad . \tag{4}$$

Now everything set forth above can be inserted into Eq. (3) [terms like $(\varepsilon\delta_1 C y_1^2)$ will be small] to give the result sought for unsteady-state diffusion of dilute gas *1* subject to decay and forced flow, namely

$$D_1 \frac{\partial^2 C_1}{\partial x^2} - v \frac{\partial C_1}{\partial x} = \varepsilon \frac{\partial C_1}{\partial t} + \varepsilon\lambda_1 C_1 \ , \tag{5}$$

where $\vec{J} = \vec{v}C$ or $J = vC$ (dropping the vector notation as we restrict the treatment to unidirectional flow), v is the total partial velocity, and C is the overall density of the gas.

Although all the equations above are referred to the bulk dimensions of the medium, units of D_1 and v seem to be mixed; they are (pore cm^3/bulk cm sec) and (pore cm^3/bulk cm^2 sec), respectively. This happens because the driving potential, $C = p/RT$, applies only to the pore volumes, not to the solids. For the same reason, an ε appears before the accumulation and decay terms. This causes no problems, since the average pressures and volumetric flow rates (determining the Cs and Js) in the pores are the same as the average values measured in free spaces external to the medium boundaries. Considerations of units should give some insight as to why all coefficients carry a geometrical factor ε'/q, which converts free space values to porous medium values. We note that ε' is that fraction of ε that carries most of the flow; q is a tortuosity factor with units of (pore cm^2/bulk cm^2). In practice, $\varepsilon'/\varepsilon \approx 10^{-2}$. For the near-normal region, $D_1 \approx (\varepsilon'/q)D_{12}$, where D_{12} is the free-space diffusion coefficient value.

3.3.1.2 Adsorbed Phase Transport

To treat this aspect of the problem separately, one envisions an adsorbed species *1* with a low vapor pressure as it moves about on a two-dimensional surface. Since species *2* (helium) does not adsorb at the temperatures of interest, and interactions with other adsorbed species are assumed to be negligible, the diffusion expression is simply

$$J_s' = -D_s' \frac{dC_s'}{dx} \quad . \tag{6}$$

The subscript s refers to the surface; the units of C_s' are (mole/surf cm^2).

Unfortunately, a form like Eq. (6) cannot be applied directly to porous media, because one must invoke a capillary surface area model that reflects proper averaging of pore dimensions and heterogeneous surface phenomena. The problem of conversion of Eq. (6) to a form suitable for application to porous media can best be circumvented through the same dogmatic approach used for gases. An apparent coefficient is defined by agreeing to measure the total flux across one of the boundary areas normal to x, then to express C_s' as C_s (mole/bulk cm^3) as it obtains from equilibrium adsorption data for large pieces of graphite. Thus

$$J_s = -D_s \frac{dC_s}{dx} \quad . \tag{7}$$

When radioactive decay is included, Eq. (7) takes the form

$$D_s \frac{\partial^2 C_s}{\partial x^2} = \frac{\partial C_s}{\partial t} + \lambda_1 C_1 \ . \tag{8}$$

3.3.1.3 Coupled Vapor-Adsorbed Phase Transport

Here again consideration is given to diffusion of an adsorbed species along surfaces, but with a vapor pressure high enough to merit inclusion of vapor phase contributions subject to the influence of a forced flow. The question is: How does the forced flow affect surface transport? Of course, if the system falls into this category, adsorption isotherms can be measured. These give equilibrium data, which can usually be described by an equation of the form

$$C_{\text{gas}}^n = \alpha C_{\text{surf}} \ , \tag{9}$$

where the units of α are (pore bulk cm^3/pore cm^3). We take values of α as given, and consider cases in which $n = 1$ (the Langmuir or Henry's Law region). The combined equation in terms of the gas concentration

is obtained by substituting Eq. (9) into (8), then adding this result to that given by Eq. (5) with subscript g for gas replacing 1. In similar fashion, one may derive an identical expression (regarding coefficients) in terms of the surface concentration wherein one may convert the surface concentrations from a bulk to pore basis by dividing both sides by ε. An addition of both forms of the combined equations gives another identical expression in terms of the overall concentrations $C_o = C_g + C_s/\varepsilon$, which is referred to the total amount of material in pore volumes and on pore surfaces, namely,

$$D_o \frac{\partial^2 C_o}{\partial x^2} - v_o \frac{\partial C_o}{\partial x} = \varepsilon\lambda C_o + \varepsilon \frac{\partial C_o}{\partial t} , \tag{10}$$

where the subscript o means overall.

The reason one might express Eq. (10) in terms of either C_g, C_s, or C_o stems from the fact that complete gas-surface coupling is implied through Eq. (9); also, the flows are parallel. Of greater importance are the forms obtained for the overall diffusion coefficient and effective velocity,

$$D_o = \frac{D_g + D_s/\alpha}{1 + 1/\alpha\varepsilon} , \tag{11}$$

$$v_o = \frac{v}{1 + 1/\alpha\varepsilon} . \tag{12}$$

It turns out that α values for cesium on graphites are quite small in the Langmuir region. For AGOT graphite at 800°C, $\varepsilon \approx 0.2$ and $\alpha \approx 10^{-12}$. Thus, according to Eq. (11), the overall coefficient will be primarily the surface coefficient, the vapor-phase contribution will be negligible. It is also clear from Eq. (12) that cesium diffusion along pore surfaces will be practically immune to helium flow effects, unless the flow rates are extremely high as compared with those required to sweep out a gaseous precursor. (Additional theoretical details are given elsewhere.[5–7])

3.3.2 Laboratory Experiments

All the experiments performed to date have been set up to utilize the classical thin-layer technique, wherein cesium concentration profiles within a small graphite specimen are determined after the specimen has been annealed for a predetermined period of time. Specimens sizes and diffusion times are adjusted to ensure that (1) transient conditions prevail throughout the anneal according to Eq. (10) with the velocity and decay terms set equal to zero, and (2) the profiles will not penetrate to the back boundary; that is,

$$D \frac{\partial^2 C_p}{\partial x^2} = \varepsilon \frac{\partial C_p}{\partial t} , \tag{13}$$

where subscript o has been replaced by p to represent pore surface and volume. Initial and boundary conditions are: $C(x,0) = 0$, $C(\infty,t) = 0$, and a "flash" or impulse of cesium is applied instantaneously at $x = 0$, $t = 0$.

Experiments are initiated by placing a thin cesium layer, with about 30% of the 137 isotope, on the surfaces of diffusion specimens in the form of cesium oxides derived from an aqueous solution. While the sample is brought to the desired diffusion anneal temperature under pure helium, the oxide converts (at about 500°C) to the metal, which produces an impulse with strength Q_0 mole per specimen area normal to x. If all conditions are satisfied, the solution to Eq. (13) becomes

$$C_p(x,t) = \frac{Q_0}{\sqrt{\pi D \varepsilon t}} \exp\left(-\frac{x^2 \varepsilon}{4DT}\right) . \tag{14}$$

The preexponential term is the time-variable surface concentration $C_p(0,t)$. Conversion to bulk concentrations as measured in the laboratory, $C'(x,t)$, is accomplished by multiplying both sides of Eq. (14) by ε.

Slicing up small specimens to determine concentration profiles directly can be an extremely arduous and time-consuming task, particularly when one must contain and collect quantities of contaminated dry graphite dust. We therefore chose to section the specimens by grinding away portions of the samples (using kerosene as a cutting fluid) and measuring

FR, the fraction of total activity remaining, as a function of grinding distance. The pertinent equation is given by:

$$FR = (1/Q_0) \int_x^\infty C'(x',t')dx' = \mathrm{erfc}\left(\frac{x}{2}\sqrt{\frac{\varepsilon}{Dt}}\right) . \tag{15}$$

A plot of Eq. (15), along with some cesium diffusion data obtained with a graphite (Hawker Siddeley) that happens to exhibit the idealized behavior demanded by Eq. (14), is presented in Fig. 3.6. To bring all the points together, the results are plotted in terms of "reduced" penetrations, u. The diffusion coefficients are based on the determination of the factor by which the experimentally determined x values must be multiplied in order to make them fall on the correct u values at appropriate FR values. This factor is $\sqrt{\varepsilon/4Dt}$. The diffusion coefficients listed in Fig. 3.6 are bulk values (i.e., D_p/ε).

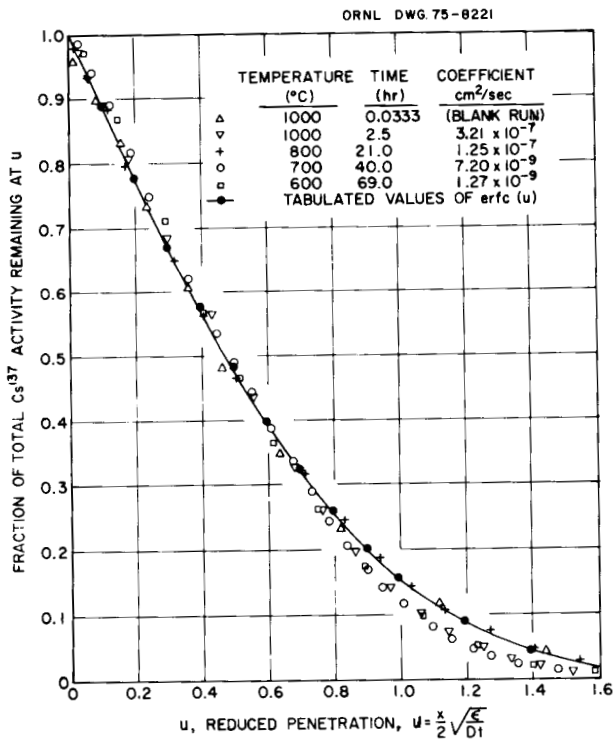

Fig. 3.6. Generalized Set of Cesium Penetration Data Obtained in Thin-Layer Experiments. The set shown pertains to cesium diffusion in a furfuraldehyde-impregnated fine-grain graphite referred to as Hawker Siddeley.

Three rather significant features of these results should be noted:

1. Consider the tabulated value of the grinding results obtained at 700°C (Fig. 3.6); the value is 7.20×10^{-9} cm^2/sec. Based on gas diffusion, permeability experiments, and mercury porosimetry data, the estimated value of D_p/ε for cesium or xenon *vapor* is about 10^{-2} cm^2/sec. The latter is much higher than the measured value.

2. A plot of the logarithm of the tabulated values of D_p/ε against the reciprocal of the absolute temperature reveals an exponential dependence and suggests an activation energy of about 155 kJ/mole (37 kcal/mole). Vapor phase coefficients, if controlling, would have a temperature dependence of approximately $T^{3/2}$, where T is the Kelvin temperature. This would yield an activation energy of only about 4 kJ/mole (1 kcal/mole).

3. The average graphite loading in these experiments ranged about 0.1 μmole/bulk cm^3. Thus, a low α value would be anticipated, and a low value applied to Eq. (11) suggests that the coefficients measured are surface values, as suggested by (1) and (2) above.

Clearly the results indicate that cesium diffusion behavior in Hawker Siddeley graphite relate directly to surface, not gas-phase, effects.

When the same experiments are performed with H-327 graphite, notable deviations from idealized behavior are observed. First, only part of Q_0 placed on the surface initially diffused into the specimen. The residual was immobilized and remained very close to the $x = 0$ surface. This did not happen with Hawker-Siddeley graphite. Secondly, the profiles tended to be linear with penetration, and did not exhibit the downward curvature (on semilog paper) that one would expect if Eqs. (13) and (14) were being followed. In fact, the curves are reminiscent of those obtained when one examines profiles for an immobilized daughter of a very mobile noble-gas precursor after diffusion into graphite under quasi-steady-state conditions.[8] Comparative plots of typical cesium diffusion results in Hawker-Siddeley and H-327 graphites are shown on Fig. 3.7. When $\tau = 0$ on this plot, the curve is described by Eq. (15), which corresponds to ideal behavior. When $\tau > 0$, other effects perturb the diffusion profiles. Additional details associated

with the data on curves of Fig. 3.7 appear in Table 3.3. We now attempt to describe the features of the model described by the various $\tau \neq 0$ curves on Fig. 3.7.

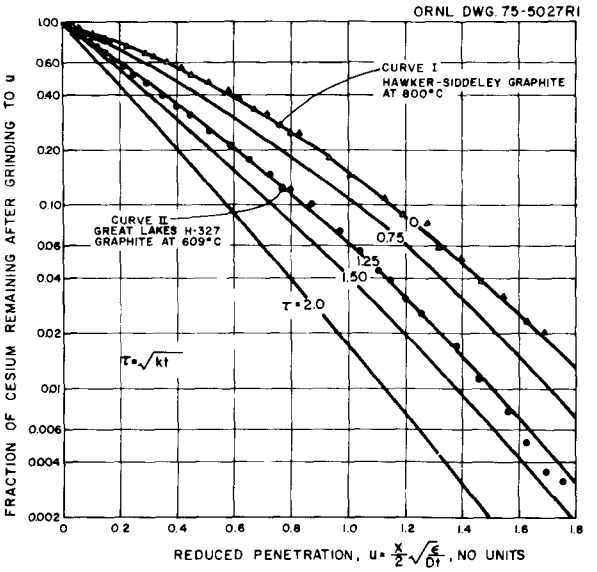

Fig. 3.7. Comparison of Cesium Penetration Data Obtained for Two Different Graphites. Grinding results are plotted as log FR versus u; solid curves represent solutions of Eq. (20) for various τ values. Data on curve I exhibit idealized ($\tau = 0$) behavior. Data on curve II indicate *in situ* plateout (or internal trapping) effects.

Table 3.3. Cesium Diffusion Results for Two Graphites as Shown on Fig. 3.7

Migration Parameters	Curve I Hawker-Siddeley Graphite (fine-grain impregnated)	Great Lakes Graphite (H-327) (large grain)
Temperature, °C	800	609
Diffusion time, min	1300	70.0
Penetration, x, at $FR = 0.5$, cm	0.093	0.096
Bulk diffusion coefficient D/ε, cm^2/sec	1.2×10^{-7}	7.9×10^{-6}
Amount of tracer[a] Q_0, $\mu mole/cm^2$	3.7×10^{-3}	1.8×10^{-3}[b]
Final surface conc. $C_T'(0,t')$ $\mu mole/cm^3$	0.026	0.013

[a] ^{137}Cs isotope plus nonradioactive species.

[b] Amount engaged in diffusion process; total amount was 2.4×10^{-3} $\mu mole/cm^2$, and $(2.4 - 1.8) \times 10^{-3}$ was held up at the $x = 0$ surface.

In line with the precursor behavior mentioned above, it was surmised, regarding H-327 results, that a trapping effect must have been occurring at the $x = 0$ surfaces and along internal pore surfaces as well. To account for these effects, deep profile data were extrapolated back to $x = 0$ to eliminate specimen surface trapping effects. Possible mechanisms of internal trapping were then explored. The first inclination was to add a first-order reversible reaction rate term like

$$r_\tau = k(\varepsilon C_p - KC_\tau) \tag{16}$$

to the right-hand side of Eq. (13), and then examine the applicability of the integrated results. Here, r_τ is the trapping (or plate-out) rate and KC_τ represents a back pressure term. Inclusion of the KC_τ term seemed desirable because one invariably is concerned about filling the traps, whereby an ultimate equilibrium like

$$K = (\varepsilon C_p / C_\tau)_{\text{equil}} \tag{17}$$

might be attained. In Eqs. (16) and (17), C_p represents the mobile or pore surface plus volume concentration, whereas C_τ denotes the concentration of filled traps in the solid grains referred to bulk volume.

However, considerations of long-term results suggest that the back pressure term might be negligible. Accordingly, the integration was carried out using only the first term in Eq. (16). The result for C_p was merely Eq. (15) multiplied by e^{-kt} *for the mobile fraction.* Grinding experiments "see" both immobile and mobile fractions, so the total bulk concentration was computed via

$$C_T'(x,t) = \varepsilon C_p e^{-kt} + \varepsilon k \int_0^t C_p e^{-kt'} dt' \ , \tag{18}$$

which yields

$$\frac{C_T'(x,t')}{C_T'(0,t')} = \frac{e^{-(u^2+\tau^2)} + (\sqrt{\pi}/2)\tau[e^{-2u\tau}\text{erfc}(u-\tau) - e^{+2u\tau}\text{erfc}(u+\tau)]}{e^{-\tau^2} + \sqrt{\pi}\,\tau[1 - \text{erfc}(\tau)]} \tag{19}$$

where

$C_T'(x,t')$ = total cesium concentration (mobile + immobile),

$u = (x/2)\sqrt{\varepsilon/Dt'}$, and

$\tau = \sqrt{kt'}$.

The corresponding fraction-remaining expression for our experimental sectioning procedure is

$$FR = e^{-2u\tau} + [e^{2u\tau}\mathrm{erfc}(\tau + u) - e^{-2u\tau}\mathrm{erfc}(\tau - u)]/2 \ . \qquad (20)$$

Figure 3.7 indicates that data for H-327 graphite give a good correlation when one assumes a value of $\tau = 1.25$ (Curve II) for this particular experiment. This gives a positive indication that the trap model, as explained above, is an adequate representation of cesium migration behavior in the H-327 material. The same model has been used to correlate long-term in-reactor experiments conducted by General Atomic Company using the same graphite but different boundary conditions.[9] However, a rather poignant feature of performing long-term experiments with H-327 graphites should be noted. After a relatively short time, the value of τ overwhelms the value of u. Complementary error functions like $\mathrm{erfc}(\tau + u)$ fade away at $\tau > 2.0$; diffusion information from discrete u values is then lost, and the only information that can be gained in this case is a value for the grouping, $2u\tau/x$, which is obtained from the slope of the curves (plotted vs x) as on Fig. 3.7 at high τ values. The value of this grouping is $\sqrt{\varepsilon k/D}$.

It should be noted that the correlation on Fig. 3.7 is really not the best illustration of the asymptotic approach to the quasi-steady-state condition, because one can continue to construct curves on this plot for τ values greater than 2.0 even though the profiles are fixed. Another and better approach is to employ the group $z = 2u\tau$ for the independent variable, as has been suggested by Rodliffe[7] for a constant-potential situation. A plot of this kind is shown on Fig. 3.8. All data following ideal behavior as on Curve I in Fig. 3.7 will remain on the FR axis of Fig. 3.8 but, if a finite k value exists, the curves

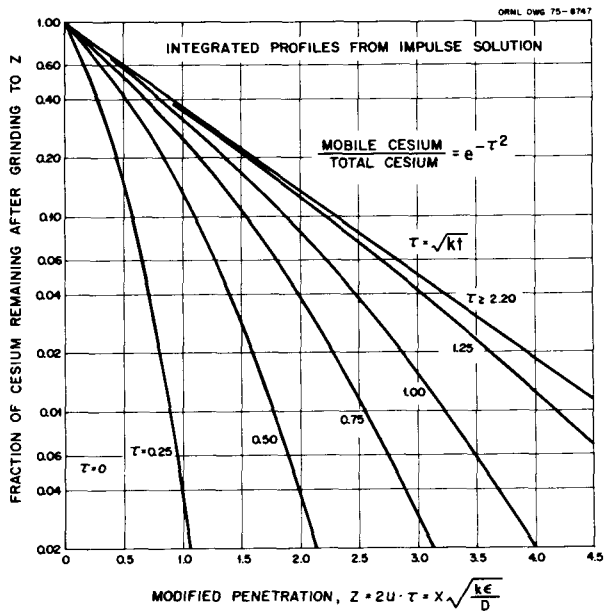

Fig. 3.8. Alternate Method of Presenting Solutions to Eq. (20) on a Semilogarithmic Basis. The independent variable has been changed from u to $z = 2u\tau$. Curves do not proceed beyond $\tau = 2.2$.

will proceed out from $z = 0$ with increasing k until the ultimate τ value of about 2.2 is reached. With further increase, the curve remains unchanged, regardless of τ values greater than 2.2. The same shapes occur when $k > 0$ if the data are plotted against x at selected diffusion anneal times. At about $\tau = 2.2$, the profile is frozen; the cesium is no longer mobile.

Finally, we point out that, while the group $\sqrt{\varepsilon k/D}$ may contain adequate information for reactor analyses, it is not sufficient for mechanistic studies. A complete understanding of cesium diffusion in highly permeable large-grained graphites such as H-327 can apparently only be gained through properly timed laboratory experiments. Current laboratory efforts are being concentrated on characterization and structural studies of Hawker-Siddeley and H-327 graphites in an effort to rationalize the dramatically different cesium diffusion results obtained with these materials.

3.3.3 Review of Peach Bottom HTGR Fuel Element Postirradiation Examination Data

This review is based on a detailed reappraisal of the results obtained by General Atomic Company through the analyses of the fuel element spines and sleeves removed from the reactor during Core I operation. Two sets of published data are available: (1) results of analyses of components from element D06-01, removed after 300 effective full-power days (EFPD), which were reported by Vanslager, Bell, Sisman, and Morgan;[10] (2) results from element D13-05, removed after 452 EFPD, which were reported by Haire and Zumwalt.[11]

Many of these data are plotted in Fig. 3.9, which presents the "as-reported" radial cesium profiles in terms of concentration (not *FR*) versus the radial distance in the fuel element for ^{134}Cs (open circles) and ^{137}Cs (closed circles) isotopes in both the spines and sleeves.

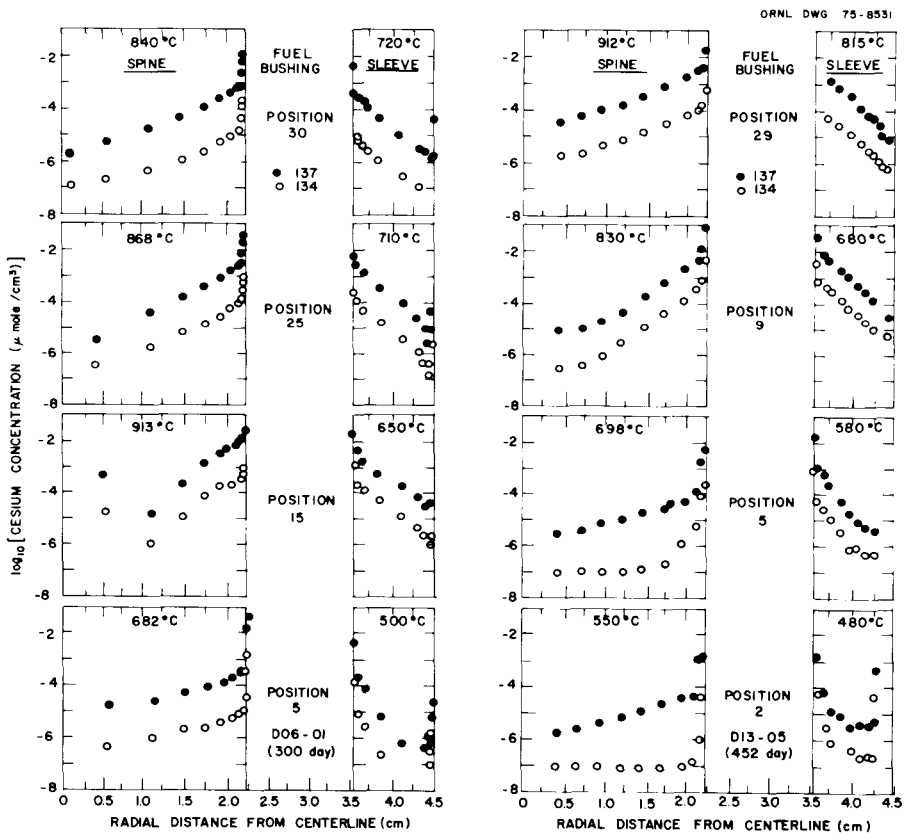

Fig. 3.9. Cesium Concentration Profiles Found in Components of Two Core I Peach Bottom Fuel Elements Removed after 300 and 452 EFPD. Open circles, ^{134}Cs. Closed circles ^{137}Cs.

(For purposes of orientation, the reader is referred to the element description in Sect. 3.5.1.) The element comprises three main parts in reference to the axial direction — namely, an upper reflector, a central fuel element section, and a lower reflector assembly, which contains fission-product traps. Data presented in Fig. 3.9 refer to the central fueled section, which is 2.29 m (90 in.) long and contains thirty 76-mm (3-in.) fuel compacts (actually fuel bushings), which are slipped over the spine, then covered by the sleeve. Helium coolant flow is upward with respect to the assembly, but a portion is induced to flow (through restrictors) down through gaps between the spine-compact interface, and also between the compact-sleeve interface. A fraction of the gap flow occurred in a radial direction through the sleeve, as a result of the average pressure drop across this component. This flow was directed to oppose leakage of fission products from the compacts (through the sleeve) into the main coolant stream.

The data available for the 300-EFPD element are limited to those appearing in Fig. 3.9. Sleeve temperatures in this case had to be estimated from available Core II temperature profiles, since only coolant temperatures were given. In contrast, the amount of data for the 452-EFPD element far exceeded those shown in Fig. 3.9. The latter included not only additional cesium diffusion profiles for spines and sleeves, but profiles for the krypton-strontium system as well.

Attention is called to the lower two sets of curves in Fig. 3.10, which pertain to the spines in the 452-EFPD element. These curves represent correlation of the ^{90}Sr and ^{89}Sr isotopes that plated out as a result of gaseous ^{90}Kr decay (half-life = 33 sec), and ^{89}Kr decay (half-life = 192 sec), respectively. It was assumed that these strontium profiles were immobilized and that they directly reflect the quasi-steady-state ($\partial C/\partial t = 0$) profiles for their krypton precursors, which migrated into the spines according to the radial flow form of Eq. (5). There might have been a minute value of transverse flow in the spines, but one might safely assume that the radial component of this flow is negligible; thus the velocity v in Eq. (5) may also be set equal to zero.

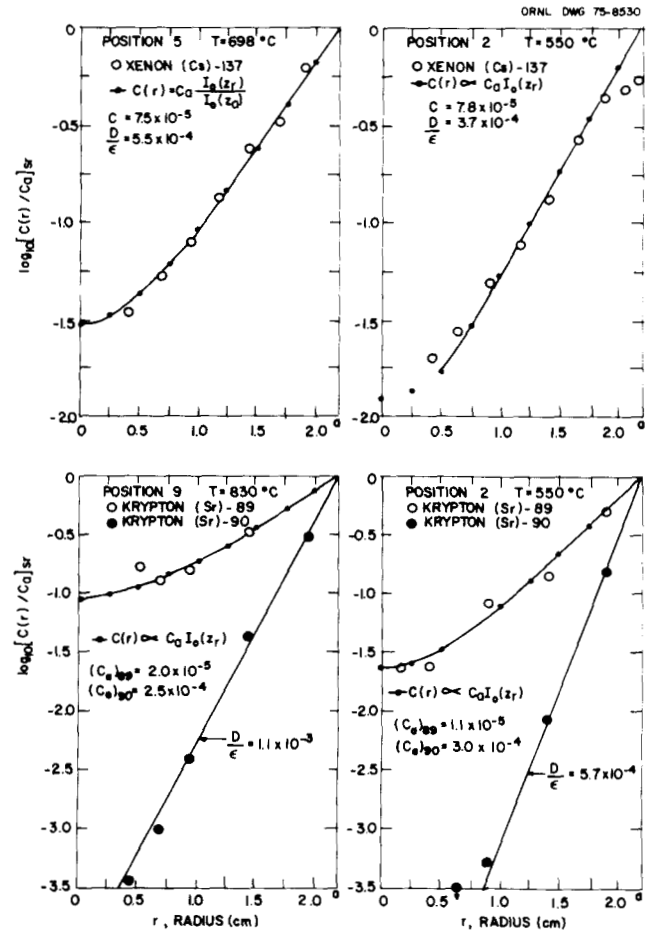

Fig. 3.10. Spine Penetration Data for Cesium and Strontium Isotopes that Reflect the Diffusion Profiles of Noble-Gas Precursors. Data pertain to the 452-EFPD fuel element.

The solution, assuming a time-constant krypton concentration at $r = a$ (an approximate boundary condition), is

$$\frac{C}{C_a} = \frac{I_0(\beta_\lambda\, r)}{I_0(\beta_\lambda\, a)}\ , \tag{21}$$

where $\beta_\lambda = \sqrt{\varepsilon\lambda/D}$. The curve fitting procedure was to pass a straight line through the ^{90}Sr data, as shown on Fig. 3.10, for which the C/C_a ratio could be approximated by the linear-flow form of Eq. (21), compute β_λ from the slope, then compute the D_{Kr}/ε value from β_λ. The ^{90}Sr data appeared to be slightly scattered, perhaps as a result of the deep penetration (from the long half-life) coupled with counting uncertainities

(measurements of this kind are quite difficult). We therefore used the D_{Kr}/ε from the ^{90}Sr data and computed a "predicted curve" for ^{89}Kr. Reference to the curves indicates good agreement between the 89 and 90 results.

Reference to the cesium profiles in the spine of the 452-EFPD element at positions 2 and 5 (Fig. 3.9) reveals two instances where the ^{134}Cs profiles are significantly different from all the other 134 profiles. The concentrations are relatively low and the profiles are relatively flat (in these cooler positions). In addition, the 137 concentrations are somewhat lower than other 137 concentrations, even though the profiles indicate significant, but shallow, concentration gradients. The cesium profiles here seem to be representative of the profile left by gaseous precursors, only this time xenon rather than krypton. Apparently the ^{134}Cs present originally migrated in as ^{133}Xe, which decayed slowly (with a long half-life of 7600 min, plenty of time to distribute uniformly) to ^{133}Cs, which, in turn, was converted *in situ* to ^{134}Cs via neutron absorption. The ^{137}Xe, on the other hand, decayed directly to ^{137}Cs, with a controlling half-life of 3.82 min. The ^{137}Cs data in this case could be treated in the same way as the ^{90}Sr data were treated by Eq. (21). The cesium results appear in the top two plots of Fig. 3.10. All the spine precursor results are summarized in Table 3.4; the values listed in the table are in good agreement with those reported previously by Haire and Zumwalt.[11]

Table 3.4. Summary of Precursor Diffusion Profile Results for the 452-EFPD Fuel Element Spine

Spine Temperature (°C)	Compact	C_a, μmole/cm^3			D/ε, cm^2/sec	
		^{89}Sr	^{90}Sr	^{137}Cs	^{90}Kr	^{137}Xe
550	2	1.1×10^{-5}	3.0×10^{-4}	7.8×10^{-5} [a]	5.7×10^{-4} [b]	3.7×10^{-4} [c]
698	5			7.5		5.5
830	9	2.0	2.5		11	
1000	18	0.68	1.3		36	

[a]Does not include cesium held up at $r = a$.

[b]Used $\lambda(^{90}Kr) = 0.021$/sec.

[c]Used $\lambda(^{137}Xe) = 3.024 \times 10^{-3}$/sec.

The cesium precursor data are of considerable importance in that they suggest rather useful indicia for the existence of a metallic cesium diffusion mechanism. Whenever the ^{134}Cs and ^{137}Cs isotopes have parallel profile shapes, a metallic state mechanism must have been controlling. Note that all cesium profiles in Fig. 3.9, other than those at spine positions 2 and 5 at 452 EFPD display such behavior. One might speculate for spine 2 and 5 that the redox-temperature conditions at these positions could not support cesium in the reduced state. The metal was immobilized, perhaps as an oxide. The only way cesium could have moved into the graphite, therefore, was in the form of a redox-insensitive noble-gas precursor.

Based on the above indicia, all other cesium profiles were treated as if the primary migration mode were a surface phenomenon involving a low-mobility species related to the metallic state. Contributions from the ^{137}Xe precursor would smear out in this case, since the xenon decay product would be free to move about. We differ at this point with the interpretations suggested by Haire and Zumwalt,[11] because we feel that both ^{137}Cs and ^{134}Cs profiles should be treated in the same way when the reduced state is suspected.

With respect to the remaining majority of the data sets displayed in Fig. 3.9, the buildup of excess immobilized cesium at the $r = a = 2.2$ cm surfaces should be noted. This is a good indication that internal trapping effects are present and have to be taken into account.

Semilogarithmic plots of the normalized cesium concentrations for both isotopes as a function of the radial distance to the first power are shown on Fig. 3.11 for the data obtained in the 300-EFPD element. The agreement between the two isotopes is almost too good to be true. Correlation of these data proceeded as follows: the solution to the cylinder-flow form of Eq. (10), with $v_o = 0$ and λ (the decay constant) replaced by a trap factor k, was rewritten in terms of Laplace transformed variables to obtain a form similar to Eq. (21), but with the time transformed variable s appearing at various places. (In all cases here, $k >> \lambda$.) The result is

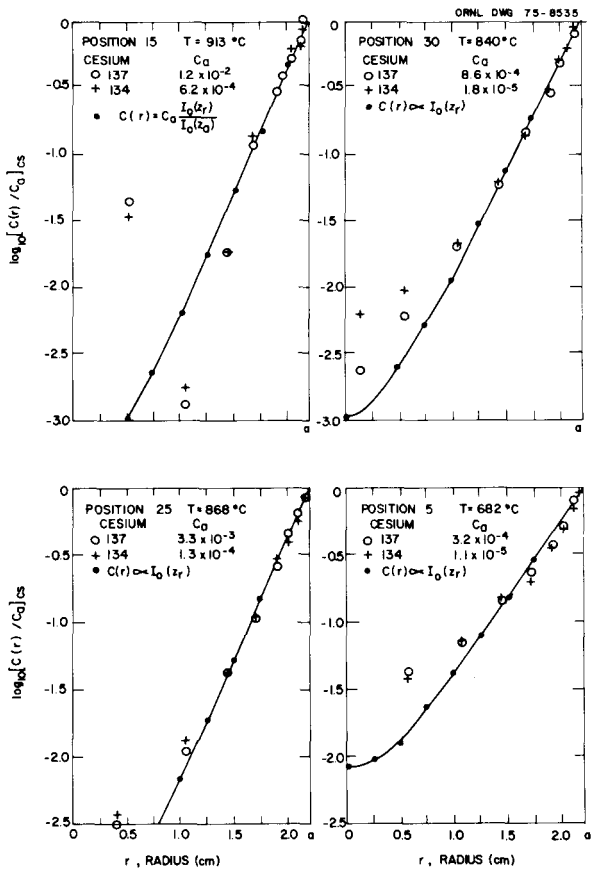

Fig. 3.11. Spine Concentration Profiles that Reflect the Nature of Metallic Cesium Diffusion in the Adsorbed State. Data pertain to the 300-EFPD fuel element.

$$\bar{c}_p(r,s) = \frac{C_a I_o[r\sqrt{\varepsilon(k+s)/D}]}{sI_o[a\sqrt{\varepsilon(k+s)/D}]} \quad . \tag{22}$$

This expression assumes a zero initial concentration over r and a constant potential C_a applied at $r = a$. Since the data curves in Fig. 3.11 are fairly steep, we could approximate Eq. (22) using a scheme described by Carslaw and Jaeger,[12] namely

$$\bar{c}_p(r,s) = C_a\sqrt{\frac{a}{r}}\left[\frac{1}{s}\exp(-\Delta r\sqrt{\varepsilon(k+s)/D})\right] \quad , \tag{23}$$

where $\Delta r = r - a$, and a is the solid spine outer radius.

The inverse of the bracketed term has been described by Crank[13] and Rodliffe,[7] and this turns out to be the answer for the pore concentration

(mobile — on pore surfaces and in pore volumes) in terms of slab geometry when $x = \Delta r$. Next, contributions of the immobilized fraction were inserted by the procedure described previously. The complete result is

$$\sqrt{\frac{r}{a}}\,\frac{C_T^{\prime}(r,t)}{C_T^{\prime}(a,t)} = \frac{(1 + \tau^2 - u\tau)e^{-2u\tau}\mathrm{erfc}(u - \tau) + (1 + \tau^2 + u\tau)e^{+2u\tau}\mathrm{erfc}(u + \tau)}{2(1 + \tau^2)} \tag{24}$$

where τ is $\sqrt{\varepsilon k/D}$, and u is $(\Delta r/2)\sqrt{\varepsilon/Dt}$. Equation (24) indicates that a small radial correction to the concentration ratio allows one to use the slab form for cylindrical cases. To obtain the form used for sleeve calculations, one need only remove the ratio of radii and substitute x for Δr.

Notice that we have changed the normalization from C_a to $C_T^{\prime}(a,t)$, since all the concentrations in our figures and tables are really $C_T^{\prime}$ values for total cesium referred to bulk volumes as measured after time t. Actually $C_T^{\prime}$ increased during a diffusion exposure from $C_T^{\prime}(a,0) - \varepsilon C_a$ to

$$C_T^{\prime}(a,t) = \varepsilon C_a(1 + kt) \ . \tag{25}$$

Plots of the right side of Eq. (24) versus u or $z = 2u\tau$ at fixed τ values look very much like the curves on Figs. 3.7 and 3.8. However, the rate of approach to quasi-steady state (with respect to τ) is somewhat slower; the ultimate useful curve, like the $\tau = 2.2$ curve in Fig. 3.8, occurred at $\tau = 5.0$. Unfortunately, the spine cesium data seemed to correlate at τ values ranging near the limiting value, which made the fitting procedures somewhat difficult and tedious.

Results of correlating the 452-EFPD spine cesium data with Eq. (24) are presented in Table 3.5. Included are previously reported values[11] that were obtained by force fitting the same equation with $\tau = 0$. Significant differences in coefficients occur for the trap and nontrap cases. Since the τ values we encountered were so high, it was doubtful that we could get a meaningful separation of k and D/ε. We simply could not perform a good transient analysis. We therefore recorrelated the data in terms of the steady-state Eq. (21), wherein β became $\sqrt{\varepsilon k/D}$ and

Table 3.5. Results of Correlating Metallic Diffusion Profiles in the 452-EFPD Fuel Element Spine Assuming Transient Flow

Compact Position	Temperature (°C)	$\sqrt{\varepsilon k/D}$ Ratio Parameter (cm^{-1})	k, Trap Factor (sec^{-1})	Coefficient D/ε, cm^2/sec	
				Calculated from Eq. (24)	Reported by Haire and Zumwalt[11]
9	830	5.65	6.4×10^{-7}	2.0×10^{-8}	2.4×10^{-9}
29	912	3.35	4.6	4.1	4.0
13	932	4.31	5.2	2.8	3.5
22	970	2.95	4.1	4.7	3.4
18	1000	3.31	4.6	4.2	3.5

D/ε now represents a surface coefficient not subject to evaluation. This is the type of correlation indicated in Fig. 3.11, and the results of correlating all available spine data are summarized in Table 3.6. Notice the nearly constant values of β with respect to temperature. It would appear that the activation energies of the k and D/ε in β tend to cancel.

Table 3.6. Summary of All Results for Metallic Cesium Diffusion in Fuel Element Spines Assuming Steady Flow

Compact Position	Temperature (°C)	Concentration,[a] μmole/cm^3		$\beta = \sqrt{\varepsilon k/D}$ Ratio Parameter[b] (cm^{-1})
		$C'_T(a,t')$ ^{137}Cs	$C'_T(a,t)$ ^{134}Cs	
		300-EFPD Element		
5	682	0.32×10^{-3}	0.11×10^{-4}	3.0
30	840	0.86	0.18	4.0
25	868	3.3	1.3	4.5
15	913	12	6.2	4.5
		452-EFPD Element		
9	830	10	6.8	5.6
29	912	3.9	1.6	3.5
13	932	13	11	4.4
22	970	40	30	3.1
18	1000	58	44	3.4

[a]Does not include cesium held up at $r = a$.

[b]Estimated by fitting data to Eq. (21).

Sleeve data analysis was clouded by possible effects of the inward helium flow, which opposed the outward flow of cesium via diffusion. To evaluate this situation, a more general form of Eq. (24) for slab geometry was derived to include both internal trapping and back flow or a negative velocity, $(-v_o)$. The latter gave rise to an additional group called γ, where $\gamma^2 = tv_o^2/4D\varepsilon$. This new parameter was scattered about in the arguments of the exponential and complementary error functions, along with the familiar u and τ. Plots of the limiting case, zero k or τ, revealed that increases in γ gave the same behavior and curve shapes as when τ was increased in the right-hand side of Eq. (24), wherein $\gamma = 0$. Identical plots have been presented by Rodliffe.[7] At large times, the general semi-infinite equation approaches the limiting form

$$\frac{C_T'(x,t)}{C_t'(0,t)} = \exp[-2u(\gamma + \sqrt{\gamma^2 + \tau^2})] = \exp\left\{-x\left[\frac{v_o}{2D} + \left(\frac{v_o^2}{4D^2} + \frac{k\varepsilon}{D}\right)^{1/2}\right]\right\} \quad (26)$$

If velocity effects were present, the value of the terms within the braces would be equivalent to the slope of the curves for typical sleeve data. Such curves for normalized 452-EFPD cesium results appear in Fig. 3.12.

About all that can be extracted from these data is in the sum of ratios as in Eq. (26) (the slope). At least two more independent pieces of information would be required to separate or evaluate the three parameters D/ε, k, and v.

In an effort to rationalize away at least the velocity term, the limited strontium precursor data available for the sleeves were examined, because the krypton profiles are much more susceptible than adsorbed cesium to backflow. Based on the description[11] of spine and sleeve graphites, the uniform pressure coefficients for krypton in the sleeve should be lower than in the spine; even lower values should result when an effective backflow exists in the sleeve. But spine and sleeve gas coefficients had about the same values at comparable temperatures. It seemed reasonable therefore to drop the v_o terms, and proceed with only the trapping mechanism.

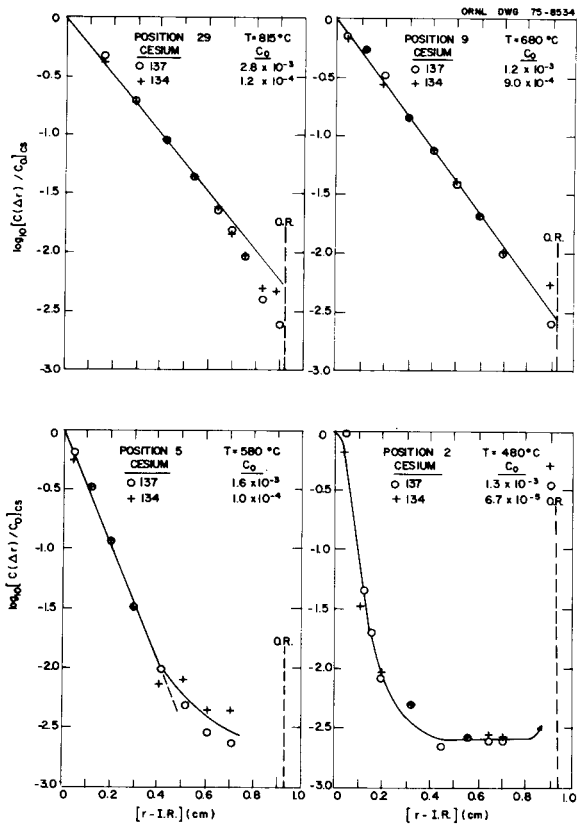

Fig. 3.12. Sleeve Concentration Profiles for Cesium Diffusion. Data pertain to the 452-EFPD fuel element.

The next facet explored related to whether or not the curves represented a transient situation or one at quasi-steady state. To examine this aspect, the slab equivalent of Eq. (24) was modified once again, this time for $C_T'(l,t) = 0$ rather than $C_T'(\infty,t) = 0$. For the first step, the profile equation for pore concentrations was derived by use of Laplace transforms along with the inversion integral. Use of Dankwert's method[13] seemed to produce a less compact solution. The result is

$$\left[\frac{C(x,t)}{C_o}\right]_p = 2\sum_{n=1}^{\infty} \frac{1 - \exp(-|S_n|t)}{|S_n|} \frac{n\pi D}{\varepsilon l^2} \sin\frac{n\pi x}{l} \quad , \tag{27}$$

where

$$S_n = k + n^2\pi^2 D/\varepsilon l^2 .$$

The solution comprises two series; the second series gives transient corrections to the first series, which converges to the steady-state solution

$$\left[\frac{C(x)}{C_o}\right]_p = \frac{\sinh[\beta(l - x)]}{\sinh[\beta l]} , \tag{28}$$

where

$\beta = \sqrt{k\varepsilon/D}$.

As before, the complete solution for $C_T'(x,t)$, including both mobile and immobile cesium, required additional operations, as described earlier. Since the results are too complex to present here conveniently, we merely note that the curves are the same as those for Eq. (24) up to regions near $x = l$, where they abruptly drop down to satisfy the zero concentration condition imposed. The initial slopes [log $C_T'(x,t)$ vs u] at high τ values are the same as those given by Eq. (24).

An approximation to $C_T'(x,t)$ can be obtained if it is assumed that Eq. (28) prevails during most of the diffusion period. When the time constant profile is converted according to Eq. (19), one obtains

$$\frac{C_T'(x,t)}{C_T'(0,t)} = \frac{\varepsilon(1 + kt)\ \sinh[\beta(l - x)]}{\varepsilon(1 + kt)\ \sinh\ (\beta l)} \approx e^{-x\sqrt{k\varepsilon/D}} , \tag{29}$$

which is the same sort of approach used ultimately for all spine data. The last approximation comes from having rather large β values. Thus, the right-hand side of Eq. (24) or Eq. (26) (with $k = 0$), along with the forms of $C_T'(x,t)$, indicates the same thing; that is, the initial slope of a semilog plot of C/C_o versus x is the main feature of the sleeve data. Table 3.7 summarizes these data.

To pursue things a bit further, we performed two cesium experiments in the laboratory using uncontaminated Peach Bottom fuel element sleeve graphite (HML-85). This gave us a fair estimate of the coefficient D/ε at 600 and 800°C but a questionable value for k (it was difficult to obtain an acceptable specimen size from this pipelike stock). On

Table 3.7. Summary of All Results of Metallic Cesium Diffusion in Fuel Element Sleeves Assuming Steady Flow

Compact Position	Temperature (°C)	$C_T'(0,t')$,[a] mole/cm^3		$\sqrt{\varepsilon k/D}$, Ratio Parameter[b] (cm^{-1})
		^{137}Cs	^{134}Cs	
		300-EFPD Element		
5	500	0.32×10^{-3}	1.1×10^{-5}	11.1[c]
15	650	4.2	26	5.7
25	710	2.9	13	6.7
30	720	0.41	0.87	6.5
		452-EFPD Element		
5	580	1.6	9.5	11.2[c]
9	680	12	90	6.3
29	815	2.8	12	5.6

[a]Does not include cesium held up at $x = 0$.

[b]Estimated by fitting data to Eq. (29).

[c]High value might be due to oxide interference.

the basis of the value of the coefficients reported by Haire and Zumwalt, as shown in the third column of Table 3.8, we weighted our results to give a reasonable temperature variation as shown in the fourth column of Table 3.8. We then used the $\sqrt{k\varepsilon/D}$ values obtained from the slopes of the curves in Fig. 3.11 along with the estimated D/ε values to obtain k values applicable to the reactor data. Utilization of Eq. (24) with the estimated D/ε and k values allowed computation of the transient curves shown on Fig. 3.13. A few points from the complete series solution are shown to demonstrate that the semi-infinite form, Eq. (24), is good enough to plot. The transient times in the right-hand column of Table 3.8 are taken as those required to reach steady state (at about $\tau = \sqrt{kt} = 4.0$).

All these estimates indicate that the system attained steady-state conditions very early; thus we can estimate $\Delta M/A$, the cumulative amount of cesium emitted at the back boundary per unit area, using Eq. (28) in the usual way:

$$\frac{\Delta M}{A} = \int_0^t -D\left(\frac{dC_p}{dx}\right)_l \, dt = \frac{(C_o)_p \beta D t}{\sinh(\beta l)} \quad . \tag{30}$$

Table 3.8. Cesium Diffusion Parameters Used to Estimate Transient Curves on Fig. 3.13 for the 452-EFPD Element

Compact Position	Temperature (°C)	D/ε, coefficient, cm^2/sec		Ratio Parameter $\sqrt{k\varepsilon/D}$ (cm^{-1})	Trap Factor k (sec^{-1})	Time[c] Up to $\tau = 4.0$ (hr)
		Reported[a]	Estimated[b]			
5	580	0.600×10^{-9}	2.18×10^{-7}	11.2	2.75×10^{-5}	162
9	680	1.40	5.07	6.33	2.03	219
29	815	1.69	5.80	5.64	1.85	240

[a]Haire and Zumwalt.[11]

[b]Based on temperature variation of the reported coefficients and ORNL diffusion experiments.

[c]Approximate time to reach steady-state diffusion.

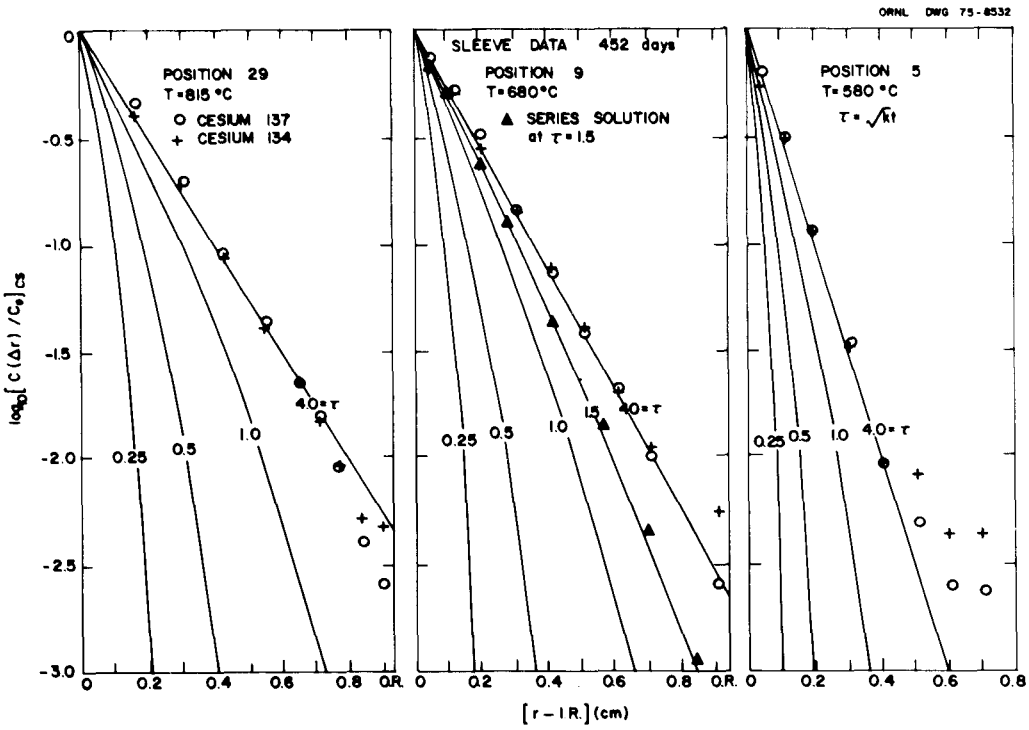

Fig. 3.13. Computed Curves Illustrating the Approach to Steady State for Cesium in the 452-EFPD Sleeve.

But $(C_o)_p \approx C_T'(0,t)/(\varepsilon kt)$; thus,

$$\frac{\Delta M}{A} \approx 2C_T'(0,t)\ e^{-\beta l}/\beta\ , \tag{31}$$

where $C_T'(0,t)$ and β are the surface concentrations and ratio parameters, which are given in Table 3.7. For example, at position 29, the cumulative ^{137}Cs evolution rate at $x = l = 0.931$ cm to the coolant was (2) $(2.8 \times 10^{-3})/(5.6)\ (183.8) = 5.44 \times 10^{-6}$ μmole/cm^2. The input at $x = 0$ turns out to be (1/2) $[\exp(\beta l)]$ times this amount (i.e., 5×10^{-4} μmole/cm^2). Therefore, about 1% of the input ^{137}Cs escaped; 99% was held up in the sleeve. This means that the sleeves serve as an effective cesium filter until either the microscopic traps fill up, or the breakover point for the Langmuir-Freundlich transition is attained at much higher loadings.

The same sort of operation as indicated previously can be applied to Eq. (21) for the spine cesium data. The amount of metallic cesium taken up by the spines is:

$$\frac{\Delta M}{A} = \frac{C_T'(a,t)}{\beta} \cdot \frac{I_1(\beta,a)}{I_0(\beta,a)} \approx (0.94)\ C_T'(a,t)/\beta\ . \tag{32}$$

Based on results in Table 3.6, the amounts of ^{137}Cs taken up at positions 9 and 29 are 1.68×10^{-3} and 1.05×10^{-3} μmole/cm^2, respectively. Comparisons of these figures with the original results in Fig. 3.9 reveal that very nearly the same amount is held up at the $r = a$ surfaces. Only 60% of the cesium in or on the spine engages in the diffusion process. This percentage value is much lower for the sleeves.

In an effort to check out the validity of the relationship $(C_a)_p \approx C_T'(a,t)/\varepsilon kt$ and, indirectly, the constant surface potential assumption used for the profile equations, plots of the diffusive C_a — that is, $[C_T'(a,t)]$ — values for cesium were prepared for both the 452- and 300-EFPD spine data; these are displayed in Fig. 3.14. We anticipated that the ratio of the concentration for the two sets of data would be about 452/300. The results in Fig. 3.14 suggest a ratio of unity, which seems

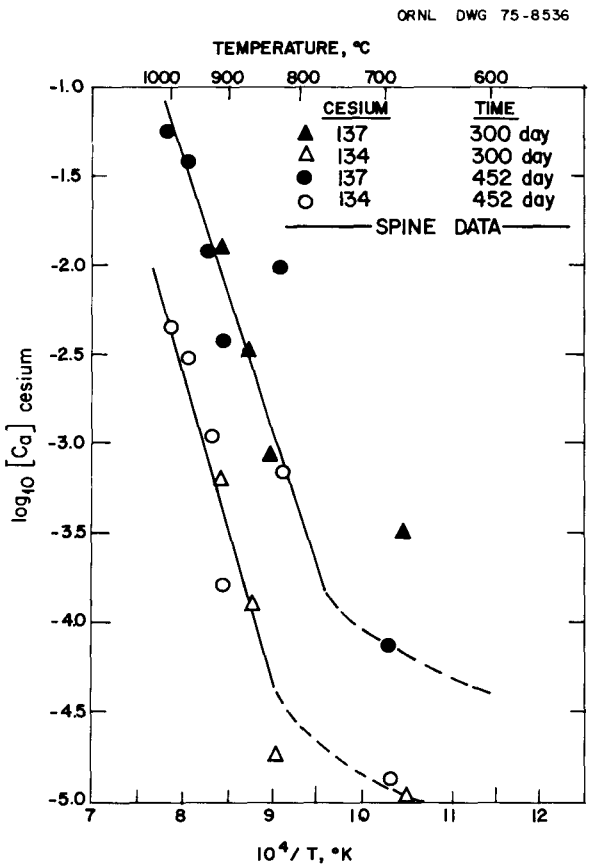

Fig. 3.14. Comparison of the Extrapolated Cesium Concentrations on Spine Surfaces from the 300- and 452-EFPD Fuel Elements. Dotted portion represents precursor-metallic state transition region.

to indicate that it will be difficult to investigate the time dependence of diffusion parameters using results from two different fuel elements at two different core positions. While these results were somewhat disappointing, we concluded that the constant-potential assumption is as good as any, particularly in the absence of detailed fuel release rate data as it applies to particular elements and positions. Perhaps effective full-power days is not indicative of effective diffusion days.

Finally, a very important feature of the long-term fuel element results as they pertain to the short-term laboratory results should be mentioned. None of the high-temperature long-term data give evidence of a back pressure for a slow relaxation of the trapped fraction via a solid-state diffusion mechanism. All that is required to correlate the profiles for metallic diffusion in the Core I results is a single

parameter β. Values of D/ε were not required, except to make some estimates regarding the length of transient times. It appears that the "need" for laboratory D/ε values for cesium transport calculations reduces to the same level as the "need" for elaborate computer codes to perform such calculations.

3.4 RADIONUCLIDE DISTRIBUTIONS IN AN HTGR — E. L. Compere, M. F. Osborne, and H. J. de Nordwall

Because the distribution and release of radiologically significant fission products are influenced by several diverse mechanisms, it is desirable to develop a scheme by which the significance of these individual mechanisms to determining radionuclide release may be ordered. Thus, the purpose of this investigation has been to identify release pathways for two selected radionuclides, tritium and iodine, to define those parameters that govern release by a given pathway, and to assess the extent to which these parameters have been determined.

3.4.1 Analysis of Tritium Distribution and Release

A report of studies of the distribution and release of tritium in an HTGR was issued.[14] An abstract of this report follows:

> Tritium will be produced in high-temperature gas-cooled reactors not only by fission, but also to a significant extent by reactions of neutrons with boron in burnable poison and control rods, with trace lithium impurity, and with ^{3}He occurring naturally in the helium coolant flowing through the core. A portion of the tritium that is formed in solids or fuel may be released to the coolant. This tritium mingles with the hydrogen in the coolant and will, in part, chemisorb on graphite. In addition, it may leak with the coolant from the reactor vessel, be removed in the helium purification system, or permeate system walls into the steam generator, where as a result of removal (blowdown) or losses it is subject to release to the environment.

The differential equations describing the above behavior are developed. Assumption of steady conditions, including hydrogen concentration, for a period makes it possible to express the distribution as well as the production in the form of coupled sets of linear first-order ordinary differential equations. A generalized analytical solution of these is presented.

The above tritium generation and distribution model has been incorporated in a computer code, TRITGO. An illustrative calculation using parameters taken from the PSAR description of the Fort St. Vrain Reactor has been made. This indicates that most of the tritium emerging from the primary coolant will have been generated by the $^{3}He(n,p)T$ reaction. A significant fraction enters the steam generator. The tritium in the steam generator blowdown, after proper dilution, may be considered for release to the environment. The effects of varying a number of system parameters are considered.

3.4.2 Iodine Behavior in an HTGR

Studies of the behavior of iodine in an HTGR have resulted in the preparation of two reports. One of these[15] is concerned primarily with identifying iodine release pathways and the mechanisms that govern release along these pathways; an abstract of this report follows:

The emission of iodine from nuclear power reactors as a result of normal operations or postulated accidents is regulated by requiring exclusion area boundaries such that the dose to any individual outside the area will be less than stipulated values. Application of the "as low as practicable" limit, proposed for light-water-cooled nuclear power reactor effluents, to the activity released from a typical reactor installation (here an HTGR), indicates that the release of ^{131}I should be as much below

13 mCi/year as is practicable using today's technology. Estimated values of primary coolant leak rate, and of the decontamination factor during passage through PCRV cracks and secondary containment, lead to a derived limit on the amount of iodine in the primary coolant gas. A consideration of the rates of removal from the primary coolant by purification and by deposition (plateout) on system surfaces, and of entry rates from failed coated particle fuel, indicates that some surface deposition is desirable. The metal surfaces of the system are expected to be oxidized. Permanent adsorption on Fe_3O_4 may be insufficient to sustain the needed deposition for the lifetime of the reactor, according to the experimental data presented. However, if iodine atoms exchange rapidly between gas and surface phases, the surface requirement is smaller and appears to be met. Formation and decomposition of volatile metal iodides around the circuit are possible, but concentrations may be too low for direction deposition to occur. In the case of postulated accidents, the iodine that is retained as deposits on primary system surfaces represents a major source of released iodine. It does not appear likely that regulatory limits would be exceeded by any accidents, provided prompt isolation of the secondary containment occurs. Even in the lack of such isolation, complete depressurization in the absence of an appreciable temperature rise in the steam generators should not cause doses at the exclusion area boundary due to release of surface sorbed iodine to exceed limits stated in the Code of Federal Regulations, Title 10, Part 100.

The second report is more directly concerned with iodine sorption and desorption characteristics. An abstract of this report[16] follows:

Safety studies of the HTGR system indicate that radioactive iodine, released from the fuel to the helium coolant, may represent a significant biological hazard. Since information on iodine behavior in this system was incomplete, experimental studies of iodine adsorption on HTGR materials were conducted in vacuum as functions of iodine pressure and adsorber temperature. Iodine coverages on Fe_3O_4 and Cr_2O_3 approached maxima of about 2×10^{14} and 1×10^{14} atoms/cm^2, respectively, whereas the iodine coverage on graphite under similar conditions was found to be less by a factor of about 100. Limited investigations of iodine desorption from the same materials into vacuum or flowing helium were conducted as functions of iodine coverage, adsorber temperature, and pure vs wet helium. The rate of vacuum desorption from Fe_3O_4 was related to the spectrum of energies of the adsorption sites. A small amount of water vapor in the helium enhanced desorption from iron powder, but appeared to have less effect on desorption from the metal oxides.

3.5 FISSION PRODUCT SURVEILLANCE IN THE PEACH BOTTOM HTGR — R. P. Wichner, F. F. Dyer, W. J. Martin, L. L. Fairchild, and R. J. Kedl

The primary objective of the Peach Bottom HTGR fission product surveillance program is to provide data to validate existing computational programs that model fission product behavior in the HTGR, or for use as a guide in modifying these codes.

The major part of the surveillance program involves the postirradiation examination (PIE) of six driver fuel elements of Core 2. Four of these elements are end-of-life elements, which had been subjected to 900 equivalent full-power days (EFPD) of service; the remaining two were withdrawn following 384 and 701 EFPD.

A second aspect of the surveillance program more directly concerns fission product behavior within the primary coolant circuit itself;

gamma radiation spectroscopy has been performed on selected parts of the Loop 1 curcuit at approximately yearly intervals since May 1971. In addition, samples of helium coolant have been taken upstream and downstream of the steam generator in Loop 1, and dust samples have been acquired from the collector beneath the cyclone separator in the primary circuit. In each case, sampling has been done more or less periodically, so that changes in fission product concentration with time could be monitored.

3.5.1 Fuel Element Examinations

A Peach Bottom driver fuel element outline and assembly are depicted in Fig. 3.15. Helium coolant flows upward (from right to left) outside the sleeve; however, a small flow from the exit plenum is diverted downward through the element. This so-called purge flow enters through an axial hole in the upper reflector, passes through the porous graphite plug, and then down the element primarily between the annular fuel compacts and the spine. Some of the purge flow passes through the outer gap between the fuel compact and the inner surface of the sleeve. Below the bottom compact and the lower reflector is positioned an internal trap assembly consisting of a graphite cylinder containing a number of axial grooves packed with about 300 cm^3 of charcoal. The purge flow passes through the charcoal trap and out the bottom of the element to the purification system.

Unlike the example in Fig. 3.15, element E06-01 is one of several instrumented fuel elements. Two 2.16- by 2.36-mm (0.085 by 0.093-in.) grooves are cut axially in the spine at the outer diameter and contain a Chromel vs Alumel and a tungsten-rhenium thermocouple. The junctions are located 1.52 m (60 in.) from the bottom of the fuel compact stack.

A Peach Bottom fuel compact is shown in Fig. 3.16. Thirty such compacts are stacked in a fuel element, yielding an active core height of 2.29 m (90 in.). (For identification, the compacts are numbered from bottom to top of the fuel element.) The fuel particles are Biso-coated thorium-uranium carbide, predominantly with a Th/U ratio of 5.5. There are also 102 thorium elements containing somewhat larger Biso particles with a higher Th/U ratio, 18.5.

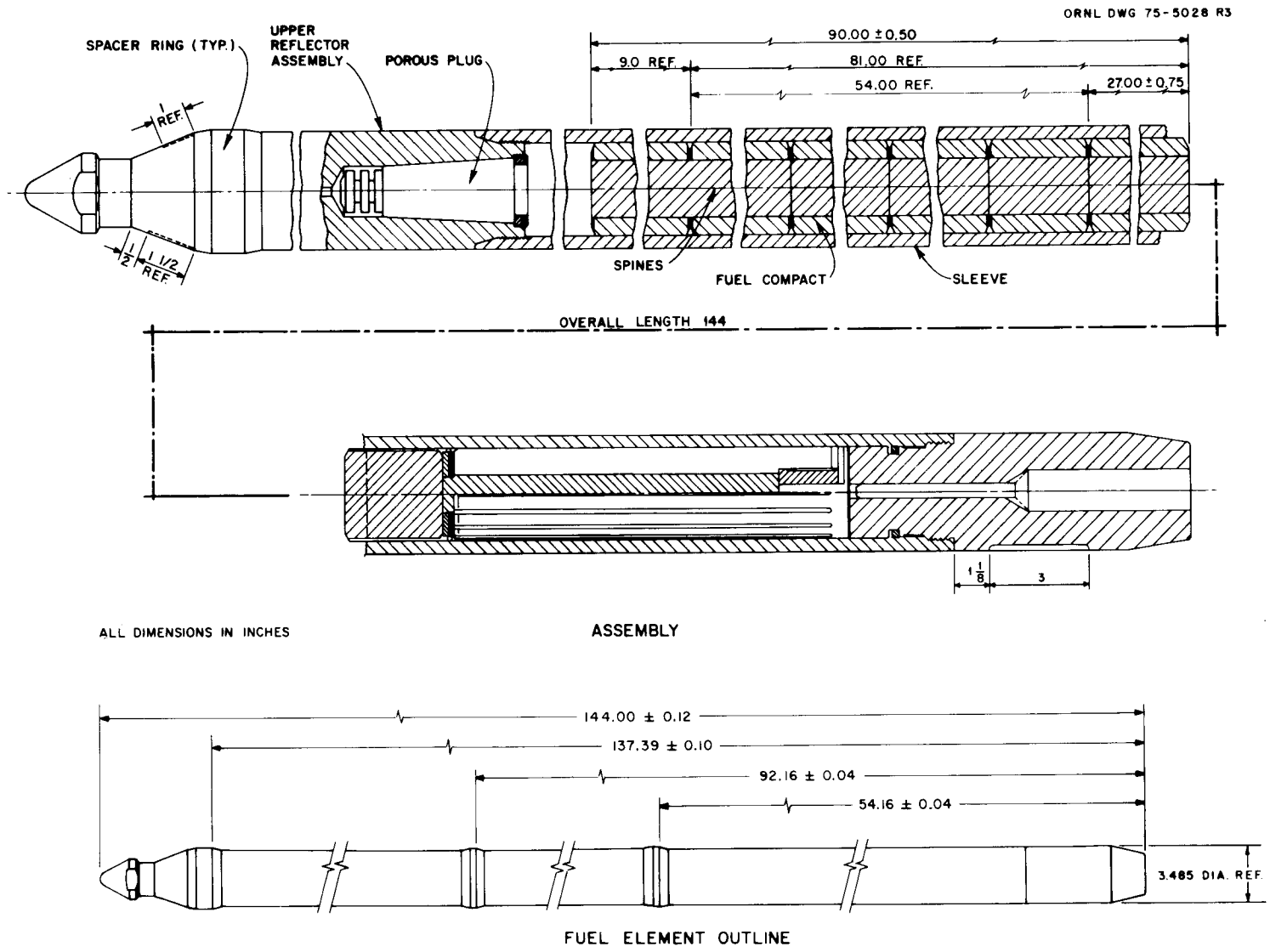

Fig. 3.15. Typical Peach Bottom Core 2 Driver Fuel Element. Some elements contain thermocouples.

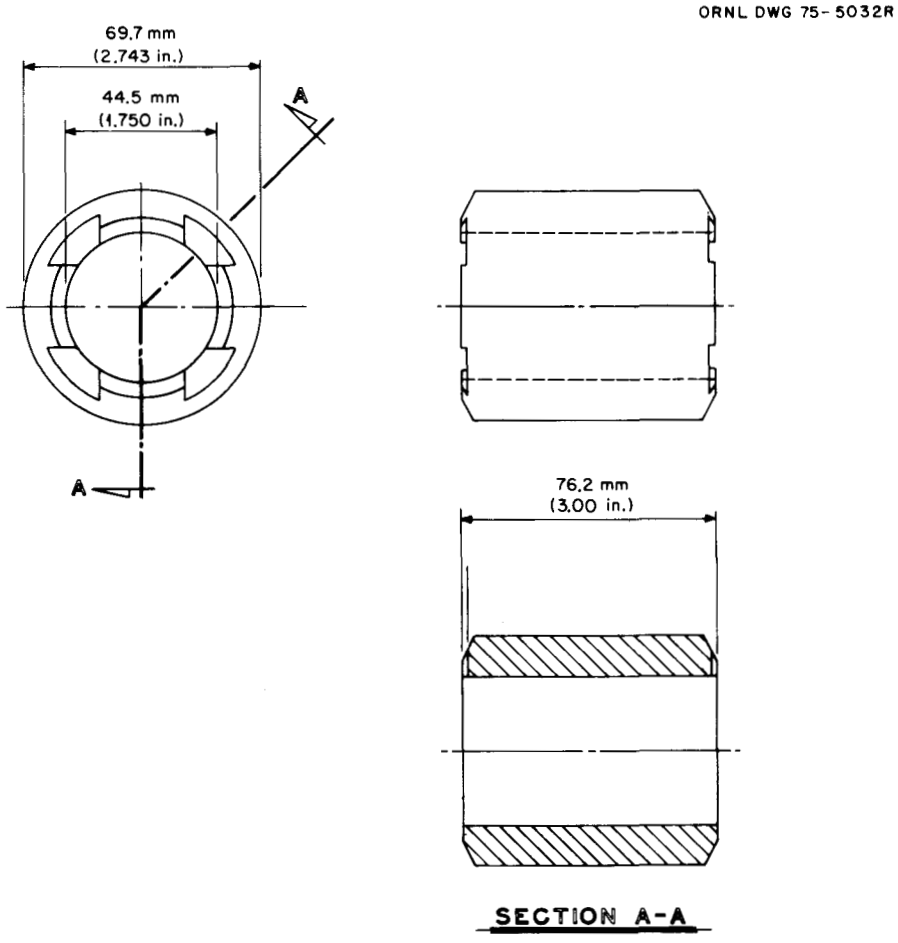

Fig. 3.16. Peach Bottom Core 2 Fuel Compact.

3.5.1.1 Postirradiation Examination Procedures

Five groups of activities constitute the postirradiation examination of a given fuel element. These are enumerated below.

1. Disassembly and Metrology — Girth cuts are made to remove the top and bottom reflector regions. The sleeve is cut into three pieces, and the element is disassembled. Photographs are taken of the compacts, spine pieces, and outside sleeve. The following critical dimensions are measured: inside and outside diameters of about seven selected fuel compacts, the length of each compact, the length and diameter of the spine pieces, and the inside and outside diameters of the sleeve at selected locations.

2. Axial gamma-scanning — About four gamma spectra are acquired for each of the 30 fuel compacts to yield gamma-emitting radionuclide

inventories. The sleeve and spine pieces are axially scanned to obtain axial distribution of gamma emitters in these components. Axial scans are also acquired in the internal trap region and along the purge flow inlet duct.

3. Radial profiles — Radial sections of sleeve and spine are obtained, by use of a lathe in a hot-cell, opposite compact locations 9, 18, and 29. The samples are gamma counted to obtain fission product concentrations as a function of radial location. When warranted, radial profiles of gamma-emitting fission products are also obtained for the sleeve and spine opposite compact 2, and in the bottom and top reflector regions.

4. Chemical analyses — Samples from four compacts are deconsolidated and analyzed for heavy metal by isotope-dilution mass spectrometry and colorometrically for a fission product monitor, zirconium, to determine fuel burnup. Additionally, ^{3}H, ^{14}C, and ^{90}Sr are determined by chemical separation and beta counting. Stable Ba and Te and ^{129}I are determined by neutron activation. Graphite samples acquired for the radial profiles are also analyzed for ^{3}H, ^{14}C, ^{90}Sr, Ba, and Te.

5. Metallography and Failed Particle Fractions — Metallographic examination is made on four fuel compacts. The failed particle fraction is estimated roughly by observing the coating integrity of from 100 to 200 particles.

3.5.1.2 Results for Driver Fuel Element E06-01

3.5.1.2.1 Operating Conditions and Element Type. Element E06-01, which was located in the sixth ring from the center of the core and the first row of Section E, was removed after 385 EFPD of operation. It is one of the 546 "light rhodium" elements (of the total number of 804) in which each of the central compacts contains 0.34 g Rh burnable poison. End-of-life fluence and temperature conditions are shown in Fig. 3.17.

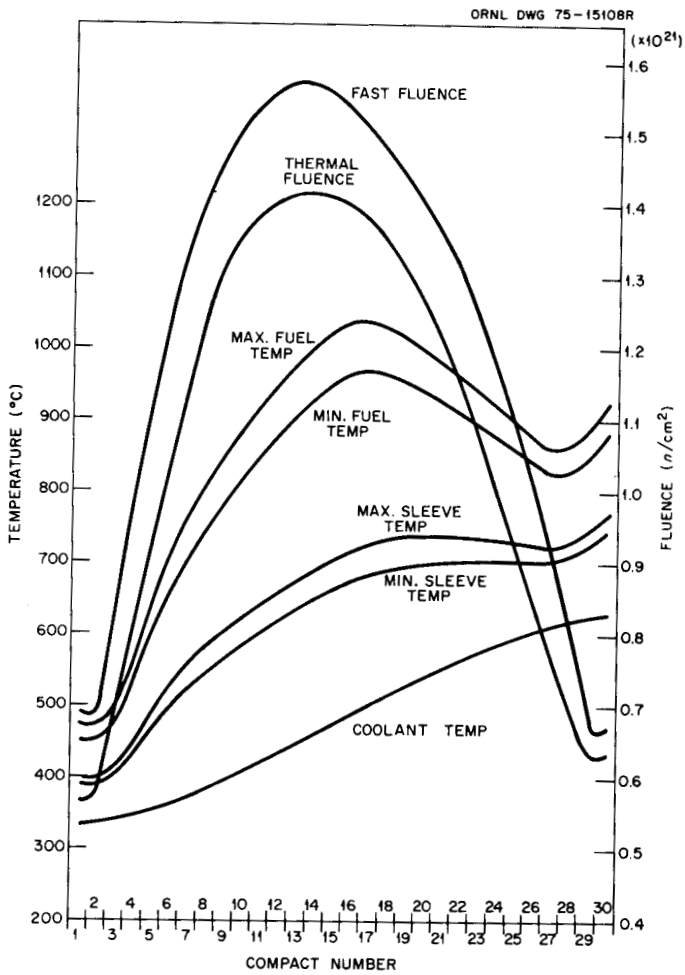

Fig. 3.17. Computed Axial Temperature and Fluence Profiles for Element E06-01 at End of Life.

3.5.1.2.2 Radionuclide Inventories in the Fuel Compacts. Inventories of radionuclides observed in the E06-01 fuel compacts are shown in Table 3.9 in terms of curies per compact, corrected for decay to the date of removal from the core. The total nuclide inventories for the fuel element are listed in the bottom row. Comparisons between observed radionuclide levels and levels calculated[17] with the ORIGEN code are listed in Table 3.10. (An average deviation of 13% between calculated and observed inventories is considered reasonable at this time.)

Table 3.9. Inventories of Gamma Emitters in E06-01 Fuel Compacts[a] as of January 6, 1972

Compact	Activity, Ci/Compact							
	^{95}Zr	^{103}Ru	^{106}Ru	^{125}Sb	^{134}Cs	^{137}Cs	^{144}Ce	^{154}Eu
1	130.49		5.89	0.22	1.61	4.49	72.47	0.03
2	128.44	59.30	5.43	0.20	1.75	4.27	74.53	0.04
3	126.38		5.14	0.32	2.04	4.15	73.12	0.04
4	152.75		6.07	0.27	2.75	5.11	85.66	0.05
5	173.30	80.90	6.71	0.27	3.47	5.77	95.45	0.07
6	198.31	88.70	7.96	0.27	4.36	6.50	107.51	0.08
7	197.28		7.66	0.27	4.48	6.38	97.10	0.09
8	201.73		8.16	0.33	4.76	6.61	115.01	0.10
9	248.31		10.25	0.42	6.06	8.00	139.81	0.17
10	224.00		9.82	0.41	5.62	7.35	126.31	0.11
11	228.10		9.31	0.38	5.88	7.43	126.55	0.14
12	122.27		4.87	0.38	3.26	4.01	65.25	0.07
13	252.76		9.48	0.38	6.54	8.10	143.03	0.13
14	243.52		9.84	0.41	6.33	7.84	136.76	0.14
15	218.51		8.96	0.37	5.70	7.11	119.70	0.15
16	227.76	95.10	8.80	0.39	5.85	7.22	128.71	0.15
17	214.75		8.34	0.34	5.61	6.95	119.36	0.14
18	223.31	88.30	9.15	0.34	5.78	7.18	126.76	0.14
19	214.06	106.00	9.00	0.38	5.58	7.04	114.29	0.11
20	230.50	110.00	9.19	0.34	5.82	7.42	127.34	0.12
21	207.55	86.20	8.52	0.35	5.36	6.92	118.06	0.12
22	203.10		8.52	0.30	5.09	6.77	114.91	0.09
23	206.87	101.00	8.58	0.31	5.10	7.07	117.79	0.12
24	184.95		7.54	0.31	4.36	6.34	105.08	0.10
25	174.67		6.75	0.27	3.92	5.86	101.41	0.09
26	167.14		7.04	0.25	3.39	5.55	90.76	0.07
27	158.58		6.65	0.24	3.03	5.39	92.89	0.09
28	140.08	71.80	6.11	0.24	2.39	4.77	82.61	0.09
29	112.68		4.51	0.22	1.70	3.83	62.03	0.04
30	132.20		5.60	0.21	1.63	4.53	79.19	0.04
SUM	5644.30	2661.00[b]	229.85	9.39	129.22	185.96	3159.40	2.92

[a]Results obtained by gamma scanning.

[b]Normalized to 30 compacts.

Table 3.10. Comparison of Computed and Measured Fission Product Inventories in E06-01 Fuel

Radionuclide	Activity, Ci		Difference[c] (%)
	Calculated[a]	Measured[b]	
^{85}Kr	264	N	
^{89}Sr	429	N	
^{90}Sr	166	N	
^{95}Zr	5180	5640	−8.2
^{103}Ru	2660	2661	−0.04
^{106}Ru	196	230	−15
^{110m}Ag	0.224	N	
^{111}Ag	24.7	N	
^{125}Sb	6.4	9.4	−32
^{127m}Te	29.9	N	
^{129}Te	1110	N	
^{129}I	5.0×10^{-5}	N	
^{131}I	3340	N	
^{134}Cs	161	129	25
^{137}Cs	168	186	−9.7
^{140}Ba	6950	N	
^{141}Ce	3180	3160	0.6
^{152}Eu	0.019	N	
^{154}Eu	3.3	2.9	14
^{155}Eu	3.94	N	

[a]Calculated by Tobias.[17]

[b]Taken from Table 3.9. N denotes that no attempt was made to measure the nuclide or its gamma rays were not detected.

[c]100(calculated activity/measured activity − 1).

3.5.1.2.3 Axial Distributions of Radionuclides. Axial distributions of observed gamma emitters in the sleeve of element E06-01, expressed as curies in the 76-mm (3-in.) section opposite the stated compact number, are listed in Table 3.11. Also listed are the ^{3}H and ^{90}Sr inventories for the indicated seven compact locations. The total inventory in the sleeve and the spine of each observed gamma emitter is shown in the last row of the table.

Table 3.11. Axial Distribution of Gamma Emitters in E06-01 Sleeve[a] — January 6, 1972

Compact[b]	Activity, μCi/Sleeve Section										
	^{46}Sc	^{60}Co	^{95}Zr	^{106}Ru	^{110}Ag	^{134}Cs	^{137}Cs	^{144}Ce	^{154}Eu	^{3}H	^{90}Sr
1	1.16	0.16	6.40	0.37	0.00	0.12	0.32	6.84	0.10	2.020	0.065
2	0.99	0.19	6.40	0.40	0.00	0.15	0.34	5.88	0.10	2.360	0.047
3	1.36	0.21	6.10	0.40	0.00	0.16	0.36	4.73	0.10	3.380	0.067
4	1.53	0.24	8.50	0.50	0.00	0.24	0.48	8.88	0.13	5.410	0.325
5	1.74	0.26	10.70	0.67	0.21	0.44	0.82	9.36	0.15	8.400	0.222
6	1.77	0.28	7.00	0.55	0.00	0.44	0.76	6.80	0.14	3.840	1.040
7	1.77	0.32	9.30	0.58	2.24	0.60	0.90	9.56	0.16	2.030	2.040
8	2.00	0.36	7.90		0.65	0.81	1.11	9.90	0.14	1.920	0.326
9	2.07	0.37	7.50		4.15	0.94	1.20	9.87	0.13		
10	2.11	0.41	9.80		5.24	1.08	1.37	10.41	0.15		
11	2.24	0.39	8.60		3.06	1.37	1.67	10.75	0.17		
12	2.18	0.41	9.00	0.70	2.45	1.26	1.54	12.76	0.16		
13	2.04	0.37	8.90		4.05	1.15	1.50	8.33	0.16		
14	2.14	0.40	10.60	0.86	3.47	1.09	1.42	11.50	0.15		
15	2.24	0.37	8.60	0.73	2.65	1.07	1.31	10.20	0.14		
16	2.00	0.37	9.20	0.00	3.33	1.10	1.37	8.30	0.17		
17	2.00	0.42	12.40	1.28	2.86	1.61	2.03	11.10	0.19		
18	1.97	0.42	10.20	1.24	2.96	1.10	1.33	10.20	0.19		
19	1.84	0.41	8.70	0.68	2.11	0.90	1.19	9.70	0.15		
20	2.62	0.53	7.30		2.42	1.33	1.84	10.20	0.18		
21	2.76	0.52	4.80		2.14	1.00	1.42	10.20	0.21		
22	7.52	0.48	9.40		2.31	1.05	1.49	11.90	0.20		
23	1.77	0.40	10.00		1.84	0.95	1.48	11.70	0.19		
24	1.63	0.31	11.00		1.97	0.87	1.43	10.20	0.11		
25	1.22	0.29	7.00		1.60	0.67	1.22	8.50	0.10		
26	3.50	0.33	8.00		1.22	0.54	1.00	6.80	0.14		
27	1.33	0.29	8.00		0.99	0.49	1.01	4.60	0.07		
28	1.43	0.27	7.00		0.71	0.41	0.93	3.40	0.07		
29	1.36	0.28	45.00	1.46	0.00	0.96	1.59	104.00	0.07		
30	1.36	0.18	0.00		0.00	0.18	0.36	0.00	0.07		
SUM	61.65	10.19	283.30	10.42	54.63	24.06	34.78	356.57	4.20		

[a]Results determined by gamma scanning as μCi/g were normalized to curies per 76 mm (3 in.) of sleeve with a measured value of 4.465 kg/m (113.4 g/in.) of sleeve.

[b]Compact number adjacent to measured sleeve section.

3.5.1.2.4 Radial Distributions in the Sleeve and Spine. Radial distributions of four observed gamma-emitting radionuclides in the sleeve graphite are given in Table 3.12 for compact locations 7, 16, and 26. Additionally, ^{3}H and ^{90}Sr concentrations, as obtained by chemical

Table 3.12. Radial Distribution of Radionuclides in E06-01 Sleeve at Three Locations on January 6, 1972

Distance From Center of Element (mm)	Thickness of Cut Milled from Sleeve (mm)	Activity, μCi/g					
		^{60}Co	^{134}Cs	^{137}Cs	^{154}Eu	^{3}H	^{90}Sr
		At Compact 7					
43.91	0.64	1.990	0.064	0.057	0.613	10.800	0.182
43.28	0.64	0.759	0.014	0.020	0.614	8.320	0.067
42.45	1.02	0.762	0.016	0.019	0.569	6.440	0.071
41.44	1.02	0.859	0.020	0.030	0.582	6.720	0.127
40.42	1.02	0.902	0.049	0.055	0.523	6.840	0.066
39.40	1.02	0.886	0.112	0.131	0.531	6.680	0.112
38.39	1.02	0.816	0.280	0.309	0.531	5.040	0.058
37.37	1.02	0.739	0.652	0.745	0.496	10.500	0.087
36.36	1.02	0.767	1.730	2.690	0.443	28.700	0.216
35.39	0.92	2.710	13.590	16.720	0.372	45.600	3.030
		At Compact 16					
43.94	0.64	2.240	0.068	0.109	0.713	28.500	0.153
43.30	0.64	0.977	0.069	0.068	0.691	25.000	0.131
42.48	1.02	0.903	0.121	0.108	0.652	19.500	0.130
41.46	1.02	1.050	0.193	0.189	0.619	17.200	0.072
40.45	1.02	1.140	0.360	0.341	0.603	15.500	0.093
39.43	1.02	1.190	0.726	0.713	0.604	16.900	0.136
38.42	1.02	1.080	1.570	1.650	0.584	15.700	0.068
37.40	1.02	1.010	3.390	3.700	0.544	10.300	0.077
35.91	1.96	2.420	15.900	19.960	0.619	11.300	12.200
		At Compact 26					
43.92	0.64	1.570	0.025	0.034	0.596	9.480	0.028
43.29	0.64	0.786	0.039	0.055	0.577	7.720	0.035
42.46	1.02	0.777	0.076	0.096	0.541	5.710	0.057
41.45	1.02	0.882	0.118	0.160	0.531	5.650	0.052
40.43	1.02	0.958	0.184	0.255	0.531	4.160	0.053
39.42	1.02	1.020	0.317	0.429	0.508	3.520	0.038
38.40	1.02	0.939	0.526	0.739	0.499	3.890	0.060
37.38	1.02	0.824	0.800	1.160	0.495	4.310	0.059
36.37	1.02	0.875	0.831	1.190	0.490	4.410	0.145
35.40	0.92	1.510	11.210	18.550	0.421	6.020	13.000

separation and beta counting, are likewise listed as a function of radial distance. Note that the cesium nuclide data, as well as the data for ^{90}Sr, clearly indicate a source at the inner radius and diffusion outward. The ^{60}Co and ^{3}H data, however, show a more complex behavior. For compact location 7, which is the coolest of the three axial locations, the predominant source of tritium in the sleeve appears to be situated at the inner surface. However, there appears to be some external source, as evidenced by the concentration elevation at

the outer surface. The situation is quite different for compact location 16, where the tritium gradient is decreasing inward instead, evidently signifying a tritium source external to the fuel element and subsequent diffusion inward.

Figure 3.18 illustrates the radial distribution of ^{134}Cs and ^{137}Cs in the sleeve of element E06-01. Most striking is the close similarity in the shape of the radial distribution for each of the cesium radionuclides at the corresponding axial locations. This close similarity indicates that each radionuclide was distributed by the identical transport mechanism, despite the fact that ^{134}Cs passes through a 5-day half-life ^{133}Xe, whereas the half-life of the xenon precursor to ^{134}Cs is only 4 min. In other words, transport of the noble gas precursor does not appear to play a significant role in cesium transport.

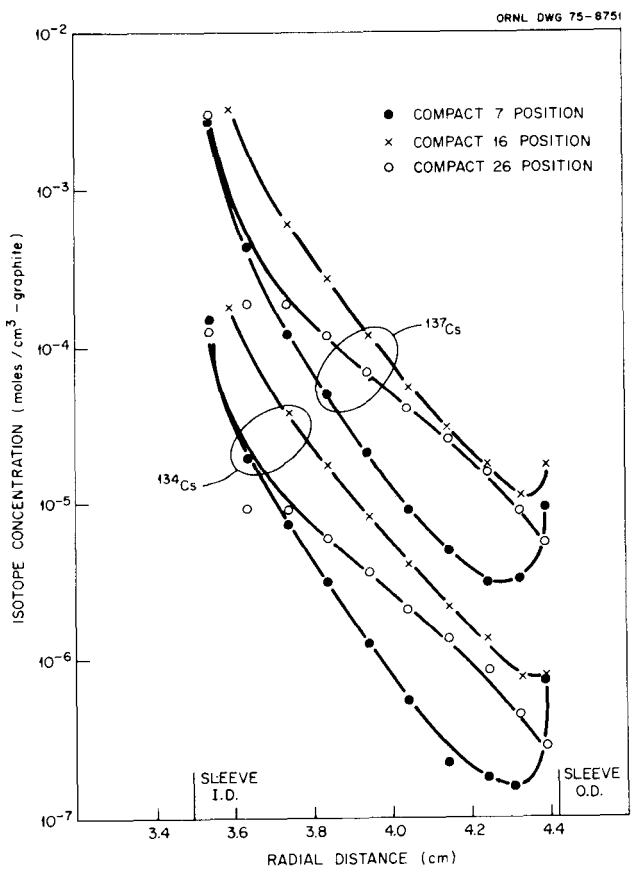

Fig. 3.18. Radial Cesium Distributions in Element E06-01 Sleeve.

This aspect was pursued further in the following manner: From the reported noble gas release-to-birth rate ratio (R/B) values for the Peach Bottom HTGR, the current of xenon leaving the sleeve outer surface can be computed. If estimated values of the mass transfer coefficient and free stream concentration of xenon are then used, one can thereby compute the outer surface concentration of xenon in the sleeve. The diffusion equation with these two boundary conditions (concentration and current on the outer sleeve surface) may then be solved for the sleeve, yielding xenon concentration profiles for assumed values of the effective xenon diffusion coefficient. The total xenon inventory and thus the total cesium inventory, which results from subsequent decay, may then be readily calculated by assuming that cesium does not diffuse out of the sleeve once it is born. (In the case of ^{134}Cs, an additional calculation is necessary since it comes from neutron capture by ^{133}Cs.)

Since the available R/B values refer to the whole core, and not particularly to element E06-01, and since xenon diffusion coefficients for sleeve graphite are not well known, estimates of this type must be regarded as approximate. That is, in the final comparison, factors of 2 or 3 must be considered negligible, so that only orders of magnitude are considered to be significant. The results of the calculations are shown in Table 3.13.

Table 3.13. Calculation of Cesium Inventories in E06-01 Sleeve Assuming Only Xenon Diffusion

	^{134}Cs	^{137}Cs
Activity in 76 mm (3 in.) of sleeve, Ci		
Measured	8.0×10^{-4}	1.2×10^{-3}
Calculated for the following values of the Xe diffusion coefficient		
1.0×10^{-4} cm^2/sec	3×10^{-9}	5×10^{-7}
2.0×10^{-5} cm^2/sec		3×10^{-4}
1.0×10^{-5} cm^2/sec	2×10^{-8}	3×10^{-2}

The ^{134}Cs results are the most definitive, since the calculated inventory does not markedly depend upon the xenon diffusivity. Note that the computed inventory of ^{134}Cs in the sleeve, assumed to originate from ^{133}Xe, is five to six orders of magnitude less than the measured inventory. This indicates rather strongly that most of the observed ^{134}Cs entered the sleeve as ^{134}Cs and ^{133}Cs.

The results for ^{137}Cs are somewhat ambiguous because of the short half-life of the ^{137}Xe precursor (3.9 min). Three values of ^{137}Cs inventory are shown, which correspond to different assumed values of the xenon diffusion coefficient over the range 10^{-4} to 10^{-5} cm^2/sec. As is obvious in the tabulation, as the diffusion coefficient changes by one order of magnitude, the computed inventory of ^{137}Cs changes by five orders of magnitude, so that the calculated results encompass the measured value. This ambiguity, however, is mitigated by the observation that the holdup time of xenon in the sleeve must be relatively short, since reported[18] R/B values obtained by sampling the purge flow and the coolant flow maintained the same ratio for half-lives ranging from 5.2 days to 3.2 min. For this to be the case, calculations show that xenon diffusion coefficients in the Peach Bottom sleeve must be approximately 1.0×10^{-4} cm^2/sec or slightly higher. Therefore, referring to Table 3.13, calculated activity levels in the sleeve for ^{137}Cs assumed to be transported by xenon diffusion are again substantially less than observed levels. Hence, we conclude that xenon transport is not significant for either ^{134}Cs or ^{137}Cs.

We can now estimate effective diffusion coefficients for cesium from the radial concentration profiles with confidence that migration of the xenon precursor and subsequent decay will not cloud the results. From the radial profiles of ^{134}Cs and ^{137}Cs in the element E06-01 sleeve, which are shown in Fig. 3.18, effective diffusion coefficients were estimated with the assistance of FIPER-Q by parametrically varying the diffusion coefficient until a best fit was obtained between the computed and observed concentration profiles. Results of these calculations are shown in Fig. 3.19 for compact locations 7, 16, and 26. The horizontal scale indicates the range of temperatures that existed in the sleeve at end-of-life (EOL) conditions.

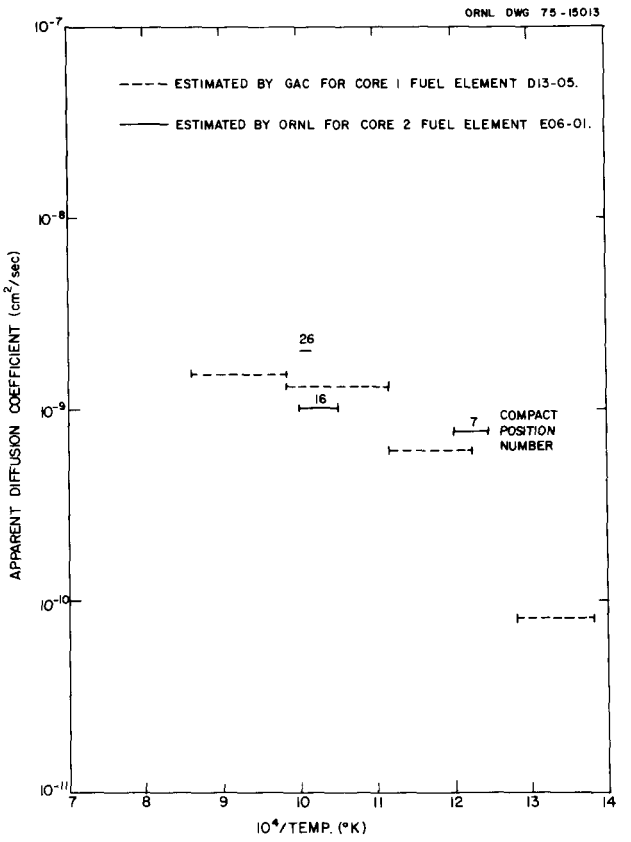

Fig. 3.19. Effective Cesium Diffusion Coefficients Estimated from Radial Profiles Observed in Peach Bottom Fuel Elements.

Included in the plot are effective diffusion coefficients computed by Haire and Zumwalt[11] from profiles taken from element D13-05 of Core I. Both elements had sleeves composed of the same graphite, HLM 85. The agreement between the two sets of estimates appears to be fairly good. However, at these small effective diffusion coefficients, profiles establish quite slowly, and hence it may be more appropriate to employ time-average rather than EOL temperatures, which would move each indicated range to the right somewhat.

3.5.1.2.5 Summary of Radionuclide Inventories in the Graphite Portions of E06-01. Inventories of selected nuclides found in the top reflector, sleeve, spine, and bottom reflector portions of the element are summarized in Table 3.14. Totals are compared in the last column with the sum observed in the 30 fuel compacts. We note that the

Table 3.14. Inventories of Radionuclides in Graphite Components of E06-01

Radionuclide	Activity,[a] μCi					
	Top Reflector[b]	Spine	Sleeve	Bottom Reflector[c]	Total	Total (% of total in 30 fuel compacts)
^{46}Sc	4	11.1	62	N	77	
^{60}Co	0.8	3.7	10	1.9	16	
^{95}Zr	N	32	283	N	315	0.0056
^{106}Ru	1.2×10^{-4}	8.6	10	0.6	19	0.0083
^{110m}Ag	0.09	17	55	N	72	
^{134}Cs	0.06	10	24	1.1	35	0.027
^{137}Cs	0.02	12	35	0.69	48	0.026
^{144}Ce	3×10^{-4}	56	356	9.6	422	0.013
^{154}Eu	0.25	3.8	4.2	N	8	0.27
^{54}Mn	3.5×10^{-4}	N	N	N	3.5×10^{-4}	
^{59}Fe	0.012	N	N	N	0.012	
^{65}Zn	N	N	N	9.2	9.2	
^{3}H	I	7.2	109	N	116	
^{90}Sr	I	4.3	16	N	20	

[a]An entry of N instead of a numerical value in the table denotes either that no attempt was made to measure the radionuclides or that it was not detected by gamma spectroscopy. An I denotes insufficient data to determine inventory.

[b]Includes only purge tube and porous plug.

[c]Includes only fission product trap.

radionuclide ^{154}Eu is present in the graphite portions of the fuel element to the greatest degree relative to the amount in the fuel. The main source for this radionuclide is evidently neutron activation of ^{153}Eu, which is present as an impurity in the sleeve graphite. The highest fission product mobilities are observed for ^{134}Cs and ^{137}Cs, where 0.027% and 0.026%, respectively, of the fuel inventory are found in the graphite. It is also worth noting that inventories in the fission product trap are quite low compared with the nuclide concentrations in the sleeve and spine.

3.5.2 Primary Circuit Gamma Activity Scans

The primary coolant piping was gamma scanned on four occasions during the life of Peach Bottom Core 2 at the locations specified in

Table 3.15. (One may refer to Figs. 10.8 and 10.9 of Kolb et al.[19] for a visualization of the main loop with most of the scanning points identified.) Plateout activities determined in these four tests are summarized in Tables 3.16 and 3.17. Each test was conducted during a shutdown period, and the data were corrected back to the time of shutdown. The relevant dates are listed for each test. Table 3.16 lists revisions of values previously reported.[19] Table 3.17 contains an augmented version of data presented previously[20] along with the results of the most recent gamma scan, taken about two weeks following the final shutdown of the reactor plus a single sampling at location 5 in May 1974.

Table 3.15. Primary Loop Sampling Locations — Loop 1

Location	Distance from Loop 1 Steam Generator (m)
1. Near steam generator	2
2. Directly upstream from valve HC 203	34
3. Downstream from valve HC 203	37
4. Compressor inlet, near entry crawl space	41
5. Compressor outlet, near entry crawl space	58
6. Compressor outlet, near steam generator	67
7. Vertical duct	99
8. Directly upstream from concentric duct	108

It is worth noting that iodine photopeaks were observed only in the September 1973 scan data, and upper detection limit activities only are recorded for the 1971 and 1974 scans. The 1972 scan was acquired far too long after reactor shutdown to offer any possibility of detecting the 8-day ^{131}I photopeak.

Figure 3.20 summarizes some interesting features of the large duct gamma-scan data. Note that the initial period of Core 2 operation saw a diminuation of ^{137}Cs activity on the cold leg of the coolant duct as a result, evidently, of removing large deposits left from Core 1 operation.

Table 3.16. Loop 1 Coolant Duct Activities During 1971 and 1972

Location[a]	Activity, μCi/m²														
	^{54}Mn	^{59}Fe	^{60}Co	^{65}Zn	^{95}Zr	^{103}Ru	^{106}Ru	^{110m}Ag	^{124}Sb	^{131}I	^{134}Cs	^{137}Cs	^{144}Ce	^{140}Ba	^{154}Eu
On April 26, 1971 — Measured May 11–13, 1971															
1	31	79	94	110	<13	<20	<90	140	34	<85	3,100	9,400	2,400	43	<4.6
4	39	26	8.2	130	<24	<46	<180	150	3.0	<190	3,400	11,100	300	38	<7.1
5	32	11	5.3	150	<16	<30	<150	110	11	<130	3,200	9,900	100	40	<4.6
6	12	45	30	22	<10	<20	<150	19	3.3	<85	850	2,500	300	12	<4.2
7	14	78	96	18	23	3.9	49	250	3.5	<15	750	2,100	400	19	4.6
On January 6, 1972 — Measured April 25–28, 1972															
1	21	36	41	59				49			1,300	4,100	250		<1.1
3	15	14	10	30	<11	<49	<64	27	1.5		1,000	3,500	87		<1.1
4	17	13	8.2	49	<6.4	<28	<30	38	8.9		1,000	3,500	60		<0.79
5	58	10	5.3	23	<22	<85	<10	29	<1.7		790	2,800	54		<2.5
6	23	100	130	42	<38	120	120	43	7.6		990	3,700	430		<7.1
8	14	41	24	28	<19	<64	<46	14	<3.4		520	1,800	160		<3.3

[a]Described in Table 3.15.

Table 3.17. Activities Found on Loop 1 Coolant Duct During 1973 and 1974

Location[a]	Activity, μCi/m² of Each Nuclide				
	^{60}Co	^{131}I	^{134}Cs	^{136}Cs	^{137}Cs
On Sept. 4, 1973 — Measured Sept. 19–21, 1973					
1		68	5.27×10^3	265	7.26×10^3
3		69	4.04	188	6.44
4		69	4.59	205	6.99
5		0.34	1.32	77	1.82
6		57	2.89	172	4.16
7		42	4.22	244	5.38
8		42	2.46	148	3.38
On May 28, 1974 — Measured June 4, 1974					
5			11.6		10.7
On Oct. 31, 1974 — Measured Nov. 4–8, 1974					
1		<100	36.9	230	30.4
2		<100	22.2	55	17.4
3	4.8	<20	22.3	73	18.2
4		<100	23.9	76	19.1
5	3.7		20.0	22	15.8
6	120	<30	21.4	120	19.1
7	420	<300	26.7	220	22.7
8	90	<200	21.4	180	17.8

[a]Identified in Table 3.15.

ORNL DWG 75-15012

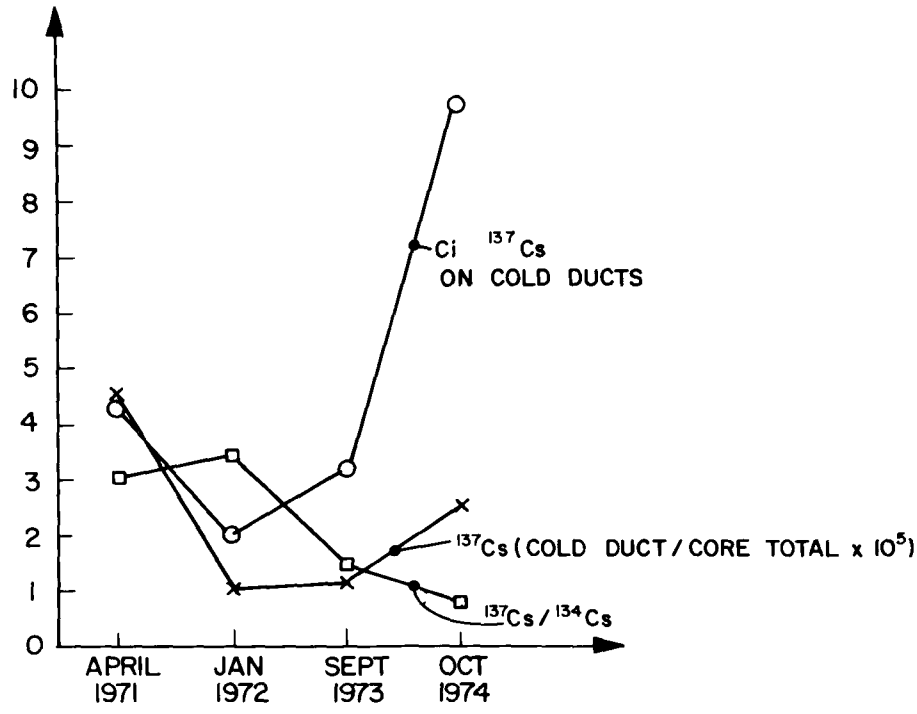

Fig. 3.20. Activity of ^{137}Cs on Both Cold-Leg Ducts of the Peach Bottom Primary Loop. (1) Total activity, (2) ratio to total core ^{137}Cs inventory, (3) ratio $^{137}Cs/^{134}Cs$ activity.

Further evidence for the observation that the early cesium activity was largely left from Core 1 is offered by the observed drop in the $^{137}Cs/^{134}Cs$ ratio. "Old" cesium would be characterized by a higher than normal quantity of ^{137}Cs by virtue of its longer half-life. Thus, the observed drop in the ratio during Core 2 operation indicates that "old" cesium was being replaced by cesium generated in Core 2. The approximate fraction of ^{137}Cs deposited on the cold ducts relative to total core inventory shows a similar initial drop from 4.5×10^{-5} for the January 1972 data, followed by an elevation to 2.5×10^{-5} at end of life.

3.5.3 Coolant Sampler Results

The Peach Bottom coolant flow was isokinetically sampled during Core 2 operation both upstream and downstream from the Loop 1 steam generator, according to the schedule shown in Table 3.18. The design

Table 3.18. Summary of Activities — Peach Botton Core 2 Coolant Sampling Program

Sampler and Designer	Location Relative to Steam Generator	Service Conditions							Components
		Temperature, °C		Operating Dates	Sampler Flowrate		Integrated Sample Flow		
		Inlet	Deposition (approx)		mg/sec	(lb_m/hr)	kg	(lb_m)	
CG,GAC	upstream	← unknown →							3 stainless steel diffusion tubes, cellulose filter, charcoal iodine absorber
C1,ORNL	downstream	300	130	7/29/71–12/14/71	≈59	≈0.47	590	1300	3 silver diffusion tubes, silver membrane filter, absolute filter, no iodine absorber
CA-1,ORNL	upstream	680	350	9/13/72–11/24/72 (1727 hr)	33	0.26			6 stainless steel diffusion tubes, silver membrane filter
CA-2,				11/17/73–5/19/74 (2681 hr)	33	0.26			same 6 diffusion tubes as CA-1, but new silver membrane filter, plus fiberglass filter, and charcoal iodine absorber
CB,ORNL	downstream	300	130	1/17/73–5/19/73 (2688 hr)	60	0.48	585	1290	4 silver diffusion tubes, a 5-stage particle impactor, silver membrane filter, fiberglass filter zeolite absorber, charcoal absorber
CC,ORNL	upstream	680	350	3/13/74–5/28/74 (1834 hr)	33	0.26	216	477	same as CA-2
CD,ORNL	downstream	300	130	3/13/74–5/28/74 (1834 hr)	48.4	0.384	319	704	same as CB

of the coolant samplers was described previously,[20] and preliminary data are presented by Malinauskas et al.,[21] de Nordwall et al.,[22] and in previous progress reports.[19,20] At the present time, a final summary report on the coolant sampler results is in progress. Recent results regarding cesium depositions in the upstream and downstream 1974 samplers are given in Table 3.19. The significance of the $^{137}Cs/^{134}Cs$ ratios listed in column five is that these values give an indication of the age of the deposited material. "Old" deposits would exhibit relatively higher ^{137}Cs levels by virtue of its longer half-life. The values shown for the 1974 coolant samplers are in agreement with the large duct scans, in signifying that the cesium observed in the 1974 tests was of recent origin. This is opposed to the 1971 to 1973 data, which showed $^{137}Cs/^{134}Cs$ ratios ranging from 1.2 to 3.9.

Table 3.19. Peach Bottom Coolant Sampler Results — Samplers CC and CD Corrected to May 1974

Sampler	Observed Activity, μCi			Ratio
	^{134}Cs	^{136}Cs	^{137}Cs	$^{137}Cs/^{134}Cs$
	Upstream Sampler (CC)			
Diffusion tubes and manifolds	13.3	0.49	8.3	0.62
Filters	1.13	0.41	0.93	0.82
TOTAL	14.4	0.53	9.23	0.64
	Downstream Sampler (CD)			
Diffusion tubes and manifolds	3.56	0.102	2.38	0.67
Impactor dust	1.93	0.048	1.32	0.68
Filters	0.0896	0.0035	0.0587	0.66
Total dust	2.02	0.052	1.38	0.68
TOTAL	5.58	0.154	3.76	0.67

3.6 REFERENCES

1. R. B. Evans III and M. T. Morgan, *Mathematical Description of Fission Product Transport in Coated Particles During Postirradiation Anneals,* ORNL-4969 (June 1974).
2. M. T. Morgan, H. J. de Nordwall, and R. L. Towns, *Release of Fission Products from Pyrocarbon-Coated HTGR Fuel Particles During Postirradiation Anneals,* ORNL-TM-4539 (December 1974).
3. M. T. Morgan, *Review of HTGR Coated Particle Stability,* ORNL-TM-4882 (August 1975).
4. C. E. Milstead, "Sorption Characteristics of the Cesium-Graphite System at Elevated Temperatures and Low Cesium Pressures," *Carbon* 7(1): 199–200 (1969).
5. E. A. Mason, A. P. Malinauskas, and R. B. Evans III, "Flow and Diffusion of Gases in Porous Media," *J. Chem. Phys.* 46: 3199–216 (1967).
6. E. A. Mason and R. B. Evans III, "Graham's Law: Simple Demonstration of Gases in Motion: Part I, Theory," *J. Chem. Educ.* 46: 358–64 (1969).
7. R. S. Rodliffe, *The Effect of Flow on Mass Transport of an Absorbing Radioactive Species in a Porous Medium,* CEGB Report RD/B/N-2375 (September 1972).
8. R. B. Evans III, J. L. Rutherford, and A. P. Malinauskas, *Gas Transport in MSRE Moderator Graphite Parts II and III,* ORNL-4389 (May 1969).
9. C. F. Wallroth, N. L. Baldwin, C. B. Scott, and L. R. Zumwalt, *Postirradiation Examination of Peach Bottom Fuel Test Element FTE-3,* USAEC Report GA-A-13004 (August 1974).
10. F. E. Vanslager, W. E. Bell, O. Sisman, and M. T. Morgan, "Fission Product Transport in HTGR Systems — A Summary," pp. 361–83 in *Proceedings of Gas-Cooled Reactor Information Meeting at ORNL, April 27–30, 1970,* CONF-700401.
11. M. J. Haire and L. R. Zumwalt, *Cesium Diffusion Coefficients and Other Results from the Analysis of Peach Bottom D13-05 Fuel Element Activity Profiles,* GA-A-12492 (July 1973).

12. H. S. Carslaw and J. C. Jaeger, *Conduction of Heat in Solids*, 2nd ed., Oxford University Press, New York, 1959.

13. J. Crank, *The Mathematics of Diffusion*, 1st ed., Oxford University Press, New York, 1957.

14. E. L. Compere, S. H. Freid, and C. W. Nestor, *Distribution and Release of Tritium in High-Temperature Gas-Cooled Reactors as a Function of Design, Operational, and Material Parameters*, ORNL-TM-4303 (June 1974).

15. E. L. Compere, M. F. Osborne, and H. J. de Nordwall, *Iodine Behavior in an HTGR*, ORNL-TM-4744 (February 1975).

16. M. F. Osborne, E. L. Compere, and H. J. de Nordwall, *Studies of Iodine Adsorption and Desorption on HTGR Coolant Circuit Materials*, ORNL-TM-5094, in press.

17. M. Tobias, *Estimates of Fission Product Activities in Fuel Element E06-01*, ORNL-TM-4705 (October 1974).

18. F. F. Dyer et al., "Fission Products in the Coolant Circuit," *ORNL Nuclear Safety Research and Development Program Bimonthly Report for July—August 1971*, ORNL-TM-3554, pp. 67—72.

19. J. O. Kolb, F. F. Dyer, and W. J. Martin, "Fission Product Behavior in the Coolant Circuit of the Peach Bottom HTGR," *GCR Programs Annu. Prog. Rep. Dec. 31, 1972*, ORNL-4911, pp. 172—78.

20. J. O. Kolb, W. J. Martin, F. F. Dyer, and L. L. Fairchild, "Fission Product Behavior in the Primary Circuit of the Peach Bottom HTGR," *GCR Programs Annu. Prog. Rep. Dec. 31, 1973*, ORNL-4975, pp. 246—55.

21. A. P. Malinauskas et al., "Fission Product Behavior During Operation of the Second Peach Bottom Core," pp. 237—48 in *Gas-Cooled Reactors with Emphasis on Advanced Systems* (Proc. Symp. Jülich Oct. 13—17, 1975), Vol. 1, International Atomic Energy Agency, Vienna, 1976.

22. H. J. de Nordwall et al., "An Interim Report on Fission Product Release During Operation of the Second Peach Bottom Core," pp. 18.1—18.4 in *Proceedings of BNES International Conference on Nuclear Fuel Performance, Oct. 15—19, 1973*, British Nuclear Energy Society, London, 1974.

4. HTGR KERNEL MIGRATION AND IRRADIATED FUEL CHEMISTRY

A. P. Malinauskas

4.1 INTRODUCTION

The main objective of this 1.5-man-year program is the understanding of the kinetic processes and thermodynamics of the fuel, fission product, coating system to a degree that permits identification and quantitative description of failure mechanisms and improved fuel performance by means of kernel chemistry modification.

4.2 KERNEL MIGRATION STUDIES — R. L. Pearson and T. B. Lindemer

In this activity quantitative data on fuel kernel migration rates are obtained out-of-reactor on unirradiated HTGR fuels. Similar in-reactor data are obtained on irradiated fuels during postirradiation examination of irradiation capsules.

4.2.1 Theory and Initial Analyses of Oxide Kernel Migration in HTGR Particles

The theory and analysis of oxide kernel migration in HTGR particles leads one to conclude that a solid-state diffusion mechanism operating across the kernel is controlling the migration rate. The experimental oxide kernel migration data are correlated by plotting the solid-state KMC, which has the units derived by (cm/sec) K^2 $(K/cm)^{-1}$, versus reciprocal absolute temperature. These analyses and conclusions were developed during a previous reporting period and published.[1] Two subsequent publications[2,3] of theory and experimental data during the present reporting period amplified these earlier analyses; the abstracts are given below:

> This report presents the currently available quantitative data for the kernel migration coefficient (KMC) in pyrolytic-carbon-coated HTGR fuel particles. The data include results obtained at Oak Ridge National Laboratory as well as information reported in the literature. In-reactor KMC values are reported for kernels composed of ThO_2, $Th_{1-z}U_zO_2$, UO_2, and ThC_2, while out-of-reactor

KMC values are reported for ThC_2, $Th_{1-z}U_zC_2$, and UC_2 kernels. The migration rates of all these kernel types appear to be controlled by solid-state diffusion processes that operate when the kernel is in a temperature gradient. To date, the migration of oxide kernels has been reported only for in-reactor experiments. There is no apparent dependence of the KMC upon the extent of fission for either carbide or oxide kernels. The relative rate of in-reactor migration of the fuel compounds was established in one set of comparative experiments and appears to have the order $ThO_2 < Th_{1-z}U_zO_2 < ThC_2$ in the temperature range of 1100 to 1900°C; UO_2 appears to exhibit the fastest migration rate at $T \leqslant 1200°C$.

Fuel kernel migration is widely observed in the coated oxide and carbide fuel particles used in high-temperature gas-cooled reactors (HTGRs). The rate of this phenomenon is generally observed to be sufficient to establish operational limits on the time-temperature-power density relationships needed for the design of the HTGR core. On the other hand, it has been difficult to establish the rate-controlling migration mechanism in oxide fuels and thus permit the rate of this mechanism to be determined unequivocally. This paper describes several new and general theoretical methods that can be used to establish experimentally the rate-controlling mechanism, and applies these developments to the analysis of recent in-reactor kernel migration observed in coated UO_2, $Th_{1-z}U_zO_2$, and ThO_2 particles. This analysis establishes that the kernel migration rate is apparently not controlled by the rate of CO/CO_2 diffusion in UO_2, $Th_{1-z}U_zO_2$, or ThO_2 particles. Furthermore, the data indicate that a solid-state diffusion

mechanism is controlling the kernel migration rate. A solid-state kernel migration coefficient (KMC) has been calculated for each particle observed in metallographic cross sections of specimens from several irradiation experiments. The KMC is defined as $(y/t)\ (T^2)\ (dT/dx)^{-1}$, in which y is the observed migration during time t. These coefficients were obtained over the temperature range 900 to 2000°C. The KMC for ThO_2 was less than that for $Th_{1-z}U_zO_2$ at a given temperature; UO_2 had the highest KMC at $T \leqslant 1200$°C. The activation energy for the UO_2 KMC was $\sim$ 19 kcal/mol, while that for ThO_2 and $Th_{1-z}U_zO_2$ was $\sim$ 44 to 45 kcal/mol. No burnup dependence of the KMC could be discerned in either ThO_2 or UO_2.

An additional analysis compared the use of the KMC to correlate extensive in-reactor UO_2 migration data with the use of a correlation coefficient based on rate control by CO-CO_2 diffusion. The latter coefficient is designated as the COKMC and is given as Eq. (12b) of ref. 1. The only major assumption in the derivation is that the krypton-plus-xenon release per fission and the oxygen release per fission, which leads to the generation of pressures of CO and traces of CO_2 in the particle, are constant at all burnups. The COKMC can then be defined as:

$$\text{COKMC} = \frac{a\,\dfrac{dy}{dt}}{T\,\dfrac{dT}{dx}\,\dfrac{\%\ \text{FIMA}}{100}}\ , \tag{1}$$

in which

a = ratio of the void volume in the buffer and kernel to the initial volume of a fully dense UO_2 or $Th_{1-z}U_zO_2$ kernel,

FIMA = fissions per initial heavy-metal atom,

$\dfrac{dy}{dt} = \dfrac{\text{observed migration}}{\text{irradiation time}}$, cm/sec,

T = temperature, K,

$\dfrac{dT}{dx}$ = temperature gradient, K/cm.

The only significant difference between the KMC and the COKMC is the inclusion of a and % FIMA in the latter quantity; the different use of temperature leads primarily to a scale factor on the ordinate. The in-reactor UO_2 kernel migration data from GA[4] and ORNL[2] were analyzed along with data provided by R. Rotterdam (HRB, Mannheim), J. Thompson (Belgonucleaire), K.S.B. Rose (AERE, Harwell), and M. Wagner-Löffler (Dragon Project, Winfirth). Comparison of the KMC and COKMC data correlations did not demonstrate that either was, by itself, sufficiently definitive to establish either the solid-state mechanism or the CO-CO_2 mechanism as rate-controlling. However, the solid-state KMC did correlate the majority of the UO_2 migration data as well as the COKMC did and certainly adequately for core design.

4.2.2 Current KMC Data for Oxides and Carbides

A report[5] presents all KMC data obtained at ORNL up to January 1976. Laboratory KMC data for as-coated particles were obtained for UC_2, $Th_{0.84}U_{0.16}C_2$, ThC_2, ThO_2, and $UO_{1.65}N_{0.25}$. The carbide data agreed exactly with that reported by Stansfield et al.[6] and the ThO_2 data agreed with other ThO_2 KMC data obtained earlier.[2,3,7] The laboratory KMC values for $UO_{1.65}N_{0.25}$, which is a UO_2-U_2N_3 solid solution, fell on the high-temperature extrapolation of the in-reactor UO_2 data, thus indicating that the nitrogen addition would not improve the migration characteristics. In-reactor tests of $UO_{1.50}N_{0.38}$ to 85% FIMA, Fig. 4.1, confirmed that the migration behavior was qualitatively comparable with that for UO_2 at 30 to 85% FIMA. Thus, nitrogen additions to UO_2-based fuels do not appear to be warranted.

Extensive additional in-reactor data were obtained. In-reactor KMC data were obtained for UO_2, ThO_2, and $Th_{1-z}U_zO_2$ (z = 0.5, 0.33, or 0.11). These KMC data all agree with other KMC data obtained earlier.[2,3] In addition, no apparent KMC differences could be detected in comparisons of Biso vs Triso particles or ^{233}U vs ^{235}U contents. In-reactor KMC data for ThC_2 from the H-1-9 irradiation[2] and from Peach Bottom irradiation E11-07, compacts 16 and 18, indicate that the in-reactor KMC values are as much as 10 times higher than the laboratory values. This

Y-130283

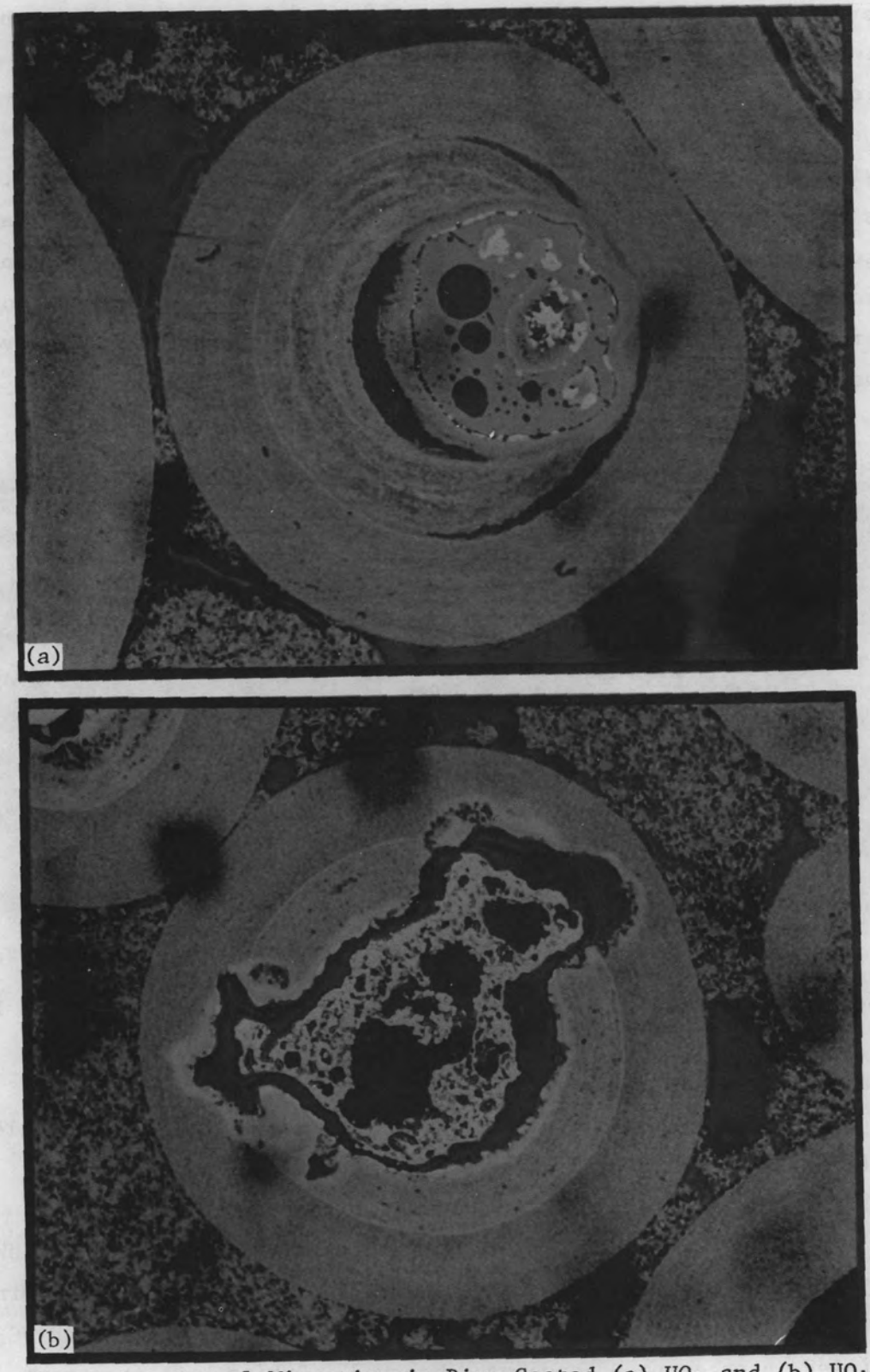

Fig. 4.1. Kernel Migration in Biso-Coated (a) UO_2 and (b) $UO_{1.50}N_{0.38}$. Both particles were irradiated to a fast fluence of 5.0×10^{21} n/cm^2 (80% FIMA) at a centerline temperature of 1280°C in HRB-7.

observation is contrary to the work of Stansfield et al.,[6] where the in-reactor and laboratory KMC values for ThC_2 and UC_2 agreed. An in-reactor test of Triso WAR $UC_{0.4}N_{0.6}$ to 85% FIMA at a maximum temperature of 1500°C revealed extensive interaction of the fuel-fission product system with the inner LTI and SiC layers, Fig. 4.2. This behavior is identical in appearance with that observed in irradiated Triso UC_2 particles. Thus, the nitrogen addition apparently does not improve the overall performance of the carbide-base fuel in spite of the fact that the $UC_{1-z}N_z$ KMC is less than that[5,8] for UC_2 at a given temperature.

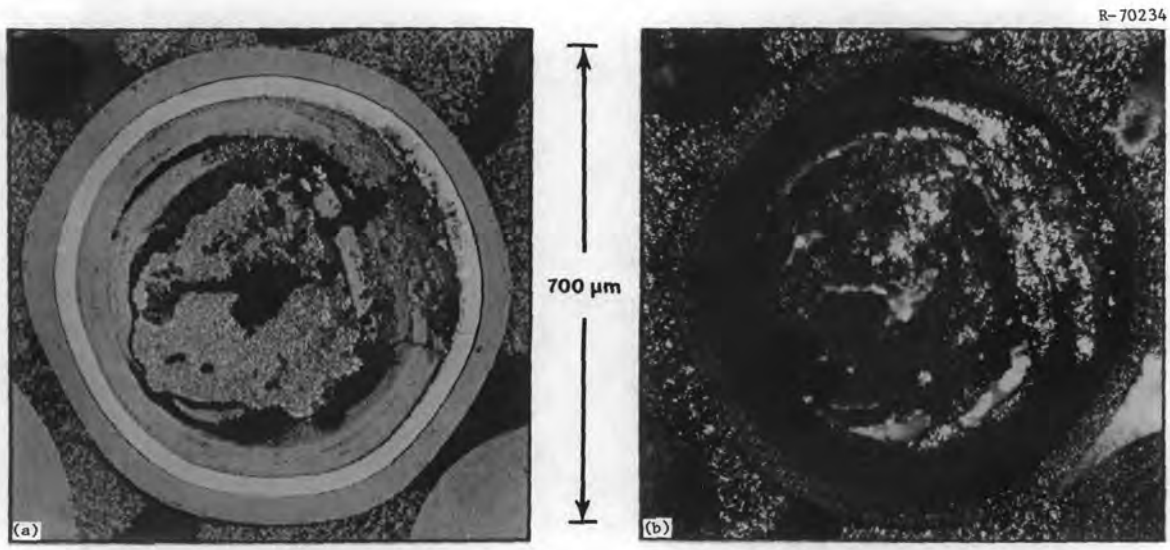

Fig. 4.2. Triso WAR $UC_{0.4}N_{0.6}$ Fuel Particle Irradiated to a Fast Fluence of 4.8×10^{21} n/cm^2 (80% FIMA) at a Nominal Centerline Temperature of 1500°C in HRB-10. (a) Bright field. (b) Polarized light.

4.2.3 WAR UC_2 Kernel Vaporization

During the kernel migration studies, a variety of fuel particles was heat-treated at a maximum temperature of 1940°C in a 278°C/cm gradient. One of the disks included in that study contained Biso particles with WAR-derived kernels fully converted to UC_2. The disks were radiographed as made and after 143, 365, and 551 hr in the furnace. Instead of kernel migration, as was observed with the bed-melted UC_2 particles, another phenomenon was observed. During heat treatment, the

kernel diameters appeared to shrink, the rate depending on the temperature. From one of the particles that was held at 1900°C the kernel completely disappeared after 551 hr, as seen in Fig. 4.3. Shrinkage of the kernels could be detected in particles heated as low as 1700°C. There is a linear relationship between kernel diameter and time at all temperatures.

Particles 22 and 23, which were heat treated at 1800°C, were photographed after metallographic sectioning of one of the disks. The structure of the resin kernel was intact; no densification had occurred. Instead, a distinct boundary line could be observed within the resin kernel. The diameter of the section enclosed by the boundary was the same as the diameter of the kernel observed in the radiograph. These same particles were submitted for microprobe analysis along with polished archive specimens of the same batch of microspheres, which were used as a standard. Electron-beam-scanning images of both particles and the average U M_{α} x-ray intensity from ten standard microspheres (chosen at random) are plotted in Fig. 4.4. Each heat-treated microsphere exhibited a depletion of uranium near the surface of the kernel. Step scans were taken every 5 μm for about 100 μm into the kernel. In particle 22, there was no uranium in the outer 25 μm. Over the next 15 to 20 μm there was a steep, linear rise in the concentration gradient. From there on into the center of the kernel, the concentration of the uranium was still the same as in the archive samples.

Two scans were made on particle 23, one parallel and one normal to the temperature gradient. Almost 50% of the uranium of kernel 22, which was 365 μm in diameter, had escaped from the kernel. About 80% of the uranium had escaped from particle 23. No uranium was detected in either the buffer or the LTI layer.

A second disk in the same furnace run contained a batch of Biso WAR (weak-acid-resin-derived) UO_2-UC_2 in which only 15% of the UO_2 was converted to UC_2; a third disk contained only bed-melted UC_2. None of the kernels in either of these disks exhibited any shrinkage. The reason for no shrinkage in the bed-melted UC_2 kernels is postulated to be related to the surface area. The surface area of UC_2 exposed in a

Y-133698

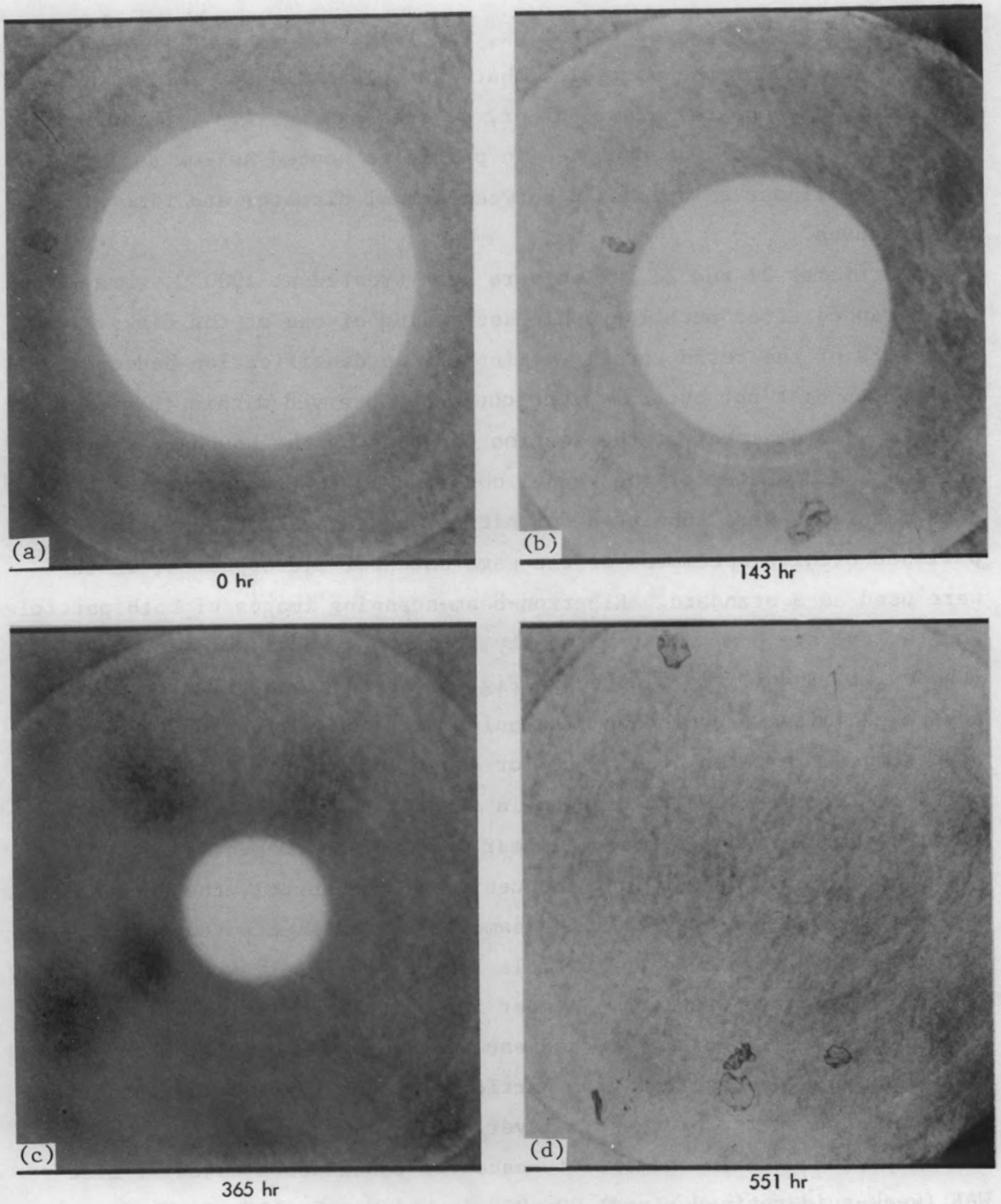

Fig. 4.3. Shrinkage of the Uranium Portion of a Biso WAR UC_2 Kernel at 1900°C vs time. The carbon structure of the resin-derived kernel remains intact. (a) Unheated. (b) 143 hr. (c) 365 hr. (d) 551 hr.

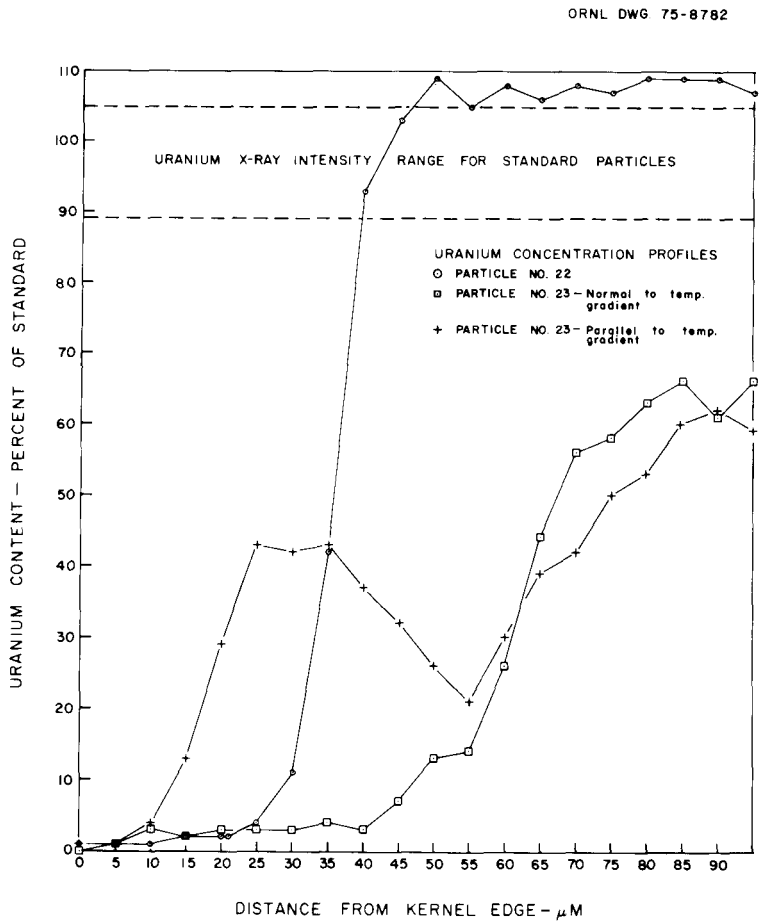

Fig. 4.4. Uranium Concentration in Biso-Coated WAR UC_2 Kernels vs Distance from Kernel Edge.

bed-melted kernel is about 0.001 of that in a WAR UC_2 kernel. If the rate of disappearance of UC_2 per unit surface area were the same for bed-melted UC_2 as it is for WAR UC_2, at 1900°C it would take about 30 years for the UC_2 kernel to shrink 2 μm, the limit of detection of the microscope. Further experiments are in progress.

The apparent activation energy for the loss of uranium from WAR UC_2 is approximately 400 kJ/mole (100,000 cal/mole). This and the containment properties of the SiC layer on the fissile particles should preclude any problem with uranium loss at nominal HTGR temperatures.

4.3 GAS PRESSURE MEASUREMENTS — T. B. Lindemer

Several types of measurement are made in this activity. Individual irradiated particles are first analyzed by gamma-ray spectrometry to determine the ^{95}Zr, ^{106}Ru, ^{137}Cs, and ^{144}Ce contents; F. F. Dyer and L.L. Fairchild perform this service. This information is used to determine the actinide burnup and cesium retention in the particle. Each particle is then heated to 1000 to 2000°C, equilibrated, and broken, and the amounts of CO and Kr + Xe are determined. From these data the fraction of Kr + Xe released into the void space of the particle by the kernel during irradiation is obtained, and the chemical potential of oxygen for the fuel-fission product system is determined as a function of temperature, burnup, and initial actinide composition. The information on oxygen potential is then used to infer the oxidation state of the actinides and the fission products.

The apparatus used for the pressure measurements has been described.[9] A particle is heated to 1000 to 2000°C and broken to release the gases into a known volume. The pressure is measured with a capacitance manometer, and then a titanium wire is heated to getter the CO, leaving the pressure of Kr + Xe to be measured.

A primary concern of this program has been the validity of the CO measurements. For some time it was not conclusively demonstrated whether the CO measurements resulted from the real CO content in the particle before it was broken or from CO produced by rapid oxide-carbon chemical reactions after it was broken. These problems were considered in part in ref. 9. This question has apparently been favorably resolved by measurements completed on Harwell 919/8 particles obtained from G. W. Horsley[10] (AERE-Harwell) and M. Wagner-Löffler (Dragon Project). These low-enriched Triso particles experienced 5.7% FIMA, with 50% being plutonium fissions. Particles from this batch were used to compare results of the mass spectrographic technique used at AERE-Harwell[11] and at ÖSGAE* (Austria)[12] with the ORNL technique.[9]

---

*Österreiche Studiengesellschaft für Atomenergie, Seibersdorf.

The experimental results are given in Table 4.1. The ORNL results for Kr + Xe through 1700°C average 2.73 mm^3 (STP) and agree with the ÖSGAE results. The somewhat lower AERE results for Kr + Xe may result from a difference in the particle breaking method; at AERE the coatings are cracked with a micrometer to release the gas, while at ORNL and probably at ÖSGAE both the coating and the kernel are fractured, thus possibly releasing more gas from closed voids. The ONRL Kr + Xe release at 2000°C is higher than the lower temperature results probably because of Kr + Xe diffusion from the kernel during the 2000°C equilibration.

Table 4.1. Gas Contents in 919/8 Particles

Temperature (°C)	ORNL Measurements				European Mass-Spectrometric Measurements, std mm^3			
	Heating Time (hr)	Delay Time[a] (sec)	Gas Found, std mm^3		AERE		ÖSGAE	
			Kr + Xe	$CO + CO_2$	Kr + Xe	$CO + CO_2$	Kr + Xe	$CO + CO_2$
1000	24	0	2.89	0.94	1.89	0.76	2.8[b]	1.1
	1	120	2.44	0.96				
1200					2.43	0.92	2.8[b]	1.6
1400	24	0	3.05	2.88	2.16	1.21	2.8[b]	2.1
	24	10	2.84	2.13				
	1	155	2.70	2.26				
1700	1	0	2.79	3.80				
	1	120	2.87	2.50				
	1	120	2.33	0.24[c]				
	1	120	2.70					
2000[d]	1	0	4.07	9.56				
	1	120	3.34	3.46				

[a]Delay after heater was turned off before particle was broken. The standard AERE treatment[11] is a 120-sec delay after 1 hr at temperature.

[b]ÖSGAE measurements are unavailable but are said[10] to be 30% higher than AERE values. Hence they were estimated by multiplying the average of the AERE values by 1.3

[c]This corresponds to in-particle P_{CO} over the $SiC-SiO_2-CO$ equilibrium.

[d]Heated at 1400°C for 50 min and then at 2000°C for 10 min.

The $CO + CO_2$ data at 1000°C lie between the AERE and ÖSGAE results; there does not appear to be any effect of delay time before breaking the particle. At 1400°C the ORNL results agree with the ÖSGAE data when the particles are broken after a delay time of either 10 or 120 sec. (At ÖSGAE a 10-sec delay time is used,[10] while a 120 sec delay is used at Harwell.[11]) On the other hand, breaking the particles immediately results in a higher $CO + CO_2$ (essentially CO) amount. The difference

between the delay and no-delay amounts increases even more at 1700 and 2000°C. It would appear that breaking the particle at the higher temperatures does release some additional CO as a result of postbreaking reactions; it may be better to break the particle after it has cooled. This conclusion will be discussed further below. Generally, however, these data intercompare very well and appear to validate the measurements by the European mass-spectrometric method and the ORNL capacitance manometer technique, which includes the hot titanium wire for separation of CO from the inert fission gases.[9]

Sufficient data were collected from Biso ThO_2 particles before the 919/8 measurements to permit an analytical treatment of oxygen release as CO from the oxide kernel, the Kr + Xe release from the kernel, and the cesium retention by the entire particle. The data were obtained from Biso ThO_2 irradiated to $1.3 \leqslant$ % FIMA $\leqslant 19.0$% in ORNL experiments HT-12 through -15 (sleeves 8, 13, 21, and 26) and to about 3% FIMA in GA experiment P13L-C4T6-10 and -11.* Also included were data from $Th_{0.81}U_{0.19}O_2$ irradiated in HRB-6-1C to 21 to 22% FIMA. All the data for oxygen release shown in Fig. 4.5 were fitted to the equation $O/f = (a + bf)\exp(-Q/RT)$, in which O/f is the measured moles of oxygen released (as CO and CO_2) per mole of actinide that fissioned, f is the fraction FIMA (not % FIMA), Q is the apparent activation energy, R is the gas constant, and T is the temperature in K. Application of the least squares theorem simultaneously to all the data gave $a = 0.234$, $b = 26.5$, and $Q = 45.6$ kJ/mole (10,900 cal/mol). These coefficients are applicable over the range $0.03 \leqslant f \leqslant 0.22$ and $1050 \leqslant T \leqslant 2000$°C. It should be noted, however, that the oxygen release measurements were made by breaking the particle at temperature, as was discussed above; the measurements at 2000°C may be a factor of 2 or 3 too high. This would also explain why the 2000°C oxygen-release results shown in Fig. 4.5 are often much higher than the indicated[1,13,14] maximum theoretical oxygen release for fission of ^{233}U and ^{235}U. Further work is being performed on particles equilibrated at 1700 and 2000°C and

---

*Particles provided by C. L. Smith of GA.

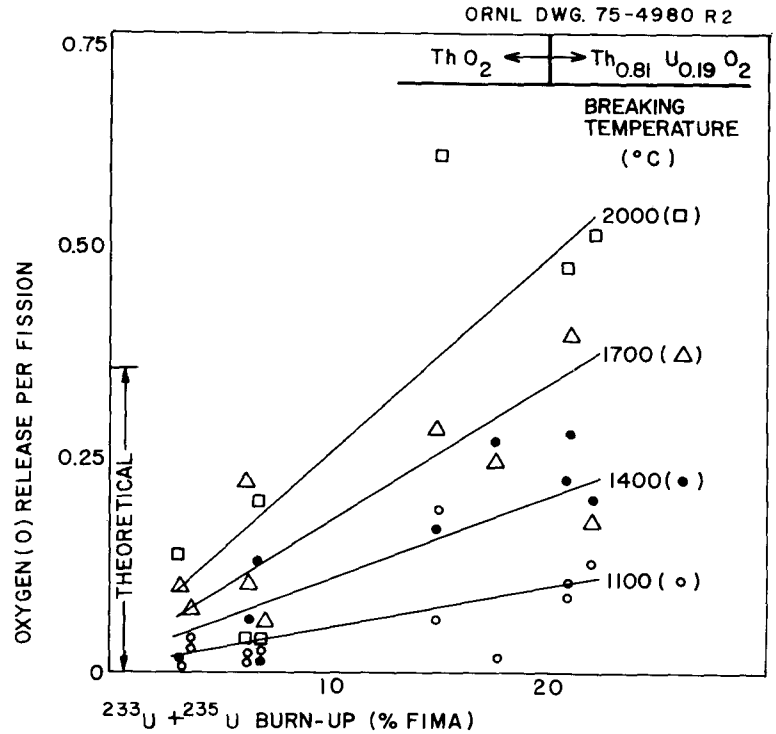

Fig. 4.5. Experimental Oxygen Release per Fission in ThO_2 and $Th_{0.81}U_{0.19}O_2$ Particles as a Function of ^{233}U Plus ^{235}U Burnup and Equilibration Temperature.

then cooled for 120 sec; we anticipate that the resulting lower oxygen-release values will have the primary effect of lowering the value of Q in the above equation. The experimental in-particle P_{CO} for most of these particles is shown in Fig. 4.6.

The observed cesium retention in the particles after irradiation is shown in Fig. 4.7. The irradiation temperatures indicated on the figure are nominal; thermal analyses of these particles will be reported elsewhere[15] and that temperature information should be used for any interpretation of the cesium loss rate.

The Kr + Xe release from the kernel into the buffer layer void space is shown in Fig. 4.8. It can be described up to 6% FIMA by the approximate equation (% release) = 10(% FIMA), and by the equation (% release) = 45 + 2.5(% FIMA) over the range $6 \leqslant$ % FIMA $\leqslant 22$. These results agree reasonably well with those reported by Janvier et al.[16] for HTGR oxide particles irradiated between 1.5 and 8% FIMA.

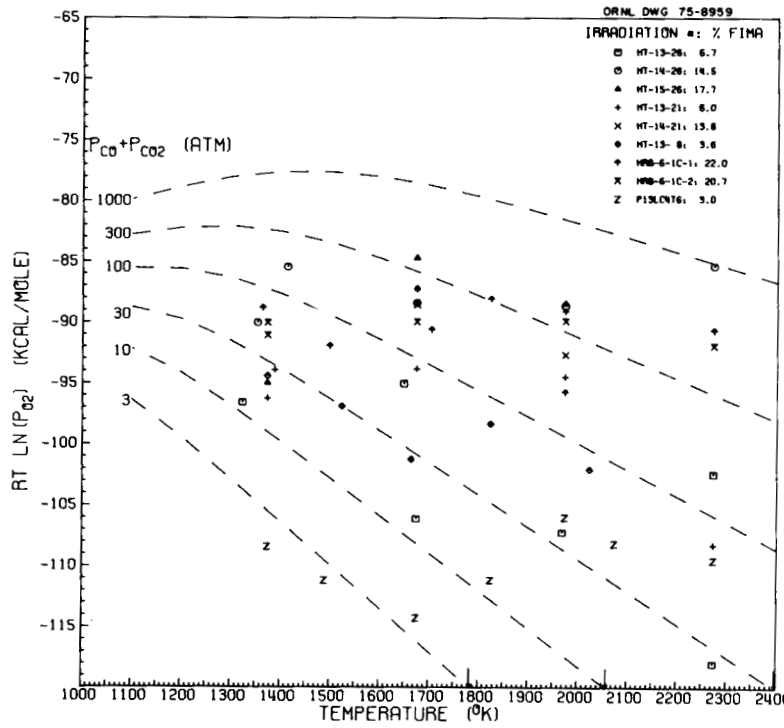

Fig. 4.6. Experimentally Derived Chemical Potential of Oxygen (RT ln P_{O_2}) vs Temperature and ^{233}U Plus ^{235}U Burnup in ThO_2 and $Th_{0.81}U_{0.19}O_2$ Particles. Also indicated is the in-particle value of $P_{CO} + P_{CO_2}$ in atmospheres.

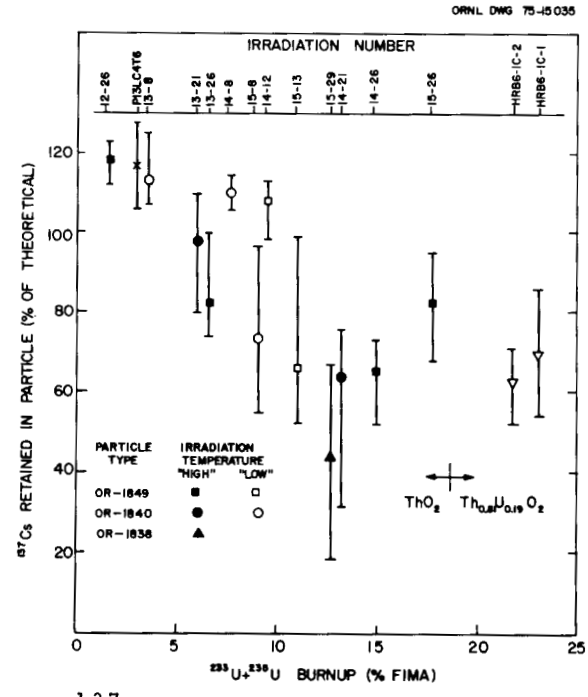

Fig. 4.7. The ^{137}Cs Retention by Biso Tho_2 Particles vs ^{233}U Plus ^{235}U Burnup. Indicated temperatures are nominal.

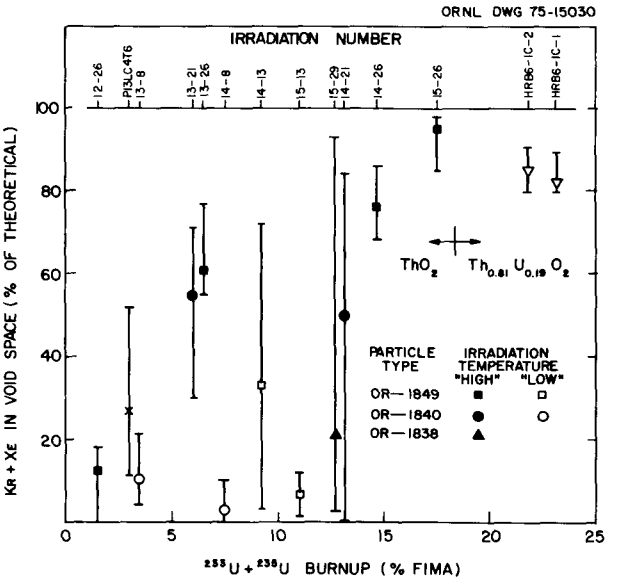

Fig. 4.8. The release of Kr + Xe into the Void Space of the particle vs ^{233}U plus ^{235}U Burnup in ThO_2 Particles.

4.4 THE CHEMICAL BEHAVIOR OF HTGR FUELS — T. B. Lindemer

This task is essentially a continuing literature review and interpretation of available phase equilibria and other thermodynamic data. This provides the fundamental chemical information necessary for interpretation of chemical phenomena observed during postirradiation examination (PIE).

The WAR UO_2-UC_2 kernel is being irradiated to evaluate the performance as a function of initial UC_2 content, as is described in Sect. 6.6. In addition, past work with full-burnup, 100% UC_2 particles has revealed extensive lanthanide interaction with the SiC layer. The following summarizes the current results of thermochemical calculations for the fissioned UO_2-UC_2 system.

The chemical potential of oxygen ($RT \ln P_{O_2}$) has been calculated as a function of temperature for the probable oxide-carbide equilibria for uranium and each fission product. Typical equilibria are:

$$UO_2 + 1.86C \rightleftarrows UC_{1.86} + O_2 \ ,$$

$$2SrO + 4C \rightleftarrows 2SrC_2 + O_2 \ ,$$

$$1.33LaO_{1.5} + 2.66C \rightleftarrows 1.33LaC_2 + O_2 \ .$$

Activity effects resulting from solid solution of fission-product oxides (primarily in UO_2) were not considered because quantitative activity data are not available. Examination of the oxygen potentials for the equilibria at all HTGR temperatures permits the following ranking in terms of increasing stability of the oxide relative to the carbide: Ba, Zr, Eu, Sr, U, Sm, (La, Pr, Nd), Ce, and Y. In other words, as the oxygen potential of the fissioned system after full burnup is made more negative by increasing the initial percentage of UC_2 in the kernel, barium will be the first to form BaC_2 instead of BaO, followed by ZrC instead of ZrO_2, and so on.

Another effect to be considered at low initial percentages of UC_2 is gettering of fission-released oxygen. At the oxygen potential of the UO_2-UC_2 kernel, all lanthanides, if present as oxides instead of dicarbides, will be present as sesquioxides. One can then perform the usual oxygen mass-balance calculations to demonstrate that the oxygen release is 0.38 oxygen atoms per ^{235}U fission. As is well known, UC_2 in the kernel will react with this oxygen to form UO_2 and prevent a significant pressure of CO.

It should also be noted that cesium and rubidium will be present as metals in the fissioned UO_2-UC_2 system. The oxygen potentials in this system are much lower than those necessary for the stability of the uranates and molybdates of these metals.

Now consider a particle at *75% FIMA* in view of the above information and of the usual fission product yields for ^{235}U. The ranking and quantitative data in Table 4.2 can be established below 1500°C to demonstrate the effect of the initial percentage of UC_2. If 14% UC_2 were present in the initial kernel, then at 75% FIMA all the oxygen would be present as UO_2 and fission-product oxides, along with an insignificant CO overpressure; no UC_2 or any other carbide would be present. With an initial 16.6% UC_2 content, the oxygen would be present as oxides and barium would be present as BaC_2. Between 16.6 and 39.6% UC_2, both ZrO_2 and ZrC would be present in addition to the previous two effects; at an initial 39.6% UC_2 addition all the zirconium would be present as ZrC. All the elements below zirconium would be present as oxides. Similar interpretations may be made for the remainder of Table 4.2

Table 4.2. Initial UC_2 Required to Give Indicated Effect at 75% FIMA in Oxide-Carbide Kernels

Function of UC_2 Addition	Initial % UC_2 Required for Each	Cumulative % UC Required
Oxygen gettering	14	14.0
BaO to BaC_2	2.6[a]	16.6
ZrO_2 to ZrC	23	39.6
$EuO_{1.5}$ to EuC_2	0.4	40.0
SrO to SrC_2	3.3	43.3
UO_2 to UC_2	25	68.3
$SmO_{1.5}$ to SmC_2	1.7	70.0
$(La,Nd,Pr)O_{1.5}$ to $(La,Nd,Pr)C_2$	18	88.0
$CeO_{1.5}$ to CeC_2	9.2	97.2
$YO_{1.5}$ to YC_2	2.3	99.5 (∿100%)

[a]For example, consider the reaction (not an equilibrium) $2C + 2BaO + UC_2 \rightarrow UO_2 + 2BaC_2$. The initial amount of UC_2 required for conversion of all BaO to BaC_2 at 75% FIMA is (7.0% Ba/fission) (0.75 fission) (1 UC_2/2BaO) = 2.6% UC_2.

A more generalized representation of the phases present in an oxide-carbide kernel is given in Fig. 4.9 as a function of initial UC_2 content and % FIMA. The several phase changes that take place at the lower initial UC_2 contents are quite evident. Cognizance of this fact may be helpful in interpreting irradiation behavior observed in UO_2-UC_2 fissile fuels, which are usually examined only at full burnup. More importantly, these calculations demonstrate that Y, La, and the lanthanide fission products are present as oxides as long as the initial UC_2 content is below 68%. This result is consistent with the post-irradiation observations that at less than about 70% initial UC_2 the La, Ce, Nd, and Pr are retained in the fissioned kernel and are not present in significant amounts in the particle coatings, while at least 75% initial UC_2 these elements are concentrated in reaction zones in the pyrocarbon and SiC coatings.

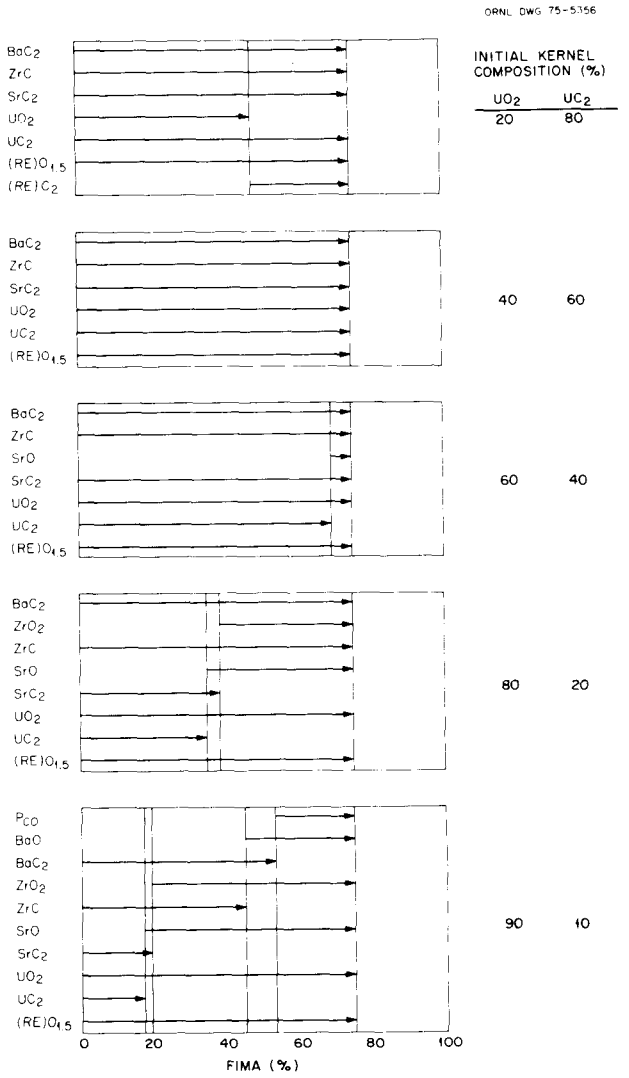

Fig. 4.9. Phases Present in a Fully Enriched UO_2-UC_2 Kernel as a Function of ^{235}U Burnup and Initial UC_2 Content. The $EuO_{1.5}$-EuC_2 system is not shown because it has a small (<1%) yield. However, its chemical behavior is different from that of the other lanthanides (RE) and it converts from the carbide to the oxide at about the same burnup as does the strontium system.

4.5 REFERENCES

1. T. B. Lindemer and H. J. de Nordwall, *An Analysis of Chemical Failure of Coated UO_2 and Other Oxide Fuels in the High-Temperature Gas-Cooled Reactor*, ORNL-4926 (January 1974).
2. T. B. Lindemer and R. A. Olstad, *HTGR Fuel Kernel Migration Data for the Th-U-C-O System as of April 1, 1974*, ORNL-TM-4493 (June 1974).

3. T. B. Lindemer, H. J. de Nordwall, and R. A. Olstad, "Analysis and Measurement of Mass Transport in Coated UO_2 and Other HTGR Oxide Particles," pp. 163–72 in *Thermodynamics of Nuclear Materials, 1974, Proc. Symp. Vienna,* International Atomic Energy Agency, Vienna, 1975.

4. *HTGR Base Program Quarterly Progress Report for Period Ending Nov. 30, 1973,* Gulf-GA-A-12818 (December 1973).

5. T. B. Lindemer and R. L. Pearson, *Kernel Migration in HTGR Fuels from the Th-U-C-O-N System,* ORNL-TM-5207 (April 1976).

6. O. M. Stansfield, C. B. Scott, and J. Chin, "Kernel Migration in Coated Carbide Fuel Particles," *Nucl. Technol.* 25: 517–30 (1975).

7. C. L. Smith, *Fuel Particle Behavior Under Normal and Transient Conditions,* GA-A-12971 (October 1974).

8. A. Naomidis and B. Thiele, "Studies of the Amoeba Effect: Carbon Transport in Coated Fuel Particles Under the Influence of a Temperature Gradient," pp. 173–86 in *Thermodynamics of Nuclear Materials 1974, Proc. Symp. Vienna,* International Atomic Energy Agency, Vienna, 1975.

9. T. B. Lindemer and R. L. Pearson, "Apparatus for Measuring Gases from Irradiated Fuel Particles," *J. Nucl. Mater.* 55: 359–61 (1975).

10. G. W. Horsley, AERE, Harwell, private communication, March 1975.

11. D. J. Clough et al., "The Determination of Gases in Coated Particle and Ceramic Fuels," paper 31 in *Post-Irradiation Examination Techniques, Proc. Conf. U. of Reading 1972,* British Nuclear Energy Society and Institute of Civil Engineers, London, 1972.

12. H. Bildstein and H. Strigl, "Determination of Free Volumes and Gas Content of Coated Fuel Particles for Gas-Cooled Reactors," paper 26 in *Post-Irradiation Examination Techniques, Proc. Conf. U. of Reacing, 1972,* British Nuclear Energy Society and Institute of Civil Engineers, London, 1972.

13. J. M. Leitnaker, "Applications of Thermodynamics for Predicting and Understanding the Performance of Fast Breeder Reactor Oxide Fuels," *J. Nucl. Mater.* 51: 95–105 (1974).

14. R. H. Flowers and G. W. Horsley, *The Influence of Oxide Kernels on the Manufacture and Performance of Coated Particle Fuel*, AERE-R-5949 (1968).

15. M. J. Kania, T. B. Lindemer, M. T. Morgan, and J M Robbins, *Irradiation Performance of HTGR Fertile Fuel in HFIR Target Capsules HT-12 to -15, Part I — Experiment Description and Fission Product Behavior*, ORNL/TM-5305 (in preparation).

16. J. C. Janvier, M. Bruet, and R. Blanchard, "Fission Gas Pressure Evolution in Irradiated Coated Particles," paper presented at the British Nuclear Energy Society Conference on the HTGR, London, 1973, Preprint 34.

5. COOLANT CHEMISTRY; THE STEAM-GRAPHITE REACTION

A. P. Malinauskas

5.1 INTRODUCTION

The graphite core and core support members readily react with steam at normal operating temperatures to produce hydrogen and carbon oxides. Moreover, radiation-induced reactions are likewise possible, and these reactions can also lead to the production of methane. The primary purpose of the coolant chemistry studies is to identify those factors that limit acceptable steam inleakages in terms of both the magnitude of the ingress and its duration. As a result, emphasis has been placed upon the elucidation of the thermal and radiation-induced reaction kinetics that are pertinent to the steam-graphite system.

5.2 ANALYSIS OF COOLANT IMPURITY COMPOSITION DATA OBTAINED DURING FORT ST. VRAIN HTGR STARTUP — G. L. Tingey and W. C. Morgan (Battelle, Pacific Northwest Laboratories)

The objective of this investigation is to gain a more complete understanding of both the thermal and radiation-induced reactions between graphite and steam as they occur in an operating HTGR, and in this manner to accurately predict the chemistry of the coolant system. The present study involves a comparison of computer-program-derived impurity compositions of the helium coolant in the Fort St. Vrain HTGR with corresponding measurements that are being made during reactor startup.

In performing this task, we have significantly modified the computer code GOP to improve the accuracy of the results. Moreover, numerous calculations of gas composition have been made for various power levels, steam leak rates, and reaction rate parameters in order to ascertain the requirements for coolant analysis during Fort St. Vrain startup.

Startup tests in Fort St. Vrain have been limited to less than 2% power during this reporting period. We have evaluated gas composition data that were obtained during the test period from April 10 to May 8, 1975. Although these data are restricted to less than 2% of design power, they nonetheless yield information that aids our understanding

of the coolant chemistry. In particular, since the maximum temperature attained during these startup tests has been only about 240°C, the thermal reactions are immeasurably small; we can thus evaluate the significance of radiolytic processes without the added complications introduced by the thermal reactions.

Table 5.1 compares the measured gas composition with values predicted by the GOP-3 computer code by varying the leak rate and dose parameters; the low level of CO in comparison with CO_2 is of particular interest. The potential sources of CO_2 include outgassing from the graphite in the system, air ingress, thermal and radiolytic reactions of O_2 or H_2O with the core graphite, and reactions of CO with O_2. Since the temperature of the coolant and graphite are so low, we do not expect any significant contribution from thermal reactions. Furthermore, the thermal reactions of steam and O_2 with carbon both yield major quantities of CO, which are not observed. Also, outgassing of oxides from graphite yields a mixture of both CO and CO_2. The removal of CO by the thermal reaction with oxygen has been shown to be insignificant up to temperatures substantially higher than the coolant temperature experienced during the test. Thus, we have concluded that the most likely source of CO_2 is the radiolytic reaction of steam with the graphite, which has been shown by Woodley[1] to yield CO_2 and H_2 but not CO.

Table 5.1. Predicted Gas Compositions at 1.9% of Design Power

Calculation Parameters	Steam-State Gas Composition, ppm				
	H_2O	H_2	CO	CO_2	CH_4
Measured value	150	1.0	<0.5	30	0.2
Reference[a]	12.8	1.8	0.008	0.94	0.02
10 × leak rate	130	16.5	0.06	8.4	0.2
10 × leak rate 5 × dose rate	100	38	2.1	23	4.6

[a]Reference condition: H_2O leak rate = 50 mg/sec (0.04 lb/hr) Coolant pressure 2.89 MPa (419 psi) Maximum radiation dose = 6.7×10^6 R/hr

The high H_2O content in the coolant is undoubtedly due to a relatively rapid desorption of moisture from the graphite in the system and is in reasonable agreement with a leak rate of 50 mg/sec (0.4 lb/hr) or ten times the reference leak rate. In order to predict the high CO_2 composition it was necessary to increase the radiation flux to 5 times the reference level. This assumption may be justified because at the low reactor power levels the actual power is not very accurately known. It may also be true that the G value of the reaction of H_2O with graphite is somewhat higher than reported. Therefore, some combination of increased radiation dose rate and $G(CO_2)$ is required to predict the high CO_2 levels. With these assumptions, reasonable agreement with measured concentrations of H_2O, CO, and CO_2 are achieved, but the predicted H_2 yield is far too high. A close evaluation of the reactor gas compositions shows that the H_2 concentration varies inversely with the O_2. We therefore conclude that H_2 is being limited by the radiolytic reaction of H_2 with O_2, a reaction process not included in the mathematical model. This reduction in H_2 would also tend to limit the CH_4 generation rate and thus explain the high predicted CH_4 level. Future tests should demonstrate the validity of these conclusions when the O_2 and N_2 impurities are eliminated.

Several adjustments have already been made in the input to the GOP code to enable it to predict the measured data. As more data are obtained, it is anticipated that further refinements will be necessary.

5.3 COMPUTER SIMULATION OF LABORATORY-SCALE STEAM-GRAPHITE REACTION EXPERIMENTS — A. P. Malinauskas, D. S. Joy, and S. C. Stem

Although most computational programs that have been developed to account for the effects of steam ingress into the primary coolant of an HTGR take into account the diffusional processes that are involved, these processes are generally ignored in analyses of laboratory-scale reaction rate data. This is ironic, since the purpose of the laboratory studies is usually to provide rate data to be used as input to the computational programs. Furthermore, unless a special effort is made to eliminate diffusion effects in the laboratory-scale experiments — for example, by limiting the studies to low temperatures or by selecting graphites that

are impermeable to steam — the mathematical aspects rapidly become unwieldy, and resort must be made to the use of computational techniques to assist in the analysis of the experimental data. One solution is to adapt the extant computer codes that are employed to investigate steam ingress effects in the HTGR. This approach is impractical, however, since steam-graphite reaction kinetics is a relatively minor consideration in these somewhat sophisticated codes, and moreover major modifications would nonetheless still be required to reduce the complex reactor core geometries modeled by these codes to the very simple configurations that are employed in the laboratory. As a consequence, we have elected to develop a much simpler code to model the laboratory experiments directly. A report that describes this computational program has been issued. An abstract of this report[2] follows:

> A mathematical model has been formulated to describe the isothermal, steady-state diffusion and reaction of steam in a graphite matrix. A generalized Langmuir-Hinshelwood equation is used to represent the steam-graphite reaction rate. The model also includes diffusion in the gas phase adjacent to the graphite matrix. A computer program, written to numerically integrate the resulting differential equations, is described.
>
> The coupled nonlinear differential equations in the graphite phase are solved using the IBM Continuous System Modeling Program. Classical finite difference techniques are used for the gas-phase calculations. An iterative procedure is required to couple the two sets of calculations. Several sample problems are presented to demonstrate the utility of the model.

5.4 REFERENCES

1. R. E. Woodley, *The Radiolytic Reaction of Graphite with Water Vapor*, BNWL-SA-1804 (April 1968).
2. D. S. Joy and S. C. Stem, *A Computer Simulation of the Steam-Graphite Reaction Under Isothermal and Steady-State Conditions*, ORNL-TM-4854 (May 1975).

6. HTGR FUEL QUALIFICATION

F. J. Homan

6.1 INTRODUCTION

The work described in this chapter is supported by the Fueled Graphite Development Program and the Thorium Utilization Program. The work supported by the Thorium Utilization Program is also reported in the progress report for that program (ORNL-5128).

The HTGR Fuel Development Program is organized around four goals. They are: (1) qualification of reference initial and makeup (IM) fuel and processes, (2) qualification of reference recycle fuel and processes, (3) qualification of backup fuels and processes to the developmental references, and (4) characterization, testing, and development in support of irradiation performance evaluations. Most of the effort associated with the ORNL program is directed toward goals (2) and (4), complementing the General Atomic Company program, which is directed mainly at goals (1) and (3). Both the ORNL and GA programs are coordinated with a third program for advanced HTGR fuel development at Los Alamos Scientific Laboratory (LASL). Irradiation space in the High Flux Isotope Reactor (HFIR) and Oak Ridge Research Reactor (ORR) is shared with LASL and GA. Some postirradiation examination (PIE) and data analysis work are done at ORNL in support of LASL and GA programs.

Most of the irradiation testing in support of HTGR fuel development has been done under accelerated conditions. Full fast-neutron exposure can be reached in about four months in the HT capsules, about ten months in the HRB capsules the way they are being operated now, and about 15 months in the ORR capsules. The Peach Bottom Elements were irradiated under real-time conditions, but the reactor was shut down in October 1974 so that the Recycle Test Elements (RTE) then under irradiation received only about half design exposure. During this reporting period an experiment was planned for the Fort St. Vrain Reactor (FSVR) in which test fuel would be loaded into standard FSVR fuel elements. In the ORNL portion of this experiment

fuel would be irradiated for 2, 4, and 6 years. Lead capsules in the ORR and HFIR would contain the same fuel so that performance under real-time conditions can be compared with performance under accelerated conditions. This very important experiment is expected to validate the conclusions that have been formed about the irradiation performance of coated particle fuels from accelerated experiments.

6.2 FUEL PARTICLE PROCESS DEVELOPMENT AND QUALIFICATION

The work described in this section is of interest to and is supported by both the HTGR Base Program and the Thorium Utilization Program. In the section on resin kernel studies, both carbonization and conversion studies are reported. The important phenomenon of fuel dispersion in the buffer coating is discussed and explained. Retained nitrogen in the kernels is reported. Both the Amberlite and Duolite resins are discussed.

In the section on coating process development, both pyrocarbon (PyC) and SiC coatings are considered. Deposition of PyC coatings with alternate coating gases is discussed, and experiments to determine the influence of various coating parameters are described. The important attribute of PyC permeability is also explored. The SiC coating studies have determined the relationships between coating rate, coating gas concentration and flow rate, coating temperature, and microstructure. Experience with several coating gases for deposition of SiC is also described.

6.2.1 Resin Kernel Studies — G. W. Weber

The current reference fissile kernel for both fresh and recycle fuel is derived from an acrylic acid-divinyl benzene copolymer loaded with uranium from uranyl nitrate. Processing of this material requires first a destructive distillation or *carbonization* procedure, which yields UO_2 dispersed in a porous carbon matrix, followed by a carbothermic reduction or *conversion* step, in which a controlled amount of the UO_2 is converted to UC_2 to optimize irradiation performance. The objective of the studies is to optimize the processes for carbonization and conversion of the loaded and dried resin microspheres.

The carbonization process can be optimized by defining critical reaction regions and appropriate control parameters. The differential thermal analysis (DTA) and thermogravimetric (TGA) behavior shown in Figs. 6.1 and 6.2, respectively, for two candidate resins, Duolite C-464 and Amberlite IRC-72, indicate the importance of the region from 200 to 500°C. Investigation of the weight loss, volume loss, and density at selected temperatures during this carbonization process produced property variations closely reflecting the TGA and DTA behavior, as shown in Fig. 6.3. A similar variation was found in particle size, as shown in Fig. 6.4, and in mercury density.

The heating rate through this critical carbonization region had a very strong effect on weight loss, volume loss, and carbon-to-uranium ratio. The final weight loss and volume loss for both resins are approximately linear with log heating rate for heating rates from 1 to 80°C/min through the critical process range, which was subsequently identified as 360 to 440°C for the Duolite resin. The variation of carbon-to-uranium ratio with carbonization rate behaved similarly for the two resins as shown in Fig. 6.5.

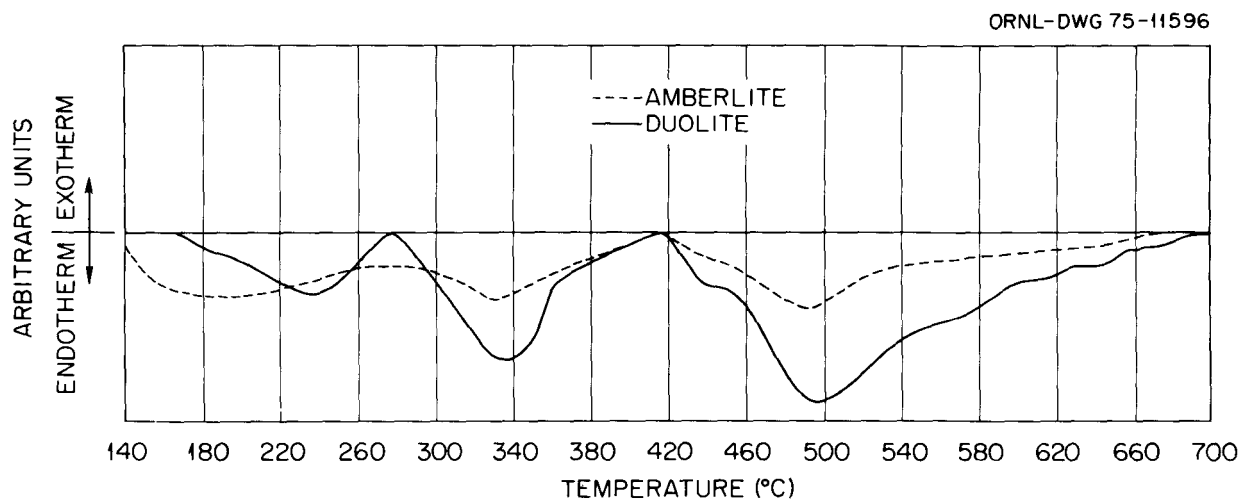

Fig. 6.1. Differential Thermal Analysis Behavior of Uranium-Loaded Duolite C-464 and Amberlite IRC-72 Weak-Acid Resins.

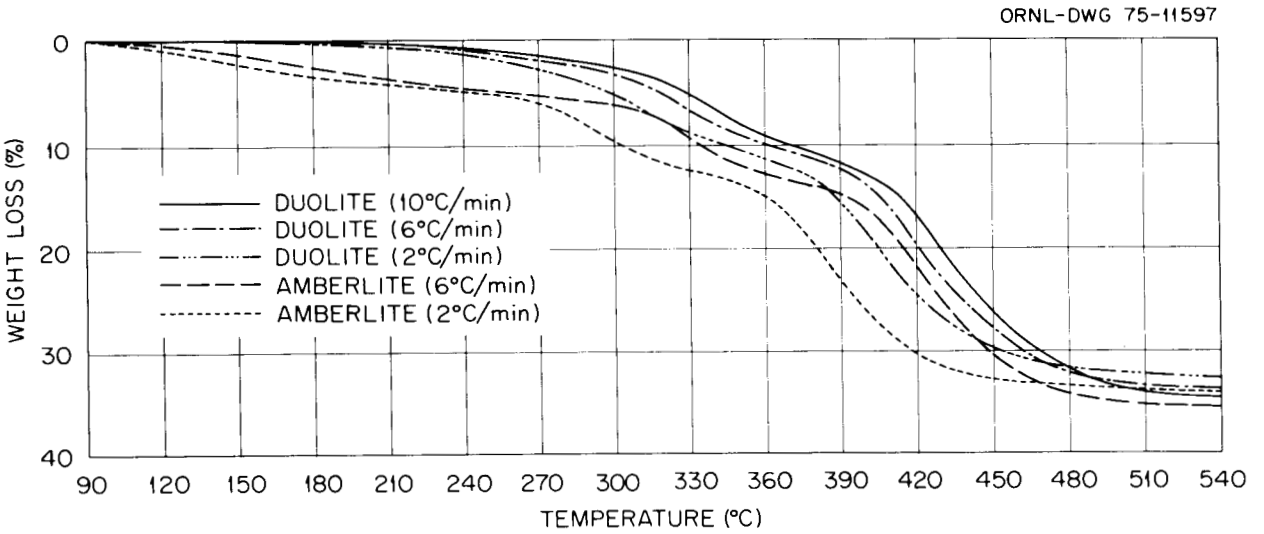

Fig. 6.2. Thermogravimetric Behavior of Uranium-Loaded Duolite C-464 and Amberlite IRC-72 Weak-Acid Resins from 90 to 540°C as a Function of Heating Rate.

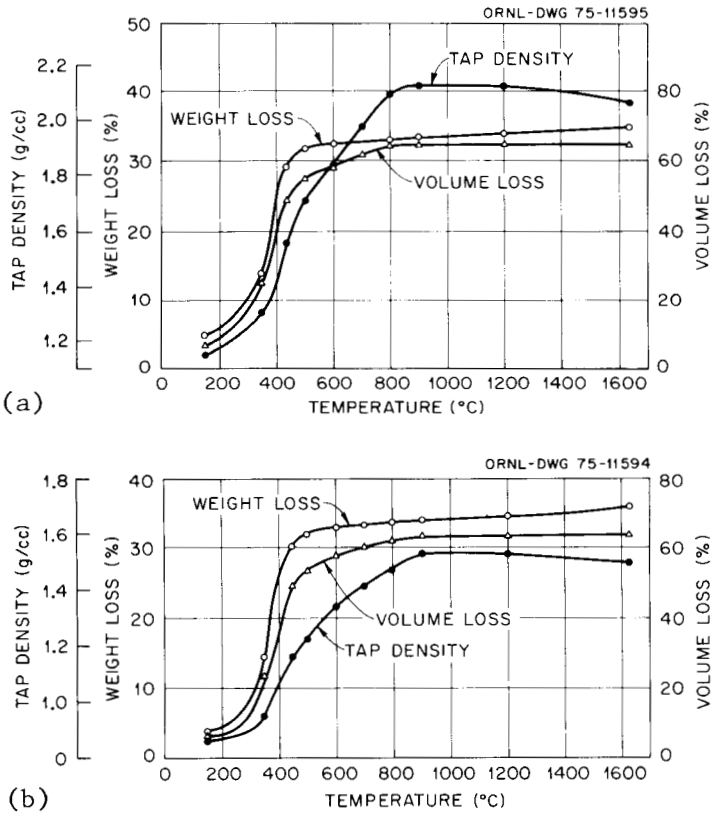

Fig. 6.3. Weight Loss, Volume Loss, and Tap Density Variation from 150 to 1625°C for Uranium-Loaded Weak-Acid Resin. (a) Amberlite IRC-72. (b) Duolite C-464.

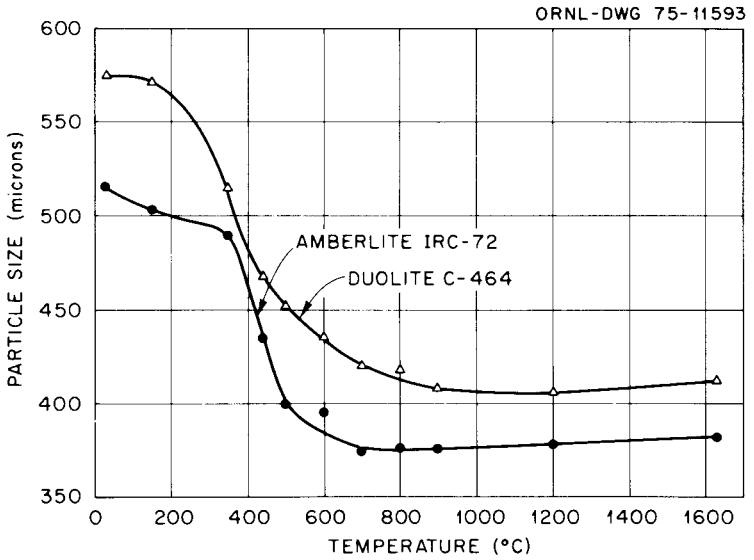

Fig. 6.4. Variation in Particle Size of Uranium-Loaded Duolite C-464 and Amberlite IRC-72 Weak-Acid Resins from 25 to 1625°C.

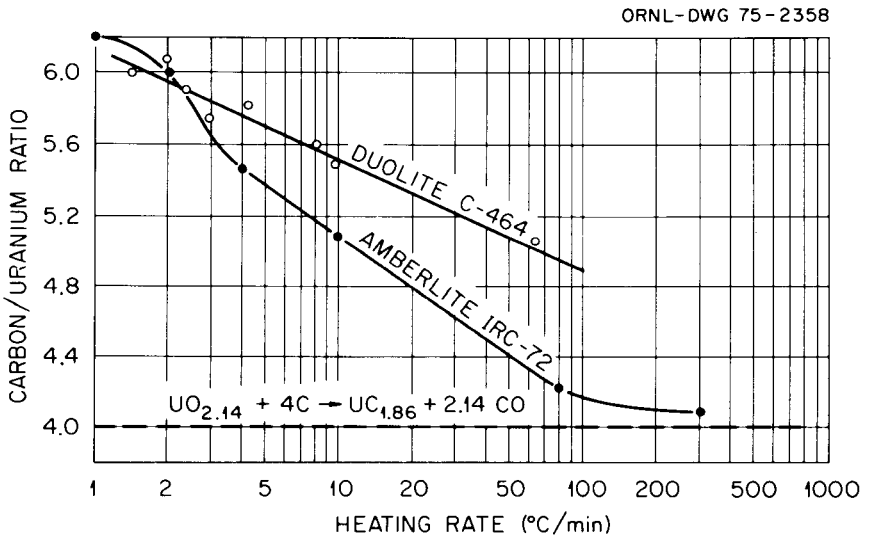

Fig. 6.5. Comparison of Carbon-to-Uranium Ratio of Carbonized (1200°C) Uranium-Loaded Weak-Acid Resins as a Function of Critical Range [Duolite (360–440°C), Amberlite (200–500°C)] Heating Rate.

The carbon-to-uranium ratio is significant in defining the fluidization behavior of the material during the subsequent conversion step. An excess of carbon is required to successfully complete this step without agglomeration. Experiments have demonstrated that a carbon-to-uranium ratio greater than about 5.8 is necessary to prevent agglomeration during typical conversion operations. The Duolite C-464 material exhibited less tendency to agglomerate during conversion because of its slightly higher carbon-to-uranium ratio.

Partial conversion of the UO_2 to UC_2 at 1600 to 1700°C in accordance with the applicable reactions is controlled by the partial pressure of CO over the material. The high available surface area (BET $\approx$ 150 m^2/g) and extensive interconnected porosity (0.015 μm diam for IRC 72 and 0.05 μm diam for C-464) of the carbonized kernels permit prediction of the rate of the UO_2 conversion to UC_2 under given conditions of specific gas flow rate and temperature. Debye-Scherrer examination of kernels processed to various conversion levels has shown that the partially converted material is a mixture of UO_2, UC_2, and UC_xO_{1-x}. The amount and proportion of the various phases can be controlled by temperature variation and by addition of hydrogen or carbon monoxide to the fluidizing gas stream.

The presence of these phases suggests the potential for uranium volatilization during conversion. However, measurements with a water-cooled collector have indicated that only about 0.035% U loss occurs during conversion under worst case circumstances. Although uranium loss during carbonization involves an aerosol that is difficult to collect, analysis has yielded a uranium loss of 0.02% during a very fast carbonization cycle under a worst case situation.

Microradiographic examination of coated WAR particles has demonstrated that under certain conditions a considerable quantity of uranium can be transferred from the kernel to the buffer coating during fabrication. This occurred during annealing of inner LTI coated particles at 1800°C and also during SiC coating. X radiographs showing the extent of uranium dispersion for the particles prepared for irradiation testing appear in Fig. 6.6. About half the particles from the two

Y-128988

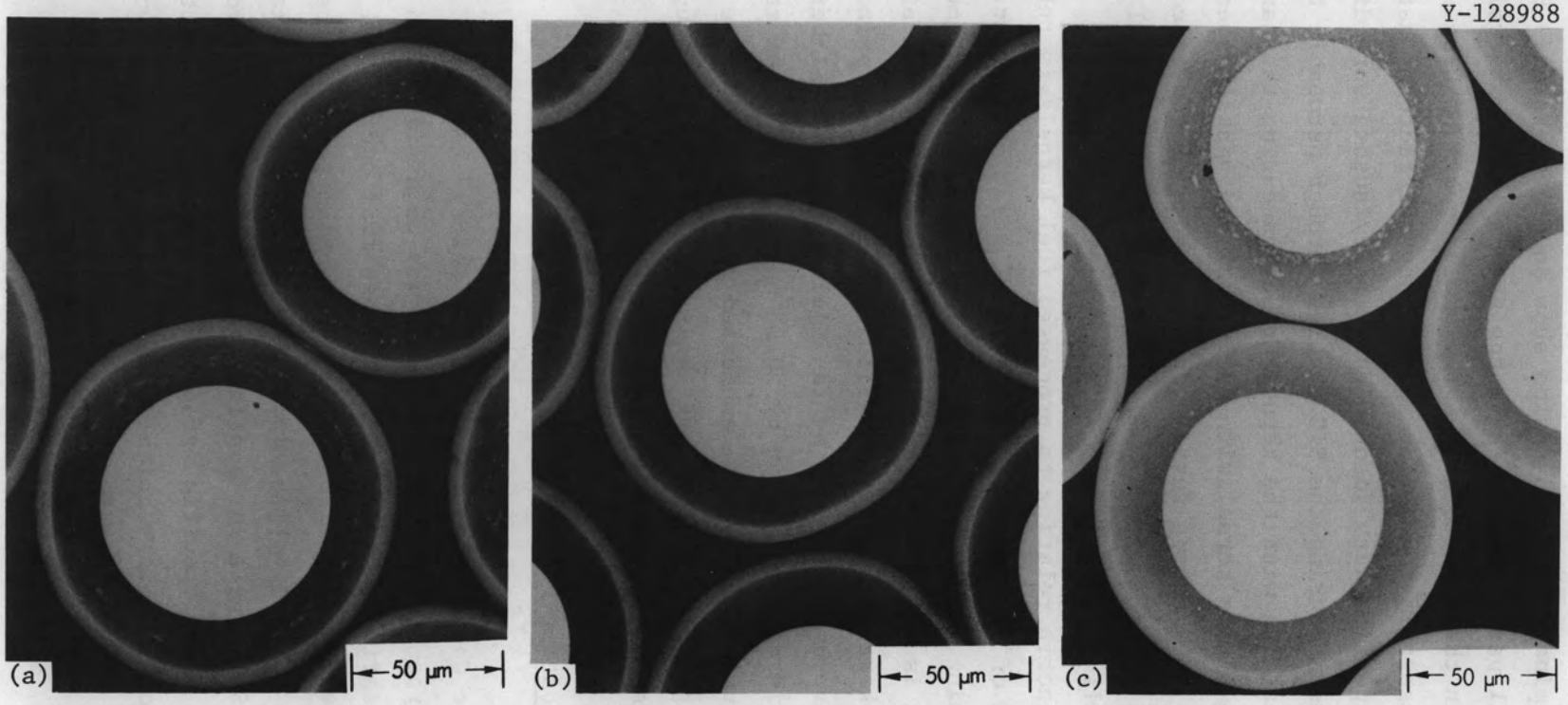

Fig. 6.6. X Radiographs of SiC-Coated Resin Showing Uranium in the Buffer Coating Layer of the Two Nominally 75%-Converted Batches. (a) Frit distributor, 69.4 ± 2.1% converted. (b) Frit distributor, 12.6 ± 2.5% converted. (c) Cone distributor, 76.6 ± 2.6% converted.

batches having nominally 75% conversion show some dispersion. However, only an occasional particle from the batch having 12.6% conversion showed dispersion, and in these cases only a few small specks of uranium-bearing material were present in the buffer layer. Several factors that can cause uranium dispersion were identified. These factors were diffusion of HCl or Cl_2 present during the SiC coating through permeable LTI coatings and subsequent reaction with the kernel, reaction during the carbon coating operation of the kernel with C_2Cl_4 that had backstreamed from the scrubber into the coating furnace, and exposure of converted kernels to the atmosphere before coating. A report describing the fuel dispersion work in more detail is available.[1]

A further concern relating to processed fuel kernels is retained nitrogen, because of the transmutation to ^{14}C, which must be accommodated in fuel reprocessing. Thus the effect of the uranium loading method on retained nitrogen is a factor in selecting the process flowsheet. Comparative data on kernels loaded by various schemes and carbonized in a similar manner have been obtained by the Kjeldahl method. Amberlite (H^+ form) with acid neutralization by NH_4OH has shown 800 ppm retained nitrogen, while Duolite (NH_4^+ form) exhibited 1200 ppm N. These values are considered significant because of their high levels, although the Kjeldahl method is not sensitive to low nitrogen levels.

6.2.2 Particle Coating Process Development

6.2.2.1 Pyrolytic Carbon Deposition — R. L. Beatty

Pyrolytic carbon (PyC) coating studies may be divided into three areas: (1) optimization of the coating process from operational considerations, (2) variation of coating process parameters to determine effects on measurable properties, and (3) fabrication of irradiation test specimens. Since relevant coating parameters for the third area will be addressed under specific irradiation experiments in Sects. 6.5 and 6.6, discussion in this section will relate to the first two areas.

6.2.2.1.1 Process Development. The major work conducted on PyC coating process development involved use of the source hydrocarbon MAPP gas to replace the widely used propylene for deposition of LTI coatings. MAPP gas is marketed by Airco, Inc., primarily to replace acetylene as a metal fabrication fuel gas.[2] Preliminary studies showing the suitability of MAPP for LTI deposition have been reported previously.[3] Calculations involving reaction enthalpies and heat capacities showed that MAPP should effect approximately 50% as much heat absorption as does propylene during the coating process.

To confirm the heat balance calculations the relative bed cooling effects of MAPP and propylene were demonstrated experimentally by using each gas undiluted to coat a 500-g batch of thoria in a 64-mm-diam (2 1/2-in.) coater. Each run was monitored simultaneously by the thermocouple immersed in the center of the bed 61 mm (2 3/8 in.) above the gas inlet and by an optical pyrometer viewing the coating chamber wall opposite the thermocouple junction. With this arrangement, the thermocouple and pyrometer recorded virtually identical temperatures while the bed was fluidized with argon. Thus, when coating gas was substituted for argon, the difference between thermocouple and pyrometer readings provided a relative measure of coating gas thermal effects. This difference between bed-center and chamber-wall readings was nearly twice as great for propylene as for MAPP gas. Thus in this particular experiment, deposition efficiency was slightly higher and density slightly lower for MAPP deposits since these parameters are highly temperature sensitive and the coating runs were controlled at the same wall temperature. Subsequent experiments in which wall temperatures were adjusted to provide the same average bed temperature showed the deposition efficiency and coating density to be essentially identical for MAPP and propylene.

During this period, MAPP gas has been used routinely for deposition of LTI coatings in laboratory coaters for preparation of irradiation test specimens. The reason for changing the process from propylene to MAPP is the improved temperature control possible with MAPP. The decision to employ MAPP rather than the alternative, blending acetylene and

propylene, to improve the coater heat balance was made for two reasons. Since most previous successful irradiation test experience had been with propylene-derived coatings, the propylene process should be viewed as a reference. On this basis the methylacetylene (propyne) and propadiene, which provide the favorable reaction enthalpy in MAPP, represent a more modest departure from established practice than does the addition of acetylene. The second reason for employing MAPP, though less important than the first, is that MAPP (like propylene) is handled as a liquid under its own vapor pressure. It is thus more convenient and safer to supply MAPP than large quantities of acetylene. The excellent irradiation performance demonstrated by MAPP-derived coatings during the past year verifies the acceptability of this process.

6.2.2.1.2 Effect of Varying Process Parameters on Coating Properties. An experiment was conducted to systematically determine effects of varying process parameters on the measurable properties of LTI coatings and on the process itself. The experiment was planned to provide a range of LTI microstructures for development of characterization techniques (see Sect. 6.4) and to provide test specimens for irradiation capsules HT-28, -29, and -30 (see Sect. 6.5.6).

Coating parameters varied included deposition temperature, MAPP gas concentration, total fluidizing gas flow rate, and bed volume (surface area). An objective of particular interest in this study was to independently vary hydrocarbon concentration and deposition rate. Since deposition rate is primarily a function of hydrocarbon flux, this necessitated varying the total gas flux or fluidizing flow relative to charge surface area.

To achieve the desired range of total gas fluxes, we varied both charge volume and density relative to standard run conditions for the 64-mm (2.5-in.) laboratory coater, as shown in Table 6.1. The more or less standard runs, footnoted *g* in Table 6.1, employed a 350-g, 125-cm^3 charge of buffer-coated thoria. To obtain higher hydrocarbon flux at a given concentraion, we decreased the charge by approximately half (footnote *f*, Table 6.1); to obtain lower hydrocarbon flux at the

Table 6.1. Deposition Parameters, Densities, and OPTAF Values of LTI Coatings[a] Prepared for Irradiation Experiments HT-28, -29, and -30

MAPP Gas[b]		Deposition			Density,[c] g/cm³			OPTAF[d]	Batch
Concentration (%)	Flux (cm³/min-cm²)	Temperature (°C)	Rate (μm/min)	Efficiency[e] (%)	As Deposited	After 15 min at 1800°C	Increase		
100	5.57[f]	1275	23.0	46.4	1.989	2.053	0.064	1.02	OR-2275-AHT
100	2.86[g]	1275	14.1	56.6	1.973	2.019	0.046	1.02	OR-2266-HT
100	1.35[h]	1275	7.3	60.4	1.948	1.982	0.034	1.02	OR-2291-HT
100	0.77[h]	1275	4.9	62.2	1.924	1.975	0.051	1.01	OR-2297-AHT
100	5.57[f]	1325	28.0	49.8	1.948	1.957	0.009	1.01	OR-2274-HT
100	2.86[g]	1325	15.7	60.8	1.918	1.949	0.031	1.01	OR-2265-HT
100	1.35[h]	1325	8.6	64.5	1.868	1.882	0.014	1.01	OR-2290-HT
100	0.77[h]	1325	5.6	66.2	1.854	1.898	0.044	1.01	OR-2296-AHT
50	2.93[f]	1275	10.7	42.1	1.974	2.015	0.041	i	OR-2271-HT
50	1.43[g]	1275	6.5	54.9	1.966	2.009	0.043	1.01	OR-2262-HT
50	0.68[h]	1275	3.6	55.9	1.934	1.961	0.027	1.02	OR-2294-HT
50	0.38[h]	1275	2.3	53.0	1.888	1.910	0.022	1.02	OR-2299-HT
50	2.93[f]	1325	12.5	45.7	1.884	1.908	0.024	1.01	OR-2269-HT
50	1.43[g]	1325	7.4	56.0	1.853	1.886	0.033	1.01	OR-2261-HT
50	0.68[h]	1325	3.9	58.5	1.813	1.832	0.019	i	OR-2293-HT
50	0.38[h]	1325	2.5	57.7	1.806	1.823	0.017	1.01	OR-2298-HT
25	1.46[f]	1275	5.2	43.2	1.968	2.009	0.041	1.01	OR-2273-HT
25	0.73[g]	1275	3.2	52.5	1.950	1.986	0.034	1.02	OR-2264-HT
25	0.34[h]	1275	1.8	54.9	1.897	1.912	0.015	1.02	OR-2295-HT
25	1.46[f]	1325	6.2	43.1	1.840	1.860	0.020	1.01	OR-2272-HT
25	0.73[g]	1325	3.6	54.4	1.816	1.837	0.021	1.01	OR-2263-HT
15	0.84[f]	1275	3.1	41.1	1.945	1.977	0.032	1.02	OR-2276-HT

[a]Deposited on fertile particles of nominal design 500-μm ThO_2 kernel, 85-μm buffer, 85-μm LTI.

[b]MAPP gas is marketed by Airco, Inc., and consists primarily of methylacetylene and propadiene with alkanes as stabilizers.

[c]Measured by gradient column technique.

[d]Measured in twofold symmetry (without analyzer), after heat treatment.

[e]Deposition efficiency is weight of carbon deposited on particles relative to weight of carbon supplied to bed.

[f]High flux obtained by using approximately half the usual charge volume.

[g]Typical flux on 350-g, 125-cm³, charge of buffer-coated fertile particles in 64-mm (2.5-in.) coating tube.

[h]Low flux obtained for given concentration by diluting bed with low-density carbon particles to reduce fluidizing flow requirement.

[i]Not determined.

same concentration, we blended low-density carbon particles with the thoria to reduce the flow rate required for fluidization (footnote *h*, Table 6.1). After coating, the carbon particles were separated from the thoria by flotation. The coating conditions achieved by carbon dilution of the bed are of particular interest because they simulate coating conditions for fissile particles.

The deposition parameters and observed densities and optical anisotropies (OPTAF) for the series of coatings prepared in this experiment are shown in Table 6.1. From these data the following observations were made.

1. *Deposition rate* varies primarily with hydrocarbon flux and secondarily with deposition temperature and hydrocarbon concentration.

2. *Deposition efficiency* increases rapidly with increasing charge volume, within the range of conditions employed. It generally increases slightly with decreasing flux, is higher for undiluted hydrocarbon than for concentrations of 50% or less, and increases with increasing temperature.

3. *Density* decreases with increasing deposition temperatures, generally decreases with decreasing gas flux, generally decreases with decreasing hydrocarbon concentration down to about 25%, then increases at lower concentration.

4. *Heat treatment* at 1800°C significantly densifies all LTI coatings, with the density increase being greater for lower deposition temperature.

5. *OPTAF* values are very low and nearly invariant for coatings deposited from MAPP gas regardless of deposition conditions within the range employed.

In a different experiment an additonal area investigated was the effect of process variables on LTI coating permeability. Previous work has shown that LTI-type coatings may have surface-connected porosity up to 15 μm deep in high-density PyC and may be permeable in any thickness of lower density PyC. In the fabrication of Triso-coated particles, this possible permeability is of particular concern in the inner LTI due to possible HCl leaching of fuel during SiC deposition.

With the objective of defining the inner LTI thickness and density requirements to assure that no fuel leaching can occur, the set of specimens shown in Table 6.2 was prepared using resin-based kernels. The seal coat indicated is a surface impregnation done at the end of LTI deposition to decrease surface roughness for SiC deposition. The seal coat is applied by lowering the coater temperature from 1275 to 1125°C and coating for about 1 min with a 50% MAPP gas concentration. The seal coat is routinely applied in preparation of irradiation test specimens. It results in appreciable bed weight gain but only very slight volume increase.

Table 6.2. Biso-Coated WAR Particles Tested for Gaseous Leaching of Uranium

Batch	Kernel Conversion (%)	Thickness, μm		Seal Coat	LTI Density[a] (g/cm^3)
		Buffer	LTI		
OR-2343	0	46.0	39.2	No	1.955
OR-2344	0	46.7	43.1	Yes	1.955
OR-2346	50	46.8	39.5	No	1.958
OR-2347	50	48.5	40.8	Yes	1.964

[a]Measured by gradient column.

High-temperature leaching was carried out on either 10- or 15-g samples. Results are shown in Table 6.3. In the first experiment, all four batches were leached at 1500°C in Cl_2 for 4 hr in 2-hr increments. The amount of uranium removed varied among the four batches, but in all cases the amount was very significant and was about the same for the second 2-hr period as for the first. This suggests a continuous steady-state leach rate characteristic of each batch. After the 4-hr leach, radiographs of all batches showed uranium dispersed in the buffer and concentrated at the buffer-LTI interface, further suggesting that the kernels had indeed been attacked by CL_2. No fuel dispersion was observed in the buffers before leaching. These data are too few to be conclusive, but they do suggest that the seal coat applied to the outside of the LTI reduced its permeability and that the 50%-converted kernels are more susceptible to Cl_2 attack than are the unconverted kernels.

Table 6.3. Uranium Removed from Biso-Coated WAR Particles by Gaseous Leaching

Batch	Fraction of Uranium Removed from Particles				
	1500°C in Cl_2		1250°C in Cl_2		1500°C in Ar
	2 hr	4 hr	2 hr	4 hr	4 hr
	$\times 10^{-4}$		$\times 10^{-4}$		$\times 10^{-4}$
OR-2343	1.18	2.62	0.54	0.68	0.42
OR-2344	0.53	1.03			
OR-2346	1.97	3.87			
OR-2347	1.62	2.99			

Since leaching for several hours in Cl_2 at 1500°C may be a more severe test than is necessary to qualify fuel and since effects on the LTI microstructure by Cl_2 are unknown, two further experiments were done. As shown in Table 6.3, one of the batches was leached in Cl_2 at 1250°C and in argon at 1500°C. The 1250°C Cl_2 leach removed about half as much uranium during the first 2 hr as did the 1500°C leach and much less during the second 2-hr period. The 4-hr treatment in argon at 1500°C removed about one-sixth as much uranium as the similar treatment in Cl_2. No evidence of damaged coatings was found in any of the experiments.

In summary, these results indicate that the standard LTI coatings are permeable to some extent, that fuel can be removed continuously through intact coatings by Cl_2 at 1500°C, and that leaching in Cl_2 at 1500°C may be too severe a test treatment (i.e., a lower temperature may be more realistic). Further experiments are needed at different temperatures for shorter and longer times, and on LTI coatings of different thickness and density to clearly establish required LTI characteristics.

6.2.2.2 SiC Deposition Process Development — J. I. Federer

Most of the laboratory-scale SiC process development activities consisted of evaluating the effects of coating conditions on coating characteristics when methyltrichlorosilane (MTS) is used as the source

for SiC. The principal variables of MTS flux, H_2/MTS ratio, and temperature were varied over wide ranges in search of trends: MTS flux was varied from 0.03 to 1.3 cm^2/min; H_2/MTS ratio was varied from 5 to 44; temperature was varied from 1225 to 1775°C. The results of this work may be summarized as follows:

1. Coating rate is affected by each of the principal variables; however, H_2/MTS ratio and temperature also affect density, whereas coating rate does not. A highly dense SiC coating can be obtained at optimum values of H_2/MTS ratio and temperature; the coating rate can then be conveniently varied by varying the MTS flux.

2. At optimum values of H_2/MTS ratio and temperature the coating rate is a linear function of MTS flux. Coating rates as high as 4 μm/min have been obtained.

3. Coating density is strongly affected by H_2/MTS ratio. Except for a few data points, the density appears to increase rapidly with increasing H_2/MTS ratio in the range 5 to 20, and is relatively insensitive to a further increase in H_2/MTS ratios. Coatings for irradiation testing were deposited at an H_2/MTS ratio of 30.

4. Since an H_2/MTS ratio of at least 20, and preferably higher, is needed for high density, the maximum coating rate is determined by the batch surface area and the coating tube size. The maximum coating rate occurs at the greatest MTS flux (and corresponding H_2/MTS ratio) that does not eject microspheres out of the coating tube. A coating rate of 1 μm/min appears to be practical in the small coating tubes used in this work. Significantly higher rates would likely require trade-offs among flow rates, batch surface area (batch size), and coating tube size.

5. The microstructure is also strongly affected by H_2/MTS ratio and temperature, but not by coating rate. Figure 6.7 shows that as the H_2/MTS ratio is varied from 5 to 25 the microstructure changes from a disorganized mass to a striated structure and finally to a grain structure. Although not evident in the microstructures, the amount of porosity decreases with increasing H_2/MTS ratio. Similarly, Fig. 6.8 shows that as temperature is increased from 1375 to 1775°C the microstructure changes from a striated structure (containing excess silicon) to a dense grain structure, and finally to a coarsely crystalline structure containing gross porosity.

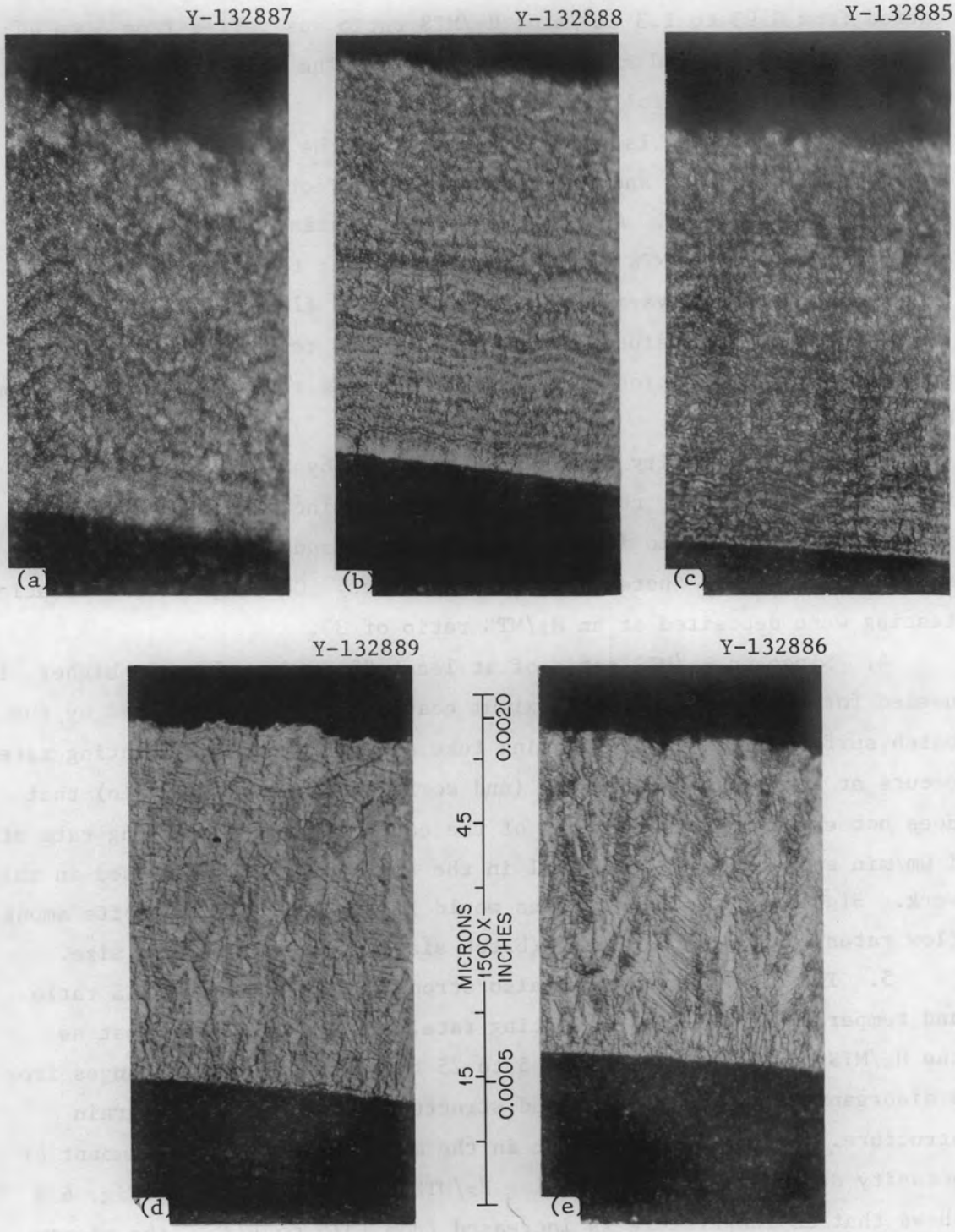

Fig. 6.7. Microstructures of Silicon Carbide Coatings Deposited at 1575°C at Various Ratios of Hydrogen to Methyltrichlorosilane. (a) 5. (b) 10. (c) 14. (d) 20. (e) 25.

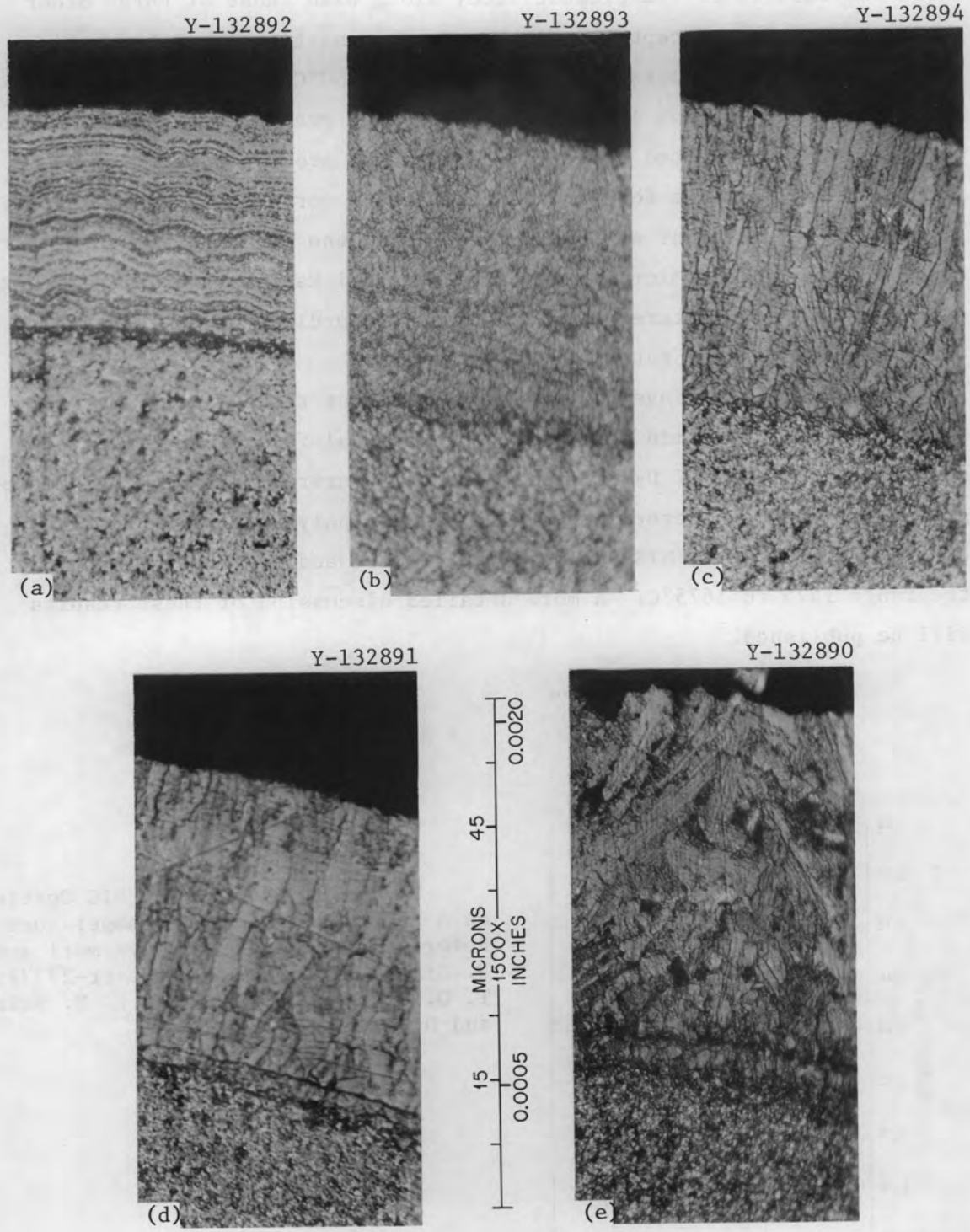

Fig. 6.8. Microstructures of Silicon Carbide Coatings Deposited at Various Temperatures and Hydrogen-to-Methyltrichlorosilane Ratio of 30. (a) 1375°C. (b) 1475°C. (c) 1575°C. (d) 1675°C. (e) 1775°C.

6. Coating density is strongly affected by temperature. Figure 6.9 shows the results of the present study along with those of three other investigators.[4—6] Except for one case[5] the densities exhibited maximum values in the temperature range 1500 to 1650°C. Coatings deposited below about 1400°C have low density due to the presence of excess silicon, while coatings deposited above 1700°C may have gross porosity, as shown in Fig. 6.8. Coatings for irradiation testing were deposited at 1575°C.

7. Heat treatment at 1800°C for 30 min, the standard treatment for consolidating coated microspheres into fuel sticks, does not significantly affect the microstructure of SiC coatings, regardless of the coating conditions or coating rate.

In summary, coatings have been deposited at rates up to 4 μm/min. A rate of about 1 μm/min appears to be practical for reasonable batch sizes. The effects of H_2/MTS ratio and temperature on density and microstructure have been determined. Highly dense polycrystalline coatings can be prepared at H_2/MTS ratios of 20 or more and at temperatures in the range 1475 to 1675°C. A more detailed discussion of these results will be published.[7]

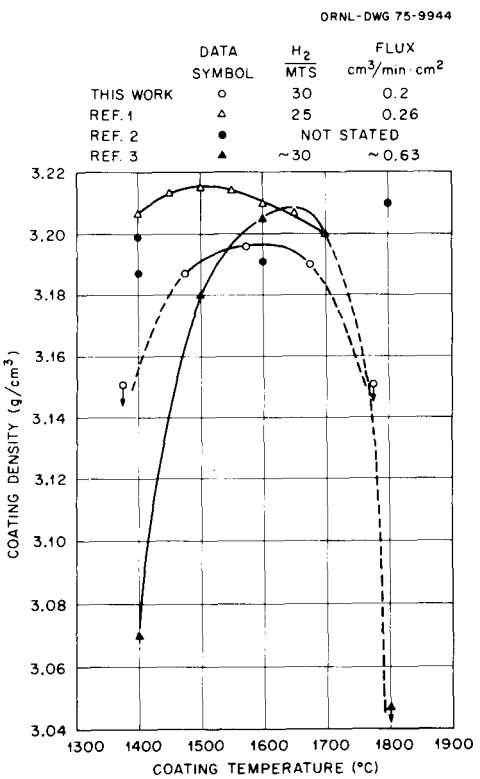

Fig. 6.9. Density of SiC Coatings as a Function of Coating Temperature. References cited are: E. Gyarmati and H. Nickel, JÜL-900-RW (ORNL-tr-2733); T. D. Gulden, GA-8275; and E. H. Voice and D. N. Lamb, DP-677.

6.2.2.3 Evaluation of Compounds Other than MTS — J. I. Federer

We are investigating the feasibility of depositing SiC from sources other than MTS (CH_3SiCl_3) because of the corrosive nature of the by-product HCl from this compound. A source compound containing less chlorine than MTS would be desirable; one with no chlorine would be preferred. Some possible compounds are silane (SiH_4), tetramethylsilane [$Si(CH_3)_4$], methylchlorosilane (CH_3SiH_2Cl), and methyldichlorosilane (CH_3SiHCl_2).

Our brief experience with SiH_4 can be summarized as follows. SiH_4 is very unstable, and it decomposes to Si and H_2 at low temperatures. In one experiment a SiC coating was deposited at 800°C from SiH_4 and acetylene (C_2H_2) in a bed fluidized with hydrogen. Large amounts of hydrogen are required to control this decomposition in a fluidized bed, and this has not always been completely successful. The possibility exists, however, of preparing SiC where the only by-product is hydrogen rather than HCl. Silane is also quite flammable and very expensive compared with MTS.

Our experience with $Si(CH_3)_4$ may be summarized as follows. Coatings of SiC have been deposited at temperatures in the range 1000 to 1500°C. However, the coatings were porous and contained excess carbon. Similar results were obtained with either hydrogen or argon as the fluidizing gas. No coatings were prepared with the acceptable density and microstructural integrity of coatings prepared from MTS, and much additional work would probably be required to achieve such a result.

6.3 FUEL ROD FABRICATION DEVELOPMENT AND QUALIFICATION — R. L. Hamner and O. J. Horne

In-block carbonization of fuel rods is now part of the reference fabrication process for large HTGR fuel elements. A limited program was initiated as a backup for in-block carbonization wherein it was proposed that a quickly thermosetting resin be used as a binder that would be amenable to the slug-injection process and would permit carbonization of fuel rods in graphite trays without additional mechanical support to prevent deformation. Such a process might offer certain advantages

in that sticking to the block should be minimal and the carbonized and heat-treated fuel rods could be inspected before insertion into the fuel block.

Three powder-type thermosetting resins, all of similar characteristics, were received from Hercules, Incorporated, for investigation. These were polyphenylene resins designated as the "H-type" that have low melt-flow temperatures (60—100°C), low viscosities at 120°C, and high coke yields (85—90%). Their properties overall suggested that they were suitable for the slug injection process. The principal variables studied were matrix composition, blending, injection time and temperature, cure time in the mold, and carbonization cycles.

The fillers used were natural graphite powder (Asbury Graphite Mills grade NF-6353) and a high-fired isotropic artificial graphite powder (derived from a Union Carbide Robinson graphite) added as 30 wt % in resin or resin-pitch mixtures (Ashland Oil Co. grade 240). The matrix components were blended both dry and with solvents such as toluene, trichloroethylene, and toluene-acetone mixtures. Injection times for a 13-mm-diam by 25-mm-long (0.5- by 2-in.) rod varied from 1 to 1.5 min, depending on the injection temperature. Forming temperatures were varied from 125 to 220°C, and cure time in the mold varied from 1 to 2.5 min. Carbonization heating rates were varied from 30 to 180°C/min. The results are summarized below.

1. Slurry blending of matrix components was much more satisfactory than dry blending; the latter resulted in very inhomogeneous mixtures. However, slurry blending posed the problem of having to remove all the solvent without heating; otherwise cracked rods resulted because of entrapped vapors. This was resolved by holding for 30 hr under vacuum.

2. The resins and resin-pitch mixtures as binders were very amenable to the slug injection fabrication process. However the use of resin alone resulted in severe cracking, apparently due to high shrinkage. This was alleviated somewhat by the addition of A-240 pitch. A nominal resin-pitch ratio of 1.0 was the most satisfactory from the standpoint of cracking and dimensional control. Higher ratios resulted in increased cracking. Ratios less than 0.75 resulted in rods that were not free standing during carbonization because of the excess of pitch.

3. Injection temperatures between 160 and 170°C were the most satisfactory. Temperatures below 160°C resulted in prohibitive hold times for partial cure. At temperatures above 170°C the matrix tended to polymerize during injection and could not be forced easily through the particle bed.

4. Nearly all specimens tended to have surface cracks, which increased with injection temperatures above 170°C and with hold times in the mold between 160 and 170°C for partial cures of 2 min or less.

5. Under the most favorable conditions for forming, a very slow heating rate (30°C/hr) was required to reduce cracking, and even then, the results were erratic.

6. Dimensional control of rods under the most favorable conditions of fabrication was reasonably good.

7. Matrix densities achieved were as high as 0.95 g/cm^3 and coke yields as high as 92%. Despite these features, however, the carbonized specimens were very weak and easily chipped. Metallographic examination showed that the matrix was badly cracked internally and matrix-coating interaction was severe.

We concluded that the "H-type" thermosetting resins were not satisfactory except for forming, although with the studies of these resins we have demonstrated that fuel rods formed within about the same time span for pitch-bonded rods could be free standing during carbonization. Other thermosetting resins, mostly phenolics, are now being investigated.

6.4 CHARACTERIZATION OF PYROCARBON COATINGS — V. J. Tennery, E. S. Bomar, J. P. Mathers,* C. S. Yust,† P. Krautwasser,‡ and R. L. Beatty

Characterization of pyrocarbon coatings in a manner enabling prediction of irradiation performance is a critical requirement for optimizing coating deposition processes, developing adequate coating

---

*Present address, Argonne National Laboratory, Argonne, Illinois.
†Work supported by Division of Physical Research, ERDA.
‡Work supported by KFA, Institut für Reaktorwerkstoffe, Jülich, FRG.

specifications, and assuring good irradiation performance. Our objective is therefore to develop a set of measurable parameters that can be uniquely correlated with irradiation performance as well as with fabrication conditions. Characterization effort has been concentrated on coating specimens prepared as sets for irradiation test experiments. These specimens were fabricated with coating deposition conditions systematically varied to provide ranges of microstructures for correlation with irradiation performance. Any characterization technique that can reveal structural differences that relate to irradiation survival is therefore of interest. Techniques under development include optical anisotropy (OPTAF), x-ray determination of the Bacon anisotropy factor (BAF), oxygen plasma etching, small-angle x-ray scattering (SAXS), transmission electron microscopy (TEM), and chemical characterization.

6.4.1 OPTAF Technique

We have continued the development reported previously[8] of an optical technique (OPTAF) for determining the anisotropy of pyrocarbon coatings on fuel particles. Problems with our system continued to make utilization of this method difficult, and the results obtained with it open to question. The major problems involved with measurement of particle coatings have been (1) the tendency for the measured curve of reflected intensity versus polarizer angle of near-isotropic pyrocarbon (PyC) to not have the symmetry predicted by the optical theory that is the basis for the measurement, and (2) the apparent critical requirements of specimen surface flatness. The causes for (1) and (2) can be eccentricity of the rotating specimen stage such that different specimen volumes are illuminated at different stage angles (or equivalent polarizer angles); the specimen surface normal varying from exactly parallel to the optic axis of the microscope as the sample is rotated; light depolarization due to scattering processes in the PyC surface; and possibly optical reflection effects unique to PyC that have not been reported by other workers.

A series of measurements was made on PyC coatings to assess the origin of the asymmetry effects often observed in the reflected light

intensity curves of near-isotropic pyrocarbons. The measurements were made on selected particles used in the loadings of the HT-17 through -19 series of irradiation experiments since those coatings were deposited with the express purpose of preparing PyC having a range of anisotropy. The basic criterion used in evaluating the OPTAF results was the symmetry of the curve of reflected light intensity as a function of specimen rotation angle. In order for the OPTAF technique to really be applied, this curve must have twofold symmetry if polarized light is used without an analyzer in the system. Results indicated that for PyC with an optical anisotropy ratio below about 1.06 it was difficult for the system to produce the required symmetrical curve. As the anisotropy decreased toward unity (isotropic condition), the amplitude of the measured curve decreased toward zero, and thus the precision of measurement became poor. Additionally, another characteristic of nearly isotropic PyC appeared to make the measurement difficult. The stage had a radial runout during rotation of about 4 μm and a vertical runout at least this large. Thus, during stage rotation, the same region of PyC was not illuminated by the 15-μm sampling beam at all times that the reflectivity was being measured. For highly anisotropic PyC, this is not too serious. However, for PyC with OPTAF less than about 1.10 this degree of stage eccentricity is apparently not acceptable. Local variations in the optical reflectivity of near-isotropic PyCs are significant on a scale of at least 4 to 5 μm. As a result, as the sample is rotated during the measurement, PyC having significantly different optical properties passes into and out of the sampling beam, distorting the measured reflectivity curve.

Comparative measurements were made on coatings of selected particles by manually rotating the microscope stage in 30° increments and repositioning the specimen field before each measurement, and by using the motor-driven stage rotation system. In all cases, reflectivity results obtained by manually rotating the stage exhibited the required twofold symmetry, whereas those obtained using the motor drive on the stage were either asymmetric or the maxima or minima had unequal intensities. Sample surface preparation also appeared to be quite critical for near-isotropic PyC coatings.

Conclusions drawn regarding the OPTAF system as well as this type of measurement in general were the following. The rotating stage of the existing system has mechanical imperfections that make it very difficult to use for measurements on near-isotropic PyC. The translational stage located on top of the rotating stage is too crude for precise positioning of a selected coating area to within a few micrometers. Factors that tend to disturb the measurement of near-isotropic PyC make it critically important that the symmetry of the reflected intensity curves be verified during a measurement. If the required two- and fourfold symmetry (for the case of crossed polarized-analyzer system) is not observed, interpretation of the reflected intensity is not possible.

With care exercised to circumvent the above equipment deficiencies, OPTAF measurements were made on PyC coatings that had also been characterized by selective etching and electron microscopy techniques. Evaluation of results of these techniques could thus be correlated with irradiation survival data. Numerous coatings produced in a 25-mm (1-in.) coater and 17 PyC samples produced in the 0.13-m (5-in.) coater were measured. Both twofold and fourfold OPTAF measurements were made on all the samples to obtain sufficient data to determine the relative merit of these two OPTAF parameters. Results for coatings made in the 0.13-m coater are given in Table 6.4. Eight of the coatings have been tested in irradiation experiments in the HFIR and ORR facilities. The coatings all have very low optical anisotropy. Postirradiation examination results on the indicated irradiation capsules will provide our first evaluation of the OPTAF technique for predicting the irradiation behavior of PyC coatings produced in the large coater. The other nine coatings indicated in Table 6.4 were produced in the 0.13-in. coater and were part of a statistical study of coated particle shape produced in the coater under systematically varied coating conditions. Specimens produced at the center and axial ends of the statistical design with no propylene diluent were selected for these measurements.[9] Increasing the propylene flow rate from 0.680 to 2.72 std liters/sec (1.44–5.76 scfm) at 1375°C with a batch charge of 1500 g resulted in a modest increase in OPTAF of the PyC from 1.02 (A-339) to 1.04 (A-369) (twofold measurement).

Table 6.4. OPTAF Values for PyC Fuel Particle Coatings Deposited from Propylene in a 0.13-m (5-in.) Coater

Sample	OPTAF[a]	Application
J-238	1.02	HRB-7, -8, and OF-1
J-262	1.02	HRB-7, -8, and OF-1
J-461	1.02	HT-26, -27
J-465	1.03	HT-26, -27
J-488	1.02	HT-30 and OF-2
J-489	1.01	HT-30 and OF-2
J-490	1.01	HT-30 and OF-2
J-491	1.01	HT-30 and OF-2
A-338	1.04	Statistical coater study
A-355	1.04	Statistical coater study
J-339	1.05	Annealed version of A-338
J-342	1.07	Annealed version of A-355
A-339	1.02	Statistical coater study
A-345	1.08	Statistical coater study
A-369	1.04	Statistical coater study
A-341	1.02	Statistical coater study
A-364	1.01	Statistical coater study

[a]Twofold measurement with 30 μm measuring aperture at 5470 Å.

Increasing the deposition temperature from 1225 to 1525°C at a propylene flow rate of 1.7 std liters/sec (3.6 scfm) and a charge of 1500 g resulted in a systematic decrease in OPTAF from 1.08 (A-345) to 1.01 (A-364).

Twenty-two PyC coating specimens produced in a 64-mm (2.5-in.) coater for irradiation evaluation in capsules HT-28, -29, and -30 were also measured. These specimens represent PyC deposited from MAPP gas over a wide range of conditions, and we hoped that they would provide a basis for determining the sensitivity of the OPTAF measurement to various coating structural variations. The OPTAF values calculated from reflectivity traces having twofold symmetry (polarized only) are given in Table 6.1 (p. 239).

An improvement in the metallographic preparation of OPTAF samples was developed for those specimens polished with 3-μm diamond before the final polish with 0.025-μm diamond. This procedure yielded specimens

with superior flatness and little rounding at the outer edge of the PyC coatings. However, some rounding still occurred at the coating-to-buffer interface.

The OPTAF values of several ORNL PyC particle coatings were measured at KFA, Jülich, and the results from KFA and ORNL agreed reasonably well.[10] The twofold-symmetry OPTAF values obtained by the two laboratories using air objectives are given in Table 6.5. The agreement between the OPTAF values obtained for a specific ORNL coating by the two laboratories is well within our estimated variance of ±0.015 OPTAF units for OPTAF values in the range 1.03 to 1.00. These results as well as those reported previously of OPTAF measurements on coatings produced at KFA-IRW indicate that values obtained for a specific PyC specimen at ORNL and KFA-IRW are essentially identical.

Table 6.5. OPTAF[a] Measurements on ORNL PyC Coatings Made at ORNL and KFA-Jülich

Particle Designation	OPTAF	
	ORNL	KFA-Jülich[b]
OR-2013-T	1.02	1.014
OR-1967-T	1.02	1.014
OR-1975-T	1.02	1.029
OR-1985-T	1.03	1.026
OR-1849-HT	1.02	1.033
OR-1749-HT	1.03	1.027

[a]Based on maximum and minimum reflectivity using polarizer only, wavelength = 5470 Å. Mid-radius value of PyC coating.

[b]Measured on Leitz MPV-II system.

In addition to the experimental work the relationship of the measured OPTAF value and the orientation of the carbon crystallites in the PyC coating was calculated theoretically. The calculation was based on an assumed dielectric susceptibility tensor for the carbon crystallites in the PyC. The tensor components were derived from published optical properties of single-crystal graphite, and local

field perturbations were neglected. Results of the calculation were reduced to a relation between OPTAF and a crystallite orientation parameter directly relatable to the Bacon Anisotropy Factor (BAF) obtained by x-ray diffraction orientation techniques. This relation has essentially the same shape but slightly different values from the OPTAF-BAF relation derived for PyC by Koizlik[11] using a much simpler model. This susceptibility tensor calculation neglects local field and optical interference effects, and the significance of these assumptions is presently unknown. Our more refined calculation does indicate that the relation between OPTAF and the BAF for PyC that has been used by various workers and is based on a relatively simple PyC model is reasonably valid.

6.4.2 X-Ray Diffraction Techniques

Development of techniques for using x-ray diffraction to characterize the LTI PyC coating on Biso particles was pursued. Two preliminary experiments were conducted to demonstrate technical feasibility. The x-ray diffracting power of the LTI must be sufficiently intense to permit extraction of orientation and crystallite size information from a diffracted beam. This capability for the LTI was demonstrated by diffracting a 50-μm-diam Cu Kα x-ray beam from a small portion of the LTI of a single particle. A 16-hr exposure on film revealed an intense (002) reflection and a moderate (10) band. This work demonstrated that with sufficient effort the LTI on a single particle could be characterized by x-ray diffraction. The other experiment measured the x-ray diffraction from a planar array of about 100 particles. Since much more LTI volume was illuminated by the x-ray beam than in the previous case of a single particle, the diffracted intensity was much higher. The data showed that the diffraction maxima customarily used to characterize bulk graphitic materials are observable for these coatings and thus should permit straightforward analysis once the measurement technique is established. The major problem with microspheres is to sufficiently collimate the incident and diffracted beams so that meaningful crystallographic information can be obtained from a relatively small volume of LTI coating.

Considerable information on the turbostratic stacking, crystallite size, and degree of graphitization in the PyC coating can be obtained from powder patterns of crushed coating samples removed from the particles. Preliminary work included analysis of samples of buffer and LTI coatings that had been removed from a number of kernels. Each of these samples had a diffraction pattern characteristic of poorly crystallized turbostratic PyC except for trace amounts of ThO_2 removed with the buffer. The (10) diffraction band of these structures has a long high-angle tail. The (11) band has similar characteristics. These data are shown in Fig. 6.10. The interplanar spacings of the (002), approximately 3.51 and 3.49 Å, respectively, for the buffer and LTI coating compared with 3.35 Å for a well-developed graphite structure. The mean crystallite sizes, L_c, were 25 Å for the buffer and 32 Å for the LTI coating, as calculated with the Scherrer equation. The (002) spacings reported here have not been corrected for the expected line shift due to these small L_c values.

We also initiated work on a method for direct determination of preferred orientation in PyC coatings on particles. This technique, developed by Pluchery,[12] employs a special sample holder that permits exposure of an equatorial band of the coating of each particle in a group of approximately 100 particles. The geometric parameters of a given particle type and the required absorption corrections are employed with a computer program to determine coating anisotropy factors. Determination of coating preferred orientation by x-ray diffraction is of interest because it should, in principle, be done fairly rapidly and quantitatively. A specimen holder for this purpose was designed and is being constructed for future work.

An additional technique planned for PyC characterization is use of small-angle x-ray scattering (SAXS). Work done at KFA, Jülich, has shown promise for correlation of SAXS measurements with irradiation stability.[13] Facilities for this work were set up and an initial evaluation of the resolution of a one-dimensional system was completed using five PyC types. Future work will include data collection on a broad range of PyC types.

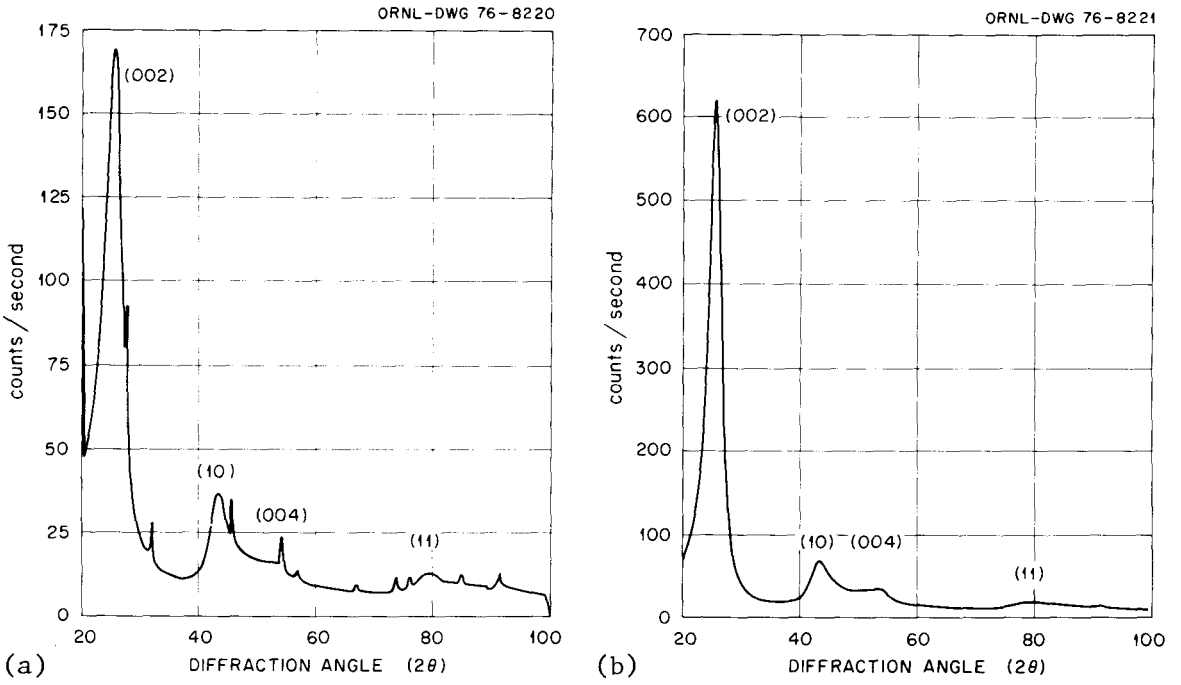

Fig. 6.10. X-Ray (Cu Kα) Diffraction Profiles of (a) Buffer Coating Removed from ThO_2 and (b) Outer Pyrocarbon Removed from OR-1978.

6.4.3 Etching Techniques

Oxygen plasma oxidation, electrolytic etching, and cathodic etching techniques have been reported[13] by German workers to provide banded etching patterns in PyC structures, which can be correlated with irradiation performance of Biso PyC coatings. Selected specimens were treated by each technique to evaluate the merits of this approach. For the initial evaluation several archive specimens from the irradiation test series HT-17 through -19 were examined with oxygen plasma oxidation and cathodic etching techniques. Five different specimen types were prepared in metal mounts and metallographically polished. These mounts were selectively etched for various times in an oxygen plasma in 12 kJ (200 W-min) increments. Others were given a cursory examination with a cathodic etcher using ionized argon. The objective of these studies was to determine if we could use these techniques to discern microstructural differences within the PyC coatings that may relate to irradiation performance. After etching, the specimen surfaces were examined optically and with a scanning electron microscope (SEM). Oxidation in the oxygen

plasma at 200 W-min of a mount of five selected Biso-coated particle types revealed significant differences in PyC from different coating runs. The microstructural features revealed were essentially below the resolution limit of the optical microscope at this oxidation stage, except for pits of the order of 1 μm, which begin to appear in circumferential arrays within the coating. Examination in the SEM revealed that what was a very smooth polished midplane surface before oxidation had a very apparent microstructure following the oxidation. Plasma oxidation of these mounts was then carried to 54 kJ (900 W-min). The banding within PyC coatings on fuel particles reported by German workers using these techniques and optical microscopy consists of arrays of pits, and these arrays have very definite geometries. The microstructure of the coatings as revealed by the plasma oxidation technique consisted of small spheroidal or ellipsoidal grainlike regions that varied in size from below 0.5 μm in their smallest dimensions to 1 to 2 μm in their longest dimension. In some coatings (near the buffer), these grainlike regions were very small and nearly equiaxed, and they tended to be much larger and not equiaxed near the outer surface of the coating. The carbon structure within the small grainlike regions appeared to consist of oxidation-resistant carbon lamellae that alternated with other regions that oxidized fairly easily. Several of these lamellae had thicknesses of about 0.1 μm. In coating regions where the grains were elongated, the long axis tended to be oriented with the coating radius, but at a small angle to it. The microstructures revealed by cathodic etching were less well defined and we decided not to pursue this technique further.

Electrolytic etching of the above coatings was briefly investigated, and the results are encouraging. The samples were etched with a solution of $K_2Cr_2O_7$ dissolved in phosphoric acid. Application of 5 V for 30 sec clearly revealed an etch structure in the coatings. Etching for an additional 30 sec accentuated these features. Coating OR-1975, which had a preirradiation OPTAF of approximately 1.02 and had only 9% survival in HT-19 at 1250°C, exhibited an etch band structure with continuous 3-μm-thick circumferential bands in the coating. These bands appeared

to contain material that alternately etched at different rates to develop the observed structure. Coating OR-2013, which had 100% survival in the 1250°C positions in both HT-18 and -19, was deposited at the same nominal rate and with the same nominal density as OR-1975. The preirradiation OPTAF value of this coating was also approximately 1.02, essentially identical to that of OR-1975. The electrolytic etch structure of this coating revealed essentially no continuous band structure. There were regions in the coating in which some banding was detectable, but the bands were very limited in circumferential extent. No qualitative estimate of the relative area amounts of material etched from these coatings was made. While the electrolytic etching did reveal microstructural differences, they were less well defined than those observed by plasma oxidation, and we decided at this point to concentrate effort primarily on the plasma technique.

We therefore continued development of the oxygen plasma etching technique so that features developed during etching could be resolved optically at magnifications in excess of 500×. An epoxy mount material was found to be necessary for use with this technique. Standard epoxy metallographic mounts containing the fuel particles of interest were polished so as to expose the midplane of the particle coatings. The polished coatings were first used for OPTAF measurements, then examined at high magnification visually in polarized light by use of an analyzer, and then were etched in the oxygen plasma. The etcher contains two chambers and the rf power (at 13.5 MHz) in each chamber was maintained at 20 W with the oxygen pressure at 100 Pa (0.75 torr). Early in this work, difficulties were encountered with the oxygen plasma charring the upper corner of the epoxy mount located nearest the incoming plasma column. Charring overheats and deforms the mount as well as contaminates the mount surface with stains due to decomposition of the epoxy. This problem was circumvented by machining a recess in the wall of the mount on the end containing the polished specimens and placing a fused silica ring on the shoulder produced by the machined recess such that the upper edge of this ring is approximately 1 mm above the mount surface.

Observations of polished surfaces of various PyC coatings in polarized light at about 60× indicate that they consist of two optically

discernible varieties of carbon. One is optically anisotropic and is visible at 500× or above as very small regions of optical activity. These have been referred to by some authors as "optical domains." These small regions exhibit four maxima and minima of reflected intensity during a 360° rotation of the polarization vector in the light beam relative to some reference direction on the PyC midplane surface. The disposition and apparent concentration of these optically active regions vary greatly in PyC coatings produced in different sized coaters and under various coating conditions. The other variety of carbon that is present in the coatings is optically inactive by microscopic observation under crossed polarizing elements. In some cases the regions containing this carbon exist over distances of several micrometers.

We demonstrated that oxidation occurs most rapidly in coating regions where the optically inactive carbon was concentrated in the LTI PyC. The regions where the optical domains were concentrated oxidized relatively slowly. It is this differential in oxidation rates that produced the surface relief in an originally polished PyC surface, and this relief could be observed with dark-field illumination. This demonstration was clearly evident in coating OR-2012, which was irradiated in HT-17, -18, and -19. The relief structure produced by plasma oxidation thus provided an indication of the locations of regions having high concentrations of the optically active carbon in the coating. Workers at KFA Jülich have reported that it is in fact the geometric disposition and concentration of the poorly oxidizable carbon that has an important bearing on the fast-neutron damage resistance of a PyC LTI coating. Coating structures in which this optically active carbon is present in continuous spherical shells in the coating have been reported by KFA Jülich to be much more sensitive to failure due to fast-neutron damage than structures in which the two varieties of carbon, deduced from etching results, are distributed in such a way that the poorly oxidizing carbon does not form continuous shells. We will designate the poorly oxidizable carbon as POC and the more readily oxidizable carbon as ROC until we know more about the crystalline structures of these carbons.

Plasma oxidation and irradiation data for coating types irradiated in HT-17 through -19 essentially confirm this concept. Coatings OR-1967, -1975, -1985, and -2012, which all had twofold OPTAFs of 1.02 or less at the coating midradius and had high irradiation failure rates, all consist of very banded structures containing very little of the ROC component.

Coatings OR-2013 and -2010, which had high survival rates in this irradiation series, exhibited structures in which the POC did not form continuous banded structures typical of the four that had very poor survival rates. In these two coatings the POC was not in continuous spherical layers in the coating (which appear as bands in the midplane cross section), but was interrupted frequently by concentrations of the ROC component.

Coatings OR-1749, -1838, and -1849, which had high survival rates at high fluence and temperature in capsules HT-12 through -15, were also examined by plasma oxidation. Coating OR-1849 contained a large quantity of ROC and had an etch structure whose features agreed fairly well with the survival criteria discussed previously. Coating OR-1838 actually consisted of two or three zones of very finely spaced bands of POC, which alternated with bands of ROC. Some particle coatings of OR-1838 contained two of the clustered bands, while others exhibited three during the etching procedure. This coating structure was unique among those studied. Coating OR-1749 had a nominal LTI design thickness of about 36 μm as a Biso particle and survived very well in the HT-12 through -15 irradiation series. This coating exhibited a structure having approximately three bands of POC alternating with two bands of ROC along the coating radius.

Numerous coatings produced in the 0.13-m (5-in.) coater and being evaluated in various irradiation experiments were also studied by this procedure. Coating J-232 along with J-262, which is the annealed version of J-232, had very similar structures consisting of rather widely spaced continuous bands of POC alternating with bands of ROC, which were approximately 10 μm in thickness. Annealing of J-232 at 1800°C for 30 min to produce J-262 reduced the amount of ROC in the coating and generally modified the geometry of the observed banding.

Coating J-461 and its annealed version, J-465, had structures reasonably similar to J-232 and J-262. Coatings J-488, -489, -490, and -491, which were prepared for irradiation capsule OF-2, contained particularly interesting structures in light of their deposition parameters and the use of the nine-hole frit distributor in the coating furnace. They all consisted of batch sizes of 2175 g of ThO_2, and were all deposited at 1350°C. Coating J-490 was deposited from 100% propylene at about 6 μm/min and contained very little ROC component. Essentially no structure could be detected, however, in the POC component, in contrast to coatings like OR-1967 discussed previously. The deposition conditions for J-489 differed from those for J-490 only in that the propylene was diluted 50% with helium. This coating contained very significant quantities of ROC and the structure could be qualitatively classified as the disrupted type.

Coating J-491 was deposited from pure propylene at about 9 μm/min. It contained significant quantities of ROC, and the POC component was quite interrupted by the ROC component. Coating J-488 was deposited under identical conditions as J-491 except for 50% dilution of the propylene by helium. This coating, deposited at 7 μm/min, also contained significant quantities of the ROC component, but in this case the POC component was organized into a more banded structure with the POC bands having a separation of about 5 μm.

Table 6.4 shows that these coatings all had essentially the same OPTAF values, but the etching data show that the coatings have significant structural differences. Postirradiation examination data for capsules containing these coatings will be very important for this work because it will allow us to correlate the etch structure with fast-neutron damage resistance and to determine the PyC structure types that are most desirable for HTGR applications.

Next, 12 of the 22 PyC coatings prepared for irradiation capsules HT-28, -29, and -30 were characterized by oxygen plasma etching. Even though the OPTAF values for all 22 of these coatings were essentially identical, oxygen plasma etching showed significant differences among the coatings. Only preliminary results are available, but they indicate

that at a deposition temperature of 1275°C and deposition rates of 4 to 7 μm/min a reduction of MAPP gas concentration from 100 to 50% results in the deposition of significantly less of the ROC component in the coatings. Similar analyses are under way for other PyC coatings in this series.[14]

Several of the HT-28, -29, and -30 series PyC coatings were then selected for use in a study to optimize the plasma etching technique by minimizing the time required to etch samples. Metallographic mounts of selected samples were etched at various positions in the unit at various radiofrequency powers, oxygen flow rates, and etching times. An experimental design was devised to establish the maximum rf power that could be applied in each chamber of the unit and still provide satisfactory etching to PyC specimens but not degrade the polymeric mounting material. The objective was to determine the minimum time that could be used to plasma etch PyC fuel particle coatings. Resistance to oxidation of two candidate epoxy resin mounting materials (Shell Epon 815 and CIBA Araldite) was evaluated at selected rf power levels at 90 Pa (0.7 torr) of oxygen. The Epon 815 material showed little degradation in the plasma at power levels up to 40 W and was thus selected as the mounting medium to be used for the plasma oxidation study. Archives of six coated fertile particles were selected from the set of 22 PyC types tested in irradiation capsule HT-30 on the basis of their deposition conditions and previous plasma oxidation data obtained at 20 W of rf power. An archive specimen of OR-2013-HT previously tested in HT-18 and -19 was also selected for incorporation into the experiment. We anticipate that results of this study will allow us to establish a standard plasma oxidation procedure for use in characterizing LTI coatings.

6.4.4 Transmission Electron Microscopy (TEM)

Recent work by Yust[15] and Kaae[16] has shown that depending upon deposition conditions LTI PyC coatings can consist of both "tangled" and "ordered" structures of carbon of a few hundred to a few thousand angstroms in cross section.

Thus, work was initiated to further delineate the microstructures of PyC fuel particle coatings and correlate the features in these structures with deposition conditions and resistance to fast-neutron damage. In the specimen preparation technique, coating fragments were hot-pressed in aluminum, and a slice of this mount was thinned by argon ion milling until sufficiently thin for electron transmission. Initially, samples of irradiation test archives and a commercial vitreous carbon were mounted. Under dark-field conditions with the diffraction aperture located on the (002) reflection of the carbon structure, coherently diffracting regions within the growth features of the coatings were imaged. Early data indicated that coating OR-1975 possessed coherently diffracting regions of the order of one-fifth to one-quarter of the volume of a growth feature, while coating OR-1849 appeared to consist of much smaller coherently diffracting regions within growth features. Coating OR-1975 experienced very poor irradiation survival in the HT-17, -18, and -19 experiments. Coating OR-1849 exhibited excellent survival in experiments HT-12, -13, -14, and -15 in both the low- and high-temperature positions.

Further examination of coatings OR-1849 and OR-2010, a batch that survived irradiation in HT-17, -18, and -19, revealed that these coatings contained structural features of essentially two sizes. The first order of spheroidal growth features contained zones about their periphery in which the carbon crystallites were coherently arranged on a dimensional scale of about 1000 Å. The carbon crystallites were arranged with their *c* axes oriented more or less with the radius of the growth feature. The cores of at least some of these growth features contained a nucleus comprising a cluster of spherical seeds with diameters of about 100 Å. The other type of feature in these structures resembled the small spherical objects observed in the cores of some growth features. These seemed to occur in bands or striations in the coating.

While a few specimens had been successfuly prepared, we encountered increased difficulty in argon ion milling foils of the PyC coatings at this point. For optimum results, the ion milling rate of the PyC should be somewhat greater than that of the supporting aluminum matrix. The

argon ion milling rate of the aluminum, however, was considerably greater than that of the PyC coatings of interest. The milling rate of the PyC coatings appeared to be a strong function of the structure of the coating. PyC structures having a large concentration of tangled carbon ribbons or tangled component within their growth features, such as those deposited from propylene at high temperatures, milled more rapidly in argon than did the more compact organized structures typified by propylene coatings deposited at temperatures near 1300°C. We analyzed the situation using available models for ion milling and determined that helium should provide more equal milling rates between the PyC samples and the aluminum matrix. This was demonstrated, and all subsequent samples were thinned with helium ions.

Helium-ion-thinned specimens of coatings from particles OR-1985-T and -2013-T were examined next. The PyC coatings of these Biso particles had initial midradius OPTAF values of 1.03 and 1.02 (twofold symmetry) and immersion densities of 2.065 and 2.002 g/cm^3, respectively. Irradiation survival of loose particles of OR-1985-T and -2013-T in the high-temperature positions of irradiation capsule HT-19 was 0 and 100%, respectively. Electron microscope observation of the structure of these coatings indicated that both were of a mosaic type consisting of spheroidal growth features having preferential orientation of the carbon crystallites within these features. We observed two differences between the structures of these coatings. First, coating OR-1985-T contained a relatively small amount of material that had a much finer orientation texture than that observed within the growth features. This material was often located in bands and between the growth features in the outer half of coating OR-2013-T and essentially throughout coating OR-2010-T described above. Both these coatings performed well to high fast-neutron fluences. Also, the growth features in OR-1985-T contained a significant amount of concentric cracking oriented about the nuclei of the features. In OR-2013-T less cracking of this type was observed near the buffer-LTI interface, and the amount decreased progressively as one moved outward along the radius of the coating. This observation for OR-2013-T correlates reasonably well with plasma oxidation results for this coating.

To examine the advantages of using thicker specimens, ion-thinned coatings J-262, -461, -465, -489, -490, OR-2275-AHT, and OR-2274-HT were examined in a 1-MV electron microscope. All these coatings had mosaic structures, and the principal difference between them was the concentration of the carbon having coherently diffracting zone sizes below 0.1 μm. In general, the spheroidal growth features were about the same size (approximately 1 μm) in all these coatings except J-490, which contained some features larger than 1.5 μm. Coatings J-262, -461, and -465 consisted of extremely finely textured PyC. The two OR coatings had a typical mosaic structure. Since all the coatings having a J prefix were deposited in a 0.13-m (5-in.) coater, and those having an OR prefix were deposited in a 64-mm (2 1/2-in.) coater, it appeared that subtle changes in coating conditions in either unit could have a dramatic effect upon the structure of the PyC produced.

Future work will employ primarily the lower energy microscope because of its greater availability. Work will continue to seek correlations between the size, shape, and distribution of microstructural features with irradiation stability.

6.4.5 Chemical Characterization of PyC

Recent measurements on PyC coatings reported by IRW-KFA Jülich indicate that certain aspects of the structure of PyC coatings from HTGR fuel particles may be relatively rapidly characterized by a chemical technique. This involves the measurement of pH change in a saline suspension of coating fragments in the presence of oxygen. Workers at KFA-Jülich[17] have correlated the observed pH change with the volume concentration of the readily oxidizable carbon (ROC) in the coating.

Three specimens of coating OR-2266-HT were examined in a small pH cell containing about 15 cm^3 of 0.1 *N* NaCl solution and an oxygen bubbler tube. The pH was measured to ±0.001 pH unit with a research pH meter. The first two specimens were hand ground with a mortar and pestle until optical examination at 50× revealed that the PyC specimen (approximately 50 mg) was a fine powder. The pH of the saline solution

with and without oxygen bubbling in the cell was approximately 7. With the hand-ground specimens, addition of the PyC specimen to the cell resulted in an immediate drop in pH to between 6 and 6.5. Subsequently, with oxygen being bubbled through the suspension, the pH began to increase and continued to rise for approximately 1.5 hr to pH 8.85. The third specimen of about 50 mg was ground in a vibratory impact grinder for 1 min. Addition of the ground PyC to the cell resulted in a sharp drop of pH to 6.1. The pH then rose to 8.82 in 1.5 hr. In all cases, the pH rose rapidly after addition of the PyC sample to the cell and was essentially constant after approximately 1.5 hr.

These results indicated that significant reaction occurred between oxygen and the PyC at 25°C under the described conditions. Previous oxygen plasma etching data for coating OR-2266-HT indicated a large concentration of ROC component in this PyC. From previously reported German data obtained with this technique, the pH change should be proportional to the volume concentration of the ROC component. The large observed change in pH with coating OR-2266-HT is therefore consistent with the plasma oxidation results. However, the procedure must be tested with a coating type known to contain a relatively small concentration of ROC to determine its usefulness. If measurements with this coating specimen indicated a small pH change and thus small ROC concentration, coatings prepared for irradiation experiments HT-28, -29, and -30 will be used to systematically evaluate this potential characterization procedure.

6.5 IRRADIATION TESTS IN HFIR TARGET FACILITY

6.5.1 Capsules HT-12 Through -15 — M. J. Kania

This experiment[18] was made up of four target capsules designated HT-12, -13, -14, and -15. It was designed to test a series of 16 batches of Biso-coated ThO_2 particles at peak temperatures of 900 and 1250°C to burnups and fast-neutron exposures up to twice the HTGR design requirements. Nine of the 16 batches were coated by ORNL and the remaining seven were coated by General Atomic Company (GA). The

ORNL-designed coatings were selected with the use of the STRETCH[19,20] computer code in order that some particles would fail while others survived. The capsules were irradiated for two, four, six, and seven HFIR cycles, respectively.

The primary objectives of this experiment were to:

1. test selected Biso-coated ThO_2 particles at conditions that would induce predictable particle failure and thereby establish minimal coating design criteria and
2. determine numerical values for the coating densification constant and the creep coefficient required in the stress analysis code, STRETCH.

In addition, several selected particle batches were investigated to determine:

1. burnup, cesium retention by particle coatings, and internal gas pressures;
2. failure and fission product release from particles; and
3. pyrocarbon coating characterization.

Detailed descriptions of the capsule design, operation history, and the postirradiation examination and analysis for each capsule have been previously reported.[21] The mechanical analysis using Modification V to the STRETCH program to determine numerical values for the coating densification constant and creep coefficient has also been reported.[22] This mechanical analysis is also described in Sect. 6.11.2 of this report. Section 3.2 of this report describes the fission product release studies during postirradiation heating of particle batches OR-1840 and -1849. Section 4.4 describes the cesium retention studies and internal gas pressure measurements for selected HT-12 through -15 test particles. Burnup calculations are described in detail in ref. 18. Pyrocarbon coating characterization studies for batches OR-1840 and -1849 are discussed in Sect. 6.4 of this report.

6.5.1.1 Thermal Analysis

Detailed thermal analysis has been performed on each of the ThO_2 test particles in capsules HT-12 through -15 using the HTCAP[23] computer

code. Maximum particle surface temperatures were determined on a day-to-day basis for each HFIR irradiation cycle. Design temperatures were 1250°C for the high-flux, high-temperature regions and 900°C for the low-flux, low-temperature regions.

Tables 6.6 and 6.7 describe in general the maximum particle surface temperature of specific particle batches for each irradiation cycle. Coated particles in holders 2 through 13 and 42 through 51 were irradiated in the low-flux, low-temperature regions of each capsule. Holders 15 through 38 were irradiated in the high-flux, high-temperature regions of each capsule. Data on specimen holder temperature and power generated per ThO_2 particle are reported elsewhere.[18]

Results from the thermal analysis indicate:

1. Specimen holders operated between 50 and 200°C higher than original design temperatures, depending on holder location in a particular sleeve.

2. Specimen holder temperatures by themselves are not adequate in describing particle operating temperatures. The maximum particle surface temperatures exceeded specimen holder temperatures by as much as 100°C after one cycle and peaked at approximately 300°C higher during the fourth cycle in the high-temperature regions and the sixth cycle in the low-temperature regions.

3. In general the particle operating temperatures were 1200 to 1300°C in the low-temperature regions and 1500 to 1600°C in the high-temperature regions.

6.5.2 Irradiation Test Capsules HT-17, -18, and -19 — R. L. Beatty

Irradiation capsules HT-17, -18, and -19 were part of a continuing series of HFIR target experiments designed to test pyrocarbon coatings on thoria kernels. The three capsules were shared by ORNL and General Atomic Company. The basic capsule design, loadings, irradiation conditions, and postirradiation examination results of HT-17 and -18 have been reported previously.[24]

The major objective of the ORNL experiment in HT-17, -18, and -19 was to define the behavior of dense pyrocarbon as a function of preferred

Table 6.6. Maximum Particle Surface Temperatures for HT-12 and -13

Holder	ORNL Particle Batch	Particle Diameter (μm)	Temperature Range, °C, for HFIR Cycles						
			Capsule HT-12		Capsule HT-13				
			82	83	83	84	85	86	87[a]
4	OR-1850	694	980–1088	1175–1198	980–1022	1048–1208	1228–1273	1295–1313	1333
5	OR-1846	482	1005–1114	1209–1225	1005–1046	1070–1239	1258–1302	1326–1342	1363
8	OR-1840	552	1013–1100	1195–1206	1013–1035	1061–1214	1236–1274	1294–1306	1328
11	OR-1749	540	1025–1147	1257–1260	1025–1073	1108–1274	1299–1335	1358–1370	1390
13	OR-1849	816	1152–1179	1293–1274	1152–1119	1152–1285	1316–1340	1369–1372	1395
17	OR-1850	694	1305–1408	1526–1509	1305–1328	1370–1528	1554–1576	1602–1606	1628
18	OR-1846	482	1315–1415	1543–1520	1315–1339	1378–1539	1563–1588	1615–1616	1642
21	OR-1840	552	1314–1379	1495–1466	1314–1311	1342–1480	1509–1529	1555–1551	1577
24	OR-1749	540	1319–1411	1532–1512	1319–1334	1376–1531	1558–1576	1603–1604	1625
26	OR-1849	816	1477–1437	1566–1515	1477–1386	1423–1534	1564–1572	1603–1594	1619
29	OR-1838	594	1319–1385	1501–1473	1319–1316	1350–1494	1522–1540	1567–1560	1586
32	OR-1826	506	1314–1417	1540–1517	1314–1338	1380–1539	1565–1588	1615–1613	1635
35	OR-1830	480	1315–1423	1546–1528	1315–1347	1383–1547	1571–1597	1623–1624	1650
38	OR-1837	452	1497–1454	1578–1534	1497–1399	1438–1548	1577–1594	1622–1617	1642
42	OR-1838	594	1025–1119	1224–1222	1042–1055	1082–1233	1258–1292	1317–1321	1344
45	OR-1826	506	1013–1137	1238–1249	1013–1058	1093–1265	1287–1326	1351–1363	1383
48	OR-1830	480	1065–1139	1237–1247	1065–1074	1103–1260	1279–1323	1342–1362	1377
51	OR-1837	452	1104–1121	1209–1211	1104–1076	1098–1222	1244–1279	1304–1320	1337

[a]HT-13 was irradiated for only one day in cycle 87, so the temperature was calculated only once.

Table 6.7. Maximum Particle Surface Temperature for HT-14 (Cycles 85 Through 90) and -15 (Cycles 85 Through 91)

Holder	ORNL Particle Batch	Particle Diameter (μm)	Temperature Range, °C, for HFIR Cycles						
			85	86	87	88	89	90	91
4	OR-1850	694	980–1088	1115–1227	1288–1294	1311–1321	1338–1329	1346–1334	1382–1334
5	OR-1846	482	1005–1114	1144–1257	1317–1323	1340–1347	1364–1362	1377–1367	1410–1359
8	OR-1840	552	1013–1100	1127–1232	1293–1290	1307–1309	1328–1319	1336–1324	1371–1313
11	OR-1749	540	1025–1147	1180–1295	1359–1346	1371–1370	1390–1378	1398–1380	1431–1372
13	OR-1849	816	1152–1179	1212–1306	1377–1351	1377–1372	1395–1377	1400–1376	1431–1362
17	OR-1850	694	1305–1408	1442–1542	1616–1587	1611–1606	1627–1606	1630–1600	1659–1588
18	OR-1846	482	1315–1415	1455–1553	1629–1597	1620–1616	1639–1621	1641–1615	1673–1597
21	OR-1840	552	1314–1379	1410–1499	1567–1537	1558–1551	1571–1553	1573–1547	1605–1532
24	OR-1749	540	1319–1411	1449–1543	1620–1584	1611–1604	1622–1603	1624–1594	1654–1580
26	OR-1849	816	1477–1437	1481–1542	1629–1578	1611–1591	1616–1593	1617–1583	1648–1566
29	OR-1838	594	1319–1385	1418–1507	1583–1548	1570–1559	1586–1559	1583–1553	1613–1539
32	OR-1826	506	1314–1417	1454–1550	1629–1597	1623–1613	1632–1613	1636–1607	1668–1592
35	OR-1830	480	1315–1423	1463–1561	1637–1608	1631–1624	1647–1624	1647–1618	1679–1606
38	OR-1837	452	1497–1454	1491–1561	1643–1599	1629–1614	1639–1616	1642–1609	1677–1595
42	OR-1838	594	1025–1119	1147–1249	1316–1305	1325–1324	1341–1332	1354–1337	1385–1323
45	OR-1826	506	1013–1137	1167–1281	1345–1342	1364–1363	1383–1376	1396–1376	1429–1373
48	OR-1830	480	1065–1139	1166–1278	1337–1336	1361–1362	1384–1375	1397–1380	1428–1377
51	OR-1837	452	1104–1121	1145–1239	1296–1297	1314–1320	1342–1335	1352–1342	1387–1339

orientation under different temperatures and fast-neutron fluences. The test particles were Biso-coated thoria. The nominal particle geometry was 500-μm kernel diameter, 75-μm buffer, and 80-μm dense outer coating for all batches except one; a peripheral experiment involved one batch with 680-μm thoria kernels and a proportionally scaled Biso coating. All the 500-μm kernels were buffer coated as a single batch to avoid buffer variations. This was done in a 0.13-m (5-in.) coater by W. J. Lackey of the Fuel Cycle Technology Group. All other coatings were deposited in a 25-mm (1-in.) laboratory coater. The dense outer coatings were deposited from propylene, with the primary process variable being propylene concentration and hence deposition rate. This is an effective means of varying the coating anisotropy. Each outer coating run was made with several graphite plates included in the batch to obtain suitable specimens for x-ray BAF measurements. The outer coating deposition conditions, densities, and BAF values are listed in Table 6.8.

In addition to the primary specimen set with varied outer coating deposition rate (varied propylene concentration with argon diluent), three specimens were included as peripheral experiments. These were the large particles mentioned above (OR-2010), a coating deposited at a gradually increasing temperature (OR-2012), and a coating deposited with CO_2 rather than argon diluent used as fluidizing gas (OR-2013). The large particles were included to determine whether the standard 500-μm thoria was near an upper size limit from the coating performance standpoint or whether the larger particle would perform satisfactorily. The large particle was omitted from the high-temperature section of the six-cycle HT-19 test because at that accumulated irradiation level (^{233}U buildup) the power generation and internal particle temperature would have been very unrealistically high. The coating deposited at variable temperature was fabricated with a programmed temperature rise designed to simulate a possible production furnace run. Since coating density is a strong function of deposition temperature, this procedure should result in a significant radial density gradient. Unfortunately, no technique currently exists for measuring the gradient, so the density

Table 6.8. Deposition Conditions, Density, and BAF of Outer Coatings on Biso-Coated Thoria Particles Irradiated in Experiments HT-17, -18, and -19

Batch	Outer Coating Deposition Conditions				Density[a] (g/cm^3)	BAF[b]
	Temperature (°C)	C_3H_6 Flux (cm^3/min-cm^2)	C_3H_6 Concentration (%)	Deposition Rate (μm/min)		
OR-2010-T[c]	1335	9.0	33.3	22.5	1.980	
OR-2013-T	1325	4.0	33.3[d]	11.5	2.002	
OR-1975-T	1315	4.0	33.3	11.8	1.982	1.00
OR-1967-T	1300	2.0	16.7	5.2	2.000	1.05
OR-2012-ST	1200–1350[e]	1.5	12.5	3.7	1.919	1.08
OR-1985-T	1275	1.25	10.4	2.9	2.065	1.12
OR-1986-T	1250	1.10	9.2	2.1	2.102	1.10
OR-1972-T	1250	1.00	8.4	2.0	2.063	1.22
OR-1987-T	1250	0.90	7.5	1.7	2.094	1.17
OR-1978-T	1240	0.50	4.2	0.8	2.072	1.73

[a]After 30 min at 1800°C, measured by gradient column on particle coatings.

[b]Average of two plate measurements, one with each side of plate toward x-ray source.

[c]Kernels nominally 680-μm-diam ThO_2; all others 500-μm-diam ThO_2.

[d]Diluent CO_2; argon diluent used with others.

[e]Temperature increased 6°C/min during run to produce radial property gradients.

reported is an average value. The coating deposited with CO_2 diluent gas was included to test a process developed earlier,[24] which showed that oxidizing fluidizing gases could be employed up to certain limits in pyrocarbon coating. The CO_2 diluent greatly reduced soot deposition in the coating chamber with no obvious detrimental effects on coating properties.

The coating set listed in Table 6.8 was intended to bracket the survival-failure line at various fluences in correlation with deposition rate and BAF. The upper limit on BAF required to survive a given fluence was not well-defined, but it was thought that deposition rates

exceeding 5 μm/min would produce coatings able to survive design HTGR fluence (≈4 HT cycles at the HFIR midplane). However, the survival rates listed in Table 6.9 show that a high deposition rate in itself does not assure a stable coating. While these coatings produced in a 25-mm (1-in.) coater cannot be considered representative of coatings deposited at similar rates in large coaters, it is very important to acknowledge that deposition rate alone is not an adequate criterion for stability. This shows the importance of characterizing coatings on the basis of measurable properties and identifying those properties that determine irradiation performance. Therefore, work was continued on characterization of archive specimens to gain a better understanding of why some of the coatings in Table 6.9 failed in spite of high deposition rates and relatively low BAF values. In addition, future experiments were planned to consider process specifications including hydrocarbon type and concentration as well as coating rate.

Table 6.9. Survival Rates Determined by Visual Observation of Particles Irradiated in Capsules HT-17, -18, and -19

Batch	Survival Rate, %					
	HT-17 (Two Cycles)		HT-18 (Four Cycles)		HT-19 (Six Cycles)	
	900°C	1250°C	900°C	1250°C	900°C	1250°C
OR-2010-T	100	100	100	86	94	a
OR-1967-T	100	0	0	0	2	0
OR-2012-ST	100	84	0	0	0	0
OR-1985-T	93	0	0	0	0	0
OR-1986-T	24	100	0	0	0	0
OR-1972-T	100	0	0	0	2	0
OR-1987-T	100	0	0	0	0	0
OR-1978-T	100	0	0	0	0	a
OR-2013-T	a	a	a	100	a	100
OR-1975-T	a	a	a	a	a	9

[a]This particle not in this test.

Further characterization studies conducted on the HT-17, -18, and -19 coatings included optical anisotropy (OPTAF) measurements, examination by oxygen plasma etching and transmission electron microscopy (TEM), and evaluation by small-angle x-ray scattering (SAXS). These are discussed in Sect. 6.4 of this report. Differences in microstructure were evidenced by all these techniques, but none has been developed sufficiently to quantitatively specify the requirements for a coating that will survive HTGR design fluence. For example, the critical difference between coatings OR-2013, which performed well, and OR-1975, which performed poorly, is not clear. These two coatings were deposited under identical conditions except for the use of CO_2 diluent gas for OR-2013 and argon for OR-1975. The average of OPTAF values measured by ORNL, by GA, and by KFA-Jülich, showed no clear distinction. Differences observed by transmission electron microscopy did not appear significant. Microstructures observed by oxygen plasma etching were quite different, but more work with this technique will be necessary to determine the significance of these differences. The SAXS measurements showed considerably more porosity smaller than 100 Å in OR-2013, the good performer, than in OR-1975. This may be significant, but more SAXS data on other irradiation test specimens are needed to establish a relationship.

The major points shown by these experiments may be summarized as follows:

1. Use of CO_2 rather than argon diluent in the coating gas resulted in a more stable coating in the one case tested. The reason for this is not yet clear.

2. Low anisotropy values alone do not assure stability of dense pyrocarbons under fast-neutron irradiation.

3. The coatings tested in this experiment may have been too dense for optimum irradiation stability.

4. Large density gradients must be considered along with absolute density values and other factors in judging detrimental effects on performance.

5. Biso coatings on dense thoria kernels as large as 680 μm can perform well under irradiation conditions that are not too accelerated.

6. High deposition rate alone is not an adequate process specification for assuring stability of dense pyrocarbon coatings.

7. Irradiation stability may be related to the amount of fine porosity as determined by SAXS.

8. Further development of product characterization techniques is needed to qualify pyrocarbon coatings for irradiation stability.

9. Future experiments should include consideration of process specifications such as hydrocarbon type and concentration as well as deposition rate.

6.5.3 Irradiation Tests HT-20 Through -23 — T. G. Godfrey, J. P. Moore, and J M Robbins

Irradiation test series HT-20 through -23 comprised four HFIR target capsules designed to measure the change in thermal conductivity (λ), electrical resistivity, (ρ), coefficient of thermal expansion (CTE), absolute Seebeck coefficient (S), and dimensions of simulated bonded fuel rods as functions of particle volume loading, temperature, and fast-neutron fluence.[25] The capsules were to be irradiated for 1, 2, 4, and 6 cycles, respectively, at a design temperature of 950°C. The centerline fluence was expected to be from about 2.4×10^{21} to 1.4×10^{22} neutrons/cm^2 (>0.18 MeV).

Specimens of five types were fabricated. One type was intrusion bonded with a matrix of 28.5 wt % Asbury Graphite Mills grade NF 6353 graphite filler in Ashland Oil, Inc., grade 240 pitch. The four remaining types were formed by extrusion with a matrix of 75.7 wt % Great Lakes Carbon Corporation grade GLCC-1008 graphite, 24.3 wt % Thermax from R. T. Vanderbilt Co., and 25 pph* Varcum (prepolymerized furfuryl alcohol) from Reichhold Chemical Corporation. All specimens were nominally 10 mm OD, 3.3 mm ID, and 51 mm long (0.40 by 0.13 by 2.0 in.).

The λ measurements required attachment of a heater and a heat sink to opposite ends of each specimen. These attachments prevented irradiation in HFIR after λ measurements. For this reason, the five most

---

*"Parts per hundred," parts of liquid added per hundred parts of solids being slurried.

uniform and homogeneous specimens of each loading were selected for the measurement series on the premise that neutron fluence would have the same effect in all specimens with the same particle loading. The specimen selections were based on knife-edge resistivity measurements at 300 K, and the results are given in Table 6.10. This table shows the nominal volume particle loadings, the matrix densities, and the fabrication series numbers.

Figure 6.11 shows the ρ and S of all unirradiated materials as functions of temperature. The ρ of each specimen decreases smoothly with increasing temperature in a fashion similar to isotropic graphites. At a constant temperature, the ρ increases smoothly with increasing particle loading for the extruded material, but the ρ of the slug-injected specimen with 58% loading is much higher than that of the extruded specimens. This is partially due to the lower matrix density of the slug-injected specimen.

Figure 6.12 shows that the CTE of each unirradiated bonded-bed fuel rod increases smoothly with increasing temperature. Each curve has been fitted with a low-degree polynomial with the coefficients given in Table 6.11. Figure 6.13 shows that the CTE increases linearly with particle loading for the unirradiated materials. This indicates that a simple mixing law describes the effect of coated particles on the CTE of a fuel rod. The fact that the slug-injected 58 vol % sample shows a CTE in accord with those of the extruded samples might be considered surprising in view of its low matrix density and different matrix composition. After carbonization, however, the ratio of graphitic carbon to nongraphitic carbon for the extrusion matrix is about 2 and for the injection matrix, about 1.5. They are, therefore, actually quite similar. A significant conclusion drawn from the 58 vol % sample data is that the apparent CTE of these coated particles is less than 4×10^{-6}/K at room temperature. Since the particles in the specimen with 58 vol % loading are in a close-packed array, the observed thermal expansion is essentially that of the particles and is only slightly affected by the matrix.

Table 6.10. Average Electrical Resistivities (After Final Machining) of Bonded Rod Specimens to be Irradiated

Average Loading (%)	Average Matrix Density (g/cm^3)	Specimen Series	Average Resistivity, μΩ-m, for Specimens to be Irradiated Each Number of Cycles (in Each Capsule)[a]				
			0	1 (HT-20)	2 (HT-23)	4 (HT-22)	6 (HT-21)
0	1.75	JI-184	17.13 (19)	17.16 (24)	17.12 (21)	17.30 (12)	17.29 (14)
13	1.70	JI-182	22.18 (30)	21.89 (18)	22.03 (28)	21.72 (37)	21.71 (28)
23	1.65	JI-185	26.55 (72)	26.44 (23)	26.90 (31)	26.40 (56)	26.64 (38)
35	1.60	JI-179	30.18 (81)	30.01 (26)	29.56 (42)	30.16 (41)	30.43 (32)
58	0.6	JI-143	78.81 (85)	80.80 (180)	76.12 (360)	81.21 (451)	82.25 (350)

[a]Number in parentheses is 10^2 × maximum deviation from average along the specimen.

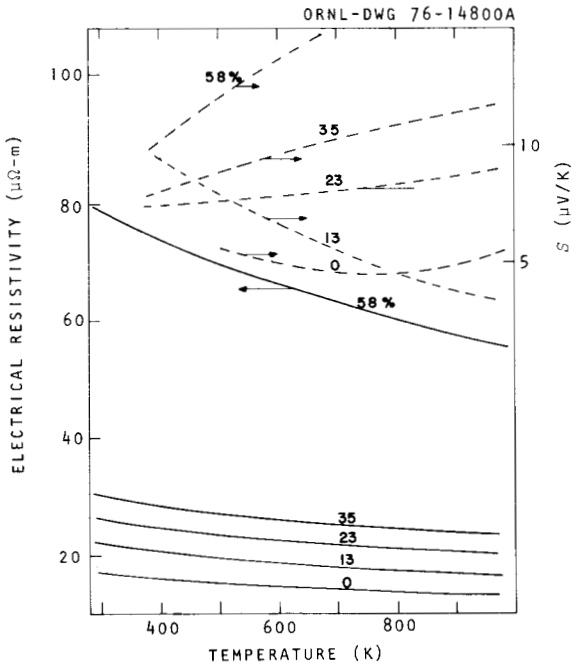

Fig. 6.11. Seebeck Coefficient and Electrical Resistivity of Unirradiated Bonded Fuel Rods as Functions of Temperature.

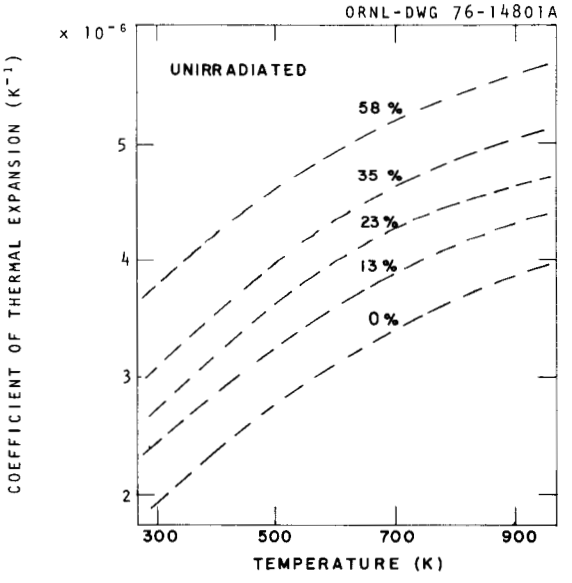

Fig. 6.12. Smoothed Values for the Coefficient of Thermal Expansion of Bonded Rod Specimens as a Function of Temperature and Coated Particle Loading.

Table 6.11. Polynomial Equations Representing the Thermal Conductivity and Coefficient of Thermal Expansion of Unirradiated Simulated Fuel

Specimen	Loading (vol %)	Coefficient of Thermal Expansion,[a] (K^{-1})	Thermal Conductivity[a] ($W\ m^{-1}\ K^{-1}$)
		$\times 10^{-6}$	
JI-184-8	0	$0.2716 + 6.280 \times 10^{-3}T - 2.586 \times 10^{-6}T^2$	$67.81 - 0.02616T$
JI-182-12	13	$0.7459 + 6.267 \times 10^{-3}T - 2.595 \times 10^{-6}T^2$	$46.54 - 0.01449T$
JI-185-14	23	$0.7607 + 7.359 \times 10^{-3}T - 3.415 \times 10^{-6}T^2$	$39.33 - 0.00851T$
JI-179-5	35	$1.1881 + 7.082 \times 10^{-3}T - 3.113 \times 10^{-6}T^2$	$30.97 - 0.00423T$
JI-143-11	58	$2.038 + 6.573 \times 10^{-3}T - 2.941 \times 10^{-6}T^2$	$16.6 - 0.00246T$

[a] T is temperature in kelvins.

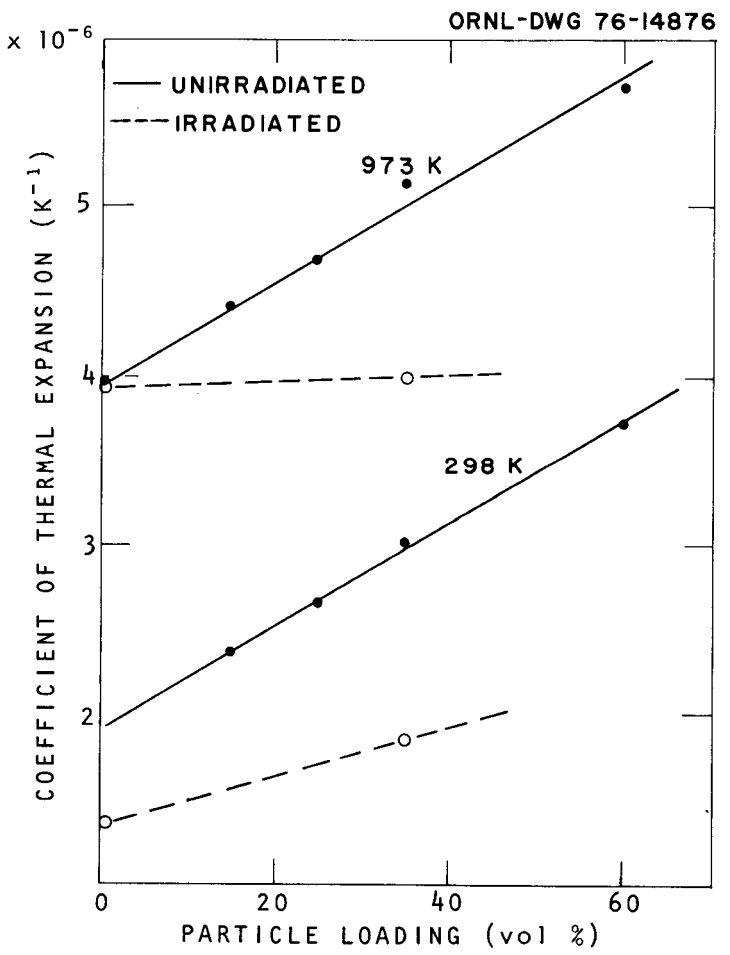

Fig. 6.13. Comparison of Coefficient of Thermal Expansion at 298 and 973 K for Unirradiated and Irradiated Samples as a Function of Particle Loading.

The λ results on unirradiated specimens are shown in Fig. 6.14. This figure indicates that λ decreases smoothly with increasing temperature and loading. The λ was fit with a linear relation in T, with the resulting parameters given in Table 6.11. All experimental data were within 1.7% of the equations with the exception of the 58 vol % specimen, where the maximum deviation of any datum from the polynomial was 5%. Previous results obtained on unirradiated materials with 0 and 28.5 vol % loadings are also shown in Fig. 6.14 from 80 to 400 K. The matrix density of these two materials was about 1.74 g/cm^3 for the 28.5% loaded specimen and 1.81 g/cm^3 for the other.[25] Although these densities are not exactly the same as those of the 13, 23, 35, and 58% loaded specimens, they serve as a comparison.

After irradiation, the ρ of all specimens was measured at room temperature (~300 K) as a prerequisite for λ measurements. The results are given in Table 6.12 and show that ρ increases with increasing neutron fluence for each volume particle loading. As irradiation was increased, the ρ of the 0 and 13% samples became much closer to each other as did those of the 23 and 35% samples. This effect may denote a basic behavior difference, which occurs between loadings of 13 and 23%.

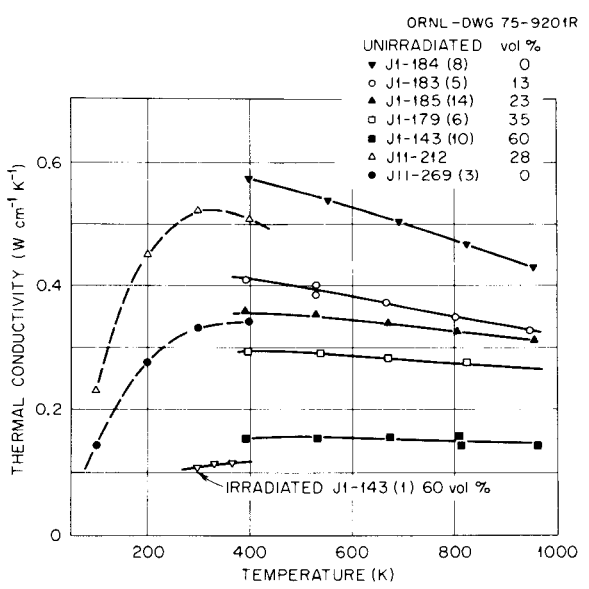

Fig. 6.14. Thermal Conductivity of Simulated Bonded Bed Fuel Rods as a Function of Temperature. Loading identified as "60 vol %" has been redetermined to be 58 vol %.

Table 6.12. Electrical Resistivity, ρ, of Bonded Rod Specimens Before and After Irradiation in HFIR

Particle Loading (vol %)	ρ, Resistivity, μΩ-m, for Each Number of Cycles				
	0	1	2	4	6
0	17.20	26.82	28.81	39.25	67.21
13	21.90	32.31	34.58	43.74	67.04
23	26.59	37.14	39.61	51.08	90.76[a]
35	30.07	38.75	40.15	51.24	b
58	79.11	95.50	c	a	c

[a]Broken but one small fragment may provide some information on ρ and λ near room temperature.

[b]Center spine still in place. If this can be removed, electrical resistivity and thermal conductivity near room temperature can be measured on one of the pieces.

[c]Broken too badly for any measurements.

The CTE of the two irradiated samples measured to date are compared with the unirradiated results at 298 and 973 K in Fig. 6.13. The decreased CTE at 298 K for the pure matrix material may be caused by residual stress and microcracks due to shrinkage under irradiation. At 973 K these effects have largely been neutralized. The large decrease in CTE observed on the 35 vol % irradiated sample clearly indicates that the coated particles have lost their additive effects. This could be caused by shrinkage of the outer pyrocarbon coating, by extensive microcracking of the adjacent matrix material, or by a combination of the two effects.

Figure 6.14 shows some low-temperature λ data obtained on the 58 vol % specimen after one cycle in HFIR. This specimen was broken during capsule disassembly and could not be assembled for the high-temperature measurements. The results indicate a λ decrease of approximately 20% at 400 K.

6.5.4 Irradiation Experiments HT-24 and -25 — R. L. Hamner and J M Robbins

Shim particles are inert diluent particles designed for use in HTGRs to provide for a range of fuel concentrations in different fuel rods having the same nominal lengths. At present they are obtained from bulk graphite, which is ground to a specific particle size range to aid in good particle blending and fabricability of fuel rods. HFIR irradiation capsules HT-24 and -25 were designed to screen several types of shim particles with respect to changes in fuel rods under irradiation. Another objective of the experiment was to determine the effect of deposition rate, and thus OPTAF, on dimensional changes of unrestrained LTI pyrolytic carbon samples prepared by GA and to obtain additional data on the relation between creep strain and the change in preferred orientation in restrained LTI pyrolytic carbon samples. The capsules were identical.

Each experiment contained 10 types of specimens nominally 9.65 mm diam by 18.80 mm long (0.380 by 0.740 in.) formed at ORNL by slug injection. The types of specimens were distinguished by five types of shim particles combined with two different volume loadings of Biso-coated carbon particles (25 and 35%) derived from desulfurized strong-acid resin to simulate fuel particles. The shim particles were added in sufficient amount to make a total particle volume loading of 60%.

Four of the shim particle types were supplied by GA and one by ORNL. The types of GA shim particles are listed below.

1. Impregnated GLCC-1099 (ground H-451 near-isotropic graphite from Great Lakes Carbon Company.

2. Impregnated Ringsdorff — V 564 (ground graphite manufactured in West Germany by Ringsdorff Werke GmbH).

3. UCC TS-1240X (ground TS-1240X near-isotropic graphite from Union Carbide Corporation.

4. Poco X-4029 (supplied by Poco Graphite, Inc. — manufacturing process proprietary).

The fifth shim was prepared at ORNL by slurry blending 50 wt % each of green Robinson coke and Thermax with 25 pph* Ashland grade 240 pitch to

---

*"Parts per hundred," parts of liquid added per hundred parts of solids being slurried.

dryness to obtain spheroids, heating to 2800°C for densification, then surface impregnating with Varcum (prepolymerized furfuryl alcohol), which was then completely polymerized. The characteristics of the shim particles are shown in Table 6.13. The matrix material, supplied by GA, for all rods consisted of 30 wt % Asbury grade NF 6353 graphite filler in Ashland grade 240 pitch containing an additive to aid in injection. The impregnated shim particles were incorporated in the rods as-cured to seal porosity and to add strength for fabrication, then carbonized *in situ* in the rods. The pyrolytic carbon strips were contained in graphite crucibles having the same nominal dimensions as the slug-injected rods. The unirradiated specimens were characterized by dimensional measurements, radiography (to detect any contamination with fuel particles), photography, metallography, electrical resistivity, and calculations for matrix density, volume loading, and coke yield.

Table 6.13. Data Summary for Shim Particles[a] for Irradiation Experiments HT-24 and -25

Capsule Position	Source	Code Number		Density, g/cm^3			Open Porosity[d] (%)
		Manufacturer	GA[b]	Tap	Helium	Mercury[c]	
1,6,20,15	Ringsdorff[e]	U564	F0150	1.10	2.01	1.98	1.49
2,7,19,14	UCC	TS-1240	F0176	0.98	2.15	1.93	10.23
3,8,18,13	ORNL[e]	S-18-1		1.12	1.97	1.92	2.54
4,9,17,12	Poco	X-4029	F0188	1.06	1.99	1.85	7.04
5,16,11	GLCC[e]	1099	F0166	1.05	2.00	1.96	2.00

[a]Shim particles are from 590 to 840 μm in diameter.

[b]General Atomic Company.

[c]As determined at 0.52 MPa (75 psi).

[d]Calculated from helium and mercury densities.

[e]Impregnated.

Matrix densities were lowest for rods containing the Poco shim particles (0.47 g/cm^3) regardless of shim particle volume loading, and highest for those containing the ORNL shim (0.55 g/cm^3). Coke yields ranged from 12.4 to 20.1%, being lowest for rods containing the Poco shim

and highest for those containing Ringsdorff, CLCC, and ORNL shims. Electrical resistivities, in general, increased with inert particle loadings, being lowest for rods containing Ringsdorff shim with 25 vol % inert particles (28 μΩ-m) and highest for rods containing the ORNL shim with 37 vol % inert particles (52 μΩ-m).

Representative sets of these specimens were selected and loaded into capsule HT-24 and -25. The capsules were irradiated in parallel in the HFIR for 2 and 4 cycles, respectively, being inserted in early June 1974. Postirradiation evaluation was performed by GA, and the results are contained in a topical report.[26] A quotation from the abstract of this report follows.

> The fuel compacts fabricated with the five different shim particle types survived irradiation at 850 to 1020°C, but were weakened by the irradiation effects and were subsequently damged during routine handling.
>
> Diametral changes of the fuel compacts fabricated with Great Lakes Carbon Company (GLCC), Union Carbide Corporation (UCC), and Poco Graphite, Inc., shim particles were negative for both axial and radial directions up to fluences of 7×10^{21} to 9×10^{21} n/cm^2 at 850 to 1020°C. Expansion was just beginning at 6×10^{21} to 7×10^{21} n/cm^2. In contrast, the dimensional changes of the fuel compacts fabricated with Ringsdorff, West Germany, shim particles showed initial contraction similar to that described above, followed by rapid expansion at about 4×10^{21} to 5×10^{21} n/cm^2, which led to net expansion at 8×10^{21} to 9×10^{21} n/cm^2. The behavior of fuel compacts fabricated with ORNL shim particles was intermediate to that of the Ringsdorff and GLCC-UCC-Poco compacts.
>
> Based on the dimensional change behavior of the fuel compacts irradiated in this experiment, shim particles fabricated from nuclear graphite blocks (such as GLCC's 1099 and UCC's TS-1240S) and the Poco shim particles are preferred over the highly anisotropic Ringsdorff particles or the agglomerated ORNL particles.

6.5.5 Test Capsules HT-26 and -27 — T. N. Tiegs

The primary objective of these experiments was to study the matrix-particle interaction phenomenon associated with the in-block carbonization technique proposed for the fabrication of HTGR fuel rods. The two capsules, HT-26 and -27, had similar loading plans and were exposed to about half and about full HTGR design fluence at the capsule

midplane, respectively. The three variables investigated were: (1) pitch coke yield, (2) strength of the particle coatings, and (3) surface texture of the coatings. Examination of the two experiments was completed and the results are being prepared for separate publication.[27] The abstract of this report follows:

> Capsules HT-26 and -27 were irradiated in the target region of the High Flux Isotope Reactor. The purpose was to study matrix-particle interaction in High-Temperature Gas-Cooled Reactor fuel rods before and after irradiation. The first objective was to fabricate fuel with a failed fuel fraction <0.1%. This was accomplished for packed Al_2O_3 and in-block carbonization techniques, using annealed Biso-coated fertile particles and either annealed or unannealed Triso-coated fissile particles. The second objective, to irradiate fuel rods and determine the failed fuel fraction (<1% for acceptable results), was not completely accomplished. In HT-26 the capsule evidently leaked, and the fuel rods suffered attack by steam. In HT-27 the fuel rods only in the high-temperature region suffered attack by zirconium (used as an oxygen getter in the capsule). These problems resulted in failed particles and consequently made it impossible to determine failure fractions due to matrix-particle interaction. Results from the other fuel rods in HT-27 showed that particle failure fractions of <1% can be obtained from fuel rods carbonized in-tube and irradiated at temperatures up to ~900°C (fuel surface temperature).

6.5.6 Irradiation Test Capsules HT-28, -29, and -30 — R. L. Beatty

The experiments HT-28, -29, and -30 were part of a continuing series of HFIR target irradiation capsules. They were planned primarily to test relative fast-neutron damage resistance of pyrolytic carbon coatings on thoria and inert carbon kernels. Capsules HT-28 and -29 contained unbonded specimens of fertile particles produced by ORNL and GA in the fuel positions. Additional specimens of inert particles with ZrC coatings and wafers of hot-pressed ZrC and extruded graphite produced by the Los Alamos Scientific Laboratory were included as unfueled spacers and in fuel magazine end plugs. Capsule HT-30 contained bonded rods with ORNL fertile particles in all fuel positions and unbonded ORNL inert particles in magazine end plugs.

6.5.6.1 Capsule Design

The three capsules were of different design with regard to fuel loading, temperature, and cover gas atmosphere. All test fertile particles for HT-28 and -29 were loaded into annular Poco graphite holders similar to those used in earlier experiments, including HT-17, -18, and -19. These capsules each contained 32 experimental thoria specimens, 22 with GA particles and 10 with ORNL particles. Both capsules also contained uranium, 6.5% enriched in ^{235}U, for heat generation during the early part of the irradiation. Capsule HT-28 was designed for a four-cycle irradiation, and as in the earlier capsules HT-12 through -15 and -17 through -19, the uranium was distributed in 20 annular loose-particle holders and four magazine end plugs, and the sealed capsule atmosphere was argon. The particle holder design surface temperatures in HT-28 were 1250°C for the two center magazines and 900°C for the end magazines. Capsule HT-29 was an isothermal design with 900°C holder surface design temperature and was irradiated for five HFIR cycles. The lower maximum temperature in HT-29 made it possible to use a helium atmosphere, which, in turn, necessitated a much higher total heavy metal loading. This required placing the uranium-containing driver particles and part of the thorium in 20 molded rods since the annular machined holders did not have sufficient fuel volume. The inert particles were placed in the end plugs of the Poco graphite magazines to avoid disturbance of the power generation profiles calculated for these capsules.

Capsule HT-30 was designed for a four-HFIR-cycle irradiation and contained only ORNL coated thoria and inert particles. All the test fertile particles were fabricated into rods by the slug-injection process. The bonded rod test specimens were selected over loose-particle holders to provide more realistic test conditions for this capsule. The rods were carbonized in natural flake graphite to 1000°C and then annealed at 1800°C. The test specimens were nominally 9.58 mm diam by 6.98 mm long (0.377 by 0.275 in.). These dimensions allowed space for 52 fuel rods, all of which contained only thoria and inert carbon particles. The uranium used in HT-28 and -29 for power generation

was deleted from HT-30 to allow an approximately 60% increase in capsule thorium loading. Advantages of the increased fertile particle test capacity were considered to outweigh the resulting lower-than-design operating temperatures during the first two irradiation cycles for this capsule. The rod surface design temperatures were 1250°C for the two center magazines and 900°C for the end magazines. The HT-30 atmosphere was neon.

6.5.6.2 Experimental Objectives

The primary objective of the ORNL tests in this series of experiments was to determine relative stabilities under fast-neutron irradiation of low-temperature isotropic (LTI) pyrolytic carbon coatings having subtle differences in microstructure. The microstructural differences of interest include all properties that can be measured and were obtained experimentally by varying deposition conditions. The primary deposition process variables studied were temperature, hydrocarbon (MAPP gas) concentration, and total fluidizing gas flux. Deposition rate, which is often quoted to characterize coatings, is a strong function of both hydrocarbon concentration and total gas flux. Thus, a major concern of this work was to distinguish between deposition rate effects *per se* and hydrocarbon concentration effects on both irradiation stability and measurable differences in microstructure.

It is well known that differences in carbon coating microstructure arising from variation of coating process parameters strongly influence resistance to fast-neutron irradiation damage. Results of many irradiation tests indicate that anisotropy or preferred orientation within the coating structure is a dominant factor in determining this resistance, though other microstructural features, most of which are poorly understood, are important as well. Accordingly, a recent series of experiments, HT-17, -18, and -19, was designed specifically to determine limits on anisotropy that would allow adequate performance as a function of fast-neutron fluence. However, results of those experiments were ambiguous and did not produce the clear-cut definition of the anisotropy limits desired. Thus, a major conclusion drawn from the experiments was that characterization

methods used were inadequate and that we do not yet have a combination of measurements capable of uniquely characterizing a carbon coating to predict its irradiation performance.

Many pyrocarbon coatings have performed very well on exposure to full-HTGR design fluence, but at present the preparation of reliable coatings necessarily includes specification of certain fabrication process parameters. In order to develop the necessary set of characterization tools and to correlate meaningfully the resulting sets of measured properties with irradiation performance, a large set of coatings with different microstructures was fabricated and tested. This set of test coatings included a wide range of process variables relating to the so-called LTI process. Further development of characterization techniques — including OPTAF, BAF, and other x-ray characteristics, definition of microstructure by various etching techniques, and scanning and transmission electron microscopy — was pursued as a major portion of the preparation and interpretation of these experiments.

Since the ultimate goal of these tests was to correlate the irradiation stability of coatings with a set of measurable properties, characterization of the coatings in terms of microstructural features was a major part of the work. However, since characterization, including development of new techniques, was necessarily continued during and after the irradiation, coatings for testing were selected on the basis of deposition conditions.

The set of LTI coatings selected for testing in these experiments was deposited in a 64-mm (2.5-in.) coater as Biso fertile particles of nominal reference design. Coating process parameters and properties are listed in Table 6.14. The grouping in Table 6.14 shows the multiple combinations of hydrocarbon concentration and deposition rate employed in preparing the coating set. Deposition rate was varied, within limits, independently of hydrocarbon concentration by using different total gas fluxes. In addition to the variations introduced by gas flow rates and compositions, density differences were superimposed by changing coating temperature. The coating set thus produced was intended to bracket the ability to survive HTGR design fast fluences and to provide a range

Table 6.14. Deposition Parameters and Properties of LTI MAPP Gas[a] Coatings[b] Irradiated in Experiments HT-28-, -29, and -30

MAPP Gas		Deposition		Surface Connected Porosity[c] (%)	Density, g/cm³			OPTAF[e]	Batch
Concentration (%)	Flux (cm³/min-cm²)	Temperature (°C)	Rate (μm/min)		As Deposited[d]	After 15 min at 1800°C[d]	Corrected[c]		
100	5.57[f]	1275	23.0	9.62	1.989	2.053	1.855	1.02	OR-2275-AHT
100	2.86[g]	1275	14.1	8.13	1.973	2.019	1.855	1.02	OR-2266-HT
100	1.35[h]	1275	7.3	8.33	1.948	1.982	1.817	1.02	OR-2291-HT
100	0.77[h]	1275	4.9	7.98	1.924	1.975	1.817	1.01	OR-2297-AHT
100	5.57[f]	1325	28.0	15.16	1.948	1.957	1.660	1.01	OR-2274-HT
100	2.86[g]	1325	15.7	9.75	1.918	1.949	1.759	1.01	OR-2265-HT
100	1.35[h]	1325	8.6	10.06	1.868	1.882	1.693	1.01	OR-2290-HT
100	0.77[h]	1325	5.6	10.86	1.854	1.898	1.692	1.01	OR-2296-AHT
50	2.93[f]	1275	10.7	5.34	1.974	2.015	1.907	i	OR-2271-HT
50	1.43[g]	1275	6.5	5.19	1.966	2.009	1.905	1.01	OR-2262-HT
50	0.68[h]	1275	3.6	4.13	1.934	1.961	1.880	1.02	OR-2294-HT
50	0.38[h]	1275	2.3	4.18	1.888	1.910	1.830	1.02	OR-2299-HT
50	2.93[f]	1325	12.5	7.91	1.884	1.908	1.757	1.01	OR-2269-HT
50	1.43[g]	1325	7.4	5.38	1.853	1.886	1.785	1.01	OR-2261-HT
50	0.68[h]	1325	3.9	5.47	1.813	1.832	1.731	i	OR-2293-HT
50	0.38[h]	1325	2.5	4.99	1.806	1.823	1.732	1.01	OR-2298-HT
25	1.46[f]	1275	5.2	3.81	1.968	2.009	1.933	1.01	OR-2273-HT
25	0.73[g]	1275	3.2	3.04	1.950	1.986	1.926	1.02	OR-2264-HT
25	0.34[h]	1275	1.8	3.10	1.897	1.912	1.852	1.02	OR-2295-HT
25	1.46[f]	1325	6.2	4.33	1.840	1.860	1.780	1.01	OR-2272-HT
25	0.73[g]	1325	3.6	3.56	1.816	1.837	1.771	1.01	OR-2263-HT
15	0.84[f]	1275	3.1	3.24	1.945	1.977	1.913	1.02	OR-2276-HT

[a]MAPP gas is marketed by Airco, Inc., and consists primarily of methylacetylene and propadiene with alkanes as stabilizers.

[b]Biso particles of nominal design 500-μm ThO_2 kernel, 85-μm buffer, 85-μm LTI.

[c]Determined by mercury porosimetry (15,000 psi) as percent of LTI volume assuming 4-μm infiltration of buffer.

[d]Measured by gradient column technique.

[e]Measured in twofold symmetry (without analyzer), after heat treatment.

[f]High flux obtained by using approximately half usual charge volume.

[g]Typical flux on 350-g, 125-cm³, charge of buffer-coated fertile particles in 2.5 in. coating tube.

[h]Low flux obtained for given concentration by diluting bed with low-density carbon particles to reduce fluidizing flow requirement.

[i]Not determined.

of microstructures suitable for correlating structure and performance. To the extent possible, these coatings were irradiated under a variety of conditions including different temperatures and fluences and as loose particles and in bonded rods. In addition to the coating set listed in Table 6.14, one capsule, HT-30, contained for comparison four candidate coatings deposited in a 0.13-m (5-in.) prototype coater and one coating produced in a 25-mm (1-in.) coater and previously irradiated without failure in capsules HT-12 through -15. These particles, all of the nominal Biso-coated fertile design, are shown in Table 6.15.

Table 6.15. Deposition Parameters and Properties of LTI Propylene Coatings[a] Irradiated in Capsule HT-30

Batch	C_3H_6 Concentration (%)	Deposition		Density[b] After 30 min at 1800°C (g/cm^3)	OPTAF[c]
		Temperature (°C)	Rate (μm/min)		
OR-1849-HT[d]	75[e]	1300	21.5	1.940	1.02
J-488[f]	50[e]	1350	7.2	1.976	1.02
J-489[f]	50[e]	1350	5.8	1.904	1.01
J-490[f]	100	1350	6.2	1.992	1.01
J-491[f]	100	1350	9.1	2.004	1.01

[a]Biso particles of nominal design 500-μm ThO_2 kernel, 80-μm buffer, 75-μm LTI.

[b]Measured by gradient column.

[c]Measured in twofold symmetry (without analyzer) after heat treatment.

[d]Deposited in 25-mm (1-in.) coater.

[e]Helium diluent.

[f]Deposited in 0.13-m (5-in.) coater.

A performance comparison between particles irradiated in bonded rods and in loose particle holders was a secondary objective of these experiments. A few anomalous results from earlier HT experiments have

raised the question of whether coatings may be broken by particle-particle ratchetting due to coating dimensional changes during irradiation. The bonded (slug-injected) rods for these tests were carbonized in natural flake graphite to minimize coating-matrix interaction effects while providing a coating test environment as realistic as possible.

A tertiary objective of these experiments was the irradiation of coatings that could be examined in detail for microstructural changes induced by the irradiation. For this purpose, particles with inert carbon kernels were included in the end plugs of capsule HT-30 at no expense to the capsule fuel capacity. We anticipated that these particles could be removed from the hot cell after irradiation. The inert test particles included all those coated along with the fertile particles denoted by footnote *f* in Table 6.15 as well as one Triso-coated lot.

6.5.6.3 Capsule Loading, Operation, Fluence, and Burnup

All capsule loading calculations, testing supervision, and fluence and burnup calculations were performed by B. H. Montgomery of the ORNL Reactor Division. Capsules HT-28 and -30 were irradiated for four HFIR cycles from February 4 to May 9, 1975. Capsule HT-29 received five cycles of irradiation from February 4 to June 3, 1975. The individual specimen irradiation conditions for HT-28, -29, and -30 are shown, respectively, in Tables 6.16 through 6.18.

All three capsules were successfully irradiated and transferred to the hot cell for examination. When the postirradiation examination is completed, results will be evaluated in terms of microstructural characteristics as well as fabrication conditions.

Table 6.16. Capsule HT-28 Loading Schedule, Design Operating Temperature, Neutron Fluences, and Heavy Metal Burnup

Capsule Position[a]	Specimen Lot	Design Temperature[b] (°C)	Estimated Fluence, n/cm^2		Estimated ^{232}Th Burnup (% FIMA)
			<0.414 eV	>0.18 MeV	
E-S-1	LASL[c]	900			
1-A	LASL[d]				
2, 4, 5, 7	GA[e]	900			
8	OR-2294-HT	900	14.3×10^{21}	6.07×10^{21}	6.30
10	OR-2266-HT	900	14.9	6.54	6.70
11, 13	GA[e]	900			
M-S-1	LASL[c]	1250			
15, 17, 18, 20	GA[e]	1250			
21	OR-2294-HT	1250	20.4	8.77	8.69
23	OR-2266-HT	1250	20.9	8.88	8.80
24, 26	GA[e]	1250			
27	GA[e]	1250			
29	OR-2273-HT	1250	21.1	8.92	8.85
30	OR-2297-HT	1250	20.9	8.88	8.80
32	OR-2262-HT	1250	20.4	8.77	8.69
33, 35, 36, 38	GA[e]	1250			
M-S-2	LASL[c]	1250			
40	GA[e]	900			
42	OR-2273-HT	900	15.4	6.77	6.90
43	OR-2297-AHT	900	14.9	6.54	6.70
45	OR-2262-HT	900	14.3	6.07	6.30
46, 48, 49, 51	GA[e]	900			
E-S-2	LASL[c]	900			

[a]Positions (1 through 52) and four end plugs not listed contained uranium (6.5% enriched in ^{235}U) for heat generation only.

[b]Graphite holder surface temperature.

[c]LASL loose inert particles in graphite end plug.

[d]LASL hot-pressed ZrC wafer placed in end (replacing graphite screw) of uranium-loaded particle holder.

[e]GA Biso-coated fertile particles.

Table 6.17. Capsule HT-29 Loading Schedule and Neutron Fluences and Heavy Metal Burnup[a]

Capsule Position[b]	Specimen Lot	Estimated Fluence, n/cm^2		Estimated ^{232}Th Burnup (% FIMA)
		<0.414 eV	>0.18 MeV	
E-S-1	LASL[c]			
1-A	LASL[d]			
2	OR-2264-HT	14.4×10^{21}	5.73×10^{21}	7.15
4	OR-2294-HT	15.6	6.40	7.85
5, 7, 8, 10, 11, 13	GA[e]			
E-L-1	LASL[c]			
M-S-1	LASL[c]			
14-A	LASL[d]			
15	OR-2291-HT	23.2	10.21	11.40
17, 18, 20, 21	GA[e]			
23	OR-2262-HT	26.2	11.12	12.20
24, 26	GA[e]			
M-L-1	LASL[c]			
M-L-2	LASL[c]			
27	GA[e]			
29	OR-2299-HT	26.5	11.17	12.30
30	OR-2261-HT	26.2	11.12	12.20
32, 33, 35, 36	GA[e]			
38	OR-2290-HT	23.2	10.21	11.40
39-A	LASL[d]			
M-S-2	LASL[c]			
E-L-2	LASL[c]			
40, 42, 43, 45, 46	GA[e]			
48	OR-2298-HT	16.2	6.69	8.20
49	OR-2293-HT	15.6	6.40	7.85
51	OR-2263-HT	14.4	5.73	7.15
52-A	LASL[d]			
E-S-2	LASL[c]			

[a]Graphite holder design surface temperature was 900°C.

[b]Positions (1 through 52) not listed contained uranium (6.5% enriched in ^{235}U) in warm-molded rods for heat generation only.

[c]LASL loose inert particles in graphite end plug.

[d]LASL extruded graphite wafer accommodated for shortening adjacent uranium-loaded rod.

[e]GA Biso fertile particles.

Table 6.18. Capsule HT-30 Loading Schedule, Design Operating Temperature, and Neutron Fluences and Heavy Metal Burnup

Capsule Position[a]	Specimen Lot		Estimated Fluence, n/cm^2		Estimated ^{232}Th Burnup (% FIMA)
	First Position	Second Position	<0.414 eV	>0.18 MeV	
E-S-1, 2	Inerts[b]	Inerts[b]		3.8×10^{21}	
1, 52	OR-2276-HT	OR-2295-HT	11.1×10^{21}	4.31	4.61
2, 51	OR-2298-HT	OR-2263-HT	11.5	4.58	4.90
3, 50	J-488[c]	J-490[c]	12.0	4.92	5.12
4, 49	OR-2299-HT	OR-2264-HT	12.5	5.11	5.40
5, 48	OR-2290-HT	OR-2269-HT	12.9	5.34	5.62
6, 47	OR-2291-HT	OR-2271-HT	13.4	5.61	5.85
7, 46	OR-2293-HT	OR-2262-HT	13.8	5.84	6.10
8, 45	OR-2294-HT	OR-2262-HT	14.3	6.07	6.30
9, 44	OR-2265-HT	OR-2296-AHT	14.6	6.31	6.50
10, 43	OR-2266-HT	OR-2297-AHT	14.9	6.54	6.70
11, 42	OR-2274-HT	OR-2273-HT	15.4	6.77	6.90
12, 41	OR-2275-AHT	OR-2272-HT	15.8	6.99	7.10
13, 40	J-489[c]	J-491	16.1	7.15	7.21
E-L-1, 2	Inerts[b]	Inerts[b]		7.4	
M-S-1, 2	Inerts[b]	Inerts[b]		7.7	
14, 39	J-489[c]	J-491[c]	18.1	8.00	8.09
15, 38	OR-2276-HT	OR-1849-HT[d]	18.5	8.15	8.21
16, 37	OR-2298-HT	OR-2263-HT	18.9	8.27	8.30
17, 36	OR-2299-HT	OR-2264-HT	19.2	8.42	8.40
18, 35	OR-2290-HT	OR-2269-HT	19.6	8.52	8.49
19, 34	OR-2291-HT	OR-2271-HT	19.8	8.61	8.59
20, 33	OR-2293-HT	OR-2261-HT	20.1	8.69	8.62
21, 32	OR-2294-HT	OR-2262-HT	20.4	8.77	8.69
22, 31	OR-2265-HT	OR-2296-AHT	20.6	8.84	8.75
23, 30	OR-2266-HT	OR-2297-AHT	20.9	8.88	8.80
24, 29	OR-2274-HT	OR-2273-HT	21.1	8.92	8.85
25, 28	OR-2275-AHT	OR-2272-HT	21.3	8.96	8.88
26, 27	J-488[c]	J-490[c]	21.5	9.00	8.91
M-L-1, 2	Inerts[b]	Inerts[b]		9.0	

[a]Specimens 1–13 and 40–52 had 900°C design surface temperature; specimens 14–39 had 1250°C design surface temperature.

[b]Magazine end plug containing inert coated particles.

[c]Biso-coated particles prepared in 0.13-m (5-in.) coater.

[d]Reference batch irradiated in HT-12 through -15.

6.6 IRRADIATION TESTS IN HFIR REMOVABLE BERYLLIUM FACILITIES — F. J. Homan

To date ten capsules have been irradiated in the HFIR Removable Beryllium (HRB) facilities. Reporting is completed on eight of these capsules, and postirradiation examination was nearly completed on the remaining two capsules by the end of this reporting period. The HFIR was shut down from June 1975 until September, and the next HRB capsules are scheduled to begin irradiation in November or December 1975.

The most significant accomplishments during the reporting period, with respect to HRB testing, is the performance of WAR fissile fuel in the HRB-7 through -10 series. We now feel we have a reference fissile particle that will give adequate performance for steam-cycle HTGRs and offers considerable potential for improvement for application in the higher temperature environments characteristic of VHTRs.

6.6.1 Capsules HRB-4 and -5 — F. J. Homan

The design, operation, and examination of HRB-4 and -5 were reported previously.[28] During this reporting period the thermal analyses of these capsules was completed, and a topical report issued.[29] The thermal analyses for each fuel rod adjacent to a Chromel vs Alumel thermocouple in the graphite sleeve are presented in Figs. 6.15 through 6.20 for HRB-4. The plots for HRB-5 are similar.[29] Shown are the graphite midwall temperatures, fuel surface and center temperatures, as functions of time during the irradiation. The report[29] also shows the fission heat rates for each specimen, and the sweep gas compositions as functions of time. All other information on these capsules was published last year.[28]

6.6.2 Capsule HRB-6 — F. J. Homan

The design, operation, and examination of HRB-6 was reported in last year's annual.[30] During this reporting period the thermal analysis of the capsule was completed, and a topical report was issued.[31] The thermal analyses for each fuel rod adjacent to a Chromel-Alumel thermocouple in the graphite sleeve are presented in Figs. 6.21 through 6.27.

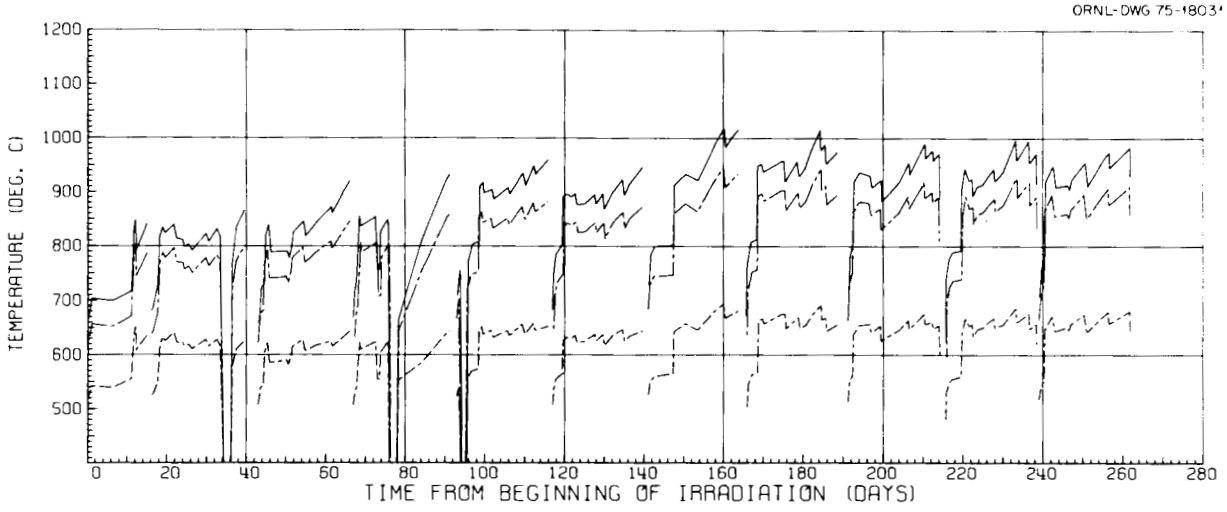

Fig. 6.15. Fuel Center, Fuel Surface, and Graphite Midwall Temperatures for HRB-4 Specimen 1B.

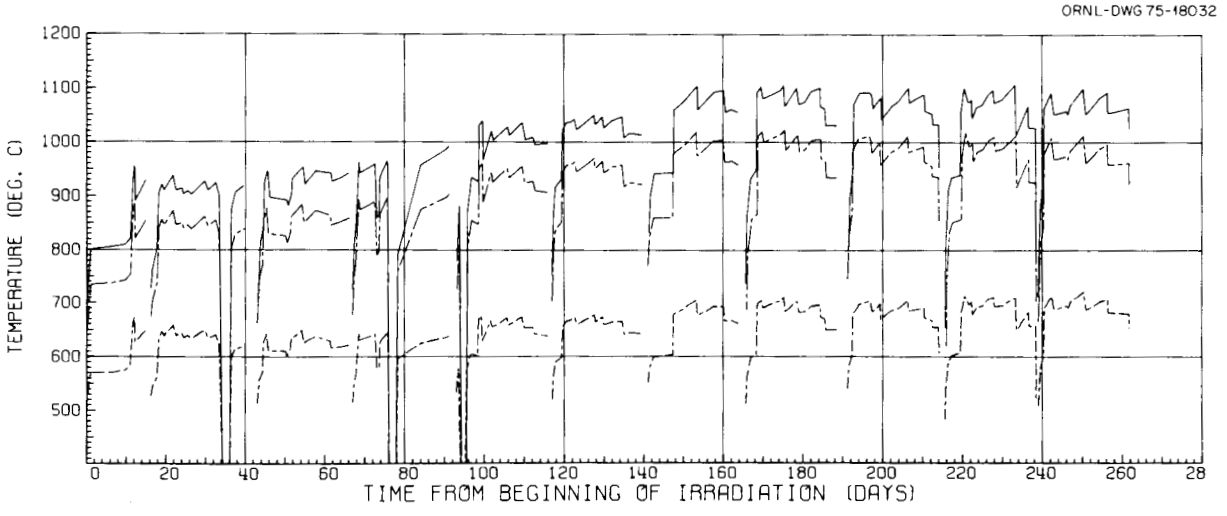

Fig. 6.16. Fuel Center, Fuel Surface, and Graphite Midwall Temperatures for HRB-4 Specimen 1C.

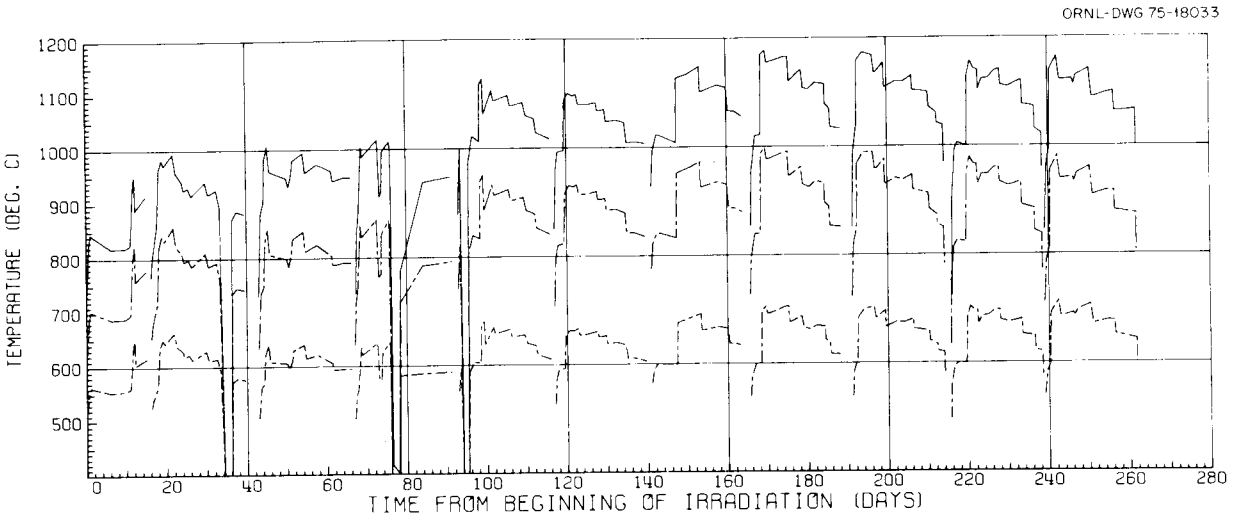

Fig. 6.17. Fuel Center, Fuel Surface, and Graphite Midwall Temperatures for HRB-4 Specimen 2B.

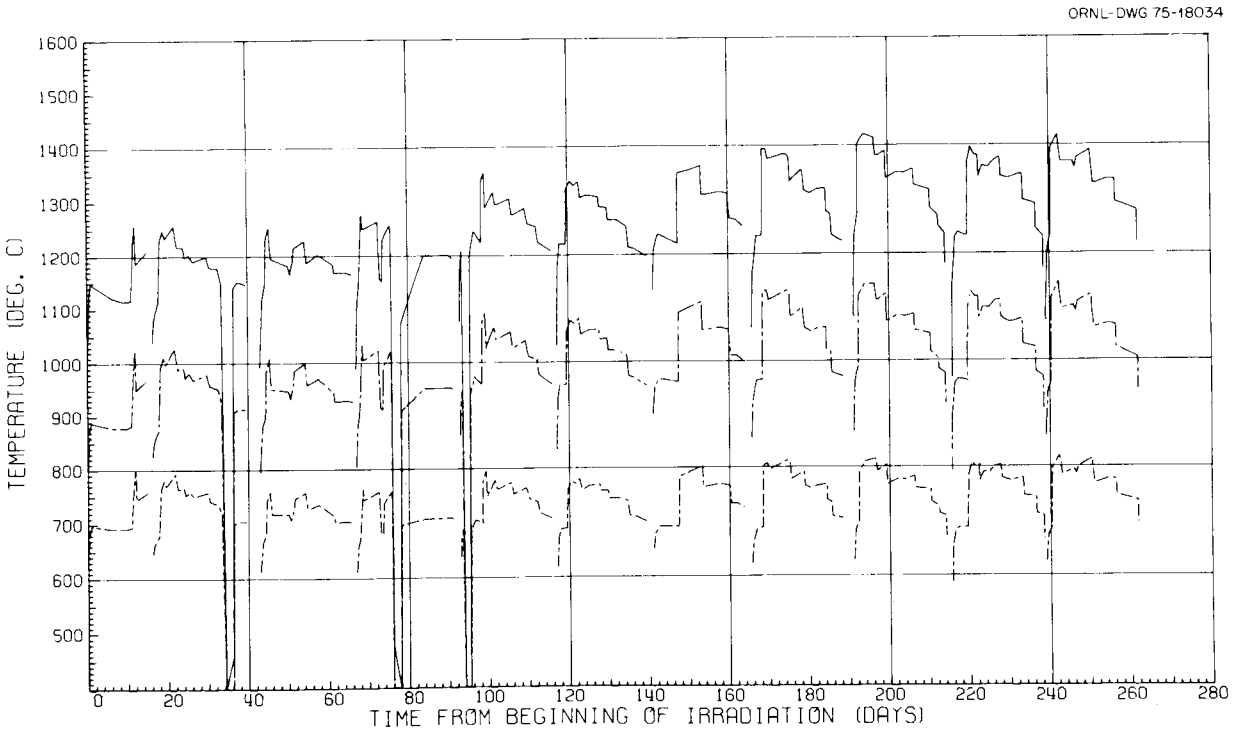

Fig. 6.18. Fuel Center, Fuel Surface, and Graphite Midwall Temperatures for HRB-4 Specimen 3A.

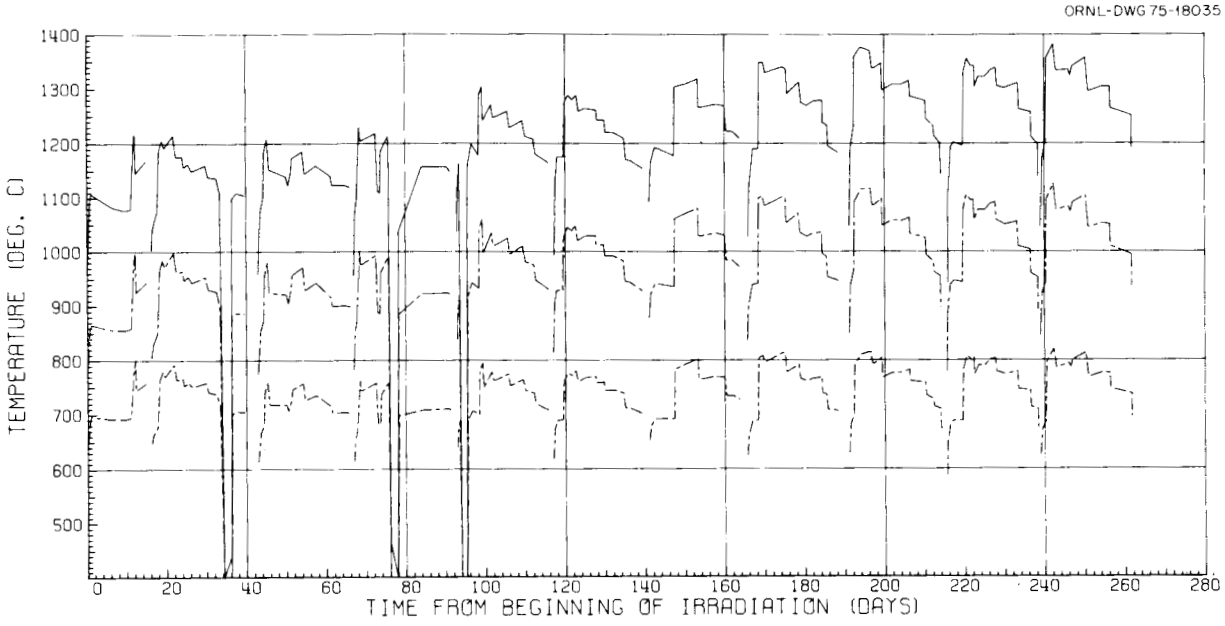

Fig. 6.19. Fuel Center, Fuel Surface, and Graphite Midwall Temperatures for HRB-4 Specimen 3B.

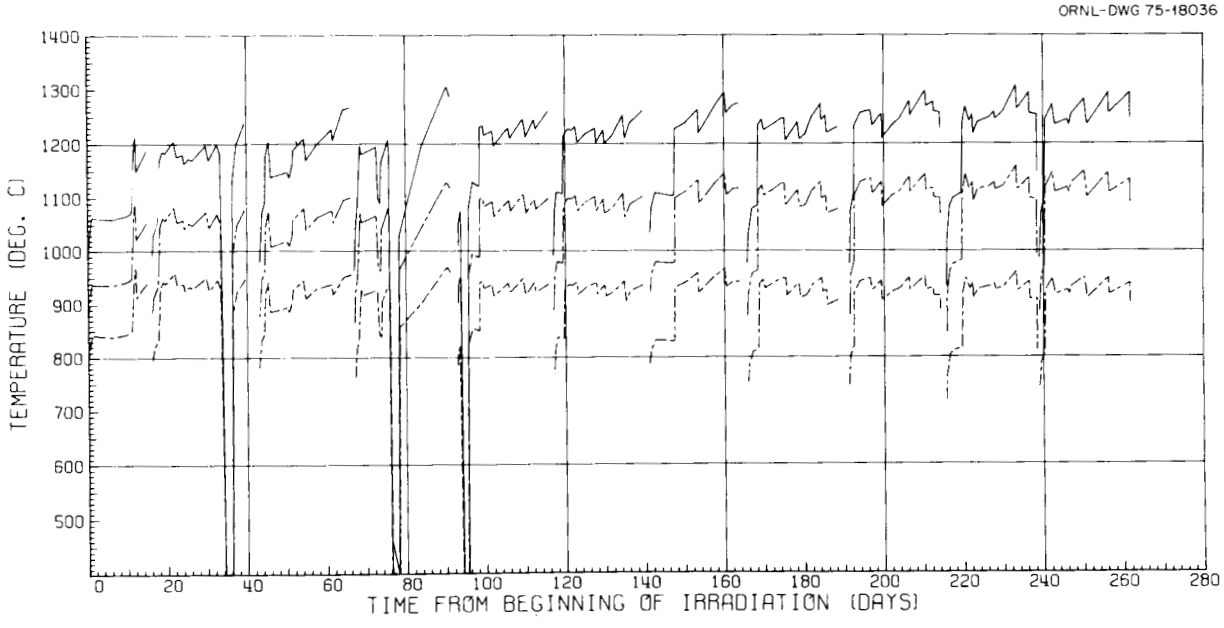

Fig. 6.20. Fuel Center, Fuel Surface, and Graphite Midwall Temperatures for HRB-4 Specimen 4B.

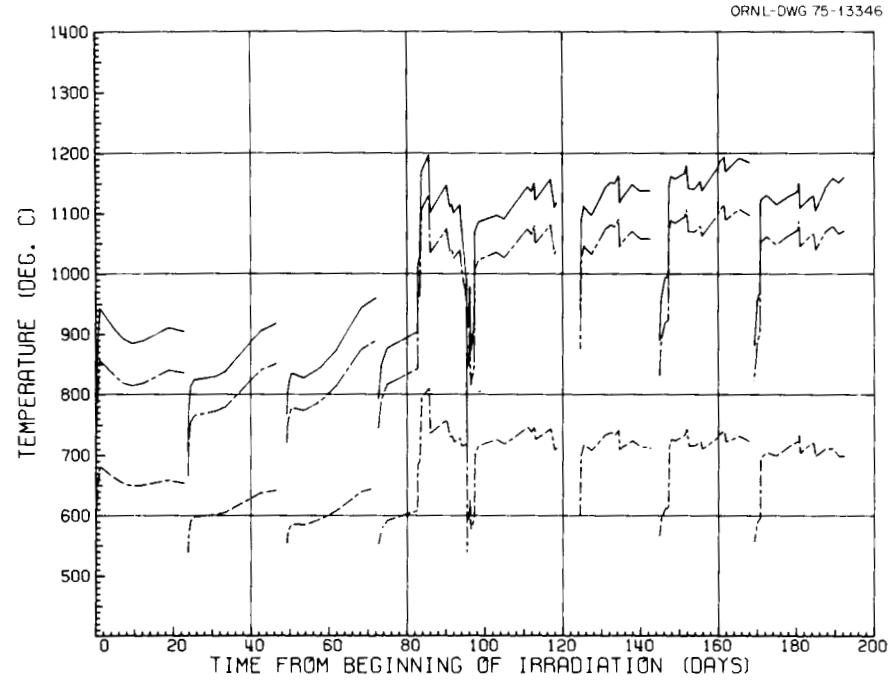

Fig. 6.21. Fuel Center, Fuel Surface, and Graphite Midwall Temperatures for HRB-6 Specimen 1B.

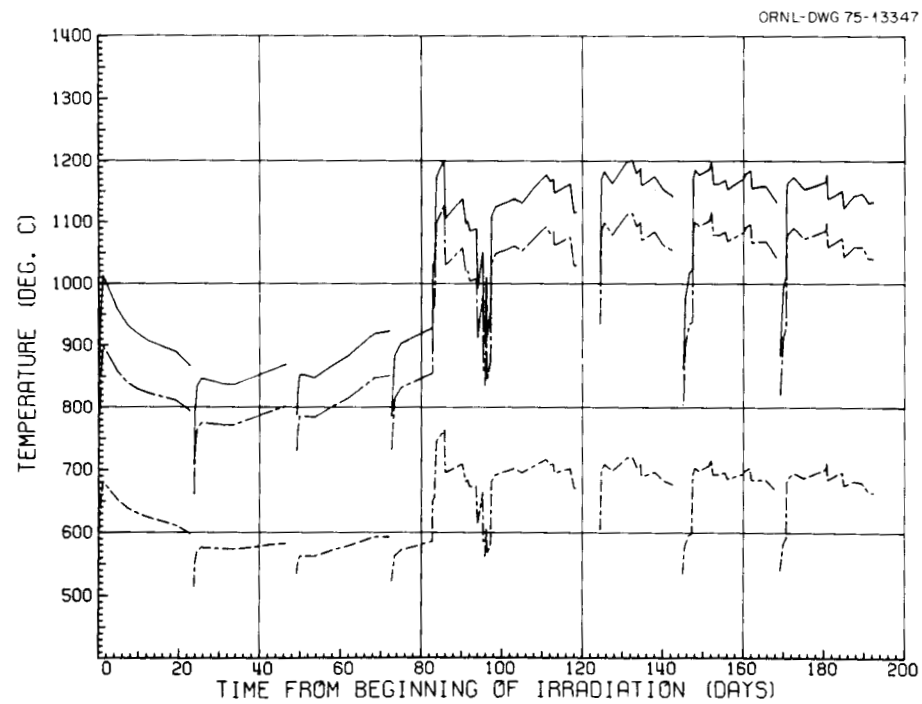

Fig. 6.22. Fuel Center, Fuel Surface, and Graphite Midwall Temperatures for HRB-6 Specimen 1C.

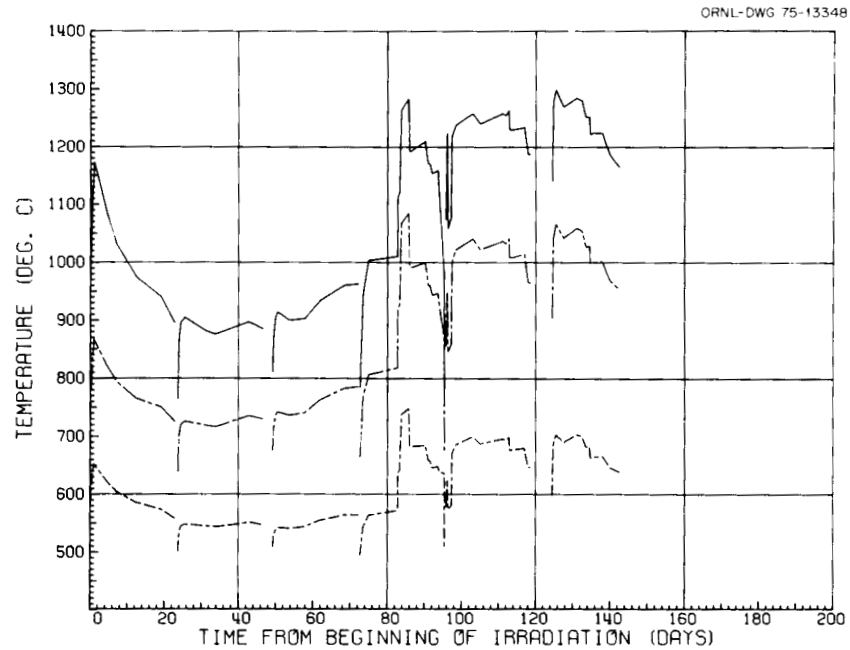

Fig. 6.23. Fuel Center, Fuel Surface, and Graphite Midwall Temperatures for HRB-6 Specimen 2B.

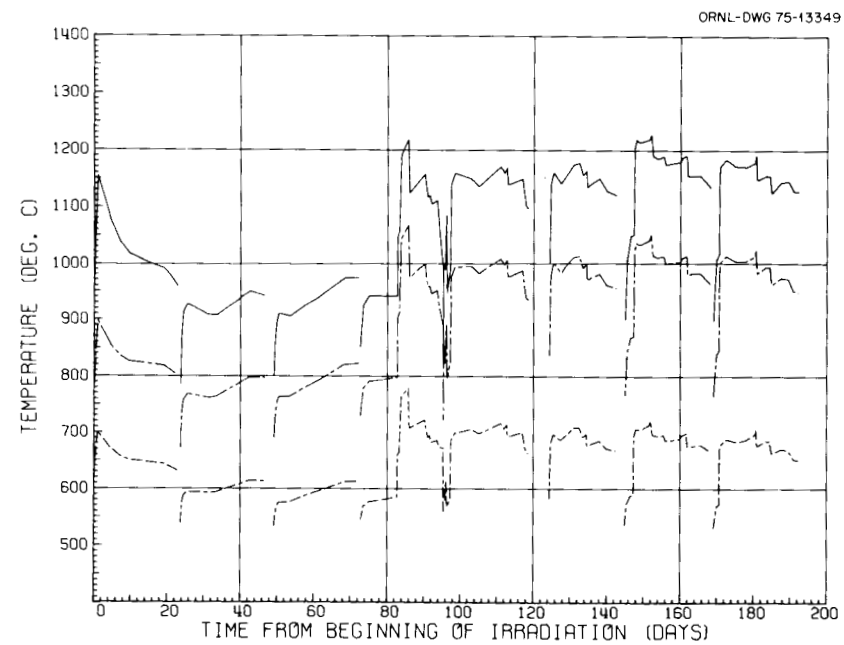

Fig. 6.24. Fuel Center, Fuel Surface, and Graphite Midwall Temperatures for HRB-6 Specimen 3A.

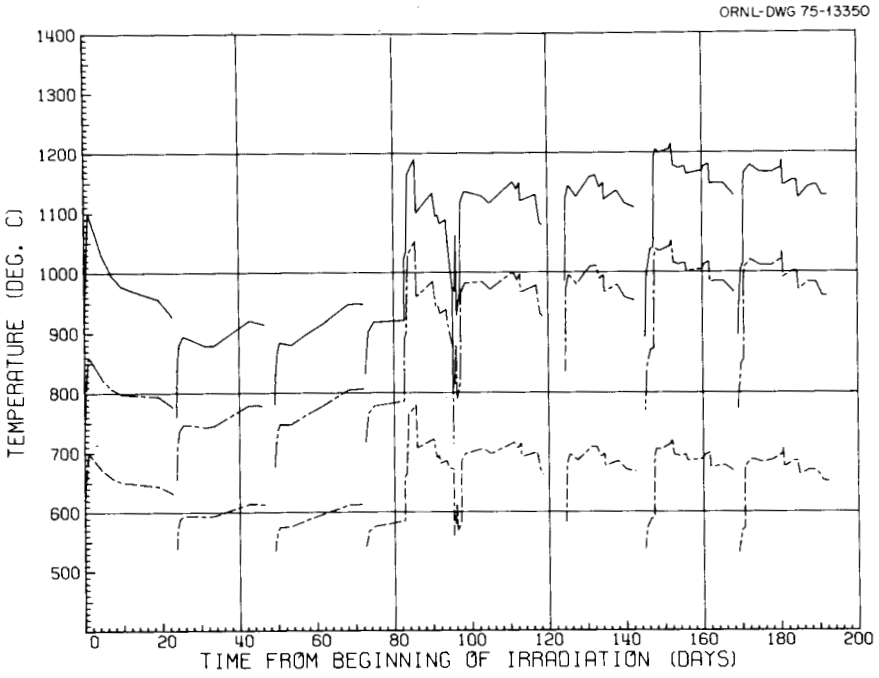

Fig. 6.25. Fuel Center, Fuel Surface, and Graphite Midwall Temperatures for HRB-6 Specimen 3B.

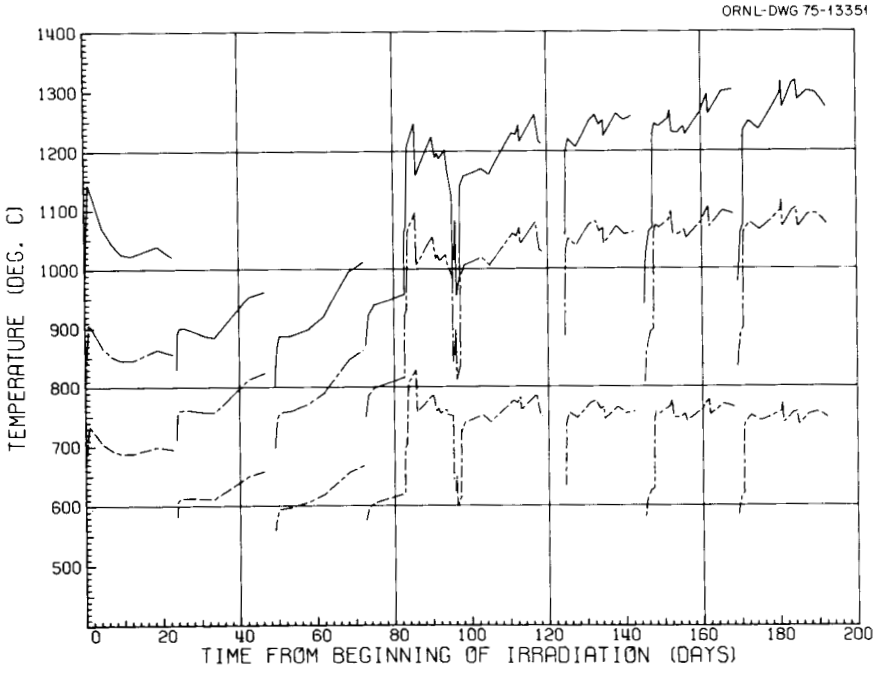

Fig. 6.26. Fuel Center, Fuel Surface, and Graphite Midwall Temperatures for HRB-6 Specimen 3C.

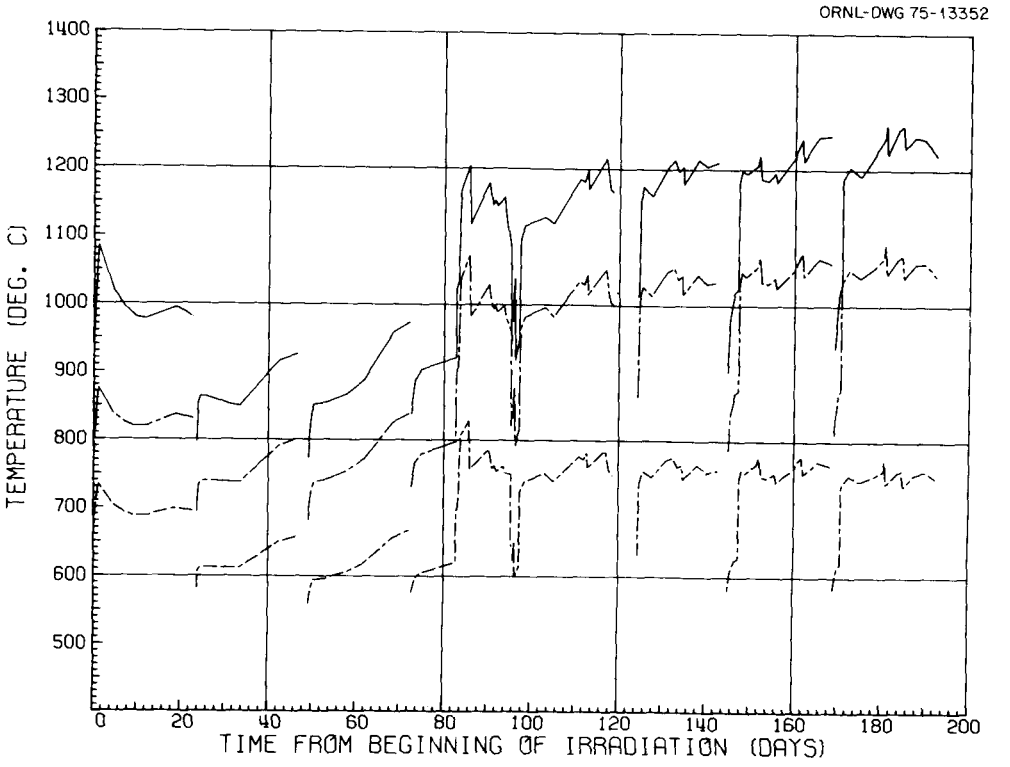

Fig. 6.27. Fuel Center, Fuel Surface, and Graphite Midwall Temperatures for HRB-6, Specimen 3D.

Shown are the graphite midwall temperatures and the fuel surface and center temperatures as functions of time during the irradiation. Also reported[31] are the fission heat rates for each specimen and the sweep gas compositions as functions of time. All other information on these capsules was published last year.[30]

6.6.3 Capsules HRB-7 and -8 — K. H. Valentine, B. H. Montgomery, R. L. Hamner, E. L. Long, Jr., and T. N. Tiegs

The analysis of results obtained from the seventh and eighth capsules in the HFIR Removable Beryllium (HRB) series of irradiation experiments is now complete. This includes the thermal analysis, postirradiation examinations, and fuel kernel migration studies. Although the experimental objectives, capsule design, and fabrication data have already been reported in detail,[32] a brief summary will be included here to provide context for the results.

The major objective of the HRB-7 and -8 irradiation experiments was to screen a relatively large number of fissile particle types for performance at high temperatures (1250–1500°C) and high burnups (about 84% FIMA for ^{235}U and 6–12% for ^{232}Th). More specific objectives are listed below.

1. To test a theoretical model for amoeba migration. The kernels of primary interest were (1) mixed oxide-carbide derived from sol-gel microspheres, because the two-phase mixture was thought to be more stable than oxide fuel kernels, and (2) uranium oxynitride derived from sol-gel microspheres, because thermochemical calculations suggested improved performance under HTGR conditions of fluence and temperature. A sol-gel UO_2 particle was used as a reference for comparison with the other two particles.

2. To test potential recycle fuel candidates. These included sol-gel UO_2, weak-acid-resin UC_2, and sol-gel $(4Th,U)O_2$. Comparisons were made between ^{233}U- and ^{235}U-bearing particles and between Biso- and Triso-coated particles.

3. To establish the relative stability of mixed-oxide sol-gel particles having Th/U ratios of 0, 1, 2, 4, and 8. The latter was also of interest to GA for first-core loadings.

4. To test advanced coating designs from GA in which ZrC was substituted for SiC in the reference makeup particle.

5. To compare the performance of a weak-acid-resin UO_2-UC_2 particle with that of GA's reference makeup particle at very high temperatures.

6. To test mixed-oxide fissile particles prepared in a production-size 0.13-m-diam (5-in.) coater.

7. To test a multijunction tungsten-rhenium alloy thermocouple for measuring centerline temperatures at different locations in the capsule.

Results pertaining to objectives (2) through (6) are presented in this section, while results pertaining to objectives (1) and (7) are discussed in Sects. 4.2 and 6.10.3, respectively.

6.6.3.1 Capsule Design

The HRB-7 and -8 capsules were similar to the earlier HRB-4, -5, and -6 capsules (see Figs. 6.28 and 6.29). They consisted of primary and secondary stainless steel containment vessels, a graphite annulus, and the fuel rods. During irradiation, capsule temperatures were controlled by altering the composition of the capsule sweep gas mixture. Major variations from previous capsules include a different method of controlling the axial temperature profile, the use of a different type of central thermocouple, and the geometry and composition of the fuel specimens. In previous HRB capsules, the graphite sleeve was tapered at the ends to provide a higher thermal resistance and thus maintain fuel temperatures in spite of the centrally peaked power density. The same objective was achieved in HRB-7 and -8 with an untapered sleeve by adjusting the heavy metal loadings so as to flatten the axial power density. Each of the capsules contained 19 equally long slug-injected fuel rods having an axial hole to accommodate a special five-junction tungsten-rhenium thermocouple.

6.6.3.2 Preparation of Test Specimens

A total of 17 types of fissile particles were tested in the HRB-7 and -8 capsules. These types and their purposes in the experiment are listed in Table 6.19. Each fuel specimen contained one type of fissile particle and various amounts of fertile ThO_2 particles, inert SAR particles, and WAR $^{238}UO_2 + UC_2$ driver particles to make up the required loadings. The characterization of all types of coated particles included in the experiment is included in Tables 6.20 and 6.21.

The coated particles already described were fabricated into fuel rods, nominally 12.4 mm diam by 20 mm long (0.49 by 0.8 in.) with a 3.35-mm (0.132-in.) central hole for placement of a multijunction tungsten-rhenium thermocouple to measure fuel centerline temperatures. An orientation-identification mark was formed on one end of each specimen so diameter measurements could be made at the same location both before and after irradiation.

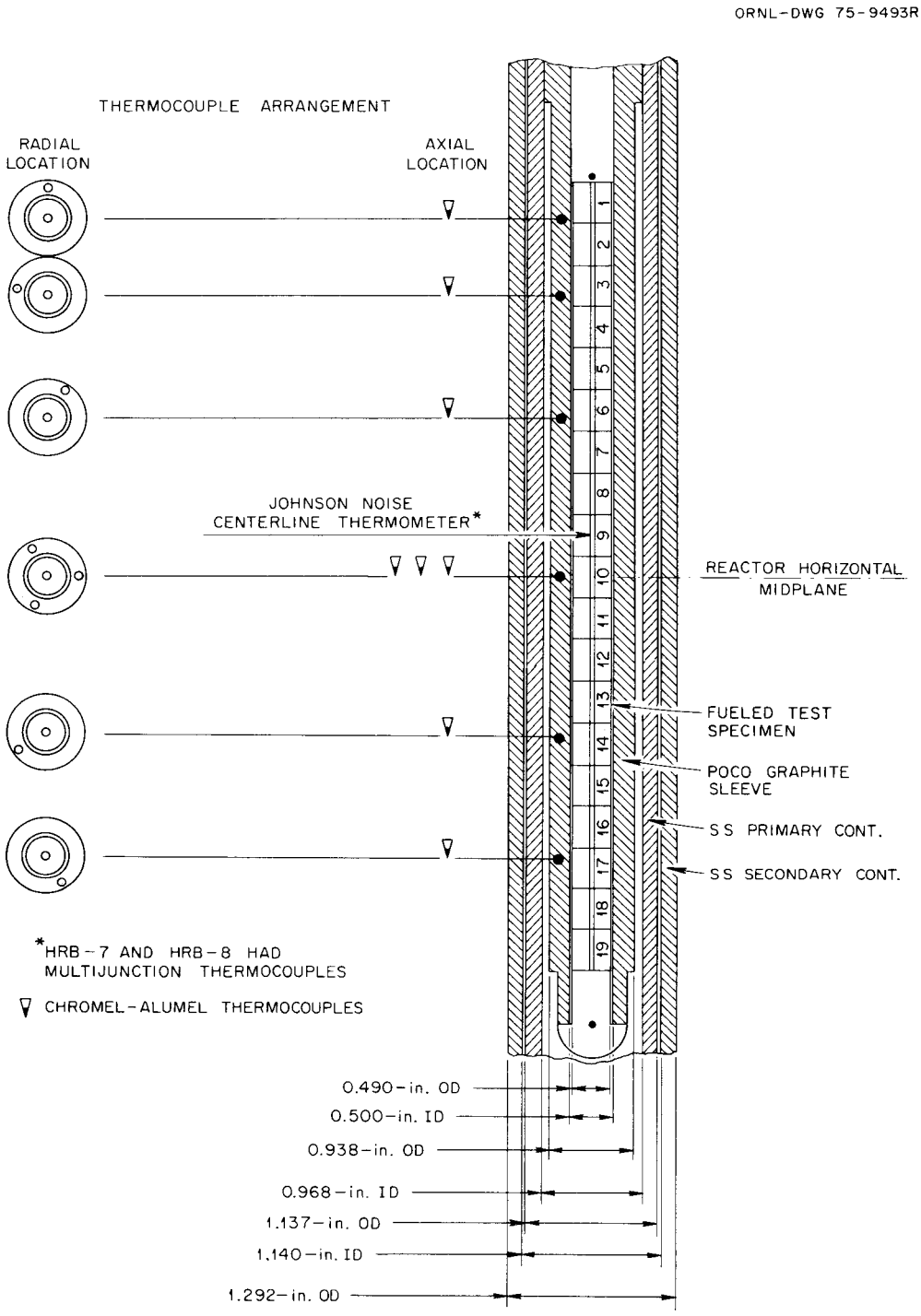

Fig. 6.28. Configuration for HRB-7, -8, -9, and -10. To convert diameters to millimeters, multiply by 25.4.

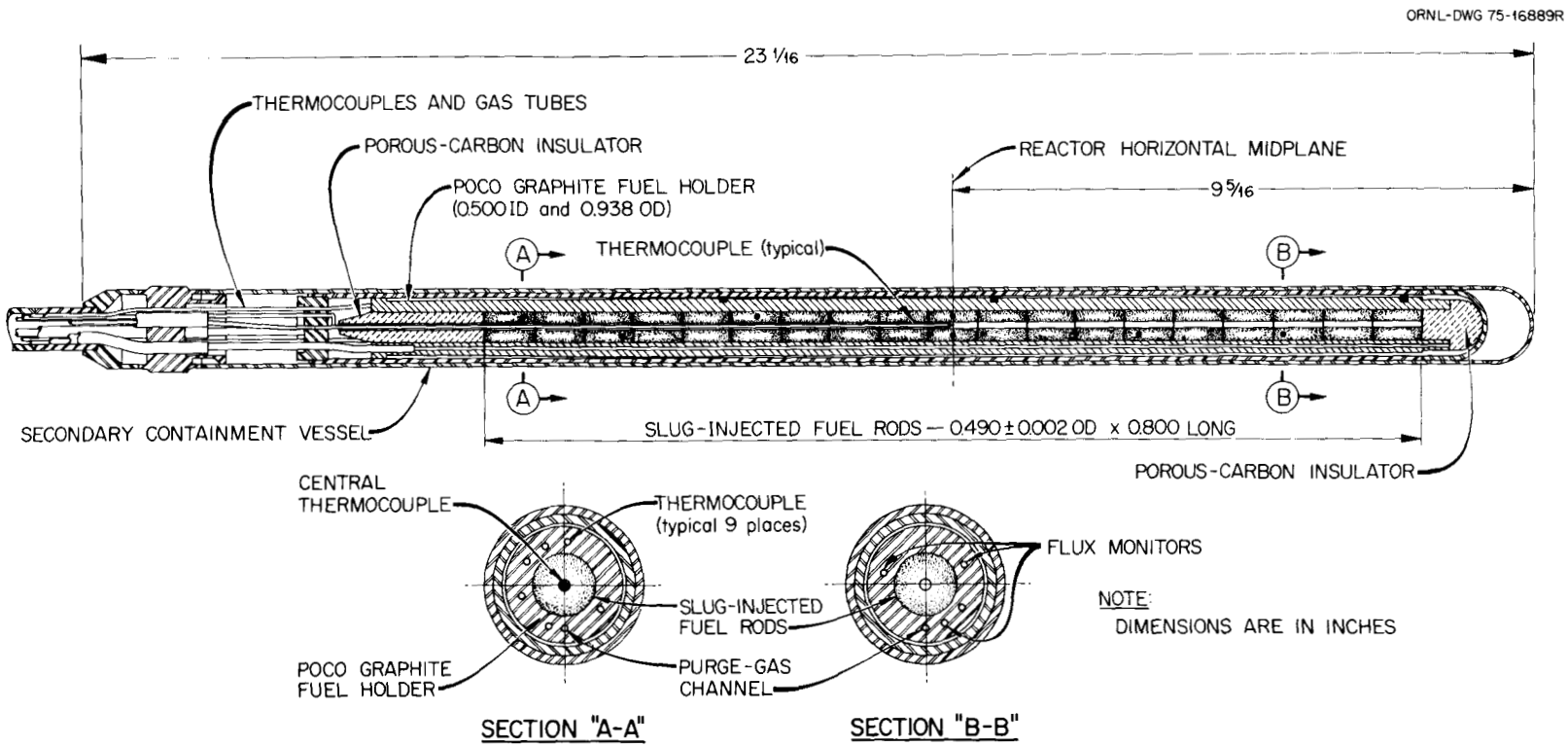

Fig. 6.29. Instrumented Capsules HRB-7 and -8. To convert dimensions to meters, multiply by 0.0254.

Table 6.19. Coated Particles and Positions in HRB-7 and -8 Capsules

Position in Capsule	Kernel Type[a]	Coating Type	Purpose in Experiments
1	$^{235}UC_2$—1% Th[b]	Triso	GA reference
2	$(4Th,^{235}U)O_2$ SG	Biso	Test particle prepared in large coater
3	$^{235}UO_2 + U_2N_3$ SG	Biso	To study amoeba effect
4	$^{235}UO_2 + UC_2$ SG	Biso	To study amoeba effect
5	$^{233}UO_2$ SG	Triso	Potential candidate for recycle; compare with $^{235}UO_2$
6	$^{235}UO_2$ SG	Biso	Reference for amoeba effect; compare Biso with Triso
7	$^{235}UO_2$ SG	Triso	Reference for amoeba effect; compare Triso with Biso
8	$(2Th,^{235}U)O_2$ SG	Biso	Relative stability; Th/U ratio
9	$(4Th,^{235}U)O_2$ SG	Triso	Recycle candidate
10[c]	$(8Th,^{235}U)O_2$[b] SG	Triso	Relative stability; Th/U ratio; interest for first-core loadings
11	$(4Th,^{235}U)O_2$ SG	Biso	Relative stability; Th/U ratio
12	$(Th,^{235}U)O_2$ SG	Biso	Relative stability; Th/U ratio
13	WAR $^{235}UO_2 + UC_2$	Triso	Compare with GA reference makeup particle
14	WAR $^{235}UC_2$	Triso	Recycle candidate; compare Triso with Biso
15	WAR $^{235}UO_2 + UC_2$	Biso	Compare Biso with Triso
16	WAR $^{235}UC_2$	Biso	Recycle candidate; compare Biso with Triso
17	$^{235}UC_2$ with ZrC in coating[b]	Triso	Test GA advanced coating design
18	$^{235}UC_2$—1% Th	Triso	GA reference
19	$(4Th,^{235}U)O_2$ SG	Biso	Test particle prepared in large coater

[a]SG = derived by sol-gel process; WAR = derived from weak-acid resin.

[b]Supplied by GA.

[c]At reactor horizontal midplane.

Table 6.20. Compositional Characterization of Coated Particles for HRB-7 and -8

Batch	Kernel Material[a]	Content, wt %		^{235}U Enrichment (at. %)	Content, ppm	
		U	Th		B	Fe
GAC6151-00-035[b]	VSM UC_2–1% ThC_2	18.86		93.15		
J-263	SG $(4Th,U)O_2$	7.25	29.74	93.17	12	40
OR-2098-H	SG UO_2-U_2N_3	23.65		93.17	5	10
OR-2097-H	SG UO_2-UC_2	24.91		93.17	20	3
Pu-303-H[c]	SG UO_2	25.5		98.05[c]	1	30
OR-2089-H	SG UO_2	22.41		93.17	5	7
OR-2114-H	SG UO_2	16.99		93.17	20	20
OR-2094-H	SG $(2Th,U)O_2$	10.44	20.79	93.17	20	20
OR-2116-H	SG $(4Th,U)O_2$	6.50	26.42	93.13	3	20
GAC6155-01020[b]	SG $(8Th,U)O_2$	5.23	43.59	93.15		
OR-2111-H	SG $(4Th,U)O_2$	7.24	29.98	93.17	5	3
OR-2090-H	SG $(Th,U)O_2$	13.5	13.36	93.17	20	80
OR-2115-H	WAR UO_2-UC_2	19.13		93.18	5	20
OR-2121-H	WAR UC_2	20.03		93.32	5	20
OR-2106-H	WAR UO_2-UC_2	21.75		93.18	20	3
OR-2120-H	WAR UC_2	23.66		93.32	2	10
GAC6171-63E[b]	VSM UC_2	20.70		93.15		
J-262	SG ThO_2		54.05			
OR-2104-H	WAR UO_2-UC_2	29.11		0.70	20	3
OR-2079-H	SAR carbon				3	10

[a]VSM = GA's proprietary process, SG = sol-gel process, WAR = weak-acid resin derived, SAR = strong-acid resin derived.

[b]Supplied by General Atomic Company.

[c]In batch Pu-303-H the fissile isotope is ^{233}U.

Table 6.21. Mean Dimensions and Densities[a] of Coated Particles for HRB-7 and -8

Batch	Kernel Diameter (μm)	Thickness, μm				Density, g/cm³				
		Buffer	Inner C	SiC	Outer C	Kernel	Buffer	Inner C	SiC	Outer C
GAC6151-00-035[b]	196 (16)	99 (10.6)	33 (3.5)	32 (5.3)	38 (5.0)	10.99	1.07	1.92	3.20	1.85
J-263	353.8 (5.9)	101.2 (13.8)			91.8 (9.6)	9.80	1.39			2.01 (0.007)
OR-2098-H	192.8 (4.7)	70.7 (9.6)			75.6 (7.2)	9.9	1.2			2.006 (0.004)
OR-2097-H	193.8 (5.8)	67.6 (8.2)			78.4 (4.9)	10.5	1.19			1.998 (0.004)
Pu-303-H	226.8 (11.0)	84.7 (10.9)	35.1 (5.7)	27.1 (1.5)	40.7 (2.9)	10.08	0.90	2.0	3.19 (0.001)	2.02 (0.005)
OR-2089-H	195.6 (5.9)	74.8 (8.6)			77.1 (4.7)	9.97	1.25			2.01 (0.003)
OR-2114-H	195.9 (5.2)	85.0 (9.8)	37.0 (3.6)	27.3 (1.8)	46.4 (2.3)	9.83	1.28	2.0	3.17 (0.009)	1.98 (0.001)
OR-2094-H	282.0 (13.2)	84.5 (7.9)			89.0 (6.2)	10.17	1.26			2.01 (0.003)
OR-2116-H	360.0 (4.7)	97.7 (8.7)	38.8 (2.9)	33.6 (1.9)	42.9 (3.0)	9.8	1.36	2.0	3.21 (0.003)	2.04 (0.002)
GAC6155-01-020[b]	502 (23.1)	106 (17.6)	32.0 (4.3)	34.0 (6.7)	42.0 (6.1)	9.77	1.24	1.93	3.22	1.81
OR-2111-H	360.0 (4.7)	95.1 (7.2)			94.6 (5.5)	9.8	1.36			2.04 (0.002)
OR-2090-H	245.5 (19.0)	78.5 (9.0)			84.4 (7.0)	8.58	1.28			2.01 (0.004)
OR-2115-H	385.8 (29.0)	40.9 (6.8)	42.9 (3.6)	32.1 (1.9)	48.8 (4.0)	3.18	1.37	2.0	3.19 (0.003)	1.99 (0.005)
OR-2121-H	315.3 (29.1)	74.6 (11.3)	36.1 (3.8)	28.4 (2.7)	49.2 (3.3)	5.28	1.10	2.0	3.19 (0.006)	1.98 (0.004)
OR-2106-H	385.8 (29)	40.9 (6.8)			99.0 (7.1)	3.18	1.37			2.00 (0.005)
OR-2120-H	315.3 (29.1)	74.6 (11.3)			88.6 (6.6)	5.28	1.10			1.99 (0.003)
GAC6171-63E[b]	197.0 (24)	102 (9.5)	8.4 (1.2)	21.0 (0.0)[c]	65.0 (3.8)		1.00	1.80	6.5[c]	1.73
J-262	497.0 (3.2)	84.0 (13.4)			86.1 (10.9)	10.0	1.19			2.01 (0.006)
OR-2104-H	426.2 (31.4)	42.3 (7.7)			83.1 (9.0)	3.34	1.11			2.02 (0.006)
OR-2079-H	471.5 (24.6)	77.3			95.3 (6.6)	1.37				1.96 (0.013)

[a]Numbers in parentheses are standard deviations.

[b]Supplied by GA.

[c]ZrC substituted for SiC.

All coated particles, except those supplied by GA, were heat-treated at 1800°C before incorporation into the fuel rods. All coatings prepared by ORNL generally shrink during heat treatment of the fuel rods unless so annealed. The matrix used for bonding the coated particles was composed of 28.5 wt % Ashbury Mills Graphite Flour, grade NF6353, in Ashland Oil Company grade 240 petroleum pitch. The matrix was injected through the particle bed at 175°C and 6.2 MPa (900 psi) pressure. A metal mold was used, and a metal rod was used to form the thermocouple hole. The mold, mandrel, and punches used to form the fuel rods are shown in Fig. 6.30. Note that the bottom punch has a small ridge at the surface contacting the specimen to make an indentation, which is the orientation-identification mark mentioned earlier. If a flat-surface punch is used, the specimen can be easily separated from the mandrel and punches by twisting, but with the ridged punch, a device was needed to push the green rod and mandrel away from the bottom punch so that the specimen could be twisted off without damage.

After forming, the specimens were carbonized by heating in argon to 1000°C at a rate of 40°C/hr. They were then heat-treated to 1800°C to dimensionally stabilize the matrix. A total of 152 specimens were prepared for the experiment, archives, and characterization.

The specimens were characterized by dimensional measurements, weights, radiography, metallography, and photography. Figure 6.31 shows pole and side views of typical specimens. A characterization summary for each specimen is given in Table 6.22. The heavy metal loadings for all specimens are given in Table 6.23.

6.6.3.3 Capsule Operation

The operating schedules for HRB-7 and -8 are shown in Table 6.24. Both capsules were irradiated for two cycles in the PB-13 (VXF13) facility before going into the RB facility. This was done to burn out sufficient ^{235}U to avoid overpowering the particles in the RB facility, as discussed in Sect. 6.6.4. The calculated burnups for the two capsules are listed in Table 6.25. Neutron fluxes and fluences are given in Table 6.26.

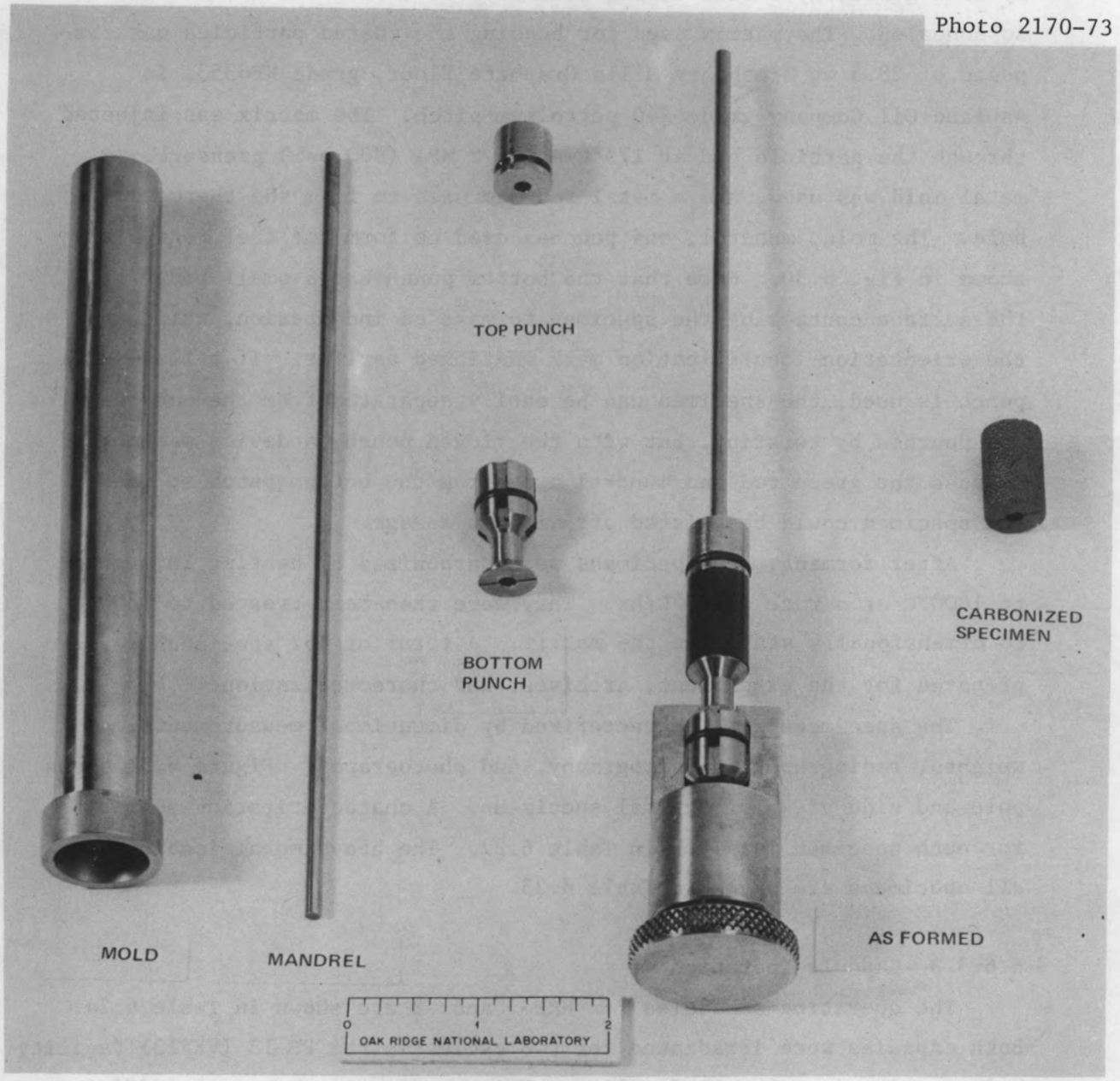

Fig. 6.30. Preparation of Specimens by Slug Injection for Irradiation Tests. Scale is 51 mm long.

Photo 2623-73

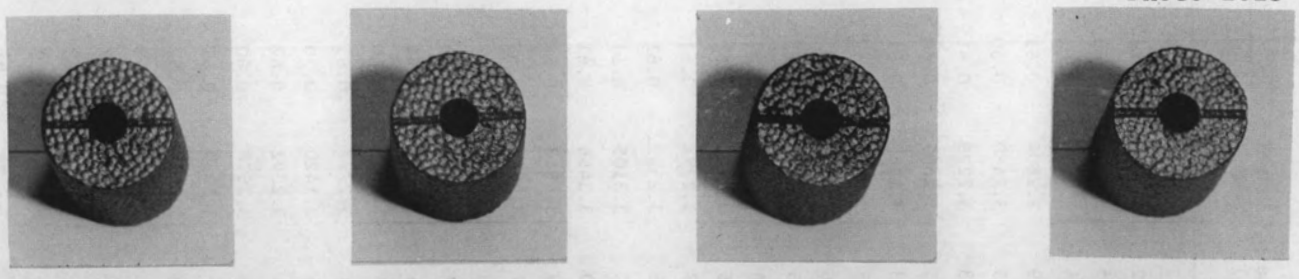

Photo 2648-73

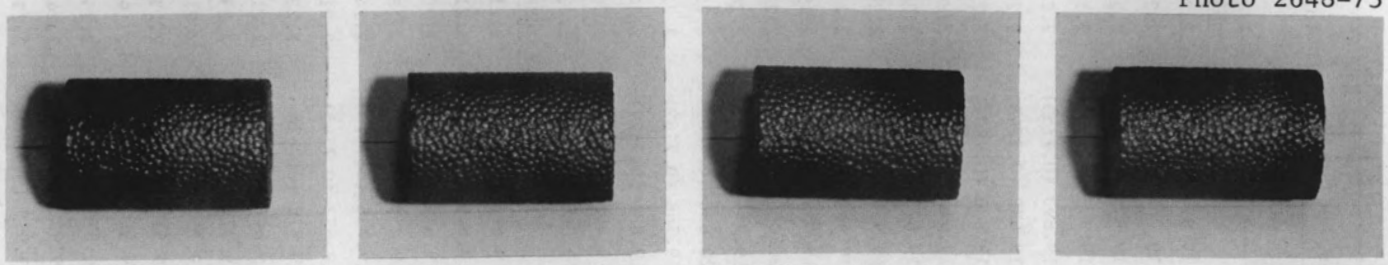

Fig. 6.31. Typical Specimens for HRB-7 and -8. 1.4×. Top: pole view. Bottom: side view. Left to right: rods 12-2, -3, -5, and -7.

Table. 6.22. Characterization of Specimens for HRB-7 and -8

Position in Capsule	Average Dimensions, mm (in.)[a]		Volume (cm^3)	Weight (g)	Density, g/cm^3		Particle Volume Loading (%)
	Outside Diameter	Length			Matrix	Total	
			Capsule HRB-7				
1	12.418 (0.4889)	19.817 (0.7802)	2.2272	3.4449	0.61	1.55	60.2
2	12.433 (0.4895)	19.705 (0.7758)	2.2205	3.4511	0.63	1.55	60.5
3	12.436 (0.4896)	19.545 (0.7695)	2.2034	3.3046	0.61	1.50	60.8
4	12.433 (0.4895)	19.393 (0.7635)	2.1859	3.2804	0.61	1.50	60.8
5	12.499 (0.4921)	19.693 (0.7753)	2.2445	3.1480	0.50	1.40	59.3
6	12.438 (0.4897)	19.680 (0.7748)	2.2193	3.2226	0.61	1.45	60.0
7	12.423 (0.4891)	19.830 (0.7807)	2.2303	3.2605	0.60	1.46	60.5
8	12.428 (0.4893)	19.616 (0.7723)	2.2083	3.1989	0.61	1.45	60.3
9	12.423 (0.4891)	19.662 (0.7741)	2.2115	3.2365	0.62	1.46	59.7
10	12.446 (0.4900)	19.924 (0.7844)	2.2498	3.2177	0.61	1.43	59.3
11	12.421 (0.4890)	19.461 (0.7662)	2.2165	3.1864	0.58	1.44	58.0
12	12.443 (0.4899)	19.479 (0.7669)	2.1986	3.1838	0.62	1.45	60.3
13	12.433 (0.4895)	20.010 (0.7878)	2.2546	3.2705	0.61	1.45	60.0
14	12.428 (0.4893)	19.944 (0.7852)	2.2452	3.2772	0.62	1.46	60.3
15	12.423 (0.4891)	20.036 (0.7888)	2.2535	3.2562	0.61	1.44	60.0
16	12.423 (0.4891)	19.766 (0.7782)	2.2232	3.3105	0.61	1.49	60.4
17	12.436 (0.4896)	19.881 (0.7827)	2.2410	3.3466	0.61	1.49	60.0
18	12.416 (0.4888)	19.995 (0.7872)	2.2459	3.4843	0.62	1.55	60.8
19	12.438 (0.4897)	19.860 (0.7819)	2.2397	3.4687	0.63	1.55	60.0
			Capsule HRB-8				
1	12.428 (0.4893)	19.680 (0.7748)	2.2157	3.4450	0.63	1.55	60.5
2	12.438 (0.4897)	19.616 (0.7723)	2.2124	3.4535	0.64	1.56	60.6
3	12.423 (0.4891)	19.632 (0.7729)	2.2083	3.2955	0.60	1.49	60.6
4	12.421 (0.4890)	19.456 (0.7660)	2.1876	3.2772	0.61	1.50	60.7
5	12.482 (0.4914)	19.736 (0.7770)	2.2426	3.1420	0.50	1.40	59.3
6	12.426 (0.4892)	19.672 (0.7745)	2.2136	3.2292	0.62	1.46	60.2
7	12.421 (0.4890)	19.878 (0.7826)	2.2348	3.2678	0.60	1.46	60.3
8	12.428 (0.4893)	19.644 (0.7734)	2.2114	3.1950	0.61	1.44	60.2
9	12.438 (0.4897)	19.774 (0.7785)	2.2300	3.2433	0.62	1.45	59.2
10	12.403 (0.4883)	19.751 (0.7776)	2.2136	3.2185	0.63	1.45	60.2
11	12.441 (0.4898)	19.812 (0.7800)	2.2352	3.1874	0.57	1.43	57.5
12	12.426 (0.4892)	19.540 (0.7693)	2.1987	3.1812	0.62	1.45	60.3
13	12.438 (0.4897)	20.010 (0.7878)	2.2566	3.2783	0.62	1.45	59.7
14	12.428 (0.4893)	19.985 (0.7868)	2.2497	3.2764	0.61	1.46	60.2
15	12.433 (0.4895)	19.975 (0.7864)	2.2534	3.2518	0.61	1.44	60.0
16	12.416 (0.4888)	19.713 (0.7761)	2.2143	3.3139	0.62	1.50	60.7
17	12.428 (0.4893)	19.863 (0.7820)	2.2360	3.3469	0.62	1.55	60.0
18	12.436 (0.4896)	20.137 (0.7928)	2.2699	3.4846	0.60	1.54	60.2
19	12.426 (0.4892)	19.715 (0.7762)	2.2184	3.4650	0.64	1.56	60.5

[a]Inside diameter = 3.35 mm (0.132 in.).

Table 6.23. Heavy Metal Loadings for HRB-7 and -8

Position in Capsule	Loading, g/cm^3, HRB-7			Loading g/cm^3, HRB-8		
	^{235}U	^{238}U	^{232}Th	^{235}U	^{238}U	^{232}Th
1	0.0185	0.1593	0.1782	0.0186	0.1602	0.1791
2	0.0186	0.1599	0.1787	0.0186	0.1605	0.1793
3	0.0166	0.1161	0.1731	0.0166	0.1159	0.1727
4	0.0167	0.1170	0.1744	0.0167	0.1169	0.1743
5	0.0149[a]	0.0833	0.1639	0.0149[a]	0.0834	0.1640
6	0.0150	0.0851	0.1657	0.0151	0.0853	0.1661
7	0.0150	0.0847	0.1649	0.0149	0.0845	0.1646
8	0.0143	0.0735	0.1634	0.0143	0.0734	0.1632
9	0.0143	0.0734	0.1632	0.0142	0.0728	0.1618
10	0.0140	0.0722	0.1604	0.0143	0.0734	0.1630
11	0.0143	0.0732	0.1628	0.0141	0.0727	0.1615
12	0.0144	0.0739	0.1641	0.0144	0.0739	0.1641
13	0.0148	0.0837	0.1631	0.0148	0.0836	0.1630
14	0.0149	0.0840	0.1638	0.0148	0.0839	0.1635
15	0.0148	0.0837	0.1632	0.0148	0.0837	0.1632
16	0.0165	0.1151	0.1715	0.0165	0.1155	0.1722
17	0.0163	0.1142	0.1701	0.0164	0.1144	0.1705
18	0.0183	0.1580	0.1767	0.0182	0.1564	0.1748
19	0.0184	0.1585	0.1772	0.0186	0.1601	0.1789

[a]96.11% ^{233}U.

Table 6.24. Capsules HRB-7 and -8 Reactor Operating History

Facility	Cycle	Begin		End		Irradiation Time, hr	
		Time	Date	Time	Date	During Cycle	Accumulated
				Capsule HRB-7			
PB-13	101	1540	12/18/73	2400	1/10/74	559.44	559.44
PB-13	102	1237	1/11/74	2400	2/3/74	562.56	1122.00
RB-7	103	1440	2/28/74[a]	1915	3/23/74	556.80	1678.80
RB-7	104	0907	3/24/74	1006	4/16/74	552.72	2231.52
RB-7	105	1750	4/17/74	1135	5/9/74	521.28	2752.80
RB-7	106	0120	5/10/74	2200	6/1/74	547.92	3300.72
RB-7	107	2326	6/4/74	0100	6/28/74	552.72	3853.44
RB-7	108	1406	6/28/74	1340	7/21/74	551.52	4404.96
				Capsule HRB-8			
PB-13	103	1440	2/28/74	1915	3/23/74	556.80	556.80
PB-13	104	0907	3/24/74	1006	4/16/74	552.72	1109.52
RB-5	105	1750	4/17/74	1135	5/9/74	521.28	1630.80
RB-5	106	0120	5/10/74	2200	6/1/74	547.92	2178.72
RB-5	107	2326	6/4/74	0100	6/28/74	552.72	2731.44
RB-5	108	1406	6/28/74	1340	7/21/74	551.52	3282.96
RB-5	109	1842	7/22/74	0400	8/15/74	546.88	3829.84
RB-5	110	1707	8/15/74	2012	9/9/74	549.60	4379.44
RB-5	111	1030	9/12/74	0736	10/5/74	548.88	4928.32
RB-5	112	0525	10/6/74	0218	10/31/74	547.20	5475.52

[a]Reactor down 24.61 days between cycles.

Table. 6.25. Calculated Specimen Burnup in HRB-7 and -8

Rod	Location[a] (mm)	Location[a] (in.)	Calculated Burnup, % FIMA: ^{235}U PB-13	^{235}U RB-7, 5	^{235}U Total	^{238}U PB-13	^{238}U RB-7, 5	^{238}U Total	^{232}Th PB-13	^{232}Th RB-7, 5	^{232}Th Total
					Capsule HRB-7						
1, 19	183	7.2	46.19	37.34	83.53	0.42	10.21	10.63	0.11	3.94	4.05
2, 18	163	6.4	48.97	34.95	83.92	0.50	11.69	12.19	0.12	4.57	4.69
3, 17	142	5.6	51.56	32.64	84.20	0.58	13.25	13.83	0.15	5.27	5.42
4, 16	122	4.8	54.02	30.66	84.68	0.65	14.45	15.10	0.16	5.93	6.09
5, 15	102	4.0	55.68	28.90	84.58	0.69	15.62	16.31	0.18	6.47	6.65
6, 14	81	3.2	57.14	27.40	84.54	0.77	16.57	17.34	0.20	6.99	7.15
7, 13	61	2.4	58.28	26.28	84.57	0.82	17.41	18.23	0.21	7.37	7.58
8, 12	41	1.6	59.14	25.57	84.71	0.86	18.04	18.90	0.22	7.71	7.93
9, 11	20	0.8	59.60	25.09	84.69	0.89	18.38	19.27	0.23	7.85	8.08
10	0	0	59.84	24.84	84.68	0.90	18.58	19.48	0.23	8.05	8.28
					Capsule HRB-8						
1, 19	183	7.2	46.19	38.03	84.22	0.42	13.96	14.38	0.11	5.89	6.00
2, 18	163	6.4	48.97	35.37	84.34	0.50	15.84	16.34	0.12	6.79	6.91
3, 17	142	5.6	51.56	32.87	84.43	0.58	17.83	18.41	0.15	7.77	7.92
4, 16	122	4.8	54.02	30.79	84.81	0.65	19.31	19.96	0.16	8.70	8.86
5, 15	102	4.0	55.68	28.95	84.63	0.69	20.75	21.44	0.18	9.45	9.63
6, 14	81	3.2	57.14	27.42	84.56	0.77	21.92	22.69	0.20	10.18	10.38
7, 13	61	2.4	58.28	26.29	84.57	0.82	22.96	23.78	0.21	10.70	10.91
8, 12	41	1.6	59.14	25.57	84.71	0.86	23.75	24.61	0.22	11.17	11.39
9, 11	20	0.8	59.60	25.09	84.69	0.89	24.17	25.06	0.23	11.36	11.59
10	0	0	59.84	24.84	84.68	0.90	24.41	25.31	0.23	11.64	11.87

[a]Distance from reactor horizontal midplane.

Table 6.26. Thermal and Fast Fluences Calculated for HRB-7 and -8 Specimens

Rod	Location[a]		Flux in PB-13, n cm^{-2} sec^{-1}		Flux in RB-7, -5, n cm^{-2} sec^{-1}		Total Fluence, n/cm^2			
							Thermal, <0.414 eV		Fast, >0.18 MeV	
	(mm)	(in.)	av Thermal <0.414 eV	Fast >0.18 MeV	av Thermal <0.414 eV	Fast >0.18 MeV	HRB-7	HRB-8	HRB-7	HRB-8
1, 19	183	7.2	4.44×10^{14}	3.42×10^{13}	6.18×10^{14}	2.95×10^{14}	0.91×10^{22}	1.15×10^{22}	3.62×10^{21}	4.78×10^{21}
2, 18	163	6.4	4.86	3.80	7.07	3.31	1.03	1.30	4.07	5.35
3, 17	142	5.6	5.22	4.31	7.95	3.66	1.15	1.46	4.50	5.92
4, 16	122	4.8	5.56	4.65	8.80	3.97	1.26	1.60	4.88	6.42
5, 15	102	4.0	5.89	4.90	9.57	4.28	1.37	1.73	5.26	6.92
6, 14	81	3.2	6.23	5.17	10.27	4.55	1.47	1.86	5.59	7.36
7, 13	61	2.4	6.57	5.40	10.90	4.78	1.55	1.97	5.87	7.73
8, 12	41	1.6	6.85	5.58	11.40	4.92	1.62	2.07	6.04	7.95
9, 11	20	0.8	6.98	5.67	11.71	5.00	1.67	2.12	6.14	8.09
10	0	0	7.03	5.70	11.80	5.00	1.68	2.14	6.14	8.09

[a]Distance from reactor horizontal midplane.

6.6.3.4 Thermal Analysis

A good deal of progress has been made recently in improving methods for the thermal analysis of HRB irradiation experiments. The entire process is now computerized, so phenomena such as fuel rod shrinkage, dependence of thermal conductivity on fluence and temperature, and time dependence of HFIR gamma heating can be easily handled. The thermal analysis has been completed for all fuel rods that were adjacent to a Chromel vs Alumel thermocouple in the graphite midwall. However, results are presented here only for rods 1 and 10 in each capsule (see Figs. 6.32 and 6.33). These two rods represent the extremes in distance from the horizontal midplane of the reactor and therefore the extremes in thermal and fast-neutron fluence. They also typify the probably temperature ranges in the capsules.

Figures 6.34 through 6.37 show results from intermediate steps in the calculational procedure. Starting with the last half of the HRB-4 experiment, the standard practice has become to periodically change the composition of the sweep gas (normally a helium-neon mixture) to 100% He. With the experimental variable of gas composition eliminated, the fission power densities shown in Figs. 6.34 and 6.35 can be accurately calculated. From these power densities, the gas composition during the entire experiment can be calculated (see Figs. 6.36 and 6.37). Note that although a spearate composition history is calculated for each fuel rod, the sweep gas is common to all rods during the experiment. Therefore, all calculated composition histories for a capsule should be similar. As can be seen, the agreement obtained between rods 1 and 10 was good for both HRB-7 and -8.

6.6.3.5 Postirradiation Examination

The physical and metallographic examination of the fuel rods from HRB-7 and -8 was completed during this reporting period. The general appearance of the fuel rods was good except for rods 5 and 10, containing respectively ^{233}U-bearing and (8 Th,U)O_2 fissile particles. An arbitrary failure grouping of rod vs number of failed particles observed on the surfaces of the rods, shown in Table 6.27, indicates relative performance.

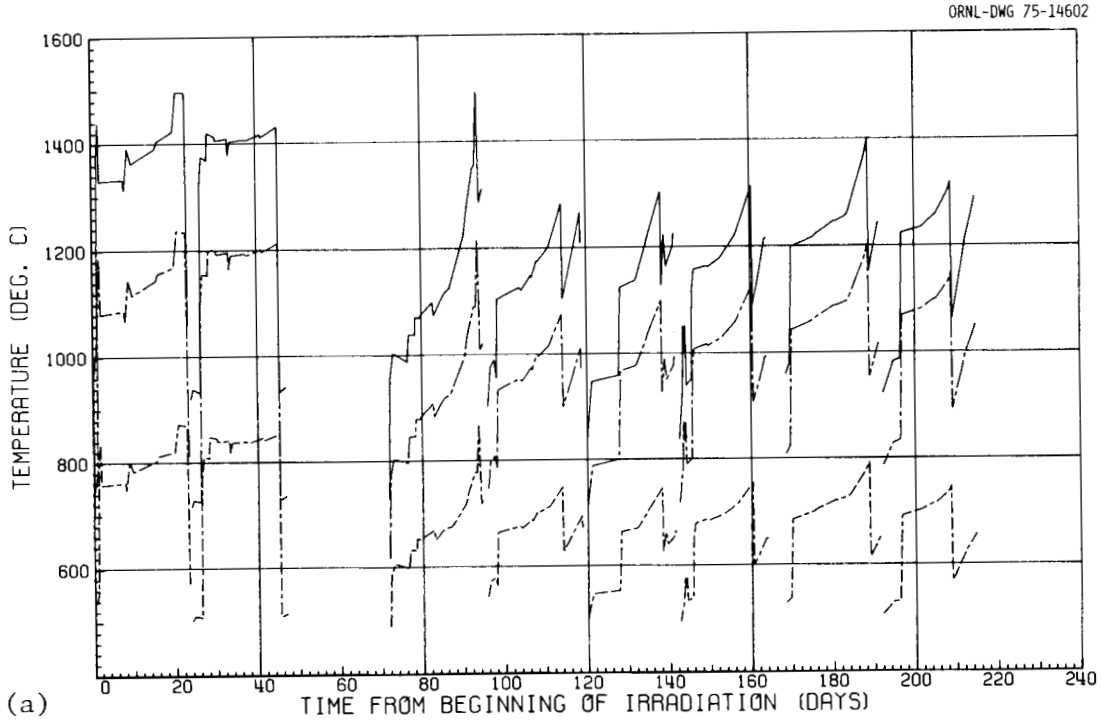

(a)

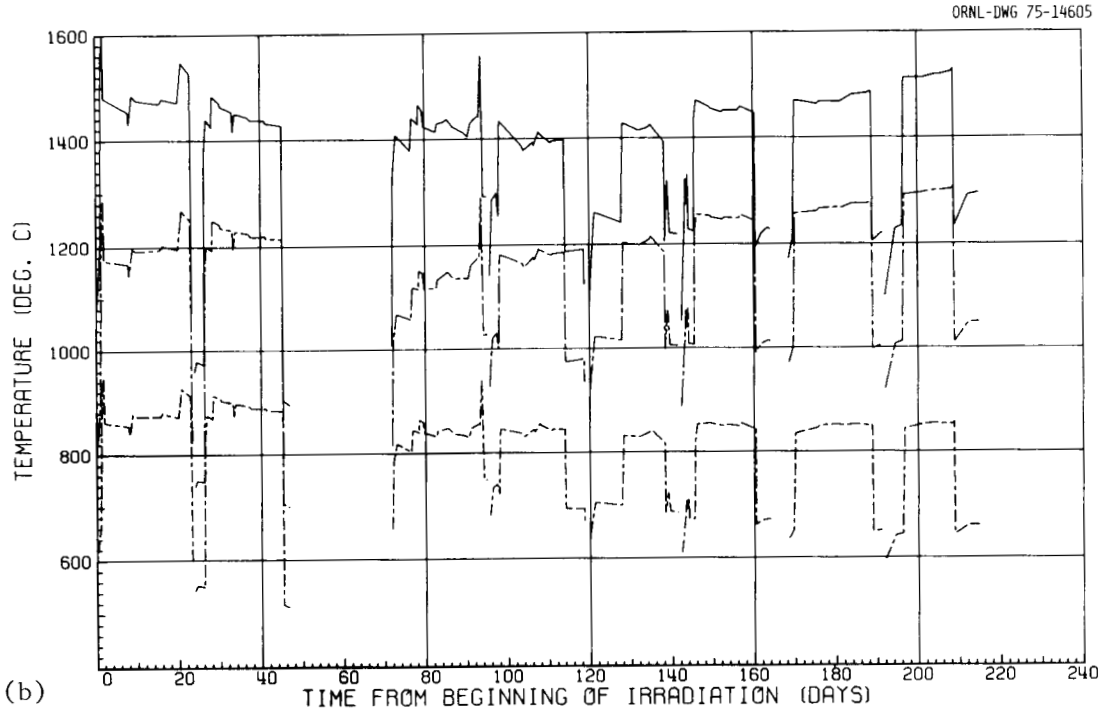

(b)

Fig. 6.32. Capsule Temperatures at Midpoint Positions of Rods in HRB-7 Experiment. From top to bottom, the traces are calculated fuel inside surface temperature, calculated fuel outside surface temperature, and measured graphite midwall temperature. (a) Rod 1. (b) Rod 10.

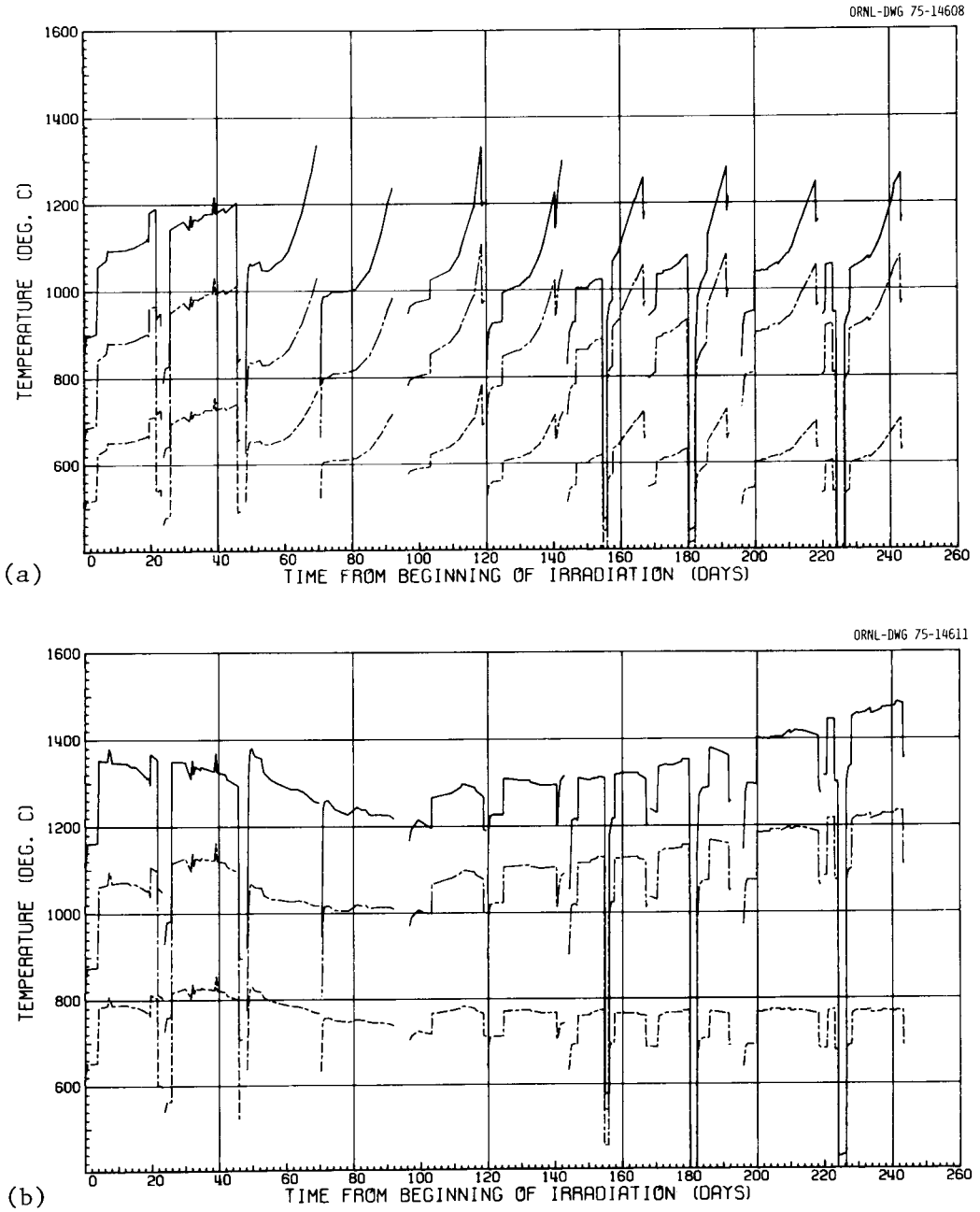

Fig. 6.33. Capsule Temperatures at Midpoint Positions of Rods in HRB-8 Experiment. From top to bottom, the traces are calculated fuel inside surface temperature, calculated fuel outside surface temperature, and measured graphite midwall temperature. (a) Rod 1. (b) Rod 10.

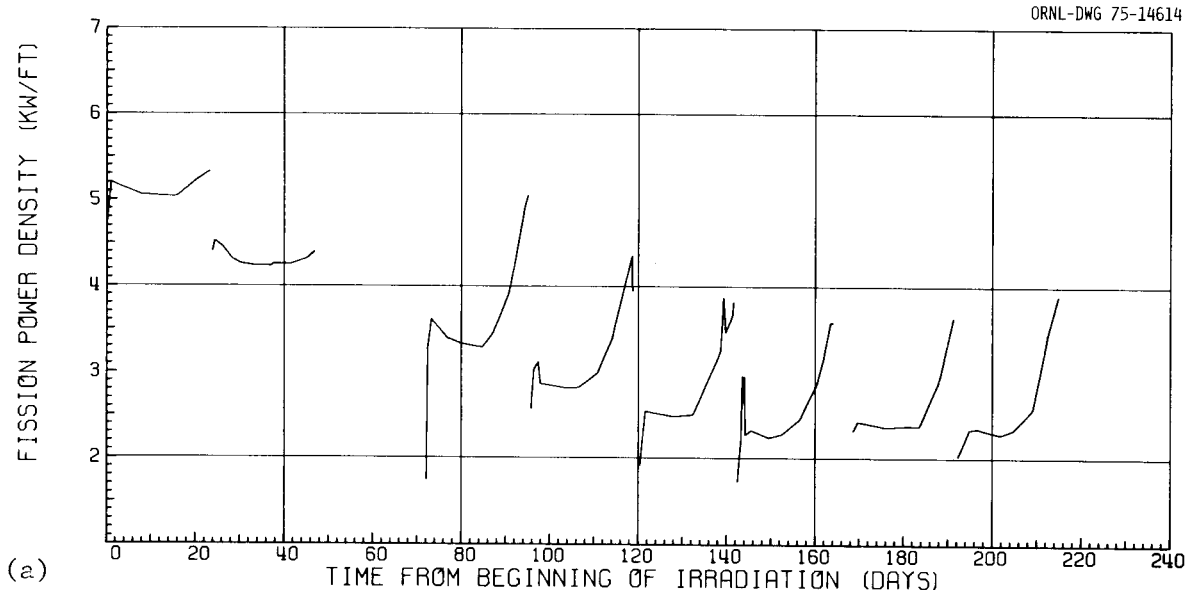

(a)

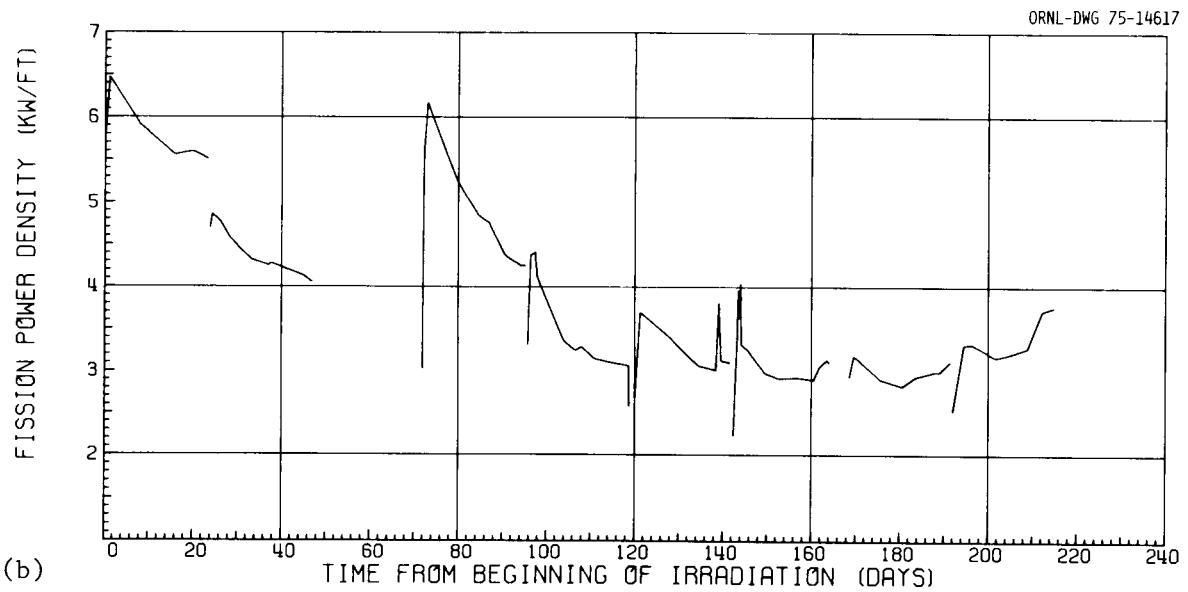

(b)

Fig. 6.34. Calculated Fuel Rod Fission Power Density for Experiment HRB-7. (Does not include gamma heating power.) (a) Rod 1. (b) Rod 10. To convert 1 kW/ft = 3.28 kW/m.

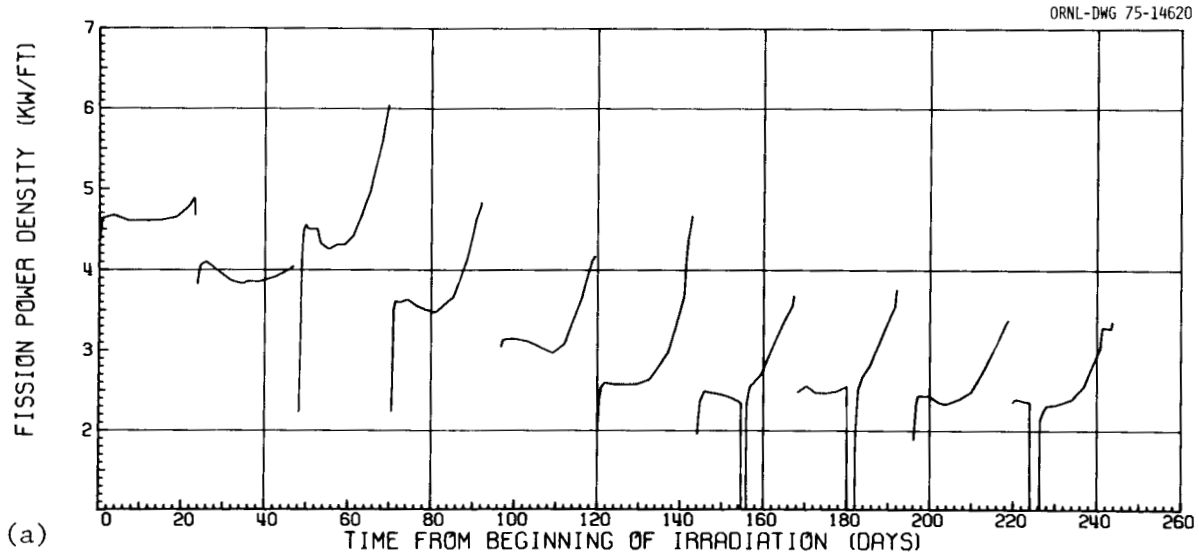

(a)

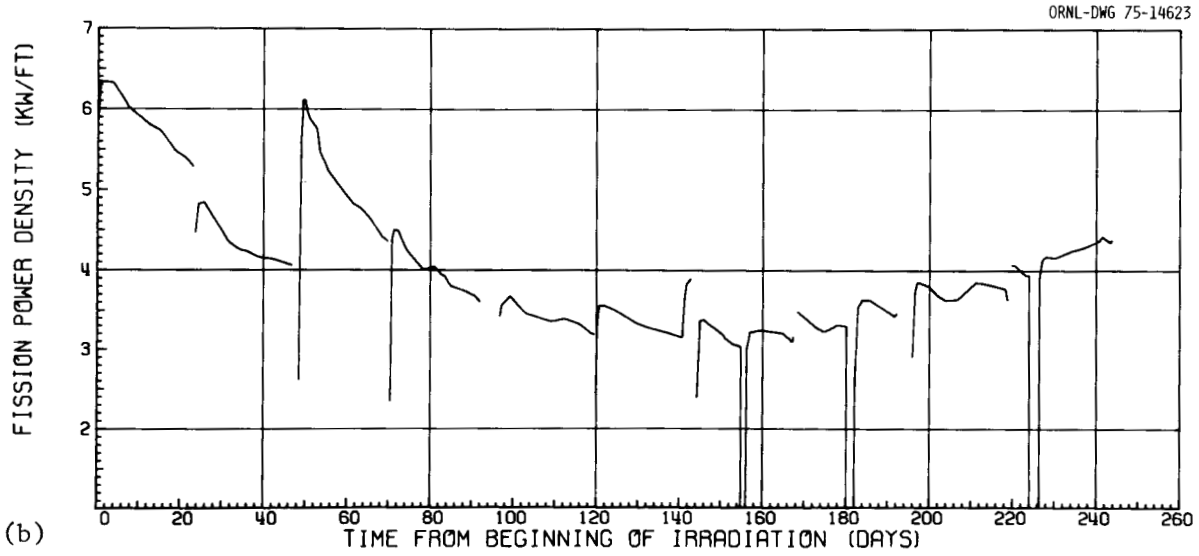

(b)

Fig. 6.35. Calculated Fuel Rod Fission Power Density for Experiment HRB-8. (Does not include gamma heating power.) (a) Rod 1. (b) Rod 10. To convert 1 kW/ft = 3.28 kW/m.

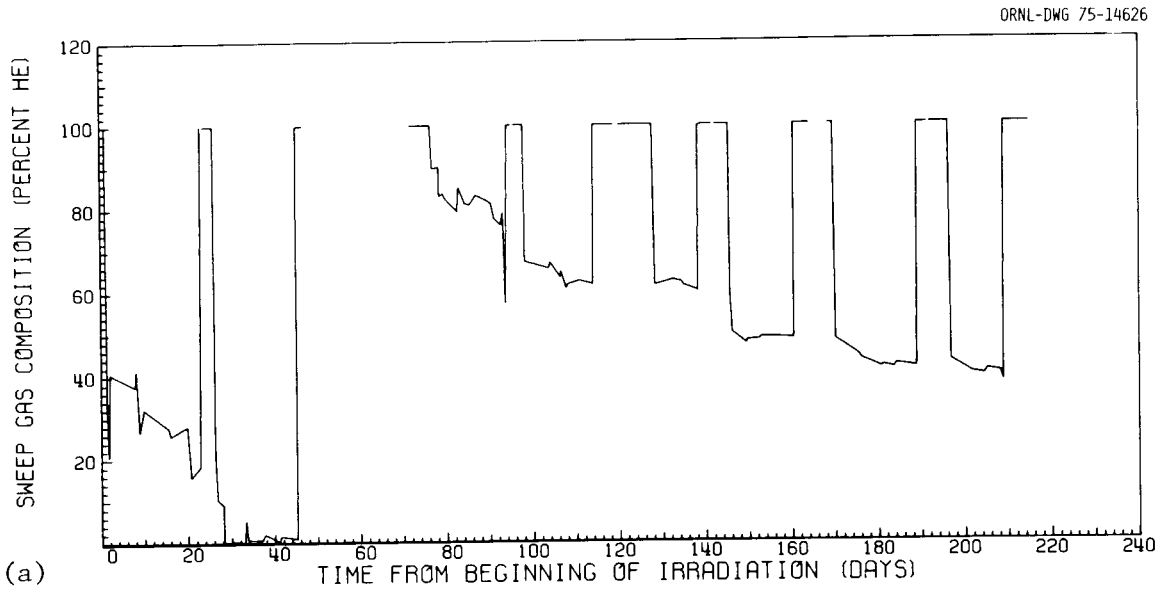

(a)

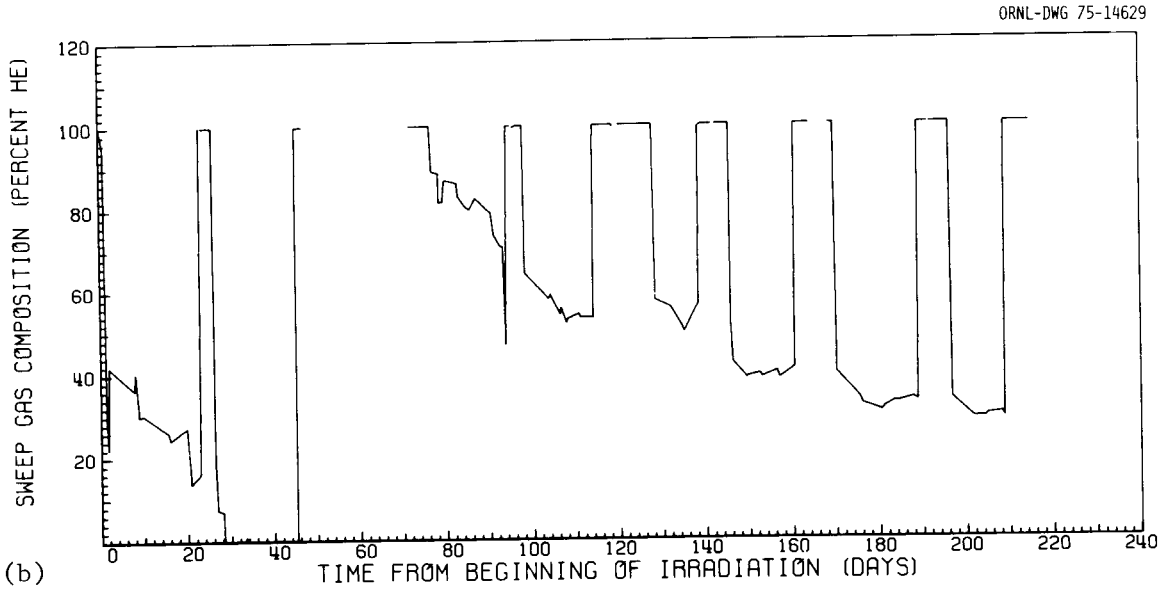

(b)

Fig. 6.36. Calculated Sweep Gas Composition (He-Ne) for HRB-7 Experiment. (a) Rod 1. (b) Rod 10.

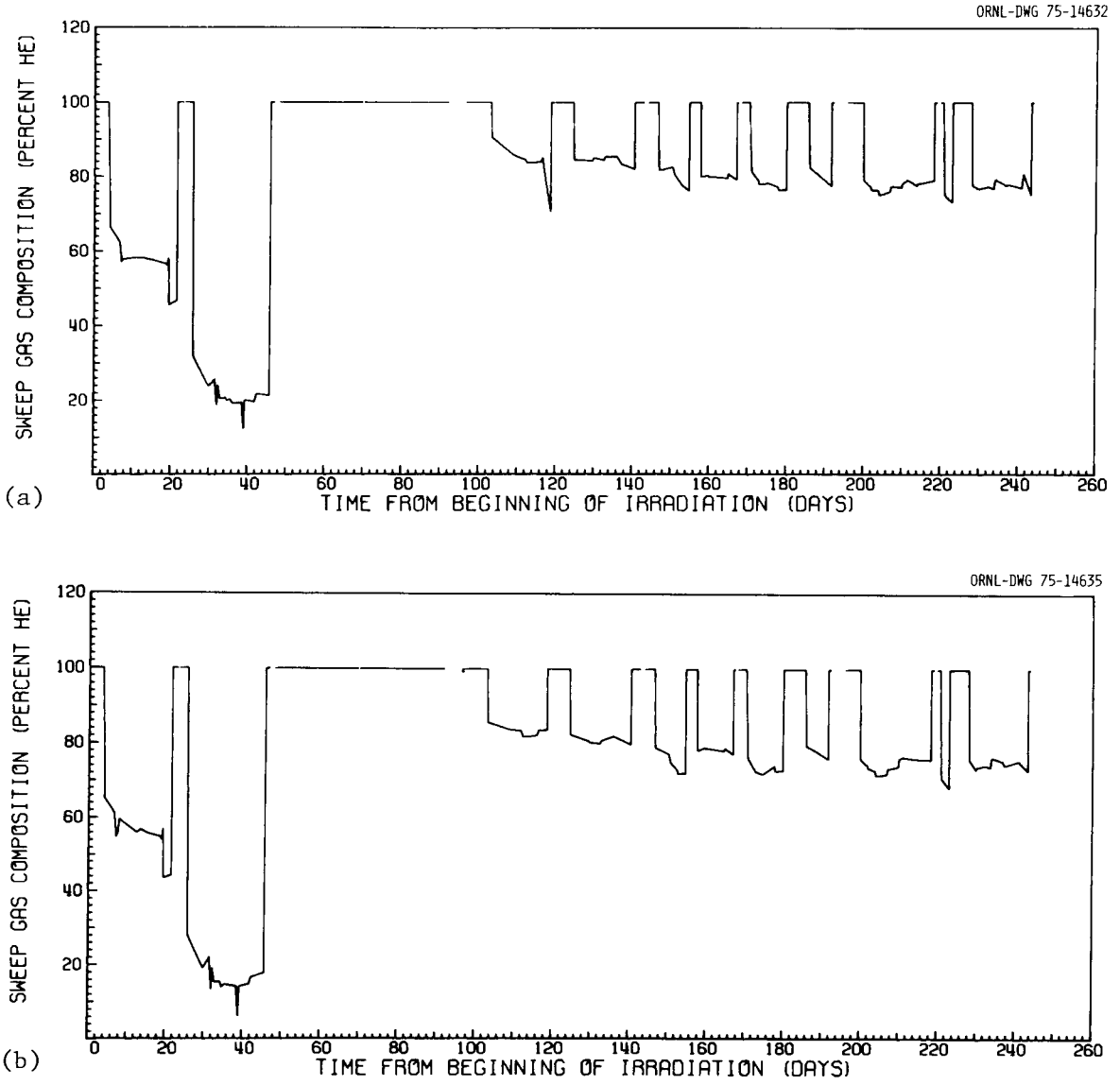

Fig. 6.37. Calculated Sweep Gas Composition (He-Ne) for HRB-8 Experiment. (a) Rod 1. (b) Rod 10.

Table 6.27. Results of Visual Examination of Fuel Rod Surfaces for Failed Particles

Failure Number Range	Rod Number	
	HRB-8	HRB-7
none	2, 8, 15, 16, 17,[a] 19	3, 8, 9,[a] 11, 13,[a] 14,[a] 15, 16
1–5	3, 4, 6, 11, 12, 13[a] 14[a]	2, 7,[a] 12, 17,[a] 19
6–10		6
11–15	1,[a] 7,[a] 10[a]	4, 5[a]
>15	5,[a] 18[a]	1,[a] 10,[a] 18[a]

[a]Triso-Biso system.

Although examination of the rod surfaces revealed about 2000 particles, only about 5 to 10% of them were fissile particles. If we assume that the only particles that failed were the fissile particles (over half the fuel rods showed only 0 to 1 failure), then the poorer performers were rods 1, 4, 5, 7, 10, and 18. Only rod 4 of the poor performers contained Biso-coated fissile particles. However, metallographic examination of the fuel rods showed that several failure mechanisms were involved.

The results of the dimensional inspection of the fuel rods are shown in Fig. 6.38. As can be seen, the rods shrank isotropically with $(\Delta D/D)/(\Delta L/L)$ values ranging from 0.8 to 1.1; and there was essentially no difference in the change in diameter of the rods that contained Triso-coated particles compared with an all-Biso system. However, this was not surprising since, as mentioned above, the Triso-Biso fuel rods contained only a small fraction of Triso particles. A difference in shrinkage rates was noted between the HRB-7 and -8 rods. The rods in HRB-7, the higher temperature experiment, and HRB-8 reached minimum dimensions at fast (>0.18 MeV) fluences of about 5×10^{21} and 6.5×10^{21} n/cm^2, respectively.

All 38 fuel rods from the two irradiation capsules were submitted for microstructural evaluation. Transverse sections were made at about the mid-length of each rod for metallographic preparation. A summary

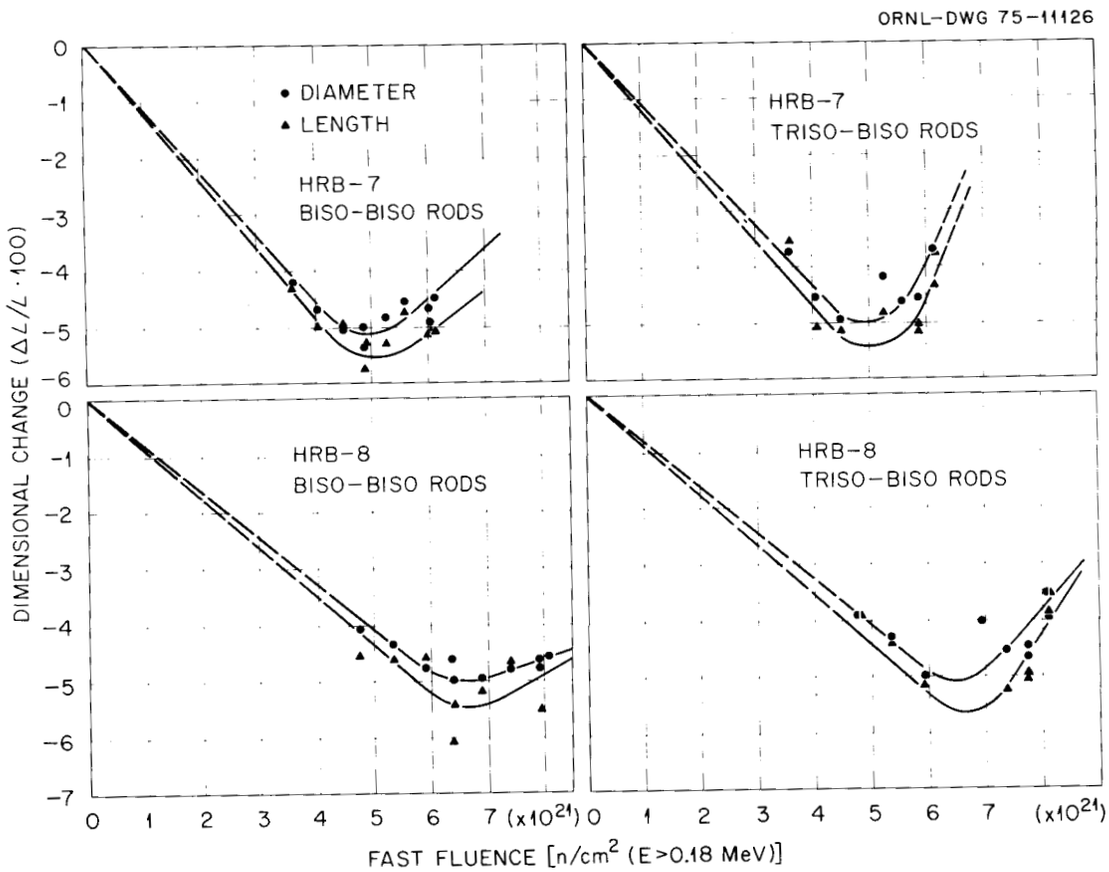

Fig. 6.38. Correlation of Dimension Change with Fast Fluence Damage in Fuel Rods from Irradiation Capsules HRB-7 and -8.

of the metallographic results for the various fissile particles is given in Table 6.28 and the appearances of the fuel particles in HRB-7 and -8 were essentially identical, with only subtle differences that could be attributed to the different operating temperatures. The following general observations were noted during the metallographic examinations:

1. No evidence of migration of the ThO_2 kernels was seen in any of the fuel rods, whereas a measurable amount of migration was observed with all the fissile-oxide kernels. The kernel migration coefficients have been calculated by Lindemer and Pearson and are reported in Sect. 4.2.

2. No evidence was seen to indicate that the palladium formed in the ^{238}U-bearing kernels had affected adjacent coated particles.

Table 6.28. Brief Description and Purpose of the Fissile Particles in HRB-7 and -8 and a Summary of the Metallographic Evaluations

Fissile Kernel	Coating Type	Fuel Rod Number	Purpose in Experiment	HRB-7			HRB-8			Metallographic Results
				Number Fissiles Examined, Failed	Amoeba	Maximum Migration (μm)	Number Fissiles Examined, Failed	Amoeba	Maximum Migration (μm)	
UC_2–1% Th (VSM)	Triso[a]	1	GA reference fissile makeup particle	9, 3	no		24, 23	no		Graphitization of cold side of inner LTI coating. Failures were mechanical, associated with cold side of particles. No fission product attack on SiC coating. Large fission-gas bubbles in kernels.
UC_2–1% Th (VSM)	Triso[a]	18	GA reference fissile makeup particle	8, 4	no		13, 13	no		Graphitization of cold side of inner LTI coating more pronounced than in above fuel rod. Failures were mechanical, primarily associated with cold side of particle, although a few straight-line cracks were in SiC on hot side. Kernels no longer resemble UC_2; no fission-gas bubbles present, only slight fission product attack on SiC (<5 μm).
UC_2–1% Th (VSM)	Triso[a]	17	Test GA advance coating design. ZrC substituted for SiC in the Triso coating.	13, 0	no		7, 0	no		Kernels no longer resemble UC_2; about half the kernels broke through the densified buffer to the ZrC (<10 μm inner LTI shrank with buffer away from ZrC). No gross attack of ZrC although it appears "peppery" across entire thickness; up to 20% penetration from inside. Four ZrC coatings contained fine straight-line fractures.
$^{235}UO_2$ (Sol-gel)	Biso	6	Reference for amoeba effect. Compare with Triso coating.	7, 0	yes	65	8, 0	yes	28	Amoeba very apparent. Rejected graphite behind kernel. Large fission-gas bubbles and metallic fission products present in kernels.
$^{235}UO_2$ (Sol-gel)	Triso	7	Reference for amoeba effect. Compare with Biso coating.	11, 1	yes	100	22, 0	yes	95	Amoeba very apparent. Kernels similar in appearance to above UO_2 fissile particles. Worm-hole type attack of SiC on cold side of particle; complete penetration of SiC on two particles in HRB-7 rod.
$^{233}UO_2$ (Sol-gel)	Triso	5	Potential candidate for recycle; compare with $^{235}UO_2$ performance.	4, 2	yes	65	7, 4	yes	100	Amoeba very apparent. General appearance of kernel similar to above UO_2 kernels. No evidence of attack of SiC coatings. Pressure vessel failures of two particles in HRB-7.
$^{235}UC_{4.39}O_{1.72}$[b] (WAR)	Triso	13	Compare with GA reference makeup particle.	5, 0	no		7, 0	no		Phase segregation occurred in all fissile kernels. Slight fission product attack of SiC on cold side of coated particle penetrated SiC to half the thickness. No graphitization of inner LTI (see comments for GA reference makeup particle). Buffer consumed by kernel.
$^{235}UC_{4.39}O_{1.72}$[b] (WAR)	Biso	15	Compare performance of WAR kernel with Triso coating (see rod 13, above).	10, 0	no		7, 0	no		No amoeba. Segregation of an oxide phase that resembles UO_2 is apparent. In most fissile particles, kernel consumed the buffer coating.

Table 6.28. (Continued)

Fissile Kernel	Coating Type	Fuel Rod Number	Purpose in Experiment	HRB-7			HRB-8			Metallographic Results
				Number Fissiles Examined, Failed	Amoeba	Maximum Migration (μm)	Number Fissiles Examined, Failed	Amoeba	Maximum Migration (μm)	
$^{235}UC_{2.61}O_{0.16}$[c] (WAR)	Triso	14	Recycle Candidate. Compare performance with GA reference makeup particles.	11, 5	no		2, 2	no		No amoeba. Graphitization of inner LTI on cold side of particle. Failures are mechanical and are associated with the cold side of the particle. Although fission products accumulated on the cold side of the inner surface of the SiC, there was not significant amount of attack.
$^{235}UC_{2.61}O_{0.16}$[c] (WAR)	Biso	16	Compare performance of this WAR kernel with a Triso coating (see rod 14, above).	8, 0	no	~100	6, 0	no		No evidence of amoeba, although the kernels did move unilaterally through the densified buffer. Movement of kernels random (not temperature-gradient dependent). No failed LTI coatings observed.
UO_2-U_2N_3 (Sol-gel)	Biso	3	Study amoeba effect.	16, 4	no	>150	7, 1	no	>150	No amoeba; multidirectional movement of kernels through coatings. In most severe case, outer coatings of adjacent particle attacked. Kernels of unfailed particles have appearance of UO_2; kernels of failed particles appear to have converted to carbides.
UO_2+UC_2 (Sol-gel)	Biso	4	Study amoeba effect.	12, 2	no	>150	5, 1	no		Same observations as rod 3, above.
$(Th,U)O_2$ (Sol-gel)	Biso	12	Study relative stability of oxide kernel as affected by Th/U ratio.	14, 1[a]	yes	55	15, 2	yes	55	Amoeba very apparent. Kernels contain relatively large fission-gas bubbles and metallic fission products. Segregation of what appear to be carbon can be seen on cold side of kernel.
$(2Th,U)O_2$ (Sol-gel)	Biso	8	Same as rod 12.	10, 0	yes	80	12, 0	no		Same as rod 12.
$(4Th,U)O_2$ (Sol-gel)	Biso	11	Same as rod 12.	12, 0	yes	75	7, 0	yes	20	Same as rod 12.
$(4Th,U)O_2$ (Sol-gel)	Biso	2	Test coated particles prepared in the large coater.	10, 0	yes	40	6, 0	yes	13	Amoeba not as apparent as in rods 8, 11, and 12.
$(4Th,U)O_2$ (Sol-gel)	Biso	19	Same as rod 2.	10, 0	yes	30	6, 0	yes	20	Same as rod 2.
$(4Th,U)O_2$ (Sol-gel)	Triso	9	Recycle candidate. Compare performance with GA reference makeup particle.	23, 0	yes	25	11, 0	yes	25	Amoeba effect is apparent. No attack of SiC coatings.
$(8Th,U)O_2$ (Sol-gel)	Triso[a]	10	Study relative stability of oxide kernel as affected by Th/U ratio. Possible interest for first-core loading.	8, 1	yes	25	14, 0	yes	85	Amoeba effect is apparent. The outer LTI coating had failed on a typical particle. No evidence of fission-product attack on any of the coatings. Fine fission-gas bubbles and globules of metallic fission products dispersed throughout kernel.

[a]Coatings applied by GA.

[b]15% converted WAR kernel.

[c]100% converted WAR kernel.

There had been speculation as to whether or not the palladium would migrate through the Biso coatings and result in failure of adjacent particles.

3. The rhenium foil used to protect the central thermocouple had not affected any of the coated particles on the inner surface of the annular fuel rods. The rhenium foil was included in the metallographic section through fuel rod 14, in case a reaction had taken place between the foil and the coated particles.

The relative performance of the various oxide fissile kernels and WAR kernels irradiated in HRB-7 is compared in Figs. 6.39 and 6.40, respectively.

Electron micorprobe analyses were performed on three types of Triso-coated fissile particles irradiated in HRB-8 — 100% reduced WAR, 15% reduced WAR, and sol-gel UO_2. One of the major factors that can limit the performance of the recycle fissile particle is the collection of the rare-earth fission products (La, Pr, Ce, and Nd) at the inner surface region of the SiC coating. If the fissile kernel does not contain sufficient oxygen to form stable oxides with the rare earths, the rare earths will distill out of the kernel and condense on the cold side of the particle. The rare earths can chemically attack and mechanically interact with the coatings, leading to particle failure.

Various thermodynamic considerations for the retention of the rare-earth fission products within the kernel are discussed in Sect. 4.4.

The results of these microprobe analyses confirmed that:

1. The 100%-reduced WAR kernel ($UC_{2.61}O_{0.16}$) rejects essentially all the rare-earth fission products (Fig. 6.41).

2. The 15%-reduced WAR kernel ($UC_{4.39}O_{1.72}$) retains the bulk of the rare earths (Fig. 6.42).

3. The sol-gel UO_2 kernel retains all of the rare earths (Fig. 6.43).

R-65778

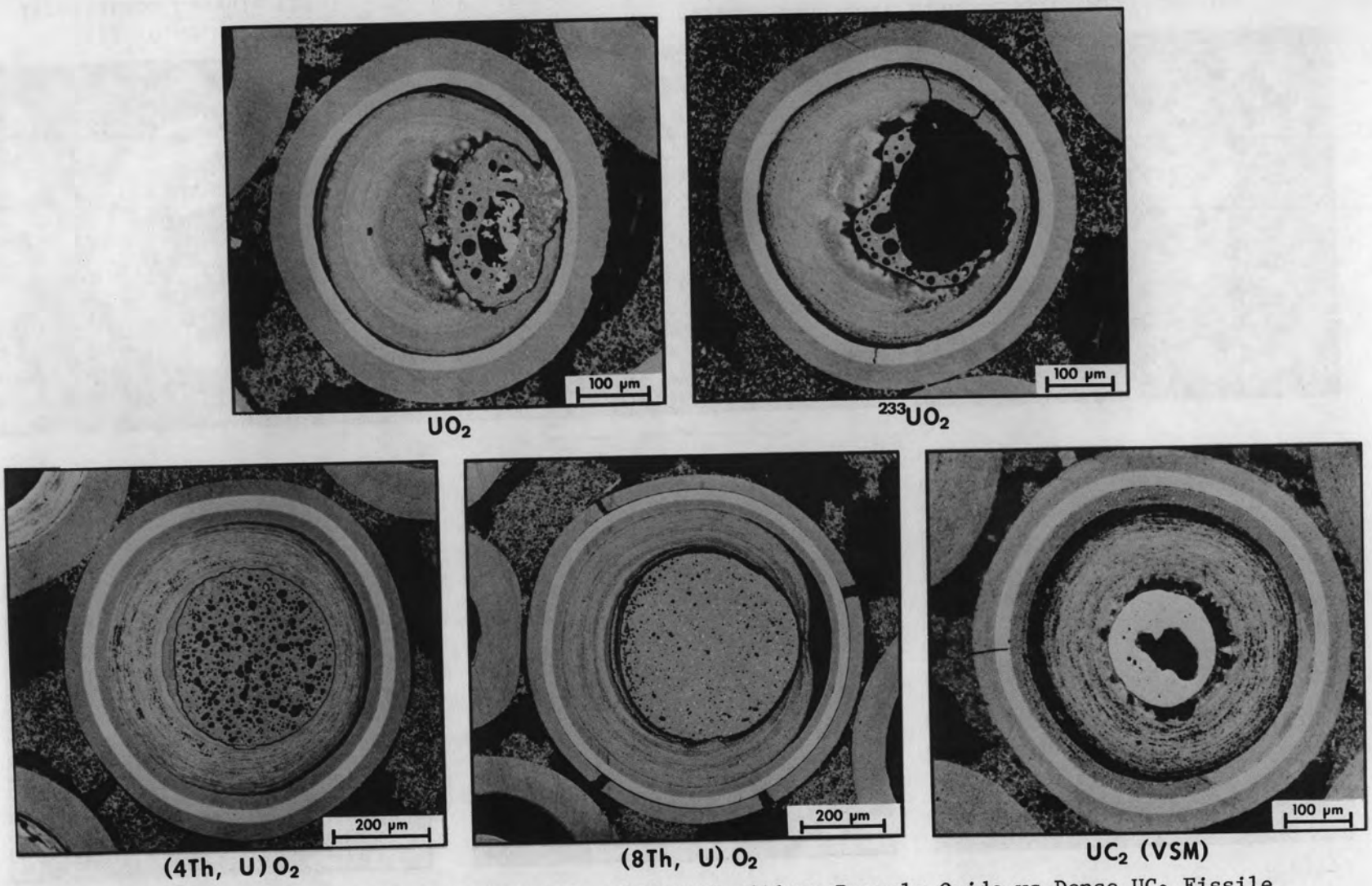

Fig. 6.39. Relative Thermal Stability of HTGR Candidate Recycle Oxide vs Dense UC_2 Fissile Particles Irradiated in HRB-7. Fast fluence: 4–6 × 10^{21} n/cm^2; maximum fuel temperature: 1500°C design. The hot side of each particle is on the right.

R-65777

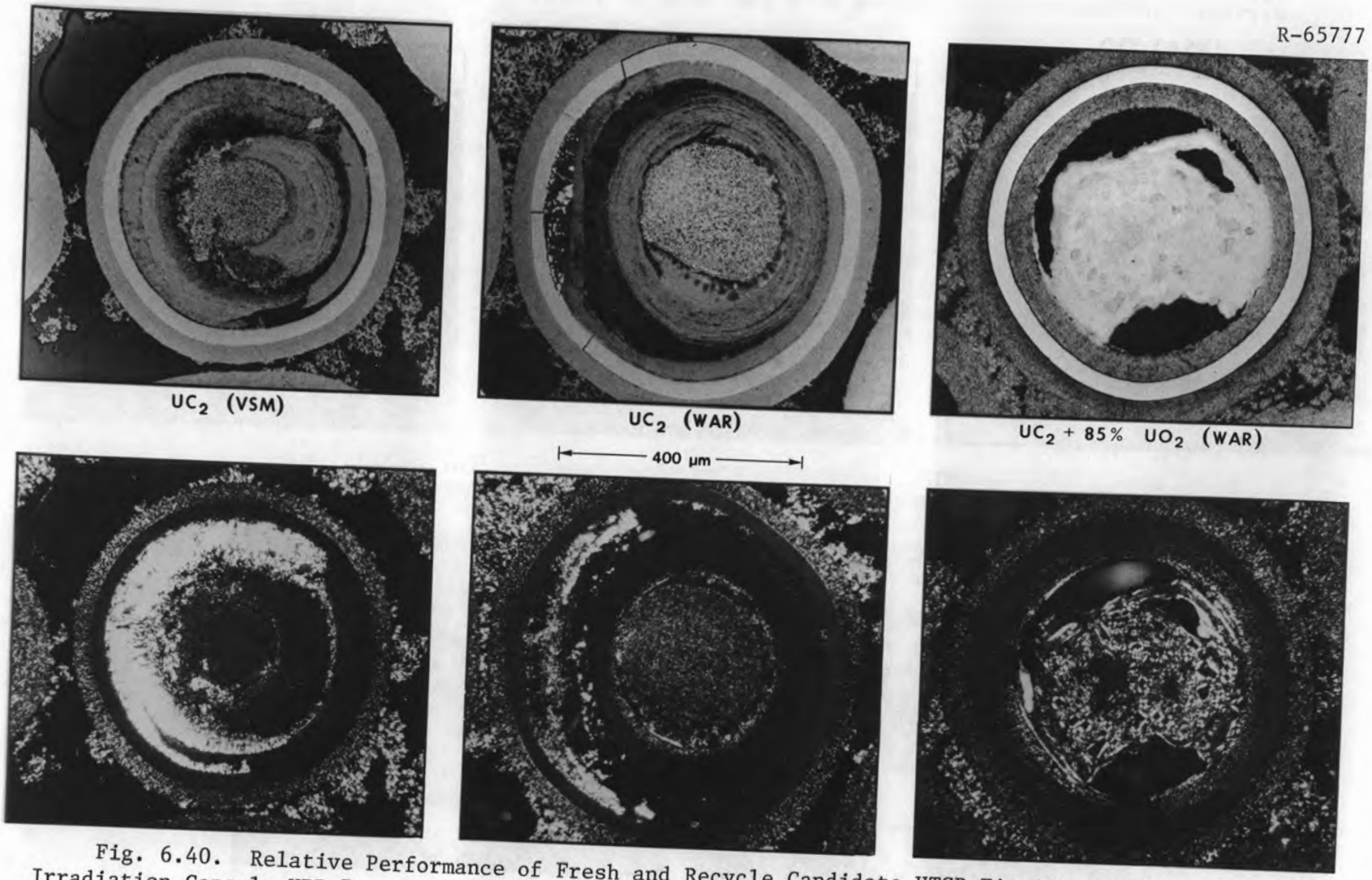

Fig. 6.40. Relative Performance of Fresh and Recycle Candidate HTGR Fissile Particles in Irradiation Capsule HRB-7. The hot side of each particle is on the right. Top row: Bright field. Bottom row: Polarized light.

Y-127988

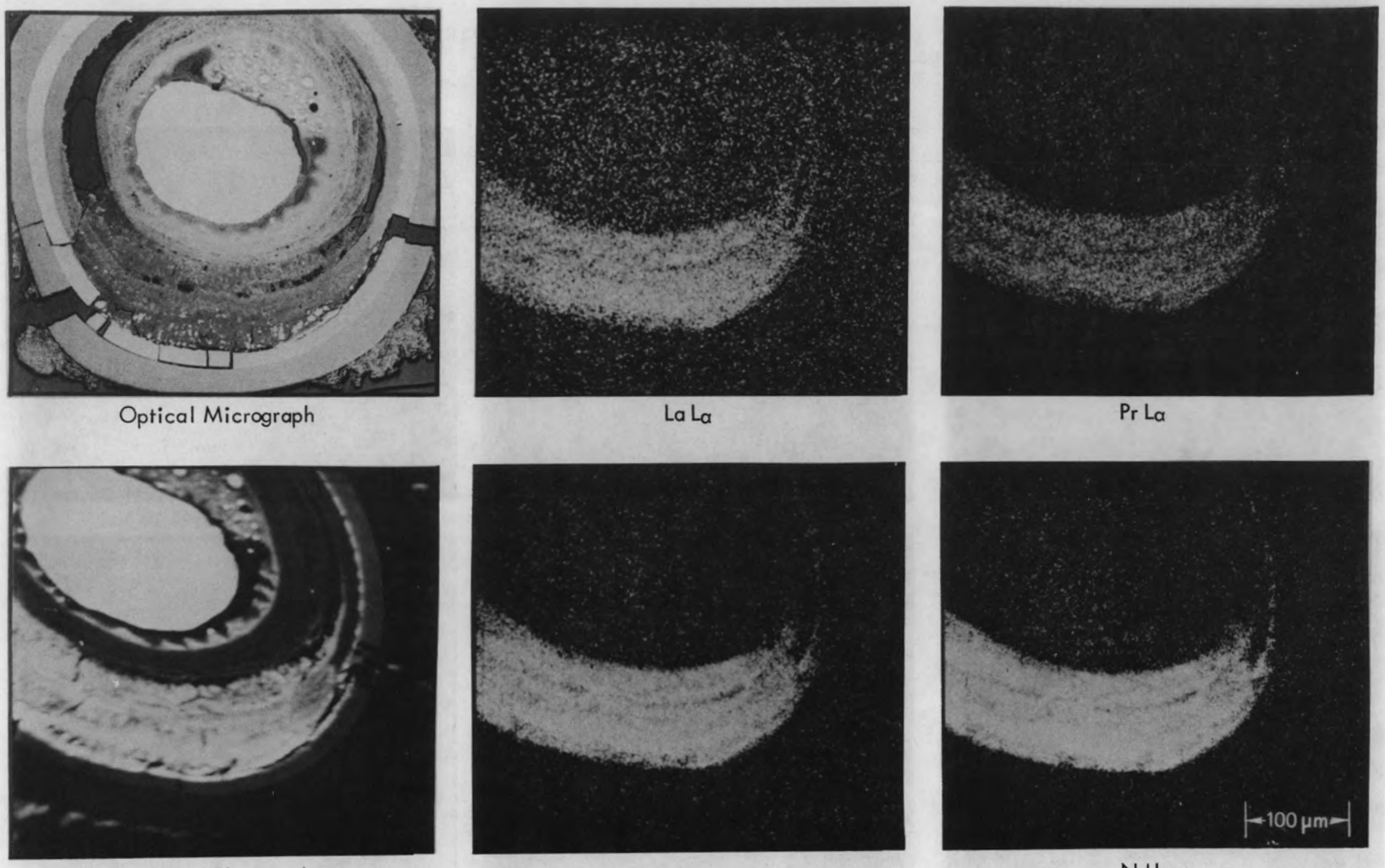

Fig. 6.41. Distribution of Rare-Earth Fission Products in a Triso-Coated 100%-Reduced Weak-Acid-Resin Particle Irradiated in HRB-8. 130×.

Y-128086

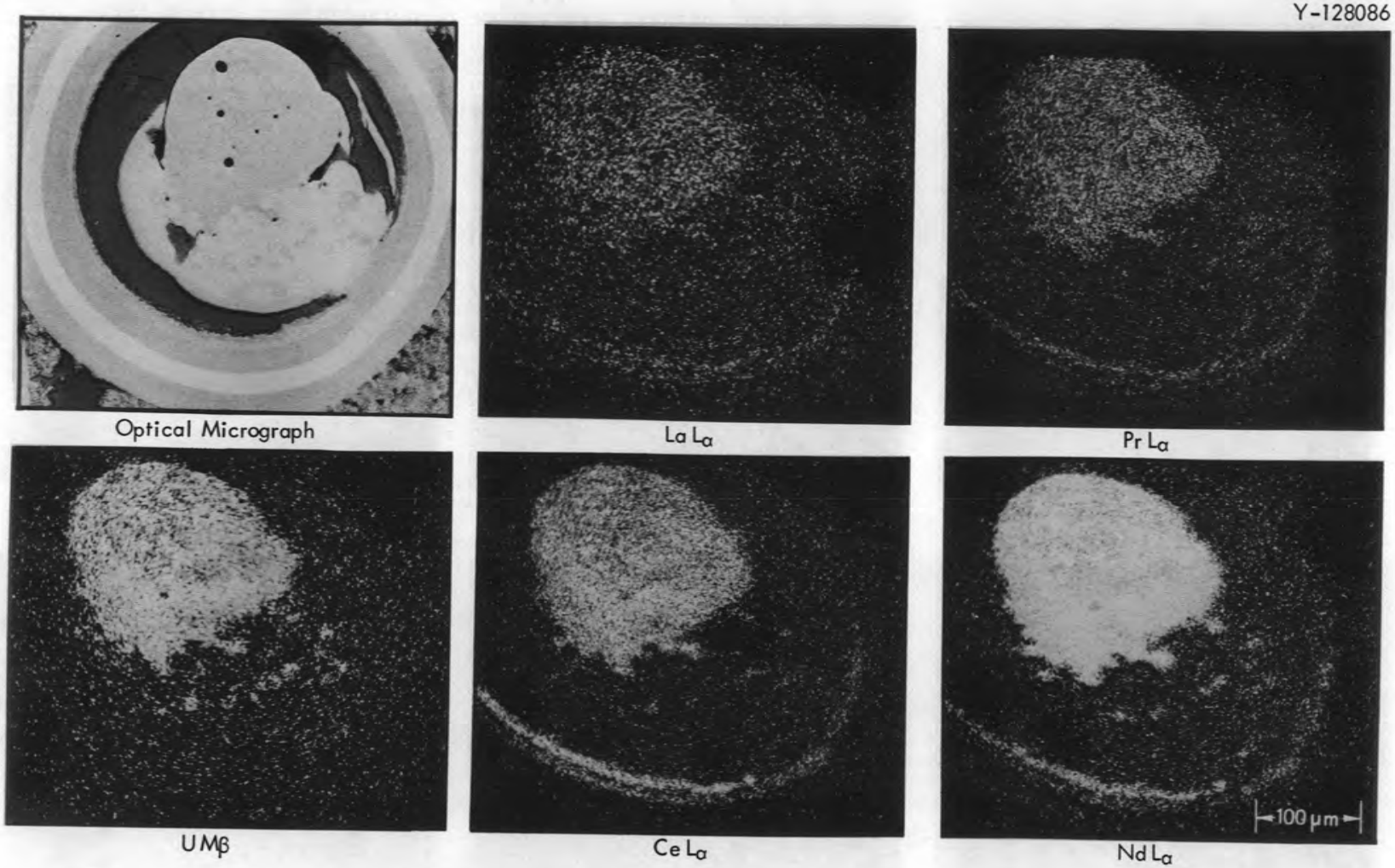

Fig. 6.42. Distribution of Uranium and Rare-Earth Fission Products in a Triso-Coated 15%-Reduced Weak-Acid-Resin Particle Irradiated in HRB-8. 130×.

Y-129593

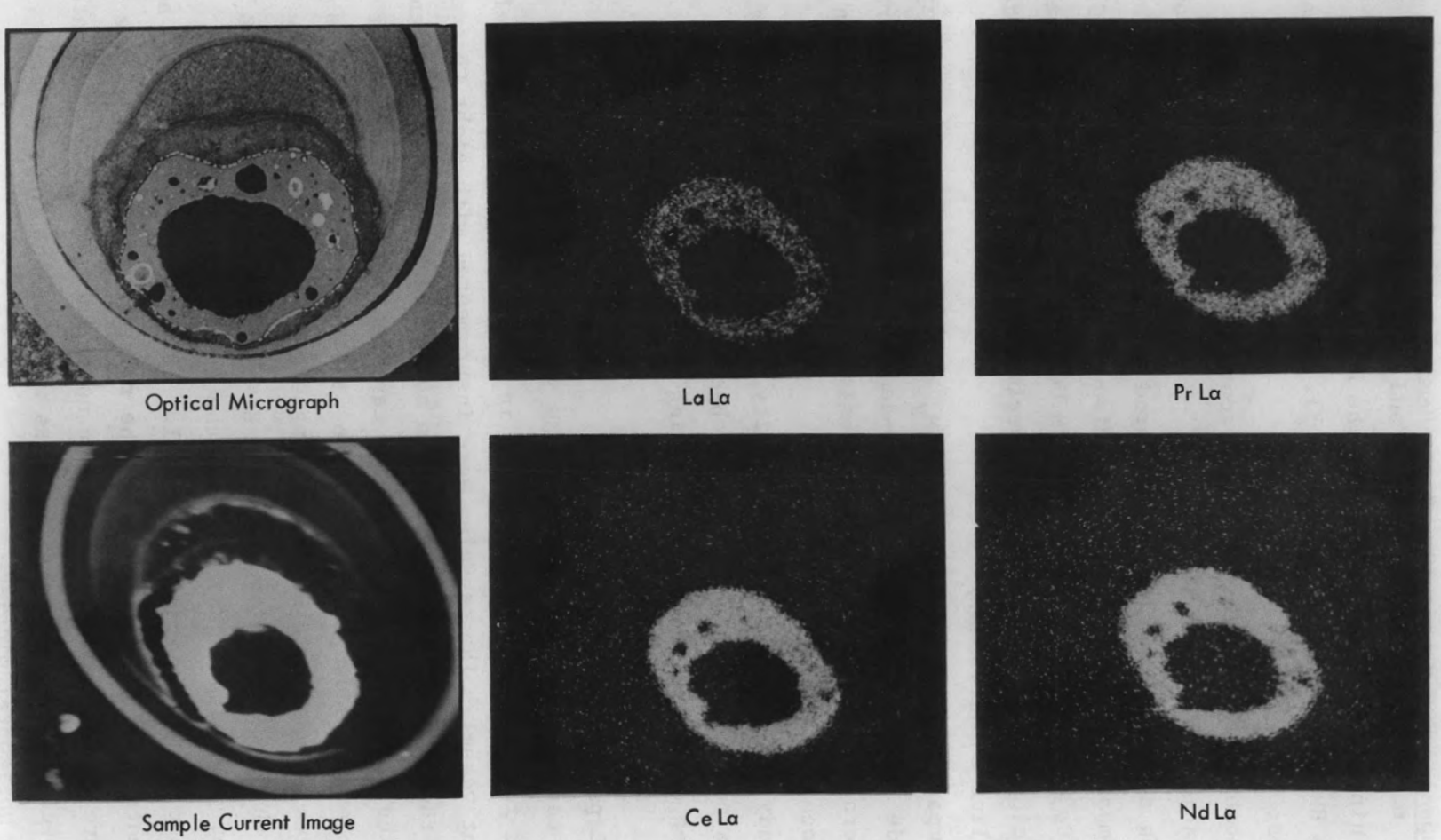

Fig. 6.43. Retention of Rare-Earth Fission Products in the Kernel of a Triso-Coated Sol-Gel UO_2 Particle Irradiated in HRB-8. 130×.

6.6.4 Capsules HRB-9 and -10 — F. J. Homan, B. H. Montgomery, E. L. Long, Jr., R. L. Hamner, and T. N. Tiegs

The ninth and tenth capsules in the HRB series were similar in design to HRB-7 and -8 (see Sect. 6.6.3). HRB-9 and -10 had four main objectives:

1. to establish the effect of oxygen content on the performance of Weak-Acid-Resin (WAR) fissile fuel — in particular, the effect on amoeba and SiC attack by fission products;
2. to compare the behavior of ORNL Triso-coated sol-gel-derived (SG) $Th_{0.8}U_{0.2}O_2$ and GA Triso-coated VSM UC_2 particles with WAR fissile particles (This portion of the experiment was intended to provide base-line comparisons.);
3. to compare amoeba rates of WAR UC_xN_y kernels and high-density WAR carbide kernels with rates for low-density carbide (or oxide-carbide) WAR kernels (This experiment was designed to provide information on amoeba mechanisms.);
4. to study the effect of a high-density, high-thermal-conductivity matrix on fuel performance. This objective was accomplished by testing a warm-molded specimen having a high matrix density.

6.6.4.1 Capsule Design

Each capsule contained 19 fuel rods in a graphite sleeve. The sleeve and fuel rods were encapsulated in a dual-wall stainless steel containment vessel. The capsules were instrumented with eight Chromel vs Alumel thermocouples and one Johnson noise thermometer. The dimensions of the various components of the capsules and the locations of all thermocouples are shown in Fig. 6.28 (p. 306). As with all previous HRB capsules, temperature control in HRB-9 and -10 was maintained by adjusting the composition of the sweep gas (helium and neon) flowing through the gaps between the fuel and the graphite and between the graphite and the stainless steel vessel. All 19 fuel rods in HRB-9 and -10 had central holes. The holes in the rods in the top half of the capsule were to accommodate the Johnson noise thermometer at the centerline of specimen 9. The remaining holes were present for symmetry around the horizontal midplane.

6.6.4.2 Preparation of Test Specimens

Nine types of fully enriched fissile particles were tested in both capsules. The particle types, their purposes in the experiment, and their positions within the capsules are briefly described in Table 6.29. The Biso-coated WAR $^{238}UC_{4.55}O_{1.71}$ driver particle was included to maintain the desired temperature after most of the ^{235}U had burned out and until sufficient ^{233}U had been bred in the fertile particles. The driver particles, along with the Biso-coated fertile particles and the inert carbon particles, were common to all specimens and were used as required for heavy metal and particle volume loadings. All particles in the experiment (except those provided by GA) were heat-treated at 1800°C to stabilize the coatings. The coated particle characteristics and coating conditions for each type of particle are given in Tables 6.30 through 6.32.

All the specimens in both capsules were fabricated by the slug-injection method except specimens 10, which were warm molded. The matrix materials for all slug-injected specimens were the same: 28.5 wt % Ashbury Natural Flake 6353 graphite filler in Ashland grade 240 pitch. The matrix materials for the warm-molded specimens were 55 wt % GLCC 1074 graphite filler, 15 wt % Thermax, and 30 wt % Ashland grade 240 pitch. The particles were blended in an air blender. The matrix was injected through the particle bed at 180°C and 6.9 MPa (1000 psi) in a metal mold and around a metal rod to form the central hole. In fabricating the warm-molded rods the coated particles were slurry blended with the matrix materials after which the mix was granulated, poured into a steel mold, and pressed at 160°C and 6.9 MPa (1000 psi). All specimens were carbonized at 900°C in a packed bed of alumina at a heating rate of 180°C/hr. They were then heat-treated at 1800°C for 30 min for dimensional stability. Approximately 115 specimens were prepared for the experiments, archives, and characterization.

The specimens were characterized by dimensional measurements, weight, radiography, metallography, and photography. Figures 6.44 and 6.45 show pole and side views, respectively, of typical specimens.

Table 6.29. Coated Particles and Positions in HRB-9 and -10 Capsules[a]

Position in Capsule[b]	Kernel Type[c]	Conversion[d] (%)	Kernel Diameter (μm)	Purpose in Experiment
1	(WAR) $UC_{3.68}O_{0.01}$ Density — 3.01 g/cm^3	100	360	Effect of O/U ratio and kernel density on amoeba
2	(SG) 4:1(Th,U)O_2 (VSM) UC_2		360 200	Provide base-line data for comparison with WAR kernels
3	(WAR) $UC_{2.61}O_{0.16}$ Density — 5.28 g/cm^3	100	315	Fffect of O/U ratio and kernel density on amoeba
4	(WAR) $UC_{4.58}O_{2.04}$ Density 3.66 g/cm^3	0	360	Effect of O/U ratio on amoeba
5	(WAR) $UC_{3.68}O_{0.01}$ Density — 3.01 g/cm^3	100	360	Effect of O/U ratio and kernel density on amoeba
6	UC_xN_y		360	Compare effect on amoeba with that of WAR with high-denisty kernel
7	(SG) 4:1 (Th,U)O_2 (VSM) UC_2		360 200	Provide base-line data for comparison with WAR kernels
8	(WAR) $UC_{4.39}O_{1.72}$	15	360	Effect of O/U ratio on amoeba
9	(WAR) $UC_{4.14}O_{0.53}$	75	360	Effect of O/U ratio on amoeba
10[e]	(WAR) $UC_{4.14}O_{0.53}$	75	360	Effect of O/U ratio on amoeba
11	(WAR) $UC_{3.68}O_{0.01}$ Density — 3.01 g/cm^3	100	360	Effect of O/U ratio and kernel density on amoeba
12	(WAR) $UC_{4.58}O_{2.04}$	0	360	Effect of O/U ratio on amoeba
13	(WAR) $UC_{4.63}O_{0.97}$	50	360	Effect of O/U ratio on amoeba
14	(WAR) $UC_{2.61}O_{0.16}$ Density — 5.38 g/cm^3	100	315	Effect of O/U ratio and kernel density on amoeba
15	(WAR) $UC_{4.14}O_{0.53}$	75	360	Effect of O/U ratio on amoeba
16	(WAR) $UC_{4.39}O_{1.72}$	15	360	Effect of O/U ratio on amoeba
17	(WAR) $UC_{4.63}O_{0.97}$	50	360	Effect of O/U ratio on amoeba
18	(WAR) UC_xN_y		360	Compare effect on amoeba with that of WAR with high density kernels
19	(WAR) $UC_{4.14}O_{0.53}$	75	360	Effect of O/U ratio on amoeba
All	(WAR) $^{238}UC_{4.55}O_{1.71}$ Biso	15	425	For fission heat generation as the ^{235}U is burned out
All	(SG) ThO_2 Biso		500	Fertile particle
All	(SAR) Carbon Biso		500	Diluent particle

[a]All particles are Triso coated unless noted otherwise.

[b]Refer to Fig. 6.28

[c]All fissile particles are ^{235}U unless noted otherwise. WAR — Derived from weak acid resin. SG — Derived by the sol-gel process. VSM — Derived by GA's process. SAR — Derived from desulfurized strong acid resin.

[d]Nominal percent of oxygen removed.

[e]Warm molded specimen at reactor horizontal midplane.

Table 6.30. Conditions for Coating Particles in Capsules HRB-9 and -10

Batch	Layer	Coating Gas	Temperature[a] (°C)	Deposition Rate (μm/min)
OR-2219-H	Buffer	C_2H_2	1125	9.47
	Inner LTI	MAPP[b]	1275	6.29
	SiC	CH_3SiCl_3	1550	0.17
	Outer LTI	MAPP	1275	6.21
OR-2208-H	Buffer	C_2H_2	1125	7.40
	Inner LTI	MAPP	1275	4.83
	SiC	CH_3SiCl_3	1550	0.15
	Outer LTI	MAPP	1275	5.71
OR-2211-H	Buffer	C_2H_2	1125	8.47
	Inner LTI	MAPP	1275	4.96
	SiC	CH_3SiCl_3	1550	0.16
	Outer LTI	MAPP	1275	6.00
OR-2116-H	Buffer	C_2H_2	1100	13.96
	Inner LTI	C_3H_6	1250	11.94
	SiC	CH_3SiCl_3	1550	0.37
	Outer LTI	C_3H_6	1250	10.73
OR-2115-H	Buffer	C_2H_2	1300	6.82
	Inner LTI	C_3H_6	1275	7.80
	SiC	CH_3SiCl_3	1550	0.34
	Outer LTI	C_3H_6	1275	6.97
OR-2121-H	Buffer	C_2H_2	1100	6.78
	Inner LTI	C_3H_6	1275	6.02
	SiC	CH_3SiCl_3	1550	0.32
	Outer LTI	C_3H_6	1275	4.92
OR-2218-H	Buffer	C_2H_2	1125	9.96
	Inner LTI	MAPP	1275	6.00
	SiC	CH_3SiCl_3	1550	0.17
	Outer LTI	MAPP	1275	6.37
OR-2233-H	Buffer	C_2H_2	1125	17.64
	Outer LTI	MAPP	1275	11.16
OR-2103-H	Buffer	C_2H_2	1300	11.6
	Outer LTI	MAPP	1275	9.5

[a]All coating temperatures are as read with an optical pyrometer on outside wall of coating tube.

[b]MAPP gas: mixture of methylacetylene and propadiene, with other hydrocarbons as stabilizers.

Table 6.31. Compositional Characterization of Coated Particles for HRB-9 and -10

Batch	Kernel Material[a]	Content, wt %		Enrichment (at. % ^{235}U)	Content, ppm	
		U	Th		B	Fe
GAC6151-00-035[b]	VSM UC_2—1% ThC_2	18.86		93.15		
OR-2219-H	WAR $U(C,N)\cdot C_x$	15.11		93.06	<10	30
OR-2208-H	WAR $UC_{3.68}O_{0.01}$	17.72		93.06	<10	10
OR-2211-H	WAR $UC_{4.63}O_{0.01}$	16.55		93.06	<10	10
OR-2216-H	SG $(4Th,U)O_2$	6.50	26.42	93.13	3	20
OR-2115-H	WAR $U_{4.39}O_{1.72}$	19.13		93.18	5	20
OR-2121-H	WAR $UC_{2.61}O_{0.16}$	20.03		93.32	5	20
OR-2218-H	WAR $UC_{4.58}O_{2.04}$	15.55		93.06	<10	30
OR-2223-H	ThO_2		52.46		<10	30
OR-2103-H	WAR $UC_{4.55}O_{1.71}$	30.59		0.7	20	20
OR-2081-H	SAR carbon				<10	10

[a]VSM = GA's proprietary process, SG = sol-gel process, WAR = weak-acid resin derived, SAR = strong-acid resin derived.

[b]Supplied by General Atomic Company.

Table 6.32. Mean Dimensions and Densities[a] of Coated Particles HRB-9 and -10

Batch	Kernel Diameter (μm)	Thickness, μm				Density, g/cm³				
		Buffer	Inner C	SiC	Outer C	Kernel	Buffer	Inner C	SiC	Outer C
GAC6151-00-035[b]	196 (16)	99 (10.6)	33 (3.5)	32.0 (5.3)	38 (5.0)	10.99	1.07	1.92	3.20	1.85
OR-2219-H	356.3 (18.8)	66.3 (9.5)	44.0 (3.8)	31.9 (1.9)	43.5 (4.6)	3.02	1.09	1.947 (0.007)	3.192 (0.005)	1.977 (0.007)
OR-2208-H	366.5 (24.2)	59.2 (8.5)	36.2 (4.1)	27.9 (1.6)	40.0 (3.6)	3.01	1.11	1.947 (0.004)	3.20 (0.006)	1.997 (0.005)
OR-2211-H	363.0 (20.0)	59.3 (8.6)	34.7 (3.8)	30.2 (1.6)	42.0 (4.1)	3.11	1.09	1.948 (0.009)	3.20 (0.003)	1.997 (0.010)
OR-2116-H	360.0 (4.7)	97.7 (8.7)	38.8 (2.9)	33.6 (1.9)	42.9 (3.0)	9.8	1.36	2.0	3.205 (0.003)	2.037 (0.002)
OR-2115-H	385.8 (29.0)	40.9 (6.8)	42.9 (3.6)	32.1 (1.9)	48.8 (4.0)	3.18	1.37	2.0	3.187 (0.003)	1.986 (0.005)
OR-2121-H	315.3 (29.1)	74.6 (11.3)	36.1 (3.8)	28.4 (2.7)	49.2 (3.3)	5.28	1.10	2.0	3.188 (0.006)	1.982 (0.004)
OR-2218-H	371.3 (15.4)	69.3 (9.8)	42.0 (3.9)	30.7 (1.7)	44.6 (4.1)	3.66	1.12	1.945 (0.006)	3.193 (0.005)	1.994 (0.007)
OR-2223-H	498.3 (2.5)	79.4 (12.2)			89.3 (6.5)	10.00	1.31			2.038 (0.004)
OR-2103-H	430.4 (29.6)	46.6 (9.7)			76.0 (6.0)	3.35	1.11			2.014 (0.005)
OR-2081-H	471.5 (24.6)	73			93.6 (5.4)	1.37	0.95			1.986 (0.006)

[a]Numbers in parentheses are standard deviations.

[b]Supplied by GA.

Photo 2221-74

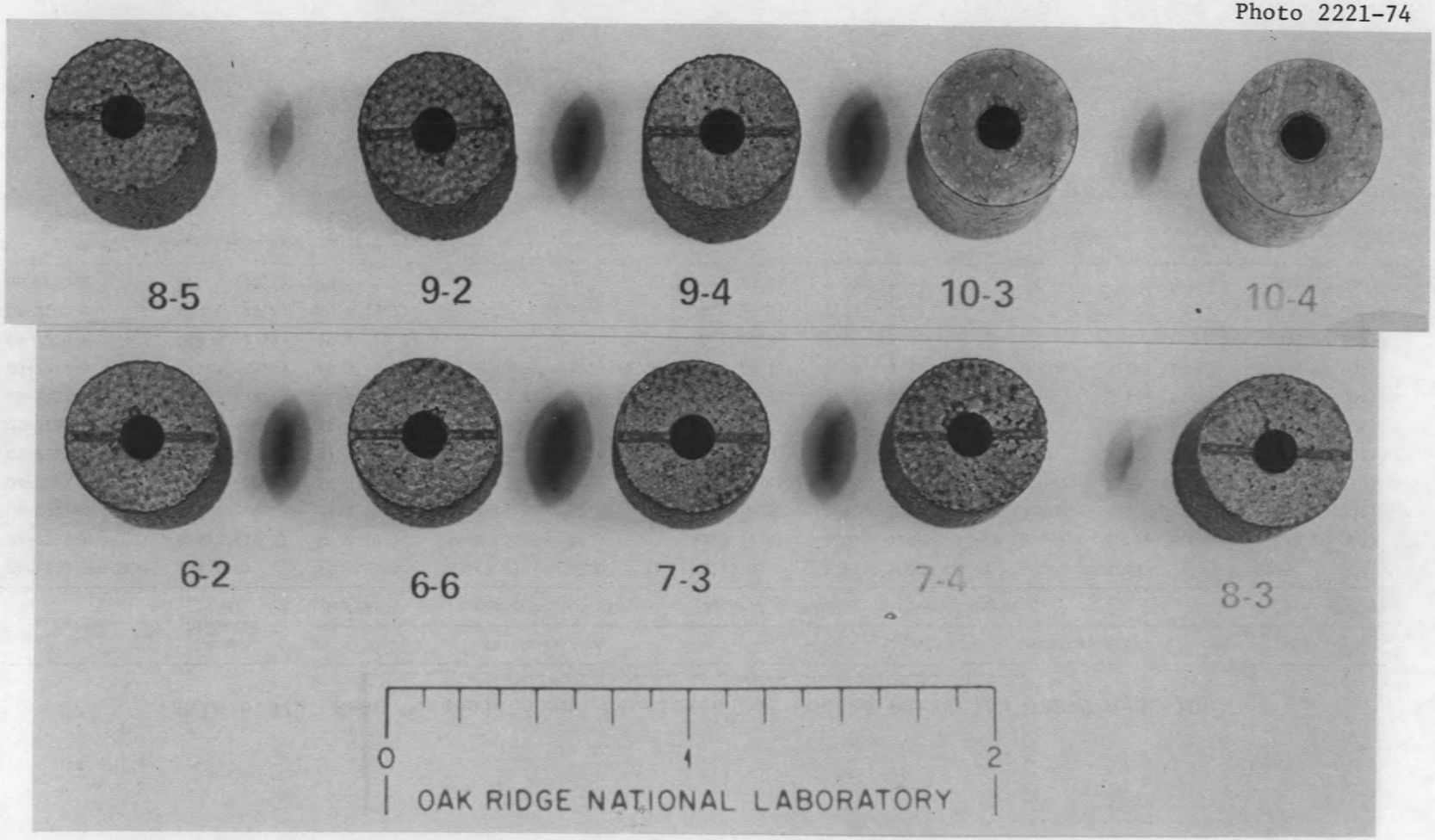

Fig. 6.44. Pole View of Typical Specimens for HRB-9 and -10. Scale length is 51 mm.

Photo 2219-74

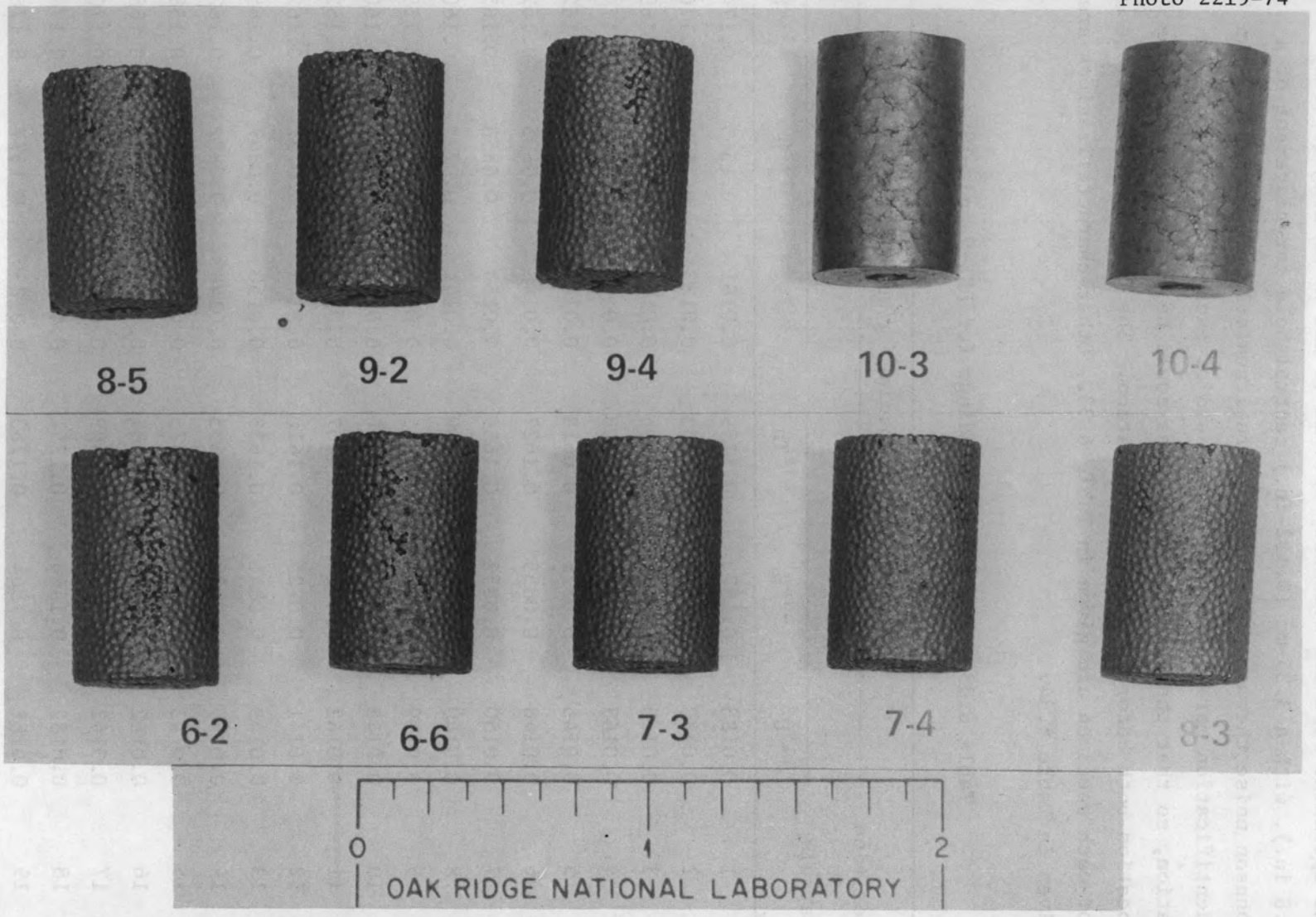

Fig. 6.45. Side View of Typical Specimens for HRB-9 and -10. Scale length is 51 mm.

The specimens were all nominally 12.4 mm OD and 20 mm long (0.49 by 0.8 in.), with a 3.35-mm (0.132-in.) central hole for placement of a Johnson noise thermometer to measure fuel centerline temperature. An identification mark was formed on one end of each specimen for orientation, so that the specimen dimensions could be measured at the same location both before and after irradiation. The heavy metal loadings for each specimen are given in Table 6.33. Other characterizations are given in Table 6.34.

Table 6.33. Heavy Metal Loadings for HRB-9 and -10

Position in Capsule	Loading, g/cm^3					
	HRB-9			HRB-10		
	^{235}U	^{238}U	^{232}Th	^{235}U	^{238}U	^{232}Th
1	0.0183	0.1573	0.1759	0.0181	0.1563	0.1748
2	0.0182	0.1570	0.1753	0.0183	0.1579	0.1763
3	0.0163	0.1138	0.1696	0.0163	0.1137	0.1697
4	0.0168	0.1175	0.1753	0.0167	0.1165	0.1740
5	0.0146	0.0828	0.0613	0.0147	0.0834	0.1623
6	0.0148	0.0835	0.1627	0.0148	0.0835	0.1626
7	0.0150	0.0852	0.1659	0.0150	0.0853	0.1659
8	0.0140	0.0719	0.1600	0.0141	0.0723	0.1607
9	0.0139	0.0715	0.1591	0.0140	0.0718	0.1597
10	0.0143	0.0732	0.1626	0.0140	0.0723	0.1608
11	0.0142	0.0723	0.1607	0.0143	0.0731	0.1627
12	0.0141	0.0725	0.1610	0.0143	0.0732	0.1627
13	0.0149	0.0841	0.1639	0.0150	0.0847	0.1651
14	0.0149	0.0838	0.1635	0.0148	0.0832	0.1624
15	0.0143	0.0808	0.1575	0.0143	0.0811	0.1580
16	0.0162	0.1132	0.1687	0.0162	0.1129	0.1683
17	0.0162	0.1133	0.1689	0.0164	0.1142	0.1704
18	0.0182	0.1566	0.1751	0.0181	0.1564	0.1749
19	0.0181	0.1564	0.1763	0.0183	0.1577	0.1764

Table 6.34. Characterization of Specimens for HRB-9 and -10

Position in Capsule	Average Dimensions, mm (in.)[a]		Volume (cm^3)	Weight (g)	Density, g/cm^3		Particle Volume Loading (%)
	Outside Diam	Length			Matrix	Total	
			Capsule HRB-9				
1	12.421 (0.4890)	19.647 (0.7735)	2.2042	3.2755	0.47	1.49	59.1
2	12.433 (0.4895)	19.647 (0.7735)	2.2091	3.3752	0.50	1.53	60.0
3	12.431 (0.4894)	19.537 (0.7692)	2.1959	3.1396	0.47	1.43	58.2
4	12.377 (0.4873)	19.080 (0.7512)	2.1246	3.1062	0.45	1.46	59.5
5	12.436 (0.4896)	19.782 (0.7788)	2.2252	3.0943	0.48	1.39	58.6
6	12.433 (0.4895)	19.634 (0.7730)	2.0277	3.0915	0.47	1.40	58.7
7	12.423 (0.4891)	19.284 (0.7592)	2.1644	3.0751	0.49	1.42	58.9
8	12.436 (0.4896)	19.583 (0.7710)	2.2029	3.0435	0.47	1.38	58.3
9	12.426 (0.4892)	19.741 (0.7772)	2.2167	3.0695	0.48	1.38	58.5
10[b]	12.408 (0.4885)	19.362 (0.7623)	2.1675	3.8065	1.45	1.76	32.4
11	12.390 (0.4878)	19.655 (0.7738)	2.1934	3.0318	0.47	1.38	58.6
12	12.428 (0.4893)	19.482 (0.7670)	2.1886	3.0410	0.48	1.39	58.4
13	12.423 (0.4891)	19.515 (0.7683)	2.1904	3.0547	0.48	1.39	57.9
14	12.410 (0.4886)	19.614 (0.7722)	2.1966	3.1055	0.50	1.41	58.7
15	12.428 (0.4893)	20.312 (0.7997)	2.2819	3.1704	0.46	1.39	58.9
16	12.423 (0.4891)	19.667 (0.7743)	2.2075	3.1785	0.48	1.44	58.9
17	12.421 (0.4890)	19.652 (0.7737)	2.2048	3.1704	0.50	1.44	58.1
18	12.423 (0.4891)	19.726 (0.7766)	2.2140	3.3205	0.49	1.50	59.4
19	12.421 (0.4890)	19.586 (0.7711)	2.1974	3.3051	0.50	1.50	59.6
			Capsule HRB-10				
1	12.426 (0.4892)	19.748 (0.7775)	2.2176	3.2770	0.47	1.48	58.8
2	12.421 (0.4890)	19.578 (0.7708)	2.1965	3.3092	0.46	1.51	60.4
3	12.418 (0.4889)	19.576 (0.7707)	2.1953	3.1401	0.47	1.43	58.2
4	12.428 (0.4893)	19.055 (0.7502)	2.1407	3.1198	0.50	1.46	58.8
5	12.431 (0.4894)	19.682 (0.7749)	2.2121	3.0871	0.46	1.40	58.9
6	12.423 (0.4891)	19.670 (0.7744)	2.2078	3.1145	0.49	1.41	58.7
7	12.423 (0.4891)	19.253 (0.7580)	2.1610	3.0591	0.48	1.42	59.0
8	12.431 (0.4894)	19.515 (0.7683)	2.1933	3.0383	0.47	1.39	58.6
9	12.428 (0.4893)	19.652 (0.7737)	2.2077	3.0625	0.47	1.39	58.8
10[b]	12.418 (0.4889)	19.550 (0.7697)	2.1924	3.7882	1.42	1.73	32.0
11	12.423 (0.4891)	19.307 (0.7601)	2.1670	3.0050	0.47	1.39	58.5
12	12.418 (0.4889)	19.319 (0.7606)	2.1665	3.0242	0.47	1.40	59.0
13	12.426 (0.4892)	19.370 (0.7626)	2.1751	3.0421	0.47	1.40	58.3
14	12.426 (0.4892)	19.700 (0.7756)	2.2122	3.0754	0.46	1.39	58.4
15	12.423 (0.4895)	20.226 (0.7963)	2.2742	3.1762	0.47	1.40	59.1
16	12.410 (0.4886)	19.751 (0.7776)	2.2120	3.1941	0.50	1.44	58.8
17	12.421 (0.4890)	19.494 (0.7675)	2.1871	3.1581	0.49	1.44	58.6
18	12.428 (0.4893)	19.728 (0.7767)	2.2163	3.3192	0.49	1.50	59.3
19	12.426 (0.4892)	19.576 (0.7707)	2.1982	3.2928	0.48	1.50	59.5

[a]Inside diameter = 3.35 mm (0.132 in.).

[b]Warm molded.

6.6.4.3 Capsule Operation

The operating schedules for HRB-9 and -10 are shown in Table 6.35. Both capsules were irradiated for two cycles in the PB-13 (VXF13) facility before going into the RB facility. This was done to burn out sufficient ^{235}U to avoid overpowering the particles in the RB facility. The PB facility is located further from the HFIR core (39 cm from the center of the core compared to 27 cm for the RB-5 facility). The neutron flux characteristics of the two positions are shown elsewhere.[33] The thermal flux in the PB facility is about 60% of the RB flux, and the fast flux is about 11%. Using the PB facility for preirradiations permits irradiation of fully enriched fissile particles, which could not be done otherwise because of very high power production rates at the beginning of the test. The Fuel Development Program currently reserves one PB facility and two RB facilities. Capsule HRB-9 was irradiated for two cycles in PB-13, and then moved to RB-7 for an additional nine cycles at a design irradiation temperature of 1250°C (for the fuel center line). Capsule HRB-10 was inserted into PB-13 at the beginning of cycle 114 (when HRB-9 was moved out) for two cycles, and then moved to RB-5 for six additional cycles at a design irradiation temperature of 1500°C (fuel center line).

The calculated burnups for the two capsules are given in Table 6.36; neutron fluxes and fluences are tabulated in Table 6.37. Some preliminary thermal analyses are given in the next two figures. Figure 6.46 shows the calculated fission heat rates at different axial locations in the two capsules. No attempt has been made to calculate fission heat rates for the two cycles each capsule was irradiated in PB-13, because no data are yet available on gamma heating characteristics for this region of the HFIR. Figure 6.47 shows preliminary calculations of the fuel surface and center temperatures for HRB-9 specimens for locations at the horizontal midplane and various distances from it.

Table 6.35. Capsules HRB-9 and -10 Reactor Power and Irradiation History

Facility	Cycle	Begin		End		Irradiation Time, hr	
		Time	Date	Time	Date	During Cycle	Accumulated
			Capsule HRB-9				
PB-13	112	0525	10/6/74	0218	10/31/74	547.20	547.20
PB-13	113	0318	11/1/74	1028	11/24/74	558.72	1105.92
RB-7	114	1332	11/25/74	0400	12/18/74	541.68	1647.60
RB-7	115	1435	12/20/74	1716	1/11/75	529.68	2177.28
RB-7	116	1700	1/12/75	2000	2/3/75	530.16	2707.44
RB-7	117	1700	2/4/75	1800	2/26/75	527.76	3235.20
RB-7	118A	1732	2/28/75	1726	3/6/75	143.28	3378.48
RB-7	119	1524	3/7/75	0233	3/30/75	539.04	3917.52
RB-7	118B	1821	3/30/75	0639	4/16/75	396.00	4313.52
RB-7	120	0153	4/17/75	0400	5/9/75	529.92	4843.44
RB-7	121	2125	5/11/75	0918	6/3/75	539.28	5382.72
			Capsule HRB-10				
PB-13	114	1332	11/25/74	0400	12/18/74	541.68	541.68
PB-13	115	1435	12/20/74	1716	1/11/75	529.68	1071.36
RB-5	116	1700	1/12/75	2000	2/3/75	530.16	1601.52
RB-5	117	1700	2/4/75	1800	2/26/75	527.76	2129.28
RB-5	118A	1732	2/28/75	1726	3/6/75	143.28	2272.56
RB-5	119	1524	3/7/75	0233	3/30/75	539.04	2811.60
RB-5	118B	1821	3/30/75	0639	4/16/75	396.00	3207.60
RB-5	120	0153	4/17/75	0400	5/9/75	529.92	3737.52

Table 6.36. Calculated Specimen Burnup in HRB-9 and -10

Specimen	Location[a]		Calculated Burnup, % FIMA								
			^{235}U			^{238}U			^{232}Th		
	(mm)	(in.)	PB-13	RB-7, -5	Total	PB-13	RB-7, -5	Total	PB-13	RB-7, -5	Total
					Capsule HRB-9						
1, 19	183	7.2	46.19	37.99	84.18	0.42	13.56	13.98	0.11	5.68	5.79
2, 18	163	6.4	48.97	35.35	84.32	0.50	15.40	15.90	0.12	6.54	6.66
3, 17	142	5.6	51.56	32.86	84.42	0.58	17.35	17.93	0.15	7.49	7.64
4, 16	122	4.8	54.02	30.79	84.81	0.65	18.80	19.45	0.16	8.39	8.55
5, 15	102	4.0	55.68	28.95	84.63	0.69	20.21	20.90	0.18	9.12	9.30
6, 14	81	3.2	57.14	27.42	84.56	0.77	21.35	22.12	0.20	9.83	10.03
7, 13	61	2.4	58.28	26.29	84.57	0.82	22.38	23.20	0.21	10.34	10.55
8, 12	41	1.6	59.14	25.57	84.71	0.86	23.15	24.01	0.22	10.80	11.02
9, 11	20	0.8	59.60	25.08	84.68	0.89	23.57	24.46	0.23	10.98	11.11
10	0	0	59.84	24.84	84.68	0.90	23.80	24.70	0.23	11.25	11.48
					Capsule HRB-10						
1, 19	183	7.2	46.19	36.39	82.58	0.42	8.02	8.44	0.11	2.89	3.00
2, 18	163	6.4	48.97	34.31	83.28	0.50	9.24	9.74	0.12	3.38	3.50
3, 17	142	5.6	51.56	32.19	83.75	0.58	10.56	11.14	0.15	3.91	4.06
4, 16	122	4.8	54.02	30.36	84.38	0.65	11.57	12.22	0.16	4.42	4.58
5, 15	102	4.0	55.68	28.68	84.36	0.69	12.55	13.24	0.18	4.84	5.02
6, 14	81	3.2	57.14	27.24	84.38	0.77	13.36	14.13	0.20	5.25	5.45
7, 13	61	2.4	58.28	26.16	84.44	0.82	14.07	14.89	0.21	5.54	5.75
8, 12	41	1.6	59.14	25.46	84.60	0.86	14.61	15.47	0.22	5.80	6.02
9, 11	20	0.8	59.60	24.99	84.59	0.89	14.91	15.80	0.23	5.91	6.14
10	0	0	59.84	24.75	84.59	0.90	15.08	15.98	0.23	6.06	6.29

[a]Distance from reactor horizontal midplane.

Table 6.37. Thermal and Fast Fluences Calculated for HRB-9 and -10 Specimens

Rod	Location[a] (mm)	Location[a] (in)	Flux in PB-13 n cm^{-2} sec^{-1} av Thermal <0.414 eV	Flux in PB-13 n cm^{-2} sec^{-1} Fast >0.18 MeV	Flux in RB-7 and -5, n cm^{-2} sec^{-1} av Thermal <0.414 eV	Flux in RB-7 and -5, n cm^{-2} sec^{-1} Fast >0.18 MeV	Total Fluence, n/cm^2 Thermal <0.414 eV HRB-9	Total Fluence, n/cm^2 Thermal <0.414 eV HRB-10	Total Fluence, n/cm^2 Fast >0.18 MeV HRB-9	Total Fluence, n/cm^2 Fast >0.18 MeV HRB-10
			$\times 10^{14}$	$\times 10^{13}$	$\times 10^{14}$	$\times 10^{14}$	$\times 10^{22}$		$\times 10^{21}$	
1, 19	183	7.2	4.44	3.42	6.18	2.95	1.13	0.76	4.68	2.96
2, 18	163	6.4	4.86	3.80	7.07	3.31	1.28	0.87	5.25	3.32
3, 17	142	5.6	5.22	4.31	7.95	3.66	1.43	0.96	5.81	3.68
4, 16	122	4.8	5.56	4.65	8.80	3.97	1.58	1.06	6.29	3.99
5, 15	102	4.0	5.89	4.90	9.57	4.28	1.71	1.15	6.78	4.30
6, 14	81	3.2	6.23	5.17	10.27	4.55	1.83	1.23	7.21	4.57
7, 13	61	2.4	6.57	5.40	10.90	4.78	1.94	1.30	7.57	4.80
8, 12	41	1.6	6.85	5.58	11.40	4.92	2.03	1.36	7.79	4.94
9, 11	20	0.8	6.98	5.67	11.71	5.00	2.08	1.39	7.92	5.02
10	0	0	7.03	5.70	11.80	5.00	2.09	1.40	7.93	5.02

[a]Distance from reactor horizontal midplane.

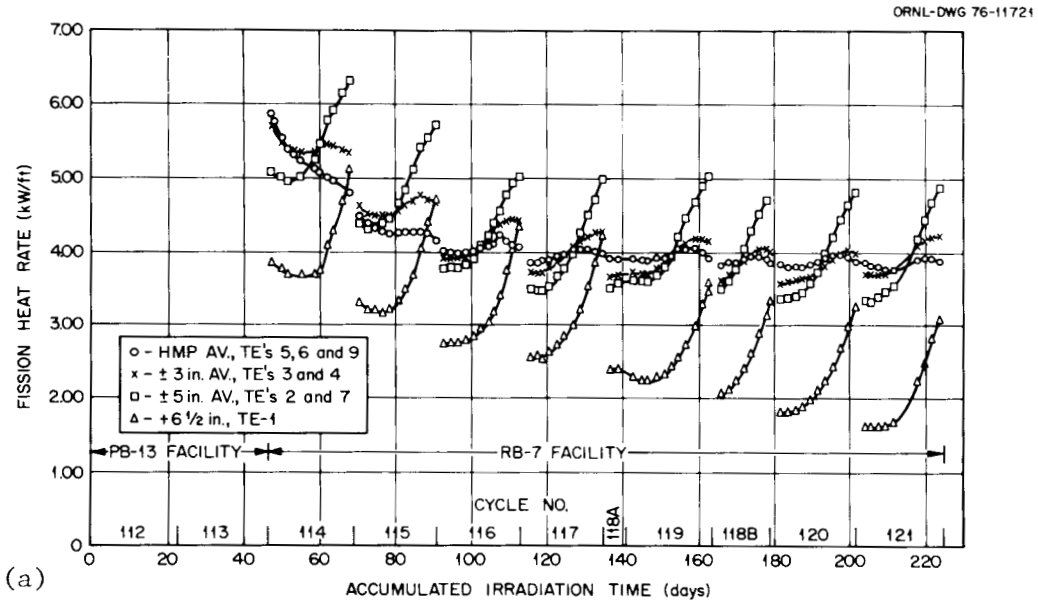

(a)

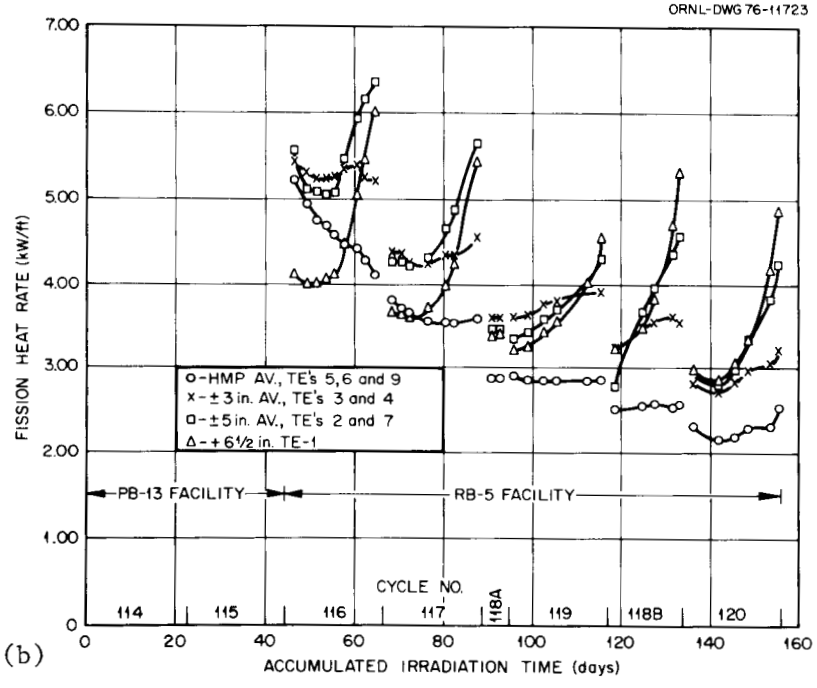

(b)

Fig. 6.46. Calculated Fission Heat Rate History for Capsules (a) HRB-9 and (b) HRB-10. Points plotted are for the averages of the following thermocouples at four axial locations: thermocouples 5, 6, and 9 at the horizontal midplane; 3 and 4 at ±76 mm (3 in.) from the midplane; 2 and 7 at ±0.13 m (5 in.); and 1 at +0.165 m (6.5 in.).

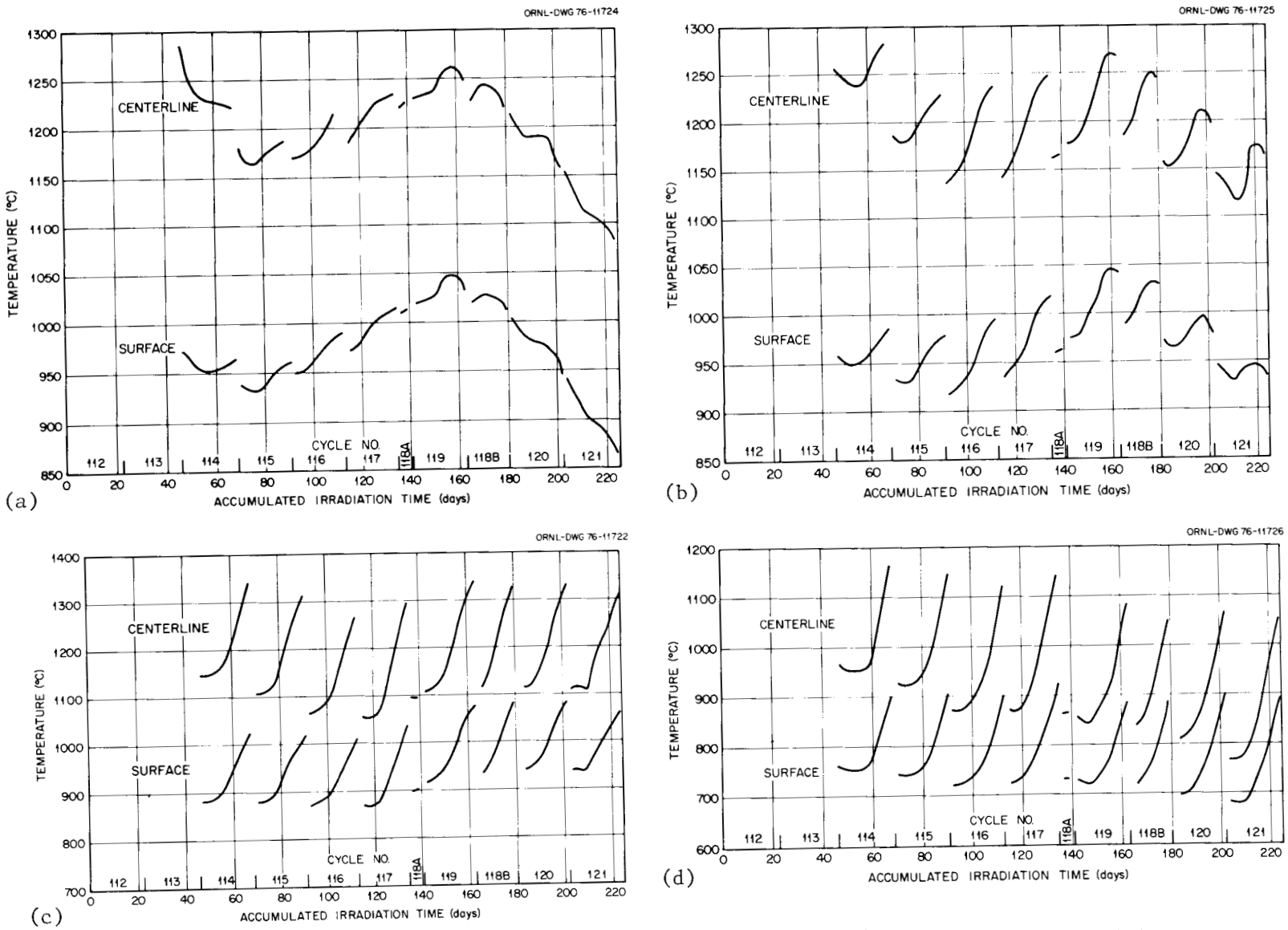

Fig. 6.47. Calculated HRB-9 Specimen Temperature History. (a) At horizontal midplane. (b) ±76 mm (3 in.) from midplane. (c) ±0.13 m (5 in.). (d) +0.165 m (6.5 in.).

6.6.4.4 Postirradiation Examination

Disassembly and physical examination of irradiation capsules HRB-9 and -10 were completed during this reporting period. The fuel rods from HRB-9 were removed in good condition. Stereoscopic examination showed that minor debonding had occurred at the edges of the rods but that all rods were intact. One broken particle was observed on the surfaces of rods 5, 6, and 14. However, the particle type could not be identified.

In removing the fuel rods from HRB-10, we found that rods 1 through 9 were bonded to the central thermocouple assembly. An attempt was made to separate the rods by cutting through the thermocouple assembly, but the rods were so fragile that they broke when cutting was started. Only rod 7 remained intact. Fuel rods 10 through 19 were removed in good condition.

Visual examination of the fragments of rods 1 through 9 showed that the particles on the inner surfaces of the rods had reacted with the rhenium foil and the molybdenum-rhenium tube. Some particles appeared to be embedded in the foil, as shown in Fig. 6.48(a). Also, the reaction did not extend around the entire circumference of the rhenium foil, but occurred only where the molybdenum-rhenium tube contacted the foil.

The surfaces of all rods appeared spotty from what appeared to be black sooty regions. The rods had varying amounts of surface covered, and no correlation with particle type was evident. A possible explanation of the spotty appearance is associated with the fact that the HRB-10 capsule was sealed off during irradiation because of a high degree of release of fission gases in the purge system. This resulted in a high buildup of fission products in the capsule. The spotty appearance may be due to condensation of volatile fission products on the fuel rod surface.

One broken particle each was observed on the surfaces of rods 13, 14, and 15; the particle types could not be identified.

A dimensional inspection of the intact rods from HRB-9 and -10 was made and is summarized in Table 6.38.

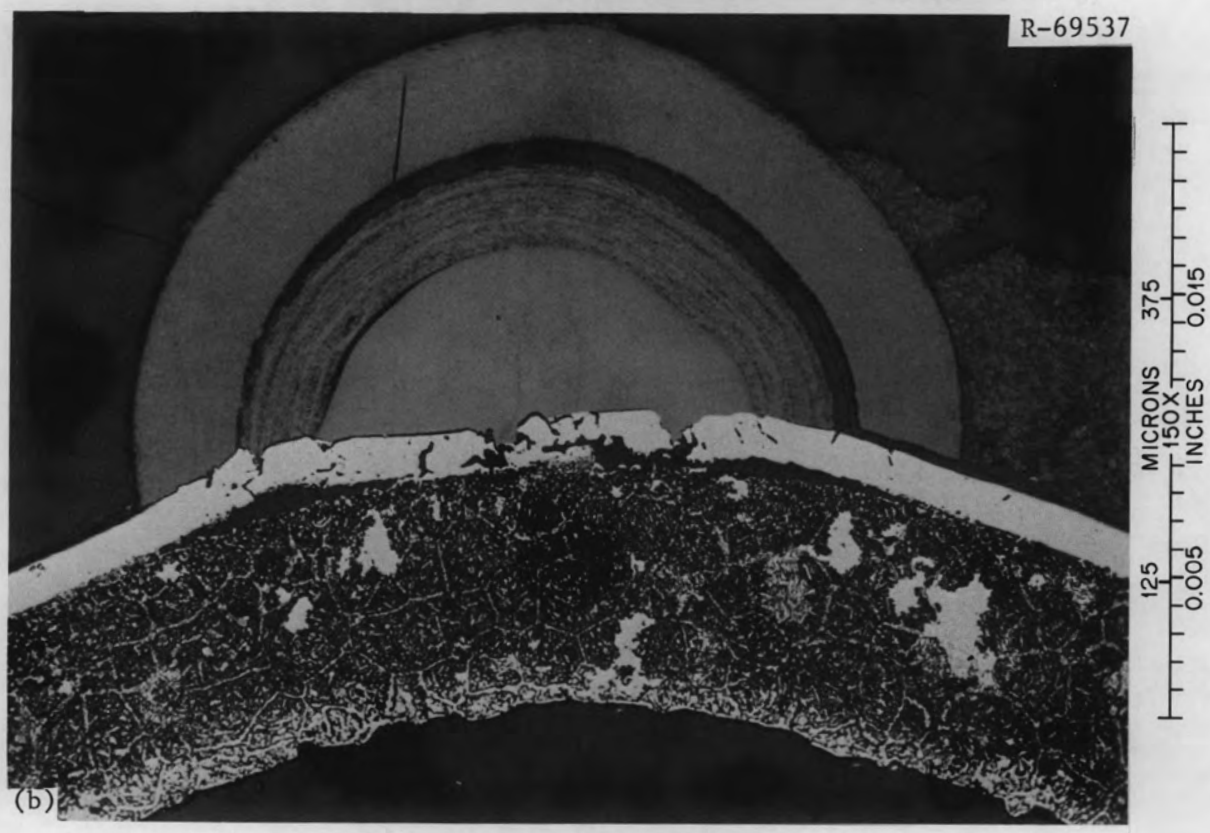

Fig. 6.48. Results of Reaction of Coated Particles with Central Thermocouple Assembly of Irradiation Capsule HRB-10. (a) Coated particles attached to rhenium foil. 10×. (b) Metallographic section through a Biso-coated inert particle attached to and partially consumed by rhenium-foil-wrapped Mo—48% Re sheath. Note massive carbide in sheath.

Table 6.38. Summary of Dimensional Changes in Fuel Rods from HRB-9 and -10

Rod	Postirradiation Diameter		Diameter Decrease		
	(mm)	(in.)	(mm)	(in.)	(%)
			Capsule HRB-9		
1	12.088	0.4759	0.333	0.0131	2.68
2	12.029	0.4736	0.404	0.0159	3.25
3	11.999	0.4724	0.432	0.0170	3.47
4	11.913	0.4690	0.465	0.0183	3.76
5	11.974	0.4714	0.462	0.0182	3.72
6	12.012	0.4729	0.422	0.0166	3.39
7	11.986	0.4719	0.437	0.0172	3.52
8	11.994	0.4722	0.442	0.0174	3.55
9	11.994	0.4722	0.432	0.0170	3.48
10	12.167	0.4790	0.241	0.0095	1.94
11	11.953	0.4706	0.437	0.0172	3.53
12	12.107	0.4731	0.411	0.0162	3.31
13	11.996	0.4723	0.429	0.0169	3.43
14	11.951	0.4705	0.460	0.0181	3.70
15	12.042	0.4741	0.386	0.0152	3.11
16	12.007	0.4727	0.417	0.0164	3.35
17	12.022	0.4733	0.399	0.0157	3.21
18	12.037	0.4739	0.386	0.0152	3.11
19	12.075	0.4754	0.361	0.0142	2.78
			Capsule HRB-10[a]		
7	11.943	0.4702	0.488	0.0192	3.93
9	11.918	0.4692	0.511	0.0201	4.11
10	12.078	0.4755	0.340	0.0134	2.74
11	11.946	0.4703	0.478	0.0188	3.84
12	11.900	0.4685	0.518	0.0204	4.17
13	11.880	0.4677	0.546	0.0215	4.39
15	11.913	0.4690	0.521	0.0205	4.19
16	11.872	0.4674	0.538	0.0212	4.34
17	11.918	0.4692	0.503	0.0198	4.05
18	11.928	0.4696	0.500	0.0197	4.03
19	12.022	0.4733	0.404	0.0159	3.25

[a]Rods 1 through 6, 8, and 14 broken too badly during disassembly to permit dimensional inspection.

Twenty-two fuel rod specimens were selected from the two capsules for metallographic examination; the results for the various fissile particles are summarized in Table 6.39. Although a few specimens remain to be examined and electron microprobe analyses will be performed later, the following general conclusions concerning the variety of fissile particles contained in these two irradiation tests can be stated.

1. The performance of the 15, 50, and 75%-converted WAR kernels appears to be superior to that of $(4Th,U)O_2$ or dense UC_2 (VSM).

2. The 100%-converted WAR does not retain the rare-earth fission products. This degrades the inner LTI and SiC layers and can lead to particle failure. The performance of the 100%-converted WAR is not unlike that of dense UC_2 (VSM).

3. The WAR UO_2 (0% converted) kernels exhibit lack of thermal stability (amoeba) and result in corrosive attack of the SiC, apparently from oxidation by the high carbon monoxide pressures expected after irradiation.

4. Although we saw no evidence of amoeba of the nitrogen-bearing WAR kernels, the inner LTI and SiC layers were severely damaged, and coating failures were observed.

Examples of WAR particles from the higher temperature capsule, HRB-10, are shown in Fig. 6.49.

In addition, we saw no evidence of amoeba in any of the Biso-coated ThO_2 kernels; nor were any failures or evidence of potential failures observed out of about 300 particles examined in these two experiments. Metallographic examination of a section through a fuel rod (No. 7) that contained a section of the rhenium foil and molybdenum-rhenium sheath revealed that particles were virtually consumed by the diffusion of carbon through the rhenium to the molybdenum-rhenium, which acted as a carbon sink. Hemispheres of coated particles were found attached to the rhenium foil where the foil and sheath were in intimate contact, and massive carbide was present in the molybdenum-rhenium sheath [Fig. 6.48(b)].

Table 6.39. Summary of Various Fissile Particles Irradiated in Capsules HRB-9 and -10

Fissile Kernel Composition	Conversion[a] (%)	Kernel Density[b] (g/cm^3)	Purpose of Experiment	Irradiation Capsule[c]	Number Fissiles Examined	Maximum Amoeba (μm)	Fuel Rod Examined[d]	Metallographic Results
(WAR) $UC_{4.38}O_{3.04}$	0	3.66	Effect of O/U ratio on fissile particle performance	HRB-9	13	~75	12	No failure of fissiles observed. Migration of oxide kernel through buffer evident in peripheral region of fuel rod; no migration at midwall to inner surface of rod; no evidence of rare-earth fission products on cold side of particle. Separation of inner LTI from SiC apparent – as much as 10-μm gap in some particles. Slight evidence of attack on inner surface of SiC on hot side of particle to a maximum depth of 2 μm.
				HRB-10	19	~90	12	One failed fissile particle observed on inner surface of fuel rod; the fissile particles showed chemical attack from slight to complete penetration of SiC layer. Amoeba apparent in particles in peripheral region of rod. No evidence of rare earth fission products on cold side of particles. Separation of inner LTI from SiC apparent – as much as 15 μm in some particles.
(WAR) $UC_{4.30}O_{1.72}$	15	3.18	Effect of O/U ratio on fissile particle performance	HRB-9	17	0	8	No failed fissile particles observed. Buffer coating consumed by kernels. Kernels segregated into two distinct phases; one phase has the appearance of an oxide and contains fission gas bubbles, the other is active under polarized light and appears having been molten during irradiation. Phase containing bubbles surrounded by other phase. No evidence of graphitization of inner LTI or collection of rare earth fission products on cold side of coatings.
				HRB-10	11	0	8	Same as observation made for HRB-9, rod 8, above.
(WAR) $UC_{4.63}O_{0.97}$	50	3.11	Effect of O/U ratio on fissile particle performance	HRB-9	11	0	13	No failed fissile particles observed. Buffer coating, although still intact, separated from inner LTI and densified around kernel. Kernel segregated into two distinct phases. The minor phase is optically active under polarized light, and appears to have been molten during irradiation. No evidence of graphitization of inner LTI and slight evidence of what may be rare earth fission products on cold side of inner surface of SiC.
				HRB-10	8	0	13	No failed fissile particles observed. Essentially identical to observations made for HRB-9, rod 13, above, except more evidence of what may be rare earth fission products in inner LTI and adjacent to inner surface of SiC on cold side of particle.

Table 6.39. (Continued)

Fissile Kernel Composition	Conversion[a] (%)	Kernel Density[b] (g/cm^3)	Purpose of Experiment	Irradiation Capsule[c]	Number Fissiles Examined	Maximum Amoeba (μm)	Fuel Rod Examined[d]	Metallographic Results
(WAR) $UC_{4.14}O_{0.53}$	75	3.03	Effect of O/U ratio on fissile particle performance	HRB-9	16	0	9	No failed fissile particles observed. Buffer coating still intact although it separated from the inner LTI and densified around kernel. Kernel segregated into two distinct phases; major phase has appearance of carbide; minor phase is optically active and appears to have been molten during irradiation. No evidence of graphitization of inner LTI and slight evidence of what may be rare earth fission products on cold side of inner surface of SiC.
				HRB-9	18	0	10	Same as observations for HRB-9, rod 9, above.
				HRB-10	12	0	9	Although intact when removed from capsule, fuel rod broke into many pieces while handling in the hot cell. Metallographic sample comprises several pieces of rod and orientation of particles relative to thermal gradient unknown. One failed Triso coating was observed (straight-line mechanical failure), and one particle was noted where the inner LTI was graphitized on what is assumed to be the cold side. An accumulation of what is assumed to be rare earth fission products was present on the inner surface of the SiC in the graphitized region described above. No kernels exposed in this plane of polish could be considered representative; an additional sample is scheduled for metallography.
				HRB-10	15	0	10	No failed fissile particles observed. The buffer separated from the inner LTI, remained intact, and densified around kernel in about half the particles examined. The buffer did not separate from the inner LTI in the remainder of the particles, and a void developed between the densified kernel and buffer. Although no graphitization of the inner LTI was observed, small amounts of rare earth fission products accumulated on the inner surface of the SiC on the cold side of the particle.
				HRB-10			15	Secheduled for metallography.
(WAR) $UC_{3.60}O_{0.01}$	100	3.01	Effect of O/U ratio on fissile particle performance	HRB-9	8	0	11	Six of the eight fissile particles exposed in the plane of polish failed as a result of accumulation of rare earth fission products on the cold side of the particle. Graphitization of the cold side of the inner LTI also evident; failures more prevalent in particles located in steep-thermal-gradient regions of rod. Two distinct phases in kernels; major phase has appearance of a carbide; minor phase is optically active under polarized light and appears to have been molten during irradiation.

Table 6.39. (Continued)

Fissile Kernel Composition	Conversion[a] (%)	Kernel Density[b] (g/cm^3)	Purpose of Experiment	Irradiation Capsule[c]	Number Fissiles Examined	Maximum Amoeba (μm)	Fuel Rod Examined[d]	Metallographic Results
(WAR) $UC_{2.61}O_{0.16}$	100	5.38	Effect of O/U ratio and kernel density of fissile particle performance	HRB-9	15	0	14	Seven of the 15 fissile particles examined failed by same mechanism described for the lower density kernel particle in the HRB-9, rod 1, described above. Chemical attack of inner surface region of SiC to over half the coating thickness observed; other observations are same as those described for HRB-9, rod 10, above.
(WAR) $UC_{3.68}O_{0.01}$	100	3.01	Effect of O/U ratio on fissile particle performance	HRB-10	17	0	11	Three of the 17 fissile particles failed by same mechanism described for HRB-9, rod 11, above; other general observations the same, also.
(WAR) $UC_{2.61}O_{0.16}$	100	5.38	Effect of O/U ratio and kernel desnity of fissile particle performance	HRB-10	10	0	14	Three of the 10 fissile particles failed by same mechanism described for HRB-9, rod 14, above; other general observations the same, also.
(WAR) UC_xN_y[e]	f	3.02	Effect of nitrogen addition on fissile particle performance	HRB-9	13	0	6	Three of the 13 fissile particles failed; two failed from straight-line fractures through coatings on cold side of particles; one failed by penetration of SiC by fission products on cold side of particles. Graphitization of inner LTI and severe attack of SiC by fission products. Kernels are two-phase structure.
				HRB-10	27	0	6, 18	Six particles of 27 examined in rods 6 and 18 failed from same mechanism described for HRB-9, rod 6, above; other general observations the same, also.
(VSM) UC_2	f	9.80	Provide base-line data for comparison with WAR kernels	HRB-9			7	Scheduled for metallography.
				HRB-10	11	0	7	Six of the 11 fissile particles examined failed. Failures were mechanical and resulted from collection of rare earth fission products on the cold side of the particle in the inner LTI adjacent to the SiC. Graphitized on cold side of particle.
(Sol-gel) 4:1$(Th,U)O_2$	f	9.80	Provide base-line data for comparison with WAR kernels	HRB-9			7	Scheduled for metallography
				HRB-10	8	~35	7	No failed fissile particles observed; however, all exhibited the amoeba effect.

[a]Nominal percent oxygen removed.

[b]Pour-volume density assuming 62% volume filling.

[c]HRB-9 design for a maximum fuel temperature of 1250°C. HRB-10 design for a maximum fuel temperature of 1500°C. Both capsules were in the PB facility of HFIR for two cycles; in addition, HRB-9 was in an RB facility for eight cycles and HRB-10 for five cycles.

[d]Fuel rod 10 was a warm-molded specimen; all other fuel rods were fabricated by the slug-injection process.

[e]$UC_{0.47}N_{0.53}$ + 3.21 C – (from chemical analysis. $UC_{0.37}N_{0.63}$ – (from lattice parameter measurements).

[f]Not applicable.

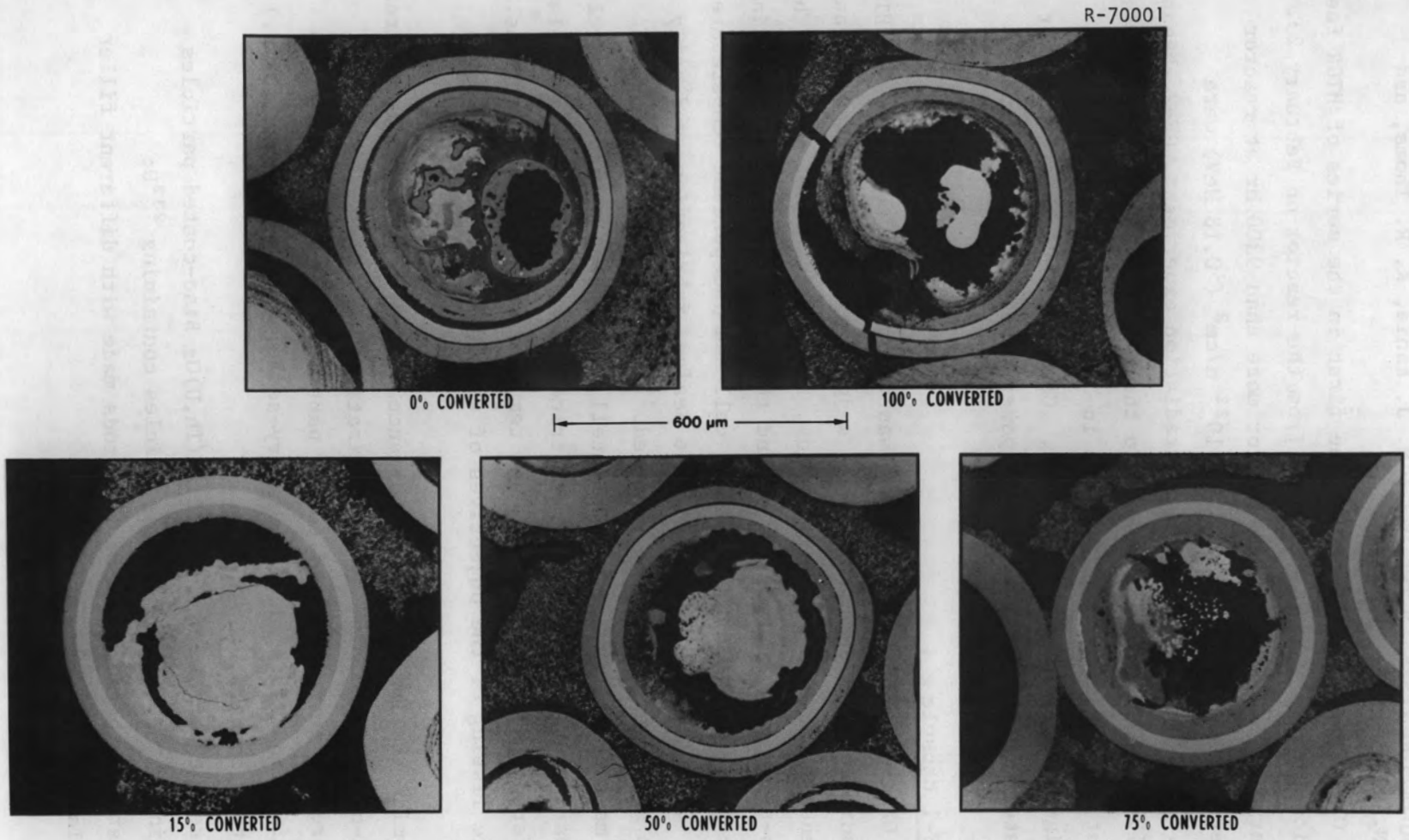

Fig. 6.49. Relative Performance of Weak-Acid-Resin (WAR) Kernels Converted Within the Range from UO_2 (0%) to UC_2 (100%). Irradiated in HRB-10. Maximum design fuel temperature — 1500°C; burnup — 80% FIMA; fast fluence — 4.3–5.0 × 10^{21} n/cm^2 (>0.18 MeV).

6.7 IRRADIATION TESTS IN THE ORR — M. J. Kania, K. R. Thoms, and T. N. Tiegs

The OF-1 irradiation capsule, the first in the series of HTGR fuel irradiations in the ORR, was removed from the reactor on February 23, 1975. This experiment had been irradiated for more than 9300 hr at reactor full power. Peak fluences of 1.08×10^{22} n/cm^2 (>0.18 MeV) were achieved. Planning for the second irradiation experiment, OF-2, began in July 1974, and it was inserted into the ORR on June 21, 1975. This experiment is scheduled to be removed in July 1976 after achieving a peak design fluence of 9×10^{21} n/cm^2. Capsule OF-2 has operated for approximately 225 hr at reactor full power as of July 30, 1975.

6.7.1 OF-1 Capsule

The OF-1 Irradiation Experiment was the first in the series of HTGR fuel irradiations in the ORR. It was a joint experiment between GA and ORNL. General Atomic Company fuel rods, in magazine P13Q, occupied the upper two-thirds of the test space, and the ORNL fuel rods, in magazine OF-1, the lower one-third. Each fuel cell had independent temperature control. Detailed descriptions of the design, fabrication, and early operation have been previously reported.[34–36]

The major objective of the ORNL cell was to test candidate recycle fissile particles and fuel bonding matrices at accelerated flux levels under reference HTGR temperatures and temperature gradient conditions. A complete listing of the objectives of the OF-1 experiment is given below:

1. determine the irradiation performance of recycle fuel rods prepared by in-block and packed-bed carbonization;
2. compare the performance of coated particles prepared to the same specifications in small (laboratory-scale) and 0.13-m-diam (5-in.) prototype coaters;
3. compare the performance of 4.2:1 $(Th,U)O_2$ Biso-coated particles containing ^{235}U with similar particles containing ^{233}U;
4. evaluate the performance of fuel rods made with different filler materials;

5. measure the in-reactor thermal conductance of a slug-injected fuel rod.

The first four objectives described above have been achieved and are reported here. Objective 5 is presently being achieved in the OF-1 thermal analysis calculations.

6.7.1.1 Capsule Operation

OF-1 was installed in the E-3 position of the ORR on August 22, 1973, and irradiation was terminated on February 23, 1975, during which time the capsule operated with the reactor at full power for 9340 hr. This time period covers ORR operating cycles 114 through 123. The capsule was out of the reactor for one entire cycle (No. 119) to repair a leak that developed in the sweep-gas system of the ORNL cell.

The two-cell design of the capsule allowed independent sampling of the GA cell and the ORNL cell sweep-gas systems. These samples were then analyzed to determine release-to-birth rate ratios (R/B) for selected fission gas isotopes. Original plans called for sampling each cell once per week; however, after about 4000 hr of irradiaion the nickel bulkhead that separated the two cells had failed, making it impossible to obtain accurate R/B data for each cell. The decision was made to cut off all sweep gas into the ORNL cell and operate the GA cell at design conditions. This mode of operation allowed continued accurate sampling of the GA cell but made it impossible to obtain R/B data in the ORNL cell. A history of R/B data for the first 3900 hr of operation of the ORNL cell is presented in Table 6.40. Although sampling continued on this cell for a short period of time after the bulkhead failure, we feel that only the data presented in Table 6.40 are accurate and representative of the behavior of the ORNL fuel rods.

The calculated average heavy metal burnup and fluence for each fuel rod is presented in Table 6.41. The relative location of each fuel rod and thermocouple can be found in Fig. 6.50. The burnup calculations and fluences are based on fluxes provided by E. J. Allen and H. T. Kerr of the Reactor Division Nuclear Analysis Group (see Sect. 6.9) and the burnups were calculated with the CACA computer code.[37]

Table 6.40. Fission Product Release Rate Data for ORNL Cell in Capsule OF-1

Sample	Date	Operating Time (hr)	Flow Rate,[a] cm^3/min		Temperature,[b] °C			Fission Product Release-to-Birth Rate Ratio, R/B ($\times 10^{-6}$)				
			He	Ne	TE-21	TE-35	TE-36	^{85m}Kr	^{87}Kr	^{88}Kr	^{133}Xe	^{136}Xe
1-2b-1	8/30/73	19.1	25.0	0	863	925	1110	1.01	0.365	0.442	0.192	c
1-2b-3	8/31/73	44.5	11.0	9.1	1000	1045	1235	c	1.12	1.35	0.845	0.056
1-2b-7	9/4/73	144	11.0	8.7	969	1000	1180	1.97	0.775	0.900	1.45	0.318
1-2b-11	9/11/73	291	7.5	8.2	989	1020	1195	1.98	0.949	1.31	1.15	0.729
1-2b-14	9/14/73	364	5.0	8.2	986	1019	1187	1.44	0.862	0.907	1.60	0.140
1-2b-16	9/18/73	458	5.0	11.8	1006	1033	1207	1.82	1.18	1.25	3.20	0.183
1-2b-18	9/26/73	647	6.8	8.0	1003	1031	1200	1.94	1.64	1.43	1.76	0.273
1-2b-20	10/5/73	862	5.0	8.0	988	1006	1178	1.78	1.21	0.895	2.30	0.128
1-2b-24	10/18/73	1081	7.5	10.6	1042	1067	1246	2.11	1.36	0.395	2.97	0.248
1-2b-26	10/26/73	1264	6.0	8.3	1030	1050	1238	2.33	1.87	2.16	3.53	0.207
1-2b-29	11/1/73	1409	5.0	11.8	1018	1043	1237	1.55	1.03	1.09	2.11	0.164
1-2b-31	11/15/73	1662	5.0	14.6	1037	1054	1239	2.07	1.10	1.36	1.98	0.164
1-2b-34	11/21/73	1794	6.0	14.5	1034	1048	1224	1.75	1.09	c	1.53	0.164
1-2b-36	11/30/73	1997	1.5	7.7	1043	1049	1230	1.58	1.16	1.41	3.37	0.177
1-2b-39	12/13/73	2199	5.0	9.7	1047	1044	1219	2.04	1.43	1.44	3.27	0.114
1-2b-42	12/20/73	2367	2.0	8.7	1040	1029	1210	2.05	1.27	1.39	3.05	c
1-2b-44	12/27/73	2529	4.0	8.7	1038	1027	1194	1.74	1.14	1.21	2.30	0.164
1-2b-47	1/10/74	2858	4.2	7.8	1024	1000	1168	1.31	1.06	1.22	2.95	0.227
1-2b-50	1/17/74	3026	1.5	10.5	1042	1013	1188	2.17	1.23	1.30	8.69	0.224
1-2b-52	1/25/74	3210	1.5	13.1	1047	1010	1188	1.85	0.840	1.25	5.97	0.346
1-2b-55	2/11/74	3497	2.0	11.2	1021	985	1164	2.29	1.44	1.58	8.26	0.355
1-2b-58	2/21/74	3720	1.5	8.5	1043	998	out	4.40	1.88	2.07	22.8	1.53
1-2b-60	3/1/74	3904	0	6.7	985	946	1113	2.50	1.17	1.28	9.68	1.28

[a]During the time period covering samples 1-2b-1 to 1-2b-20 there was a leak in the helium emergency cooling selenoid valve, which was estimated to be 5 cm^3/min. Therefore the helium flow rates reported for these samples are estimated and not actually measured.

[b]The temperatures presented here are those indicated by the thermocouples shown. TE-35 and -36 were tungsten-rhenium thermocouples, and they decalibrated severely during the test. An attempt to determine the amount of decalibration is currently under way.

[c]The data for these samples were lost through malfunction of analysis equipment.

Table 6.41. Calculated Burnup and Fluence for the ORNL Fuel Rods Irradiated in Capsule OF-1

Fuel Rod[a] Location	Rod	Calculated Average Burnup, % FIMA			Calculated Average Fluence, n/cm^2	
		^{235}U	^{238}U	^{232}Th	Thermal, <1.86 eV	Fast, >0.18 MeV
1-1	M105A077	80.2	14.4	4.93	8.57×10^{21}	10.8×10^{21}
1-2	M105A075	78.7	12.5	4.16	7.57	9.58
1-3	M105A072	76.1	10.2	3.27	6.49	8.00
1-4	M105A068	73.5	8.56	2.67	5.48	5.72
2-1	M105A094	79.0	12.8	4.28	7.73	9.85
2-2	M105A093	77.5	11.2	3.67	6.83	8.61
2-3	M105A092	74.9	9.38	2.97	5.99	6.99
2-4	M105A091	72.3	8.00	2.47	5.21	4.88
3-1	M105A114	79.0	12.8	4.28	7.73	9.85
3-2	M105A113	77.5	11.2	3.67	6.83	8.61
3-3	M105A121	75.6	9.81	3.13	6.12	7.40
3-4	M105A117	73.7	8.67	2.71	5.58	5.92
3-5	M105A122	71.6	7.66	2.35	5.04	4.37
4-1	M115A079	80.2	14.4	4.93	8.57	10.8
4-2	M115A078	78.7	12.5	4.16	7.57	9.58
4-3	M115A077	76.1	10.2	3.27	6.49	8.00
4-4	M115A076	73.5	8.56	2.67	5.48	5.72
5-1	M105A135	88.7[b]	13.5	4.55	3.10	10.4
5-2	M105A125	78.1	11.8	3.89	7.20	9.18
5-3	M105A137	83.5[b]	9.70	3.09	6.22	7.48
5-4	M105A127	73.0	8.31	2.58	5.31	5.25

[a]Fuel rod location is defined as follows: the first number designates the hole and the second designates the elevation as shown in Fig. 6.50.

[b]These two fuel rods were fueled with ^{233}U instead of ^{235}U, and the burnup numbers presented are for ^{233}U.

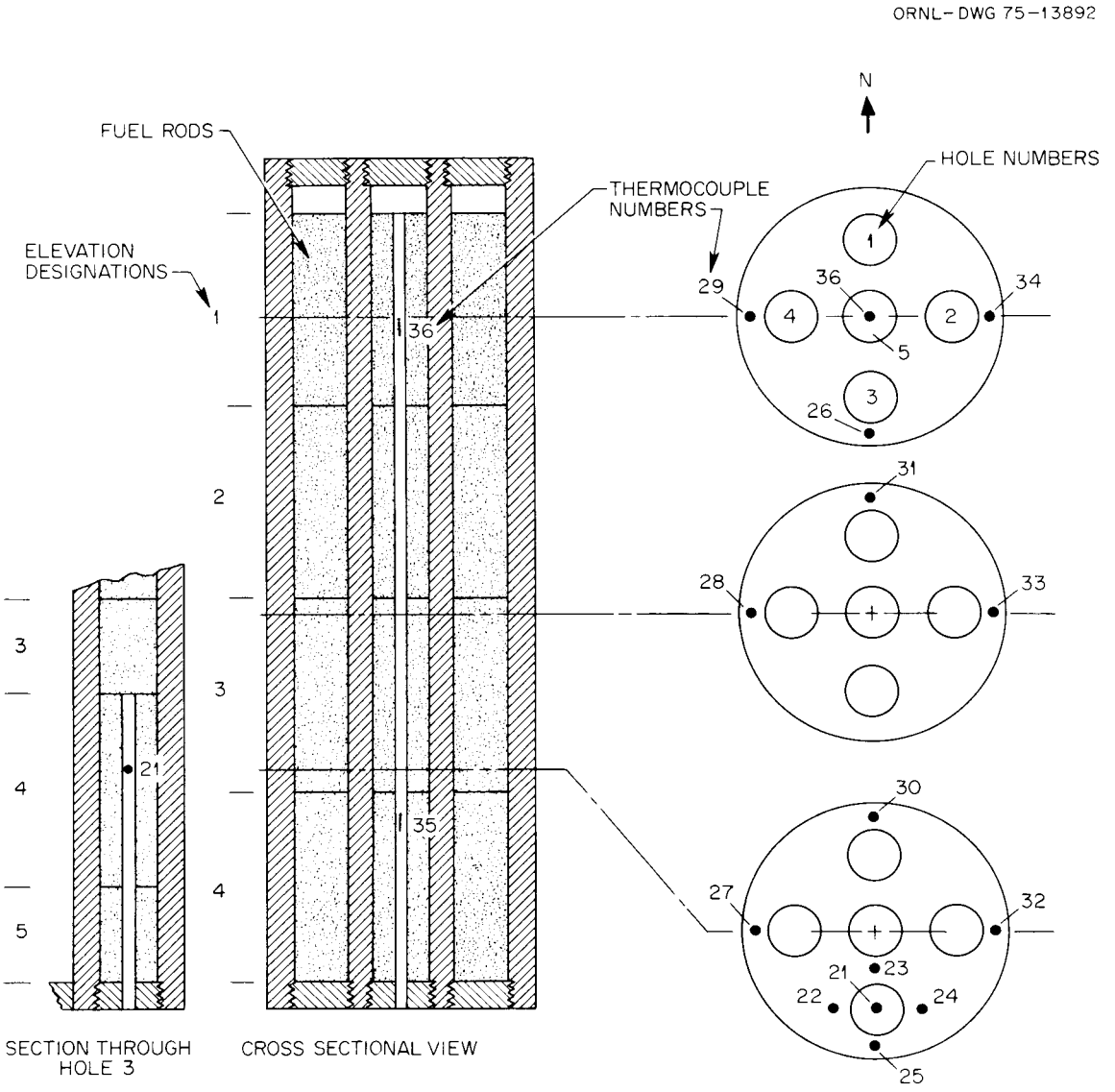

Fig. 6.50. Specimen and Thermocouple Diagram for Experiment OF-1.

The reliability of thermocouples in this capsule was not good. The ORNL cell contained a total of 16 thermocouples of which there were 14 Chromel vs Alumel (C/A) and two tungsten-rhenium. The C/A were all sheathed with stainless steel and insulated with alumina. Four of the C/A thermocouples were 1.6 mm (1/16 in.) OD and 10 were 1.0 mm (0.040 in.) OD. All the 1.6-mm C/A thermocouples operated throughout the test, but seven of the smaller thermocouples had failed by the end of irradiation. The two tungsten-rhenium thermocouples (Nos. 35 and 36), which measured the fuel center-line temperatures in hole 5, were severely decalibrated. The degree of decalibration cannot be determined until the thermal analysis is completed, but it appears that the error is from 200 to 300°C. A complete history of thermocouple operation appears in Table 6.42.

6.7.1.2 Postirradiation Examination

After the irradiation was terminated the two portions of the capsule were separated, and the GA section was shipped to San Diego for detailed examination.

The general appearance of the ORNL OF-1 magazine, made of H-451 graphite, was excellent. The fuel rods carbonized in packed Al_2O_3 were removed easily, while those carbonized in-block required cutting the graphite magazine open for removal. Table 6.43 describes the results of the visual examination of the ORNL fuel rods.

The results of the dimensional analysis of the fuel rods are given in Table 6.44. Because of the inability to inspect the rods after in-block carbonization, only those carbonized in packed Al_2O_3 could be analyzed for dimensional changes. As expected from previous irradiation tests,[33] the slug-injected rods at the higher fast (>0.18 MeV) flux and temperature positions experienced the greatest shrinkages.

All fuel rods contained Biso-coated $(4.2Th,U)O_2$ fissile particles, Biso-coated ThO_2 fertile particles, and coated inert particles. The fissile particles were from three different batches: (1) coated in a 0.13-m-diam (5-in.) prototype coater; (2) coated in a 25-mm-diam (1-in.)

Table 6.42. Operating History of Thermocouples in the ORNL cell of Capsule OF-1

Thermocouple	Type[a]	Sheath Diameter		Operating Temperature Range (°C)	Operating[b] Time (hr)	Fluence at End of Test or Time of Failure, n/cm^2	
		(mm)	(in.)			Thermal <1.86 eV	Fast >0.183 MeV
21	K	1.6	1/16	700–1050		5.72×10^{21}	6.25×10^{21}
22	K	1.6	1/16	650–850		5.72	6.25
23	K	1.6	1/16	700–950		5.72	6.25
24	K	1.6	1/16	650–850		5.72	6.25
25	K	1.02	0.040	600–800	8950	5.48	5.99
26	K	1.02	0.040	750–950	9000	7.52	9.56
27	K	1.02	0.040	600–800		6.05	7.23
28	K	1.02	0.040	750–850	3270	2.47	3.10
29	K	1.02	0.040	800–975	4990	4.60	5.78
30	K	1.02	0.040	550–750		6.05	7.23
31	K	1.02	0.040	600–700	5850	4.42	5.54
32	K	1.02	0.040	550–800	8440	5.17	5.65
33	K	1.02	0.040	725–825	4040	2.73	3.40
34	K	1.02	0.040	775–975		7.80	9.92
35	W-Re		Bare Wire	1100–1250[c]		5.58	6.05
36	W-Re		Bare Wire	950–1100[c]		8.14	10.4

[a]Type K thermocouples are Chromel-P vs Alumel and W-Re are W–3% Re vs W–26% Re.

[b]Operating time is given only for those thermocouples that gave indications of failure. All other thermocouples were still operating at the end of the 9340-hr test.

[c]These are the estimated ranges based on early operation. At the end of the test both thermocouples were indicating that they were operating in the 600 to 800°C range.

Table 6.43. Summary of Results of Visual Examination from OF-1

Rod Number[a]	Rod Type	Carbonization Technique	Fissile Particle Coater	Filler Type[b]		Thermo-couple	General Condition of Rod	Stereoscopic Examination
				GLC-1089[c]	6353[d]			
1-1	1	Packed bed	5 in.		x		Rod in 2 pieces, but no extensive debonding.	No broken particles observed.
1-2	1	Packed bed	5 in.		x		Rod in 2 pieces, but no extensive debonding.	No broken particles observed.
1-3	1	Packed bed	5 in.		x		Rod in 2 pieces, but no extensive debonding.	No broken particles observed.
1-4	1	Packed bed	5 in.		x		Rod in 2 pieces, but no extensive debonding.	A number of broken inert particles observed on surface, but no broken fissile particles.
2-1	2	In-block	5 in.		x		Rod intact with slight debonding at top.	No broken particles observed.
2-2	2	In-block	5 in.		x		Rod in 2 pieces, but no extensive debonding. One-half of rod is bonded to 2-3.	No broken particles observed.
2-3	2	In-block	5 in.		x		Rod in 2 pieces, but no extensive debonding. One half of rod is bonded to 2-3.	No broken particles observed.
2-4	2	In-block	5 in.		x		Rod intact with no debonding. Bonded to half of 2-3.	No broken particles observed.
3-1	4	Packed bed	Laboratory		x		Rod in 2 pieces, but no extensive debonding.	No broken particles observed.
3-2	4	Packed bed	Laboratory		x		Rod esssentially intact, with some debonding at top.	No broken particles observed.
3-3	6	Packed bed	5 in.		x	x	Rod intact, with slight debonding at top.	No broken particles observed.
3-4	5	Packed bed	5 in.		x	x	Rod intact with slight debonding at top.	No broken particles observed.
3-5	6	Packed bed	5 in.		x	x	Rod intact with slight debonding at top.	No broken particles observed.
4-1	3	In-block	5 in.	x			Rod essentially intact, with some debonding at both ends.	No broken particles observed.
4-2	3	In-block	5 in.	x			Completely debonded.	A few broken particles (3) were observed; but was unable to identify what type
4-3	3	In-block	5 in.	x			Rod intact with some debonding at the top. Bonded to 4-4.	No broken particles observed.
4-4	3	In-block	5 in.	x			Rod intact and bonded to 4-3.	No broken particles observed.
5-1	8	Packed bed[e]	Laboratory		x	x	Completely debonded.	A large number of broken particles (>20) observed with cracked and missing coatings. Unable to identify the type of particles.
5-2	7	Packed bed	Laboratory		x	x	Rod intact with some debonding on bottom.	No broken particles observed.
5-3	8	Packed bed[e]	Laboratory		x	x	Rod essentially intact with debonding at top.	A large number of broken particles (10) observed with cracked and missing coatings. Unable to identify the type of particles.
5-4	7	Packed bed	Laboratory		x	x	Rod intact with slight debonding at top.	No broken particles observed.

[a]The first number is the hole number and the second is the relative rod position from top to bottom.

[b]A-240 pitch binder.

[c]About 34 wt % filler.

[d]About 29 wt % filler.

[e]^{233}U fuel.

Table 6.44. Summary of Dimensional Changes for Fuel Rods in Capsule OF-1

Rod	Dimensional Change					
	Diameter			Length		
	(mm)	(in.)	(%)	(mm)	(in.)	(%)
1–1	0.343	0.0135	−2.74			
1–2	0.348	0.0137	−2.78			
1–3	0.297	0.0117	−2.38			
1–4	0.246	0.0097	−1.97			
3–1	0.373	0.0147	−2.98			
3–2	0.338	0.0133	−2.70			
3–3	0.325	0.0128	−2.61	0.650	0.0256	−2.78
3–4	0.272	0.0107	−2.17			
3–5	0.234	0.0092	−1.87	0.465	0.0183	−1.99
5–2	0.391	0.0154	−3.14	1.430	0.0563	−3.07
5–3	0.203	0.0080	−1.62			
5–4	0.262	0.0103	−2.09	1.323	0.0521	−2.89

laboratory coater; and (3) coated in a laboratory coater but containing ^{233}U as the fissile material. The same batch of ThO_2 fertile particles was used in all fuel rods.

Summaries of the metallographic examination after irradiation and a comparison with the preirradiation examination[35] for the various fuel types follow:

Fuel Type 1: No failed particles observed on postirradiation examination (PIE). Amoeba (<5 μm) observed in some of the $(4.2Th,U)O_2$ particles (batch J-263) in the peripheral region of the fuel rod. The matrix densified and pulled away from the coated and shim particles with no matrix-particle interaction.

Fuel Type 2: No failed particles on PIE. Amoeba (<5 μm) observed in some of the $(4.2Th,U)O_2$ particles (batch J-263). The matrix densified

and pulled away from the coated and shim particles. Two relatively minor cases of matrix-particle interaction were found.

Fuel Type 3: No failed particles on PIE. Amoeba (≤20 μm) observed in some of the $(4.2Th,U)O_2$ particles (batch J-263). Densification of the matrix was evident but caused no matrix-particle interaction where the two had separated.

Fuel Type 4: No failed particles on PIE. Amoeba (<20 μm) observed in the $(4.2Th,U)O_2$ particles (batch OR-1977). The matrix densified and pulled away from the coated and shim particles with no matrix-particle interaction.

Fuel Type 5: No failed particle or amoeba observed in the $(4.2Th,U)O_2$ particles (batch J-263) on PIE. Densification of the matrix was evident and caused no matrix-particle interaction where the two had separated.

Fuel Type 7: No failed particle or amoeba observed in the $(4.2Th,U)O_2$ particles (batch OR-1977) on PIE. Densification of the matrix was evident but caused no matrix-particle interaction where the two had separated.

Fuel Type 8: A number of failed $(4.2Th,^{233}U)O_2$ particles (batch Pu-291) were observed, and amoeba (≤15 μm) was apparent. Failure fractions of 15 and 80% were recorded in two samples. These particles had very dense buffers, and property gradients were found in the outer pyrocarbon coatings. Also, several particles had been broken during fabrication.

All Fuel Types: No failures or amoeba effects were associated with the fertile ThO_2 particles (batch J-262). The appearance of the shim particles remained relatively unchanged.

The most common problem associated with the fissile particles was migration of the kernel up the temperature gradient. Figures 6.51 through 6.53 show typical polished sections of the three fissile particle types before and after irradiation. As shown, the performance of the fissile particles from the two coaters (batches J-263 vs OR-1977) was essentially identical. Both experienced small amoeba migration but no failures.

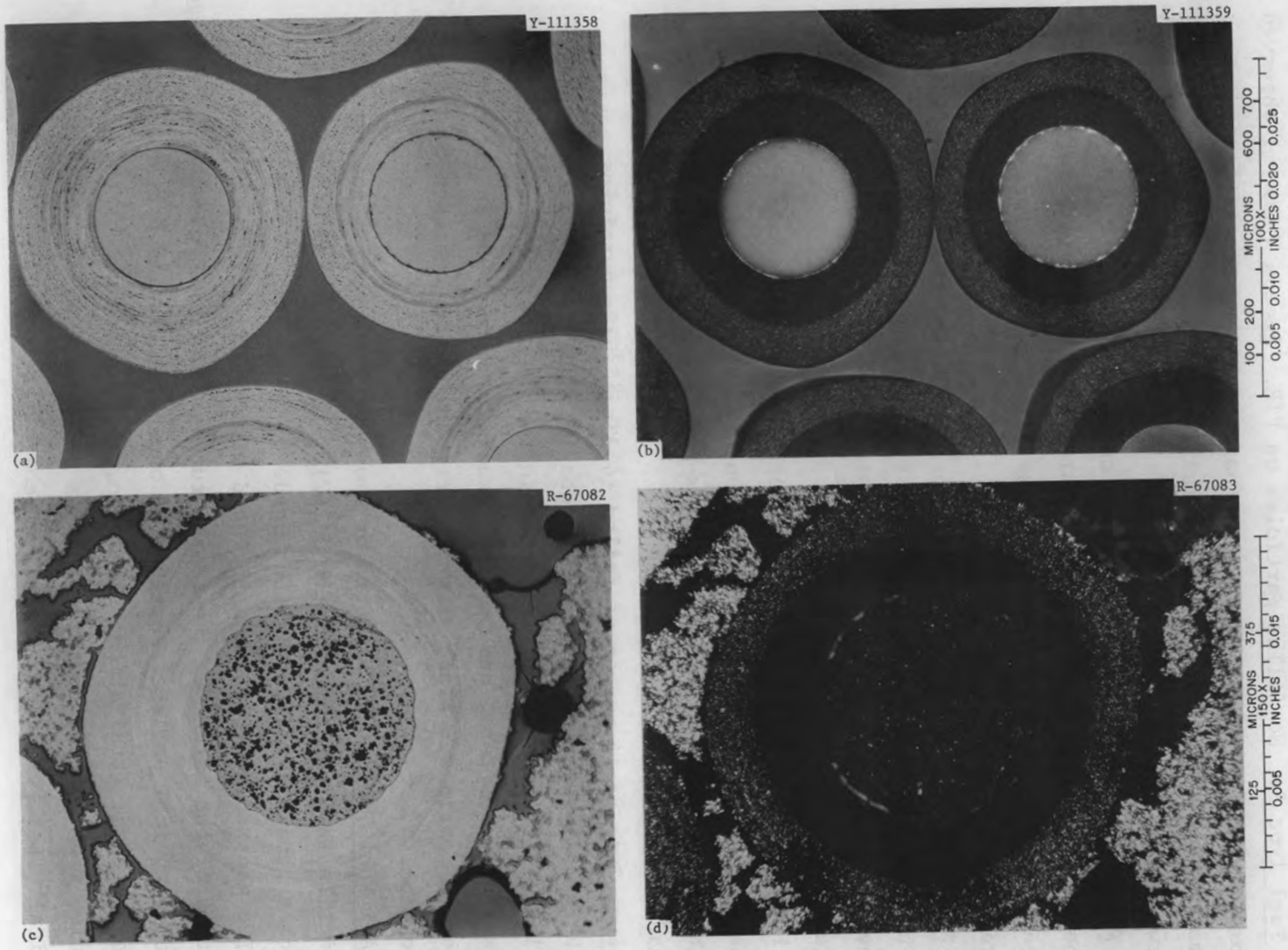

Fig. 6.51. Biso-Coated $(4.2Th,U)O_2$ Particles Coated in a 0.13-m-diam (5-in.) Coater (Batch J-263) and Irradiated in OF-1 Capsule. (a) and (b) Preirradiation polished section under bright field and polarized light, respectively. (c) and (d) Typical postirradiation polished section under bright field and polarized light, respectively. Note slight amoeba migration of kernel to the right (up the temperature gradient).

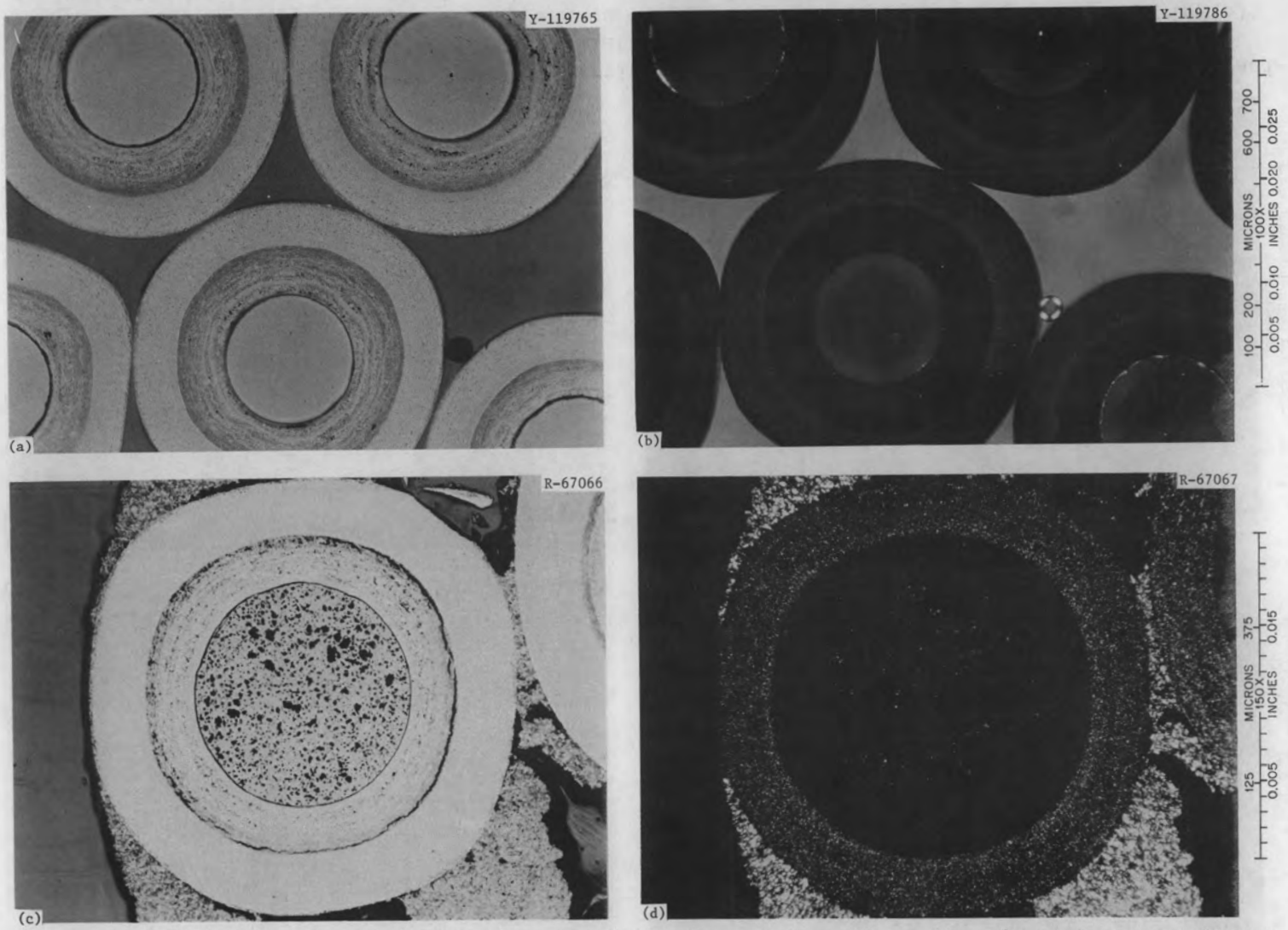

Fig. 6.52. Biso-Coated $(4.2Th,U)O_2$ Particles Coated in a 25-mm-diam (1-in.) Coater (Batch OR-1977) and Irradiated in OF-1 Capsule. (a) and (b) Preirradiation polished sections under bright field and polarized light, respectively. (c) and (d) Typical postirradiation polished sections under bright field and polarized light, respectively. Note slight amoeba migration of the kernel to the right (up the temperature gradient).

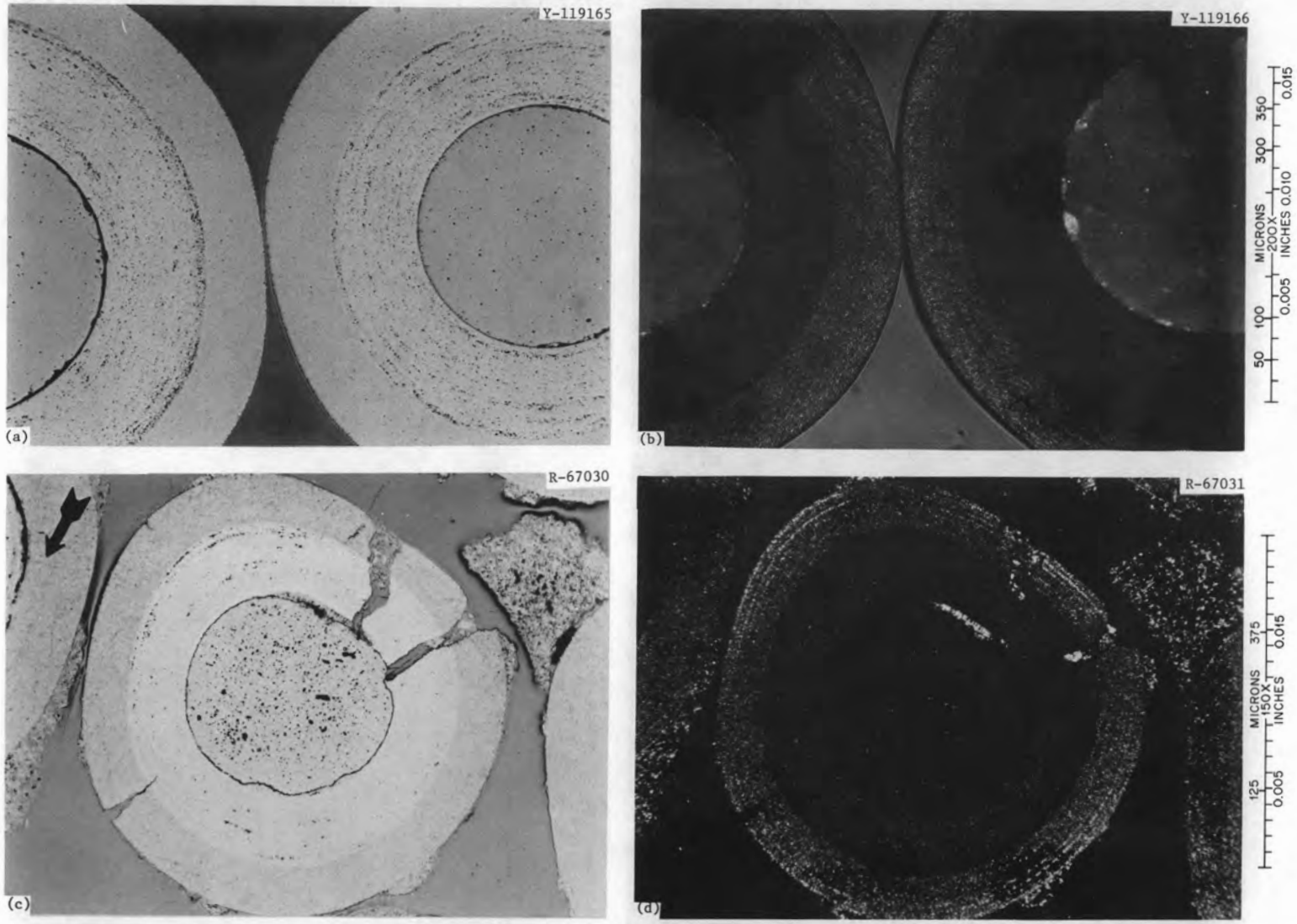

Fig. 6.53. Biso-Coated $(4.2Th,U)O_2$ Particles Contained in Batch Pu-291 (^{233}U) and Irradiated in OF-1 Capsule. (a) and (b) Preirradiation polished sections under bright field and polarized light, respectively. Note presence of property gradients in outer coatings in (b) as indicated by change in optical activity. (c) and (d) Typical postirradiation polished sections under bright field and polarized light, respectively. Note that property gradients are exaggerated as compared to preirradiation.

The fissile particles containing ^{233}U (batch Pu-291) experienced gross coating failures. They were first observed in the visual examination and confirmed with the metallographic examination. Under polarized light, property gradients in the coatings (shown by optical anisotropy or activity) are visible before and after irradiation. Cracking of the coatings resulted from differential shrinkage during irradiation. These same observations were made in the HRB-6 irradiation test,[31] where the same batch of particles was used. As with the HRB-6 fuel, the performance of the ^{233}U-containing kernels was comparable to that of the ^{235}U-containing kernels.

As expected, the ThO_2 fertile particles (batch J-262) exhibited excellent irradiation behavior. No failures or amoeba was observed with any of the polished sections examined.

Individual filler particles were barely discernible in the matrices of rods that had been carbonized in packed Al_2O_3, whereas before irradiation they were clearly visible. The matrices had definitely densified. The matrices of the rods carbonized in the fuel body had the same dense "blocky" appearance (where the filler particles are not discernible) as they did before irradiation. No real difference was observed between matrices containing different filler particle types.

Matrix-particle interaction, which was observed during preirradiation examination[36] of fuel type 3, was found only in fuel type 2 upon post-irradiation examination. Both these fuel types had been carbonized by the in-block process, where the matrices have very different microstructures. No matrix-particle interaction was found in any of the rods carbonized in packed Al_2O_3 in either the pre- or postirradiation examination.

Good irradiation performance was observed for fuel rods carbonized by the in-block and packed-Al_2O_3 processes. Rods carbonized in-block were more susceptible to matrix-particle interaction, tended to bond to the graphite magazine, and had matrices with very dense microstructures. The different carbonization techniques had no effect on the performance of the fuel particles.

6.7.1.3 Thermal Analysis

The OF-1 capsule was designed so that real-time temperature data could be obtained during irradiation in the ORR. Sixteen thermocouples were placed inside the capsule to monitor fuel centerline temperatures and H-451 graphite magazine temperatures. Beginning-of-life (BOL) temperature calculations have been made at two axial positions along the magazine at two irradiation times, 260 hr corresponding to a pure helium sweep-gas and 290 hr corresponding to a mixed helium and neon sweep-gas.

Two two-dimensional (R-θ) models were used in conjunction with the HEATING3 Heat Conduction Code.[38] Figure 6.54 describes these grid models applicable to one-eighth of a circular cross section of the OF-1 magazine. The origin of model 1-A is located at the center of the central fuel rod. This model accurately describes the temperature distribution within the central fuel, central gas gap, outer portion and surface of the graphite block, and double-walled stainless steel containment vessel. Model 2-A has its origin located at the center of the peripheral fuel rod and accurately describes the temperature distribution within the peripheral fuel rod, peripheral gas gap, and central graphite region. Model 2-A uses the outer surface temperature of the graphite magazine as calculated in model 1-A as an input boundary condition.

Figure 6.55 describes the calculated temperatures as functions of radial distance at axial distances of 127 and 235 mm (5.00 and 9.25 in.) from the bottom of the capsule for a pure helium sweep-gas and for a He—32% Ne mixed sweep-gas. Data are shown along a radius vector from the midpoint of the central fuel through the center of the peripheral fuel to the outer surface of the graphite magazine. Also compared are calculated temperatures, both models 1-A and 2-A, and the real-time temperatures observed. In each case excellent agreement is shown at the 127-mm level and less than 7% difference at the 235-mm level. The temperature observed with the tungsten-rhenium thermocouple (No. 36) was disregarded because of decalibration. For the mixed-sweep-gas case the temperature gradient at the peripheral fuel rod surface was calculated to be 600°C at the 235-mm level and 440°C at the 127-mm level. Both are within the normal range expected for HTGR fuel.

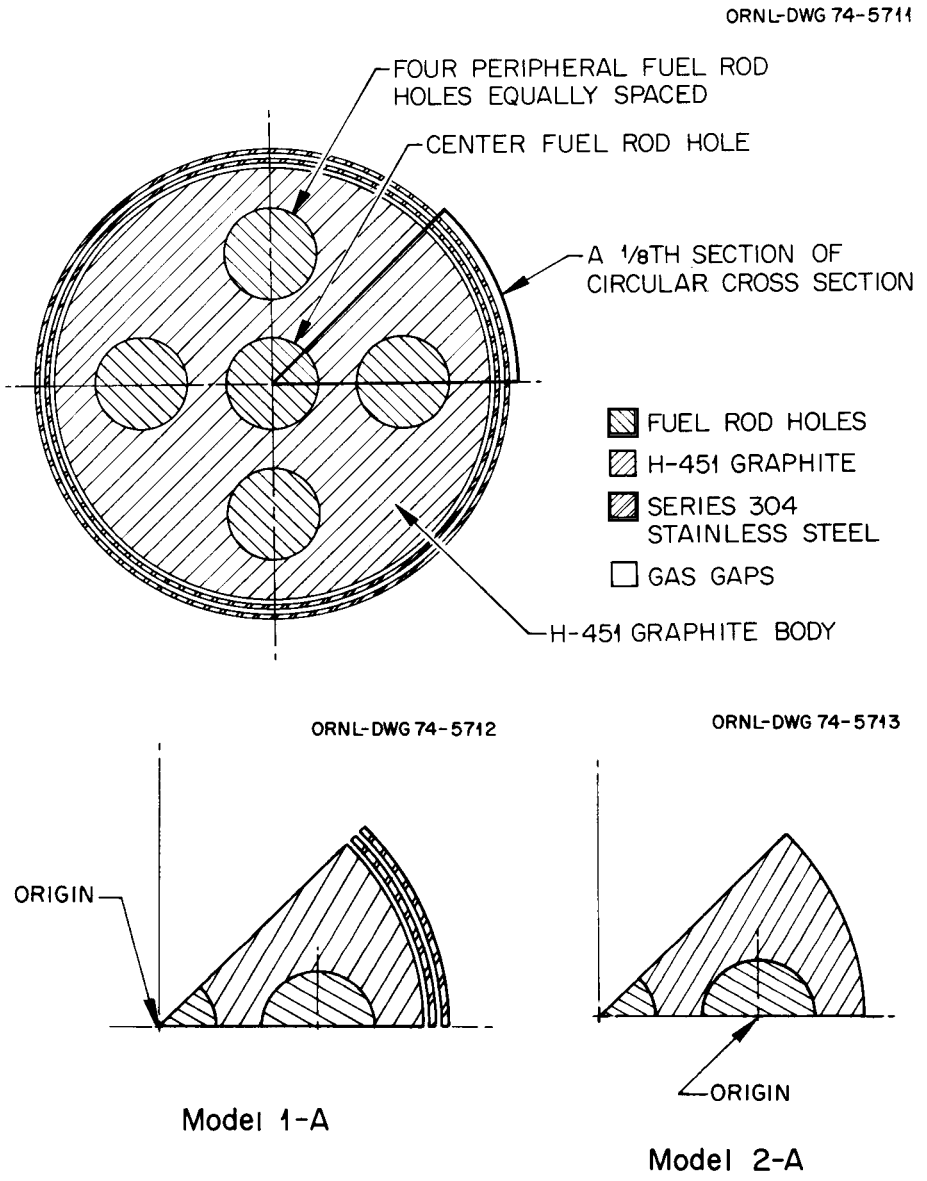

Fig. 6.54. Cross Section of OF-1 Capsule. On the bottom are one-eighth-section R-θ grid models used in thermal analysis.

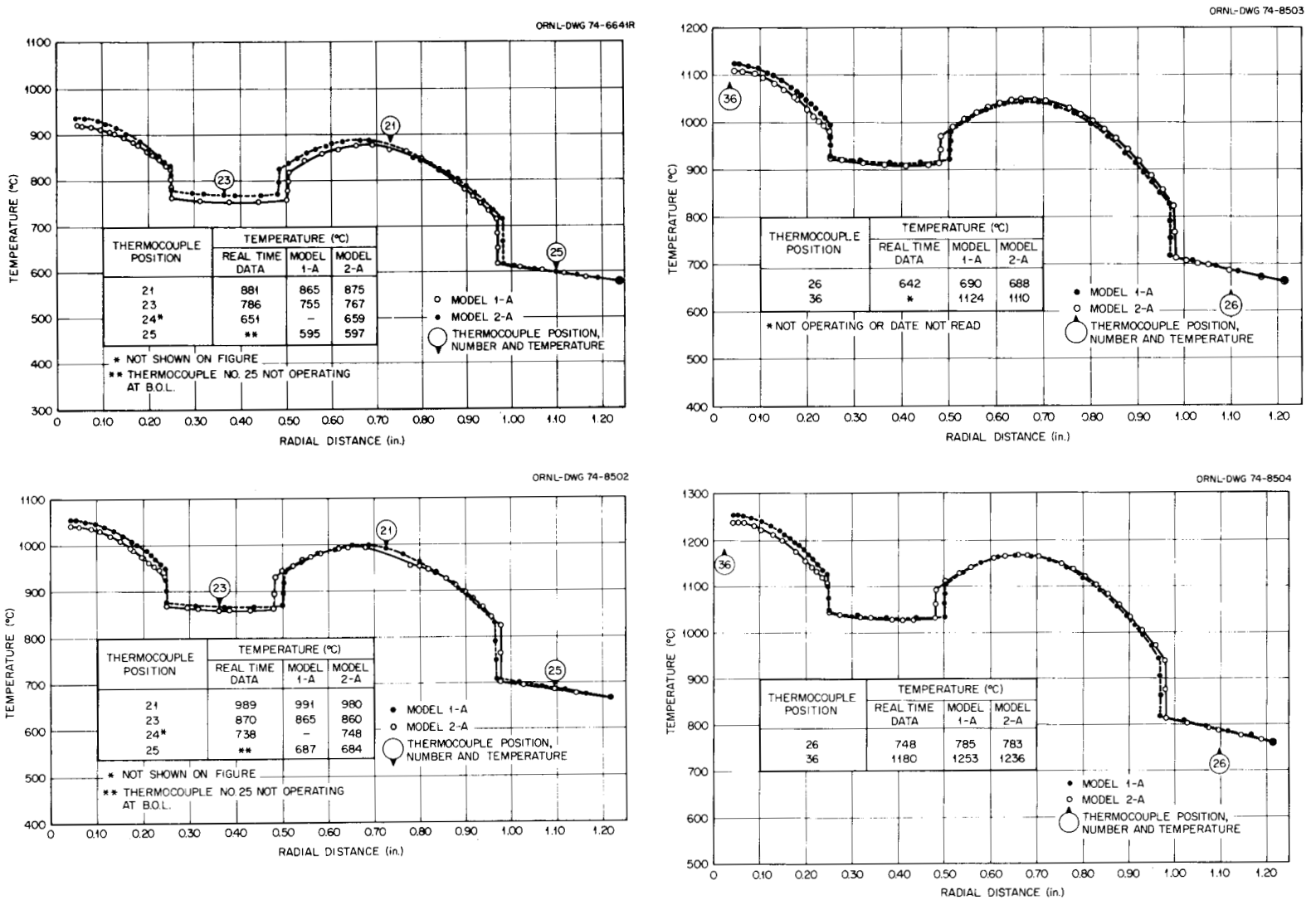

Fig. 6.55. Radial Temperature Profiles in Capsule OF-1. Sweep gas 100% He for top drawings and He–32% Ne for bottom. Left: 127 mm (5.00 in.) from bottom of capsule; right: 235 mm (9.25 in.). To convert radial distance scale to millimeters, multiply by 25.4.

Both models predict that the maximum peripheral fuel temperature occurs away from the center of the peripheral fuel rod. For the mixed sweep gas, the maximum temperature calculated with Model 2-A is 1165°C, compared with 1152°C at the center of the rod. For the 100% He sweep gas, the maximum is 1045°C, compared with 1033°C at the center of the rod.

The results reported here are for beginning-of-life conditions for the OF-1 capsule. The detailed thermal analysis for the remaining irradiation period is presently being conducted. This analysis includes thermal conductance calculations as a function of temperature and fast neutron fluence for slug-injected fuel rods.

6.7.2 Capsule OF-2

The OF-2 Irradiation Experiment is the second in a series of HTGR fuel irradiations in the Oak Ridge Research Reactor (ORR). Prototype fuels and fuel-rod matrix designs irradiated in the OF series are typically selected from best performing experimental fuels and fuel-rod designs irradiated in the HT and HRB of HFIR Irradiation Experiments. However, because of the temporary shutdown of HFIR and the need for verification of performance for fuels to be used in the Fort St. Vrain Reactor, OF-2 departed from this selection concept. In addition to containing prototype fuels in the usual manner, OF-2 represents the first test of Triso-coated fissile fuel fabricated in the large-diameter (0.13-m) coater at ORNL.

A complete list of the objectives of this experiment are:

1. to test the performance of reference Triso-coated weak-acid-resin fissile particles and reference Biso-coated fertile particles, both coated in the 0.13-m-diam furnace;
2. to investigate the matrix-particle interaction phenomena, involving a study of the effects of particle strength, matrix type, and particle surface conditions on irradiation performance;
3. to investigate the irradiation behavior of various coating microstructures arising from a variation of the coating process parameters: gas concentration, deposition rate, deposition temperature, and batch size;

4. to investigate the influence of stoichiometry and kernel density on the irradiation performance of weak-acid-resin-derived fuels;
5. to verify the adequate performance of fissile and fertile fuel that will be irradiated later in early proof-test elements in the Fort St. Vrain Reactor;
6. to compare the performance of coatings deposited in the 0.13-m coater using a fritted and cone gas distribution systems. (The fritted system is the present reference for the HTGR Recycle Demonstration Facility.);
7. to test the ability to remove fuel rods from the graphite holder after full-life irradiation, particularly as this applies to in-block carbonization.

6.7.2.1 Description of the OF-2 Capsule and Fuel Specimen Holders

The OF-2 irradiation capsule is similar in design to the OF-1 capsule.[35] It is a double-walled water-cooled stainless steel vessel. The total active test space is a cylinder 0.635 m long by 60.5 mm diam (25.0 by 2.38 in.). This test space is divided into two compartments by a copper bulkhead brazed in the primary containment tube 85.73 mm (3.375 in.) below the reactor horizontal midplane. The upper compartment (designated cell 2) contains three-fifths of the test space and is oriented toward objectives 2, 3, and 4. The lower compartment (designated cell 1) contains the remaining two-fifths of the test space and is oriented toward objectives 1, 5, 6, and 7. Each compartment has its own sweep-gas system and can be independently swept with a helium and neon gas mixture to control temperatures and monitor fission gas release. The entire in-core section of the capsule is shown in Fig. 6.56.

The upper experimental compartment (cell 2) contains two H-451 graphite* specimen holders with a 9.53-mm-diam (0.375-in.) central spline hole and four 15.95-mm-diam (0.628-in.) peripheral fuel holes. The upper holder, specimen holder A, is 168.3 mm (6.625 in.) long by 61.34 mm (2.415 in.) diam and designed to operate at a maximum temperature of

---

*H-451 graphite manufactured by Great Lakes Carbon Company (GLCC), New York.

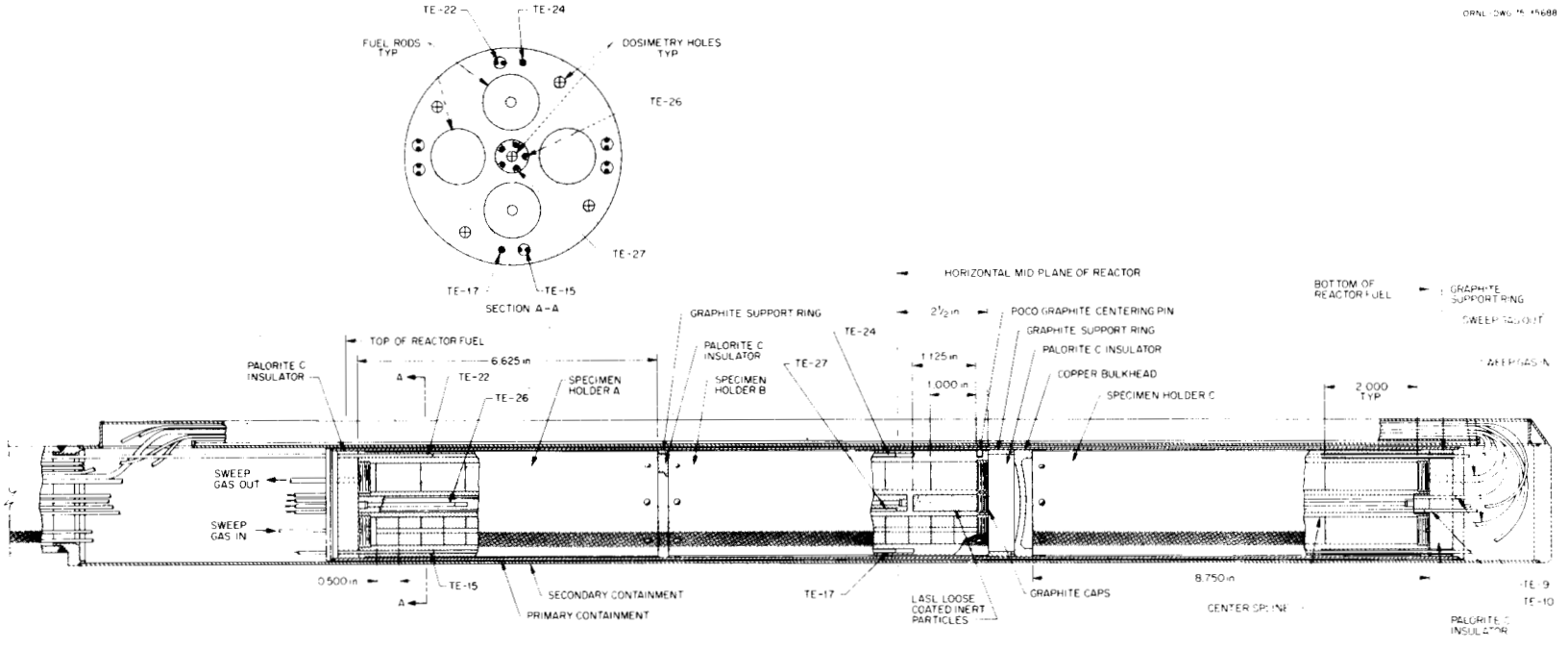

Fig. 6.56. In-Core Section of OF-2 Capsule. To convert dimensions to millimeters, multiply by 25.4.

1150°C. The lower holder, specimen holder B, is 168.3 mm (6.625 in.) long by 61.16 mm (2.408 in.) diam and is designed to operate at a maximum temperature of 1350°C. Each specimen holder contains 36 fuel rods; Fig. 6.57 and 6.58 are representative of specimen holders A and B, respectively. Holes 1 and 2 each contain six 25.4-mm-long by 15.75-mm-diam (1.00 by 0.620 in.) fuel specimens; holes 3 and 4 each contain twelve 12.7-mm-long by 15.75-mm-diam (0.50 by 0.620 in.) fuel specimens. In addition, specimen holder B contains approximately 2 cm^3 of LASL loose coated inert particles.

Specimen holder A contains 12 thermocouples — 11 Chromel-P vs Alumel (C/A) and one platinum-molybdenum (Pt/Mo). Specimen holder B contains seven thermocouples — 6 C/A and 1 Pt/Mo. These are used to monitor axial, peripheral, and centerline graphite temperatures. Flux monitors are also incorporated into each specimen holder and central graphite spline.

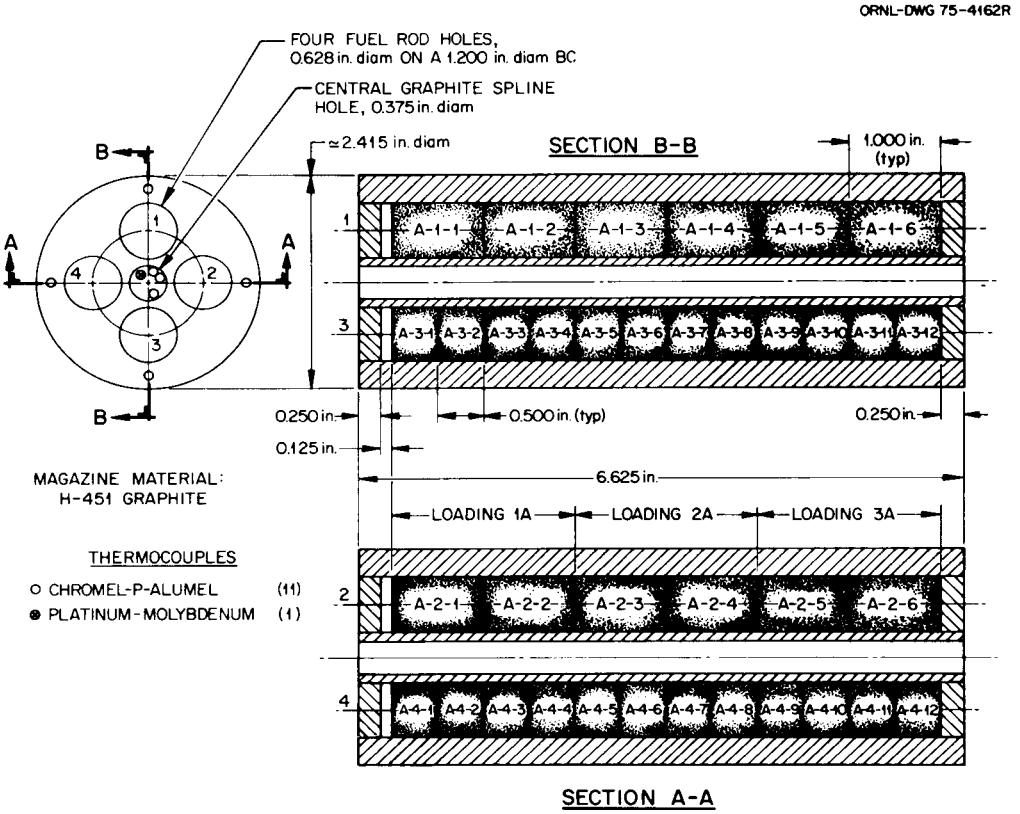

Fig. 6.57. Specimen Holder A of Irradiation Capsule OF-2. To convert dimensions to millimeters, multiply by 25.4.

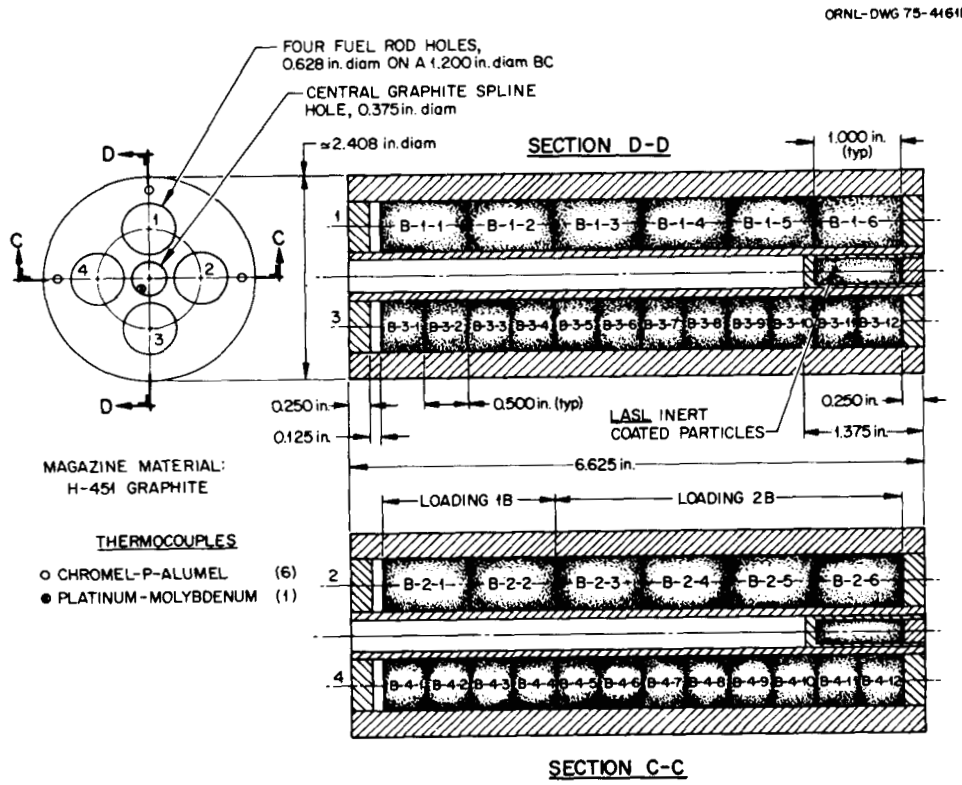

Fig. 6.58. Specimen Holder B of Irradiation Capsule OF-2. To convert dimensions to millimeters, multiply by 25.4.

The lower experiment compartment (cell 1) contains one H-451 graphite specimen holder with a 9.53-mm-diam (0.375 in.) central spline hole and four 15.95-mm-diam (0.628 in.) peripheral fuel holes. This holder, specimen holder C, is designed to operate at a maximum temperature of 1350°C and is 222.25 mm (8.750 in.) long by 61.054 mm (2.4037 in.) diam. Figure 6.59 describes specimen holder C. Each fuel hole contains four 50.8-mm-long by 15.75-mm-diam (2.00 by 0.620 in.) fuel rods. Nine C/A thermocouples are incorporated to monitor axial, peripheral, and centerline graphite temperatures. Flux monitors are placed in the central graphite spline only.

6.7.2.2 Design Thermal Analysis

The design thermal analysis for OF-2 was aimed at determining the outside diameter for each of the specimen holders A, B, and C; and predicting fuel loadings necessary to maintain the desired fuel centerline

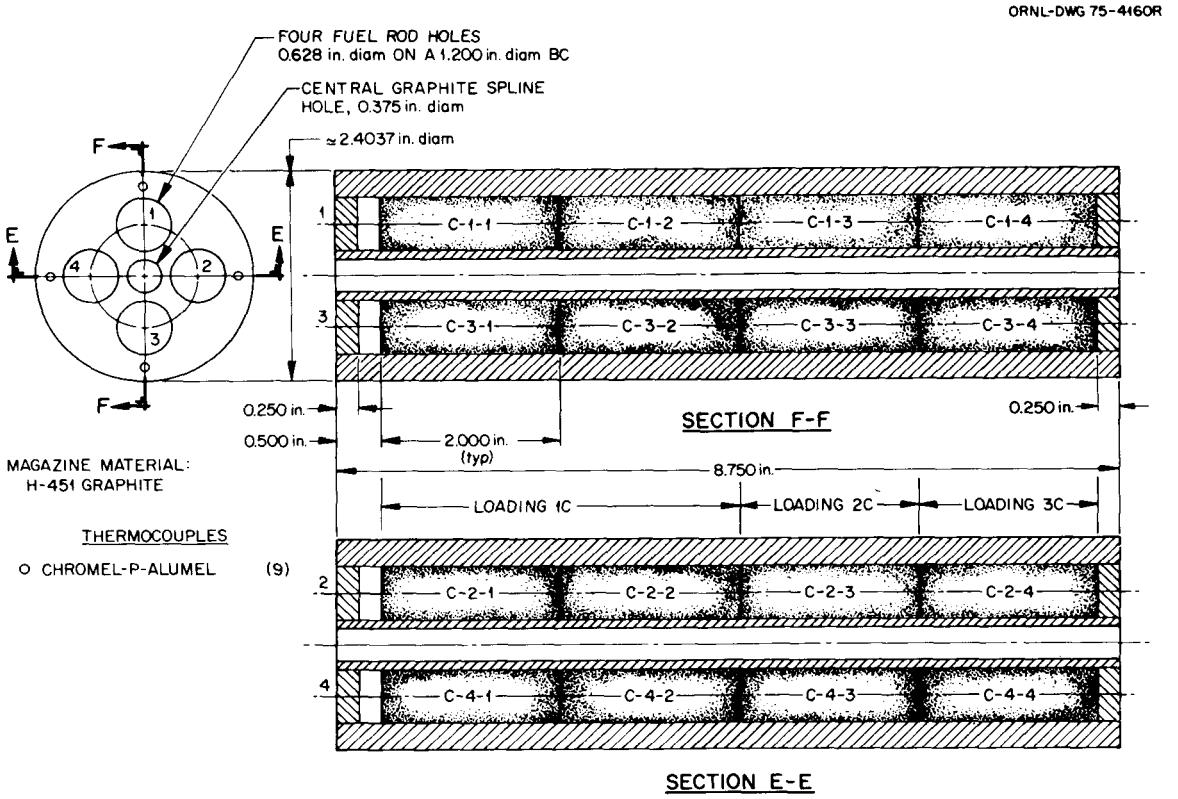

Fig. 6.59. Specimen Holder C of Irradiation Capsule OF-2. To convert dimensions to millimeters, multiply by 25.4.

temperatures throughout the life of the capsule. The design specified linear heat generation rates of all fuel rods should be approximately 20 kW/m (5 kW/ft), and the fuel loadings should be varied along the length of the capsule in an effort to flatten the temperature and power gradients that a single fuel loading would produce.

The initial phase was to perform a three-dimensional thermal analysis on each fuel specimen holder at beginning-of-life (BOL) conditions. The HEATING3 computer code[38] was used to perform this analysis. Axial dependent gamma heating and thermal neutron flux (fission heating) profiles as well as temperature-dependent material thermal conductivities were incorporated into the HEATING3 code. An iterative process was used to determine the outside diameter of the graphite specimen holders and peak linear heat generation rates for each of the eight fuel loadings also shown in Figs. 6.57 through 6.59.

At the axial location of peak fuel temperatures for each fuel loading, two-dimensional models of the capsule cross section were made. These were necessary in order to analyze end-of-life (EOL) conditions since irradiation-induced dimensional changes vary along each specimen holder. The EOL capsule geometries were based on an operating life of 9600 hr, at which the peak damage fluence would be 9.0×10^{21} n/cm^2 (>0.18 MeV). Using an axially dependent damage flux profile the appropriate fluences were determined for each of the two-dimensional models. Based upon these fluences, material thermal conductivities[39,40] and dimensional changes[41–43] were calculated for the fuel rods and graphite holders at EOL. An iterative process was again used to determine heat generation rates necessary to maintain maximum fuel centerline temperatures. A summary of BOL and EOL heat generation rates, heat transfer gaps, and maximum temperatures for each fuel loading is presented in Table 6.45.

Based upon total reaction rates provided for the E-7 position of the ORR core ^{235}U and ^{232}Th loadings were calculated. The ^{235}U loadings were calculated from the required BOL heat generation rates determined in the three-dimensional thermal analysis. The ^{232}Th loadings were calculated with the FABGEN[44] computer code. An iterative process was used to predict the required ^{232}Th loading based upon EOL heat generation rates necessary to maintain design fuel centerline temperatures. The resulting fuel loadings are presented in Table 6.46.

Table 6.45. Summary of Beginning-of-Life and End-of-Life Fission Powers, Heat Transfer Gaps, and Maximum Temperatures for Capsule OF-2

Graphite Holder	Fuel Loading	Peak Heat Generation Rate		Radial Gaps, μm (mils)				Peak Temperature,[a] °C		
				Fuel to Holder		Holder to Primary Tube		Fuel Center	Holder TC	Holder Peripheral TC
		(kW/m)	(kW/ft)	Room Temp.	Design Temp.	Room Temp.	Design Temp.			
				Beginning-of-Life Conditions						
A	1A	19.7	6.0	102(4.0)	91(3.6)	302(11.9)	292(11.5)	1170	935	745
	2A	16.4	5.0	102(4.0)	91(3.6)	302(11.9)	292(11.5)	1160	970	770
	3A	16.4	5.0	102(4.0)	91(3.6)	302(11.9)	292(11.5)	1135	965	770
B	1B	16.4	5.0	102(4.0)	91(3.6)	394(15.5)	348(13.7)	1320	1140	905
	2B	16.4	5.0	102(4.0)	91(3.6)	394(15.5)	348(13.7)	1350	1180	950
C	1C	16.4	5.0	89(3.5)	71(2.8)	467(18.4)	414(16.3)	1330	1250	990
	2C	18.0	5.5	89(3.5)	71(2.8)	467(18.4)	414(16.3)	1345	1250	990
	3C	19.7	6.0	89(3.5)	71(2.8)	467(18.4)	414(16.3)	1270	1150	925
				End-of-Life Conditions						
A	1A	12.1	3.7		254(10.0)		318(12.5)	1120	940	675
	2A	9.8	3.0		338(13.3)		391(15.4)	1150	980	720
	3A	9.8	3.0		378(14.9)		427(16.8)	1145	980	730
B	1B	9.5	2.9		404(15.9)		643(25.3)	1350	1210	930
	2B	8.9	2.7		404(15.9)		643(25.3)	1350	1210	940
C	1C	10.2	3.1		206(8.1)		757(29.8)	1330	1255	1020
	2C	11.5	3.5		234(9.2)		724(28.5)	1340	1255	1000
	3C	13.1	4.0		277(10.9)		691(27.2)	1265	1195	915

[a]Peak temperature data for BOL were obtained from three-dimensional mockups, while EOL data were obtained from two-dimensional mockups.

Table 6.46. Design Fuel Loadings for Capsule OF-2

Specimen Holder	Loading	Loading, g/m (g/in.)	
		^{235}U	^{232}Th
A	1A	9.37 (0.238)	156.7 (3.98)
	2A	5.32 (0.135)	102.8 (2.61)
	3A	4.17 (0.106)	86.2 (2.19)
B	1B	3.21 (0.0815)	60.2 (1.53)
	2B	2.72 (0.0691)	49.6 (1.26)
C	1C	2.63 (0.0669)	54.7 (1.39)
	2C	3.13 (0.0795)	68.1 (1.73)
	3C	7.16 (0.182)	155.5 (3.95)

6.7.2.3 Description of OF-2 Fuel Specimens — Coated Particles

Capsule OF-2 required 88 fuel specimens. Of these 86 were fabricated at ORNL and two specimens at LASL. The Triso-coated fissile particle test set consisted of: 12 batches of weak-acid-resin-derived (WAR) particles of a wide range of stoichiometries, from uranium oxide to uranium carbide; one batch of WAR U(C,N) particles; one batch of sol-gel $(4Th,U)O_2$ particles; and one batch of General Atomic Company's VSM UC_2 particles. Each fissile particle batch is described completely in Table 6.47. All the particle batch types except type 15 were included in the fuel specimens in the upper experimental compartment, cell 2. Particle types 13, 14, and 15 were fabricated for the lower experimental compartment, cell 1, by use of the large-diameter coating furnace. Types 13 and 14 were coated with the reference fritted gas distribution system and type 15 with the cone distribution system. Particle types 1 through 11 were annealed at 1800°C for 10 min in a fluidized bed after the outer LTI coating had been deposited. Particle types 13 through 15 were similarly annealed after the inner LTI coating was deposited.

Sixteen batches of Biso-coated fertile particles were selected for OF-2. Nine of the fertile batch types were coated in the large-diameter coating furnace. Batch types G through J and M through P used the fritted gas distributor and batch type K the cone distribution system.

Table 6.47. Fissile Particle Test Set for OF-2

Type	Batch	Kernel Composition	Nominal Reduction (%)	Carbonization Rate (°C/min)	Kernel Density[a] (g/cm^3)	Coater		Anneal	Mean Dimensions,[b] μm				
						Diam (mm)	Type		Kernel	Buff	ILTI	SiC	OLTI
1	OR-2332-H	WAR $UC_{5.43}O_{1.95}$	0	2	3.23	64	Cone	Yes	373.1	39.2	32.3	32.9	32.2
2	OR-2329-H[c]	WAR $UC_{5.53}O_{1.97}$	0	2	3.22	64	Cone	Yes	371.9	23.0	40.6	31.8	30.8
3	OR-2218-H[d]	WAR $UC_{4.58}O_{2.04}$	0	40	3.66	64	Cone	Yes	371.3	69.3	42.0	30.7	44.6
4	OR-2322-H[e]	WAR $UC_{5.54}O_{1.69}$	15	2	3.12	64	Cone	Yes	379.7	49.8	35.7	32.3	39.4
5	OR-2320-H	WAR $UC_{5.12}O_{1.54}$	25	2	3.17	64	Cone	Yes	374.0	43.8	36.8	34.3	38.6
6	OR-2211-H[d]	WAR $UC_{4.63}O_{0.97}$	50	2	3.11	64	Cone	Yes	363.0	59.3	37.5	30.2	42.0
7	OR-2207-H[d,f]	WAR $UC_{4.14}O_{0.53}$	75	2	3.03	64	Cone	Yes	366.4	62.7	38.9	31.1	42.7
8	OR-2208-H[d]	WAR $UC_{3.68}O_{0.01}$	100	2	3.01	64	Cone	Yes	366.5	59.2	38.4	27.9	40.0
9	OR-2121-H[d,f,g]	WAR $UC_{2.61}O_{0.16}$	100	6	5.28	64	Cone	Yes	315.3	74.6	36.1	28.4	49.2
10	OR-2219-H[d]	WAR $UC_{3.68}N_{0.53}$		2	3.02			Yes	365.3	66.3	44.0	31.9	43.5
11	OR-2321-H[e]	Sol-gel $Th_{0.8}U_{0.2}O_2$			9.9			Yes	361.1	83.3	37.2	34.4	41.1
12	6151-00-035	VSM UC_2			10.99				196.0	99	33	32	38
13	A-601	WAR	75	2	3.03	127	Frit	No	354.2	58.8	35.4[h]	30.0	35.8
14	A-611	WAR	15	2	3.10	127	Frit	No	366.4	47.6	36.8	30.5	35.5
15	A-615	WAR	75	2	3.08	127	Cone	No	354.1	51.0	30.7[h]	29.5	32.4

[a]Mercury gradient column measurement, uncorrected.

[b]Kernel diameter; buffer, inner LTI, SiC, and outer LTI thicknesses.

[c]Thin buffer.

[d]Irradiated in HRB-9 and -10.

[e]Similar batch irradiated in HRB-7, -8, -9, -10, and MET VII.

[f]Irradiated in Dragon MET VII.

[g]Irradiated in HRB-7 and -8.

[h]Buffer thickness corrected for uranium entering it during subsequent coating.

Specific coating parameters, deposition rates, geometries, and densities are described in Table 6.48. Fertile particle types A through L were annealed at 1800°C for 10 min in a fluidized bed, and the remaining types were unannealed.

6.7.2.4 Fuel Rods

For each fuel rod specimen fabricated, one batch each of fissile and fertile particles was selected from their respective test sets and combined with a particular matrix type. The matrix test set for OF-2 is described in Table 6.49.

For the upper experimental compartment 72 fuel rod specimens were fabricated. Each specimen contained a mixture of Triso-coated fissile particles, Biso-coated fertile particles and Biso-coated carbon particles. All specimens were fabricated by the slug-injection technique. We fabricated 46 to nominal dimensions of 15.75 mm OD by 3.30 mm ID by 12.70 mm long (0.620 by 0.130 by 0.500 in.) using matrix type d with 28.5 wt % Asbury 6353 graphite in Ashland Oil Company A-240 petroleum pitch. Specimens were injected at 180°C and 4.1 MPa (600 psi) and carbonized in a bed of high-fired (3000°C) graphite flour at a heating rate of 1°C/min. The remaining 26 fuel specimens were fabricated to nominal dimensions of 15.75 mm diam by 25.4 mm long (0.620 by 1.00 in.) with matrix types a, b, and c. Matrix types a and b are the same as used in the 12.70-mm (0.500-in.) long specimens and matrix type c is GA's proprietary matrix. Specimens were injected at 180°C and 5.5 MPa (800 psi) except for those containing unannealed fertile batches M and N, which used 4.1 MPa (600 psi). Eight fuel rods of matrix type a were carbonized in a bed of Al_2O_3 at a heating rate of 6°C/min, producing a coke yield of 18.3%; eight rods using matrix type b were carbonized in-tube at a heating rate of 2°C/min, producing a coke yield of 37.1%; and eight fuel rods using matrix type c were carbonized in-tube at a heating rate of 11.5°C/min, producing a coke yield of 29.8%. All specimens were subjected to a final heat treatment at 1800°C in argon for 30 min. For each of the fuel rods in specimen holders A and B (Figs. 6.57 and 6.58)

Table 6.48. Fertile Particle Test Set for OF-2

Type	Batch	Coater		Coating Parameters			LTI Deposition		Dimensions,[a] μm			Density,[b] g/cm³		Anneal
		Type	Diam (mm)	Gas	Concentration (%)	Diluent (%)	Temperature (°C)	Rate (μm/min)	Kernel	Buffer	LTI	Uncorrected	Corrected	
A	OR-2266-HT[c]	Cone	64	MAPP[d]	100		1275	14.1	506	94.8	91.3	2.02		Yes
B	OR-2265-HT[c]	Cone	64	MAPP	100		1325	15.7	508	96.1	94.2	1.95		Yes
C	OR-2262-HT[c]	Cone	64	MAPP	50	50 Ar	1275	6.5	507	98.0	85.1	2.01		Yes
D	OR-2261-HT[c]	Cone	64	MAPP	50	50 Ar	1325	7.4	506	95.8	88.9	1.89		Yes
E	OR-2264-HT[c]	Cone	64	MAPP	25	75 Ar	1275	3.2	507	96.5	91.6	1.99		Yes
F	OR-2263-HT	Cone	64	MAPP	25	75 Ar	1325	3.6	506	92.8	90.5	1.84		Yes
G	J-488[c,e]	Frit	127	C_3H_6	50	50 He	1375	7.4	497.9	82.7	80.7	1.98	1.87	Yes
H	J-489[c]	Frit	127	C_3H_6	50	50 He	1375	5.8	499.0	81.4	77.7	1.90	1.79	Yes
I	J-490[c]	Frit	127	C_3H_6	100		1375	6.2	495.9	80.2	74.7	1.99	1.86	Yes
J	J-491[c]	Frit	127	C_3H_6	100		1375	9.3	497.1	79.5	77.5	2.00	1.86	Yes
K	J-262[f]	Cone	127	C_3H_6	100		1350	8.4	497	84.0	86.1	2.01		Yes
L	OR-1849-HT	Cone	25	C_3H_6	75	25 He	1400[g]	21.5	508	79.4	74.7	1.94		Yes
M	J-481[h]	Frit	127	C_3H_6	50	50 He	1375	7.4	497.9	82.7	80.7	1.94	1.84	No
N	J-483	Frit	127	C_3H_6	100		1375	6.2	495.9	80.2	74.7	1.96	1.83	No
O	J-482	Frit	127	C_3H_6	50	50 He	1375	5.8	499.0	81.4	77.7	1.88	1.78	No
P	J-487	Frit	127	C_3H_6	100		1375	9.3	497.1	79.5	77.5	1.95	1.81	No

[a]Mean dimensions for kernel diameter, buffer and LTI thickness.

[b]Mercury-gradient column measurement.

[c]Irradiated in HT-30.

[d]MAPP gas is marketed by AIRCO, Inc., and consists primarily of methylacetylene and propadiene with alkanes as stabilizers.

[e]Batch J-488 rupture load = 26.33 N (5.92 lb), strong particle in matrix interaction experiment.

[f]Irradiated in HRB-7 and -8, OF-1.

[g]Temperature measured at different point in furnace; actual bed temperature approximately 1325°C.

[h]Batch J-481 rupture load = 22.42 N (5.04 lb), weak particle in matrix interaction experiment.

Table 6.49. Matrix Test Set for OF-2

Type	Pitch	Additive	Filler	Expected Coke Yield (%)	Carbonization Technique
a	A-240	None	Asbury 6353	15–25	Al_2O_3
b	A-240	None	Asbury 6353	35–40	In tube
c	GA	Proprietary		20–25	In block
d	A-240	None	Asbury 6353	15–20	Graphite flour

Tables 6.50 and 6.51 describe the fissile and fertile particle types and matrix type used along with the total weights of ^{235}U and ^{232}Th contained in each rod.

For the lower experimental compartment 16 fuel rod specimens were fabricated. Each specimen contained a mixture of Triso-coated fissile particles, Biso-coated fertile particles, and Triso- and Biso-coated carbon particles, and H-451 shim particles. To keep fuel rod dimensional changes uniform in this compartment the ratio of Biso- to Triso-coated particles was kept constant for each loading. Each specimen contained 20 vol % shim particles. Specimens were fabricated to nominal dimensions of 15.75 mm diam by 50.8 mm long (0.620 by 2.00 in.) by the slug-injection technique with matrix type c. Specimens were injected at 180°C and 5.5 MPa (800 psi) except for rods containing unannealed fertile particle types M and N, which used 4.1 MPa (600 psi). Placement of fuel rod specimens in cell 1 (Fig. 6.59) was based upon a statistical experimental design to minimize interaction effects. Rods were carbonized by the reference in-block technique with a heating rate of 11.5°C/min, producing a coke yield of 25.7%. All fuel rods were subjected to a final heat treatment at 1800°C in argon for 30 min. Table 6.52 describes the fissile and fertile particle types along with the total weights of ^{235}U and ^{232}Th used in each fuel rod of specimen holder C.

Table 6.50. Fuel Rods for OF-2 Irradiation Capsule, Holder A

Specimen Location[a]	Particle Types		Matrix Type	Loading, g	
	Fissile	Fertile		^{235}U	^{232}Th
	25.4-mm-long (1.00-in.) Specimens				
1-1	14	M	b	0.2380	3.980
-2	13	M	a	0.2380	3.980
-3	14	G	a	0.1350	2.610
-4	14	G	c	0.1350	2.610
-5	13	G	b	b.1060	2.190
-6	13	M	c	0.1060	2.190
2-1	14	M	a	0.2380	3.980
-2	14	G	b	0.2380	3.980
-3	13	M	b	0.1350	2.610
-4	13	G	c	0.1350	2.610
-5	14	M	c	0.1060	2.190
-6	13	G	a	0.1060	2.190
	12.7-mm-long (0.50-in.) Specimens				
3-1	12	M	d	0.1190	1.990
-2	2	I	d	0.1190	1.990
-3	11	H	d	0.1190	1.990
-4	2	G	d	0.1190	1.990
-5	4	K	d	0.0675	1.805
-6	6	J	d	0.0675	1.805
-7	8	G	d	0.0675	1.805
-8	10	H	d	0.0675	1.805
-9	4	I	d	0.0530	1.095
-10	2	C	d	0.0530	1.095
-11	8	A	d	0.0530	1.095
-12	12	B	d	0.0530	1.095
4-1	9	G	d	0.1190	1.990
-2	1	H	d	0.1190	1.990
-3	9	I	d	0.1190	1.990
-4	1	J	d	0.1190	1.990
-5	3	A	d	0.0675	1.805
-6	5	B	d	0.0675	1.805
-7	7	C	d	0.0675	1.805
-8	11	D	d	0.0675	1.805
-9	3	E	d	0.0530	1.095
-10	1	F	d	0.0530	1.095
-11	7	A	d	0.0530	1.095
-12	LASL	LASL	LASL	0.0530	1.095

[a]Hole number followed by position from top.

Table 6.51. Fuel Rods for OF-2 Irradiation Capsule, Holder B

Specimen Location[a]	Particle Types		Matrix Type	Loading, g	
	Fissile	Fertile		^{235}U	^{232}Th
	25.4-mm-long (1.00-in.) Specimens				
1-1	13	M	b	0.0814	1.530
-2	13	G	a	0.0814	1.530
-3	13	G	c	0.0690	1.260
-4	14	M	a	0.0690	1.260
-5	14	G	b	0.0690	1.260
-6	14	M	c	0.0690	1.260
2-1	13	G	b	0.0814	1.530
-2	14	M	b	0.0814	1.530
-3	14	G	a	0.0690	1.260
-4	13	M	a	0.0690	1.260
-5	13	M	c	0.0690	1.260
-6	14	G	c	0.0690	1.260
	12.7-mm-long (0.50-in.) Specimens				
3-1	12	A	d	0.0407	0.765
-2	2	B	d	0.0407	0.765
-3	4	C	d	0.0407	0.765
-4	6	D	d	0.0407	0.765
-5	8	E	d	0.0345	0.630
-6	10	F	d	0.0345	0.630
-7	2	L	d	0.0345	0.630
-8	4	G	d	0.0345	0.630
-9	3	H	d	0.0345	0.630
-10	8	I	d	0.0345	0.630
-11	2	J	d	0.0345	0.630
-12	4	K	d	0.0345	0.630
4-1	11	G	d	0.0407	0.765
-2	1	H	d	0.0407	0.765
-3	3	I	d	0.0407	0.765
-4	5	J	d	0.0407	0.765
-5	7	A	d	0.0345	0.630
-6	9	B	d	0.0345	0.630
-7	1	C	d	0.0345	0.630
-8	3	D	d	0.0345	0.630
-9	5	E	d	0.0345	0.630
-10	7	F	d	0.0345	0.630
-11	1	A	d	0.0345	0.630
-12	LASL	LASL	LASL	0.0345	0.630

[a]Hole number followed by position from top.

Table 6.52. Fuel Rods for OF-2 Irradiation Capsule, Holder C[a]

Specimen Location[b]	Particle Types		Loading, g	
	Fissile	Fertile	^{235}U	^{232}Th
1-1	13	N	0.1338	2.780
-2	13	I	0.1338	2.780
-3	14	G	0.1590	3.460
-4	13	O	0.3640	7.900
2-1	15	O	0.1338	2.780
-2	13	G	0.1338	2.780
-3	15	H	0.1590	3.460
-4	15	P	0.3640	7.900
3-1	14	M	0.1338	2.780
-2	14	P	0.1338	2.780
-3	13	J	0.1590	3.460
-4	14	M	0.3640	7.900
4-1	15	H	0.1338	2.780
-2	14	J	0.1338	2.780
-3	13	I	0.1590	3.460
-4	13	N	0.3640	7.900

[a]All specimens 50.8 mm (2.00 in.) long, fabricated with type c matrix.

[b]Hole number followed by position from top.

6.7.2.5 Capsule Irradiation

The OF-2 capsule was inserted into the E-7 position of the ORR core, and reactor start-up began on June 21, 1975. The sweep gas was kept at 100% He until June 23. This corresponds to approximately 60 hr of irradiation. With the pure helium sweep gas, fuel centerline temperatures were estimated to be between 100 and 200°C below desired operating conditions. Initial thermocouple readings indicated that the ends of the capsule, specifically loadings 1A and 3C, were operating at a somewhat higher heat generation rate than anticipated. On June 23 the capsule

was brought up to operating temperatures with the addition of neon to the sweep gas in both cells. The amount of neon added to cell 1 was less than design because of the high peripheral graphite temperatures in loading 3C. In cell 2 the sweep gas mixture was set at design criteria, and thermocouple readings agreed well with design thermal analysis.

An investigation into the increased temperatures at the ends of the capsule revealed that total reaction rates were higher in these two regions because of a change in the neutron spectrum at the end of the capsule. The result was an increase of approximately 20% in heat generation rate for loadings 1A and 3C at the ends of the capsule.

A new thermal analysis was initiated to determine the effect of this increased heat generation rate. The analysis was performed after approximately 170 hr of irradiation and included corrected heat generation rates for both cells 1 and 2. The results of these calculations using the HEATING3 computer code and three-dimensional models are shown in Table 6.53. Results presented here represent calculations using a thermal conductivity 85% of that used in the design analyses[43] for H-451 graphite. Good agreement is shown with calculated thermocouple temperatures and real-time thermocouple readings. The major changes shown are that loading 1A of specimen holder A will operate at approximately 100°C above design temperature, and that the maximum temperature, 1350°C, in cell 1 will occur in loading 3C rather than loading 2C.

As of June 30, 1975, OF-2 had operated for approximately 225 hr at ORR full power. A history of release-to-birth rate ratio (R/B) for several fission gases during initial irradiation are shown in Table 6.54. It should be noted that for samples 1-A-1 and 2-A-2 OF-2 was operating below design temperatures (pure helium sweep gas), and for samples 1-A-2 and 2-A-4 OF-2 was at design temperatures (mixed helium and neon sweep gas).

Table 6.53. Temperature History of OF-2 After 170 hr of Irradiation in ORR

Fuel Loading[a] or Location	Temperatures Predicted with HEATING3 Code, °C				Observed Temperatures, °C		
	Fuel Center	Graphite		ΔT Graphite Center to Periphery	Graphite		ΔT Graphite Center to Periphery
		Center	Periphery		Center	Periphery	
				Specimen Holder A			
1A	1290	1052	785	267	1060	771	289
2A	1187	1022	776	246	1021	767	254
3A	1155	998	765	233	1000[b]	752	248
				Specimen Holder B			
1B	1336	1177	893	284	c	906	c
2B	1380	1226	922	304	1233	930	303
				Specimen Holder C			
1C	1250	c	917	c	c	907	c
2C	1295	c	950	c	c	910	c
3C	1357	c	962	c	c	961	c
240.8[d]		1040			1010		
256.7[d]		533[e]			521[e]		

[a]As designed in Table 6.46.

[b]The temperatures at this location is measured by both a Chromel vs Alumel and a Platinum-Molybdenum alloy thermocouple. The reported 1000°C was indicated by the C/A thermocouple, while the Pt/Mo indicated 1060°C.

[c]There are no thermocouples located at the graphite centerline for these fuel loadings.

[d]Distance in millimeters from copper bulkhead dividing OF-2 into two compartments.

[e]This thermocouple is located on the surface of the stainless steel primary containment bulkhead.

Table 6.54. Release-to-Birth Rate Ratios (R/B) for Capsule OF-2

Sample	Operating Time (hr)	R/B Ratios × 10^5				
		^{85m}Kr	^{87}Kr	^{88}Kr	^{133}Xe	^{135}Xe
1-A-1	53.7	1.48	0.895	0.711	1.67	0.504
1-A-2	79.1	2.09	1.44	1.31	4.09	0.574
2-A-2	53.9	0.075	0.327	0.224	0.916	0.294
2-A-4	79.3	11.2	1.43	2.26	23.5	0.948

6.8 IRRADIATION TESTS IN PROTOTYPE REACTORS — E. L. Long, Jr.

Irradiation testing in prototype reactors has included experiments in the Peach Bottom Reactor and the Dragon Reactor. In addition, some preliminary planning has been done for a test element series in the Fort St. Vrain Reactor. During this reporting period the Peach Bottom Reactor was shut down, terminating irradiation of four Recycle Test Elements (RTE) at about half of peak large HTGR exposure. Three RTEs had been previously removed, and some results from examination of these elements were reported previously.[45,46] Examination of these three elements was completed during the reporting period, and the examination of RTE-8, the first of four elements irradiated to half of HTGR design exposure, was begun. Results from these examinations have so far been consistent with results from irradiation tests in accelerated capsule experiments. Detailed results and discussion of the examinations are reported elsewhere.[47]

The Dragon MET VII Experiment began irradiation in January 1975, and is scheduled to operate until Spring 1979. An interim nondestructive examination is scheduled for Spring 1976, at approximately one-fourth exposure. The MET VII capsule contains several fuel types for comparison: UC_2(VSM), weak-acid-resin-derived (WAR) uranium carbide, $(4Th,^{235}U)O_2$, and $(4Th,^{233}U)O_2$. This test is designed to compare the performance of candidate fissile particles, as well as the performance of fuels containing ^{233}U and ^{235}U, under real-time irradiation conditions. Further, the test is expected to confirm that the conclusions about fuel performance,

which have been made from accelerated testing results, can be applied to real-time situations. This last result is especially important in view of the substantial body of accelerated testing data that have been collected by ORNL and GA and the extended periods of time required to collect real-time irradiation data.

The FSVR test element program will not begin until Spring 1977, when the first elements are scheduled to begin irradiation. Preliminary planning was accomplished during the reporting period, and more substantive accomplishments will be reported later. Briefly, the ORNL portion of the test element program will include about 90 test fuel rods to be irradiated in each of three FSVR fuel elements. The remaining fuel in the elements will be either production FSVR fuel or test fuel from other sites. General Atomic Company will coordinate the test with the reactor owner (Public Service Company of Colorado), and will be testing fuel and graphite in the same test element series. The fissile fuel for the FSVR test elements was manufactured during the reporting period and is undergoing preliminary capsule testing in the OF-2 capsule. Similar fuel, manufactured in laboratory-scale equipment, performed very well in the HRB-9 and -10 capsules. All the fuel for the FSVR test elements will be manufactured in engineering-scale equipment being developed for the HTGR Recycle Demonstration Facility. General Atomic Company will provide the fertile fuel, shim material, and matrix material for the test.

6.9 NUCLEAR ANALYSIS IN SUPPORT OF IRRADIATIONS — H. T. Kerr, E. J. Allen, and D. L. Reed

The nuclear analysis effort during this reporting period has included a variety of activities. Computational analyses and experimental flux mappings have been made for irradiation facilities in the HFIR and the ORR to determine spatial variations of neutronic parameters required for the design and operation of test capsules. Time variations of the neutronic parameters have been investigated but have not been fully resolved. We have developed and tested a computational model that accurately calculates spatial variations of the neutron fluxes and energy spectra in the ORR. Considerable effort has also been given to

improvement of dosimetry materials and to identification of the appropriate parameters for characterizing irradiation test data. Also a computer code, CACA, has been written to estimate neutronic-related engineering parameters required during the design and operation of irradiation test capsules. A development program has been initiated to produce a calorimetric device for directly measuring gamma and/or fission heat rates in selected materials. Brief descriptions of these efforts and limited results are presented below; more detailed information can be obtained from the referenced topical reports for each subject.

6.9.1 Characteristics of the HFIR Facilities

HTGR test capsules are irradiated in various facilities of the HFIR. The uninstrumented HT capsules are irradiated at peripheral target-rod positions in the central target cavity. The instrumented HRB capsules are irradiated primarily in the large RB facilities of the removable beryllium reflector; the heavily fueled HRB capsules are initially irradiated in the PB-13 (VXF13) facility of the permanent beryllium reflector to achieve partial fuel burnup without excessive capsule power.

Neutron fluxes and isotopic reaction rates within the HFIR facilities have steep spatial gradients and vary with time during the 23-day fuel cycle. These spatial and time dependences are generally reproduced during each HFIR fuel cycle so that test capsule performance indices determined during any cycle are generally valid for similar capsules in other fuel cycles. Performance indices for HTGR capsules in HFIR are based on the following computational analyses and dosimetry experiments:

1. A fuel burnup analysis of HFIR was made by use of a nine-group two-dimensional diffusion theory model in the CITATION code.[48] The experimental facilities could not be explicitly represented in this analysis, so the calculated spatial and time variations of the neutron fluxes are not directly applicable for test capsule evaluations. However the calculated fluxes are useful for relative comparisons, and they can be modified to account for perturbations caused by the test capsules.

2. Detailed neutron energy spectra were calculated for HFIR start-of-cycle conditions with a 123-group one-dimensional transport theory model in the ASISN code.[49] These detailed spectra were coupled with the fluxes calculated in the CITATION model to produce a reference library of "unperturbed" spatial and time-dependent neutron fluxes for HFIR.

3. A dosimetry mapping experiment was done in one of the peripheral facilities in the HFIR target cavity. Dosimeter packages were placed at seven axial positions and two radial positions in an aluminum capsule. The axial and radial activation profiles produced during the one-cycle irradiation were interpreted as cycle-averaged neutron fluxes. The experimentally derived fluxes were about 8% lower than the unperturbed fluxes obtained from the computational models.

4. Neutron dosimeters were irradiated in the graphite annuli of several HRB capsules, but the resulting activation data were of limited value. Physical repositioning of the HRB capsules after each fuel cycle changed the spatial positions of the dosimeters, and the high fluence irradiations required large dosimeter depletion corrections. Also some of the dosimeter materials used were not suitable for the high-temperature environment and were not recovered in a usable form.

5. Neutron dosimeters were recovered from an aluminum research experiment irradiated for two cycles in the RB-7 facility of HFIR. Dosimeter packages were positioned at 51-mm (2-in.) intervals along the capsule axial centerline, and the resulting activation profiles were interpreted as cycle-averaged neutron fluxes. The results were internally consistent and in expected good agreement with the calculated "unperturbed" fluxes. Complete details are reported.[50]

6. None of the computational analyses or the preceding dosimetry data were directly applicable to the HRB capsules in the beryllium reflector facilities. Therefore, special one-cycle dosimetry mappings of the RB-3 and the PB-13 facilities were made with dosimetry capsules resembling the HRB capsules. Axial activation profiles were determined at several radial positions in both facilities and are shown in Fig. 6.60. The analysis of these data is continuing and will provide

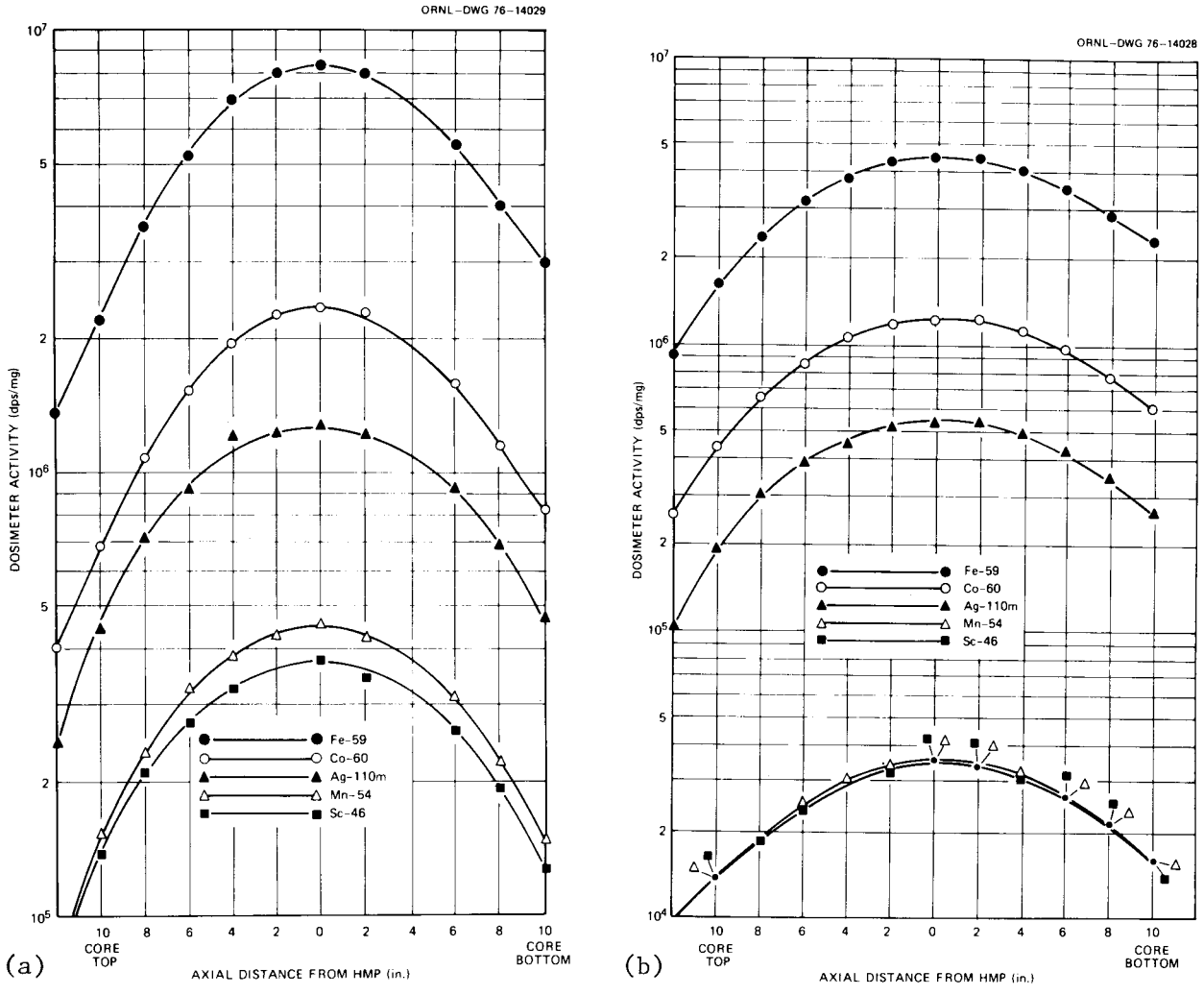

Fig. 6.60. Dosimeter Activity Profiles from Flux Maps of HFIR Facilities. (a) RB-3. (b) PB-13. To convert the axial distance from the horizontal midplane to millimeters, multiply by 25.4.

complete spatial flux and reaction rate profiles for the HRB capsules. A second mapping experiment will be done after replacement of the HFIR reflector to determine if neutronic conditions have changed.

The preceding computational and experimental efforts are reported[51] in detail and provide the basis for current evaluations of HFIR facilities. The cycle-averaged neutron fluxes and isotopic reaction rates recommended for HTGR test capsules in the HFIR facilities are summarized in Fig. 6.61 and in Tables 6.55 and 6.56.

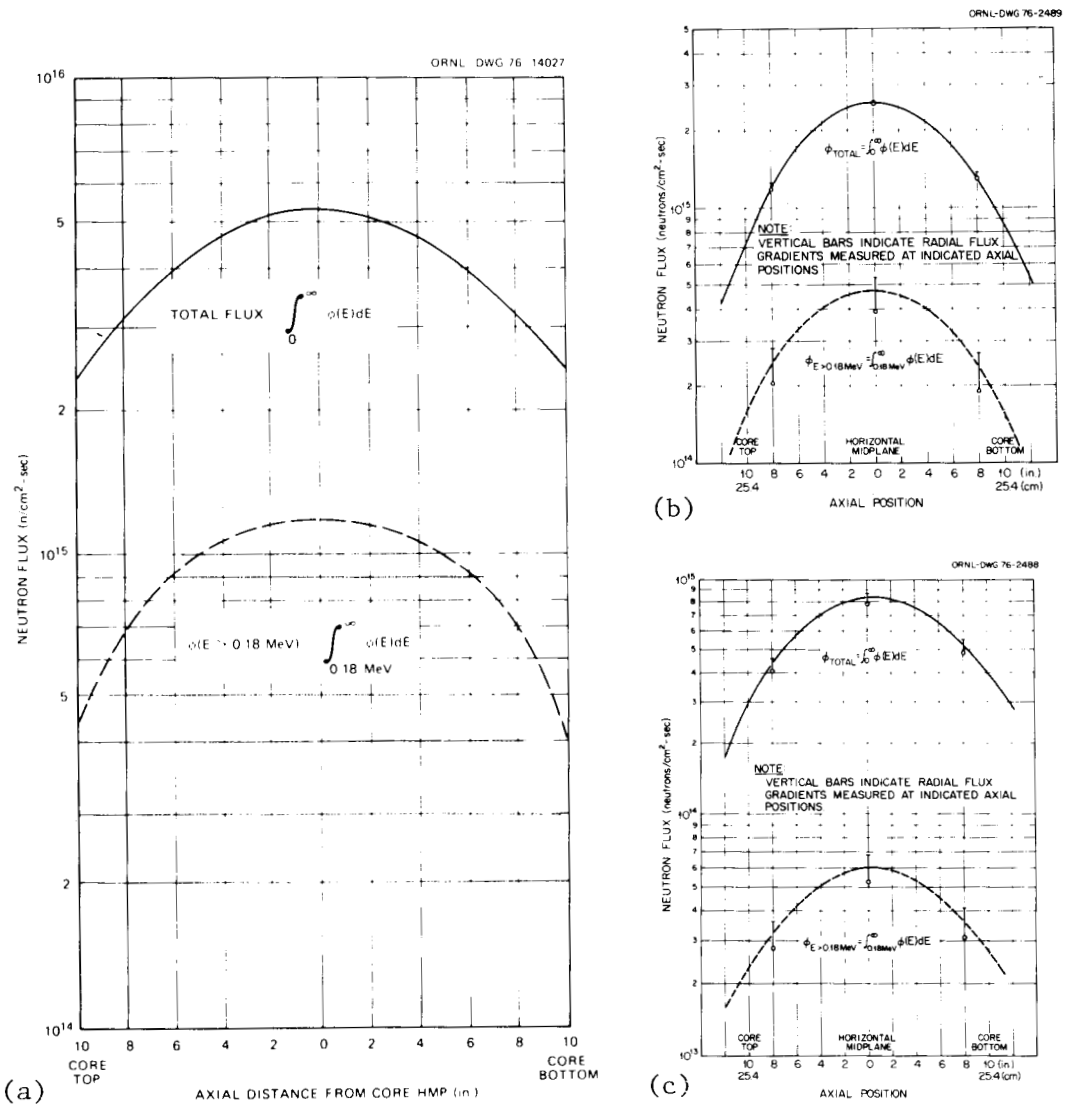

Fig. 6.61. Axial Flux Profiles for HTGR Capsules Irradiated in HFIR. (a) HT capsules in A-2 facility. (b) HRB capsules in RB-3 facility. (c) HRB capsules in PB-13 facility.

Table 6.55. Characteristics of HFIR and ORR Facilities Used for HTGR Capsule Irradiations

Facility	Capsule Series	ϕ_{tot}, max Total Flux ($n\ cm^{-2}\ sec^{-1}$)
HFIR		
A-2	HT	5.3×10^{15}
RB-3	HRB	2.6
PB-13	HRB	0.84
ORR		
E-3	OF	0.96

Table 6.56. Effective Total Cross Sections for HTGR Capsules Irradiated in the HFIR and ORR

Reaction	σ_{tot}, Effective Total Cross Section,[a] b			
	A-2	RB-3	PB-13	ORR E-3
$^{232}Th(n,\gamma)$	4.32	3.96	5.21	2.94
$^{233}U(n,\gamma)$	22.0	16.1	24.3	11.4
$^{233}U(n,f)$	215.0	151.0	243.0	101.0
$^{234}U(n,\gamma)$	48.1	40.1	52.6	28.0
$^{235}U(n,\gamma)$	39.3	27.9	44.0	18.5
$^{235}U(n,f)$	215.0	144.0	241.0	91.2
$^{238}U(n,\gamma)$	5.42	8.44	6.72	6.89
$^{239}Pu(n,\gamma)$	153.0	141.0	206.0	102.0
$^{239}Pu(n,f)$	351.0	281.0	432.0	194.0
$^{240}Pu(n,\gamma)$	356.0	287.0	342.0	270.0
$^{241}Pu(n,\gamma)$	142.0	109.0	175.0	73.0
$^{241}Pu(n,f)$	442.0	329.0	532.0	217.0

[a] $\sigma_{tot} = \int_0^\infty \sigma(E)\ \phi(E)\ dE \ / \int_0^\infty \phi(E)\ dE,$

$\sigma_{tot}\ \phi_{tot}$ = reaction rate.

6.9.2 Characteristics of the ORR Facilities

HTGR test capsules are irradiated at several in-core lattice positions of the ORR as shown in Fig. 6.62. During each irradiation the ORR core is arranged so that fuel elements surround the test capsules in all avialable positions. However the ORR fuel elements are replaced on a nominal two-week cycle, and significant core configuration changes are frequently made to accomodate other experiments. Consequently neutron fluxes and isotopic reaction rates in the ORR facilities exhibit configuration-dependent variations in addition to the cycle-dependent variations. Therefore, nuclear parameters for ORR capsules must be routinely evaluated during the irradiation interval.

Extensive computational analyses and experimental flux mappings have been done in conjunction with HTGR capsule irradiations in the ORR. Brief descriptions of each major effort and important results are given.

1. The OF-1/P13Q capsule irradiated in the E-3 facility was a joint effort by ORNL and GA, and neutron dosimeters were placed inside both compartments of the capsule for full-term high-fluence dosimetry data. These internal dosimeters gave relative indications of the exposure in each column of fuel specimens and substantiated the spatial flux gradients obtained from computational models. Data from the GA dosimeters in the P13Q compartment and the ORNL dosimeters in the OF-1 compartment were compared and found to be consistent and in good agreement with calculated flux profiles. Nominal fluxes for the fuel specimen in the OF-1/P13Q capsule are shown in Fig. 6.63(a), and isotopic reaction rates are given by Tables 6.55 and 6.56. Many additional dosimeters were irradiated for short times in special slots machined in the corners of the aluminum core piece. These dosimeters showed the changes in the E-3 facility fluxes resulting from changes in the ORR core configuration. For example the fluxes in E-3 increased by about 10% when the OG-1 capsule was removed from the C-3 facility.

2. The OG-1 capsule was designed by GA and irradiated in the C-3 lattice position of the ORR. Dosimeters were loaded inside the capsule and analyzed by GA. Other dosimeters were irradiated in the dosimeter slots in the aluminum core piece and analyzed by ORNL. Both dosimeter

ORNL-DWG 76-5732

Be — Beryllium element

Exp — Experiment or experimental facility

POOL

W

	A-1 Be	A-2 Exp	A-3 Fuel	A-4 Fuel	A-5 Fuel	A-6 Fuel	A-7 Be	A-8 Be	A-9 Be
	B-1 Be	B-2 Fuel	B-3 Fuel	B-4 SR	B-5 Fuel	B-6 SR	B-7 Fuel	B-8 Be	B-9 Be
	C-1 Be	C-2 Fuel	C-3 Exp	C-4 Fuel	C-5 Fuel	C-6 Fuel	C-7 Fuel	C-8 Fuel	C-9 Be
S	D-1 Be	D-2 Fuel	D-3 Fuel	D-4 SR	D-5 Fuel	D-6 SR	D-7 Fuel	D-8 Exp	D-9 Be	N
	E-1 Be	E-2 Fuel	E-3 Exp	E-4 Fuel	E-5 Exp	E-6 Fuel	E-7 Exp	E-8 Fuel	E-9 Be
	F-1 Be	F-2 Fuel	F-3 Fuel	F-4 SR	F-5 Fuel	F-6 SR	F-7 Fuel	F-8 Be	F-9 Be
	G-1 Be	G-2 Be	G-3 Be	G-4 Be	G-5 Be	G-6 Be	G-7 Be	G-8 Be	G-9 Be

E

Fig. 6.62. Typical ORR Core Configuration Showing Locations of Experimental Facilities for HTGR Experiments. SR — Shim Safety Rod.

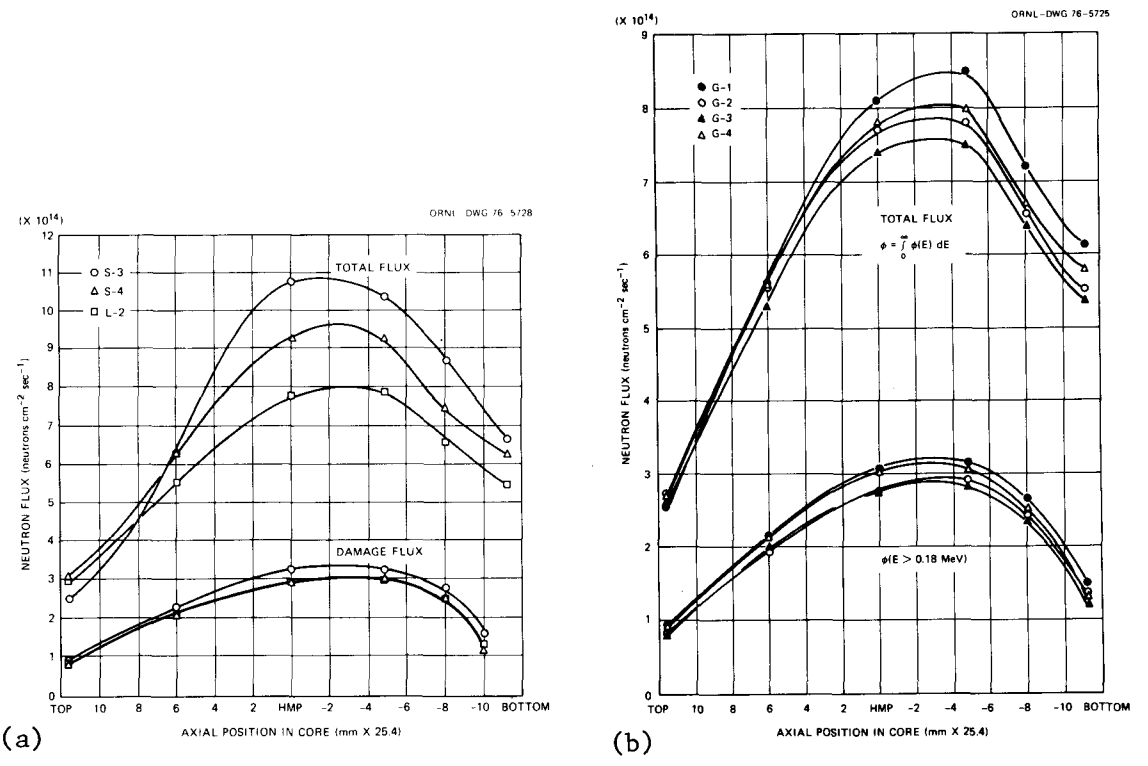

Fig. 6.63. Typical Axial Flux Profiles in HTGR Capsules Irradiated in the ORR. (a) P13Q/OF-1. (b) OG-1.

sets showed the same flux spatial profiles and were consistent with results from computational models. Typical fluxes for the OG-1 capsule are shown in Fig. 6.63(b).

3. Additional ORR in-core facilities were needed for HTGR capsules, and a core configuration was proposed with experimental facilities in the C-3, E-3, E-5, and E-7 lattice positions. Typical values of neutron fluxes in these facilities were determined by direct experiment dosimetry and are presented in Fig. 6.64. Fluxes in the C-3 and E-3 facilities were only slightly affected by the new configuration and are generally higher than the fluxes in the E-5 and E-7 facilities. Differences in the axial flux profiles result from the absence of fuel assemblies in some positions adjacent to the E-5 and E-7 facilities.

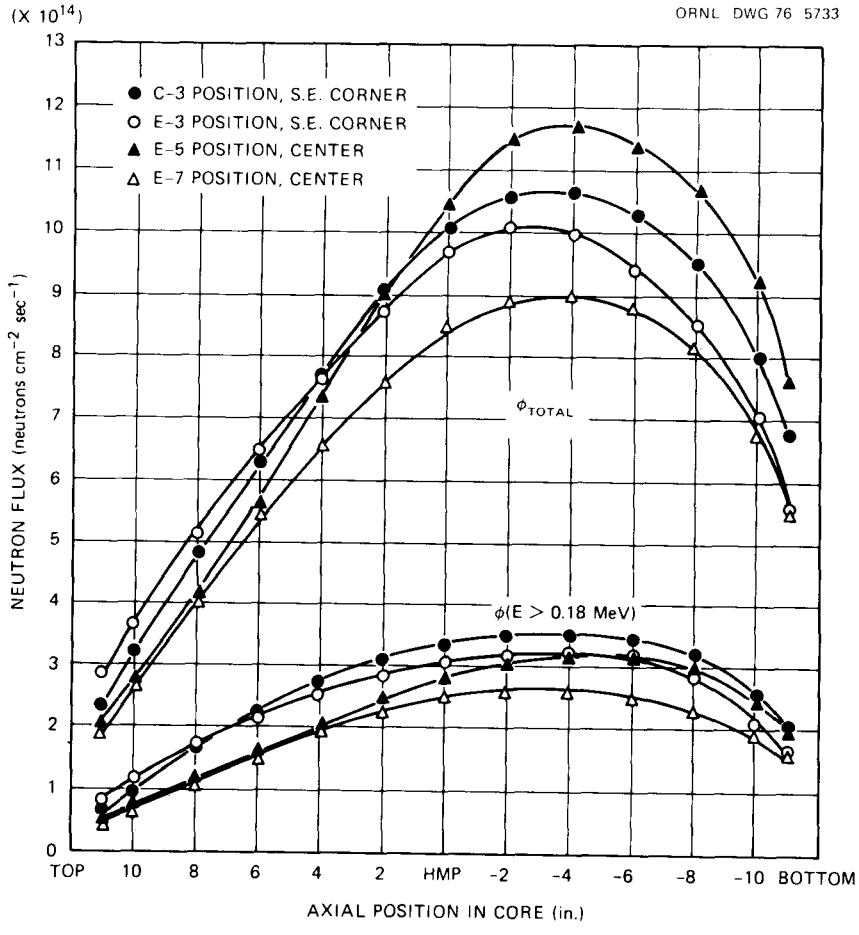

Fig. 6.64. Typical Axial Flux Profiles in the C-3, E-3, E-5, and E-7 Irradiation Facilities of the ORR.

4. Nuclear parameters for the ORR core facilities are very configuration-dependent and have previously been obtained by irradiating flux monitors in mockup capsules and inferring values from the induced monitor activities. Unfortunately, this procedure is time consuming, is costly, and gives no indication of perturbations associated with changes in the core configuration. Computational analyses have been attempted, but the three-dimensional structure of the ORR could not be adequately represented within the spatial mesh limits of available computer codes. In particular, axial flux profiles calculated with the CITATION code differed significantly from activation profiles obtained experimentally, especially in facilities near the control rods.

The computer code system BOLD-VENTURE has been developed,[52] and the only practical limitation on the spatial mesh in this code is computing cost. Consequently, a computational model using the VENTURE code was developed for ORR analyses. Multigroup neutron fluxes can now be calculated accurately and economically for any configuration of fuel elements, reflector elements, experiments, and control rods.

For routine use of this computational model, an auxiliary data processing code was developed. Approximations for axial gradients of fuel and fission-product concentrations were incorporated, greatly simplifying input data handling for VENTURE. Also, unique broad-group cross sections were produced for each of several characteristic compositions of the ORR. A representative cross section set is selected for each region of the calculational model.

The adequacy of this computational model was verified by direct comparison of calculated and experimentally measured dosimeter activation profiles. Approximately 2700 flux monitors were positioned in a typical ORR core configuration, and a detailed activation mapping was produced. Activation profiles for this same configuration were then calculated with the VENTURE model and compared with the experimentally derived profiles. The agreement was generally within 10%. Calculated activation profiles for other core configurations have shown similar agreement with available experimental data. Complete descriptions of the computational

model, the input instructions, and typical results have been reported.[53] This model should greatly simplify future evaluations of changes in the ORR core configuration.

Details of the preceding experimental and computational efforts for the ORR facilities are summarized in a report that is being prepared.

6.9.3 Development of the CACA Code

Depletion-burnup analyses of fueled irradiation tests were previously performed by programs such as ORIGEN[54] or FABGEN.[44] However, difficulties with computer turnaround time, cross section inaccessibility, large output in an undesired form, time-step limitations, power treatment, and fission-product limitations restricted the use of these programs. A computer code, CACA, was written to alleviate these difficulties but yet be simple and applicable to a wide variety of depletion-burnup problems. It can be used to calculate nuclide concentration histories, fission rates, and burnups for fueled experimental capsules subjected to neutron irradiations. A fourth-order Runge-Kutta calculational method is used; 16 heavy nuclides and 13 user-specified fission products are considered. Either constant power density or time varying fluxes for each time interval may be specified. Burnup is calculated in terms of fissions/cm^3, FIMA, and MWd/metric ton. FIMA is the fissions per initial heavy-metal atom and MWd/metric ton is the megawatt days per metric ton of heavy metal based on 180 MeV/fission. The output consists of the concentrations of the 29 nuclides, the birth rates of the fission-product nuclides, flux, power, fission rate, and the three burnup measures. A complete description of the program and input instructions was published.[55] The input and output for a sample problem are included. Program source decks are available on request.

6.9.4 Summary of Graphite Damage Terminology

Investigations of radiation-induced property changes in graphite and other materials require extensive testing in a variety of experimental facilities. The magnitude and the rate of irradiation damage for a specific material in a particular facility is a function of both the

nuclear properties of the material and the nuclear characteristics of the facility. The interpretation and comparison of graphite irradiation data has been complicated by the variety of conventions and parameters used for reporting data. Therefore a report was prepared[56] to describe the parameters required to quantify irradiation damage in graphite and define indices for comparing graphite irradiation data from different reactor facilities. Multigroup elastic scattering cross sections for carbon and corresponding Thompson-Wright displacement weighting functions are tabulated in the memo, and atomic displacement rates in several reactor facilities are compared. Several effective damage fluence conventions were defined to facilitate direct comparisons of data from different facilities. These conventions simply express graphite displacement data in terms of a neutron fluence for a reference neutron spectrum.

6.9.5 Development of a Gamma and Fission Calorimeter (GAFI)

The design and operation of irradiation test capsules require a knowledge of the heat generation rates in the capsules. Present methods for estimating these heat rates are cumbersome and provide indirect values, which are not easily extrapolated to different materials or conditions. A simple method was needed for determining the heat rates of selected materials in specific irradiation facilities.

A calorimetric instrument has been designed for direct measurements of gamma heat rates in selected structural materials and fission heat rates in standard fission foils. The general design is illustrated in Fig. 6.65. Basically the instrument consists of a central rod of the selected structural material with three thermocouples embedded at known positions. The containment shell is evacuated so the central rod is cooled essentially on one end, and the heat generation rates are determined by response differences in the three thermocouples. Standard fission foils can be mounted on the hot end of the rod, and fission rates in the foils can be determined.

Prototypes of these instruments are presently being fabricated with aluminum used as the structural material. Operational tests will be

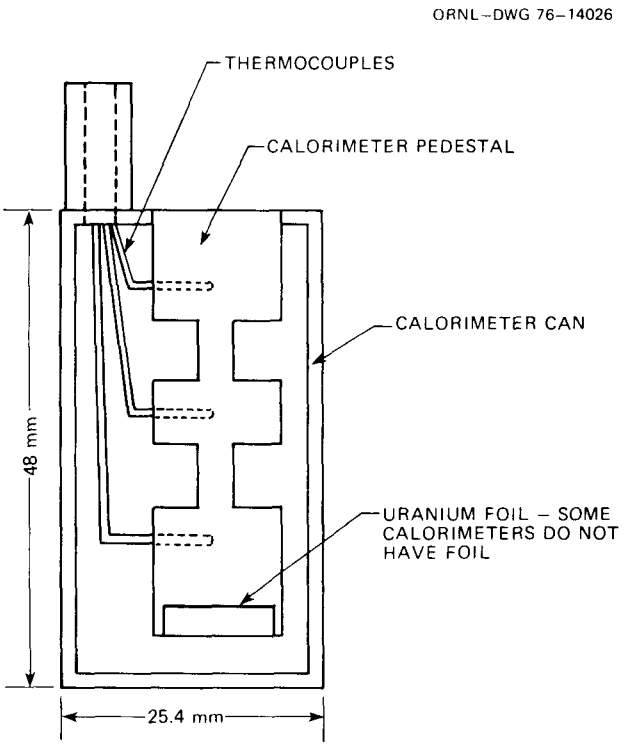

Fig. 6.65. Sketch of GAFI — The Gamma and Fission Rate In-Core Calorimeter.

conducted in the ORR, and if successful, instruments will be fabricated from other structural materials.

6.9.6 Development of Dosimetry Materials

Dosimetry programs for HTGR test capsules have been severely limited because relatively few existing dosimetry materials are stable and compatible in the high-temperature high-fluence environments of most HTGR capsules. In many cases dosimetry material failures have prevented recovery of any dosimetry data or introduced large anomalies relative to other existing data. For example, the activation profile of ^{54}Mn in metallic iron wires in the HRB capsules indicated axial peaking of the fast flux profile at the bottom of the HFIR fuel region. The indicated flux profile was not realistic and was attributed to diffusion of the manganese from the hot regions of the iron wires. The same situation existed with the iron dosimeters in the OF-1 capsule. Therefore the development of suitable dosimetry materials was essential for successful HTGR dosimetry programs.

An alloy containing 0.215 wt % Co in vanadium was developed as a thermal flux monitor. Another alloy containing 0.54 wt % of isotopically enriched iron in vanadium was developed as a high-energy flux monitor [the iron was 88% enriched in ^{54}Fe to enhance the $^{54}Fe(n,p)^{54}Mn$ reaction]. The isotopic analyses of these alloys were determined by activation analysis relative to known standards and by mass spectrometer analysis. The isotopic analysis of all samples tested was within 2% of the nominal isotopic analysis. Photomicrographs of the alloys showed complete homogeneity, with no precipitate forming at the grain boundaries. Vanadium-alloy specimens in beryllium oxide insulators were heated in an induction furnace to 1000°C with minor oxidation, and vanadium-alloy monitors have been irradiated in HTGR test capsules at temperatures up to 900°C. Other vanadium alloys are being considered, and attempts are being made[57] to obtain more high-purity vanadium metal free of undesirable impurities such as tantalum.

Some dosimeter materials cannot be used in the bare elemental form, and must be encapsulated. A method has been developed at ORNL for encapsulating well-defined quantities of dosimeter materials in high-purity vanadium capsules. Dosimeters of ^{6}Li, ^{10}B, ^{45}Sc, ^{232}Th, ^{235}U, ^{238}U, ^{237}Np, ^{238}Pu, ^{239}Pu, and ^{241}Pu have been prepared by this method. Normally the elemental form is used for the stable dosimeter materials and the oxide form is used for the radioactive materials. The vanadium capsules used to encapsulate the dosimeter materials have a 1.27 mm diameter but vary in length from 3.05 to 8.64 mm. The internal cavity is 0.76 mm in diameter and varies in depth from 2.28 to 7.87 mm. Amounts of dosimeter material loaded into each capsule can vary from about 1 to 10 mg, depending upon the particular isotope. The contained isotope is identified by the length of the capsule, and each individual capsule is identified by a dot coding system. These dosimeters have been used in some HTGR capsules, but they are not presently suited for general use.

Some development effort was expended to prepare ceramic wires from powdered oxide material. Ceramic wires can be produced from a powdered oxide material by use of a high-viscosity organic binder. No solvents are used. The wax-like binder is warmed to melting, and the oxide powder

is slowly mixed in until a paste is obtained. This paste can be readily extruded through a small-diameter die (~0.75 mm) at moderate pressure [~3.4 MPa (500 psi)]. The subsequent green wire can be handled easily without deformation and is finally fired in air at a temperature that yields maximum density with the least friability (especially in the bending mode).

The first ceramic wires were fabricated from the $^{235}U_3O_8$ and $^{238}U_3O_8$ materials normally used for the vanadium-encapsulated monitors. Subsequently, stronger uranium oxide wires were prepared from UO_2. The resulting wires were completely uniform and had the same isotope-to-oxide ratio as the original oxide material. Other dosimeter materials, such as cobalt and scandium, have been fabricated in the oxide wire form. The use of scandium in this form eliminates the tantalum contamination inherent in commercially available metallic scandium.

Although the oxide wires can withstand temperatures above 1500°C, they are more fragile than metallic wires and should be encapsulated. One technique being considered for encapsulating dosimetry materials for high-temperature application is to apply coatings of carbon and/or silicon carbide by use of the fluidized-bed technology developed for fabrication of gas-cooled reactor fuels. Coatings can be applied to any suitably refractory material that can be levitated in the bed and is chemically compatible with the coating fluid. The coating thickness, density, porosity, etc. can be controlled by varying process parameters such as fluid type, flow rate, and coating temperature. Some of the coated dosimeters could conceivably be used at operating temperatures as high as 1800°C in environments compatible with carbon.

Spherical oxide kernels of thorium and highly enriched uranium have been coated and tested for use as neutron dosimeters. The particles were coated with three layers of pyrolytic carbon and one layer of silicon carbide; the four layers provide complete containment of fission products. The thorium-containing particles have 47.36 wt % Th. The kernels are sol-gel thoria of essentially theoretical density, 10.0 g/cm^3, and have a nominal diameter of 500 μm with a standard deviation of 2.55 μm. In a sample of 90 particles, the largest and smallest kernel diameters

measured 508 and 496 μm, respectively. Accuracy of the microradiographic technique is about ±1 μm. The mean thorium content per particle is 5.77×10^{-4} g.

The kernels for the uranium-containing particles were obtained from an ion exchange resin and are very good spheres. The kernel diameters are nominally 350 μm but vary over a wide range. The diameter can be determined for each individual dosimeter particle with a microradiograph. The kernels have 73.2 wt % U and a density of 3.66 g/cm^3. A nondestructive assay technique has been developed to determine the ^{235}U content of individual coated particles to a relative accuracy less than 1%. This technique is based on delayed neutron counting and has shown a precision of 0.2% in tests conducted at ORNL.[58] Both the thorium and uranium particles are compatible with graphite at temperatures above 1800°C.

Additional effort is needed to develop a complete set of high-quality dosimeters for high-temperature applications. The availability of existing dosimetry materials and the fabrication requirements of dosimeters need to be established. High-temperature performance data need to be compiled, including such information as (1) homogeneity, (2) isotopic content, (3) mass determination, (4) physical properties and chemical compatibility, and (5) analytical considerations such as self-shielding.

6.10 CAPSULE THERMOMETRY — R. L. Shepard, J. K. East, J. L. Horton, R. J. Fox, T. G. Kollie, B. H. Montgomery, K. R. Thoms, M. W. Waddell, and R. K. Williams

A series of thermometry experiments is being conducted in the HRB instrumented irradiation capsules.* These experiments are aimed at providing more accurate and reliable measurements of the fuel centerline temperatures in HTGR fuel tests. The approach used is (1) to improve the quality of thermocouples, (2) to develop new methods for verifying

---

*This program is supported jointly by the LMFBR program for the development of fuel thermometers and by the GCR Base Program, which provides the capsule space and irradiation facility for testing fuel thermometers.

the integrity and calibration of centerline thermometers, and (3) to develop new sensors that avoid the limitations of conventional thermometers.

Centerline thermometers in the HRB fuel irradiation capsules must measure temperatures from about 900°C to as high as about 1500°C for periods of 2000 to 6000 hr. During this time, they will accumulate a neutron fluence of up to about 3×10^{22} n/cm^2 (thermal) and about 8×10^{21} n/cm^2 (fast). They must survive in an atmosphere containing carbon and various fission products. Considerations of HRB capsule and HFIR core design limit the thermometer outside diameter to a maximum of about 3.2 mm (0.125 in.) and require a 3-m (10-ft) lead length and about 9-m (30-ft) extension cable lengths.

A temperature measurement accuracy of better than 10°C at 1200°C is required for significant determinations of fuel thermal conductivities and particle coating diffusion kinetics. The typical level of confidence is not better than 100°C in most cases. Chromel vs Alumel thermocouples could provide the desired accuracy and radiation stability[59] up to about 900°C; too low for fuel centerline temperatures in most HRB experiments. Tungsten-rhenium thermocouples have sufficient temperature range and out-of-reactor stability but have large calibration drifts[59] due to thermal neutron transmutation of the high-cross-section wires. Thermocouples using materials with low neutron cross sections, made from Pt, Mo, Ru, and Nb alloys, could be useful to 1500°C but are still in an early state of development. Platinum-sheathed, alumina-insulated, Pt—5% Mo vs Pt—0.1% Mo thermocouples are being tested for measuring temperatures up to 1500°C in the HFIR and ORR irradiation capsules. Ultrasonic thermometers, developed first in England by Jacques and Bell for the Dragon Project, provide sufficient temperature range and accuracy and a wide choice of sensor materials but exhibit a large calibration shift in-reactor. Johnson noise thermometers are being developed for absolute measurements of fuel centerline temperatures with no limitations due to radiation or chemical effects.

Tungsten-rhenium thermocouples were used to measure centerline temperatures in HRB-3 -4, -7, and -8 capsules. The thermocouple output dropped from 75°C at 1000°C in 2000 hr in HRB-4 to as much as 530°C at

1500°C in 5500 hr in HRB-8. In these experiments, an additional pair of wires was connected to the thermocouple to provide means for accurate measurement of the thermocouple loop resistance. Irradiation caused a decrease in thermocouple output and a corresponding increase in loop resistance. Analysis of this pair of property changes was used to update calibration. A study was begun to use measured Seebeck coefficient values of alloys simulating the irradiated tungsten-rhenium thermocouple wires for predicting the calibration drifts of tungsten-rhenium thermocouples undergoing transmutation in an irradiation experiment. An in-pool, whole-capsule, calibration furnace facility was used to show the pronounced effect of axial temperature gradient on the temperature indications from irradiated, thermoelectrically inhomogeneous tungsten-rhenium thermocouples.

Ultrasonic thermometers (UST) with rhenium sensing elements were installed in fuel centerline positions in HRB-5 and -6 experiments. The rhenium UST operated successfully for over 2500 hr at 900 to 1100°C in HRB-5 but changed calibration by a very large amount because of the transmutation of half the rhenium to osmium; a 7% change in the room-temperature transit time was observed and corresponds to about a 600°C error at 900°C. The UST output was measured each time the reactor was shut down at the end of an irradiation cycle and isothermal conditions were obtained, and a careful in-place calibration was performed in the in-pool furnace at the end of the irradiation. Combining these data with the preirradiation calibration, we could obtain the corrected temperatures, which agreed within 50°C of the corrected thermocouple readings in the companion HRB-4 experiment. The UST has incompletely developed potential advantages for use at very high temperatures (over 2000°C), but it is sensitive to radiation damage and to mechanical interference, as encountered in the HRB-6 experiment (see previous report[60] for more details).

A Johnson noise thermometer (JNT) has been successfully used to measure fuel centerline temperatures in HRB-9 for 4500 hr at 1250 to 1500°C with no apparent decalibration. The JNT is an absolute thermometer, and its development represents the main present problem for this program.

6.10.1 Johnson Noise Thermometer Development — R. L. Shepard, C. J. Borkowski, T. V. Blalock,* J. K. East, R. J. Fox, and J. L. Horton

A Johnson noise thermometer (JNT) was developed by C. J. Borkowski and T. V. Blalock.[61] It utilizes the noise power produced by a passive resistance element to provide an absolute measurement of temperature, independent of composition, irradiation, or past history of the sensor. It behavior follows the Nyquist equation:

$$\sqrt{\overline{P_n^2}} = K \cdot 4kT\ \Delta f\ ,$$

by which the temperature T can be calculated from measurement of the noise voltage and noise current — their product being the noise power P_n — over a frequency bandwidth Δf, by use of low-noise amplifiers with a measured gain K and a known value of Boltzmann's constant k. Noise currents of about 6 nA and noise voltages of about 0.5 μV were detected in the frequency bandwidth of 60 to 100 kHz from an 85-Ω rhenium resistor at 1000°C, by use of voltage and current preamplifiers having equivalent noise resistance of 16 and 11 Ω, respectively. An integration time of 10 sec provides a theoretical accuracy of 0.2% at this bandwidth.

Fuel centerline JNTs were built and used in the HRB-9 and -10 irradiation capsules and provided credible temperature measurements of 1350 to 1500°C during the 4500-hr HRB-9 irradiation. An 18-Ω rhenium resistor, insulated with beryllia, was contained in a Mo—48% Re sheath, 2.5 mm OD (0.098 in.), as shown in Fig. 6.66. The sensor extended 23 cm (10 in.) into the 3.4-mm-ID (0.135-in.) hollow fuel elements, and was joined to a 3.7-m (144-in.) stainless-steel-sheathed extension cable. The entire sensor was contained within primary fission gas containment.

An electronic system for measuring noise voltage and noise current was built and connected to a digital data processor, using a PDP-8/S computer, which logged data and provided a digital record of the noise voltage, noise current, sensor temperature, and sensor resistance.

---

*Professor of Electrical Engineering, University of Tennessee, Knoxville.

ORNL DWG 74-10564

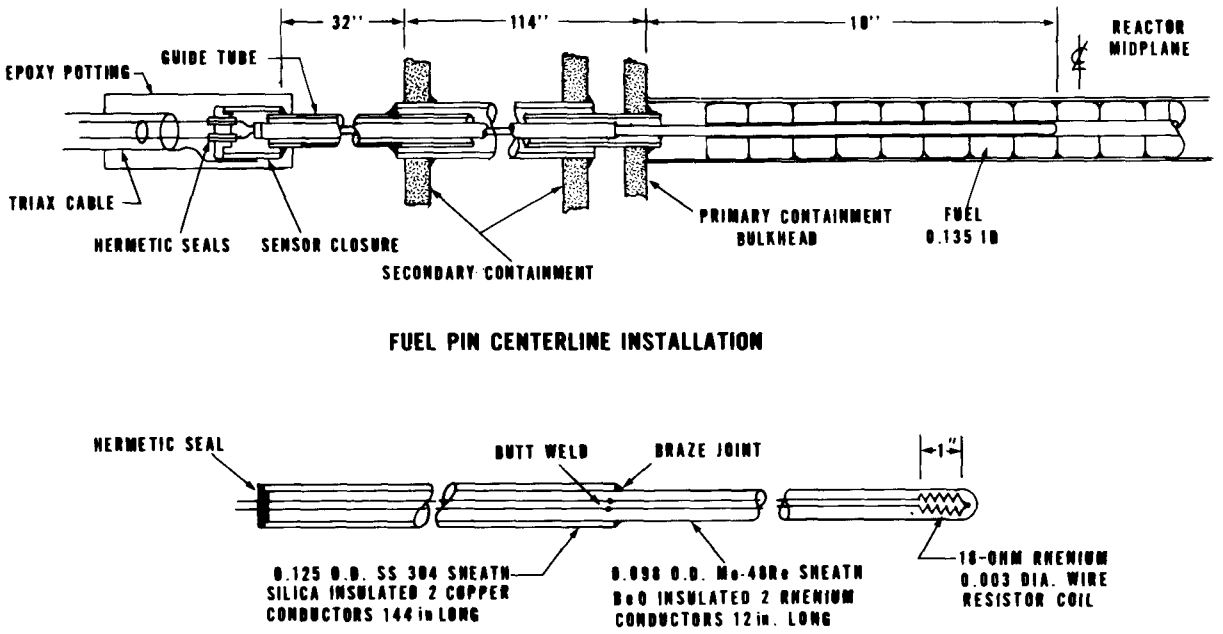

Fig. 6.66. Johnson Noise Thermometer Used in Capsule HRB-9. Dimensions are in inches; multiply by 25.4 to convert to millmeters.

An analog signal from the noise voltage was provided for recording on a strip chart recorder. The system operated unattended for the entire irradiation.

The HRB-9 JNT operated successfully for 4500 hr in the HFIR indicating changes in centerline temperature with changes in the helium-neon capsule sweep gas composition and variations in fuel power during each reactor fuel cycle. Changes in the electrical resistance of the rhenium sensor of about 15% were observed by measuring the ratio of noise voltage to noise current, as the rhenium sensor transmuted to about 80% osmium. Occasional periods of interference due to external electrical noise and to irradiation of the electrical insulation were observed, but the thermometer was still operating well and indicating a centerline temperature of about 1350°C at the end of nine irradiation cycles during which it had accumulated a thermal neutron fluence of 2.7×10^{22} n/cm^2. The sensor failed open circuit during the start-up

of the tenth irradiation cycle after the capsule had been removed from and then reinserted into the irradiation facility between reactor fuel cycles.

The HRB-10 JNT, identical to that used in HRB-9, provided similar temperature data during two irradiation cycles in the HFIR PB-13 irradiation facility and for part of the next cycle after the capsule was moved to the HFIR RB-7 irradiation facility. It then failed open circuit after a total of 1300 hr. These experiments were described in a paper presented in December 1974 at the Petten Fuel Thermometry Colloquium.[62]

In postirradiation examination of the HRB-10 capsule, severe interaction due to carbon migration was observed between the sensor molybdenum-rhenium sheath, a wrap of 38-μm-thick rhenium foil that surrounded the sheath, and the inner surface of the coated fuel particles where they were in intimate physical contact. No interaction was seen in other places where the fuel and sheath did not touch, nor in the HRB-9 capsule. Some JNT temperature readings in HRB-10 in the PB-13 facility were as high as 1650°C, which may have been in part due to gamma heating of the sensor; no readings in HRB-9 exceeded 1500°C, and the sensor was more loosely spaced in the fuel centerline hole.

We concluded that these experiments demonstrated the feasibility of using JNT in fuel irradiation capsules, that they provide credible temperature in spite of very large radiation-produced changes in sensor composition, and that a more effective carbon barrier is required for protection between the fuel coating and the sensor sheath.

6.10.2 Low-Cross-Section Thermocouple Development — R. L. Shepard, R. L. Beatty, J. K. East, R. J. Fox, G. W. Weber, and R. K. Williams

Tungsten-rhenium thermocouples have been widely used to measure centerline temperature in fuel irradiation experiments, and while they have good out-of-reactor stability and more than adequate range for GCR tests, they have been shown[59,63] to drift because of cumulative effects of irradiation by as much as 400°C at 1000°C in 6000-hr irradiations. A review[64] of development of thermocouples made from alloys

of metals having low cross sections for neutron capture — Pt, Mo, Ru, Nb — suggests that these materials may be suitable for in-reactor thermometry to 1500°C, although chemical compatibility problems were reported.[65] One experiment reported[66] at Battelle PNW Laboratories showed that Pt—5% Mo vs Pt—0.1% Mo thermocouples did not change significantly in calibration during an irradiation in ETR to 1.5×10^{21} n/cm^2 (fast) and 1.5×10^{21} n/cm^2 (thermal) neutron fluence.

Thermocouple wire and platinum-sheathed alumina-insulated Pt—5% Mo vs Pt—0.1% Mo thermocouples were obtained from Engelhard Industries for test and evaluation. Two sheathed thermocouples 1.57 mm OD (0.062 in.) were installed in the graphite spine of the OF-2 irradiation capsule to measure temperatures of 1000 to 1150°C. Platinum-molybdenum thermocouple wire was used in the fabrication of a composite, centerline thermometer, which included a pair of platinum-molybdenum thermocouples, a Pt—1% Mo resistance thermometer, and a platinum-molybdenum-sensor JNT. This thermometer was intended for OF-2 but was not used because of the incompatibility of the molybdenum-rhenium sheath with the fuel coating observed in the HRB-10 postirradiation examination. It will be used instead for furnace testing to determine drift and high-temperature performance of the platinum-molybdenum thermocouples.

A 1.5-m-long (5 ft) platinum-sheathed, Pt—5% Mo vs Pt—0.1% Mo thermocouple was modified for use as the HRB-11 centerline thermometer by adding a stainless-steel-sheathed pair of Chromel vs Alumel thermocouples to measure the cold junction temperature of the platinum-molybdenum thermocouple. This modification provided sufficient extension length 2 m (6 ft), and permitted accurate, four-wire loop resistance measurements of the platinum-molybdenum thermocouple. This sensor shown in Fig. 6.67 was fabricated and installed in HRB-11 for use at 1350°C. A rhenium foil wrap was used to separate the platinum sheath from the coated fuel particles.

Two platinum-sheathed, alumina-insulated Pt—5% Mo vs Pt—0.1% Mo thermocouples were tested in an out-of-reactor graphite compatibility furnace for 513 hr at 1500°C. One thermocouple, wrapped with rhenium foil, maintained a steady 39—40 mV for the duration of the test and retained its high 10^{12}-Ω room-temperature insulation resistance. The

ORNL-DWG 75-18069

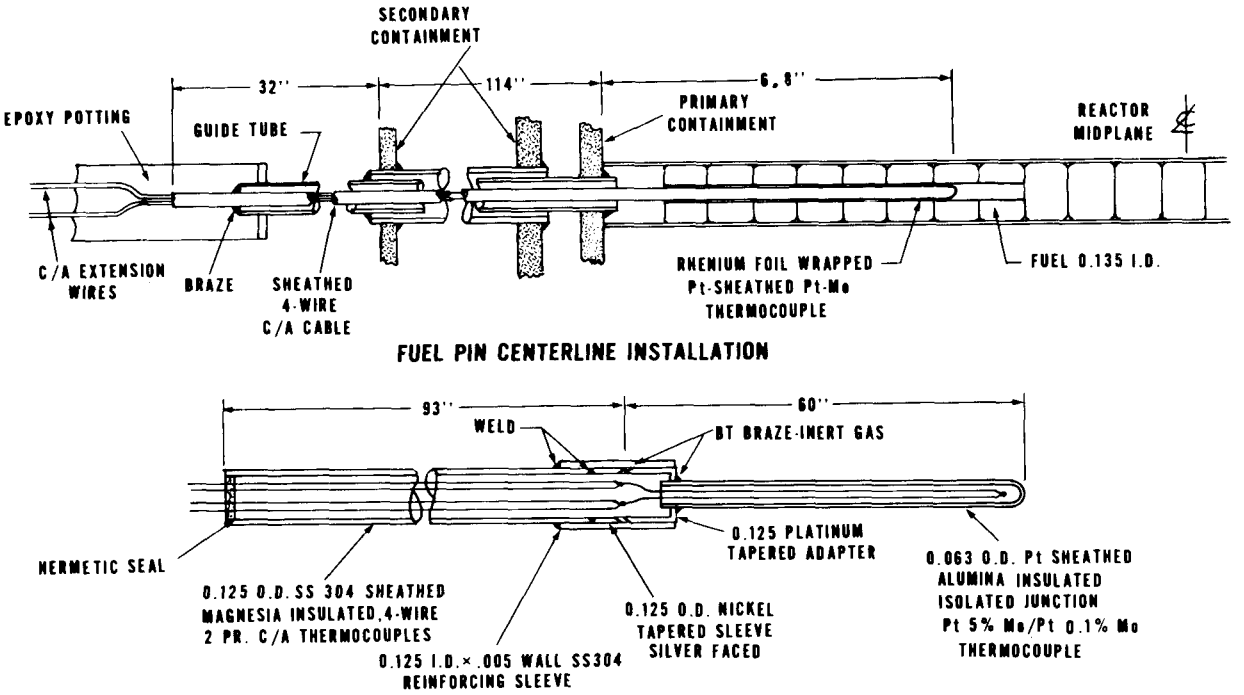

Fig. 6.67. Platinum-Molybdenum Thermocouple for Capsule HRB-11. Dimensions are in inches; to convert to meters, multiply by 0.0254.

other thermocouple, not protected with rhenium foil, decreased in output 6 mV and dropped in insulation resistance to about 100 Ω. Post-test examination showed some minor sheath carbonization of the protected thermocouple and a sheath rupture of the unprotected thermocouple.

In concurrent work the Seebeck coefficients of a group of low-cross-section platinum-base alloys including Pt-Mo, Pt-Ru, and Pt-Nb have been obtained. These wires will be used in future thermocouple studies.

6.10.3 Thermometry in HRB Capsules — R. L. Shepard and B. H. Montgomery

Fuel centerline temperatures from 900 to 1600°C have been measured in a series of HTGR fuel capsules irradiated in the HFIR. The purpose of these experiments was (1) to provide temperature data for calculating fuel thermal conductivity and evaluating coated particle kernel migration kinetics, (2) to determine calibration drift of tungsten-rhenium thermocouples, and (3) to demonstrate feasibility of the use of new types of temperature sensors — ultrasonic and Johnson noise thermometers. The

same general design of capsules has been used in each experiment. As shown in Fig. 6.68, the centerline sensor is inserted in hollow fuel elements extending nearly to the reactor horizontal midplane. Stainless-steel-sheathed Chromel vs Alumel (C/A) thermocouples are inserted into the peripheral graphite cyclinder surrounding the fuel elements, with three in the same axial location as the centerline sensor, and four or five more at other axial locations. The capsules were operated on the basis of the temperature indications from the C/A thermocouples. Heat removal from the fuel was controlled by varying the composition of the helium-neon sweep gas outside the graphite liner. The liner was machined to vary the gas gap along the capsule to provide an approximately flat axial temperature distribution. Since the centerline sensor was directly exposed to the fuel, some sheath was required. The sheath generally was wrapped with rhenium foil to prevent carbon migration from fuel to sheath, and primary fission gas containment was provided in the design of the sensor installation in the capsule. The later versions of capsule design incorporated a 4.7-mm-OD by 0.51-mm-thick (0.1875- by 0.020-in.) stainless steel guide tube into which different sensors could be installed without redesign of the capsule.

An extremely valuable adjunct to the HFIR facility was provided by an in-pool, whole capsule, resistance heated furnace — Fig. 6.69 — which permitted calibration to 800°C of the sensors in the capsule between irradiation cycles with the capsule removed from the HFIR reflector, or at the end of irradiation. This facility was used to determine the drift of the ultrasonic thermometer used in HRB-5 and -6 and the effects of temperature gradient on the calibration of tungsten-rhenium thermocouples in HRB-7 and -8.

A summary is presented of the experiments performed in this HRB series:

HRB-3 (Jan. 7, 1972 to Oct. 2, 1972)

Centerline sensor: A W–3% Re vs W–25% Re thermocouple with provision for measuring loop resistance of the 3-m (10-ft) length of thermocouples.

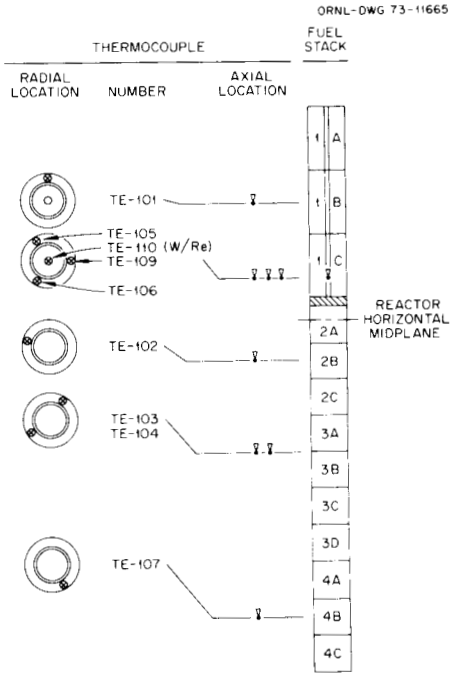

Fig. 6.68. Fuel Specimen and Thermocouple Locations in Capsule HRB-3.

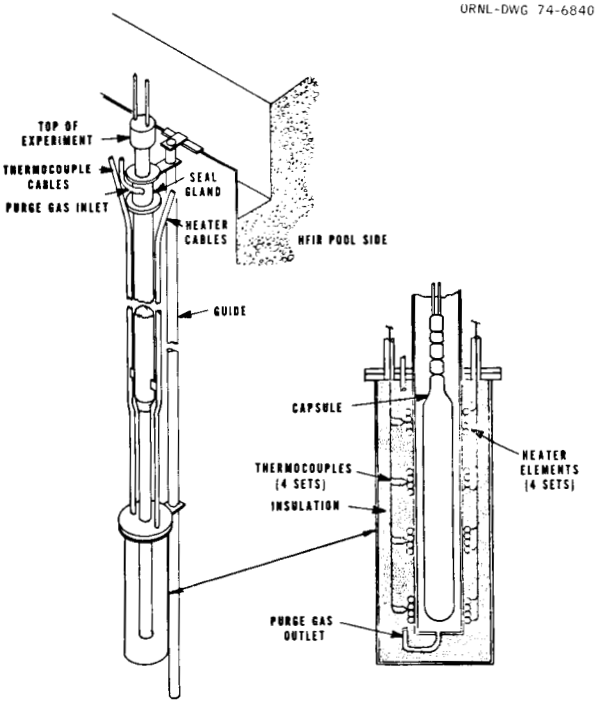

Fig. 6.69. In-Pool Calibration Furnace HRB-X.

Conditions: Operated for 6100 hr at temperatures to 1100°C accumulating a neutron fluence of 2.7×10^{22} n/cm^2 (thermal) and 8×10^{21} n/cm^2 (fast).

Performance:[60] Thermocouple drifted −300°C in 6000 hr compared with calculated centerline temperatures. Loop resistance increased 17.5%.

Postirradiation Condition: Composition changes in tungsten-rhenium wires and separation of a second phase, probably sigma-phase rhenium-rich W-Re-Os.

HRB-4 (Oct. 8, 1972 to June 26, 1973)

Centerline sensor: A W–3% Re vs W–25% Re thermocouple with provision for measuring the resistance of the 12.5-cm-long (5-in.) thermocouple loop within the fuel.

Conditions: Irradiated for 5872 hr at 1000°C, accumulating same fluence as HRB-3.

Performance:[60] Thermocouple failed open circuit after 2000 hr irradiation, showing a −75°C calibration drift and an increase of 18% in loop resistance. Resistance change was used to obtain a correction of calibration drift.

Postirradiation Condition: Thermocouple bead was broken, apparently because of swelling of beryllia insulators.

HRB-5 (Oct. 8, 1972, to Feb. 3, 1973)

Centerline sensor: A 5-cm-long (2-in.) rhenium ultrasonic thermometer, 0.5 mm OD (0.20 in.) emplaced without sheath directly exposed to fuel inner surface.

Conditions: Irradiated 2578 hr at 900 to 1100°C accumulating a neutron fluence of 1.1×10^{22} n/cm^2 (thermal) and 3.1×10^{21} n/cm^2 (fast).

Performance:[60] Satisfactory performance for entire irradiation; a 7% decrease in transit time corresponding to a −600°C calibration drift at 900°C. In-pool furnace used to measure calibration drift.

Postirradiation Condition: Analyzed a 50% transmutation of rhenium sensor to osmium. Metallographic evidence of grain boundary separation and void formation in rhenium.

HRB-6 (Feb. 27, 1973, to Sept. 8, 1973)

Centerline sensor: A rhenium ultrasonic thermometer as used in HRB-5.

Conditions: Irradiated 4400 hr at 900°C, accumulating a neutron fluence of 2×10^{22} n/cm^2 (thermal) and 6×10^{21} n/cm^2 (fast).

Performance:[60] Sensor failed during first reactor cycle by sticking of ultrasonic transmission line in 1.59-mm-OD (0.0625-in.) guide tube; intermittent performance thereafter.

Postirradiation Condition: Sensor recovered intact. Same metallographic condition as HRB-5 sensor.

HRB-7 (Dec. 19, 1973 to July 21, 1974)

Centerline sensor: A multiwire W–5% Re vs W–26% Re thermocouple with five measuring junctions along central axis of fuel column.

Conditions: Irradiated 4400 hr at 1500°C, accumulating a neutron fluence of 2×10^{22} n/cm^2 (thermal) and 6×10^{22} n/cm^2 (fast).

Performance: Thermocouple calibration drifted –330°C at 1500°C in 2200 hr. Thermocouple then failed open circuit. In-pool calibration after 1120 hr irradiation confirmed drift calculations based on changes in loop resistance, approximately –80°C at 610°C, but showed that the correction depends on the furnace axial temperature gradient.

Postirradiation Condition: The thermocouple was broken. Beryllia insulators had swelled about 3%. Absence of interaction between fuel and rhenium foil surrounding the insulators and between foil and insulators was noted.

HRB-8 (Feb. 28, 1974, to Oct. 4, 1974)

Centerline sensor: Five-junction W—5% Re vs W—26% Re thermocouple as in HRB-7.

Conditions: Irradiated 5500 hr at 1250°C, accumulating a neutron fluence of 28×10^{22} n/cm^2 (thermal) and 8×10^{21} n/cm^2 (fast).

Performance: Thermocouple calibration drifted —530°C at 1500°C in 3500 hr. Thermocouple survived entire irradiation intact. Loop resistance increased 2.7 times initial value. In-pool furnace calibration at the end of irradiation showed effect of furnace gradient on apparent decalibration. At a constant true temperature of 700°C at the middle W-Re junction, decalibration could be varied from —120°C to —210°C by changing the axial temperature gradient. The decalibration for the first 3000 hr irradiation was calculated from changes in loop resistance,[62] by use of an analysis based on Matthiesen's rule, and agreed well with in-pool furnace calibrations performed after 2163 hr irradiation.

Postirradiation Condition: Thermcouple intact: no other examination was performed.

HRB-9 (Oct. 6, 1974, to June 3, 1975)

Centerline sensor: A Johnson noise thermometer with a single rhenium resistor (described in Sect. 6.10.1).

Conditions: Irradiated for 5400 hr at 1250–1500°C two cycles in the HFIR PB-13 facility and eight cycles in the HFIR RB-7 facility, accumulating a neutron fluence of 2.8×10^{22} n/cm^2 (thermal) and 8×10^{21} n/cm^2 (fast).

Performance: The JNT provided fuel centerline temperature of 1350 to 1400°C during most of the irradiation until the sensor failed open circuit at the beginning of the last reactor cycle after 4500 hr of service. Some periods of interference from external electrical noise sources and from radiation effects on cable insulators were observed. The sensor resistance changed about 15%, partly because of an estimated 80% transmutation from rhenium to osmium.

Postirradiation Condition: Thermometer open circuit near sensing resistor end; sheath intact. No significant fuel-sheath-insulator interaction.

HRB-10 (Nov. 25, 1974, to June 9, 1975)

Centerline sensor: Rhenium sensor JNT, as in HRB-9.

Conditions: Irradiated for 3738 hr at 1500°C nominal, two cycles in HFIR PB-13 facility and five cycles in HFIR RB-5 facility, accumulating a neutron fluence of 1×10^{22} n/cm^2 (thermal) and 4×10^{21} n/cm^2 (fast).

Performance: The JNT indicated temperatures as high as 1650°C during the first irradiation cycle in PB-13. More typical readings were 1400–1550°C. The thermometer became erratic in the RB-5 facility and then failed open circuit after 1300 hr irradiation.

Postirradiation Condition: The molybdenum-rhenium sheath had reacted with fuel particle coatings, by carbon diffusing through the rhenium foil barrier where the sheath was pressed against the fuel. This catastrophic failure caused high fission gas activity in the experiment sweep-gas current and eliminates that choice of sheath material from further sensor fabrications.

Neutron fluences were calculated from the fluxes given in Table 6.57.

Table 6.57. Flux in HFIR HRB Irradiation Facilities

Facility	RB (Measured)	PB (Estimated)
Neutron Flux, n cm^{-2} sec^{-1}		
Thermal (<0.41 eV)	$1.4–1.8 \times 10^{15}$	$7–9 \times 10^{14}$
Epithermal	5×10^{14}	
Fast (>0.18 MeV)	5×10^{14}	5×10^{13}
Gamma Intensity		
R/hr	6.3×10^{9}	2×10^{9}
W/g graphite	14.7 (0.1–10 MeV)	5

In summary, these eight irradiation experiments have provided data for comparing the behavior of tungsten-rhenium thermocouples, rhenium ultrasonic thermometers (UST), and Johnson noise thermometers (JNT) in-reactor under similar irradiation conditions and show the very marked differences between the effect of irradiation on their calibration. As seen in Fig. 6.70, the UST used in HRB-5 decalibrated most, although it may be somewhat corrected for by isothermal calibration updating,[62] the tungsten-rhenium thermocouple decalibrated significantly in HRB-3 (and also HRB-4, -7, and -8), but the JNT used in HRB-9 showed no decalibration.

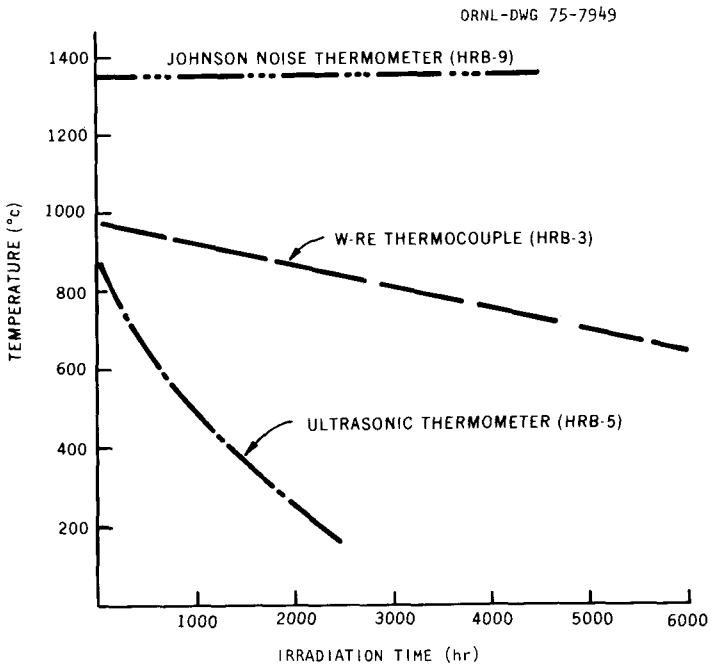

Fig. 6.70. Fuel Irradiation Centerline Thermometers.

6.10.4 Thermometry in ORR Capsules — R. L. Shepard and K. R. Thoms

Thermometry support has been provided for a series of fuel irradiation and creep test capsules for the ORR. These irradiations are typically longer than HRB irradiations and at lower neutron fluxes: 3×10^{14} n cm^{-2} sec^{-1} (fast) and 2×10^{14} n cm^{-2} sec^{-1} (thermal). Capsules provide slightly lower temperatures (900–1300°C) and accomodate shorter sensors [0.3–1.5 m (1–5 ft)] with less restriction on size of extension cables and transition joints.

Most O-series capsules have used sheathed Chromel vs Alumel (C/A) thermocouples to measure peripheral temperatures and C/A or tungsten-rhenium thermocouples to measure fuel temperatures. A short review of their performance is given:

OG-1 (June–December 1973)

This capsule was irradiated 3200 hr in the ORR, accumulating a neutron fluence of about 2×10^{21} n/cm^2 (thermal) and 3×10^{21} n/cm^2 (fast). Eight sheathed thermocouples 50- to 180-mm long (2–7 in.) measured central temperatures in cell 1 from 700 to 1000°C. Five

thermocouples were C/A sheathed in 1.60-mm-OD (0.063-in.) Inconel. Three were W—3% Re vs W—25% Re wires insulated with beryllia, and sheathed in 1.60-mm-OD tantalum. The sheathed thermocouple wires were then wrapped with tungsten wire and emplaced in Nb—1% Zr tubes. Five additional C/A thermocouples measured outer peripheral temperatures. In a similar arrangement, eight thermocouples in cell 2 measured temperatures from 600 to 1400°C.

All thermocouples survived the test and were intact when photographed in postirradiation examination. Thermocouples were furnished by General Atomic.

OF-1 (August 1973 Through February 1975)

This capsule was irradiated 9340 hr in the ORR, accumulating an estimated neutron fluence of 1.1×10^{22} n/cm^2 (fast, >0.18 MeV). Two bare wire W—3% Re vs W—25% Re thermocouples were made with a single four-hole beryllia insulator to measure fuel centerline temperatures in two places of 950—1100°C and 1100—1250°C. The tungsten-rhenium thermocouples survived the irradiation but decalibrated 200—300°C. Four 1.60-mm-OD (0.063-in.) stainless-steel-sheathed C/A thermocouples survived temperatures of 650 to 1050°C, but seven of ten 1.02-mm-OD (0.040-in.) sheathed C/A thermocouples measuring temperatures from 550 to 950°C failed before the end of irradiation.

OF-2 (Started Irradiation June 1975)

This capsule was designed to operate 9600 hr in ORR to a neutron fluence of 9×10^{21} n/cm^2 (fast, >0.18 MeV). Two 1.60-mm-OD (0.063-in.) platinum-sheathed, alumina-insulated, Pt—5% Mo vs Pt—0.1% Mo thermocouples were installed to measure graphite spine temperatures in the upper and the middle fuel cells. A stainless-steel-sheathed C/A thermocouple was positioned near the upper platinum-molybdenum thermocouple for comparative readings. The two platinum-molybdenum thermocouples have operated to date for 3500 hr without failure and no evident drift at about 1050 and 1200°C. The comparison C/A thermocouple failed open circuit after 880 hr at temperatures as high as 1095°C. Eleven 1.60-mm-OD stainless steel-sheathed C/A thermocouples were installed in the upper cooler cell and seven in the middle hotter cells to measure graphite fuel holder temperatures of 500 to 950°C. None of these have failed to date.

6.10.5 Correction of Tungsten-Rhenium Thermocouple Data — M. W. Waddell, R. K. Williams, O. W. Hermann, R. L. Shepard, and T. G. Kollie

6.10.5.1 Analytic Method

Tungsten-rhenium alloy thermocouples have been used to measure the temperature of the fuel irradiated in several of the HRB experiments. However, their value has been limited because of rapid decalibration, which may be due to transmutation-induced composition changes. An analytic method of correcting tungsten-rhenium thermocouple temperature measurements for composition changes is currently being developed. This method will be evaluated by correcting the fuel temperatures in the HRB-3 experiment and comparing these values with calculated temperatures.

6.10.5.1.1 Theory. The emf produced by two dissimilar metals where junctions are at different temperatures can be described by:

$$\text{emf} = \int_{T_1}^{T_2} S_A(t)\ dt + \int_{T_2}^{T_1} S_B(t)\ dt\ , \qquad (1)$$

where

S_A = absolute Seebeck coefficient of the positive thermoelement,
S_B = absolute Seebeck coefficient of the negative thermoelement,
T_1 = temperature at the cold junction, and
T_2 = temperature at the hot junction.

When the two thermoelements are both homogeneous and metallurgically stable materials, the emf generated by the thermocouple depends only on the two junction temperatures and can be calculated from the temperature-dependent absolute Seebeck coefficient values for each thermocouple leg. In a reactor experiment, the tungsten-to-rhenium and rhenium-to-osmium transmutation rates are significant, and this change of composition is one factor that causes decalibration. Also, since the neutron flux and energy profiles are spatially dependent, irradiation generates a range of compositions along each thermoelement. This gives rise to a temperature gradient sensitivity. The expression for the emf can be

generalized to include the composition changes:

$$\text{emf} = \int_{T_1}^{T_2} S_A(t,x)\ dt + \int_{T_2}^{T_1} S_B(t,x)\ dt\ . \tag{2}$$

Then if the position dependence of the temperature and composition are known, the emf can be calculated from Eq. (2) and the error due to transmutation effects obtained. It should be noted that this model directly includes the effect of temperature gradients along the leads.

The centerline thermocouple compositions in the HRB-3 experiment were computed with the ORIGEN code,[54] using cross sections prepared with the CASDAR code.[67] ORIGEN solves this type of problem using the matrix exponential equation, which has been found to be a very powerful method for obtaining accurate and complete results. Compositions were computed as functions of irradiation time and axial position in the reactor.

The temperature gradient along the thermocouple wires in the HRB-3 capsule is not precisely known; temperatures are known accurately at only four points. As a first approximation the fuel is assumed to be isothermal and elsewhere the temperature gradient is assumed to be linear between the known temperatures.

Having determined the spatial variation of the temperature and thermocouple composition for a fixed irradiation time (fluence), the emf of an irradiated thermocouple can be calculated from Eq. (2) if the composition and temperature variation of S_A and S_B are known. This information is being experimentally obtained for tungsten-rhenium thermoelements as part of this study. Temperature corrections are then readily obtained by computing the emf of an irradiated thermocouple as a function of the hot junction temperature and finding the calculated emf that corresponds to the measured value. The temperature measurement error is then obtained by computing the difference between this corrected temperature and the temperature obtained by employing the measured emf and the standard thermocouple table.

6.10.5.1.2 Data. Table 6.58 lists the absolute Seebeck coefficients (S) of several W-Re and W-Re-Os alloys. These values were obtained from either direct measurements against platinum or from emf versus temperature curves from the literature. After more data are obtained on other W-Re-Os alloys, the results will be fitted to isothermal curves of Seebeck coefficients versus rhenium and osmium contents. Equation (2) can then be integrated numerically. Other alloys prepared include W–3% Re–0.66% Os, W–5% Re–0.66% Os, W–5% Re–1.80% Os, W–24.7% Re–0.62% Os, and W–19% Re–21% Os. Some of these composition occur during the course of an irradiation experiment and others have been included to obtain more general information on the effects of osmium additions. For the higher rhenium-content alloys, the data indicate that osmium tends to lower the S values, but the effect is roughly equivalent to the decrease that a further rhenium addition would produce. The decrease in S produced by osmium seems to be greater in the low-rhenium alloys, and the noncompensating S shifts in the two thermoelements probably produces the negative decalibrations observed.

Work to be completed before the model is evaluated includes:

1. Additional S data on W-Re-Os alloys will be obtained.

2. The sensitivity of the temperature error calculations to changes in the assumed temperature gradient will be determined.

3. The temperature gradient along the thermocouple will be calculated with the HEATING3 code if the calculations are too sensitive to changes in the temperature gradient.

4. The required cross-section values may be determined more accurately.

6.10.5.2 Empirical Method

Complementary to the thermoelectric calculations described above, an empirical method of determining *in situ* corrections of tungsten-rhenium thermocouple data was explored. This approach does not require knowledge of the time of irradiation or neutron fluence experienced by the thermocouple, and perhaps not of the temperature gradient. Experiments with in-pool furnace calibrations of the multijunction

Table 6.58. Absolute Seebeck Coefficients in the Tungsten-Rhenium-Osmium System

Composition (wt %)		Source	Absolute Seebeck Coefficient, μV/K, at Each Temperature in °C														
Re	Os		0	100	200	300	400	500	600	700	800	900	1000	1100	1200	1300	1400
0	0	a	0.8	3.6	6.9	10.0	13.3	15.8	17.6	18.9	19.8	20.1	20.3	20.4	20.4	20.3	20.2
3	0	bc	9.0	11.4	13.9	16.2	18.2	19.5	20.2	20.5	20.4	20.0	19.3	18.9	18.4	18.0	17.3
5	0	bc	12.9	13.8	15.2	16.7	18.2	19.1	19.5	19.5	19.1	18.5	18.7	17.1	16.4	15.9	15.2
9	0	d	12.1	12.8	13.4	13.8	14.2	14.5	14.6	14.6	14.5	14.3	14.0	13.6	13.1	12.4	11.6
20	0	be	−0.1	−0.7	−0.4	0.3	1.4	2.1	2.4	2.6	2.6	2.4	2.1	1.9	1.8	1.8	1.5
26	0	bc	−0.5	−1.8	−1.9	−1.6	−0.8	−0.3	−0.1	0.0	−0.1	−0.3	−0.7	−0.7	−0.8	−0.6	−0.9
24.83	0.24	bf	−0.3	−1.5	−1.7	−1.4	−0.5	0.0	0.2	0.3	0.2	0.0	−0.4	−0.4	−0.4	−0.3	−0.5
24.65	0.48	bf	−0.4	−1.6	−1.8	−1.4	−0.6	−0.1	0.1	0.2	0.1	−0.1	−0.5	−0.6	−0.6	−0.5	−0.8
23.98	1.45	bg	−0.4	−1.6	−1.8	−1.5	−0.7	−0.3	−0.1	0.0	−0.1	−0.4	−0.8	−0.8	−0.9	−0.8	−1.1
23.18	2.78	bh	0.0	−1.4	−1.8	−1.6	−0.9	−0.6	−0.5	−0.5	−0.7	−1.1	−1.5	−1.6	−1.7	−1.7	−2.0
9	3.62	d	3.2	3.9	4.6	5.2	5.7	6.2	6.6	6.9	7.3	7.5	7.7	7.8	7.9	7.9	7.8
22	6.51	d	−0.7	−0.9	−1.1	−1.4	−1.6	−1.8	−2.0	−2.2	−2.3	−2.5	−2.7	−2.8	−2.9	−3.1	−3.2
19	13.3	d	0.2	−0.2	−0.7	−1.2	−1.6	−2.1	−2.6	−3.1	−3.5	−4.0	−4.5	−4.9	−5.4	−5.9	−6.3

[a] J. P. Moore, R. S. Graves, W. Fulkerson, and D. L. McElroy, pp. V-G-1-V-G-35 in *The 5th Conference on Thermal Conductivity, Held at Denver, Colo., Oct. 20–22, 1965*, Denver University, 1967.

[b] Derived from emf vs temperature curves.

[c] *1975 Annual Book of ASTM Standards*, part 44, American Society for Testing and Materials, Philadelphia, pp. 770–76.

[d] Results of this study.

[e] G. W. Burns, National Bureau of Standards, private communication.

[f] General Electric Co., *High Temperature Materials Program Progr. Rep. 43, Part A*, GEMP-43A, pp. 71–73.

[g] Ibid., *Rep. 39, Part A*, GEMP-39A, pp. 33–35.

[h] Ibid., *Rep. 37, Part B*, GEMP-37B, pp. 67–70.

tungsten-rhenium thermocouple in HRB-8 showed the dependence of the irradiated thermocouple output on temperature gradient. The in-pool furnace maintained a constant true temperature of 700°C at the middle tungsten-rhenium junction, as measured by a C/A thermocouple in the capsule and in the furnace. The temperature gradient above the middle junction was then changed, by adjusting separate heater sections, to produce a flat, moderate, or steep axial temperature profile. With a flat gradient, shown in Fig. 6.71, the temperature error was −120°C with a steep gradient, the error increased to −210°C.

ORNL-DWG 76-12996

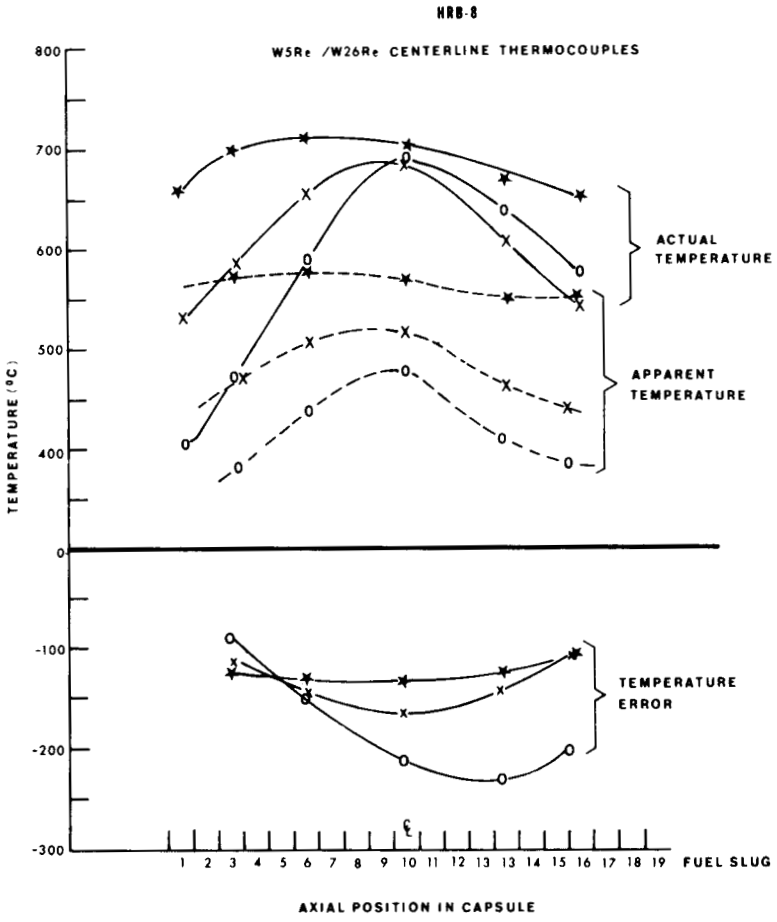

Fig. 6.71. Effect of Temperature Gradient on Decalibration of W–5% Re vs W–26% Re Centerline Thermocouples in Capsule HRB-8.

The thermometric purpose of the HRB-8 experiment was, however, to relate the thermoelectric output to the loop resistance of the irradiated centerline tungsten-rhenium thermocouple, continuing studies started in HRB-3 and -4. During start-up of reactor cycles, measurements of resistance of thermocouple loops and single wires, using the current-potential method, gave data that could be plotted as straight lines against thermocouple apparent temperatures. These lines shifted progressively with additional irradiation, as shown in Fig. 6.72. Their behavior was analyzed graphically by use of the assumption that the thermocouple alloys followed Matthiesen's rule — namely, that a temperature-independent increase of resistance at a given true temperature increased linearly with irradiation. This apparently held true for the first 2000 hr irradiation. The analytic method, shown in Fig. 6.73, allowed a correction to be made for the difference (εT) between the indicated and true temperatures. The calculated calibration drift is shown in Fig. 6.74, which also shows the effect of gradient observed in the in-pool furnace test.

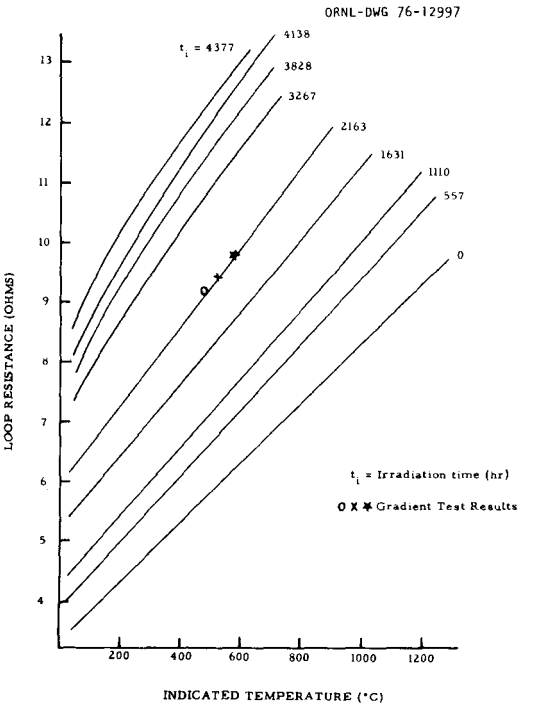

Fig. 6.72. Decalibration of Tungsten-Rhenium Thermocouples Irradiated in HRB-8.

ORNL-DWG 76-12993

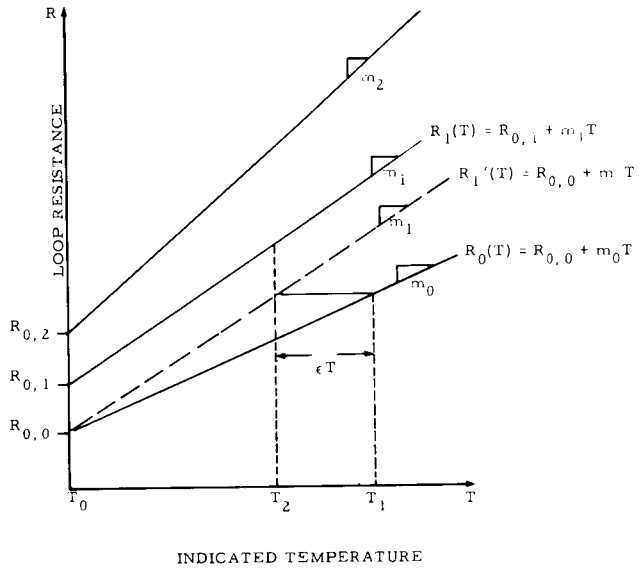

Matthiesen's Rule: $R = R_0 + R_T$

For: $R_1'(T_2) = R_0(T_1)$,

Then: $R_{0,0} + m_1T_2 = R_{0,0} + m_0T_1$

From which: $\epsilon T = T_1 - T_2 = \frac{(m_1 - m_0)}{m_1} T_1$

Fig. 6.73. Irradiated Tungsten-Rhenium Thermocouple Calibration Correction Using Matthiesen's Rule.

ORNL-DWG 76-12998

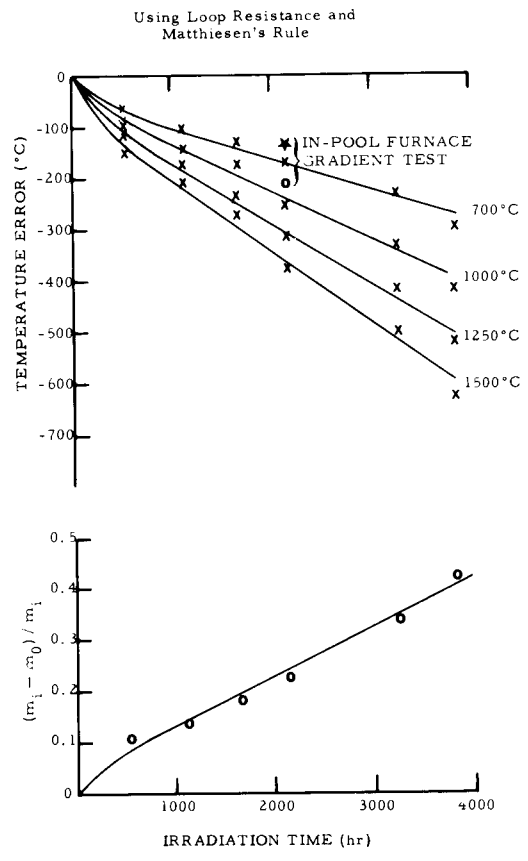

Fig. 6.74. Calibration Drift in Irradiated Tungsten-Rhenium Thermocouples in HRB-8.

A singular finding was that the three sets of thermoelectric emf and loop resistance data obtained in the in-pool furnace gradient testing all fell on the same line in Fig. 6.72. This result suggests that both the Seebeck coefficient and electrical resistivities of the irradiated tungsten-rhenium wires are affected similarly by irradiation and that their ratio is not strongly temperature dependent. It has been proposed that the study of properties of these wires, described in Sect. 6.10.5.1, be expanded to include resistivity measurements so that both equivalent circuit models shown in Fig. 6.75 can be evaluated for irradiation alloys.

ORNL-DWG 76-12992

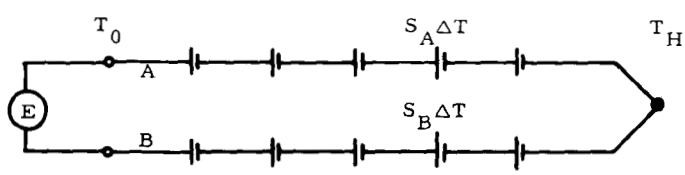

$$E = \sum_{T_0}^{T_H} S_A(T,t)\,\Delta T - \sum_{T_0}^{T_H} S_B(T,t)\,\Delta T$$

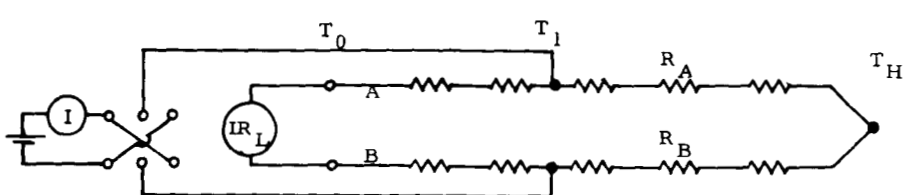

$$IR_L = I\sum_{T_1}^{T_H} R_A(T,t) + I\sum_{T_1}^{T_H} R_B(T,t)$$

$$V_0 = E \qquad T_H = f(E, T_0)$$

$$V_1 = E + IR_L \qquad R_L = \frac{V_1 - V_2}{2\,I}$$

$$V_2 = E - IR_L$$

Fig. 6.75. Equivalent Circuit Models for Thermal emf and Loop Resistance of Irradiated Thermocouples.

6.11 PERFORMANCE ASSESSMENT OF COATED PARTICLE FUELS — F. J. Homan

Information gained through irradiation testing is interpreted and applied to process and equipment development and specification writing. Most of the attention during this reporting period has been directed at thermal analysis and the determination of failed particle fractions. A little work was done to adapt computer models for coated particle mechanical analysis for use in direct evaluation of the data from loose particle irradiations in HFIR Target (HT) capsules. Dynamic testing methods were studied briefly to determine whether our thermal analysis procedures could be improved through such testing, but we concluded that the cost of this work was not justified by the additional information we would get. The studies of fission product reaction with SiC represent a new field, where additional work is planned for the future.

6.11.1 Thermal Analysis — F. J. Homan

During the reporting period the procedures for thermal analysis of several types of irradiation experiments were formalized. These procedures are now being applied routinely to the analysis of irradiation experiments in HFIR, the ORR, the Dragon Reactor, and the Peach Bottom Reactor. A brief outline of the procedures is given below: Each procedure is being thoroughly documented in a topical report.

6.11.1.1 HT Capsules

The thermal analysis procedure for HT (HFIR target) capsules was developed by Kania.[23] Before the development of this procedure the operating temperatures of the loose coated particles in the HT capsules were assumed equal to the design temperatures for the specimen holders, which were determined by a one-dimensional radial heat flow calculation.[68] Kania's procedure considers the temperature rise from the Poco graphite sleeve to the specimen holders (a schematic diagram of a typical HT capsule for the irradiation of loose coated particles is shown as Fig. 7.28 of ref. 21) and from the inner surface of the specimen holder annulus to the particles themselves. Axial heat flow is considered as

well as radial. Temperatures of several hundred degrees above the design graphite sleeve temperatures have been calculated. Examples of the calculation are shown in Fig. 6.76 for 900 and 1250°C design graphite temperatures. Since the HT experiments are uninstrumented the calculations are the only temperature information available in the analysis of HT data. We feel that the temperatures calculated by Kania's procedure are more accurate than the design temperatures used previously and have significantly improved the quality of information coming from these experiments.

6.11.1.2 HRB Capsules

The basic procedures for thermal analysis of the HRB capsules were outlined by Homan[69,70] and expanded by Valentine.[71] Before the development of this procedure the HRB capsule fuel temperatures were calculated with GENGTC[68] from fission heat rates calculated with FABGEN.[44] Calculation of accurate fission heat rates requires knowledge of the time variation of the fission rates at each axial position in the capsule. Good cross-section data are also needed. The neutron fluxes increase with time during the 23-day HFIR cycles, as the control elements are withdrawn (see ref. 33 for a brief description). The shape of the flux vs time curve is known only at the reactor horizontal midplane, and even this information is suspect because it applies only to an empty HRB facility. The influence of a capsule on the neutron fluxes is not known. Calculating the graphite midwall temperatures with the GENGTC-FABGEN thermal analysis could not achieve good agreement with the temperatures measured with Chromel vs Alumel thermocouples. Because the HRB capsules were highly instrumented, we decided to use the instrumentation to advantage in the thermal analysis. A mathematical model was developed[70] to calculate fission heat rates and sweep gas composition as functions of time during each HFIR cycle. This information was then used, with the same model, to calculate fuel specimen surface and center temperatures. While the capsules have all had centerline thermometry, the centerline temperature data have never been good because the centerline devices decalibrated.

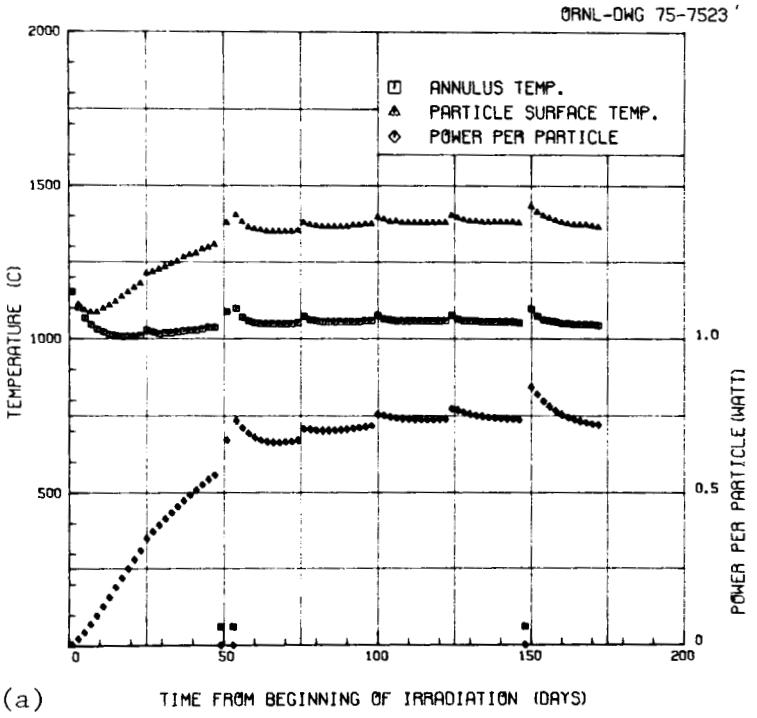

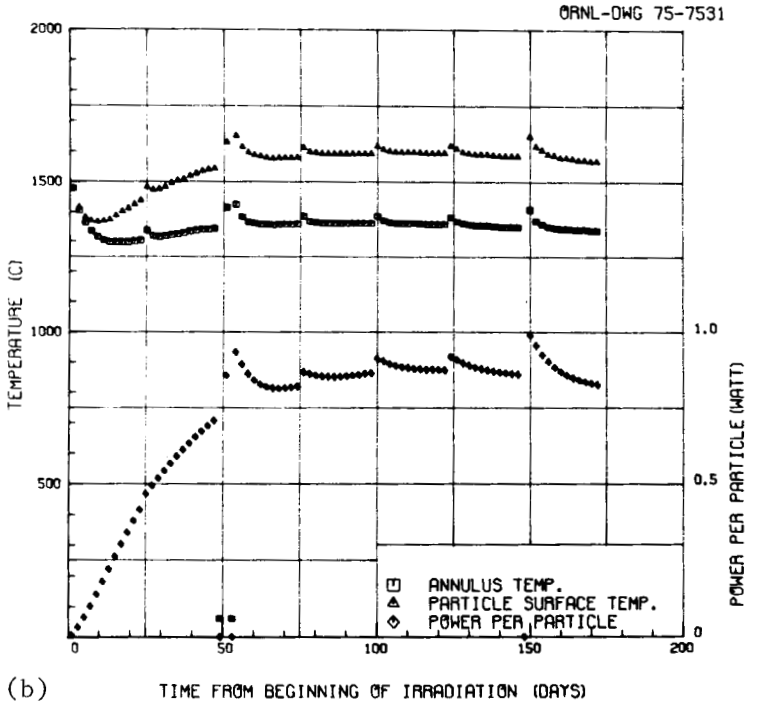

Fig. 6.76. Examples of Temperature and Power Calculations for Loose Particles in an HT Capsule. Batch OR-1849 816-μm-diam particles in holders (a) 13 and (b) 26 of capsules HT-14 and -15.

Techniques are being developed (see Sect. 6.10.5 of this report) to correct the centerline temperature data on previous HRB capsules. In addition, absolute temperature measuring devices are being developed (see Sect. 6.10.2), which hopefully will not decalibrate. Eventually we hope that a direct comparison of measurement with calculation will be possible for fuel center temperatures. This comparison will reflect directly on the quality of the thermal analysis procedures being used.

Valentine[71] improved on the procedure described above by developing a capability for considering nonsymmetric geometries (asymmetric gaps). Also, Valentine's method is highly automated and has removed many of the hand operations described in ref. 69. The ENCTRK code is coupled with a plotting package, which permits graphical display of graphite midwall, fuel surface, and fuel center temperatures for each specimen, for each HFIR cycle. Fission heat rates and sweep gas composition can also be plotted.

6.11.1.3 ORR Capsules

The geometry of the ORR capsules is somewhat more complex than that of the HT and HRB capsules. The first ORR capsule, OF-1, had five fuel holes; the second, OF-2, has four. Because of the complex geometry, simple, one-dimensional radial heat flow models such as those used for the HT and HRB capsules could not be used. Kania and Thoms have developed methods for the thermal analysis of ORR capsules, using the HEATING3 computer code.[38] The two R-θ grid models employed for the OF-1 analysis are shown in Sect. 6.7.1 of this report, in Fig. 6.54. Sample temperature calculations for the OF-1 capsule are shown in Fig. 6.55 of Sect. 6.7.1. A detailed description of the thermal analysis procedures for ORR capsules is given elsewhere.[72]

6.11.1.4 Recycle Test Elements

The Recycle Test Elements (RTEs) were irradiated in the Peach Bottom Reactor. The fuel for these elements was fabricated at ORNL, and the elements were loaded by General Atomic Company. The present

status of these experiments is covered in Sect. 6.8 of this report. All coordination between Philadelphia Electric Company (the owner of the Peach Bottom Reactor) and the experimenters was done by General Atomic personnel. General Atomic had a number of Fuel Test Elements (FTE) and Proof Test Elements (PTE) in the Peach Bottom Reactor at the same time as the RTEs and has developed methods for thermal analysis for these elements.[73] The thermal analysis of the Recycle Test Elements has been subcontracted to General Atomic Company. The results and methods of their analysis will be reported with the final report on the RTE series, which is scheduled for September 1977.

6.11.1.5 Dragon Reactor Experiment

The MET VII Experiment was inserted into the Dragon Reactor in January 1975. The experiment is scheduled to run slightly over four years. When the experiment was planned it was assumed that thermal analysis of the ORNL specimens would be performed by personnel from the Dragon Project. However, with the present uncertainty about the status of the Dragon Project, it is unlikely that there will be sufficient manpower available for this work. Therefore, a thermal analysis similar to the one outlined earlier for ORR capsules will be performed if fuel temperatures are not provided by Dragon. The status of the MET VII Experiment is covered in Sect. 6.8 of this report.

6.11.2 Mechanical Analysis of HT-12, -13, -14, and -15 Experiments

Several modifications have been made to the stress analysis code, STRETCH, in an attempt to improve agreement between the calculated and observed behavior of pyrocarbon-coated fuel particles during irradiation in a reactor environment. Specific areas of the code that were modified include the neutron-induced densification model and the neutron-induced creep calculation. Also, the capability for modeling surface temperature variations was added. HFIR Target experiments HT-12 through -15 were simulated with the modified code, and the neutron-fluence vs particle-failure predictions compared favorably with the experimental results. This work is described completely by Valentine[22] along with listings of the modified FORTRAN IV main program and user instructions.

6.11.3 Coated Particle Failure Analysis — F. J. Homan

The failed particle specification is a very important aspect of large HTGR fuel development. Currently an accurate, inexpensive way to measure this parameter is lacking. Metallography has been valuable for determining failure mechanisms but is too expensive and time consuming for measuring failure statistics. Too many particles must be examined. Chlorine leaching has potential, but it is expensive, and many uncertainties are still associated with it. For example, one cannot establish unequivocally (with present technology) whether a given concentration of uranium or thorium in the leaching solution is due to a few failed particles, or due to a small amount of heavy metal being leached through intact coatings on all particles. Further, it is not known whether the leaching process itself damages the coatings.

The Irradiated Microsphere Gamma Analyzer (IMGA) system we have developed provides an inexpensive, quick examination of each particle within a fuel rod. The rod is first electrolytically disintegrated, and then each recovered particle is examined by a Ge-Li detector to determine its gamma spectrum. A decision is then made whether the particle is failed or intact, and particles can then be segregated according to preset gamma spectrum characteristics for further examination. The entire process (after disintegration) is computer controlled. The ORNL unit is the only one of its kind in the world. Hot operation is scheduled for March 1976.

6.11.3.1 Failure Mechanisms — E. L. Long, Jr.

Five mechanisms that can either cause or lead to failed particles have been identified. Two are classified as thermochemical and three are considered mechanical. These mechanisms are discussed in more detail below.

The term "amoeba" was adopted to described kernel migration toward the hotter side of the particle. Amoeba is primarily a function of time, temperature, and thermal gradient, and can result in coating failure as the kernel migrates through coating layers. All fissile and fertile fuels considered to date have the potential of exhibiting amoeba,

although kernel migration has not been observed to date with partially converted weak-acid-resin-derived fissile kernels, and ThO_2 has proved to be very stable and meets performance requirements. An example of amoeba is shown in Fig. 6.77. Detailed studies have been under way with irradiated and unirradiated particles at ORNL and GA to quantify amoeba and establish predictable performance limits of various fuels (see Chap. 4 of this report).

Another failure mechanism, which is also thermochemical and occurs only in Triso-coated particles, involves volatile high-yield fission products. In this failure mechanism the lanthanides (La, Pr, Ce, Nd) distill out of the kernels and collect on the cold side of the particle adjacent to the inner surface of the SiC layer. The collection of the rare earths on the cold side of the particle typically results in graphitization of the inner LTI layer and can result in either mechanical failure of the SiC and outer LTI layer or failure from chemical attack of the SiC. The thermal gradient across a particle is a significant factor since the SiC and outer LTI fail mechanically primarily in the peripheral regions of fuel rods, where a steep thermal gradient exists. At temperatures above reference HTGR design, the SiC is subject to chemical attack by the rare earths, which can limit the fuel performance.[74] Examples of fission product interaction are shown in Figs. 6.78 and 6.79. Fortunately, the rare earths can be contained within the kernel by providing sufficient oxygen to form stable rare-earth oxides.

A third failure mechanism, pressure vessel failure, is mechanical and occurs when the gas pressure within the Triso- or Biso-coated particle exceeds the strength of the coating. This can occur when either a particle does not meet design specifications or the coating properties have degraded from either of the above thermochemical mechanisms. An example of pressure-vessel failure is shown in Fig. 6.80.

A second mechanical failure mechanism has been identified[75] and is the result of mechanical interaction between the coating and matrix during irradiation. Small tears can be initiated in coatings during fuel rod fabrication. If the bond between the matrix and coating is sufficiently strong, these tears can lead to coating failure as a

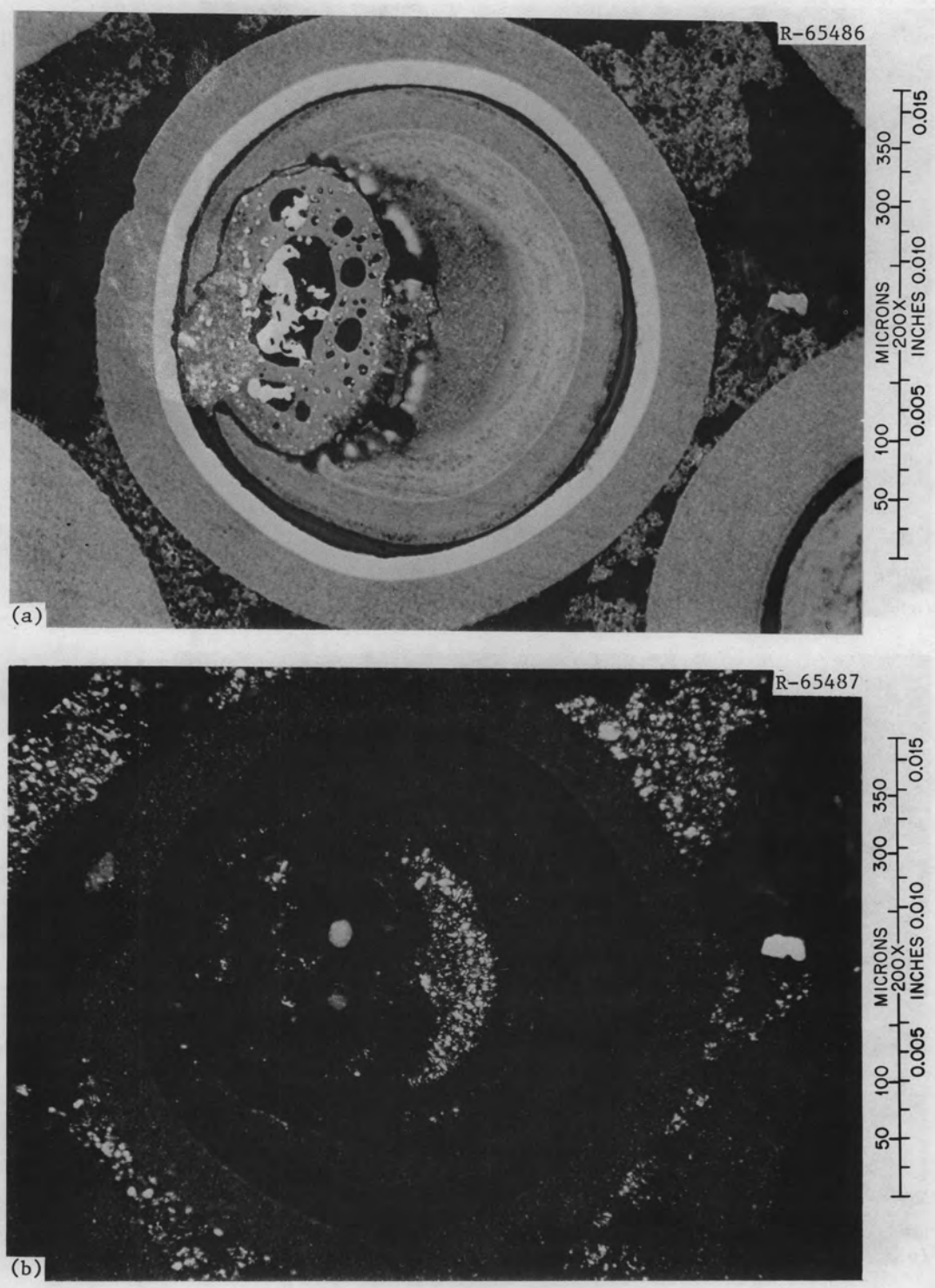

Fig. 6.77. Unidirectional Migration (Amoeba) of UO_2 Kernel Toward the Hot Side of the Particle. (a) Bright field. (b) Polarized light.

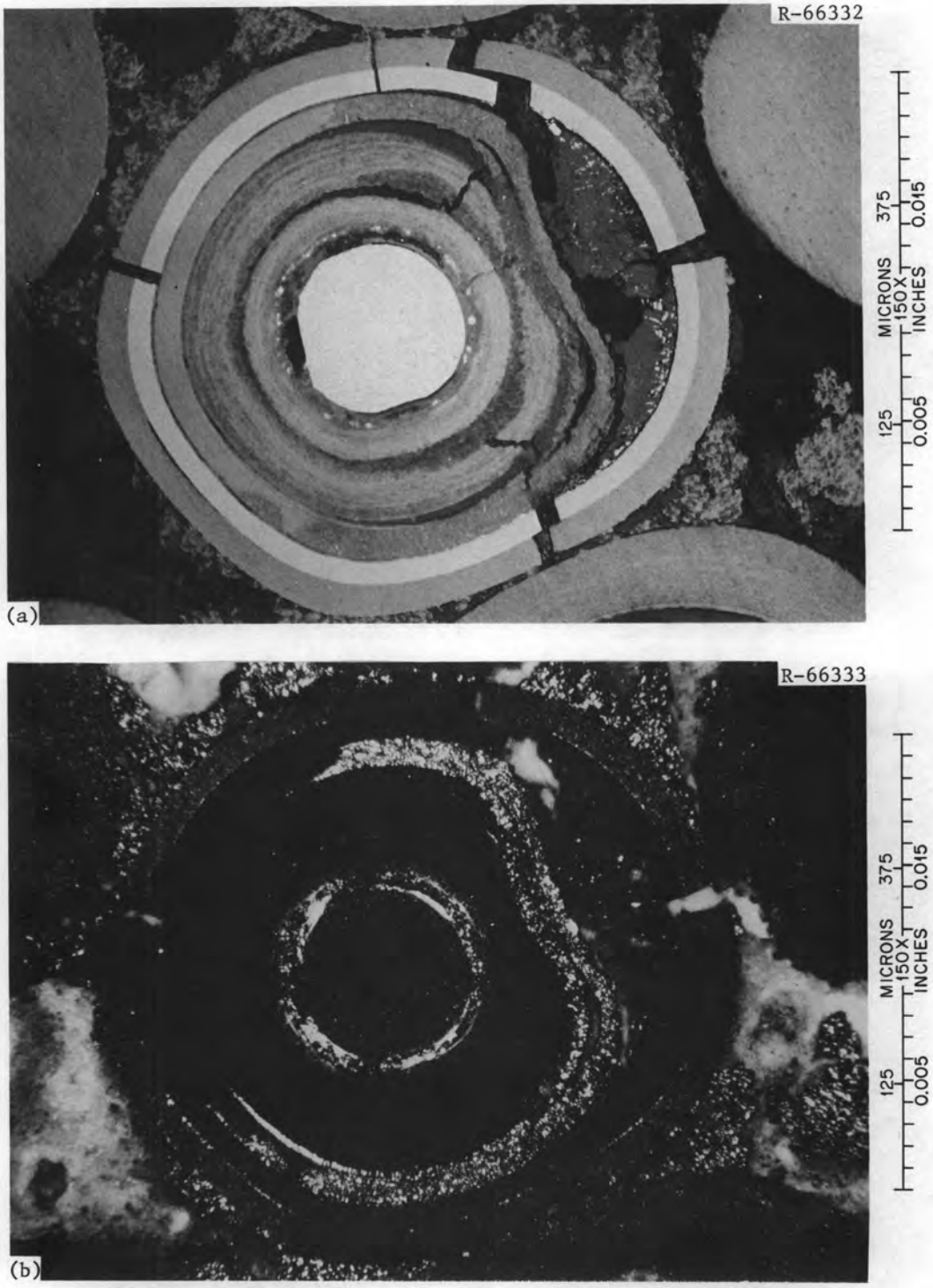

Fig. 6.78. Failure Caused by Collection of Rare Earth Fission Products La, Pr, Ce, and Nd on the Cold Side of the Particle. 150×. (a) Bright field. (b) Polarized light. Note graphitization and deformation of inner pyrocarbon layer due to collection of fission products adjacent to SiC layer.

Fig. 6.79. Example of Attack of SiC Layer by Rare-Earth Fission Products La, Pr, Ce, and Nd on the Cold Side of the Particle. This particle operated above the present design limits for HTGR.

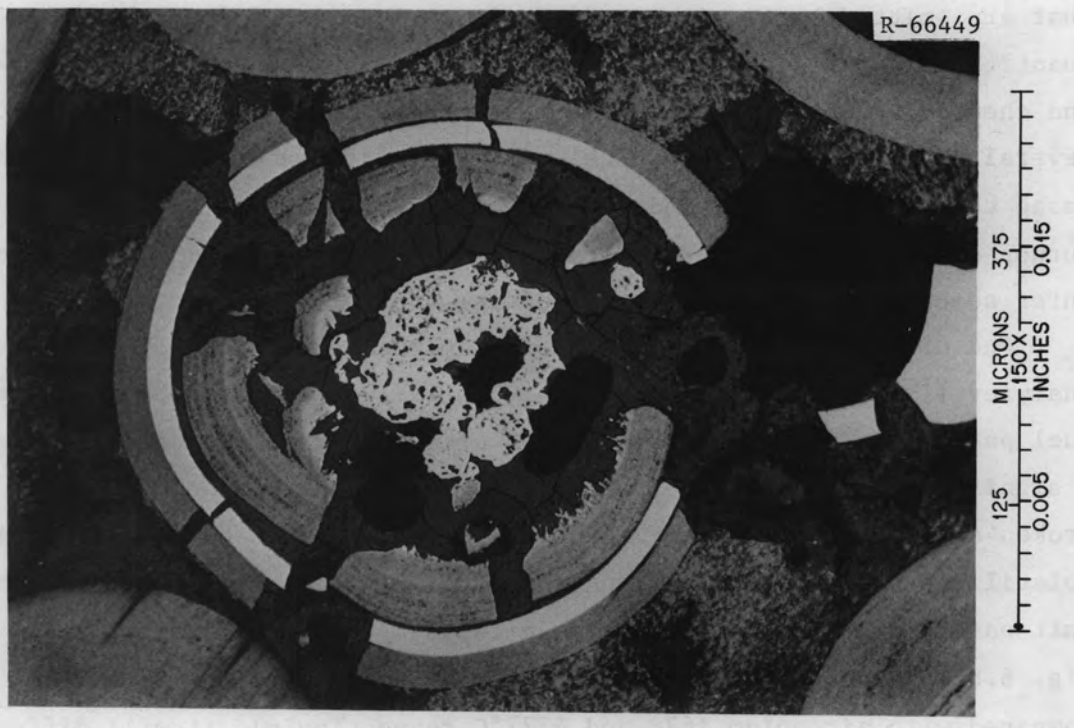

Fig. 6.80. Example of a Pressure-Vessel Failure. The kernel was originally UO_2 but reacted after coating failure to a carbide form.

result of irradiation-induced shrinkage. To date this failure mode has been observed only in rods that had been carbonized in graphite tubes to simulate in-block carbonization and did not meet design specifications for pitch-coke yield or microporosity.

The last category of failure mechanisms consists of fabrication defects that can be introduced during coating, handling, or fuel rod fabrication operations. These defects are generally in the form of missing or defective coating layers, out-of-specification (weak) particles that are broken during rod fabrication, or coatings with poor properties that fail during irradiation, as shown in Fig. 6.81.

6.11.3.2 Irradiated Microsphere Gamma Analyzer System — K. H. Valentine

A new system is being designed and fabricated to provide ORNL with the capability for making statistically accurate determinations of HTGR fuel particle performance. Very basically, the system consists of a high resolution Ge-Li gamma detector, a computer-based pulse height analysis system (PHA), and an automatic sample changer. The major purpose of this system is to record the energy spectra of gamma rays that are emitted by fission products in an irradiated fuel particle. Quantitative analysis of the gamma spectra plus knowledge of the physical and chemical properties of the gamma emitters then allows us to evaluate several important aspects of fuel particle performance during irradiation. Among these are fission product retention properties of the coatings and burnup of heavy metal in the kernels. Perhaps we may even be able to infer something about kernel and coating operating temperatures.

One of the primary functions of the Irradiated Microsphere Gamma Analyzer (IMGA) will be to determine the failure fraction of irradiated fuel particles; that is, the fraction of fuel particles that have lost a significant amount of their fission products through defective or broken coatings. This determination is made possible by the different volatilities of the two fission products ^{95}Zr and ^{137}Cs, both of which emit easily detectable gamma rays in the 600 to 800 keV range (see Fig. 6.82). Because of the relatively low boiling point of cesium compared with zirconium (678 and 4377°C respectively), it will diffuse or escape from a defective particle and much more readily than zirconium

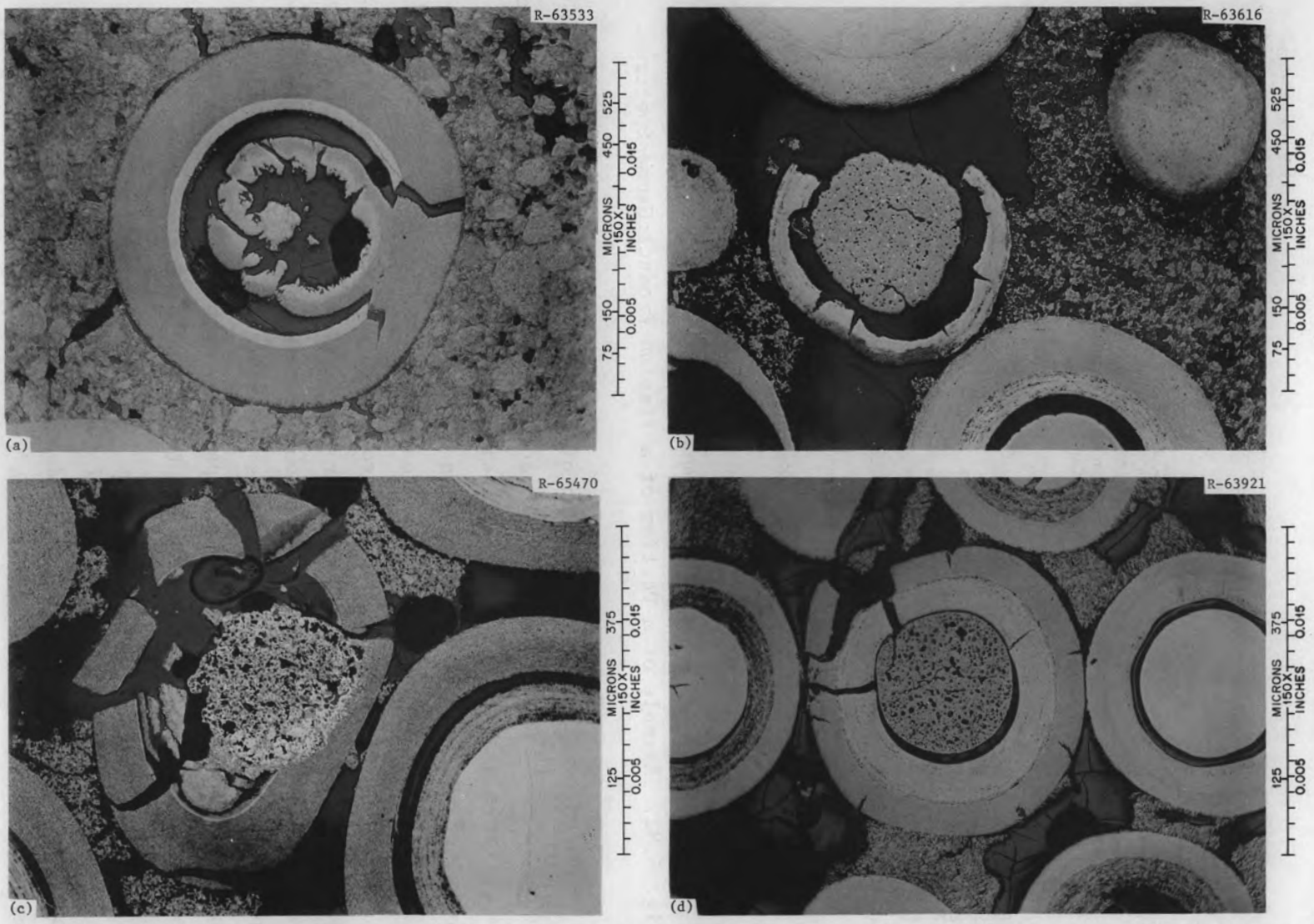

Fig. 6.81. Examples of Particles That Failed Because of Manufacturing Defects. (a) Portion of SiC missing. (b) Buffer missing. (c) Nonspherical particle. (d) Poor coating properties.

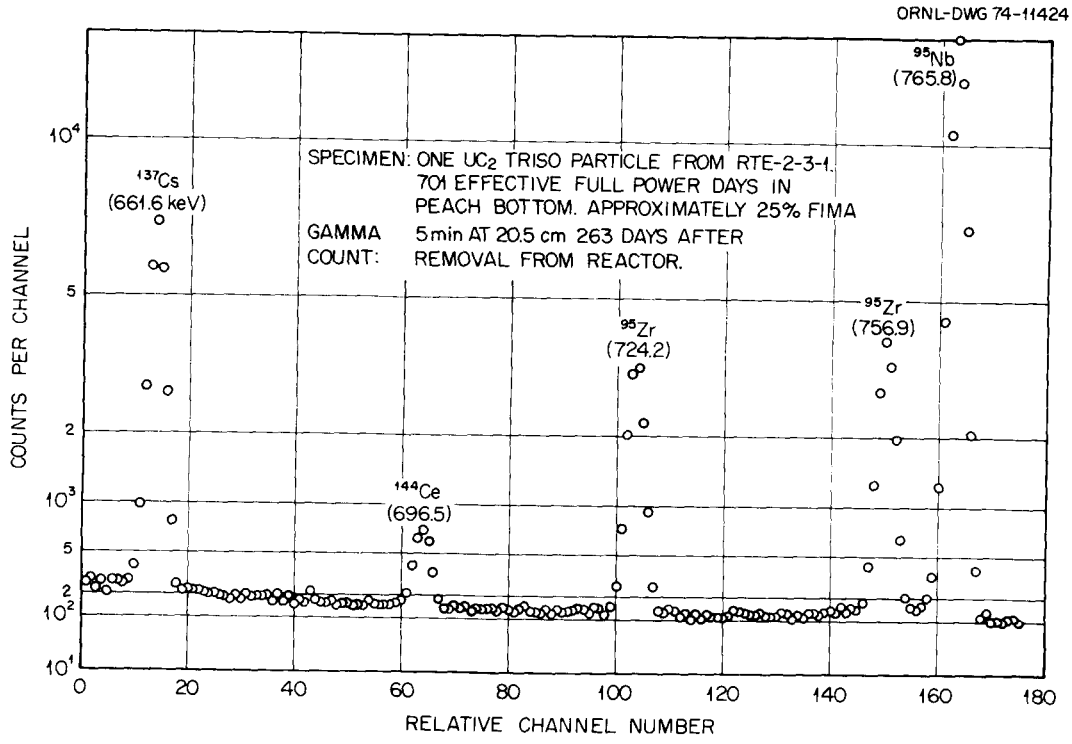

Fig. 6.82. Example of a Portion of a Fission Product Gamma Spectrum.

in the high-temperature environment of the HTGR. Thus a measurement of the ratio of ^{137}Cs activity to ^{95}Zr activity provides a direct measure of the particle's ability to retain fission products. An attractive feature of the ratio determination is its insensitivity to variations in the kernel size and heavy metal loading.

Any high-resolution gamma spectroscopy system could be used to make the ratio measurement for one or two particles. However, statistical considerations (see next section) dictate that from several hundred to several thousand particles be examined to accurately determine the failure fraction of a multiparticle sample. This would be a staggering task if each particle had to be handled individually, but it is a relatively simple task for IMGA.

Figure 6.83 is a diagram made of the system during the initial planning stage. Although the final design of the particle handler and sample changer diverges somewhat from that shown, it still illustrates

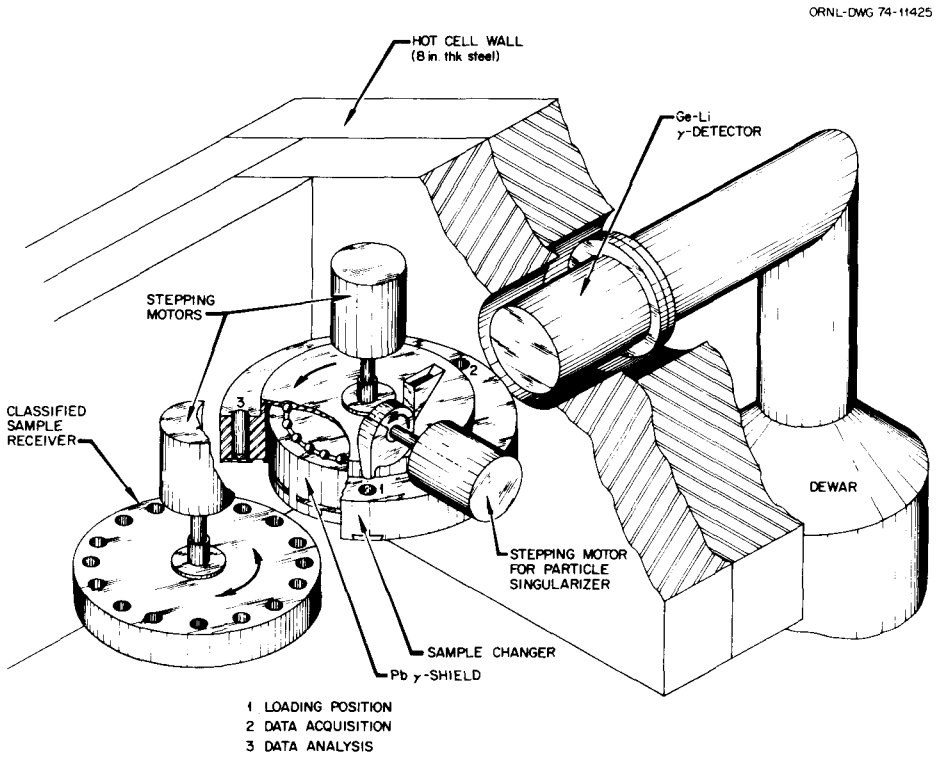

Fig. 6.83. Proposed Design for Irradiated Microsphere Gamma Analyzer. Steel cell wall thickness is about 20 cm.

the basic functions of IMGA. From Fig. 6.83, the automated particle handler is seen to consist of a particle singularizer with feed hopper, a sample changer, and a sample receiver, all of which are controlled by an on-line computer. The sequential operation of the system is as follows:

1. A preprogrammed number of particles (only one for failure fraction determination) is loaded into the sample changer at position 1.

2. A 120° rotation of the sample changer aligns the particle with the Ge-Li gamma detector. Data acquisition is initiated and a fission-product gamma spectrum is accumulated. The next particle is loaded at position 1.

3. When the predetermined data acquisition time elapses, another 120° rotation of the sample changer aligns the next particle with the detector. The spectrum for the first particle is shifted to another part of the core memory and data acquisition is again initiated. After

loading the third particle at position 1, the central processor (CPU) is free to analyze the spectrum of the first particle, which is holding at position 3.

4. From results of the spectrum analysis, the CPU makes a logical decision and aligns one of the 20 bins of the sample receiver under position 3 of the sample changer. The particle is then released into the bin. The analysis is recorded on magnetic tape.

5. The cycle is repeated until interrupted by operator intervention.

Projected particle examination rates are on the order of 5 to 10 per minute, which means that the failure fraction for a sample of particles can be estimated in just a few hours. Although the system is designed to operate only with loose particles, the particles from bonded rods can also be examined after electrolytic deconsolidation of the rod.

The ability of IMGA to segregate particles according to selected properties of their fission product gamma spectra should also prove extremely useful for studying the various particle failure mechanisms. It will allow us to prepare metallographic specimens that contain only failed particles, thereby reducing substantially the time and cost of metallographic preparation.

6.11.3.3 Statistical Basis for Failure-Fraction Determinations
K. H. Valentine

Up to and including the present, failure fraction determinations have been based on visual observation of polished metallographic cross sections or, in a few cases, on visual observation of loose particles. In a typical metallographic cross section of a 13-mm-diam (1/2-in.) experimental fuel rod, one may see from 10 to 50 particles of the type of interest. If we are optimistic and assume a sample size of 100, then Fig. 6.84 shows the relationship between what is observed and what is likely to be true.

The solid line of Fig. 6.84 is a plot of estimated failure-fraction against the number of observed failures. For example, one observed failure implies a failure fraction of 1% and 10 failures implies a value of 10%. This observed value is exact for the particles in the

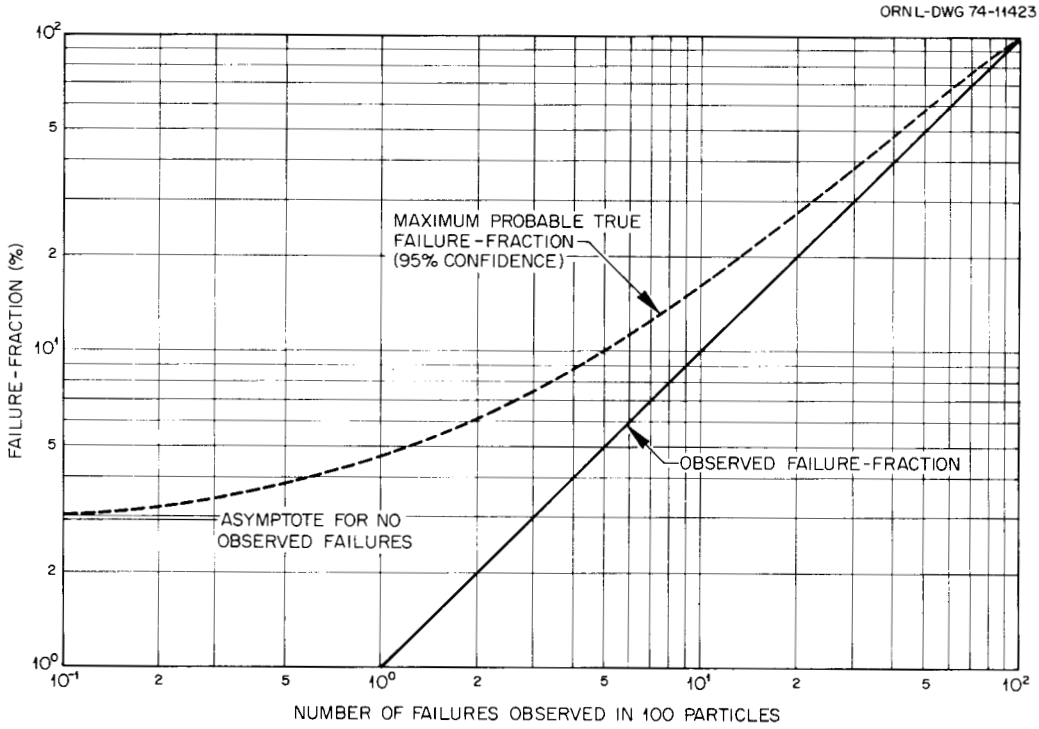

Fig. 6.84. Failure Fraction Determination from Examination of 100 Particles.

cross section. However, we must now ask the question, "How well does the observed failure fraction represent all the particles in the rod?" The dashed curve of Fig. 6.84 represents one possible answer to this question. It represents the locus of failure fraction values that are larger than the true failure fraction for the entire fuel rod* with 95% confidence.† Thus if the observed failure fraction is 10%, then one can be 95% confident that the true value is less than 16.1%. Similarly, an observed failure fraction of 1% implies a true value that is less than 4.6%. However, even if no failures are observed, we can only be 95% certain that the true value is less than 3.1%. In view of the current design limit on fuel particle failure fraction of 1% at end-of-life, we clearly need to look at many more than a hundred particles.

---

*Based on the assumption that the fuel rod contains an infinite population of fuel particles.

†To make a statement with 95% confidence means that there is a 95% probability that the statement is true.

Figure 6.85 shows the magnitude of the problem of demonstrating that a particulate fuel satisfies the current design limit on fuel failure fraction. The curve labeled "95% confidence that failure fraction <0.01" is similar to the curve of Fig. 6.84 except that in the present case, the number of observed failures is specified rather than the failure fraction. Points on this curve represent conditions that must be satisfied in order to state with 95% confidence that the failure fraction is less than 0.01. For instance, one observed failure out of 480 particles or 80 observed failures out of 9500 particles are both sufficient conditions.

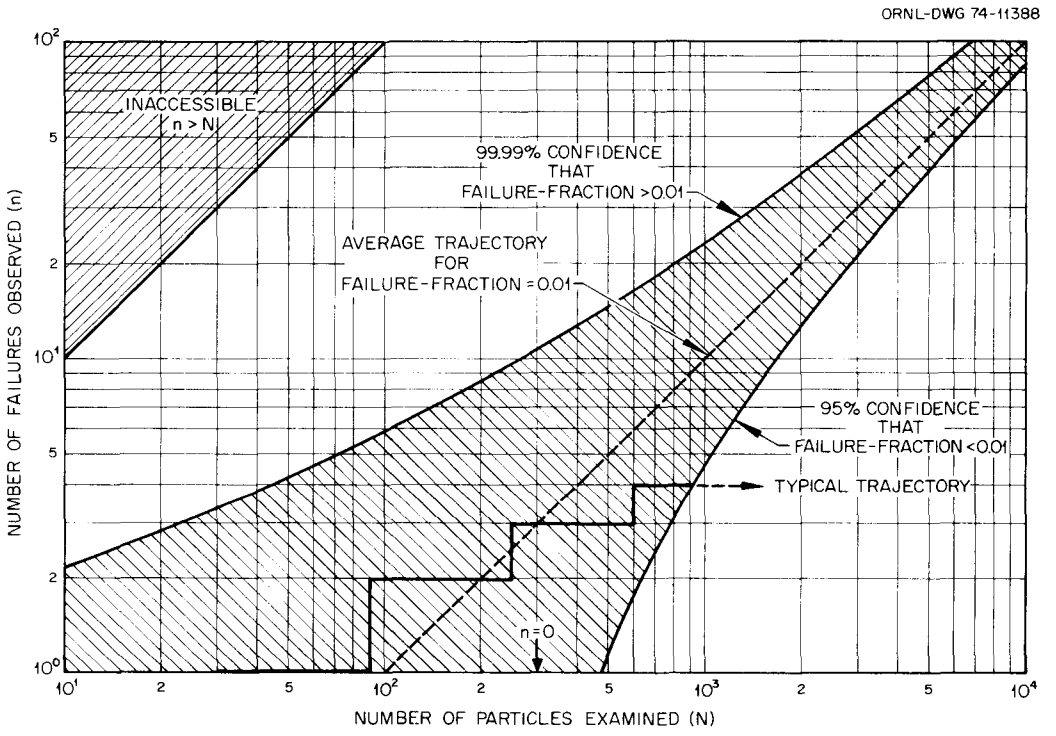

Fig. 6.85. Confidence Limits for Fuel Particle Examination.

Knowledge of the 95% confidence level curve also allows us to establish a simple algorithm for qualifying the various HTGR fuel concepts with a system such as IMGA. For this application, fuel particles are fed through the system individually and failed, not-failed decision is made for each particle. A typical trajectory for

this procedure is shown in the figure. The first failure is found during the 30th examination, the second during the 90th, the third during the 250th and the fourth during the 600th. No more failures are detected up to the 911th examination at which time the trajectory crossed the 95% confidence curve. The intersection of a trajectory with any point on this curve yields 95% confidence that the failure fraction is less than 0.01 and therefore demonstrates (with 95% confidence) that the design limit has been satisfied. Similarly, the intersection of a trajectory with any point on the line labeled "99.99% confidence that failure fraction >0.01" yields 99.99% confidence that the failure fraction is greater than 0.01. This line is included to provide a clear-cut criterion for terminating the examination of fuels that have a true failure fraction in excess of 0.01. Although the 99.99% confidence was chosen arbitrarily for illustrative purposes, practical values should probably be fairly high to minimize the probability of rejecting a fuel that is actually acceptable.

For purposes of calculating points on the confidence curves, n (number of observed failures) was assumed to be a binomial variable to make the results completely general and unrestricted. Therefore, the probability, $P(n)$ of seeing n failures out of N examinations is given by

$$P(n) = \frac{N!}{n!\,(N-n)!}\,\eta^{n}(1-\eta)^{N-n} , \tag{1}$$

where η is the true failure fraction for the sample. The equations that relate the failure fraction and confidence coefficient to n and N are:

$$I_{\eta}(n+1,\ N-n+1) = C , \tag{2}$$

$$I_{\eta}(n+1,\ N-n+1) = 1-C , \tag{3}$$

where I_{η} is the incomplete beta function defined as:

$$I_\eta(j,k) = \frac{1}{B(j,k)} \int_0^\eta t^{j-1}(1-t)^{k-1}\, dt$$

$$= 1 - (1-\eta)^{j+k+1} \sum_{i=0}^{j-1} \binom{j+k+1}{i} \left(\frac{\eta}{1-\eta}\right)^i ,$$

where $B(j,k)$ is the (complete) beta function, and C is the confidence coefficient. The solution of Eq. (2) for η yields the value of the failure fraction that is greater than the true failure fraction with $C \times 100\%$ confidence; and solution of Eq. (3) yields the value that is less than the true failure fraction with $C \times 100\%$ confidence. Solutions of Eqs. (2) and (3) were used to generate the 95 and 99.99% confidence curves of Fig. 6.85. For example, at $n = 5$, Eqs. (2) and (3) become respectively

$$I_{0.01}(6,N-4) = 0.95 \Rightarrow N \approx 1047 \text{ and}$$

$$I_{0.01}(6,N-4) = 0.0001 \Rightarrow N \approx 71 .$$

In general, solution of the above equations for any one of the four variables (n, N, η, C) is tedious and is best done by a computer using iterative techniques.

Up to this point, we have tacitly assumed that it is possible to establish with 100% confidence, whether or not a particle is failed. However, when the failure criteria are based on the ratio of two fission product activities (e.g., Cs/Zr), as determined by gamma counting, then the statistics of the gamma-counting process must also be considered.

Eventually we hope to be examining end-of-life HTGR fuel particles that will have particle failure fractions (fissile + fertile) of 1% or less. Thus, if only one particle in a hundred is erroneously classified, the resulting error in the failure fraction can be quite large. A good deal of insight can be obtained by assuming normal distributions for the two fission product activities, since the resulting distribution for the ratio can then be solved for analytically. Denoting the two fission product gamma counts by x and y, the distributions for the measured counts of a group of similar particles are:

$$P_x(x) = \exp[-(x - M)^2/2\sigma_x^2]/\sigma_x\sqrt{2\pi} \quad , \tag{4}$$

$$P_y(y) = \exp[-(y - N)^2/2\sigma_y^2]/\sigma_y\sqrt{2\pi} \quad , \tag{5}$$

where M and N are the mean values of x and y, respectively, and σ_x and σ_y are the standard deviations of the distributions, P_x and P_y. It can be shown that the distribution of the ratio, $R = y/x$, is given by

$$P(R) = \int_0^\infty P_x(t)P_y(Rt)t \quad dt \approx \int_{-\infty}^\infty P_x(t)P_y(Rt)t \quad dt \ . \tag{6}$$

Performing the indicated integration and defining $R_M = N/M$, $s_x = x/M$, $s_y = y/N$, and $s^2(R) = R^2 s_x^2 + R_M^2 s_y^2$, the result is

$$P(R) = \frac{1}{\sqrt{2\pi}\ s(R)} \frac{R_M(Rs_x^2 + R_M s_y^2)}{s^2(R)} \exp[-(R - R_M)^2/2s^2(R)] \ . \tag{7}$$

The distribution for the ratio is seen to be a normal-like distribution with a maximum near $R = R_M$. The major difference is that it rises to the maximum more rapidly and falls from the maximum more slowly than a true normal distribution.

The problem of separating failed particles from unfailed particles can now be stated in the following terms. Let the main group of unfailed particles be characterized by the ratio R_g and failed particles by $R \lesssim R_b$ where $R_g > R_b$. To accurately determine the failure fraction, the mixing of the two groups must be kept to an acceptable minimum or:

$$\int_{-\infty}^{R_b} P(R_g) \quad dR_g \ll \text{failure fraction} \ . \tag{8}$$

In many, if not most, cases the above integral involves only a tail of the distribution $P(R_g)$. Since the normal approximation, being a low-order expansion, is not accurate in the tails, more accurate (but less tractable) Poisson statistics should be applied. This was done, and the results are shown in Fig. 6.86 for several different values of M with $N = M$. Note that the variables x, y, M, and N used in the discussion appear as M, N, $\langle M \rangle$, and $\langle N \rangle$, respectively, in the figure. Considering

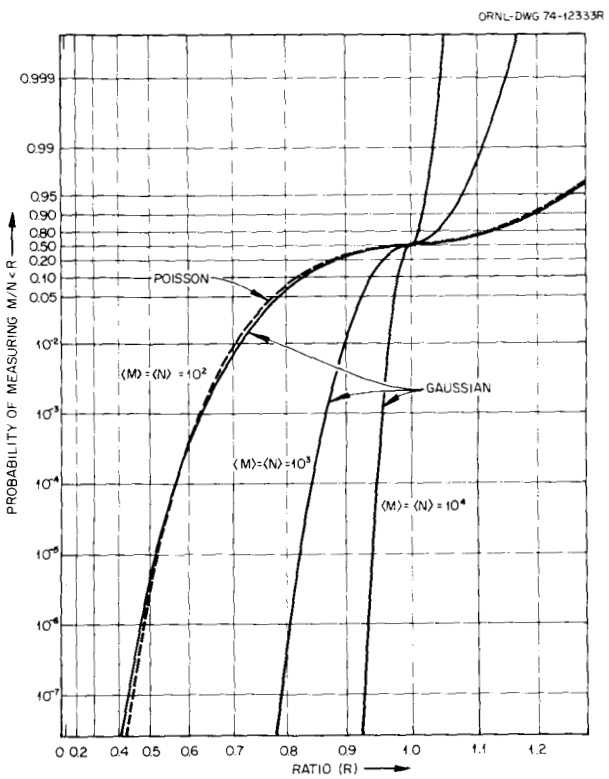

Fig. 6.86. Reliability for Ratio Determinations Involving Two Statistical Numbers (M and N).

the curve for $M = N = 1000$, we see that if $R_g = 1$ and $R_b = 0.8$ (20% Cs loss), then the probability of cross mixing is about 6×10^{-7}. In other words, less than one particle in a million will be erroneously classified. Note also that for M and N greater than 1000, results obtained using the normal approximation (Gaussian distribution) nearly coincide with those obtained from the Poisson distribution.

Recent measurements have been made with RTE-8 fuel particles under conditions similar to those to be encountered during operation of IMGA. These measurements demonstrated that data can easily be accumulated in the full energy peak of ^{137}Cs at rates up to 500 counts/sec and in the two zirconium peaks at rates up to 300 counts/sec. While the absolute accumulation rates depend on the reactor operating time, the burnup, and the cooling time, the time required by IMGA to make the failed, not-failed decision will clearly be only a few seconds.

6.11.4 Performance Comparison of Candidate Fissile Fuels — F. J. Homan

At the beginning of the reporting period the reference recycle fissile particle was the mixed thorium-uranium-oxide $Th_{0.8}U_{0.2}O_2$ kernel with a Biso coating. The reference kernel had been observed to migrate thermally (amoeba effect) under irradiation, removing carbon from the hot side of the particle and rejecting it from the cold side. The extent to which thermal migration can be tolerated has been defined and is described in Fig. 6.87. Migration through the buffer layer and into the pyrocarbon coating during the operating lifetime of the fissile particle is not permitted. The kernel migraion coefficients (KMC, discussed by Lindemer and Olstad[76]) associated with migration into the buffer layer as a function of the time-dependent fuel temperatures in various regions of an HTGR core are shown in the figure.[77] Thermal migration characterized by coefficients above the cross-hatched region are unacceptable. The "average" behavior of the dense mixed-oxide kernels is shown to be marginal with respect to the cross-hatched region. The 95% confidence interval (shown by the outer dashed lines in Fig. 6.87) for the dense oxide KMC curves extends well into the critical region.

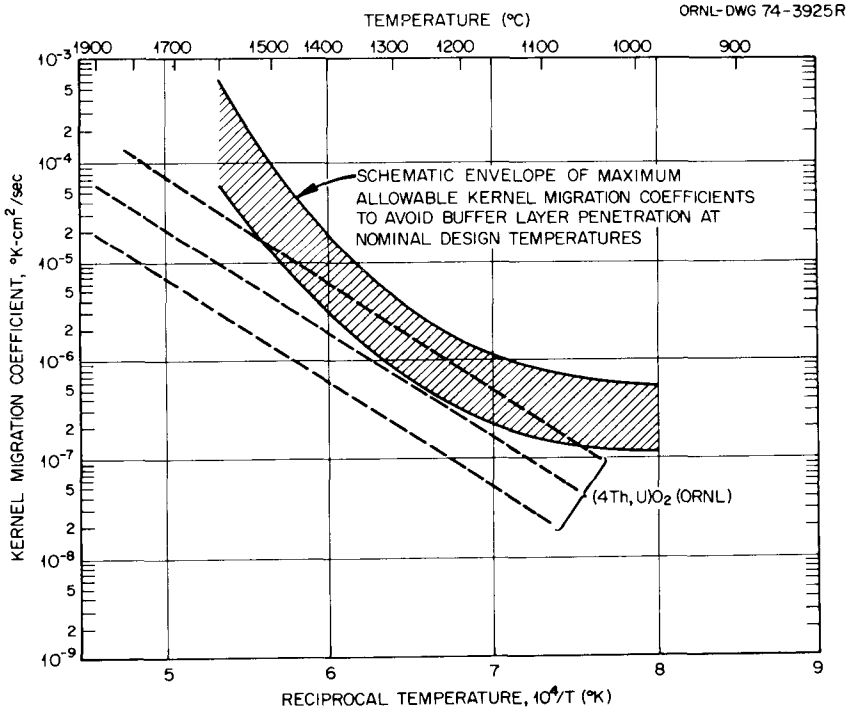

Fig. 6.87. Average Kernel Migration Coefficients for $Th_{0.8}U_{0.2}O_2$.

Because of the thermal migration problem with the dense mixed oxide, a new recycle fissile kernel was sought.[78] A limited amount of irradiation data had been collected on fissile fuel derived from uranium-loaded, ion exchange resins. We felt at the time that the resin-derived fuel demonstrated superior irradiation performance to the dense mixed oxide, and had the potential for superior economics as well. Very little was known at the time about the economics of the resin-derived fuel, but we felt that the advantages associated with a pure fissile particle (reducing the amount of heavy metal that must be refabricated remotely) and the capability for some quality control steps (such as sizing and screening the resin beads before loading) outside the hot cell could be considerable.

Irradiation experience with the new reference fuel, weak-acid-resin-derived (WAR) oxide-carbide, was meager, and the fuel that had been irradiated had been poorly characterized. Therefore, a series of experiments was designed to gain more information on the new reference fuel, and to directly compare its performance with that of the dense mixed oxide. These experiments, HRB-7 and -8, are reported in Sect. 6.6.3 of this report. Capsules HRB-7 and -8 contained dense mixed-oxide kernels with thorium-to-uranium ratios of 0 (UO_2), 2, 4, and 8. The ratio of 8 is significant because this represents the overall ratio in recycle fuel elements, making further dilution with thorium impossible. The capsules also contained WAR UC_2 and UC_2—85% UO_2.*

The results of HRB-7 and -8 are summarized completely in Sect. 6.6.3 of this report and in a topical report,[42] so just a brief summary will be given here. As in all previous irradiations, the migration of the

---

*Uranium is loaded into ion-exchange resins in oxide form. Thermodynamic calculations and irradiation testing have shown that a two-phase system (UO_2 + UC_2) performs better, hence the terminology WAR oxide-carbide. A conversion step is necessary to get to the two-phase system, and the extent of the conversion defines the stoichiometry. The 15%-converted fuel irradiated in HRB-7 and -8 was 15% carbide, 85% oxide. It is sometimes desirable to express the stoichiometry in terms of the O/U ratio, rather than percent conversion. This transformation can be made as follows: If X = O/U, and Y = fraction conversion, then $X = 2(1 - Y)$ or $Y = 1 - X/2$.

UO_2 kernels exceeded acceptable limits. Dilution with ThO_2 reduced the migration, but the 8:1 Th/U kernels showed no measurable improvement in the resistance to migration over the 4:1 Th/U. Since 8:1 is the maximum ratio that can be considered for a recycle fuel element no dense mixed oxide appears acceptable. The WAR fissile kernels performed much better. There was no amoeba, but there was considerable fission product attack of the SiC and iLTI coatings in the WAR UC_2 particles; the same phenomenon is observed in irradiated fully dense UC_2 Triso particles. The WAR UC_2—85% UO_2 particles performed even better. There was little evidence of chemical interaction, although some gross phase segregation in the kernels was observed. These phases are presently the subject of some intensive microprobe analyses, which will be reported subsequently.

The results of the HRB-7 and -8 experiments were very encouraging. On the basis of the irradiation performance of the candidate fissile fuels in this set of experiments, the tentative switch from the dense mixed oxide to the WAR oxide-carbide was finalized. All development work on the mixed-oxide system was terminated, and additional experiments to further characterize the irradiation behavior of the WAR system were planned. In addition, the WAR fissile system was adopted by GA as the reference development fresh fuel, and they began to build a body of irradiation data to support this fuel as their reference fresh fuel, to replace the VSM dense UC_2 system.

To further define the influence of kernel stoichiometry on irradiation performance, a wide range of stoichiometries was included in the HRB-9 and -10 experiments. The tests included 0, 15, 50, 75, and 100% conversions. The results of the HRB-9 and -10 experiments are covered in detail in Sect. 6.6.4 of this report and in a separate topical report,[79] and will be summarized only briefly here.

The 0- and 100%-converted fuels behaved very much like dense UO_2 and UC_2, respectively. Good performance was noted for the 15-, 50-, and 75%-converted fuels. The 15%-converted material behaved very much like it did in the HRB-7 and -8 experiments; the iLTI and SiC appeared to be in good physical condition, although the buffer was consumed by the kernel and there was little evidence of fission product migration

out of the kernels. However, the phase segregation noted earlier in the kernel was observed again. The 75%-converted fuel performed well, although there was considerably more evidence of rare earth fission product accumulation at the SiC-LTI interface on the cold side of the particle than with either the 15- or 50%-converted fuels. While statistics on the failed particle fraction are not yet available, we felt that the 50%-converted fuel performed as well as or better than any fissile particle we have yet seen.

From a processing standpoint, it is desirable to stay as close to the oxide side as possible with respect to kernel stoichiometry. On the basis of the HRB-9 and -10 experiments, the best stoichiometry for this system lies somewhere between 15 and 50% converted, with probably a large suitable range around the optimal stoichiometry. The HRB-11 and -12 experiments have as their major objective determination of the optimal stoichiometry.

In addition to the HRB tests already mentioned, the WAR oxide-carbide system is being tested in several other experiments. There is some WAR fuel in the Dragon MET VII Experiment (see Sect. 6.8); the same fuel irradiated in HRB-9 and -10 (15-, 75%-converted) is being irradiated under less accelerated conditions in OF-2 (see Sect. 6.7.2); and a real-time test of these same fuels will be conducted in the Fort St. Vrain Reactor early validation tests, which will be reported later.

6.11.5 Effect of Fissile Kernel Diameter on Operating Temperatures of Large HTGRs — F. J. Homan

When the reference fissile particle was switched from the dense mixed-oxide kernel to the porous WAR kernel, there was some concern over how the kernel shrinkage under irradiation would affect the operating temperatures of the WAR kernels. The dense mixed-oxide kernels are of nearly theoretical density, whereas the WAR kernels are less than one-third of theoretical density. Under irradiation the WAR kernels shrink drastically, resulting in a large gap between the kernels and the coatings. In many instances the buffer layer is completely consumed by the kernel. Since the gap formed under irradiation will be filled largely with low-conductivity fission gas, there is

concern that the kernel temperatures might be excessive. From a processing standpoint it is desirable to use large kernels (about 400 μm in diameter) rather than the small kernels (200 μm in diameter), which were considered for the reference fresh fuel (dense VSM UC_2). Larger kernels mean higher power output per particle, which will exaggerate any potential temperature problem.

Initial studies found that the problem of the gap was relatively minor because of the contribution of radiative heat transfer across the gap. The presence of the gap by itself would not preclude the use of 400-mm-diam kernels. However, during the course of the studies some questionable assumptions were made about the thermal conductivity of the coatings. Solid-phase control over the thermal conductivity of the coatings was assumed. Thermophysical data[80] were used for SiC and PyC of theoretical density, and a Maxwell-Eucken correction for porosity was made. This same treatment was used for the kernel. Very little data exist for the WAR oxide-carbide system, so approximations based on UO_2 data and sketchy UC_2 data were used. Tennery pointed out that his experience with porous ceramic fuels[81] has shown that gas-phase conductivity control is more likely than solid-phase control. The studies were redone with gas-phase control in the buffer and kernel assumed, with the gas phase consisting of 85% Xe and 15% Kr (typical fission gas composition). Under these assumptions the calculated operating temperatures for larger kernels (400 μm) were very high for power production per particle values representative of large HTGRs. If these calculations are accurate, then the fissile particles irradiated in HRB capsules should have melted. These capsules operate under considerably accelerated conditions compared with an HTGR, and the power production per particle is therefore several times the values calculated for HTGR operating conditions. Since the WAR fissile particles have performed rather well in HRB capsules (see Sects. 6.6.3, 6.6.4, and 6.11.4), with little sign of kernel melting, the assumptions used in these calculations appear somewhat conservative.

For one thing, the power production per particle is highest at the beginning of irradiation for fissile particles when the fissile inventory is highest. This is also when the system contains very little fission gas.

The gas phase present in the buffer and kernels at the beginning of irradiation is primarily hydrogen,[82] which has a thermal conductivity at least 25 times that of fission gas over the temperature range of interest. This is a considerably better situation than the one for which the calculations were made. Another conservative assumption is that the buffer layer is not consumed. A porous buffer layer containing low-conductivity fission gas in the pores is a much more insulating medium than would exist if the buffer had been consumed by the kernel. Radiation enhances thermal conductance across the gap between the kernel (plus consumed buffer) and the coatings; this is impossible with the buffer in place.

Much more work is clearly necessary to provide a good understanding of kernel operating temperatures in irradiation experiments, as well as those projected for commercial HTGRs. Some assessments are necessary of gas-phase composition and particle power production as functions of time. Additional analyses of coating conductivities and the influence of irradiation exposure on these conductivities are also required.

6.11.6 Dynamic Testing of HRB Capsules — F. J. Homan and N. J. Ackermann

In the HRB-8 capsule, we investigated whether dynamic testing of HRB capsules in the HFIR would provide useful information regarding capsule heat transfer characteristics that could not be obtained from static temperature measurements. The reactor power was perturbed, and the temperature responses at four locations within the HRB-8 capsule were measured. The perturbation was in the form of a pseudorandom binary sequence, introduced by the reactor control rod servo system, to oscillate the reactor power demand by about 1.5% in the frequency range 0.016 to 1.5 Hz. The neutron flux signal from the EF-2 chamber near the facility and the signals from the midplane centerline thermocouple TE113 and three peripheral thermocouples in the graphite sleeve (TE105, 106, 109) were recorded and frequency analyzed. (See Sect. 6.6.3 of this report for the location of these thermocouples.) The resulting gains and phases of the temperature responses to neutron flux perturbations were compared with the predictions of mathematical models.

Several interesting observations were made from this study:

1. The time constant between perturbation of the reactor power and the reponse by the fuel centerline thermocouple was about 20 sec. This is compared with a time constant of about 8 sec for the same type of experiment conducted with the HRB-3 capsule.[83] This time constant is considerably larger than that predicted with the model. This discrepancy between experiment and prediction may be explained by a stagnant gas gap surrounding the thermocouple. The model assumed that the thermocouple would have an instantaneous response to changes in temperature in the fuel. Experimental data from the literature[84] have indicated that the time constant associated with the response of a sheathed, mineral-insulated thermocouple in air increases markedly in flows of decreasing Reynolds number. This slow thermocouple response is unfortunate. One of the capabilities hoped for from dynamic testing was a method for correcting the centerline thermocouples for the decalibration experienced during irradiation due to transmutation effects. The slow thermocouple response will make this correction difficult.

2. The Chromel vs Alumel thermocouples located in the graphite sleeve did not responde to the power perturbation as rapidly as predicted from the model. Since these thermocouples are also located in a stagnant gas, the explanation for the long-time constant is probably the same as for the centerline thermocouple. Since the Chromel vs Alumel thermocouples do not decalibrate under irradiation, this slow response does not affect the quality of information received from the thermocouples.

3. Gamma heating was thought to be present in both the Chromel vs Alumel and the tungsten-rhenium thermocouples. The lower atomic numbers of the Chromel vs Alumel couples makes this problem less severe than for the tungsten-rhenium couples. Significant gamma heating in the tungsten-rhenium thermocouples could cause some problems if the data from these couples are used to determine fuel thermal conductivity. If the couples read higher temperatures than representative of the fuel, then a lower than actual thermal conductivity would be inferred. Because of the decalibration of the tungsten-rhenium couples, temperature readings from them have never been used to determine fuel thermal conductivities,

although this objective has been included in a number of HRB tests. We still hope (see Sect. 6.10.5 of this report) that the centerline thermocouple readings can be analytically corrected. If this is possible, then the gamma heating of thermocouple materials will have to be considered. The report on the feasibility study suggested that dynamic testing might help solve this problem.

Several conclusions and recommendations came out of this study. They are:

1. Future work on dynamic testing should emphasize improvement of the theoretical model used in the calculations. This work would require an estimated 0.5 man-year. Features to be included in the improved model were identified as (a) the effect of the helium gas gap on the heat transfer process to the thermocouples, particularly in the centerline region; (b) the effect of gamma heating in the thermocouple junctions; and (c) the effect of a variable, correlated fluctuation in capsule cooling water temperature.

2. The potential benefits to the HTGR Fuel Development Program that could be realized from dynamic testing in HRB capsules were primarily associated with evaluation of the gamma heating characteristics in tungsten-rhenium thermocouples. In the area of primary concern, decalibration of these thermocouples, dynamic testing could provide very little help because of the excessive (20-sec) time constant between power perturbation and thermocouple response. Installation in future capsules of thermocouples with better thermal contact with the fuel may alleviate this problem.

3. Those responsible for the feasibility study estimated that capability to routinely collect information through dynamic testing would cost in excess of $80,000. This expense would cover model improvement and additional experimentation. In the end it was felt that the information that would be routinely available would be of only marginal value. It was pointed out, however, that additional techniques and methods of significant benefit to the HTGR Program could be discovered during the development aspects of this work.

Because of the uncertain advantages of dynamic testing and the expense associated with continued development of those techniques, we decided not to continue the work for the present. This decision will be reassessed from time to time on the basis of the changing needs of the HTGR fuels program.

6.11.7 Reaction of Fission Products with SiC — J. I. Federer

Metallographic examination of coated microspheres irradiated in capsule HRB-4 at 1000 to 1200°C revealed a reaction at the inner surface of the SiC coating. In some cases the reaction zone penetrated 80% of the SiC thickness. Palladium and rare-earth fission products were identified in the reaction zone, apparently having diffused from the WAR UC_2 kernels through intervening PyC layers to reach the SiC.[85] As an aid in understanding the reaction, SiC has been separately reacted with palladium and cerium. Samples of Pd-SiC were prepared by cold-pressing a mixture of palladium powder and either SiC-coated microspheres or SiC fragments from coated microspheres. These were held for various times at 1000, 1100, and 1200°C in an inert atmosphere. Samples for reaction of cerium with SiC were prepared by coating small graphite disks with a 30-μm-thick layer of SiC in a fluidized bed. Small pieces of cerium metal were placed on the disks, which were held at 825°C for 1 to 2 hr in an inert atmosphere.

Metallographic examination of Pd-SiC samples revealed no reaction layer in the SiC after 150 hr at 1000°C. The SiC had darkened from the original translucent green color to black. After 100 hr at 1100°C most of the SiC fragments had been consumed by reaction. Some original palladium particles were surrounded by a once-molten matrix. After 30 hr at 1200°C a light-gray reaction layer surrounded each SiC fragment, as shown in Fig. 6.88. The reaction had even proceeded along the interface between PyC and SiC. The white phase is unreacted palladium. Figure 6.89 shows the microstructure of the sample after 70 hr at 1200°C. None of the original SiC fragments could be identified. Electron microprobe analysis revealed that the microstructure consisted of globules of

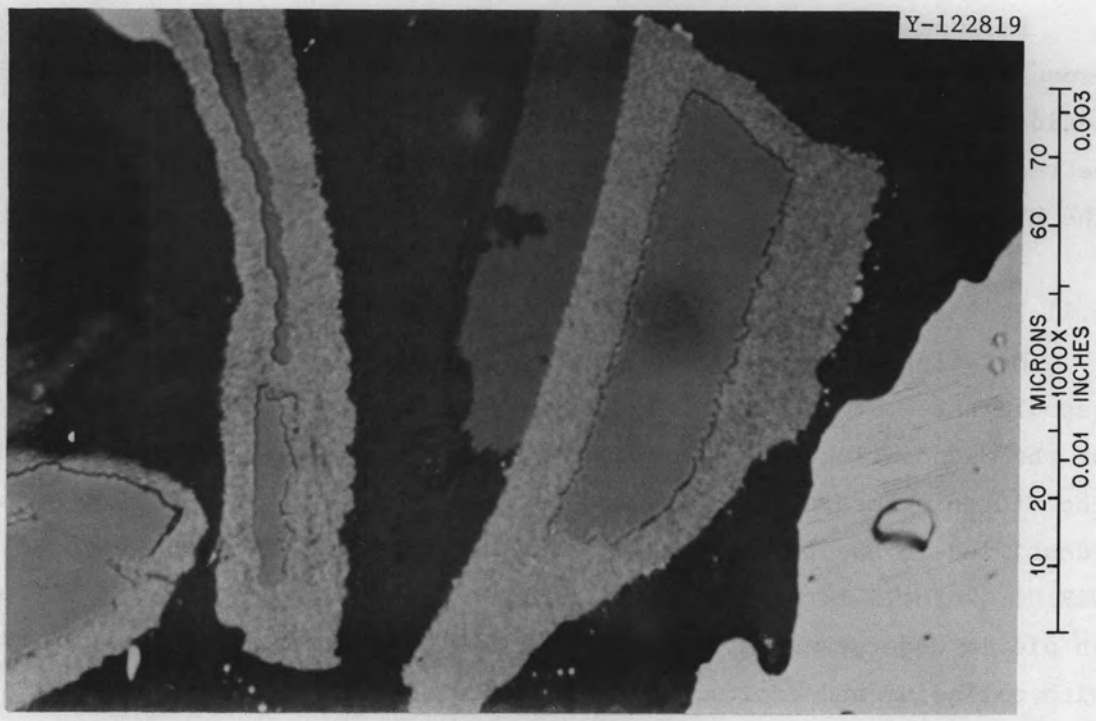

Fig. 6.88. Reaction Layer in SiC Fragments After 30 hr at 1200°C. As-polished.

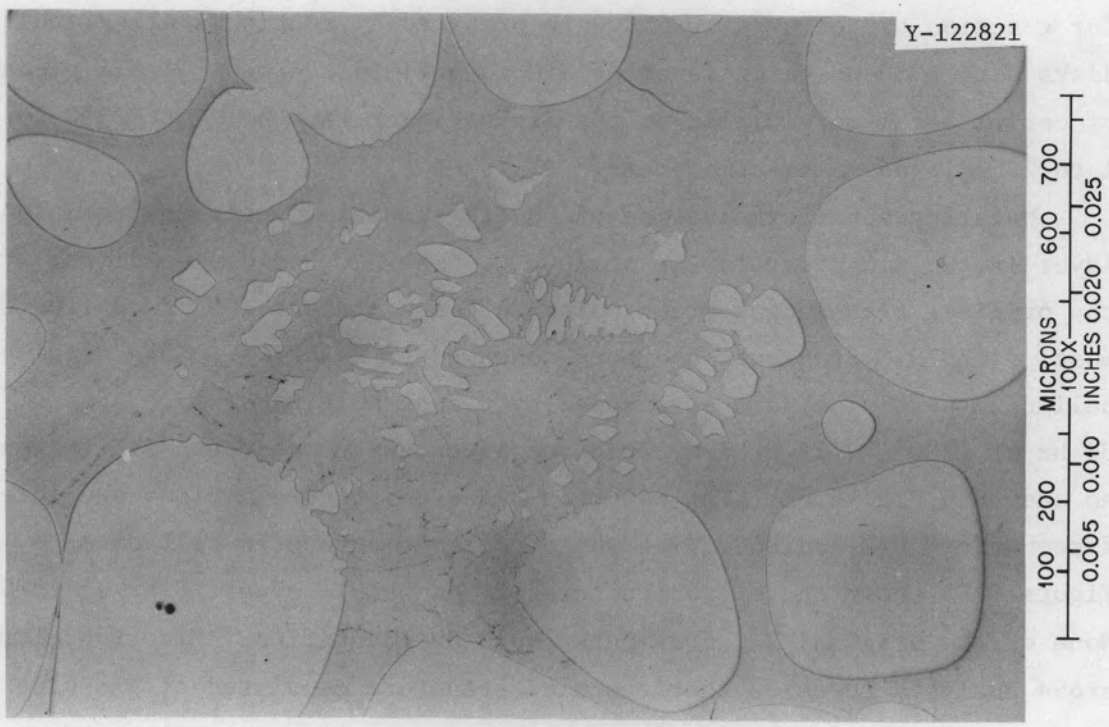

Fig. 6.89. Microstructure of Pd-SiC Sample After 70 hr at 1200°C. As-polished.

pure palladium in a once-molten matrix containing about 7 wt % Si. These observations agree qualitatively with the Pd-Si phase diagram,[86] which shows that an alloy containing 7 wt % Si would be molten at 1200°C.

Visual examination of Ce-SiC samples after 1 to 2 hr at 825°C (Ce mp, 795°C) revealed a hole in the SiC layer at the point of contact with the cerium and disappearance of the cerium metal. Subsequent metallographic examination revealed that the cerium was absorbed into the graphite disk on which the SiC had been coated. There was no discernible reaction layer in the SiC in the vicinity of the breakthrough. Thermodynamic data[87] indicate CeC_2 to be stable relative to SiC at any temperature of interest.

These experiments have shown that both palladium and cerium are capable of destroying the integrity of SiC coatings. Other rare-earth fission products, in addition to cerium, may behave similarly to cerium, but none have been examined yet.

6.12 REFERENCES

1. G. W. Weber, R. L. Beatty, V. J. Tennery, and W. J. Lackey, Jr., *Uranium Dispersion in Coated Weak-Acid-Resin-Derived HTGR Fuel*, ORNL/TM-5133 (February 1976).
2. R. D. Green, "The Search for a High Energy Fuel," *Met. Prog.* 107(6): 84–7 (June 1975) ibid., 108(2): 71–4 (July 1975).
3. R. L. Beatty, "Carbon Coating Process Developments," *Gas-Cooled Reactor Programs Annu. Prog. Rep. Dec. 31, 1973*, ORNL-4975 pp. 77–79.
4. E. Gyarmati and H. Nickel, *Stationary and Dynamic Deposition of Silicon Carbide on Coated Fuel Particles*, JÜL-900-RW (November 1972). ORNL-tr-2733.
5. T. D. Gulden, *Deposition and Microstructure of Vapor-Deposited Silicon Carbide*, GA-8275 (Dec. 1, 1967).
6. E. H. Voice and D. N. Lamb, *The Deposition and Structure of Pyrolytic Silicon Carbide*, Dragon Project Report DP-677 (October 1969).
7. J. I. Federer, *Fluidized Bed Deposition and Evaluation of Silicon Carbide Coatings on Microspheres*, ORNL/TM-5152 (in preparation).

8. R. L. Beatty and E. S. Bomar, "Characterization of Coatings," *Gas-Cooled Reactor Programs Annu. Prog. Rep. Dec. 31, 1973*, ORNL-4975, p. 82.

9. W. J. Lackey, W. H. Pechin, and J. D. Sease, *Measurement and Control of the Shape of Fuel Particles for High-Temperature Gas-Cooled Reactors*, ORNL-TM-4673 (November 1974).

10. H. Luhleich, KFA Jülich, West Germany, private communication.

11. P. Koss and K. Koizlik, "Optical Determination of Anisotropy of Pyrocarbon Coatings," *11th Bienn. Conf. Carbon, Extended Abstracts*, CONF-730601, pp. 169–71 (Gatlinburg, Tenn, May 1973).

12. M. Pluchery, *Determination of the Anisotropy of the Pyrocarbon Part of the Fuel Particles of the High Temperature Nuclear Reactor by X-Ray and Electron Diffraction*, thesis, University of Grenoble, 1973.

13. K. Bongartz et al., *Methods for the Characterization of Pyrolytically Deposited Carbon* (compiled by H. A. Schulze), KFA Report JÜL-1078-RW (GERHTR-134), June 1974.

14. J. P. Mathers, V. J. Tennery, and E. S. Bomar, *Equipment Variables and Deposition Conditions Affecting the Plasma Oxidation of Pyrocarbon Coatings on HTGR Fuel Particles*, ORNL/TM-5308 (June 1976).

15. C. S. Yust and H. P. Krautwasser, "Transmission Electron Microscopy of Propene-Derived Pyrolytic Carbon Coatings," *Carbon* 13: 125 (1975).

16. J. L. Kaae, *Carbon* 13: 55 (1975).

17. E. A. Wolfrum, *Investigations of Structure and Texture Dependent Surface Reactions Between Pyrocarbon and Oxygen at Room Temperature*, JÜL-1194 (May 1975), (in German, thesis, University of Aachen).

18. M. J. Kania, T. B. Lindemer, M. T. Morgan, and J M Robbins, *Irradiation Performance of HTGR Fertile Fuel in HFIR Target Capsule HT-12 Through HT-15: Part 1 – Experiment Description and Fission Product Behavior*, ORNL/TM-5305 (in preparation).

19. J. W. Prados and J. L. Scott, *Mathematical Model for Predicting Coated-Particle Behavior*, ORNL-TM-1405 (March 1966).

20. J. W. Prados and T. G. Godfrey, *STRETCH, A Computer Program for Predicting Coated-Particle Irradiation Behavior; Modification IV, December 1967*, ORNL-TM-2127 (April 1968).

21. Anon., "Capsules HT-12 Through -15," *Gas-Cooled Reactor Programs Annu. Prog. Rep Dec. 31, 1973,* ORNL-4975, pp. 128–31.

22. K. H. Valentine, *Modification V to the Computer Code, STRETCH, for Predicting Coated-Particle Behavior,* ORNL-TM-4867 (April 1975).

23. M. J. Kania, *HTCAP, A FORTRAN IV Program for Calculating Coated Particle Operating Temperatures in HFIR Target Irradiation Experiments,* ORNL/TM-5332 (May 1976).

24. J M Robbins and W. P. Eatherly, "Capsules HT-17 Through -19," *Gas-Cooled Reactor Programs Annu. Prog. Rep. Dec. 31, 1973,* ORNL-4975, pp. 133–38.

25. W. P. Eatherly and J M Robbins, "Capsules HT-20 Through -23," *Gas-Cooled Reactor Programs Annu. Prog. Rep. Dec. 31, 1973,* ORNL-4975, p. 138.

26. W. R. Johnson, R. L. Hamner, J M Robbins, and B. H. Montgomery, *Postirradiation Examination of Capsules HT-24 and HT-25,* GA-A-13486 (Sept. 15, 1975).

27. T. N. Tiegs, A. J. Caputo, E. L. Long, Jr., and B. H. Montgomery, *Irradiation Performance of HTGR Fuel Rods in HFIR Experiments HT-26 and -27,* ORNL/TM-5404 (August 1976).

28. B. H. Montgomery and E. L. Long, Jr., "Capsules HRB-4 and -5," *Gas-Cooled Reactor Programs Annu. Prog. Rep. Dec. 31, 2975,* ORNL-4975, pp. 99–120.

29. F. J. Homan, E. L. Long, Jr., R. L. Hamner, B. H. Montgomery, and K. H. Valentine, *Irradiation Performance of HTGR Fuel Rods in HFIR Experiments HRB-4 and -5,* ORNL-5115 (June 1976).

30. R. L. Hamner, "Capsule HRB-6," *Gas-Cooled Reactor Programs Annu. Prog. Rep. Dec. 31, 1973,* ORNL-4975, pp. 120–22.

31. F. J. Homan, E. L. Long, Jr., B. H. Montgomery, and R. L. Hamner, *Irradiation Performance of HTGR Fuel Rods in HFIR Experiment HRB-6,* ORNL-TM-5011 (December 1975).

32. R. L. Hamner, "Capsules HRB-7 and -8," *Gas-Cooled Reactor Programs Annu. Prog. Rep. Dec. 31, 1973,* ORNL-4975, pp. 121–27.

33. F. J. Homan, J. H. Coobs, R. L. Hamner, J. A. Conlin, B. H. Montgomery, E. L. Long, Jr., and J. L. Scott, *Irradiation Performance of HTGR Fuel Rods in HFIR Experiment HRB-3 and ETR Experiment P13N*, ORNL-TM-4526 (October 1974), p. 12.

34. J. A. Conlin, K. R. Thoms, and R. B. Fitts, "Irradiations in ORR Core Facilities," *Gas-Cooled Reactor Programs Annu. Prog. Rep. Dec. 31, 1972*, ORNL-4911, pp. 115–16.

35. K. R. Thoms and A. W. Longest, "Irradiation Tests in ORR In-Core Facility," *Gas-Cooled Reactor Programs Annu. Prog. Rep. Dec. 31, 1973*, ORNL-4975, pp. 138–47.

36. C. C. Smith, *Preirradiation Report. Fuel Materials for Irradiation P13Q*, GA-A-13265 (June 1975).

37. E. J. Allen, unpublished work.

38. W. D. Turner and M. Siman-Tov, *HEATING3: An IBM-360 Heat Conduction Program*, ORNL-TM-3208 (February 1971).

39. R. J. Price, *Review of Thermal Conductivity of Nuclear Graphite Under HTGR Conditions*, GA-A-12615 (September 1973).

40. W. R. Johnson, *Thermal Conductivity of Large HTGR Fuel Rods*, GA-A-12910 (March 1974).

41. R. J. Price and L. A. Beavan, *Final Report on Graphite Irradiation Test OG-1*, GA-A-13809 (August 1974).

42. K. H. Valentine, F. J. Homan, E. L. Long, Jr., T. N. Tiegs, B. H. Montgomery, and R. L. Hamner, *Irradiation Performance of HTGR Fuel Rods in HFIR Experiments HRB-7 and -8*, ORNL/TM (in preparation).

43. W. R. Johnson et al., *Postirradiation Examination of Capsules HT-24 and HT-25*, GA-A-13486 (September 1975).

44. H. C. Roland, *FABGEN, A Transient Power-Generation and Isotope Birth Rate Calculator*, ORNL-TM-4750 (April 1975).

45. E. L. Long, R. B. Fitts, and F. J. Homan, *Fabrication of ORNL Fuel Irradiated in the Peach Bottom Reactor and Postirradiation Examination of Recycle Test Elements 7 and 4*, ORNL-TM-4477 (September 1974).

46. E. L. Long, Jr., "Recycle Test Elements," *Gas-Cooled Reactor Programs Annu. Prog. Rep. Dec. 31, 1973*, ORNL-4975, p. 153.

47. E. L. Long and T. N. Tiegs, "Peach Bottom Recycle Test Elements," *Thorium Utilization Program Prog. Rep. Jan. 1, 1974–June 30, 1975*, ORNL-5128, pp. 278–304.

48. T. B. Fowler, D. R. Vondy, and G. W. Cunningham, *Nuclear Reactor Core Analysis Code: CITATION*, ORNL-TM-2496, Rev. 2 (July 1971).

49. W. W. Engle, Jr., *A User's Manual for ANISN*, USAEC Report K-1693, Oak Ridge Gaseous Diffusion Plant (March 1967).

50. H. T. Kerr, E. J. Allen, and J. H. Swanks, *Analysis of Dosimetry Data from the Aluminum and Beryllium Irradiation Experiment in the RB-7 Facility of HFIR*, ORNL-TM-4725 (January 1975).

51. H. T. Kerr, *Dosimetry and Neutron Fluxes in the HFIR*, ORNL/TM-4358 (in preparation).

52. D. R. Vondy, T. B. Fowler, and G. W. Cunningham, *VENTURE: A Code Block for Solving Multigroup Neutronic Problems Applying the Finite-Difference Diffusion-Theory Approximation to Neutron Transport*, ORNL-5062 (October 1975).

53. E. J. Allen and H. T. Kerr, *Neutron Flux Computational Model of the Oak Ridge Research Reactor*, ORNL-TM-4814 (April 1975).

54. M. J. Bell, *ORIGEN — The ORNL Isotope Generation and Depletion Code*, USAEC Report ORNL-4628 (May 1973).

55. E. J. Allen, "CACA-2," *Revised Version of CACA, A Heavy Isotope and Fission-Product Concentration Calculational Code for Experimental Irradiation Capsules*, ORNL/TM-5266 (February 1976).

56. H. T. Kerr, E. J. Allen, and D. L. Reed, *Lattice Displacement Calculations and Comparisons for Different Irradiation Facilities*, ORNL/TM-5269 (March 1976).

57. H. T. Kerr, H. L. Adair, and E. J. Allen, "Dosimetry Materials for High-Temperature Applications," paper presented at First ASTM-EURATOM Symposium on Reactor Dosimetry: Developments and Standardization, Petten, Netherlands, Sept. 22–26, 1975.

58. R. W. Knoll and J. D. Jenkins, Oak Ridge National Laboratory, unpublished internal document (May 1975).

59. N. L. Sandefur, J. S. Steibul, and R. J. Grenda, *EMF Drift of Chromel/Alumel and W–3% Re/W–25% Re Thermocouples Measured in-Pile to High Neutron Exposures,* GULF-GA-A-12501 (May 24, 1973).

60. R. L. Shepard, R. M. Carroll, and J. K. East, "Capsule Thermometry," *Gas-Cooled Reactor Programs Annu. Prog. Rep. Dec. 31, 1973,* ORNL-4975, pp. 160–70.

61. C. J. Borkowski and T. V. Blalock, "A New Method of Johnson Noise Thermometer," *Rev. Sci. Instrum.* 45(2): 151–62 (February 1974).

62. R. L. Shepard, C. J. Borkowski, J. K. East, R. J. Fox, J. L. Horton, and T. V. Blalock, "Ultrasonic and Johnson Noise Fuel Centerline Thermometry," pp. 737–74 in *Proceedings of International Colloquium on High-Temperature In-Pile Thermometry* (held at Petten, Netherlands, Dec. 12–13, 1974). EUR-5395, Vol. 2, 1975.

63. R. L. Shepard, and T. G. Kollie, "Correction of Irradiation-Produced Drift in W-Re Fuel Centerline Thermocouples," pp. 237–68 in *Proceedings of International Colloquium on High-Temperature In-Pile Thermometry* (held at Petten, Netherlands, Dec. 12–13, 1974). EUR-5395, Vol. 1, 1975.

64. E. D. Zysk, "Noble Metals in Thermometry: Recent Developments," *Engelhard Ind. Tech. Bul.* V(3): 69–99 (1964).

65. F. A. Reichardt, *Temperature Measurements in the Dragon Reactor,* Dragon Project Report DPR-157 (May 1963).

66. W. J. Gray, "The Effect of Neutron Irradiation on the EMF Stability of a Pt5% Mo/Pt0.1% Mo Thermocouple," *J. Nucl. Mater.* 44: 239–40 (1972).

67. G. W. Cunningham III, Computer Sciences Division, Oak Ridge National Laboratory, private communication.

68. H. C. Roland, *GENGTC, A One-Dimensional CEIR Computer Program for Capsule Temperature Calculations in Cylindrical Geometry,* ORNL-TM-1942 (December 1967).

69. F. J. Homan, *Thermal Analysis of HTGR Fuel Rods Irradiated in the HFIR Removable Beryllium Facility,* ORNL/TM report (in preparation).

70. F. J. Homan, *HTRANS — A FORTRAN IV Computer Program for Thermal Analysis of Coated Particle Fuels,* ORNL/TM report (in preparation).

71. K. H. Valentine, *ENCTRK, A Computer Program to Model Heat Transfer Across Asymmetric Gaps in Cylindrical Fuel Rods,* ORNL/TM report (in preparation).

72. K. R. Thoms and M. J. Kania, *Design, Fabrication, and Initial Operation of HTGR-ORR Capsule OF-2,* ORNL/TM report (in preparation).

73. TREVOR, unpublished computer code, property of General Atomic Company.

74. C. L. Smith, *Fuel Particle Behavior Under Normal and Transient Conditions,* GA-A-12971, p. 28 (October 1974).

75. E. L. Long, Jr., "Postirradiation Examination of HRB-4 and -5," *Gas-Cooled Reactor Programs Annu. Prog. Rep. Dec. 31, 1973,* ORNL-4975, pp. 110–20; note especially Figs. 7.20 and 7.21.

76. T. B. Lindemer and R. A. Olstad, *HTGR Fuel Kernel Migration Data for the Th-U-C-O System as of April 1, 1974,* ORNL-TM-4493.

77. T. D. Gulden, J. L. Scott, and C. Moreau, *Present Thorium-Cycle Fuel Concepts and Performance Limitations,* GA-A-12877 (February 1974).

78. F. J. Homan et al., "Reference Fissile Particles for Recycle HTGR Fuel Elements," unpublished internal ORNL memo (May 1974).

79. F. J. Homan et al., *Irradiation Performance of HTGR Fuel Rods in HFIR Experiment HRB-9 -10,* report in preparation.

80. Y. S. Touloukian, ed., *Thermophysical Properties of High-Temperature Solid Materials,* Thermophysical Properties Research Center, Purdue University, Macmillan, New York; Vol. I for PyC, Vol. 5 for SiC.

81. V. J. Tennery, "Heat Transfer and Thermal Conductivity of Multi-Hundred Watt $^{238}PuO_2$ Fuel Spheres," *J. Nucl. Mater.* 54: 73–78 (1974).

82. W. P. Eatherly and R. L. Beatty, private communication.

83. Private communications from D. N. Fry to R. L. Shepard, Feb. 22 and 26, 1974.

84. A. Thomson, "The Thermal Response Time of Sheathed Mineral-Insulated Thermocouples," *Trans. Soc. Instrum. Technol.* 17(2): 49–56 (June 1965).

85. E. L. Long, Jr., "Postirradiation Examination of HRB-4 and -5," *Gas-Cooled Reactor Programs Annu. Prog. Rep. Dec. 31, 1973,* ORNL-4975, pp. 110–20.

86. M. Hansen, *Constitution of Binary Alloys*, 2nd ed., McGraw-Hill, 1958, pp. 1125–26.

87. K. A. Gschneider and N. Kippenhan, *Thermochemistry of the Rare-Earth Carbides, Nitrides, and Sulfides for Steelmaking*, IS-RIC-5 (August 1971).

7. CHARACTERIZATION AND STANDARDIZATION OF GRAPHITE

W. P. Eatherly and J. A. Conlin

7.1 INTRODUCTION

The fast-neutron dimensional distortion produced in graphite can produce high internal stresses in graphite. In general, these stresses do not become severe because of fast-neutron radiation-induced creep, which provides a stress relaxation mechanism. It is apparent that, for the proper design for safety and operation of reactors that use graphite in their cores, the creep coefficients must be well known. This is necessary not only to calculate anticipated static stress loads in regions of the core where thermal and fluence gradients occur, but also to evaluate abnormal transient conditions such as thermal stress on shutdown and start-up and superimposed cyclic loading. Data exist for a number of graphites of United States, European, and Russian origin. These data are scattered — over a factor of 3 to 5, and the graphites do not correspond to the coarse-grained isotropic graphite grades being considered for large-scale HTGRs. It is obviously necessary to develop such creep data for these materials to fulfill our responsibilities for the characterization and standardization of graphite for the HTGR program.

Our basic objective in this is to determine the primary and secondary creep coefficients for the neutron-induced creep of these graphites at 600, 900, and 1250°C for accumulated fluences of at least 8×10^{21} n/cm^2 (>0.18 MeV), the full design fluence for the HTGR.

7.2 PROGRAM OBJECTIVES AND DESIGN CRITERIA — W. H. Cook

The program to study the fast-neutron-induced creep of graphite will consist of a series of irradiation capsules, OC-series, for which the source of fast neutrons will be the Oak Ridge Research Reactor (ORR). The program has two main objectives. These are to (1) design and construct a flux-trapped irradiation facility in the ORR E-5 position, and (2) determine both the primary and secondary creep coefficients and other property data required for the constitutive equations for graphites employed in high-temperature reactors.

The best way to accurately determine the creep coefficients for any set of conditions would be to continuously monitor the creep strain during the test; however, the complications involved in the test design and the maintenance of the integrity of strain gages or dilatometers makes this impractical at this time for tensile or compressive tests. We selected the simplest test, a constant-stress compressive test, as the basis for our design. This type of test is less complex and, therefore, less expensive than tension stress tests. It has the additional advantage that the secondary creep strains are reported[1] to be approximately equal for compression and tension stresses.

In our basic objective, the primary and secondary creep coefficients will be determined as functions of fluence, temperature, stress, and Young's modulus of elasticity. A series of irradiation capsules will be alternately irradiated at 900, 600, and 1250°C in a geometric progression of fast (>0.18 MeV)* fluence increments. The compressive stresses at each temperature will be 13.8 and 20.7 MPa (2000 and 3000 psi). The dimensions, Young's modulus, and sheat modulus for each graphite specimen will be determined before neutron irradiation and after each accumulated increment of fluence, approximately 1.0×10^{21} n/cm^2, one cycle in the ORR. Each capsule will contain a set of unstressed control specimens that match the stressed specimens and are also characterized before and after irradiations. Basically, the total creep strains are determined by the dimensional differences between stressed specimens and their matching control specimens after each cycle in the ORR. The primary creep strain has been found to be recoverable under irradiation if the stress is removed.[1] Therefore, selected stress-tested specimens will be irradiated again at their test temperature to recover and thereby determine their primary creep strains. One set of control and test specimens will be used for each test temperature, and the three sets will be alternated in the ORR facility until each has accumulated a fluence of at least 8×10^{21} n/cm^2, the full design fluence of the HTGR.

---

*Unless otherwise stated, all fast-neutron energies shall be of this value.

Our purpose is to acquire the creep data to an accuracy within 10%; that is, reasonably good engineering design data are sought. To do this requires a minor rearrangement of the ORR core loading pattern to permit a fourth flux-trap irradiation facility to be constructed. However, beyond this, the accuracy and precision required plus the complexity of this most direct approach for creep testing requires the incorporation of sophisticated equipment into the design of the irradiation test facility. A general-purpose, 16-bit digital computer and other ancillary equipment are necessary for the required test control, data acquisition, and data processing. The design, construction, and integration of the basic test capsule, the irradiation facility, and the computer are described in Sect. 7.3.

The selection of the first materials for these tests is predominantly influenced by the current reactors in operation and/or design. The core material, graphite grade H-327, for the Fort St. Vrain reactor will be represented by sufficient numbers of specimens to substantiate its anticipated creep behavior. A small number of specimens of graphite grade AXF-8QBG previously irradiated at the Battelle Pacific Northwest Laboratories to 1.0×10^{22} n/cm^2 (>0.18 MeV) will be included to extend data on creep behavior to very high fluences after breakaway expansion. The major portion of the specimens in these tests shall be from grade H-451 graphite. This is a near-isotropic material manufactured by the Great Lakes Carbon Corporation and is one of the principal contenders for 1000-MW(e) HTGR application. It was selected as the major material to start this series because it, at this time, is the most thoroughly characterized material of its kind. It appears to be an acceptable material. Grade TS-1240 is also a near-isotropic graphite manufactured by the Union Carbide Corporation; it has potential for the cores of HTGRs. Specimens of this material will make up the second major group of specimens in these experiments. As the tests progress, test sites will become available for the inclusion of additional grades of graphite.

As indicated, these tests are primarily and currently directed toward the immediate needs of operational HTGRs and those that are being designed. As these series of tests are designed and with the

material selected for testing, the data obtained should also be useful to other reactor designs such as the Molten Salt (breeder) and fusion reactors. As indicated above, test sites may become available for other specific grades of graphite as the series of tests progresses. Beyond storage of archival samples, no provision is now being made to determine primary creep and secondary creep under tension. A decision to do such measurements will depend upon the accuracy and precision obtained in the compressive experiments, the quality and applicability of such determinations currently being made in Europe, and the criticality of the values for core stress analyses.

7.3 DESIGN OF ORR FACILITY AND 900°C CREEP CAPSULE — R. L. Senn

The design of the Oak Ridge Research Reactor (ORR) capsule OC-1, the first of a series of capsules intended to evaluate the creep characteristics of various graphites at elevated temperatures and to high fast fluences, as described in the previous section, was completed. The necessary instruments and controls to operate the capsules as well as a computer to control capsule temperatures and to handle other facets of the experiment during irradiation were procured. The capsules will be operated sequentially in the ORR E-5 core facility. This location within the ORR core and the configuration are shown in Figs. 7.1 and 7.2. The E-5 core position provides a 76 × 76 mm (3 × 3 in.) water-cooled facility, which will accommodate an experiment of up to about 71 mm (2.8 in.) overall diameter.

Capsule OC-1 is designed to irradiate twenty-eight 15.24-mm-diam by 25.4-mm-long (0.600- by 1.00-in.) specimens at 900°C to the first planned exposure level of 1×10^{21} n/cm^2 (>0.18 MeV). A compressive stress of 13.8 MPa (2000 psi) is applied to 22 of the specimens in each test by means of a metal bellows expanded by gas pressure against the specimen columns. Six of the specimens in the two columns have a reduced diameter so as to increase the stress to 20.7 MPa (3000 psi). Each capsule also includes 28 unstressed control specimens made of the same types of graphite as are the test specimens.

Dimensional measurements to determine graphite creep characteristics will be made on the specimens at the end of each irradiation period when

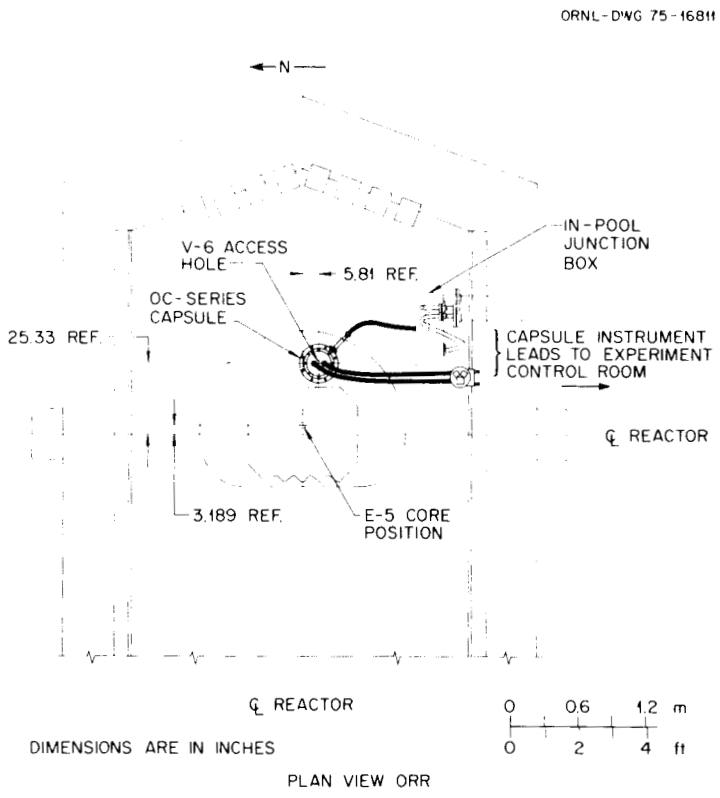

Fig. 7.1. A Top View of an OC-Series Capsule Installed in the ORR E-5 Core Position. To convert indicated dimensions to meters, multiply by 0.0254.

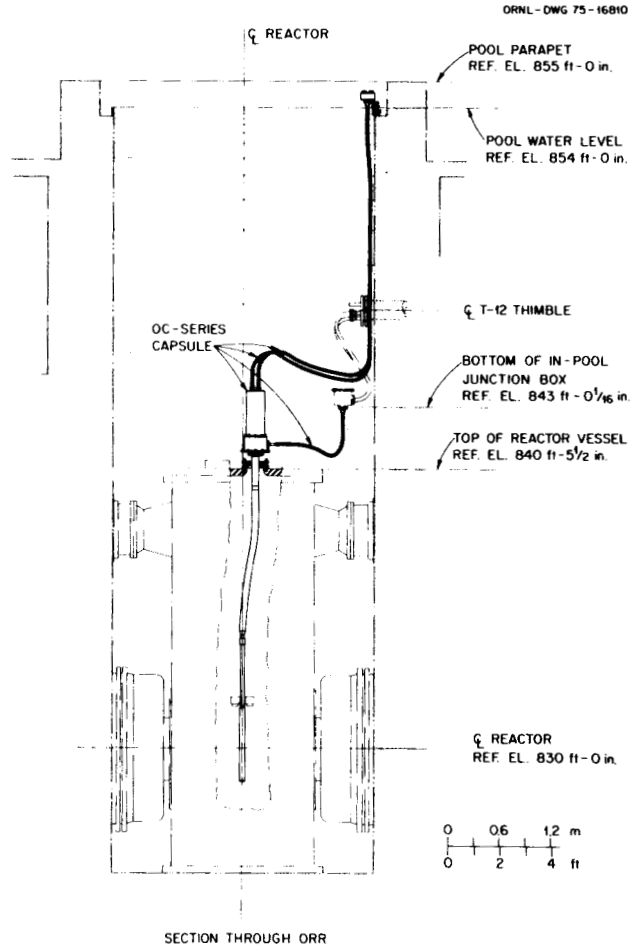

Fig. 7.2. An Elevation View of an OC-Series Capsule Installed in the ORR E-5 Position. The elevation given, from the reactor centerline upward, are 252.98, 256.17, 256.95, 260.30, and 260.60 m.

the capsule has been removed from the reactor. Each set of specimens will require a 15-months total irradiation time to attain the desired fluence.

Special features of the capsule design include (1) movable center-line thermocouples, which measure the temperature profile along the axes of the control specimens of the capsule; (2) special linear variable differential transformer (LVDT) load cells to monitor the applied load; and (3) computerized temperature control designed to achieve accurate and precise uniform longitudinal temperatures over the 0.51 m (20.0 in.) length of the test specimen columns. These features are described in more detail below.

Cross-sectional views of the in-core portion of the capsule are shown in Figs. 7.3 and 7.4. Figure 7.3 shows the stressed specimen columns. The specimens each have shallow holes in each end to accommodate the graphite pins that pass through the spacers to serve as centering guides for the specimen column. The spacers center the column by means of longitudinal centering ridges protruding from their cylindrical

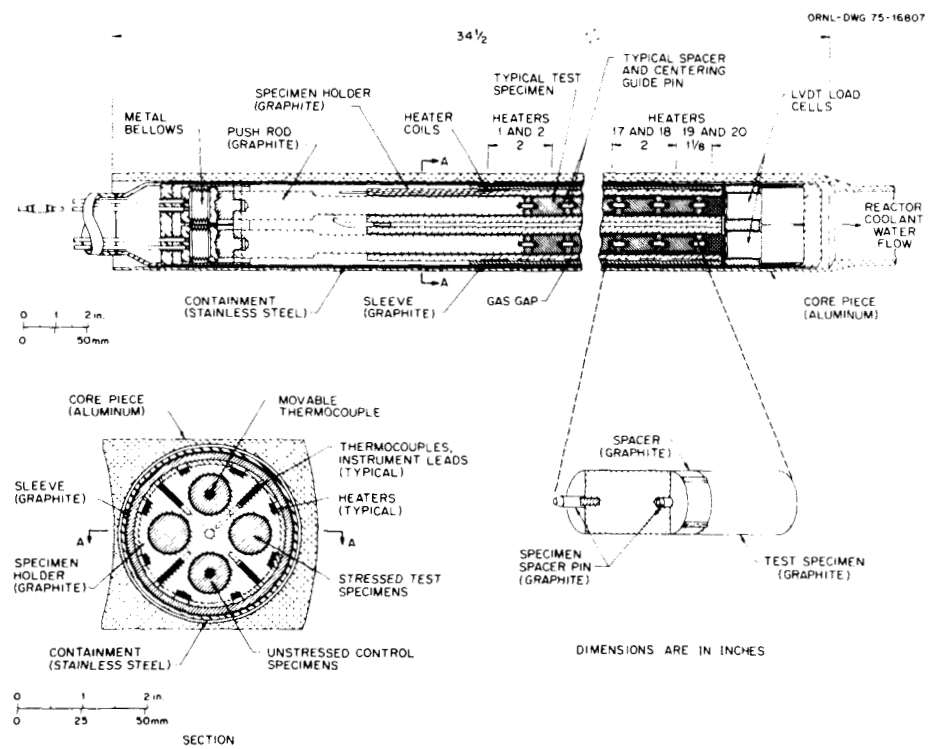

Fig. 7.3. A Cross-Sectional View of the In-Core Portion of the ORR Capsule OC-1 Showing the Stressed Columns. The overall length shown is 0.876 m.

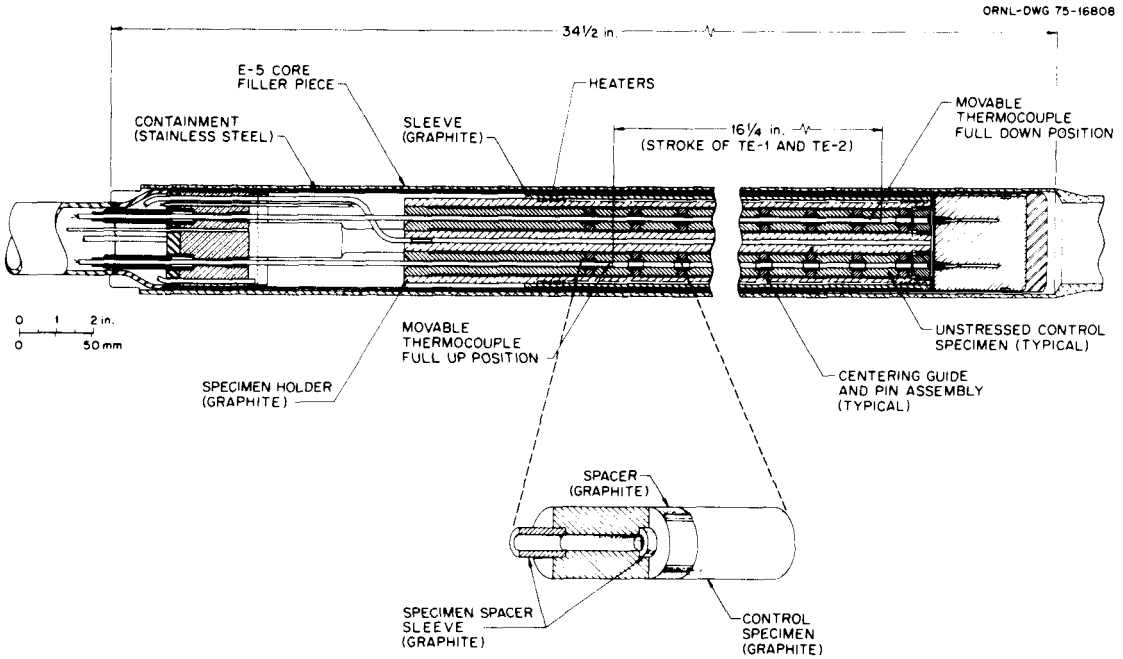

Fig. 7.4. A Cross-Sectional View of the In-Core Portion of the ORR Capsule OC-1 Showing Unstressed Specimen Columns. Length shown is 0.876 m; stroke is 0.413 m.

surfaces. This centering is important to the proper loading and temperature control of the specimens. Each metal bellows, shown at the top of the two specimen columns, will be pressurized with helium gas to 5.89 MPa (854 psig) to provide a load of 2515 N (565.4 lb), which gives the required compressive stress. Force from the bellows is transmitted to the specimen column through a graphite push-rod. At the end of each specimen column, the force is sensed by an LVDT load cell. This device is designed to measure up to 3115 N (700 lb) at 480°C. Although monitoring the pressure in the bellows will be the primary measure of the load being applied to the specimen columns, the LVDT load cell will provide backup information during the early stages of the irradiation and ensure that the force is indeed transmitted through all the specimen column. The load cell is expected to suffer radiation damage and decalibration at exposures exceeding 3×10^{20} n/cm^2 (>0.18 MeV), but it will provide valuable information during the initial stages of capsule operation.

The unstressed control specimen columns are shown in the cross-sectional view in Fig. 7.4. These specimens are stacked and centered in

a manner similar to the stressed specimens, except that a longitudinal hole has been provided to serve as a guide for the 3.2-mm-diam (1/8-in.) stainless-steel-sheathed Chromel vs Alumel movable thermocouple that is installed in each column. These thermocouples can be moved through a 0.413 m (16 1/4 in.) stroke, thus providing temperature traverses from the midplane of the uppermost specimen to the midplane of the lowest specimen in each column. The sheathed thermocouples pass up through the various bulkheads and through a 6.4-mm-diam (1/4-in.) guide tube to the junction box located just above the reactor vessel top flange. This junction box houses the rack-and-pinion assemblies that drive the thermocouples. A rack is attached to the top end of each movable thermocouple. An electrically driven motor drives the rack-and-pinion gear assembly and the attached thermocouple up and down at a rate of 0.83 mm/s (2 in./min). A variable resistor driven by a gear from the rack provides a signal related to the position of the thermocouple. By operation of the motor the thermocouple position can be controlled to less than ±3.2 mm (±1/8 in.) in longitudinal elevation. The thermocouple signal is transmitted to lead wire by means of sliding contacts that move along a gold-plated insulated strip that serves as the conduit from the contacts to the lead wire.

In addition to the two movable thermocouples, twenty-five 1.6-mm-diam (1/16-in.) stainless-steel-sheathed MgO-insulated Chromel vs Alumel thermocouples have been provided to monitor capsule temperatures. Twenty-three of these are located within the graphite specimen holder adjacent to the test specimens at various elevations along the capsule.

As stated previously, one of the important objectives of the experiment is to maintain accurate and precise temperature control along the specimen column. In order to achieve adequate control, the capsule is designed to operate on gamma heat alone approximately 100°C below design temperature. The gamma heat rate in this experiment position in the reactor varies from a low of about 5.4 W/g to a high of about 10 W/g, as shown in Fig. 7.5. A thermal resistance helium-filled gas gap between the specimen holder and the water-cooled capsule vessel is stepped in a manner that provides five different radial gaps.

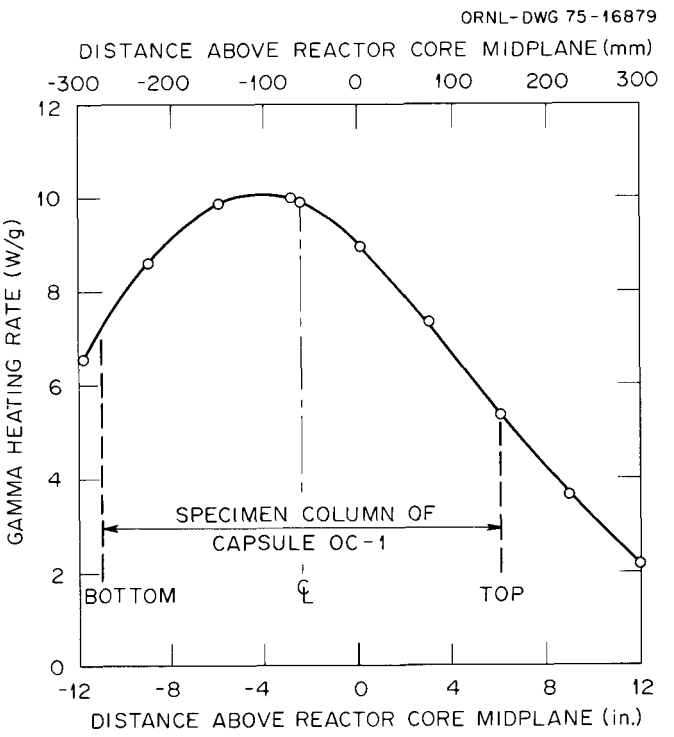

Fig. 7.5. Results of Gamma Heating Measurements Made in the E-5 Core Facility of the ORR on September 19, 1974.

These gaps accommodate the variation in gamma heating rate and establish approximately the desired constant longitudinal temperature level.

Design operating temperature and control of it are acheived by twenty 3.2-mm-diam (1/16 in.) stainless-steel-sheathed MgO-insulated Nichrome V heaters wrapped around the specimen holder as shown in Figs. 7.3 and 7.4. Ten 51-mm-long (2-in.) heated zones, each with two heaters operated in parallel, are positioned along the 0.51 m (20 in.) length of the specimen holder. Each heater is capable of operation at up to 2 kW/linear m (50 W/linear in.); however, they are expected to operate well below this maximum to maintain the design operating temperature of 900°C for the specimens.

Because of the requirement to maintain a ±10°C temperature control* along the specimen column and the intricate interaction of each heater zone with respect to adjacent heater zones, a computer is required to

*This corresponds to a ±3% change in apparent creep coefficient.

control the experiment temperatures automatically. A Digital Equipment Corporation PDP 11/40 computer with the required ancillary equipment was procured to operate the capsule heaters and monitor and record the data from the experiment. Algorithms have been developed to relate the various thermocouple temperatures to the specimen temperatures and thus permit the computer to adjust the heaters to the required operating levels. Ten solid-state heater control devices are used (one for each zone) and operate under computer control as long as the computer is operating. If the signal from the computer is lost, the controller will sense the latest temperature from its control thermocouple and continue to control the heater output to maintain this temperature. Computer control is resumed as soon as it is operating again.

The capsule will be swept with high-purity helium gas to sweep out any contaminants that may be emitted from the graphite holder or specimens. This will minimize the possibility of corrosive attack on the specimens. Only high-purity gas will be used, and this will receive additional purification by being passed through activated molecular seives and a hot titanium sponge cleanup system.

The first capsule in this series, OC-1, is scheduled for insertion into the ORR during January 1976. The design, as described above, was essentially completed, and parts for the first capsules were ordered during this reporting period.

7.4 REFERENCE

1. R. J. Price, *Review of Irradiation-Induced Creep in Graphite Under HTGR Conditions*, GA-A-12332 (Nov. 1, 1972).

GAS-COOLED REACTOR PROGRAMS

DECEMBER 31, 1975

P. R. KASTEN, DIRECTOR CMO
JUNE ZACHARY, SECY. CMO
J. H. COOBS,* ASSOC. DIR. M&C
DARLENE KECK, SECY. M&C
A. L. LOTTS,* ASSOC. DIR. M&C
PATRICIA VILES, SECY. M&C

DIVISION MANAGERS AND COORDINATORS
J. P. CALLAHAN* R
F. R. MYNATT NP
D. A. COSTANZO* AC
A. L. LOTTS* M&C
R. E. MacPHERSON R
A. P. MALINAUSKAS* CT
K. J. NOTZ* CT
I. SPIEWAK R

THORIUM UTILIZATION PROGRAM
A. L. LOTTS,* MGR. M&C

REPROCESSING
K. J. NOTZ,* MGR. CT
MILDRED PAYNE, SECY. CT

REPROCESSING DEVELOPMENT (110)
K. J. NOTZ,* PROJ. LDR. CT

GENERAL DEVELOPMENT
K. J. NOTZ* CT

HEAD-END PROCESSING
V. C. A. VAUGHEN* CT
C. L. FITZGERALD CT
E. E. McCOMBS CT
J. H. SHAFFER* CT
D. J. KINGTON CT
R. J. SHANNON* CT

SOLVENT EXTRACTION PROCESSING
R. H. RAINEY* CT
R. J. SHANNON* CT

OFF-GAS CLEANUP
A. D. RYON CT
R. D. ACKLEY CT
R. E. BARKER CT
J. T. BELL* C
C. W. FORSBERG CT
D. W. FULLER* C
T. M. GILLIAM CT
R. W. GLASS CT
L. M. TOTH* C
W. M. WOOD CT
V. L. FOWLER CT
D. J. INMAN CT

PRODUCT PREPARATION
J. W. SNIDER* CT

WASTE TREATMENT & DISPOSAL
K. H. LIN*
D. W. HOLLADAY CT

REPROCESSING HOT ENGINEERING TESTS (120)
K. J. NOTZ,* PROJ. LDR. CT

OPERATIONS PLANNING
J. W. SNIDER* CT
W. L. CARTER CT
K. H. LIN* CT
D. C. WATKIN CT

REFABRICATION HOT ENGINEERING TESTS (220)
J. D. SEASE,* PROJ. LDR. M&C

OPERATIONS PLANNING
A. R. OLSEN* M&C
J. E. VAN CLEVE M&C

REFABRICATION
J. D. SEASE,* MGR. M&C
RHONDA CASTLEBERRY, SECY. M&C

REFABRICATION PROCESS DEVELOPMENT (210)
J. D. SEASE,* PROJ. LDR. M&C

URANIUM FEED PREPARATION
F. E. HARRINGTON* CT

RESIN LOADING
K. J. NOTZ* CT
P. A. HAAS CT
C. D. BOPP* CT
J. P. DRAGO CT
D. L. MILLION CT
J. H. SHAFFER* CT
R. D. ARTHUR CT
T. V. DINSMORE CT
C. W. GREEN CT
C. F. KECK CT
W. E. SHOCKLEY CT

RESIN CARBONIZATION
W. J. LACKEY* M&C
B. J. BOLFING* I&C
J. A. CARPENTER M&C
W. R. HAMEL* I&C
J. E. MACK* M&C
D. P. STINTON M&C
W. M. BRADLEY M&C
J. B. FLYNN M&C
C. L. GARRISON* M&C
D. R. MILLER I&C

MICROSPHERE COATING
W. J. LACKEY* M&C
B. O. BARRINGER* I&C
B. J. BOLFING* I&C
D. A. COSTANZO* AC
J. I. FEDERER M&C
W. R. HAMEL I&C
D. P. STINTON* M&C
R. R. SUCHOMEL M&C
G. W. WEBER* M&C
C. E. DeVORE M&C
C. L. GARRISON* M&C
D. E. LaVALLE* AC
D. R. MILLER* I&C

FUEL ROD FABRICATION
D. R. JOHNSON* M&C
P. ANGELINI M&C
S. P. BAKER I&C
M. M. CHILES* I&C
R. W. KNOLL* R
S. R. McNEANY* R
J. E. RUSHTON R
S. W. COOK M&C
A. G. MASON M&C
D. R. MILLER* I&C
W. B. STINES* M&C

FUEL ELEMENT ASSEMBLY
D. R. JOHNSON* M&C
B. O. BARRINGER* I&C
A. J. CAPUTO M&C
H. E. COCHRAN I&C
J. G. GRUNDMANN* I&C
W. R. HAMEL* I&C
J. C. McLAUGHLIN M&C
D. R. MILLER I&C
W. B. STINES* M&C

RECYCLE FUEL IRRADIATIONS AND EXAMINATIONS (230)
F. J. HOMAN,* PROJ. LDR. M&C

PEACH BOTTOM IRRADIATION TESTS
T. N. TIEGS* M&C

LARGE SCALE IRRADIATION TESTS
E. L. LONG, JR.* M&C

PROGRAM MANAGEMENT AND ANALYSIS (310)
W. H. PECHIN, PROJ. LDR. M&C

PROGRAM PLANNING AND CONTROL
W. H. PECHIN* M&C
R. K. KIBBE* GAC
T. F. SCANLAN* M&C

PROGRAM ANALYSIS
J. D. JENKINS* R
M. S. JUDD* M&C
S. V. KAYE ES
J. W. SNIDER* CT
W. E. THOMAS R
M. L. TOBIAS R

HTGR FUEL RECYCLE DEMONSTRATION FACILITY (320)
(VACANT), PROJ. LDR.

REFABRICATION PROCESS ASSOCIATED DEVELOPMENT (210)
J. D. SEASE,* PROJ. LDR. M&C

GENERAL DEVELOPMENT
A. R. OLSEN* M&C
R. A. BRADLEY* M&C
S. R. McNEANY* R
H. R. LIVESEY M&C

SAMPLE INSPECTION
W. H. PECHIN* M&C
D. A. COSTANZO* AC
J. E. MACK* M&C
J. L. BOTTS* AC
M. S. HENDRICKS* M&C
D. E. LaVALLE* AC
L. J. TURNER M&C

PLANT MANAGEMENT
W. R. HAMEL* I&C
B. O. BARRINGER* I&C
B. J. BOLFING* I&C
R. A. BRADLEY† M&C
B. C. DUGGINS* I&C

WASTE HANDLING
J. D. JENKINS* R
M. E. GALYON* I&C
M. S. JUDD M&C
J. E. VAN CLEVE M&C
M. S. HENDRICKS* M&C

MATERIAL HANDLING
W. R. HAMEL* I&C
R. A. BRADLEY† M&C
J. G. GRUNDMANN* I&C
R. C. MULLER* I&C

RECYCLE FACILITIES & EQUIPMENT PROJECT ENGINEERING
D. P. REID,* PROJ. ENGR. E
C. C. HAWS,* ASSOC. PROJ. ENGR. CT
J. P. JARVIS, ASSOC. PROJ. ENGR. E
T. F. SCANLAN*, QA MGR. M&C

HOT ENGINEERING TEST FACILITY
D. P. REID,* PROJ. ENGR. E
P. E. STEIN,* PRINCIPAL ENGR. E
R. BLUMBERG* R
S. E. HAMBLEN E
J. D. HUGGIN E
O. A. KELLY E
C. S. MEADORS* E

REPROCESSING HOT ENGINEERING TEST EQUIPMENT (120)
C. C. HAWS,* PROJ. ENGR. CT
F. E. HARRINGTON,* PRINCIPAL ENGR. CT
R. BLUMBERG* R
L. C. HENSLEY* E
J. R. HORTON* E
M. V. KEIGAN* E
C. S. MEADORS* E
P. E. STEIN* E

REFABRICATION HOT ENGINEERING TEST EQUIPMENT (220)
D. P. REID,* PROJ. ENGR. E
L. C. HENSLEY,* PRINCIPAL ENGR. E
R. BLUMBERG* R
F. E. HARRINGTON* CT
J. L. HECK* E
M. V. KEIGAN* E
C. S. MEADORS* E
P. E. STEIN* E

REFABRICATION DEVELOPMENT TEST EQUIPMENT (210)
D. P. REID,* PROJ. ENGR. E
F. C. DAVIS, PRINCIPAL ENGR. E
J. R. HORTON,* PRINCIPAL ENGR. E
R. J. BRAATZ* E
J. E. BREWER E
W. G. COBB E
R. M. DeLOZIER E
J. L. HECK* E
G. M. LAWSON E
M. K. PRESTON E

REPROCESSING DEVELOPMENT TEST EQUIPMENT (110)
C. C. HAWS, PROJ. ENGR. CT
J. R. HORTON,* PRINCIPAL ENGR. E
R. J. BRAATZ* E
P. E. STEIN* E

HTGR FUEL RECYCLE DEMONSTRATION FACILITY (320)
C. C. HAWS,* PROJ. ENGR. CT
L. C. HENSLEY,* PRIN. MECH. ENGR. E
F. E. HARRINGTON,* PRIN. PROC. ENGR. CT

HTGR BASE PROGRAM
J. H. COOBS,* MGR. M&C

PCRV DEVELOPMENT
J. P. CALLAHAN* R
D. A. CANONICO M&C
W. G. DODGE R
R. K. NANSTAD M&C
M. N. RAFTENBERG* R
J. E. SMITH* R
C. C. HURTT R

ASSESSMENT AND EVALUATION STUDIES
L. L. BENNETT R

HTGR STRUCTURAL MATERIALS STUDIES
J. R. DISTEFANO* M&C
W. R. CORWIN* M&C
J. C. GRIESS* M&C
A. A. LYSTRUP*** M&C
J. P. STRIZAK* M&C
E. BOLLING M&C
S. W. CHAPMAN Y-12
L. K. EGNER M&C
E. H. LEE M&C
E. B. PATTON M&C
C. A. REEVES Y-12

HTGR CHEMISTRY STUDIES
A. P. MALINAUSKAS* CT

FISSION PRODUCT TECHNOLOGY
M. T. MORGAN CT
R. L. TOWNS CT
R. B. EVANS* CT
R. P. WICHNER* CT
L. C. BATE** AC
F. F. DYER** AC
R. J. KEDL* R
W. J. MARTIN CT
L. L. FAIRCHILD CT

IRRADIATED FUEL CHEMISTRY
T. B. LINDEMER* CT
R. L. PEARSON CT

COOLANT CHEMISTRY
A. P. MALINAUSKAS* CT
G. L. TINGEY§ BPNL
T. C. TUCKER* CS

ANALYTICAL CHEMISTRY STUDIES
D. A. COSTANZO* AC
J. L. BOTTS* AC
D. E. LaVALLE* AC
F. L. LAYTON AC
D. A. LEE AC
M. E. PRUITT AC
W. F. ROGERS AC
A. J. WEINBERGER AC

SPECIAL ASSIGNMENT
R. A. BRADLEY† M&C
P. L. RITTENHOUSE†† M&C

HTGR WELDMENTS
J. R. DISTEFANO* M&C
J. F. KING* M&C

CHARACTERIZATION AND STANDARDIZATION OF GRAPHITE
W. P. EATHERLY* M&C
J. A. CONLIN* R
W. H. COOK* M&C
R. L. SENN R

FUELED GRAPHITE DEVELOPMENT
F. J. HOMAN* M&C

FABRICATION AND CHARACTERIZATION
W. P. EATHERLY* M&C
R. L. BEATTY M&C
J. I. FEDERER* M&C
R. L. HAMNER M&C
C. S. MORGAN M&C
J. M. ROBBINS M&C
G. W. WEBER* M&C
B. R. CHILCOAT M&C
J. W. GEER M&C
C. HAMBY, JR. M&C
H. KEATING M&C
W. W. PROAPS M&C
D. E. ROSSON M&C

IRRADIATION TESTING
J. A. CONLIN* R
R. L. SHEPARD* I&C
K. R. THOMS R
R. M. FLANDERS R
C. R. HYMAN R
B. H. MONTGOMERY R
L. J. SHERSKY R
J. R. SHUGART R
C. A. WALLACE R

NUCLEAR ANALYSIS
H. T. KERR R
E. J. ALLEN R
R. W. KNOLL* R

POSTIRRADIATION EXAMINATION AND EVALUATION
F. J. HOMAN* M&C
M. J. KANIA* M&C
E. L. LONG, JR.* M&C
T. N. TIEGS* M&C
K. H. VALENTINE I&C
E. L. RYAN M&C

HTGR SAFETY PROGRAM

HTGR SAFETY STUDIES FOR ERDA
T. E. COLE, MGR. R
SUE BEGLEY,* SECY. R

SYSTEMS AND SAFETY ANALYSIS
DUNLAP SCOTT, JR. R
S. J. BALL* I&C
O. W. BURKE* I&C
J. C. CLEVELAND* R
J. C. CONKLIN R
I. T. DUDLEY R
J. B. FUSSELL§ UT
R. C. GWALTNEY R

FISSION PRODUCT TECHNOLOGY
E. L. COMPERE* CT

PRIMARY COOLANT TECHNOLOGY
R. P. WICHNER* CT
R. J. KEDL* R

CONFINEMENT COMPONENTS
J. P. CALLAHAN* R
E. G. BURDETTE§ UT
D. N. FANNING R
D. W. GOODPASTURE§ UT
M. N. RAFTENBERG* R

PRIMARY SYSTEM MATERIALS TECHNOLOGY
J. R. DISTEFANO* M&C
R. G. DONNELLY* M&C
W. P. EATHERLY* M&C

SAFETY INSTRUMENTATION
J. L. ANDERSON* I&C
R. E. BATTLE* I&C
M. J. ROBERTS* I&C

HTGR SAFETY STUDIES FOR NRC
J. P. SANDERS,* MGR. R
SUE BEGLEY,* SECY. R

HTGR SAFETY STUDIES FOR DSS THERMAL ANALYSIS
W. D. TURNER* CS
B. R. BECKER* CS

TRANSIENT SYSTEM RESPONSE
K. W. CHILDS* CS
R. M. DEVAULT* CS
G. E. GILES, JR.* CS

COMPONENT ANALYSIS
D. D. PAUL* R

HTGR SAFETY STUDIES FOR RSR
S. J. BALL,* CODRO. I&C

CODE IMPLEMENTATION AND EVALUATION
J. P. SANDERS* R
D. D. PAUL* R

SYSTEMS DYNAMICS AND SAFETY ANALYSIS
S. J. BALL* I&C
N. E. CLAPP, JR.* I&C
J. C. CLEVELAND* R
T. W. KERLIN§ UT

GCFR PROGRAM
URI GAT, MGR. R
PEGGY McNUTT, SECY. R

PRESSURE VESSELS AND CLOSURES
J. P. CALLAHAN* R
M. N. RAFTENBERG* R
G. C. ROBINSON* R

FUEL IRRADIATION
J. A. CONLIN* R
A. W. LONGEST R
R. M. FLANDERS* R
L. J. SHERSKY* R

CORE FLOW TEST LOOP
A. G. GRINDELL R
D. L. GRAY* E
J. T. HAN* R
P. G. HERNDON* I&C
T. L. HUDSON* E
R. W. McCULLOCH* R
H. J. METZ* I&C
M. J. ROBERTS* I&C
H. C. YOUNG* R

SHIELDING STUDIES
D. E. BARTINE* NP
C. O. SLATER NP

* PART TIME/DUAL CAPACITY
** ON LOAN
*** GUEST SCIENTIST-DANISH AEC
\# ASSIGNED FROM GAC
† ON ASSIGNMENT TO KFA, JULICH, WEST GERMANY
†† ON ASSIGNMENT TO OECD DRAGON PROJECT, AEE WINFRITH, ENGLAND
§ SUBCONTRACT
AC ANALYTICAL CHEMISTRY DIVISION
C CHEMISTRY DIVISION
CMO CENTRAL MANAGEMENT OFFICE
CS COMPUTER SCIENCES DIVISION
CT CHEMICAL TECHNOLOGY DIVISION
E UCC-ND ENGINEERING
I&C INSTRUMENTATION AND CONTROLS DIVISION
M&C METALS AND CERAMICS DIVISION
NP NEUTRON PHYSICS DIVISION
R REACTOR DIVISION
ES ENVIRONMENTAL SCIENCES DIVISION

ORNL-5108
Distribution
Category UC-77

INTERNAL DISTRIBUTION

1–2. Central Research Library
3. Document Reference Section
4–5. Laboratory Records Department
6. Laboratory Records, ORNL RC
7. ORNL Patent Office
8. E. J. Allen
9. R. L. Beatty
10. R. A. Bradley
11. K. B. Brown
12. C. R. Brinkman
13. J. P. Callahan
14. D. A. Canonico
15. J. A. Carpenter
16. J. A. Conlin
17–21. J. H. Coobs
22. W. R. Corwin
23. D. A. Costanzo
24. F. L. Culler
25. F. C. Davis
26. J. R. DiStefano
27. W. G. Dodge
28. R. G. Donnelly
29. F. F. Dyer
30. W. P. Eatherly
31. R. B. Evans III
32. D. N. Fanning
33. G. G. Fee
34. D. E. Ferguson
35. Uri Gat
36. J. C. Griess
37. P. A. Haas
38. R. L. Hamner
39–40. M. R. Hill
41. F. J. Homan
42. J. D. Jenkins
43. D. R. Johnson
44. M. J. Kania
45–53. P. R. Kasten
54. C. R. Kennedy
55. H. T. Kerr
56. R. K. Kibbe
57. J. F. King
58. W. J. Lackey
59. K. H. Lin
60. T. B. Lindemer
61. E. L. Long, Jr.
62. A. L. Lotts
63. A. P. Malinauskas
64. W. R. Martin
65. D. L. McElroy
66. J. P. Moore
67. C. S. Morgan
68. M. T. Morgan
69. R. K. Nanstad
70. D. J. Naus
71. F. H. Neill
72. K. J. Notz
73. C. B. Oland
74. A. R. Olsen
75. R. L. Pearson
76. W. H. Pechin
77. S. Peterson
78. H. Postma
79. J M Robbins
80. G. C. Robinson
81. J. P. Sanders
82. Dunlap Scott
83. R. L. Senn
84. J. H. Shaffer
85. R. L. Shepard
86. G. M. Slaughter
87. D. P. Stinton
88. J. P. Strizak
89. K. R. Thoms
90. T. N. Tiegs
91. D. B. Trauger
92. V.C.A. Vaughen
93. J. R. Weir
94. G. D. Whitman
95. R. P. Wichner
96. R. G. Wymer

EXTERNAL DISTRIBUTION

97—104. ERDA DIVISION OF NUCLEAR FUEL CYCLE AND PRODUCTION, Washington, DC 20545

Director (2)
R. G. Bradley (1)
W. S. Schieb (5)

105—106. ERDA DIVISION OF REACTOR NUCLEAR RESEARCH AND APPLICATIONS, Washington, DC 20545

Director

107—108. ERDA IDAHO OPERATIONS OFFICE, P.O. Box 2108, Idaho Falls, ID 83401

C. E. Williams, Manager
Barry Smith

109. ERDA OFFICE OF PROGRAM MANAGEMENT, RESEARCH AND SPACE PROGRAMS, P.O. Box 81325, San Diego, CA 92138

J. B. Radcliffe

110. ERDA SAN FRANCISCO OPERATIONS OFFICE, 1333 Broadway, Wells Fargo Building, Oakland, CA 94612

R. D. Thorne, Manager

111—113. ERDA OAK RIDGE OPERATIONS OFFICE, P.O. Box E, Oak Ridge, TN 37830

Director, Reseach and Technical Support Division
Director, Reactor Division
F. E. Dearing, Reactor Division

114—284. ERDA TECHNICAL INFORMATION CENTER, P.O. Box 62, Oak Ridge, TN 37830

For distribution as shown in TID-4500 Distribution Category, UC-77 (Gas-Cooled Reactor Technology)

☆ U.S. GOVERNMENT PRINTING OFFICE: 1976-748-189/41